Structure in the Milky Way

Trey Vaughn Wenger
Fort Wayne, Indiana

B.A. Astronomy and Physics, Boston University, 2009
M.S. Astronomy, University of Virginia, 2015

A Dissertation Presented to the
Graduate Faculty of the

University of Virginia

in Candidacy for the Degree of

Doctor of Philosophy

Department of Astronomy

University of Virginia
May 2019

Committee Members:
Dana S. Balser
Nitya J. Kallivayalil
Steven R. Majewski
Maïté Brandt-Pearce
Alberto D. Bolatto

© Copyright by
Trey Vaughn Wenger
All rights reserved
May 19, 2019

Abstract

The structure of the Milky Way is a constraint on theories of Galactic formation and evolution. H II regions, the zones of ionized gas surrounding recently formed high-mass stars, are important tracers of structure in both the Milky Way and other galaxies. Using the most complete sample of these Galactic high-mass star forming regions (HMSFRs) to date, we investigate the morphological and chemical structures in the Milky Way disk.

Mapping Galactic structure with HMSFRs requires accurate distances to these tracers. Unfortunately, only kinematic distances are available for most of the HMSFRs in the Galaxy. We develop a novel Monte Carlo kinematic distance method and compare the kinematic distances and parallax distances of 75 Galactic HMSFRs. The Monte Carlo method gives more accurate kinematic distances than those derived using traditional methods. The median difference between the Monte Carlo kinematic distances and parallax distances is 17% (0.42 kpc). We find that, for a large portion of the Galaxy, the kinematic distance uncertainty is up to 10 times smaller than the parallax distance uncertainty.

The census of Galactic H II regions is vastly incomplete in the southern sky. The Southern H II Region Discovery Survey (SHRDS) is completing this census by identifying new H II regions from their radio recombination line (RRL) emission. We use the Australia Telescope Compact Array to measure 4–10 GHz radio continuum and hydrogen RRL emission from H II region candidate targets. Thus far, the SHRDS has discovered 295 heretofore unknown Galactic H II regions. This increases the number of known nebulae in the surveyed zone by 82% to 568. Upon the completion of the SHRDS, we will have a catalog of all Galactic H II regions ionized by at least one O-type star.

The metallicity structure of the Milky Way disk stems from the chemodynamical

evolutionary history of the Galaxy. We use the National Radio Astronomy Observatory Karl G. Jansky Very Large Array to measure the RRL-to-continuum brightness ratios of 82 Galactic H II regions. We then derive the electron temperatures and metallicities for these nebulae. Since collisionally excited lines from metals (e.g., oxygen) are the dominant cooling mechanism in H II regions, the nebular metallicity can be inferred from the electron temperature. Including previous single dish studies, there are now 167 nebulae with accurate electron temperature and distance determinations. We find an oxygen abundance gradient across the Milky Way disk with a slope of $0.052^{+0.004}_{-0.003}$ dex kpc^{-1}. We also find azimuthal structure in the metallicity distribution. The slope of the gradient varies by a factor of $\sim$2 with Galactocentric azimuth. This azimuthal structure is consistent with simulations of Galactic chemodynamical evolution influenced by spiral arms.

Finally, we explore the spiral structure of the Milky Way by constructing a simple morphological model and using it to constrain the spiral structure of the Galaxy. The model posits the neutral gas, molecular gas, and HMSFR distributions and includes parametrizations of the kinematics of the Galactic disk, the morphology of the spiral arms, and the warp of the Galactic plane. We compare the modeled emission with observations in a novel way. We use a Bayesian Markov Chain Monte Carlo analysis to estimate the optimal model parameters that reproduce the observed Galactic longitude, latitude, and velocity distributions of H I 21 cm hyperfine emission, ^{12}CO ($J = 1 \rightarrow 0$) emission, and the number of H II regions. This is an ongoing study. Our analysis is able to recover the correct model parameters for simulated datasets, but it fails to reproduce the observed gas and HMSFR distributions. We identify degeneracies between parameters as the likely cause and assess the future capabilities of our model.

Acknowledgements

I am grateful for the countless people who have inspired, supported, and encouraged me throughout my life, especially during the past several years. The road to this dissertation was long (22 years of school!), exciting, stressful, enlightening, and, at times, overwhelming. I have finally reached my goal because of the people who believed in me. Below, I name some of the people who helped me along the way. These lists are by no means exhaustive, and I apologize to those whom I have forgotten.

The University of Virginia Department of Astronomy and the National Radio Astronomy Observatory have been welcoming places to study and work over the past six years. I thank the friendly staff and faculty at UVA and NRAO, including Aaron E., Amanda K., Brett M., Brian M., Charlie T., Connie R., Craig S., Ed M., Fred S., Jackie H., Jeff M., Jim B., Jim C., Kelsey J., Ken K., Nitya K., Remy I., Scott R., Steve M., Tony R., Tracy H., and Whitney R., who were always eager to offer their guidance, advice, and stimulating conversation. I also appreciate the time, consideration, and comprehensive feedback that my dissertation committee gave to this work.

My fellow graduate students provided much needed support during my tenure at UVA. I am happy to have made new and long-lasting friendships with many of them, including Allison M., Andrew B., Bill D., Cameron C., Chris I., Dominique M., George P., Guillermo D., Jake B., John A., Kim S., Kristen J., Lauren B., Loreto B., Matt P., Patrick K., Rachael B., Robert W., Sandy L., Scott S., Sean L., Thankful C., and Tim P. I take with me many memories of late nights studying in the big grad office, darts and karaoke at Dürty Nelly's, adventures under the stars in the southwest, conversations around a camp fire, praising Carl in the woods of rural Virginia, dancing the night away at Escafé, and much more. I thank them for these memories and the support network they provided throughout my time in graduate

school.

I was fortunate to be involved with several communities in Charlottesville, including the Jefferson Scholars Foundation, the Raven Society, and *Dark Skies, Bright Kids*. Through these and other groups, I met some amazing people, including Adam F., Ben S., Ben V., Bill W., Devin G., Drew S., Evan W., Karen T., Katie C., Kay N., LeighAnn L., Molly K., Riley H., Sandy G., Sean M, Theresa C, and Wayne C. I thank them for the kindness and friendship they shared with me.

My interests in science, mathematics, astronomy, and physics were inspired by my teachers in grade school, especially Janet Braun, my AP Physics teacher, and BJ "Starlady" Harper, the planetarium director and astronomy teacher at Northrop High School. My skills were fostered by numerous mentors, including Teresea Brainerd, who was brave enough to give me my first professional research project; Quinn Sykes and Jeff Sanborn, who taught me more "practical" skills; Tapasi Ghosh and Chris Salter, who introduced me to the thrills of radio astronomy; Tom Bania, who taught me the joys of H II regions, Emacs, and LaTeX; and, of course, Dana Balser. Dana was a patient and inspiring advisor who supported me and all of the crazy ideas and Monte Carlo analyses in this dissertation.

Finally, I thank my family, who encouraged me to reach my full personal and academic potential. Some of my earliest memories are of my Mama teaching me about math, science, and how to tell time. These experiences, without a doubt, laid the foundation for my academic career. My parents, Koral and Scott, my grandparents, Mama, Pawpaw, Sheri, Steve, and Suzy, and our many family friends have always supported me, and for that I am forever grateful.

Trey V. Wenger
Charlottesville, VA

Table of Contents

Abstract **iii**

Acknowledgements **v**

List of Figures **xiii**

List of Tables **xv**

1 Introduction **1**
1.1 The Milky Way 1
1.2 H II Regions 3
1.3 Contributions 4

2 Brief History of Galactic Structure **7**
2.1 17th Century 7
2.2 18th Century 7
2.3 19th Century 8
2.4 20th Century 10

3 Kinematic Distances: A Monte Carlo Method **19**
3.1 Introduction 19
3.2 Sample Selection 21
3.3 Parallax Distances 22
3.4 Kinematic Distances 28
3.4.1 Method A: Traditional Method, Brand & Blitz (1993) GRM . 32
3.4.2 Method B: Updated Solar Motion Parameters, Reid et al. (2014) GRM 34
3.4.3 Method C: Monte Carlo Method, Reid et al. (2014) GRM . . 36
3.5 Kinematic Distance Uncertainty 37
3.6 Kinematic Distance Ambiguity (KDA) 50
3.7 Discussion 52
3.8 Conclusions 59

4 The Southern H II Region Discovery Survey **65**
4.1 Introduction . . . 65
4.2 Target Sample . . . 67
4.3 Observations . . . 70
4.4 Data Reduction and Analysis . . . 101
4.4.1 Calibration . . . 101
4.4.2 Imaging . . . 104
4.4.3 Continuum Data Products . . . 105
4.4.4 RRL Data Products . . . 105
4.5 SHRDS: The Bright Catalog . . . 106
4.5.1 Continuum Catalog . . . 107
4.5.2 Radio Recombination Line Catalog . . . 108
4.6 Properties of Bright Catalog Nebulae . . . 140
4.6.1 Survey Completeness . . . 174
4.7 Summary and Future Work . . . 178

5 Metallicity Structure in the Milky Way Disk **181**
5.1 Introduction . . . 181
5.2 Target Sample . . . 183
5.3 Observations and Data Reduction . . . 185
5.3.1 Calibration . . . 193
5.3.2 Imaging . . . 195
5.4 Data Reduction and Analysis . . . 195
5.5 Results . . . 198
5.5.1 VLA Data Products . . . 198
5.5.2 Electron Temperatures . . . 204
5.5.3 Comparison with Single Dish . . . 209
5.5.4 Distances . . . 221
5.5.5 Electron Temperature and Metallicity Structure . . . 225
5.6 Discussion . . . 232
5.7 Summary and Future Work . . . 241

6 Galactic Morphological Structure **245**
6.1 Introduction . . . 245
6.2 Structure Tracers . . . 247
6.2.1 Neutral Gas . . . 247
6.2.2 Molecular Gas . . . 248
6.2.3 H II Regions . . . 250
6.3 Model . . . 252
6.3.1 Solar Galactocentric Radius . . . 256
6.3.2 Kinematics . . . 256
6.3.3 Warm Neutral Medium (WNM) . . . 257

6.3.4 Cold Neutral Medium (CNM) and Spiral Arms 259
6.3.5 Molecular Gas 262
6.3.6 H II Regions 265
6.3.7 Galactic Warp 265
6.4 Radiative Transfer 267
6.5 Results 272
6.6 Discussion 278
6.6.1 Model A 278
6.6.2 Model B 282
6.6.3 Model C 282
6.6.4 Model D 289
6.6.5 Model E 289
6.7 Summary and Future Work 289

7 Conclusions 295

Appendix A Galactocentric Position Uncertainty Derivations 299

Appendix B WISP: A General Radio Interferometry Data Reduction Package 303
B.1 Calibration 305
B.2 Imaging 306

Appendix C SHRDS Bright Catalog: Multiple Detections 311

Appendix D Electron Temperature Derivations 335
D.1 Single Dish Observations 338
D.2 Averaging Single Dish RRLs 340
D.3 Interferometric Observations 348
D.4 Averaging Interferometric RRLs 348

Appendix E Logarithmic Spiral Derivations 351

References 355

Biographical Sketch 369

Curriculum Vitae 373

List of Figures

1.1 The Milky Way 2

2.1 Herschel's Map of the Galaxy 9
2.2 Proctor's Spiral Model of the Galaxy 11
2.3 Easton's Spiral Model of the Galaxy 12
2.4 Conflict Between Shapley's and Kapteyn's Milky Way 14

3.1 Parallax probability distribution function example 23
3.2 Representative parallax distance probability distribution functions . . 29
3.3 Difference between Equation 3.1 and Monte Carlo parallax distances . 30
3.4 Schematic of the kinematic distance technique 31
3.5 Anderson et al. (2012) kinematic distance uncertainty model 33
3.6 Reid et al. (2014) universal rotation curve 38
3.7 Monte Carlo kinematic distance probability distribution functions . . 39
3.8 Monte Carlo kinematic distance uncertainties 40
3.9 Difference between parallax distances and Method A kinematic distances 42
3.10 Difference between parallax distances and Method B kinematic distances 48
3.11 Difference between parallax distances and Method C kinematic distances 49
3.12 Difference between radio recombination line and maser or molecular line velocity 53
3.13 Difference between radio recombination line and maser velocity Method C kinematic distances 54
3.14 Difference between Method A, B, and C kinematic distances along $\ell = 30°$ 57
3.15 Ratio of Method C to Anderson et al. (2012) kinematic distance uncertainty along $\ell = 30°$ 58
3.16 Face-on Galactic view of typical parallax distance uncertainty 60
3.17 Ratio of Method C to typical parallax distance uncertainty along $\ell = 30°$ 61
3.18 Face-on Galactic view of typical parallax distance uncertainties in Galactocentric coordinates 62
3.19 Face-on Galactic view of Monte Carlo kinematic distance uncertainties in Galactocentric coordinates 63

4.1 *WISE* infrared image of typical H II region 69
4.2 Positions of SHRDS targets 71
4.3 Typical SHRDS *uv*-coverage 102
4.4 Representative SHRDS continuum images 109
4.5 Representative SHRDS RRL spectra 141
4.6 Differences between SHRDS and previously measured RRL velocities and widths 142
4.7 Distribution of RRL line widths 171
4.8 Longitude-velocity diagram of all known H II regions 172
4.9 Longitude-velocity diagram of fourth quadrant H II regions 173
4.10 Distribution of SHRDS continuum flux densities 175
4.11 Distribution of SHRDS RRL flux densities 176
4.12 Difference between predicted and measured continuum flux densities . 177

5.1 Galactocentric positions and Milky Way disk coverage of the VLA survey H II regions 186
5.2 Watershed Segmentation Regions 197
5.3 Example VLA RRL spectra 203
5.4 Comparison between single dish and VLA RRL parameters 218
5.5 Comparison between single dish and VLA RRL-to-continuum brightness ratios and electron temperatures 219
5.6 Monte Carlo Parallax Distance Example 222
5.7 Monte Carlo Kinematic Distance Example 224
5.8 Nominal Radial Electron Temperature and Metallicity Gradients . . . 226
5.9 Most Likely Radial Electron Temperature Gradient 228
5.10 Most Likely Radial Metallicity Gradient 229
5.11 Nominal Kriging Map of Nebular Electron Temperatures 230
5.12 Nominal Kriging Map of Nebular Metallicities 231
5.13 Most Likely Kriging Map of Nebular Electron Temperatures 233
5.14 Most Likely Kriging Map of Nebular Metallicities 234
5.15 Nominal Azimuthal Variations in the Electron Temperature and Metallicity Gradient 238
5.16 Most Likely Azimuthal Variations in the Electron Temperature and Metallicity Gradient 239
5.17 Uncertainties in Azimuthal Variations in the Metallicity Gradient . . 240
5.18 Kriging Map residuals 242

6.1 HI4PI ℓ-$V_{\rm LSR}$ Diagram 249
6.2 Dame et al. (2001) ^{12}CO ℓ-$V_{\rm LSR}$ Diagram 251
6.3 *WISE* Catalog H II Region ℓ-$V_{\rm LSR}$ Diagram 253
6.4 Initial Model WNM Parameters 258
6.5 Initial Model Midplane CNM Density 261

6.6 Initial Model Total H I Surface Density 263
6.7 Initial Model ^{12}CO Distribution 264
6.8 Initial Model H II Region Distribution 266
6.9 Initial Model Galactic Warp 268
6.10 Initial Model H I ℓ-$V_{\rm LSR}$ Diagram 273
6.11 Initial Model ^{12}CO ℓ-$V_{\rm LSR}$ Diagram 274
6.12 Initial Model H II Region ℓ-$V_{\rm LSR}$ Diagram 275
6.13 Model A Parameter Subset 283
6.14 Model A Parameter Covariances 284
6.15 Model B Parameter Subset 285
6.16 Model B Parameter Covariances 286
6.17 Model C Parameter Subset 287
6.18 Model C Parameter Covariances 288
6.19 Model D Parameter Subset 290
6.20 Model D Parameter Covariances 291
6.21 Model E Parameter Subset 292
6.22 Model E Parameter Covariances 293

A.1 Relationship between the uncertainty in distance to the uncertainty in Galactocentric position 302

B.1 WISP Calibration Pipeline 307
B.2 WISP imaging pipeline 307
B.3 ATCA primary beam profile 309

E.1 Minimum distance to logarithmic spirals 354

List of Tables

3.1 High-mass Star Forming Region Sample 24
3.2 Universal Rotation Curve Parameters from Reid et al. (2014) 35
3.3 Monte Carlo Parallax and Derived Kinematic Distances 43
3.4 Distance Difference Statistics 51

4.1 Bright Catalog Fields and Targets 72
4.2 Observation Summary 99
4.3 Correlator Setup 103
4.4 Non-tapered Image Continuum Properties 110
4.5 *uv*-tapered Image Continuum Properties 126
4.6 Non-tapered Image RRL Properties 143
4.7 *uv*-tapered Image RRL Properties 157

5.1 VLA Electron Temperature Survey Targets 187
5.2 VLA Observation Summary 192
5.3 VLA Correlator Setup 194
5.4 VLA Continuum Data Products 199
5.5 VLA RRL Data Products 205
5.6 H II Region Distances and Properties 210
5.7 Radial Metallicity Gradients 235

6.1 Model Parameters 254
6.2 MCMC Results 279

C.1 Non-tapered Image Continuum Properties of Multiple Detections . . 313
C.2 *uv*-tapered Image Continuum Properties of Multiple Detections . . . 319
C.3 Non-tapered Image RRL Properties of Multiple Detections 324
C.4 *uv*-tapered Image RRL Properties of Multiple Detections 330

D.1 Single Dish Electron Temperature Corrections 347

Chapter 1

Introduction

1.1 The Milky Way

The Sun is just one of billions of stars in our Galaxy, the Milky Way. From Earth, the Milky Way appears as a band of light bisected by dark dust lanes (Figure 1.1). This is the disk of the Galaxy, and the bright regions are the combined light of billions of distant stars. Stars are just one component of the Galactic disk, which also contains gas (in various phases of molecular, neutral, and ionized) and dust (an important component in the formation of planets). Surrounding the disk is the Galactic halo, a roughly spherical collection of old stars, globular clusters, and satellite galaxies (e.g., Bland-Hawthorn & Gerhard, 2016).

The Milky Way is one of a few hundred billion galaxies in the observable universe. These galaxies have various morphologies, they appear in different environments, and they span a wide range of observable and measurable properties. How galaxies form and evolve into such a diverse population is an outstanding question in astrophysics (Conselice, 2014). The vast distances to external galaxies limit our ability to probe the minute details that might be important for individual systems. Only in nearby galaxies, like the Andromeda Galaxy and other members of the Local Group, are we able to resolve individual stars, star forming regions, and other structures that reveal the galaxy's history. Therefore, the Milky Way is the perfect laboratory to uncover the specific processes that govern the formation and evolution of galaxies across the Universe.

The structure of the Milky Way today is a vital constraint on models and simulations of galaxy formation and evolution. Unfortunately, our location within the

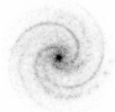

Figure 1.1: The Milky Way as viewed from Earth. The bright streak is the combined light of billions of stars, and the dark lane through the center of the Galaxy is caused by dust extinction. (Image credit: ESO/S. Brunier).

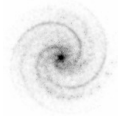

Galactic disk hinders our ability to obtain a clear picture of the Galaxy. Extinction by intervening dust limits our ability to see much farther than ∼1 kpc through the Galactic plane at optical wavelengths. We must infer Galactic structure using tracers that are bright, associated with structural features like spiral arms, can be seen through blankets of dust, and have accurate distances. Furthermore, we must be able to locate these tracers across the Galactic disk.

1.2 H II Regions

H II regions are the classic tracer of Galactic structure at radio wavelengths. These nebulae of ionized gas, which surround recently formed high-mass stars, are primarily located in the spiral arms of galaxies (Rosse & Parsons, 1880). Their cm-wavelength thermal emission is unaffected by dust, and thus we can see H II regions across the entire Galactic disk. Radio recombination lines (RRLs) are the spectral fingerprint of ionized gas. The RRL properties of an H II region reveal its kinematics and physical properties, and from these we can estimate its distance and metallicity. Therefore, H II regions are an ideal tracer of Galactic morphological, kinematic, and chemical structure.

In this dissertation, we aim to better constrain the structure of the Milky Way as traced by Galactic H II regions. Ultimately, this structure will inform formation and evolution models of the Galaxy. This work is divided into four projects: (1) the accuracy of H II region distances, (2) completing the census of Galactic H II regions, (3) the chemical structure of the Galactic disk, and (4) the morphological structure of the Galactic disk.

The most important characteristic of a Galactic structure tracer is an accurate distance. For the vast majority of Galactic H II regions, we derive the distances kinematically by measuring their radial velocity and assuming a model of Galactic rotation (e.g., Anderson et al., 2012). Few studies have tested the accuracy of these kinematic distances by comparing them to other distance determination techniques, such as parallax (e.g., Reid et al., 2014). Moreover, the traditional kinematic distance method does not typically characterize the uncertainty in the distance derivation. In Chapter 3, we develop a new kinematic distance technique and test the accuracy of kinematic distances for a sample of Galactic high-mass star forming regions.

The latest catalog of Galactic H II regions contains nearly 2000 nebulae, yet the vast majority of these objects are located in the northern sky (Anderson et al., 2014).

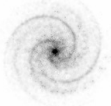

Most of the fourth quadrant of the Galaxy ($-90° < \ell < 0°$) is only visible from the southern hemisphere. The most recent RRL H II region survey in the southern sky was over three decades ago (Caswell & Haynes, 1987). In Chapter 4, we expand the H II Region Discovery Surveys to the fourth Galactic quadrant with the goal of completing the census of Galactic H II regions.

The metallicities of H II regions reveal the present day chemical structure of the Galactic disk. Stellar abundances are often difficult to interpret because the stars have unknown and/or significant ages and they migrate away from their birth locations throughout their lives (Sellwood & Binney, 2002). H II regions live for $\lesssim$10 Myr, so they represent the current chemical enrichment of the interstellar medium. Taken together, the Galactic stellar abundance structure and nebular metallicity structure place differing, but fundamental constraints on the chemodynamical history and evolution of the Milky Way. In Chapter 5, we explore the chemical structure of the Galactic disk using H II region metallicities.

Finally, H II regions are the archetypal tracer of Galactic morphological structure, such as spiral arms (Rosse & Parsons, 1880). An accurate map of this structure is essential for understanding the spiral arm formation mechanism, how the Galactic bar affects the gravitation potential of the Galaxy, and the impact of the local environment of the Milky Way (e.g., satellite galaxies) on its morphology and kinematics (Bland-Hawthorn & Gerhard, 2016). In Chapter 6, we use several tracers of Galactic morphological structure, including H II regions, to estimate some parameters of Milky Way morphology, including the number and pitch angles of the Galactic spiral arms.

1.3 CONTRIBUTIONS

The research contained within this dissertation was led by the author with contribution from several collaborators. Chapter 3 is published in the Astrophysical Journal with co-authors D. Balser, L. Anderson, and T. Bania, each of whom provided useful feedback on both the methods and the manuscript. Chapter 4 is published in the Astrophysical Journal Supplement Series with co-authors J. Dickey, C. Jordan, D. Balser, W. Armentrout, L. Anderson, T. Bania, J. Dawson, N. McClure-Griffiths, and J. Shea. Each person contributed to the design of the survey, and many also helped with the observing, data reduction, and manuscript preparation. Feedback on the remaining chapters was provided primarily by D. Balser with input from L. Anderson, T. Bania, and W. B. Burton.

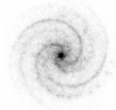

The author was supported by several funding sources for his dissertation work, including the D. N. Batten Foundation Jefferson Fellowship from the Jefferson Scholars Foundation, the Grote Reber Doctoral Fellowship from the National Radio Astronomy Observatory, the Raven Fellowship from the Raven Society at the University of Virginia, the Graduate Research Fellowship from the Virginia Space Grant Consortium, and the Achievement Rewards for College Scientists (ARCS) Scholarship from the Metro-Washington chapter of the ARCS Foundation.

Chapter 2

Brief History of Galactic Structure

2.1 17th Century

Like many aspects of modern astronomy, the field of Galactic structure began with Galileo Galilei. The telescope was invented in the late 16th century or early 17th century, and the first (unsuccessful) patent on the telescope was filed in the Netherlands by Hans Lippershey in 1608 (King, 2003). Only a few years passed before Galileo built an improved version of the telescope and turned his gaze upon the heavens.

Galileo presented the first astronomical observations with a telescope in his work, *Sidereus Nuncius* ("Starry Messenger" Galilei, 1610). In particular, Galileo discovered that there are far more stars in the sky than can be seen with the unaided eye. The bright band of light in the Milky Way, for example, can be resolved into many faint, individual stars. He writes, "For the Galaxy is nothing else than a congeries of innumerable stars distributed in clusters" (pp. 64, Galilei, 1610). With this discovery, the field of Galactic structure was born.

2.2 18th Century

Over the next two hundred years, many theories regarding the size and morphology of the Milky Way were debated. Among the first widely publicized hypotheses was that of Thomas Wright in his publication, "An original theory or new hypothesis of the Universe" (Wright, 1750). Wright proposed that the Sun is just one of the

many stars, and that the stars are arranged in a flat, circular sheet. This theory was further developed in a publication by Immanuel Kant a few years later (Kant, 1755). Notably, Wright and Kant were the first to offer observational evidence to suggest that the Milky Way is one of many island "universes."

Perhaps the most famous Galactic structure experiment of the 18th century was William Herschel's map of the Milky Way. Herschel's experiment was simple and relied on an elementary assumption: "The stars being supposed to be nearly equally scattered, and their number, in a field of view of a known angular diameter, being given, to determine the length of the visual ray" (Herschel, 1785). If stars appear in a similar density throughout the Galaxy, then the total number of stars visible along any line of sight should be proportional to the length of that line of sight. Essentially, by counting the number of stars he sees through his "40-foot telescope" (note that the telescope had a 40 foot focal length and only a 48 inch diameter primary mirror), Herschel estimated the size and morphology of the Milky Way. Figure 2.1 shows Herschel's map of the Galaxy, where the extent of the stellar disk is proportional to the number of stars visible along that line of sight.

Due to the inaccuracies of his assumptions, Herschel's drawing is only vaguely reminiscent of the modern picture of the Galaxy. His experiment accurately suggests, however, that the Milky Way is a flattened disk with a much larger extent in the direction of the Galactic plane compared to the direction of the Galactic poles. Extinction by intervening dust, and the poor resolving power of his telescope, resulted in his underprediction of the number of stars in the direction of the Galactic center. Herschel was intrigued by what he called "An Opening in the Heavens," the "parts of our [Galaxy, which have] suffered greater ravages of time than others" (Herschel, 1785). Today, we know that this dark band is not due to a lack of stars or some great ravage, but to dust lanes in the Galactic plane.

2.3 19th CENTURY

In his thorough review of the field, Stephen Alexander summarized the work of both William Herschel and his son, John Herschel, in an attempt to develop a new theory about the Milky Way (Alexander, 1852). Alexander considered the recent discovery of the spiral nature of some nebulae, including the Triangulum Galaxy (M33), by Lord Rosse (Rosse, 1850), and he concluded that the Milky Way might be a similar spiral nebulae with several "branches" or "arms."

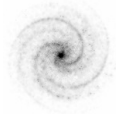

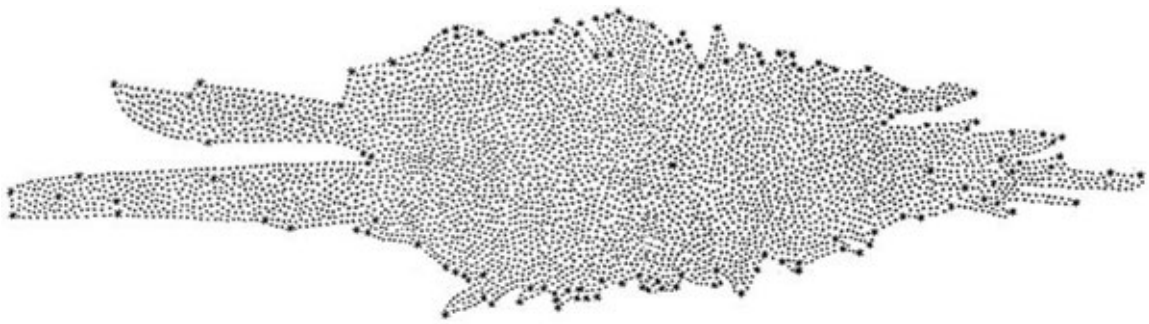

Figure 2.1: William Herschel's map of the Milky Way (Herschel, 1785). The Sun is located at the large star near the center of the diagram, and the Galactic Center is to the left. The extent of the Galaxy in each direction is proportional to the number of stars visible in that direction. The indent in the direction of the Galactic Center, which Herschel called "An Opening in the Heavens," is due to dust blocking the view of distant stars.

Richard Proctor, in 1869, created the first map of spiral structure in the Milky Way (Proctor, 1869, see Figure 2.2). Using the Herschels' observations of the Milky Way's stellar "streams," Proctor developed a two arm sprial-like model to reproduce these observations (N.B. these are not "streams" as in what we today call stellar streams, but rather the "streams" of stars in the Galactic plane). Like William Herschel, Proctor was ignorant of dust extinction, so he assumed that the dark bands through the Galactic plane delineated different "spiral arms." He accepted that his model was likely inaccurate: "It must be admitted, however, that the problem of interpreting this wonderful stream is one of enormous difficulty. Perhaps it is one which men will never be able to accomplish in a perfectly satisfactory manner" (Proctor, 1869).

2.4 20th CENTURY

The first theory of Galactic structure that resembles our modern understanding appeared at the start of the 20th century. In "A New Theory of the Milky Way," Cornelis Easton, a Dutch journalist and semi-professional astronomer[1], discussed the limitations of existing Milky Way models, such as those by the Herschels and Proctor (Easton, 1900). Easton proposed a simple "spiral" model of the Galaxy to explain the varying brightness of the Galactic disk across the sky (Figure 2.3). Although this picture is extremely reminiscent of our modern understanding of spiral galaxies, Easton still fell victim to the effect of dust extinction. To explain the lack of stars through the center of the Galactic plane, he suggested that "this galactic spiral would not be situated in a single plane, but principally in two planes forming an angle of about 20°" (Easton, 1900). Nevertheless, Easton immediately recognized that this model of the Galaxy closely resembled photographs of the "spiral nebulae," which we now know to be external spiral galaxies.

The discovery of the period-luminosity relation of Cepheid variable stars by Henrietta Leavitt revolutionized our ability to trace structure in the Galaxy (Leavitt, 1908). Harlow Shapley used variable stars, which he incorrectly classified as Cepheid variables instead of RR Lyrae variables, to determine the distances to 69 Milky Way globular clusters. By assuming the clusters were equally distributed in the Galaxy, he estimated the size of the Milky Way and the distance to the Galactic Center (Shapley, 1918). This was, perhaps, the first application of *astrophysics* in the field of Galactic

[1]Despite publishing original research in professional astronomical journals, he did not receive a formal astronomy education nor was he ever employed as an astronomer.

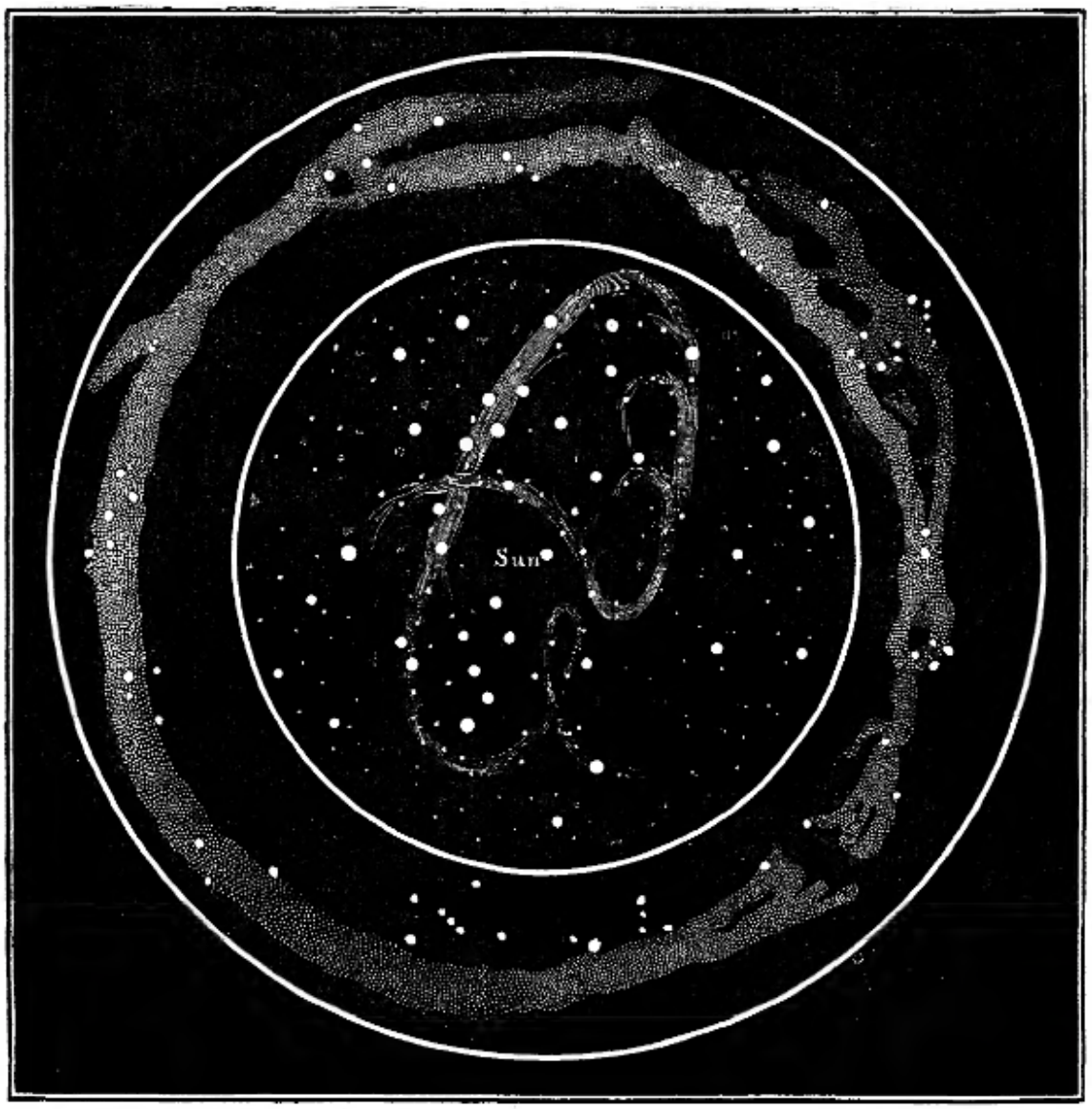

Figure 2.2: Richard Proctor's two arm spiral-like model of the Milky Way (Proctor, 1869). The outer ring is a representation of the Milky Way based on the drawings and descriptions by John Herschel. The inner circle is Proctor's spiral model, with the Sun located at the center of the diagram. This model reproduces the observed Milky Way structure when projected onto the celestial sphere.

Figure 2.3: Cornelis Easton's spiral model of the Milky Way (Easton, 1900). The Sun is located at the central star, and the Galactic Center is to the left (in the direction of Cygnus).

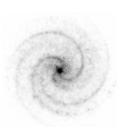

structure.

A few years later, Jacobus Kapteyn created the first astrophysical model of the Milky Way. Using the parallaxes and proper motions of a handful of nearby stars, Kapteyn extrapolated the spatial distribution of stars in the Galaxy based on star counts and apparent magnitudes, incorrectly assuming that fainter stars must necessarily be more distant. He created a gravitational model of the Galaxy to explain this spatial distribution and found that the Galaxy must be a flattened disk with the Sun offset from the center by a few hundred parsecs (Kapteyn, 1922). This model was not without criticism, however, as it predicted a Milky Way much different in size than Shapley's globular cluster distribution had suggested (see Figure 2.4). Extinction and interstellar reddening caused Kapteyn to overestimate the distances to stars.

The 1920s was an important decade in the advancement of our understanding of both the Milky Way and its place in the universe. The "Great Debate" between Harlow Shapley and Herber Curtis (a UVA alumnus) in 1920 was finally settled when Edwin Hubble measured the distances to spiral nebulae using Cepheid variables, showing that they were external to the Milky Way (Hubble, 1925)[2]. With this discovery, the Milky Way became a laboratory for understanding these "galactic systems" across the universe.

Jan Oort and Bertil Lindblad developed our modern understanding of the kinematics of stars in the Galaxy. In his first astronomical publication, Oort investigated the high velocity stars in the solar neighborhood and found that their kinematics are similar to those of the distant globular clusters (Oort, 1922). This was the first evidence of the Galactic halo as a separate stellar component of the Galaxy. Motivated by this discovery, Lindblad proposed that the Milky Way contains several of these components, or "sub-systems," each of which is centered on the same principle axis but has its own kinematics (Lindblad, 1925, 1926). The high velocity stars and globular clusters must belong to one such sub-system (now known as the Galactic halo), and the field stars must belong to another (the Galactic disk). Oort used the proper motions and radial velocities of field stars to confirm Lindblad's hypothesis (Oort, 1927). In this work, Oort developed the now-famous "Oort Constants" to characterize the rotation of the Galaxy, define the local standard of rest, and lay the foundation of the kinematic distance method.

[2]The first announcement was actually published in the *New York Times* on 22 November 1924, incorrectly attributed to "Dr. Hubbell."

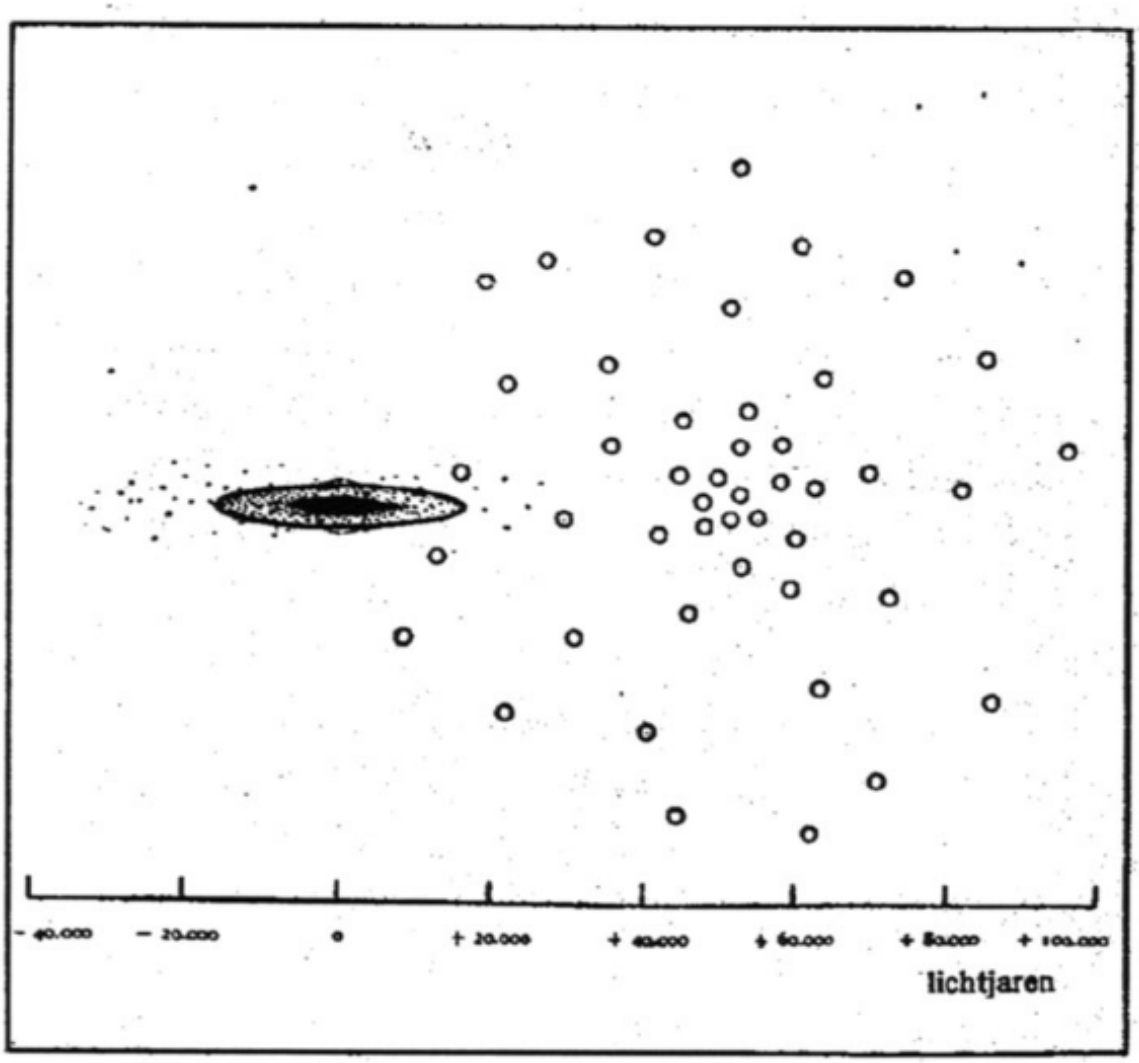

Figure 2.4: The conflict between Shapley's globular clusters and Kapteyn's gravitational model (from de Sitter, 1934). The small disk represents Kapteyn's model, and the open points are Shapley's globular clusters. (This figure was published in the 1934 Dutch version of de Sitter's "Kosmos", and it was credited to Jan Oort.)

Perhaps the most important 20th century advancement in our understanding of Milky Way stellar structure and chemical evolution was the discovery of chemically distinct stellar populations in the Milky Way, the Andromeda Galaxy (M31), and its satellite galaxies. In 1944, Walter Baade used the 100 inch Hooker telescope at Mount Wilson Observatory to resolve individual stars in M32, NGC205, and the inner region of M31. He discovered that the Hertzprung-Russell (H-R) diagram of these stars closely resembled that of Milky Way globular clusters (Baade, 1944). He coined the name "Type II" or "Population II" to distinguish this population of stars from the group of "Population I" disk stars, which occupy different parts of the H-R diagram. Furthermore, Baade recognized that this Type II population was the same as the kinematically distinct population identified by Oort in 1922. This work culminated in the Vatican Symposium of 1957, where the attendees recognized that several sub-populations of stars exist (thin and thick disk, bulge, and halo stars) and that they arise from different pathways of chemical evolution (Blaauw, 1995).

The first concrete evidence for spiral structure in the Milky Way was presented by William M. Morgan at the 1951 Winter meeting of the American Astronomical Society (Gingerich, 1985). Morgan, Stewart Sharpless, and Donald Osterbrock determined the spectrophotometric distances of massive OB-stars and star forming regions, known as H II regions, and traced out two arm-like features across several kpc. According to Otto Struve, "Morgan's paper on galactic structure was greeted by an ovation such as I have never before witnessed" (Struve, 1953). Other than a short research note (Morgan et al., 1952), this work was never published and was quickly superseded by the rapid development of radio astronomy.

Extinction by dust limits our ability to discern Milky Way stellar structure much farther than a kiloparsec or so through the Galactic disk. In 1933, Karl Jansky discovered "cosmic static," or radio waves, originating from outer space (Jansky, 1933). There was now an extinction-free tool to peer through the dusty Galaxy. Oort recognized the potential application of a radio spectral line to the field of Galactic structure and he tasked his student, Hendrik Christoffel van de Hulst, with predicting the frequencies of such spectral lines. In 1945, van de Hulst published a prediction for a hyper-fine transition of the most abundant element in the universe, neutral hydrogen, H I, at 21 cm (van de Hulst, 1945). Radio engineers around the world raced to develop antennas and receivers to search for this emission. The Dutch group was on the verge of the discovery when their receiver and equipment were destroyed in a

laboratory fire in 1950 (van de Hulst et al., 1954). Therefore, it was not until 1951 that Harold "Doc" Ewen and Edward Purcell discovered the H I 21 cm line (Ewen & Purcell, 1951). This discovery was quickly confirmed by the Dutch group (Muller & Oort, 1951) and Australian group (Pawsey, 1951).

The first H I map of the Galaxy was published in 1952 by the Australian group (Christiansen & Hindman, 1952a,b). The Dutch group, with the insight of Oort at their disposal, was the first to create a "face-on" view of the Galaxy from the Galactic longitude–velocity H I data (van de Hulst et al., 1954). Using Oort's kinematic distance method, they estimated the distances to the H I emission peaks and troughs and created a map of the neutral hydrogen distribution exterior to the Solar orbit. This map revealed the first evidence of spiral arms in the H I content of the Galaxy.

As technology improved, so did our maps of Galactic H I. By the mid 1970s, several people began to study the detailed structure and kinematics of neutral hydrogen in the Milky Way disk. For example, Burton (1973) used the new spiral density wave theory of spiral arms (Lin & Shu, 1964) to explore the dynamics of the H I disk. He showed that the effects of non-circular motions, or "streaming" motions, can influence kinematic distances and create apparent spiral arms in face-on maps of Galactic H I emission due to its pervasiveness throughout the disk. Discrete tracers or a less abundant tracer of Galactic structure was needed.

Radio recombination lines (RRLs) from high-mass star forming regions, known as H II regions, in the Milky Way were discovered in 1965 with the National Radio Astronomy Observatory (NRAO; now Green Bank Observatory) 140 Foot telescope (Hoglund & Mezger, 1965a,b). Since H II regions are the classic tracer of spiral structure in external galaxies, this extinction-free spectral line was a new way to uncover Galactic structure (e.g., Morgan et al., 1952). Furthermore, since H II regions are discrete objects that trace recent star formation, the inferred structure is not as ambiguous as what is seen in, for example, H I maps of the Galaxy. The first radio wavelength investigation into Galactic spiral structure traced by H II regions was in Georgelin & Georgelin (1976). They combined both optical and radio observations of the nebulae with supplementary information about the exciting stars to create a map of the Galaxy's spiral arms. Despite the relatively small sample (by today's standards) of H II regions, and the lack of reliable distances, it was clear that H II regions would provide an important constraint on Galactic structure.

Finally, the discovery of radio-wavelength spectral lines from molecules, which

probe regions of dense gas, opened a new view into the structure of the Milky Way. This gas is much less abundant than neutral hydrogen, but it is also more closely associated with features of Galactic spiral structure, such as giant molecular clouds and high-mass star forming regions. The most common tracers of interstellar molecular gas is carbon monoxide, discovered in the Orion Nebula by the NRAO 36 foot telescope on Kitt Peak (Wilson et al., 1970a). Within a few years, the first CO maps of the Galaxy were created. Bania (1977), for example, mapped the CO distribution of the inner Galaxy and he identified the molecular components associated with such kinematic features as the "near" 3-kpc arm, the nuclear disk, and Bania's "Clumps" 1 and 2. These and other molecular spectral lines are now an important tracer of structure and star formation in both the Milky Way and external galaxies.

Chapter 3

Kinematic Distances: A Monte Carlo Method

3.1 Introduction

Revealing the morphological and chemical structure of the Milky Way requires knowing the locations of objects on a Galaxy-wide scale. In the solar neighborhood, the distances to stars can be accurately derived by measuring their parallax. Far from the solar neighborhood, distances to stars may be determined using spectrophotometric techniques (e.g., Moisés et al., 2011) and red clump stars (e.g., Bovy et al., 2014). Distances to gas clouds can be gotten from both Very Long Baseline Interferometry (VLBI) parallax measurements of molecular maser emission from high-mass star forming regions (HMSFRs) (e.g., Reid et al., 2014) as well as kinematic distance determinations (e.g., Anderson et al., 2012).

Kinematic distances are derived by measuring the local standard of rest (LSR) velocity, $V_{\rm LSR}$, of an object and assuming a model of Galactic rotation. If the object is on a circular orbit following this Galactic rotation model (GRM), then the LSR velocity of the object uniquely identifies the object's Galactocentric radius, R. Beyond the solar orbit, this technique also uniquely determines the object's Galactocentric azimuth, θ, and distance from the sun, d. Within the solar orbit, kinematic distances

This chapter previously appeared in the Astrophysical Journal. The original citation is as follows: T. V. Wenger, D. S. Balser, L. D. Anderson, and T. M. Bania. "Kinematic Distances: A Monte Carlo Method." *Astrophysical Journal*, 856:52, March 2018.

suffer from the kinematic distance ambiguity (KDA). Here, a single LSR velocity may correspond to two distances: a "near" and "far" kinematic distance. We must use additional information to identify the kinematic distance ambiguity resolution (KDAR). The kinematic method is commonly used to determine the distances to HMSFRs in the study of Galactic structure. Recently, for example, Balser et al. (2015) used H II region kinematic distances to probe the metallicity distribution across the Galactic disk.

The Green Bank Telescope H II Region Discovery Survey (GBT HRDS) and its successors discovered more than ∼1000 new Galactic H II regions by measuring their centimeter wavelength radio recombination line (RRL) emission (Bania et al., 2010, 2012; Anderson et al., 2015a). H II regions are the zones of ionized gas surrounding recently formed high-mass (OB-type) stars. They are the archetypal tracer of Galactic spiral structure. Anderson et al. (2012) derived the kinematic distances to 149 H II regions in the original GBT HRDS, and today the *WISE* Catalog of Galactic H II Regions (Anderson et al., 2014) lists ∼1500 H II region kinematic distances.

Errors in kinematic distances are caused by both inaccurate GRMs and incorrect KDARs. The rotation of the Milky Way is affected by non-circular streaming motions induced by the Galactic bar and spiral arms (e.g., Burton, 1971; Gómez, 2006; Moisés et al., 2011). These deviations from circular motion will affect the accuracy of GRMs. A variety of techniques have been used to resolve the KDA for Galactic H II regions, for example, H I emission/absorption experiments (Kuchar & Bania, 1994; Kolpak et al., 2003; Anderson & Bania, 2009; Anderson et al., 2012; Urquhart et al., 2012; Brown et al., 2014), H I self-absorption experiments (Roman-Duval et al., 2009; Urquhart et al., 2012), and H_2CO absorption experiments (Araya et al., 2002; Watson et al., 2003; Sewilo et al., 2004). If these KDAR techniques are inaccurate, the derived kinematic distances will be as well.

Very Long Baseline Interferometric (VLBI) trigonometric parallax measurements of molecular masers are an independent and accurate way to measure the distances to HMSFRs. Over the past decade, the Bar and Spiral Structure Legacy Survey (BeSSeL)[1], the Japanese VLBI Exploration of Radio Astrometry (VERA)[2], and the European VLBI Network (EVN)[3] projects have accumulated a sample of more than

[1] http://bessel.vlbi-astrometry.org/
[2] http://veraserver.mtk.nao.ac.jp/
[3] http://www.evlbi.org/

100 VLBI parallaxes and proper motions for masers associated with HMSFRs (Reid et al., 2014). These trigonometrically derived distances do not suffer from the same problems as kinematic distances. With a typical parallax uncertainty of $\sim$20 μas, these parallax distances are accurate to about 10% at distances of 5 kpc(Reid & Honma, 2014).

Although parallaxes are the "gold standard" distances for HMSFRs, they are difficult and time-consuming to measure. To constrain the parallax and proper motion of four HMSFRs, including W51 Main/South, Sato et al. (2010) used the National Radio Astronomy Observatory (NRAO) Jansky Very Large array to locate background extragalactic position reference objects together with the NRAO Very Long Baseline Array (VLBA) for the accurate astrometry. The VLBA observations totaled $\sim$28 hours spread over $\sim$12 months. Such observations are impractical to make for all $\sim$4000 H II regions in the *WISE* Catalog. Furthermore, the majority of the H II regions in the *WISE* Catalog will not have detectable maser emission.

With such a large sample of HMSFR maser parallaxes, we can now compare the parallax and kinematic distances and judge the accuracy of the kinematic distance technique. Reid et al. (2009c) performed a similar study in which they compared the kinematic and parallax distances of 18 HMSFRs. They found that the kinematic distance method gives distances much larger (up to a factor of 2) than the parallax distances for a majority of their sample. After correcting the LSR velocities using updated solar motion parameters, however, the mean difference between the kinematic and parallax distances became close to zero and only half of their sample had kinematic distances larger than their parallax distances. Here, we expand upon the Reid et al. (2009c) analysis using a larger sample of HMSFRs.

3.2 Sample Selection

Our sample of HMSFRs comes from the maser parallax catalog in Reid et al. (2014) that contains parallaxes and proper motions for 103 HMSFRs and HMSFR proxies in the Milky Way. These data stem from measurements made using the NRAO VLBA, the VERA project, and the EVN. The Reid et al. (2014) catalog contains the parallax, maser LSR velocity, and their associated uncertainties for each HMSFR. This provides the necessary information to derive both the parallax distance and kinematic distance to each object.

Kinematic distances are unreliable in the direction of the Galactic Center (GC;

$\ell = 0°$) and the Galactic Anti-center (GAC; $\ell = 180°$) due to velocity crowding; LSR velocities due to circular motion tend toward zero in these directions. As in previous studies using kinematic distances (e.g., Balser et al., 2015), we exclude all objects within 15° of the GC and 20° of the GAC.

Our final sample contains 72 HMSFRs and 3 red supergiants (HMSFR proxies). The positions, parallaxes, and LSR velocities ($V_{\rm LSR}$) from the Reid et al. (2014) catalog are reproduced in Table 3.1. According to Reid et al. (2014), the listed LSR velocities are those of methanol masers when available; otherwise, they are the ^{12}CO emission line velocities from associated giant molecular clouds (GMCs). The LSR velocity uncertainties include both measurement uncertainties as well as an added uncertainty relating the maser spot motion to the bulk HMSFR motion. This added component ranges from $5\,{\rm km\,s^{-1}}$ to $20\,{\rm km\,s^{-1}}$ (see Reid et al., 2014).

3.3 Parallax Distances

The parallax distance is defined as

$$D_P = \frac{1}{\pi} \tag{3.1}$$

where the parallax distance, D_P, has units of kpc when the parallax, π, has units of milli-arcseconds (mas). If the parallax uncertainty, σ_π, is small compared to the parallax, i.e. $\sigma_\pi/\pi \ll 1$, then the parallax distance uncertainty, σ_P, is determined by propagating the parallax uncertainty through Equation 3.1,

$$\sigma_P = \frac{\sigma_\pi}{\pi^2}. \tag{3.2}$$

If the fractional parallax uncertainty is large, however, the shape of the parallax distance probability distribution function (PDF) is skewed. Thus, the peak (D_P) and the shape of the wings change and the parallax distance uncertainty is nonsymmetric around the peak (see Kovalevsky, 1998). Figure 3.1 shows an example of the parallax distance PDF skew for different parallax uncertainties.

We derive a Monte Carlo parallax distance for each HMSFR by resampling the measured parallaxes within their uncertainties, assuming a Gaussian parallax PDF. We sample the parallax 10^5 times and use Equation 3.1 to derive the parallax distance distribution. To approximate the parallax distance PDF, we fit a kernel density

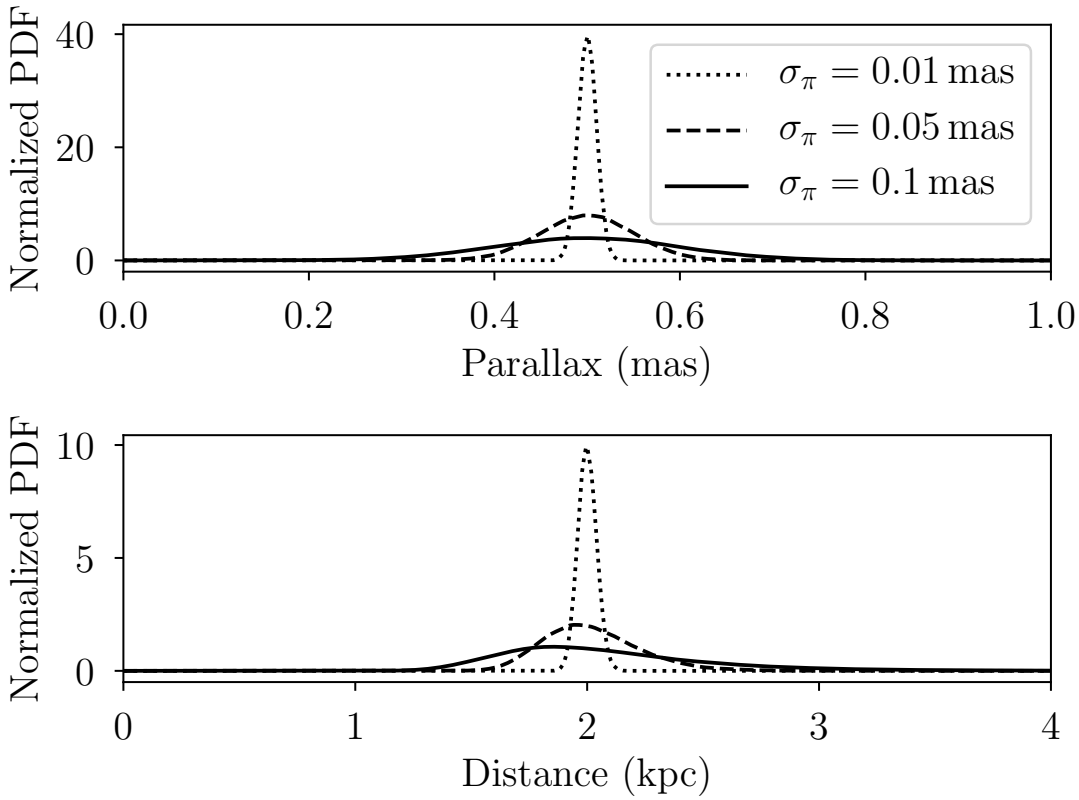

Figure 3.1: Normalized parallax probability distribution function (PDF; top) and parallax distance PDF (bottom). The parallax in this example is $\pi = 0.5$ mas and the parallax uncertainty is $\sigma_\pi = 0.01$ mas (dotted), 0.05 mas (dashed) and 0.1 mas (solid). The parallax distance PDF is determined by Monte Carlo resampling the Gaussian parallax PDF. For large relative parallax uncertainties, the parallax distance PDF is skewed.

Table 3.1: HMSFR Sample

Name	Alias	RA (J2000) (hh:mm:ss)	Decl. (J2000) (dd:mm:ss)	Parallax (mas)	$V_{\rm LSR}$ (km s^{-1})	Refs.
G015.03−00.67	M 17	18:20:24.81	−16:11:35.3	0.505 ± 0.033	22 ± 3	10
G016.58−00.05		18:21:09.08	−14:31:48.8	0.279 ± 0.023	60 ± 5	4
G023.00−00.41		18:34:40.20	−09:00:37.0	0.218 ± 0.017	80 ± 3	11
G023.44−00.18		18:34:39.19	−08:31:25.4	0.170 ± 0.032	97 ± 3	11
G023.65−00.12		18:34:51.59	−08:18:21.4	0.313 ± 0.039	83 ± 3	12
G023.70−00.19		18:35:12.36	−08:17:39.5	0.161 ± 0.024	73 ± 5	7
G025.70+00.04		18:38:03.14	−06:24:15.5	0.098 ± 0.029	93 ± 5	4
G027.36−00.16		18:41:51.06	−05:01:43.4	0.125 ± 0.042	92 ± 3	10
G028.86+00.06		18:43:46.22	−03:35:29.6	0.135 ± 0.018	100 ± 10	4
G029.86−00.04		18:45:59.57	−02:45:06.7	0.161 ± 0.020	100 ± 3	6
G029.95−00.01	W 43S	18:46:03.74	−02:39:22.3	0.190 ± 0.019	98 ± 3	6
G031.28+00.06		18:48:12.39	−01:26:30.7	0.234 ± 0.039	109 ± 3	6
G031.58+00.07	W 43Main	18:48:41.68	−01:09:59.0	0.204 ± 0.030	96 ± 5	6
G032.04+00.05		18:49:36.58	−00:45:46.9	0.193 ± 0.008	97 ± 5	4
G033.64−00.22		18:53:32.56	+00:31:39.1	0.153 ± 0.017	60 ± 3	1
G034.39+00.22		18:53:18.77	+01:24:08.8	0.643 ± 0.049	57 ± 5	13
G035.02+00.34		18:54:00.67	+02:01:19.2	0.430 ± 0.040	52 ± 5	2
G035.19−00.74		18:58:13.05	+01:40:35.7	0.456 ± 0.045	30 ± 7	14
G035.20−01.73		19:01:45.54	+01:13:32.5	0.306 ± 0.045	42 ± 3	14
G037.43+01.51		18:54:14.35	+04:41:41.7	0.532 ± 0.021	41 ± 3	2
G043.16+00.01	W 49N	19:10:13.41	+09:06:12.8	0.090 ± 0.007	10 ± 5	15
G043.79−00.12	OH 43.8−0.1	19:11:53.99	+09:35:50.3	0.166 ± 0.005	44 ± 10	2
G043.89−00.78		19:14:26.39	+09:22:36.5	0.121 ± 0.020	54 ± 5	2

Table 3.1 continued

Table 3.1: HMSFR Sample (continued)

Name	Alias	RA (J2000) (hh:mm:ss)	Decl. (J2000) (dd:mm:ss)	Parallax (mas)	$V_{\rm LSR}$ (km s^{-1})	Refs.
G045.07+00.13		19:13:22.04	+10:50:53.3	0.125 ± 0.005	59 ± 5	2
G045.45+00.05		19:14:21.27	+11:09:15.9	0.119 ± 0.017	55 ± 7	2
G048.60+00.02		19:20:31.18	+13:55:25.2	0.093 ± 0.005	18 ± 5	15
G049.19−00.33		19:22:57.77	+14:16:10.0	0.189 ± 0.007	67 ± 5	2
G049.48−00.36	W 51 IRS2	19:23:39.82	+14:31:05.0	0.195 ± 0.071	56 ± 3	16
G049.48−00.38	W 51M	19:23:43.87	+14:30:29.5	0.185 ± 0.010	58 ± 4	17
G052.10+01.04	IRAS 19213+1723	19:23:37.32	+17:29:10.5	0.251 ± 0.060	42 ± 5	18
G059.78+00.06		19:43:11.25	+23:44:03.3	0.463 ± 0.020	25 ± 3	16
G069.54−00.97	ON 1	20:10:09.07	+31:31:36.0	0.406 ± 0.013	12 ± 5	19,20,21
G074.03−01.71		20:25:07.11	+34:49:57.6	0.629 ± 0.017	5 ± 5	21
G075.29+01.32		20:16:16.01	+37:35:45.8	0.108 ± 0.005	-58 ± 5	22
G075.76+00.33		20:21:41.09	+37:25:29.3	0.285 ± 0.022	-9 ± 9	21
G075.78+00.34	ON 2N	20:21:44.01	+37:26:37.5	0.261 ± 0.030	1 ± 5	23
G076.38−00.61		20:27:25.48	+37:22:48.5	0.770 ± 0.053	-2 ± 5	21
G078.12+03.63	IRAS 20126+4104	20:14:26.07	+41:13:32.7	0.610 ± 0.030	-4 ± 5	24
G078.88+00.70	AFGL 2591	20:29:24.82	+40:11:19.6	0.300 ± 0.024	-6 ± 7	25
G079.73+00.99	IRAS 20290+4052	20:30:50.67	+41:02:27.5	0.737 ± 0.062	-3 ± 5	25
G079.87+01.17		20:30:29.14	+41:15:53.6	0.620 ± 0.027	-5 ± 10	21
G080.79−01.92[a]	NML Cyg	20:46:25.54	+40:06:59.4	0.620 ± 0.047	-3 ± 3	26
G080.86+00.38	DR 20	20:37:00.96	+41:34:55.7	0.687 ± 0.038	-3 ± 5	25
G081.75+00.59	DR 21	20:39:01.99	+42:24:59.3	0.666 ± 0.035	-3 ± 3	25
G081.87+00.78	W 75N	20:38:36.43	+42:37:34.8	0.772 ± 0.042	7 ± 3	25
G090.21+02.32		21:02:22.70	+50:03:08.3	1.483 ± 0.038	-3 ± 5	21

Table 3.1 continued

Table 3.1: HMSFR Sample (continued)

Name	Alias	RA (J2000) (hh:mm:ss)	Decl. (J2000) (dd:mm:ss)	Parallax (mas)	$V_{\rm LSR}$ (km s^{-1})	Refs.
G092.67+03.07		21:09:21.73	+52:22:37.1	0.613 ± 0.020	-5 ± 10	21
G094.60−01.79	AFGL 2789	21:39:58.27	+50:14:21.0	0.280 ± 0.030	-46 ± 5	18,28
G095.29−00.93		21:39:40.51	+51:20:32.8	0.205 ± 0.015	-38 ± 5	28
G097.53+03.18		21:32:12.43	+55:53:49.7	0.133 ± 0.017	-73 ± 5	27
G100.37−03.57		22:16:10.37	+52:21:34.1	0.291 ± 0.010	-37 ± 10	28
G105.41+09.87		21:43:06.48	+66:06:55.3	1.129 ± 0.063	-10 ± 5	21
G107.29+05.63	IRAS 22198+6336	22:21:26.73	+63:51:37.9	1.288 ± 0.107	-11 ± 5	29
G108.18+05.51	L 1206	22:28:51.41	+64:13:41.3	1.289 ± 0.153	-11 ± 3	19
G108.20+00.58		22:49:31.48	+59:55:42.0	0.229 ± 0.028	-49 ± 5	28
G108.47−02.81		23:02:32.08	+56:57:51.4	0.309 ± 0.010	-54 ± 5	28
G108.59+00.49		22:52:38.30	+60:00:52.0	0.398 ± 0.031	-52 ± 5	28
G109.87+02.11	Cep A	22:56:18.10	+62:01:49.5	1.430 ± 0.080	-7 ± 5	30
G111.23−01.23		23:17:20.79	+59:28:47.0	0.288 ± 0.044	-53 ± 10	28
G111.25−00.76		23:16:10.36	+59:55:28.5	0.294 ± 0.016	-43 ± 5	28
G111.54+00.77	NGC 7538	23:13:45.36	+61:28:10.6	0.378 ± 0.017	-57 ± 5	30
G121.29+00.65	L 1287	00:36:47.35	+63:29:02.2	1.077 ± 0.039	-23 ± 5	19
G122.01−07.08	IRAS 00420+5530	00:44:58.40	+55:46:47.6	0.460 ± 0.020	-50 ± 5	31
G123.06−06.30	NGC 281	00:52:24.70	+56:33:50.5	0.355 ± 0.030	-30 ± 5	32
G123.06−06.30	NGC 281W	00:52:24.20	+56:33:43.2	0.421 ± 0.022	-29 ± 3	19
G133.94+01.06	W 3OH	02:27:03.82	+61:52:25.2	0.512 ± 0.010	-47 ± 3	33,34
G134.62−02.19[a]	S Per	02:22:51.71	+58:35:11.4	0.413 ± 0.017	-39 ± 5	35
G135.27+02.79	WB 89−437	02:43:28.57	+62:57:08.4	0.167 ± 0.011	-72 ± 3	36
G209.00−19.38	Orion Nebula	05:35:15.80	−05:23:14.1	2.410 ± 0.030	3 ± 5	43,44,45

Table 3.1 continued

Table 3.1: HMSFR Sample (continued)

Name	Alias	RA (J2000) (hh:mm:ss)	Decl. (J2000) (dd:mm:ss)	Parallax (mas)	$V_{\rm LSR}$ (km s^{-1})	Refs.
G211.59+01.05		06:52:45.32	+01:40:23.1	0.228 ± 0.007	45 ± 5	1
G229.57+00.15		07:23:01.84	−14:41:32.8	0.221 ± 0.014	47 ± 10	28
G232.62+00.99		07:32:09.78	−16:58:12.8	0.596 ± 0.035	21 ± 3	40
G236.81+01.98		07:44:28.24	−20:08:30.2	0.298 ± 0.018	43 ± 7	28
G239.35−05.06[a]	VY CMa	07:22:58.33	−25:46:03.1	0.855 ± 0.057	20 ± 3	46,47
G240.31+00.07		07:44:51.92	−24:07:41.5	0.212 ± 0.021	67 ± 5	28

[a] Red supergiants

References — (1) BeSSeL Survey unpublished; (2) Wu et al. (2014); (4) Sato et al. (2014); (6) Zhang et al. (2014); (7) Sanna et al. (2014); (10) Xu et al. (2011); (11) Brunthaler et al. (2009); (12) (12) Bartkiewicz et al. (2008); (13) Kurayama et al. (2011); (14) Zhang et al. (2009); (15) Zhang et al. (2013); (16) Xu et al. (2009); (17) Sato et al. (2010); (18) Oh et al. (2010); (19) Rygl et al. (2010); (20) Nagayama et al. (2011); (21) Xu et al. (2013); (22) Sanna et al. (2012); (23) Ando et al. (2011); (24) Moscadelli et al. (2011); (25) Rygl et al. (2012); (26) Zhang et al. (2012b); (27) Hachisuka et al. (2015); (28) Choi et al. (2014); (29) Hirota et al. (2008); (30) Moscadelli et al. (2009); (31) Moellenbrock et al. (2009); (32) Sato et al. (2008); (33) Xu et al. (2006); (34) Hachisuka et al. (2006); (35) Asaki et al. (2010); (36) Hachisuka et al. (2009); (40) Reid et al. (2009a); (43) Sandstrom et al. (2007); (44) Menten et al. (2007); (45) Kim et al. (2008); (46) Choi et al. (2008); (47) Zhang et al. (2012a)

estimator (KDE) to the distribution. We use the linear combination KDE technique from Jones (1993), which is accurate even in the presence of physical boundaries such as the requirement that distances be greater than 0. The parallax distance PDFs for four sources are shown in Figure 3.2. The peak of the PDF (i.e. the most likely value) is the parallax distance. In every case, this distance is smaller than the distance given by Equation 3.1. We derive the uncertainty in the parallax distance by determining the lower and upper bounds of the PDF such that 1) the value of the PDF at both bounds is equal and 2) the integral of the normalized PDF between the bounds is equal to 0.683 (i.e., 68.3% of the total area under the PDF). This uncertainty is therefore the 68.3% confidence interval.

The difference between the parallax distances derived using Equation 3.1 and our Monte Carlo-derived parallax distances is small; the median difference is 0.03 kpc and the largest difference is 1.32 kpc for G025.70+00.04 (Figure 3.2, panel (d)). Figure 3.3 shows the distribution of parallax distance differences between these two methods for our HMSFR sample (Table 3.1). The majority of objects in our sample have less than 0.1 kpc difference between the Equation 3.1 and Monte Carlo parallax distances.

3.4 Kinematic Distances

A fundamental assumption of the kinematic distance method is that the chosen GRM, which gives the Galactic orbital speed, Θ, at all Galactocentric radii, R, accurately models the Galaxy. Several different techniques have been employed to derive $\Theta(R)$, such as, for example, the tangent point method (e.g., McClure-Griffiths & Dickey, 2007) or use of the full phase-space kinematics of masers associated with HMSFRs (e.g., Reid et al., 2014). The former method is only reliable in the inner Galaxy (within the solar orbit) whereas the latter method works across the entire Galactic disk. Reid & Dame (2016) demonstrated that both methods predict similar rotation curves in the inner Galaxy.

The GRM rotation curve is used to transform the Galactic longitude, Galactic latitude, distance space (ℓ, b, d) to Galactic longitude, Galactic latitude, LSR velocity space $(\ell, b, V_{\rm LSR})$. A schematic of the kinematic distance technique is shown in Figure 3.4.

Many studies have shown that HMSFRs in the Milky Way do not have perfectly circular orbits; there are significant non-circular motions due to streaming in the vicinity of the Galactic bars and spiral arms (e.g., Burton, 1971; Gómez, 2006; Reid

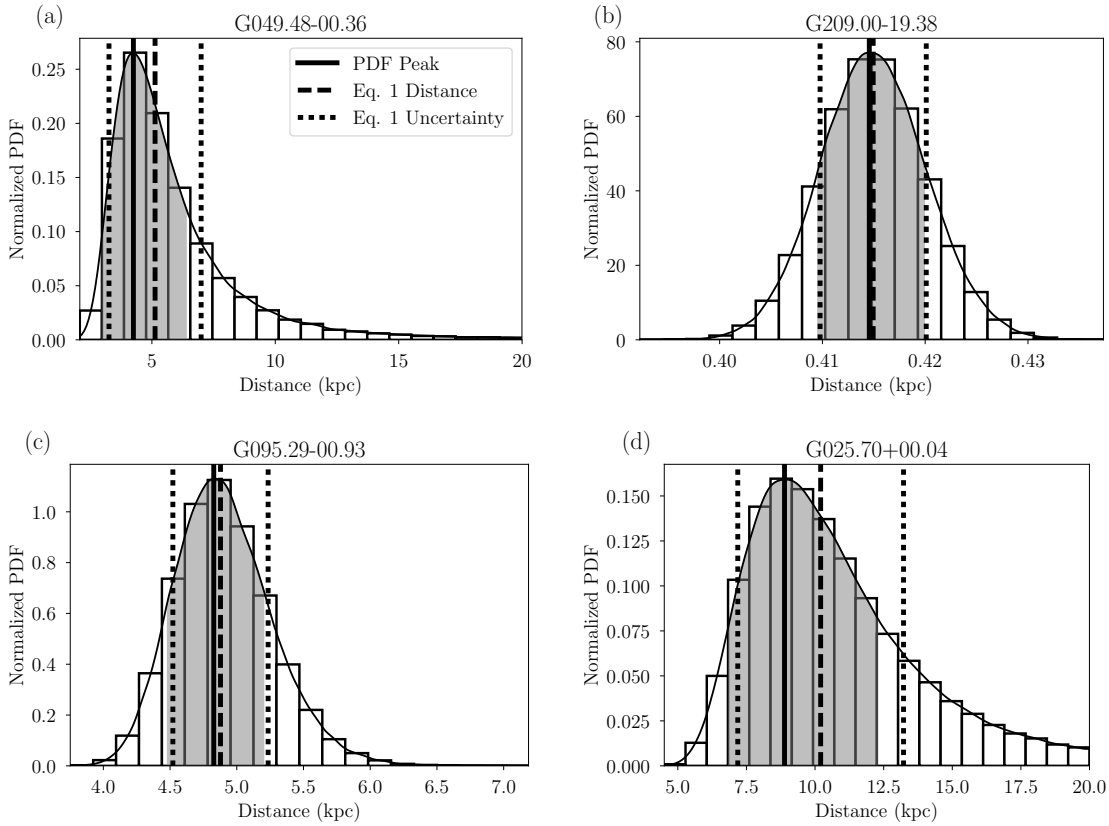

Figure 3.2: Normalized parallax distance probability distribution functions (PDFs) for four HMSFRs. The solid curve is the kernel density estimator (KDE) of the distribution; the solid vertical line is the peak of the KDE and our assigned parallax distance. The dashed vertical line is the parallax distance given by Equation 3.1. The vertical dotted lines span the symmetric uncertainty range in the parallax distance derived by propagating the parallax uncertainty through Equation 3.1. The filled region is the uncertainty range derived using the KDE (see text). Panel (a) (G049.48−00.36; W 51 IRS2) has the largest fractional parallax uncertainty and thus has the most skewed PDF. Panel (b) (G209.00-19.38; Orion Nebula) has the smallest fractional parallax uncertainty and has the PDF closest to a Gaussian distribution. Panel (c) (G095.29-00.93) has a typical fractional parallax uncertainty. Panel (d) (G025.70+00.04) has a large fractional parallax uncertainty. It has the largest deviation from the Monte Carlo-defined parallax distance and the parallax distance derived using Equation 3.1.

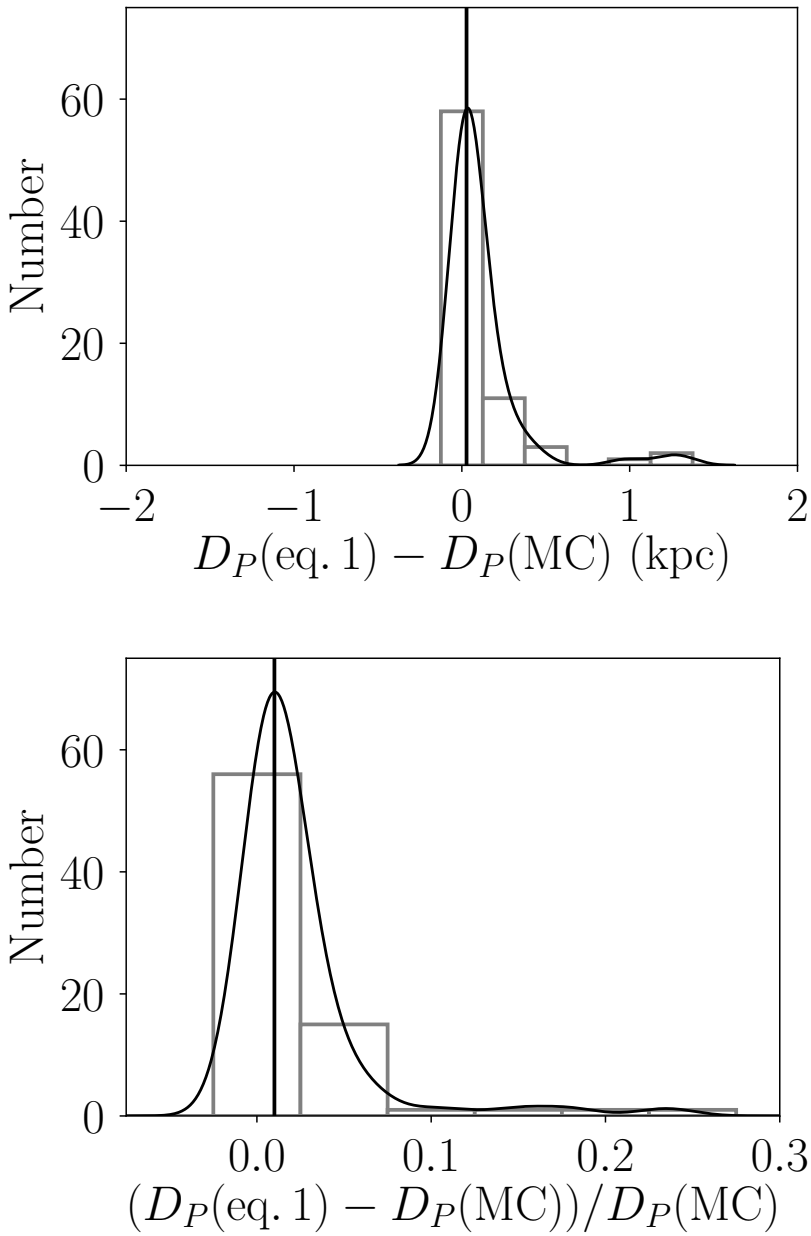

Figure 3.3: Difference (top) and fractional difference (bottom) between parallax distances derived using Equation 3.1, $D_P(\mathrm{eq.\,1})$, and those derived using the Monte Carlo method, $D_P(\mathrm{MC})$. The solid curve is the KDE fit to the difference distribution and the solid vertical line is the median of the distribution.

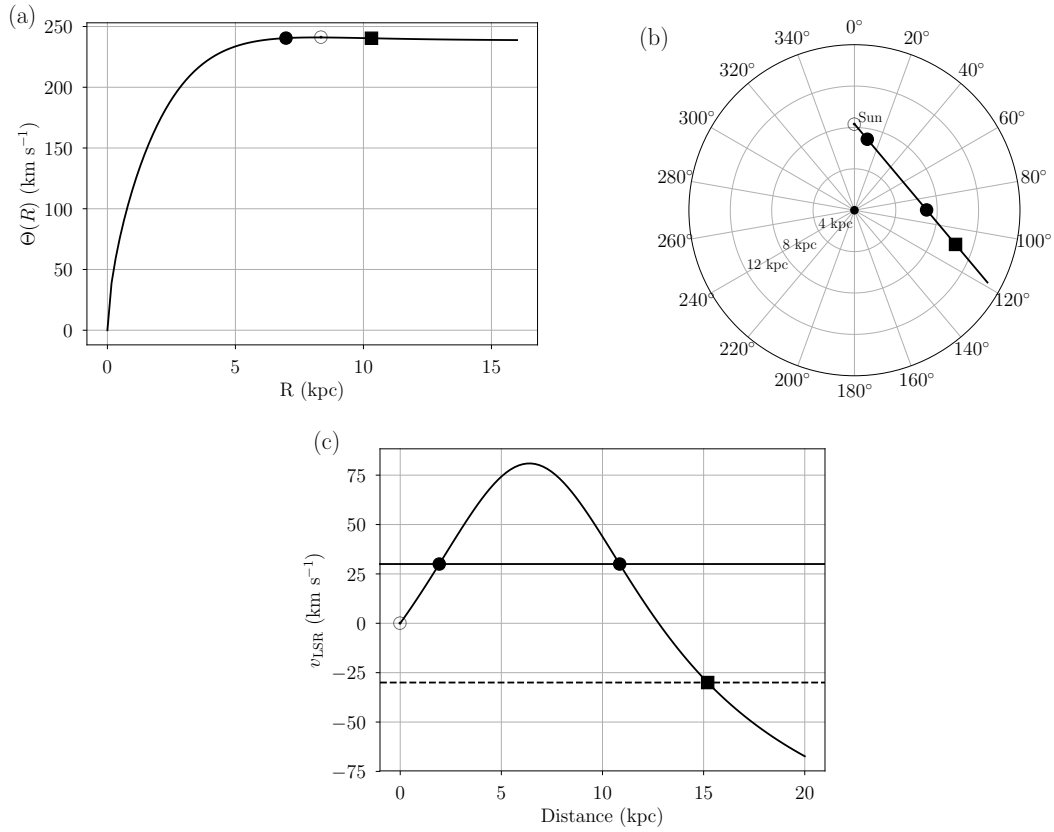

Figure 3.4: Schematic of the kinematic distance technique. Panel (a) is the Reid et al. (2014) rotation curve. Panel (b) is a face-on view of the Galaxy with the Galactic Center located at the center and the sun located 8.34 kpc in the direction $\theta_{\rm Az} = 0°$. The concentric circles are 4, 8, and 12 kpc in R and $\theta_{\rm Az}$ is given in degrees. The solid line is a line of sight through the Galaxy with $\ell = 40°$. Panel (c) is the LSR velocity profile along this line of sight. An object with $V_{\rm LSR} = 30\,{\rm km\,s^{-1}}$ in this direction (solid horizontal line) is an inner Galaxy object and has two possible kinematic distances (black circles). An object with $V_{\rm LSR} = -30\,{\rm km\,s^{-1}}$ (dashed horizontal line) is an outer Galaxy object and has only one possible kinematic distance (black square). Open circles show the location of the sun.

et al., 2009c, 2014). These streaming motions compromise the accuracy of kinematic distances in a complicated, uncertain way and are typically not accounted for in the derivation of kinematic distances.

A face-on view of the Anderson et al. (2012, hereafter A12) kinematic distance uncertainty model is shown in Figure 3.5. The A12 model includes uncertainties that stem from: (1) the variation in kinematic distances when using different GRMs; (2) the adopted values of the solar Galactocentric radius, R_0, and solar circular orbit speed, Θ_0; and, (3) including a global $7\,\mathrm{km\,s^{-1}}$ streaming motion uncertainty. This streaming motion uncertainty is an estimate of the true global streaming motion uncertainty, which may be between 5 and $10\,\mathrm{km\,s^{-1}}$ (Burton, 1966). They did not, however, consider uncertainties with the GRMs or in the solar motion parameters that define the LSR.

Here, we discuss three methods for calculating kinematic distances: the traditional method using the Brand & Blitz (1993) GRM (Method A), the traditional method using updated solar motion parameters and the Reid et al. (2014) GRM (Method B), and a new Monte Carlo technique using the Reid et al. (2014) GRM (Method C).

3.4.1 Method A: Traditional Method, Brand & Blitz (1993) GRM

The traditional method for calculating kinematic distances uses a GRM and the measured position and LSR velocity, $(\ell, b, V_{\mathrm{LSR}})$, of an object to determine the distance(s) that correspond to the measured LSR velocity. This is typically accomplished by finding the minimum difference between the GRM LSR velocity and the measured LSR velocity (see Figure 3.4).

We derive the Method A kinematic distances for our sample of HMSFRs using the Brand & Blitz (1993) GRM and the uncertainty model from A12. This rotation curve and uncertainty model provide the kinematic distances and distance uncertainties listed in the *WISE* Catalog. We resolve the KDA by finding the kinematic distance closest to the parallax distance. If the region has an LSR velocity within $20\,\mathrm{km\,s^{-1}}$ of the tangent point velocity, we assign it to the tangent point. A12 used a similar tangent point strategy, but with a velocity cutoff of $10\,\mathrm{km\,s^{-1}}$. Our $20\,\mathrm{km\,s^{-1}}$ cutoff is more conservative and is more consistent with the GRM uncertainties discussed in the following sections.

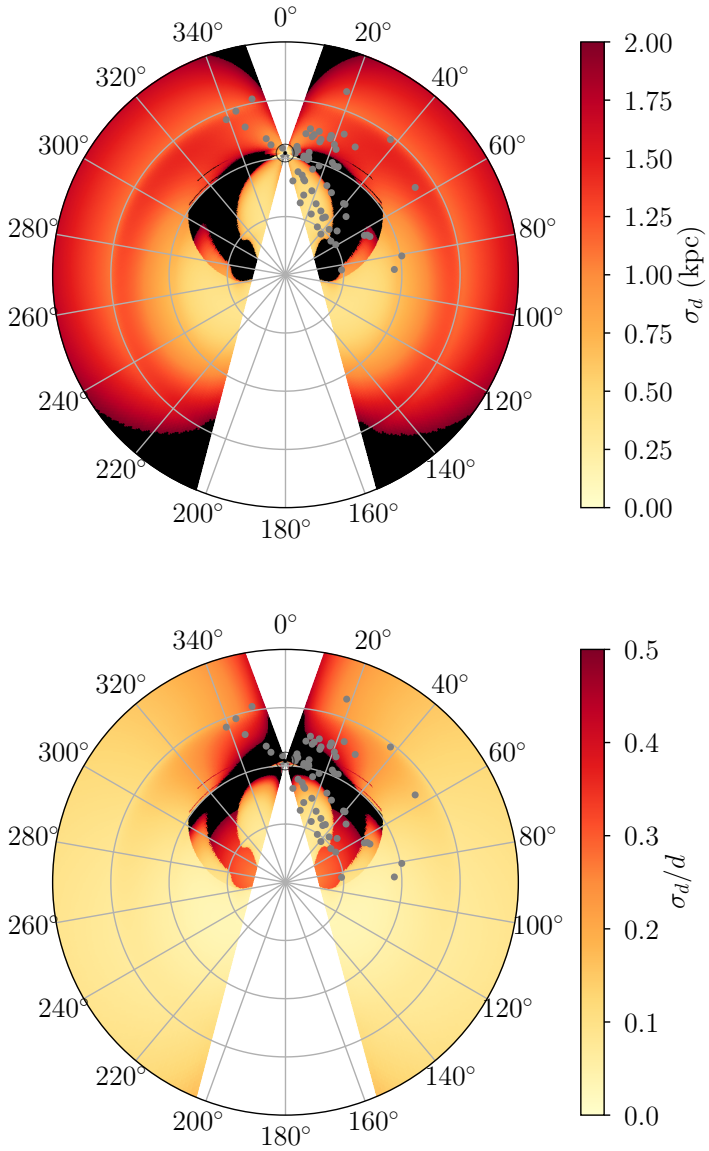

Figure 3.5: Face-on Galactic view of the A12 kinematic distance uncertainty model. The top panel is the absolute distance uncertainty and the bottom panel is the fractional distance uncertainty. The Galactic Center is located at the origin and the sun is located 8.34 kpc in the direction $\theta_{\rm Az} = 0°$. The concentric circles are 4, 8, and 12 kpc in R and $\theta_{\rm Az}$ is given in degrees. The color represents the distance uncertainty. The regions $-15° < \ell < 15°$ and $160° < \ell < 200°$ are masked (white) since kinematic distances are very inaccurate toward the Galactic Center and Galactic Anti-center. The black regions represent distance uncertainties greater than $\sigma_d = 2\,$kpc (top) or $\sigma_d/d = 0.5$ (bottom). The gray points are the HMSFRs in our sample.

3.4.2 Method B: Updated Solar Motion Parameters, Reid et al. (2014) GRM

In 1985, the LSR was *defined* by the International Astronomical Union Commission 33 as $220\,\mathrm{km\,s^{-1}}$ in the direction $(\ell, b) = (90^\circ, 0^\circ)$ with a solar non-circular motion of $20\,\mathrm{km\,s^{-1}}$ in the direction $\alpha = 18^\mathrm{h}$, $\delta = +30^\circ$ (1900) (Kerr & Lynden-Bell, 1986). Precessing to the modern epoch (J2000), the solar non-circular motion is defined in Galactic Cartesian coordinates as $U_\odot^\mathrm{Std} = 10\,\mathrm{km\,s^{-1}}$ in the direction of the GC, $V_\odot^\mathrm{Std} = 15\,\mathrm{km\,s^{-1}}$ in the direction of the solar orbit, and $W_\odot^\mathrm{Std} = 7\,\mathrm{km\,s^{-1}}$ in the direction of the North Galactic Pole. Since this definition was adopted, many authors have published more accurate derivations of the solar non-circular motion parameters. For example, Reid et al. (2014) derived updated solar motion parameters by fitting a Persic et al. (1996) universal rotation curve to the full phase-space kinematics of a sample of maser parallaxes and proper motions toward HMSFRs. The Persic et al. (1996) universal rotation curve is a physically motivated GRM, rather than an empirical model, that includes the gravitational potential of both the disk and halo. The Persic et al. (1996) universal rotation curve is given by

$$\Theta(R) = a_1 \left[\frac{1.97\beta x^{1.22}}{(x^2 + 0.78^2)^{1.43}} + (1-\beta)\, x^2 \frac{1 + a_3^2}{x^2 + a_3^2} \right]^{1/2} \tag{3.3}$$

where $x = R/(a_2 R_0)$ and $\beta = 0.72 + 0.44 \log_{10}[(a3/1.5)^5]$. Here, a_1, a_2, and a_3 are the parameters fit by Reid et al. (2014). These parameters, as well as the updated solar motion parameters fit by Reid et al. (2014), are listed in Table 3.2.

To correct the LSR velocities in our sample for the updated solar non-circular motion parameters, we first convert the measured LSR velocity to a heliocentric velocity via

$$V_\mathrm{helio} = V_\mathrm{LSR} - \left(U_\odot^\mathrm{Std} \cos\ell + V_\odot^\mathrm{Std} \sin\ell \right) \cos b - W_\odot^\mathrm{Std} \sin b. \tag{3.4}$$

Next, we use the Reid et al. (2014) solar motion parameters to derive the revised LSR velocity, $V_\mathrm{LSR}^\mathrm{Rev}$:

$$V_\mathrm{LSR}^\mathrm{Rev} = V_\mathrm{helio} + \left(U_\odot^\mathrm{Rev} \cos\ell + V_\odot^\mathrm{Rev} \sin\ell \right) \cos b + W_\odot^\mathrm{Rev} \sin b. \tag{3.5}$$

Table 3.2: Universal Rotation Curve Parameters from Reid et al. (2014)

Parameter	Value
$U_{\odot}^{\mathrm{Rev}}$ (km s^{-1})	10.5 ± 1.7
$V_{\odot}^{\mathrm{Rev}}$ (km s^{-1})	14.4 ± 6.8
$W_{\odot}^{\mathrm{Rev}}$ (km s^{-1})	8.9 ± 0.9
R_0 (kpc)	8.31 ± 0.16
a_1 (km s^{-1})	241 ± 8
a_2	0.90 ± 0.06
a_3	1.46 ± 0.16

Note — These rotation curve parameters are derived for the Persic et al. (1996) universal rotation curve (see equation 3.3).

The uncertainty in this LSR velocity ($\sigma_V^{\rm Rev}$) includes contributions from the uncertainty in the measured LSR velocity (σ_V) and the uncertainties in the Reid et al. (2014) solar motion parameters, $\sigma_{U\odot}^{\rm Rev}, \sigma_{V\odot}^{\rm Rev}, \sigma_{W\odot}^{\rm Rev}$. The combined uncertainty in the revised LSR velocity is

$$\sigma_V^{\rm Rev^2} = \sigma_V^2 + \left(\sigma_{U\odot}^{\rm Rev} \cos\ell\cos b\right)^2 + \left(\sigma_{V\odot}^{\rm Rev} \sin\ell\cos b\right)^2 + \left(\sigma_{W\odot}^{\rm Rev} \sin b\right)^2 \tag{3.6}$$

For simplicity, we ignore the cross-terms between the solar motion parameter uncertainties. Including these cross-terms would have little effect since Reid et al. (2014) finds that the magnitude of the Pearson product-moment correlation coefficients between these parameters is small, ranging between 0.011 and 0.017.

To compute the Method B kinematic distances to our sample of HMSFRs, we use the Reid et al. (2014) fits to the Persic et al. (1996) universal rotation curve and these revised LSR velocities. As before, we assign the near or far KDAR by determining which kinematic distance is closest to the parallax distance. If the HMSFR has an LSR velocity within $20\,{\rm km\,s^{-1}}$ of the tangent point velocity, we assign it to the tangent point distance. The Method B kinematic distance uncertainties are again determined by the A12 kinematic distance uncertainty model.

3.4.3 Method C: Monte Carlo Method, Reid et al. (2014) GRM

Here, we develop a method to derive kinematic distances and their uncertainties in a more statistically robust way. With this method we resample all measured and derived parameters within their uncertainties and determine the PDF of kinematic distances.

We first correct the measured LSR velocities as described above. We then resample the revised LSR velocities from a normal distribution centered on the nominal revised LSR velocity, $V_{\rm LSR}^{\rm Rev}$, with a width $\sigma_V^{\rm Rev}$. The width of this distribution is the total revised LSR velocity uncertainty, which includes both the measured uncertainty and the uncertainties in the solar motion parameters.

We also resample the Reid et al. (2014) universal Galactic rotation curve parameters, including R_0, from a normal distribution centered on the nominal values and a width equal to the uncertainty (see Equation 3.3 and Table 3.2). The variation of this resampled rotation curve is shown in Figure 3.6. Unlike A12, we do not add any additional streaming motion uncertainty into these calculations because the derivation of the Reid et al. (2014) rotation curve inherently includes uncertainties due to

streaming motions.

By resampling the above parameters 10^5 times for each HMSFR, we derive the kinematic distance PDF for each object (see example for G032.04+00.05 in Figure 3.7). Each panel in Figure 3.7 represents one distance we derive: the Galactocentric radius, R, the Galactocentric radius of the tangent point, $R_{\rm tan}$, the near kinematic distance, $d_{\rm near}$, the far kinematic distance, $d_{\rm far}$, and the tangent point kinematic distance, $d_{\rm tan}$. The shapes of the PDFs are determined by the uncertainties in the LSR velocities, the Galactocentric radius of the solar orbit, and the parameters of the rotation curve model.

We fit each PDF with a KDE derived using the linear combination technique from Jones (1993). The peak of this KDE is the most probable kinematic distance, and the width and shape of the KDE describe the range of possible kinematic distances. Similar to how we defined parallax distances, we define the Method C kinematic distance as the peak of the KDE. The uncertainty in this distance is the 68.3% confidence interval.

We resolve the KDAR in the same way as in the previous two methods. If the object has a velocity in excess of the magnitude of the tangent point velocity, then the uncertainty in the tangent point distance is the formal Monte Carlo uncertainty (i.e., the 68.3% confidence interval). If the object's velocity is smaller than the magnitude of the tangent point velocity but still within $20\,{\rm km\,s^{-1}}$, then the tangent point distance uncertainty is the total range from the near distance to the far distance. In this velocity range, traditional KDAR techniques are inaccurate and the object could be anywhere between the near and far kinematic distance (A12).

A face-on Galactic view of the Monte Carlo kinematic distance uncertainties is shown in Figure 3.8. To construct these maps we use the Monte Carlo technique to compute the kinematic distance and distance uncertainties in bins of 2° in Galactic longitude and $2\,{\rm km\,s^{-1}}$ in velocity, with 10^4 Monte Carlo samples in each bin. Since the kinematic distance uncertainties derived in this method are not symmetric, we show the uncertainties in both the positive direction (away from the sun) and the negative direction (toward the sun).

3.5 Kinematic Distance Uncertainty

We assess the accuracy of kinematic distances by comparing the parallax and kinematic distances for each of the three kinematic distance methods. Table 3.3 lists

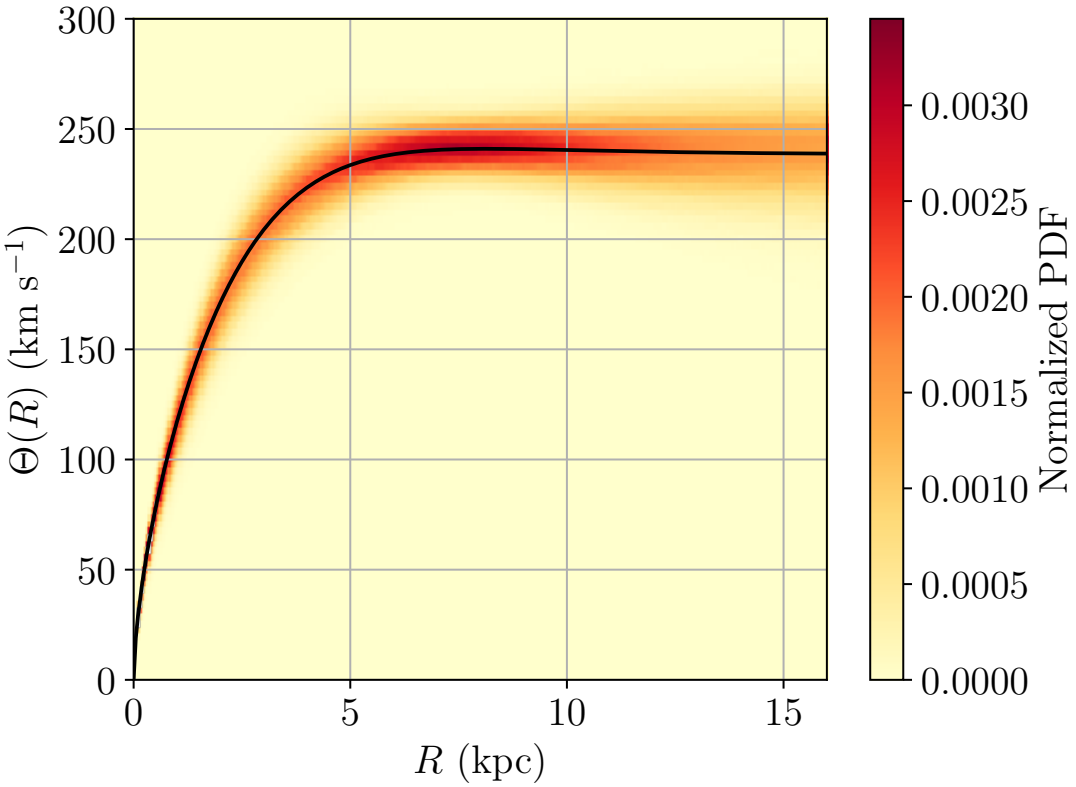

Figure 3.6: The Reid et al. (2014) universal rotation curve. The solid line is the nominal rotation curve using the parameters listed in Table 3.2. The colors represent the probability distribution function (PDF) derived by Monte Carlo resampling the rotation curve parameters within their uncertainties.

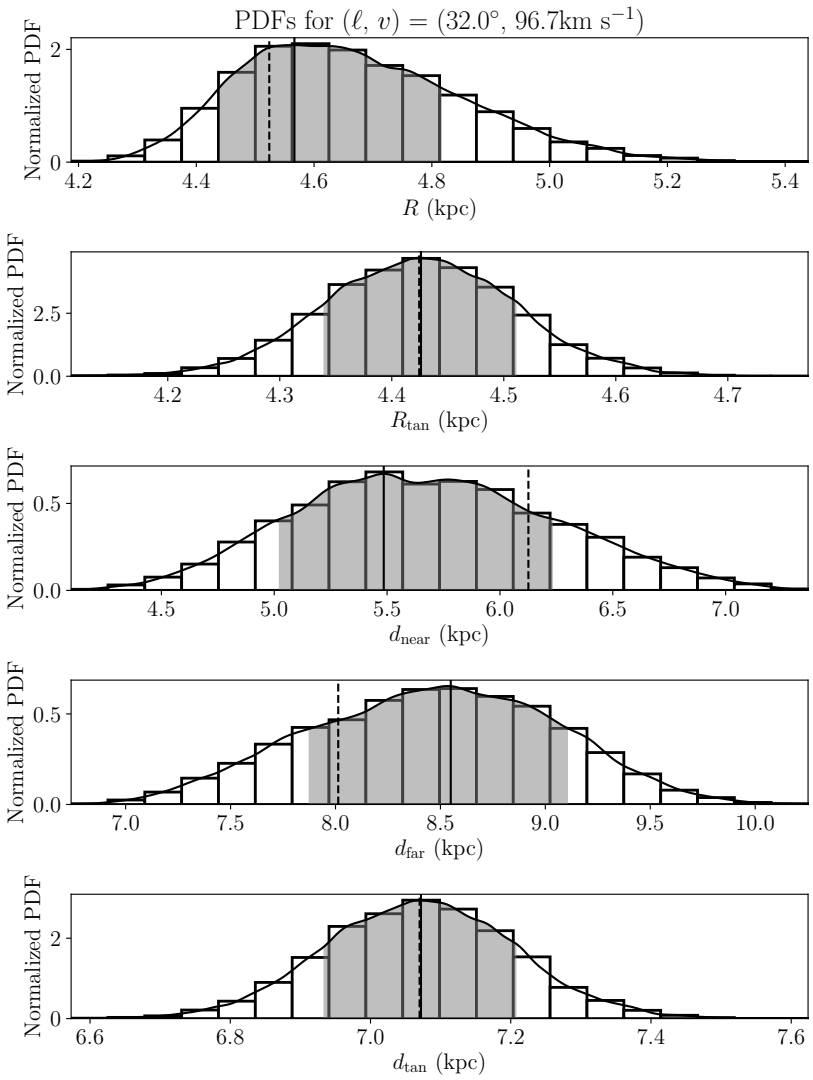

Figure 3.7: Normalized probability distribution functions (PDFs) of the Method C kinematic distances derived for G032.04+00.05, $(\ell, V_{\rm LSR}) = (32.0°, 96.7\ {\rm km\,s^{-1}})$. Shown from top to bottom are the kinematic distance PDFs for: Galactocentric radius, R, Galactocentric radius of tangent point, $R_{\rm tan}$, near kinematic distance, $d_{\rm near}$, far kinematic distance, $d_{\rm far}$, and tangent point kinematic distance, $d_{\rm tan}$. The PDFs are determined by Monte Carlo resampling the Reid et al. (2014) rotation curve within the uncertainties in the rotation curve parameters and then deriving the kinematic distances. The solid curve is the kernel density estimation (KDE) derived using the linear combination technique from Jones (1993). The dashed vertical line is the distance derived using the "traditional" kinematic techniques whereas the solid vertical line is the peak of the KDE. The gray region is the 68.3% confidence interval.

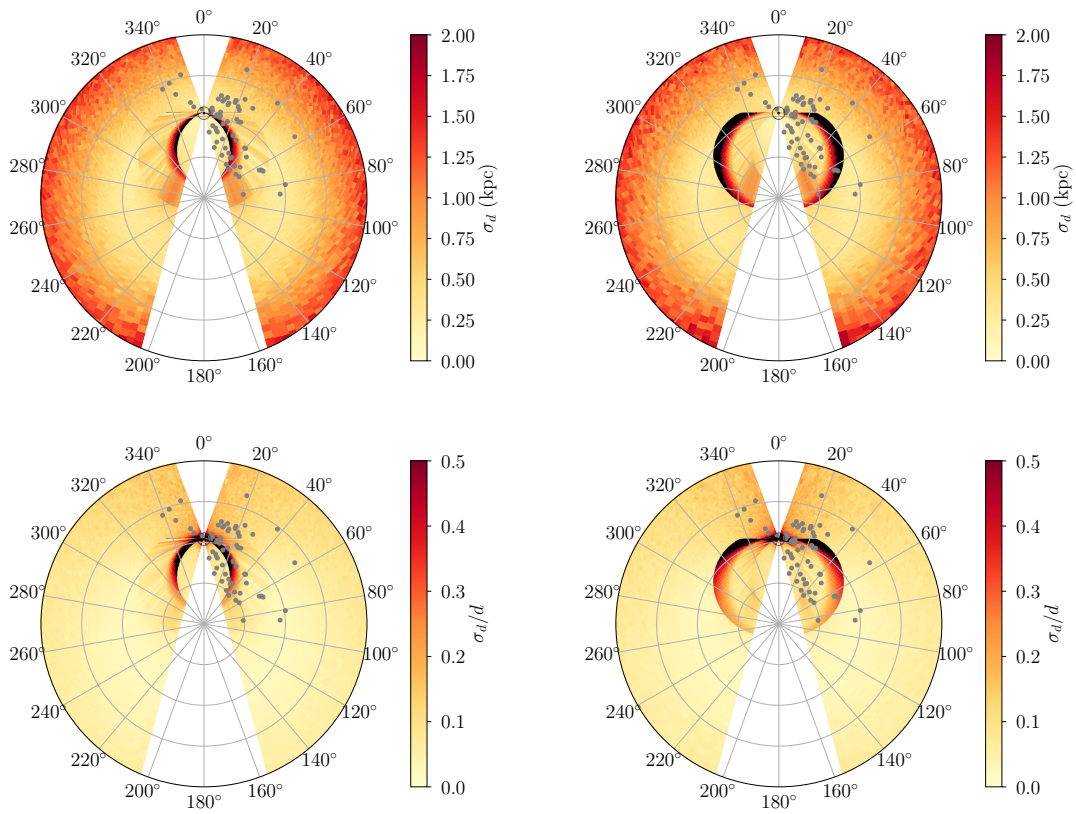

Figure 3.8: Face-on Galactic view of the Monte Carlo kinematic distance uncertainties. These uncertainties are not symmetric; the left panels are the uncertainty in the negative direction (toward the sun) and the right panels are the uncertainty in the positive direction (away from the sun). The top panels are the absolute distance uncertainties and the bottom panels are the fractional distance uncertainties. The Galactic Center is located at the origin and the sun is located 8.34 kpc in the direction $\theta_{\rm Az} = 0°$. The concentric circles are 4, 8, and 12 kpc in R and $\theta_{\rm Az}$ is given in degrees. The color represents the distance uncertainty. The regions $-15° < \ell < 15°$ and $160° < \ell < 200°$ are masked (white) since kinematic distances are very inaccurate toward the Galactic Center and Galactic Anti-center. The black regions represent distance uncertainties greater than $\sigma_d = 2\,$kpc (top) or $\sigma_d/d = 0.5$ (bottom). The gray points are the HMSFRs in our sample.

the derived distances for our sample: the Monte Carlo parallax distance, D_P, the kinematic distances using each of the three methods, D_A, D_B, and D_C, and their associated KDARs, KDAR$_A$, KDAR$_B$, and KDAR$_C$.

Here, we investigate the differences between the parallax distances and kinematic distances and compare those differences to the kinematic and parallax distance uncertainties. For each kinematic distance method we generate six figures: (1) a histogram of the difference between the kinematic distance and the parallax distance; (2) a histogram of the fractional distance difference; (3) a scatter plot of the distance difference as a function of the parallax distance; (4) a scatter plot of the distance difference minus the median difference as a function of the parallax distance; (5) a cumulative distribution function (CDF) of the ratio of the distance difference to the uncertainty in the distance difference; and (6) a CDF of the ratio of the distance difference minus the median difference to the difference uncertainty.

The distance difference histograms reveal any systematic differences between the kinematic and parallax distances. The scatter plots uncover correlations between the distance difference and the parallax distance. Finally, the CDFs characterize the accuracy of the kinematic and parallax distance uncertainties; if the kinematic and parallax distance uncertainties are random and are an accurate representation of the data, the CDF should follow a normal distribution.

We first compare the parallax distances to the Method A kinematic distances, D_A. The distance differences are shown in Figure 3.9. We compute the mean, median, and standard deviation of the distance difference (i.e., $D_A - D_P$), the absolute distance difference (i.e., $|D_A - D_P|$), the fractional distance difference (i.e., $(D_A - D_P)/D_P$), and the absolute fractional distance difference (i.e., $|D_A - D_P|/D_P$). These values are listed in Table 3.4. The fractional distance difference distribution in Panel (b) has a long tail toward larger kinematic distances.

After subtracting the median offset, the kinematic distance uncertainties from the A12 model fit the differences between the kinematic and parallax distances well. Panel (f) of Figure 3.9 shows that the ratio of the distance difference (minus the median difference) to the difference uncertainty follows a normal distribution, indicating that the kinematic and parallax distance uncertainties accurately represent the random errors in the distances. The K–S statistic for this distribution is 0.121 which corresponds to a p–value of 0.203. Panel (d), however, shows that some of the error bars are large even when the difference between the kinematic and parallax distance

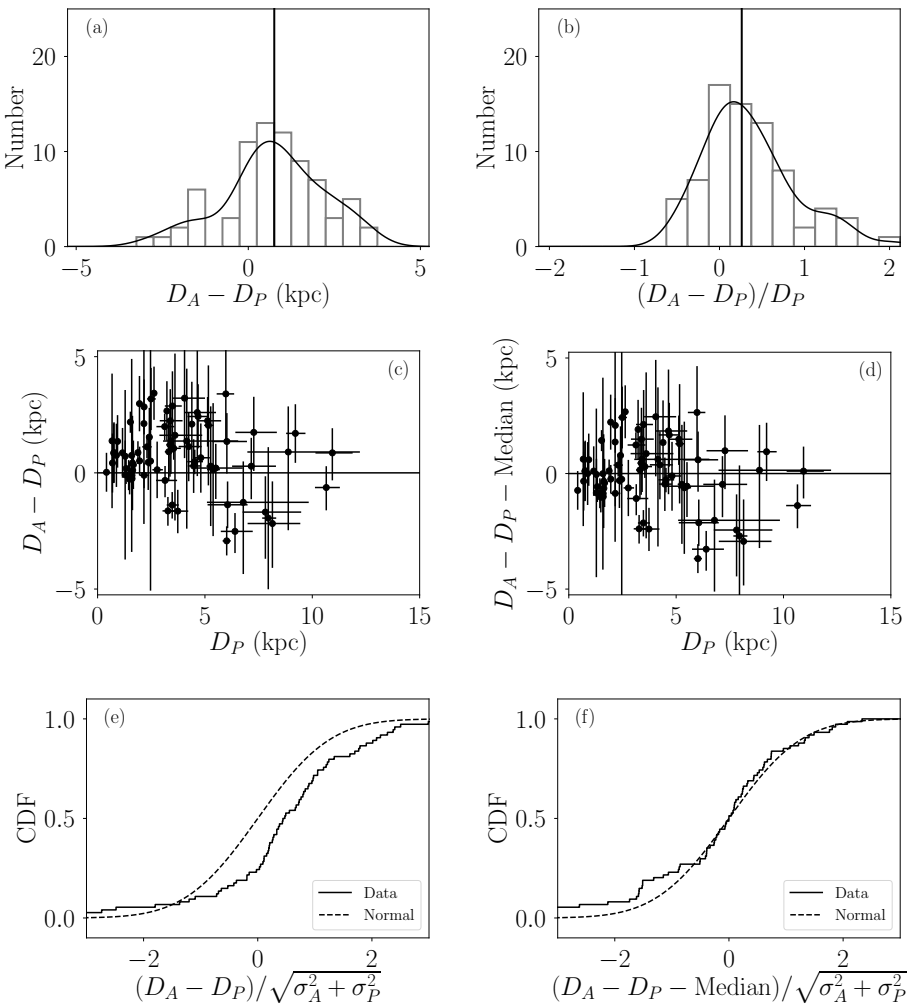

Figure 3.9: Difference between parallax distances and Method A kinematic distances. Panel (a): histogram of distance difference. The solid curve is the KDE fit to the difference distribution and the solid vertical line is the median of the distribution. Panel (b): histogram of the fractional distance difference. Panel (c): scatter plot of distance difference as a function of parallax distance. Panel (d): scatter plot of the distance difference minus the median distance difference as a function of parallax distance. Panel (e): cumulative distribution function (CDF) of the ratio of the distance differences to the distance difference uncertainties. Panel (f): CDF of the ratio of the distance differences minus the median difference to the distance difference uncertainties. The dashed curve in Panels (e) and (f) is the expected CDF for a normal distribution centered on zero. The CDF does not go to 0 on the left nor to 1 on the right because there is at least one source beyond the limits of the abscissas.

Table 3.3: Monte Carlo Parallax and Derived Kinematic Distances

Name	D_P (kpc)	D_A (kpc)	KDAR$_A$	D_B (kpc)	KDAR$_B$	D_C (kpc)	KDAR$_C$
G015.03−00.67	$1.96^{+0.15}_{-0.11}$	2.47 ± 0.60	N	2.33 ± 0.57	N	$2.39^{+0.31}_{-0.41}$	N
G016.58−00.05	$3.54^{+0.33}_{-0.27}$	4.60 ± 0.36	N	4.56 ± 0.36	N	$4.49^{+0.50}_{-0.40}$	N
G023.00−00.41	$4.53^{+0.38}_{-0.35}$	5.01 ± 0.38	N	4.96 ± 0.38	N	$4.80^{+0.56}_{-0.32}$	N
G023.44−00.18	$5.50^{+1.25}_{-0.94}$	5.71 ± 0.45	N	7.65 ± 0.60	T	$7.65^{+1.91}_{-2.04}$	T
G023.65−00.12	$3.12^{+0.45}_{-0.39}$	5.11 ± 0.39	N	5.07 ± 0.39	N	$4.92^{+0.56}_{-0.36}$	N
G023.70−00.19	$6.05^{+0.93}_{-0.93}$	4.68 ± 0.37	N	4.58 ± 0.37	N	$4.58^{+0.45}_{-0.49}$	N
G025.70+00.04	$8.88^{+3.34}_{-1.91}$	9.78 ± 0.46	F	9.50 ± 0.45	F	$9.60^{+0.58}_{-0.62}$	F
G027.36−00.16	$6.79^{+3.05}_{-1.69}$	5.52 ± 0.48	N	7.41 ± 0.65	T	$5.16^{+0.75}_{-0.32}$	N
G028.86+00.06	$7.16^{+1.15}_{-0.89}$	7.44 ± 0.83	T	7.30 ± 0.82	T	$7.30^{+1.73}_{-1.80}$	T
G029.86−00.04	$6.02^{+0.94}_{-0.68}$	7.37 ± 1.01	T	7.23 ± 1.00	T	$7.24^{+1.46}_{-1.52}$	T
G029.95−00.01	$5.12^{+0.63}_{-0.46}$	7.36 ± 0.92	T	7.23 ± 0.90	T	$7.24^{+1.56}_{-1.64}$	T
G031.28+00.06	$4.05^{+0.95}_{-0.54}$	7.26 ± 2.40	T	7.13 ± 2.35	T	$7.10^{+0.91}_{-0.94}$	T
G031.58+00.07	$4.64^{+0.87}_{-0.58}$	7.24 ± 2.59	T	7.10 ± 2.55	T	$7.11^{+1.59}_{-1.66}$	T
G032.04+00.05	$5.16^{+0.24}_{-0.20}$	7.20 ± 2.57	T	7.07 ± 2.52	T	$7.07^{+1.48}_{-1.59}$	T
G033.64−00.22	$6.40^{+0.83}_{-0.66}$	3.88 ± 0.43	N	3.65 ± 0.41	N	$3.56^{+0.48}_{-0.35}$	N
G034.39+00.22	$1.53^{+0.15}_{-0.10}$	3.71 ± 0.44	N	3.48 ± 0.41	N	$3.37^{+0.54}_{-0.41}$	N
G035.02+00.34	$2.30^{+0.22}_{-0.22}$	3.42 ± 0.44	N	3.19 ± 0.41	N	$3.17^{+0.47}_{-0.43}$	N
G035.19−00.74	$2.17^{+0.24}_{-0.21}$	2.06 ± 0.50	N	1.93 ± 0.47	N	$1.87^{+0.59}_{-0.46}$	N
G035.20−01.73	$3.14^{+0.56}_{-0.42}$	2.82 ± 0.46	N	2.62 ± 0.43	N	$2.60^{+0.35}_{-0.35}$	N
G037.43+01.51	$1.88^{+0.07}_{-0.08}$	2.75 ± 0.48	N	2.56 ± 0.45	N	$2.50^{+0.41}_{-0.33}$	N
G043.16+00.01	$10.93^{+0.94}_{-0.79}$	11.79 ± 0.71	F	11.52 ± 0.70	F	$11.40^{+0.65}_{-0.42}$	F
G043.79−00.12	$6.01^{+0.19}_{-0.19}$	3.09 ± 0.60	N	2.85 ± 0.55	N	$9.16^{+0.92}_{-0.72}$	F
G043.89−00.78	$7.82^{+1.67}_{-1.06}$	6.13 ± 1.12	T	6.01 ± 1.10	T	$6.01^{+2.50}_{-2.40}$	T

Table 3.3 continued

Table 3.3: Monte Carlo Parallax and Derived Kinematic Distances (continued)

Name	D_P (kpc)	D_A (kpc)	KDAR$_A$	D_B (kpc)	KDAR$_B$	D_C (kpc)	KDAR$_C$
G045.07+00.13	$7.95^{+0.37}_{-0.28}$	6.00 ± 3.04	T	5.89 ± 2.98	T	$5.91^{+1.96}_{-1.86}$	T
G045.45+00.05	$8.14^{+1.30}_{-1.16}$	5.96 ± 1.40	T	5.85 ± 1.37	T	$5.84^{+2.31}_{-2.22}$	T
G048.60+00.02	$10.65^{+0.63}_{-0.53}$	10.02 ± 0.75	F	9.83 ± 0.73	F	$9.83^{+0.58}_{-0.54}$	F
G049.19−00.33	$5.27^{+0.21}_{-0.20}$	5.55 ± 2.57	T	5.45 ± 2.55	T	$5.44^{+0.97}_{-0.95}$	T
G049.48−00.36	$4.15^{+2.40}_{-1.10}$	5.52 ± 2.91	T	5.42 ± 2.91	T	$5.43^{+1.37}_{-1.41}$	T
G049.48−00.38	$5.38^{+0.32}_{-0.29}$	5.52 ± 2.85	T	5.42 ± 2.84	T	$5.42^{+1.29}_{-1.15}$	T
G052.10+01.04	$3.60^{+1.27}_{-0.72}$	5.22 ± 3.44	T	5.12 ± 3.45	T	$5.15^{+1.94}_{-1.91}$	T
G059.78+00.06	$2.16^{+0.10}_{-0.10}$	4.28 ± 4.32	T	4.20 ± 2.82	T	$4.20^{+2.14}_{-2.16}$	T
G069.54−00.97	$2.46^{+0.08}_{-0.08}$	2.97 ± 5.57	T	2.91 ± 5.87	T	$2.91^{+2.05}_{-2.09}$	T
G074.03−01.71	$1.59^{+0.05}_{-0.04}$	2.34 ± 4.15	T	2.29 ± 0.98	T	$2.30^{+2.12}_{-2.05}$	T
G075.29+01.32	$9.21^{+0.47}_{-0.43}$	10.91 ± 1.18	F	9.75 ± 1.02	F	$9.61^{+1.09}_{-0.93}$	F
G075.76+00.33	$3.48^{+0.31}_{-0.26}$	2.09 ± 0.50	T	2.05 ± 0.47	T	$2.06^{+3.30}_{-2.05}$	T
G075.78+00.34	$3.73^{+0.49}_{-0.42}$	2.09 ± 0.82	T	2.05 ± 0.73	T	$2.04^{+2.54}_{-2.03}$	T
G076.38−00.61	$1.29^{+0.10}_{-0.08}$	2.00 ± 0.67	T	1.96 ± 0.62	T	$1.97^{+2.67}_{-1.96}$	T
G078.12+03.63	$1.63^{+0.08}_{-0.08}$	1.75 ± 0.60	T	1.72 ± 0.55	T	$1.72^{+2.85}_{-1.71}$	T
G078.88+00.70	$3.27^{+0.33}_{-0.25}$	1.64 ± 0.54	T	1.61 ± 0.51	T	$1.61^{+2.67}_{-1.60}$	T
G079.73+00.99	$1.33^{+0.14}_{-0.10}$	1.51 ± 0.65	T	1.49 ± 0.59	T	$1.48^{+2.43}_{-1.47}$	T
G079.87+01.17	$1.60^{+0.08}_{-0.06}$	1.49 ± 0.57	T	1.47 ± 0.52	T	$1.47^{+2.63}_{-1.46}$	T
G080.79−01.92	$1.60^{+0.13}_{-0.13}$	1.36 ± 0.65	T	1.33 ± 0.58	T	$1.33^{+2.42}_{-1.32}$	T
G080.86+00.38	$1.45^{+0.09}_{-0.08}$	1.35 ± 0.64	T	1.32 ± 0.58	T	$1.32^{+2.36}_{-1.31}$	T
G081.75+00.59	$1.49^{+0.09}_{-0.07}$	1.22 ± 0.65	T	1.20 ± 0.57	T	$1.20^{+2.33}_{-1.19}$	T
G081.87+00.78	$1.28^{+0.08}_{-0.07}$	1.20 ± 3.65	T	1.18 ± 4.01	T	$1.18^{+1.44}_{-1.17}$	T
G090.21+02.32	$0.67^{+0.02}_{-0.02}$	2.05 ± 2.90	F	1.48 ± 1.49	F	$2.23^{+0.84}_{-1.14}$	F

Table 3.3 continued

Table 3.3: Monte Carlo Parallax and Derived Kinematic Distances (continued)

Name	D_P (kpc)	D_A (kpc)	KDAR$_A$	D_B (kpc)	KDAR$_B$	D_C (kpc)	KDAR$_C$
G092.67+03.07	$1.62^{+0.06}_{-0.05}$	2.05 ± 2.03	F	1.52 ± 1.31	F	$2.23^{+1.11}_{-1.31}$	F
G094.60−01.79	$3.49^{+0.43}_{-0.35}$	6.36 ± 1.45	F	5.48 ± 1.23	F	$5.30^{+1.04}_{-0.82}$	F
G095.29−00.93	$4.81^{+0.42}_{-0.32}$	5.46 ± 1.44	F	4.68 ± 1.22	F	$4.72^{+0.84}_{-0.99}$	F
G097.53+03.18	$7.28^{+1.07}_{-0.86}$	9.02 ± 1.27	F	7.61 ± 1.07	F	$7.28^{+1.33}_{-0.85}$	F
G100.37−03.57	$3.42^{+0.14}_{-0.10}$	4.79 ± 1.42	F	4.06 ± 1.18	F	$4.03^{+1.24}_{-1.24}$	F
G105.41+09.87	$0.88^{+0.06}_{-0.04}$	1.63 ± 1.36	F	1.21 ± 0.94	F	$1.22^{+0.81}_{-0.81}$	F
G107.29+05.63	$0.76^{+0.07}_{-0.06}$	1.64 ± 1.30	F	1.24 ± 0.92	F	$1.19^{+0.83}_{-0.69}$	F
G108.18+05.51	$0.75^{+0.11}_{-0.08}$	1.60 ± 1.28	F	1.21 ± 0.90	F	$1.17^{+0.74}_{-0.65}$	F
G108.20+00.58	$4.24^{+0.60}_{-0.47}$	5.38 ± 1.37	F	4.48 ± 1.11	F	$4.18^{+1.13}_{-0.68}$	F
G108.47−02.81	$3.23^{+0.11}_{-0.10}$	5.89 ± 1.28	F	4.91 ± 1.02	F	$4.77^{+1.01}_{-0.84}$	F
G108.59+00.49	$2.49^{+0.22}_{-0.18}$	5.67 ± 1.32	F	4.72 ± 1.06	F	$4.75^{+0.81}_{-1.05}$	F
G109.87+02.11	$0.69^{+0.04}_{-0.04}$	1.12 ± 1.27	F	0.79 ± 0.81	F	$0.81^{+0.67}_{-0.67}$	F
G111.23−01.23	$3.38^{+0.57}_{-0.49}$	5.63 ± 1.27	F	4.67 ± 1.01	F	$4.54^{+1.33}_{-1.13}$	F
G111.25−00.76	$3.37^{+0.20}_{-0.17}$	4.58 ± 1.36	F	3.80 ± 1.10	F	$3.63^{+0.99}_{-0.78}$	F
G111.54+00.77	$2.63^{+0.13}_{-0.11}$	6.06 ± 1.14	F	5.01 ± 0.92	F	$4.88^{+1.00}_{-0.92}$	F
G121.29+00.65	$0.93^{+0.03}_{-0.04}$	2.28 ± 1.13	F	1.83 ± 0.88	F	$1.86^{+0.63}_{-0.73}$	F
G122.01−07.08	$2.17^{+0.11}_{-0.10}$	5.00 ± 1.18	F	4.10 ± 0.92	F	$3.92^{+1.02}_{-0.73}$	F
G123.06−06.30	$2.77^{+0.27}_{-0.22}$	2.91 ± 1.19	F	2.37 ± 0.95	F	$2.19^{+0.84}_{-0.60}$	F
G123.06−06.30	$2.36^{+0.14}_{-0.12}$	2.81 ± 1.18	F	2.29 ± 0.94	F	$2.35^{+0.54}_{-0.71}$	F
G133.94+01.06	$1.95^{+0.04}_{-0.04}$	4.93 ± 1.19	F	3.97 ± 0.95	F	$3.81^{+0.96}_{-0.69}$	F
G134.62−02.19	$2.41^{+0.11}_{-0.10}$	3.95 ± 1.25	F	3.19 ± 0.98	F	$3.07^{+0.85}_{-0.77}$	F
G135.27+02.79	$5.97^{+0.39}_{-0.43}$	9.37 ± 1.96	F	7.32 ± 1.53	F	$7.34^{+1.26}_{-1.51}$	F
G209.00−19.38	$0.41^{+0.01}_{-0.01}$	0.44 ± 0.84	F	0.24 ± 0.45	F	$0.07^{+0.64}_{-0.06}$	F

Table 3.3 continued

Table 3.3: Monte Carlo Parallax and Derived Kinematic Distances (continued)

Name	D_P (kpc)	D_A (kpc)	KDAR$_A$	D_B (kpc)	KDAR$_B$	D_C (kpc)	KDAR$_C$
G211.59+01.05	$4.39^{+0.13}_{-0.15}$	6.49 ± 1.82	F	5.06 ± 1.41	F	$4.79^{+1.45}_{-1.16}$	F
G229.57+00.15	$4.47^{+0.33}_{-0.27}$	4.77 ± 1.11	F	3.83 ± 0.88	F	$3.48^{+1.39}_{-1.09}$	F
G232.62+00.99	$1.67^{+0.11}_{-0.10}$	2.01 ± 1.04	F	1.59 ± 0.79	F	$1.52^{+0.58}_{-0.53}$	F
G236.81+01.98	$3.31^{+0.24}_{-0.18}$	4.22 ± 1.25	F	3.43 ± 0.98	F	$3.19^{+1.13}_{-0.70}$	F
G239.35−05.06	$1.16^{+0.09}_{-0.08}$	2.02 ± 1.07	F	1.59 ± 0.81	F	$1.62^{+0.52}_{-0.66}$	F
G240.31+00.07	$4.68^{+0.44}_{-0.49}$	7.11 ± 1.30	F	5.75 ± 1.04	F	$5.75^{+1.03}_{-1.13}$	F

is small. This implies that the kinematic distance uncertainty model is overpredicting the kinematic distance uncertainties in some cases. The median Method A kinematic distance uncertainty (i.e., σ_A/D_A) is 28.0%.

Next, we compare the parallax distances to the Method B kinematic distances, D_B. The differences between these two distances are shown in Figure 3.10, and the mean, median, and standard deviation statistics are listed in Table 3.4. The mean and median distance differences are significantly smaller than those found using Method A. The fractional distance difference distribution is both centered closer to zero and narrower than the Method A distribution. The tail toward larger fractional differences is not nearly as long using this method.

Once again, the A12 kinematic distance uncertainty model seems to accurately represent the typical differences between the parallax and kinematic distances. The K–S statistic for the median-corrected CDF is 0.081 with a p–value of 0.716, thus strongly implying that the uncertainties are sampled from a normal distribution. The kinematic distance errors are, however, large for sources with kinematic distances and parallax distances in good agreement. The median Method B kinematic distance uncertainty is the same as with method A at 28.0%.

Finally, we compare the parallax distances to the Method C kinematic distances, D_C. The distance differences using this method are shown in Figure 3.11 and the mean, median, and standard deviation statistics are in Table 3.4. These statistics and distributions are nearly identical to those found using Method B.

The kinematic distance uncertainties derived using the Monte Carlo method (Method C) are just as accurate as those given by the A12 kinematic distance uncertainty model (Methods A and B). Panel (f) of Figure 3.11 shows that the kinematic distance uncertainties follow a normal distribution with a K–S statistic of 0.083 (p–value is 0.681). This distribution and K–S statistic are nearly the same as that of Method B, yet the distance uncertainties are not assigned based on a model but rather derived based on the data and GRM. The median Method C kinematic distance uncertainty is slightly smaller than that of Method B at 25.8%. More than half (56%) of the Method C kinematic distance uncertainties are smaller than the Method B uncertainties. Despite these smaller error bars, panel (f) of Figure 3.11 shows that these kinematic distance uncertainties fit the data just as well as the A12 model used in Method A and B.

Table 3.4 summarizes the aforementioned results for the three kinematic distance

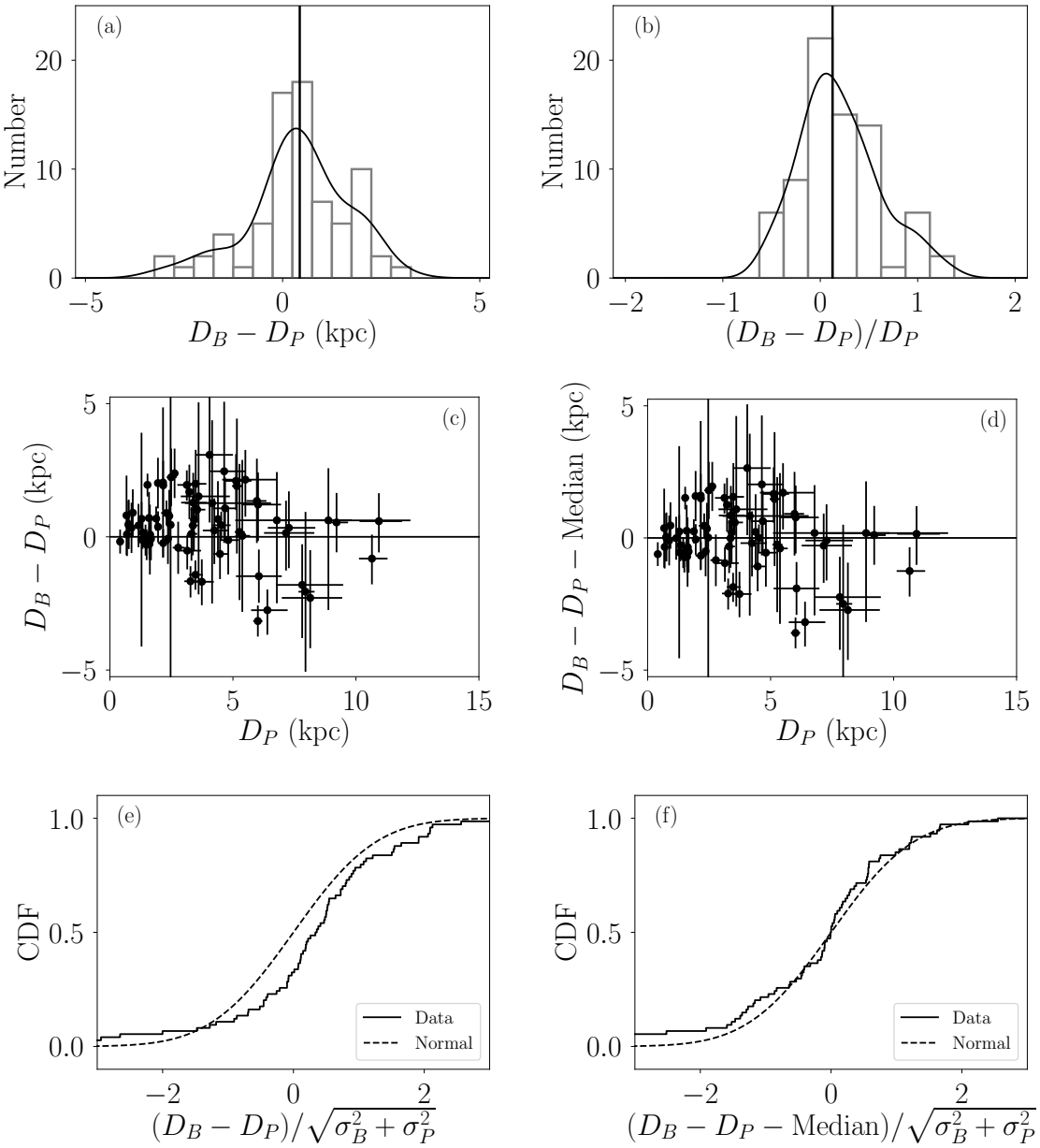

Figure 3.10: Same as Figure 3.9 but using Method B kinematic distances.

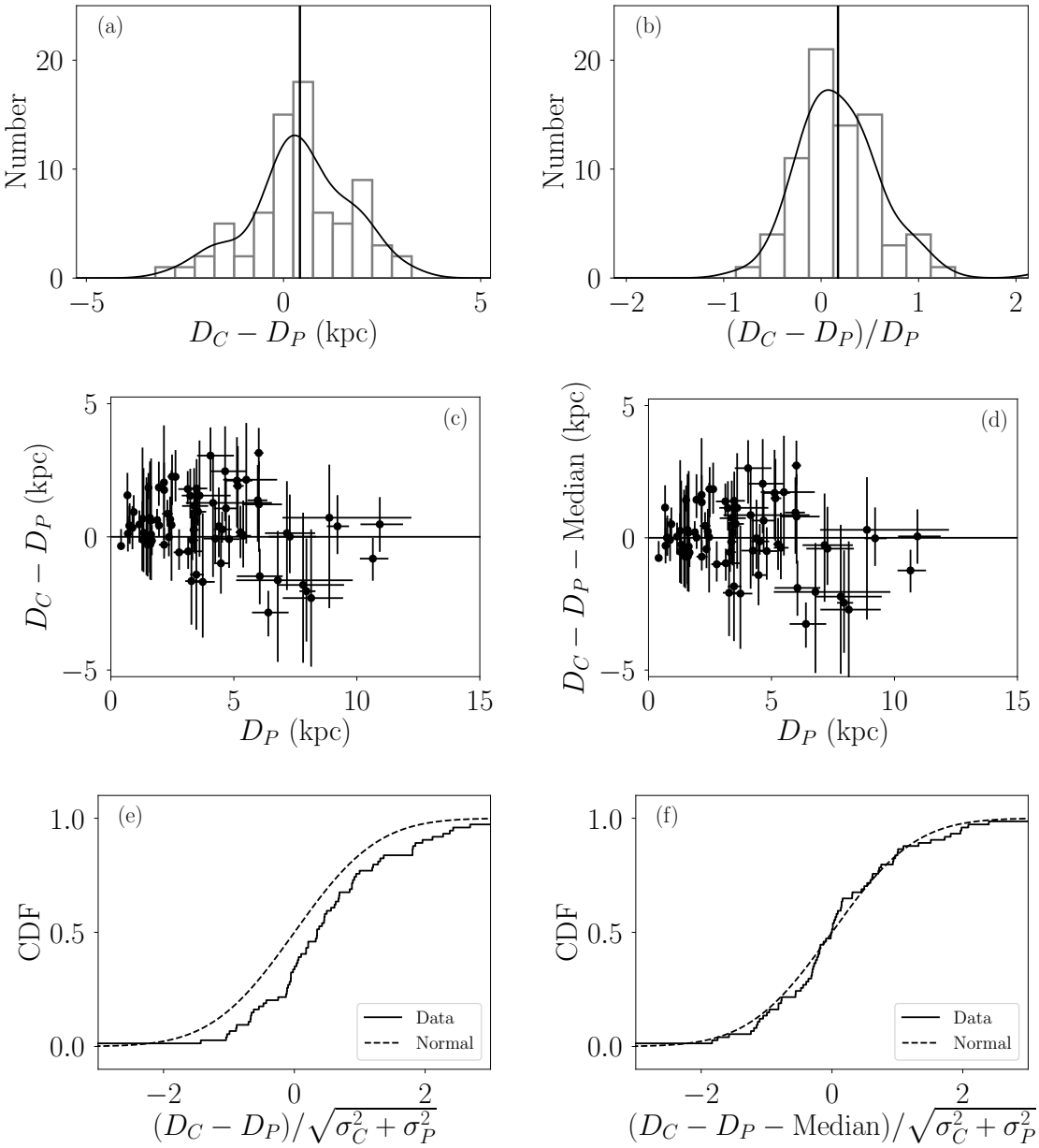

Figure 3.11: Same as Figure 3.9 but using Method C kinematic distances.

methods. The median absolute distance difference is nearly ∼40% smaller using Methods B and C, with a ∼12% smaller standard deviation. The median-corrected K–S statistic is about 30% smaller using Methods B and C, and nearly identical between Methods B and C. This suggests that the Monte Carlo-derived kinematic distance uncertainties (Method C) are just as accurate as the A12 kinematic distance uncertainty model (Method B). The median kinematic distance uncertainty, σ_D/D, is the smallest using Method C.

3.6 Kinematic Distance Ambiguity (KDA)

Thus far we resolved the KDA by assigning the kinematic distance closest to the parallax distance, or by assigning objects within $20\,\mathrm{km\,s^{-1}}$ of the tangent point velocity to the tangent point distance. The *WISE* Catalog of Galactic H II Regions (Anderson et al., 2014) contains the KDAR for 34 of our sources determined using a variety of KDAR techniques. Here, we compare our parallax-based KDARs to the *WISE* Catalog KDARs.

We first compare the LSR velocities of non-maser transitions in the *WISE* Catalog to the maser velocities from Reid et al. (2014). The *WISE* Catalog contains RRL velocities and/or non-maser molecular spectral line velocities for 34 HMSFRs: 6 regions with only RRL velocities, 11 regions with only molecular line velocities, and 17 regions with both. Since the RRL emission comes from the ionized gas of the HMSFR and the non-maser molecular line emission comes from molecular clouds associated with the HMSFR, the LSR velocities of these transitions need not be the same as that of the maser emission, which originates within the molecular envelope of the high-mass stars. Figure 3.12 shows the difference between the RRL and maser velocities and the difference between the molecular line velocities and maser velocities. The median difference is $-0.70\,\mathrm{km\,s^{-1}}$ with a standard deviation of $3.83\,\mathrm{km\,s^{-1}}$ for RRL velocities and $0.55\,\mathrm{km\,s^{-1}}$ with a standard deviation of $2.73\,\mathrm{km\,s^{-1}}$ for molecular line velocities. These distributions are consistent with the expected $\sim 10\,\mathrm{km\,s^{-1}}$ difference between maser spot emission region motions and bulk gas motions (e.g., Reid et al., 2009c, 2014). The difference in LSR velocities corresponds to differences in kinematic distances. The differences between the Method C kinematic distances derived using the RRL, molecular, and maser velocities are shown in Figure 3.13. The median difference is 0 kpc for both the RRL and maser distance difference and the molecular and maser distance difference, with standard deviations of 0.25 kpc and 0.21 kpc,

Table 3.4: Distance Difference Statistics

	Method A	Method B	Method C
$D - D_P$ (kpc)			
Median	0.75	0.43	0.42
Mean	0.74	0.40	0.42
Std. Dev.	1.42	1.24	1.23
$\lvert D - D_P \rvert$ (kpc)			
Median	1.13	0.68	0.71
Mean	1.29	1.00	1.01
Std. Dev.	0.95	0.83	0.83
$(D - D_P)/D_P$ (percent)			
Median	26	13	17
Mean	35	20	21
Std. Dev.	52	40	46
$\lvert D - D_P \rvert / D_P$ (percent)			
Median	33	24	26
Mean	46	34	36
Std. Dev.	43	30	36
σ_D/D (percent)			
Median	28.0	28.0	25.8
$(D - D_P - \text{Median})/\sqrt{\sigma_D^2 + \sigma_P^2}$			
K–S statistic	0.121	0.081	0.083
K–S p–value	0.203	0.716	0.681

respectively. The maximum fractional difference is 20% in both cases, which implies that the choice of LSR velocity tracer has a moderate impact on the derived kinematic distance.

If we limit our sample to inner Galaxy *WISE* Catalog objects more than 20 km s^{-1} from the tangent point velocity using the Reid et al. (2014) GRM, there are 9 HMSFRs. Of these, the KDAs are resolved using: H I emission/absorption and self-absorption experiments based on RRL velocities (2 objects; Anderson & Bania, 2009; Anderson et al., 2012), H I self-absorption experiments based on molecular line velocities (2 objects; Urquhart et al., 2012; Roman-Duval et al., 2009), and H_2CO absorption experiments (4 objects; Araya et al., 2002; Watson et al., 2003; Sewilo et al., 2004). One object is a visible H II region and thus likely located at the near distance.

Based on the KDAR determined using the Method C kinematic distance method and selecting the distance closest to the parallax distance, the *WISE* Catalog has incorrect KDARs for 3 of our sample objects: one source (G034.39+00.22) using an H I self-absorption experiment based on RRL velocities (Anderson & Bania, 2009) and two sources (G023.70-00.19, G035.02+00.34) using H_2CO absorption experiments (Watson et al., 2003; Sewilo et al., 2004). The Anderson & Bania (2009) KDAR resolution for G034.39+00.22 was determined only with H I self-absorption techniques, and, as the authors show in that paper, H I self-absorption techniques are much less reliable than H I emission/absorption techniques. Too, this object had a low confidence H I self-absorption detection (quality factor B in that paper). The H_2CO absorption spectra for the other two sources are marginal detections. The absorption feature for (G023.70−00.19) is on the wing of the RRL (Sewilo et al., 2004), and the absorption feature for G035.02+00.34 is weak and ∼5 km s^{-1} beyond the tangent point velocity (Watson et al., 2003). This sample size is too small to make any definitive conclusions about the accuracy of the KDAR techniques. Authors using the *WISE* Catalog KDARs should investigate the original KDAR work to assess the quality of the distance resolution.

3.7 Discussion

Based on the results of this analysis, we recommend the following prescription for deriving kinematic distances: (1) correct the measured LSR velocity using the Reid et al. (2014) solar motion parameters and Equations 3.4 and 3.5; (2) use the corrected

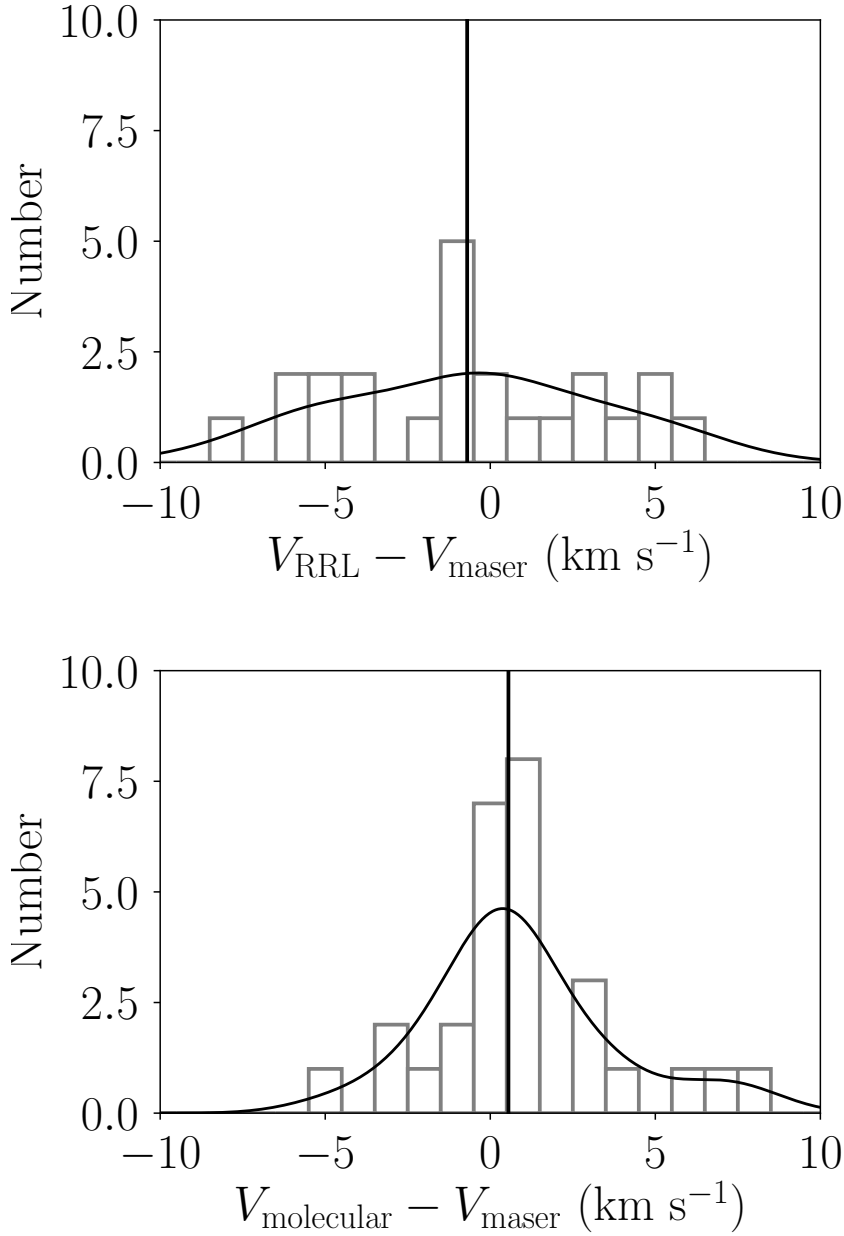

Figure 3.12: Difference between RRL and maser LSR velocity (top) and molecular line and maser LSR velocity (bottom). The solid curve is the KDE fit to each distribution, and the vertical line is the median.

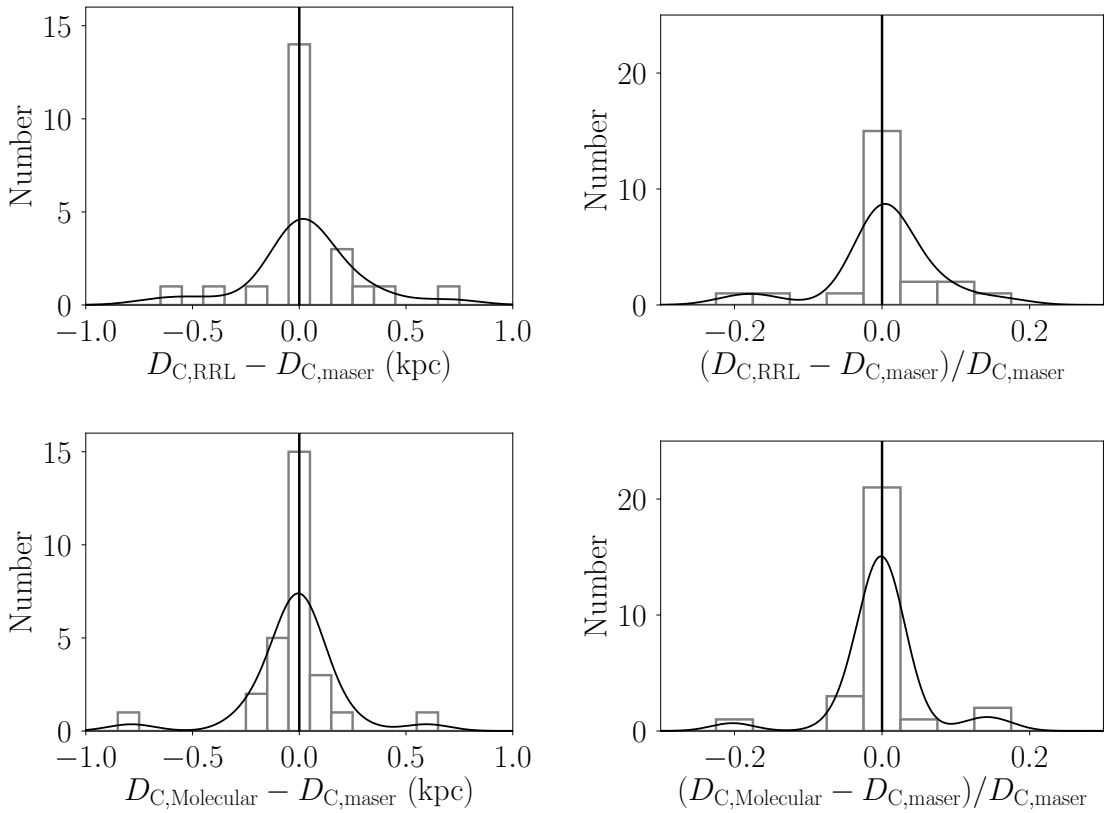

Figure 3.13: Difference between the Method C kinematic distances derived using the RRL and maser LSR velocities (top) and molecular line and maser LSR velocities (bottom). The absolute difference is shown in the left panels and the fractional difference is shown in the right panels. The solid curve is the KDE fit to each distribution, and the vertical line is the median.

LSR velocity and the Monte Carlo method (Method C) to derive the kinematic distances and uncertainties; and (3) use only the highest quality KDARs from the *WISE* Catalog (if available) to resolve the kinematic distance ambiguity. The *Python* code we used to calculate the Monte Carlo kinematic distances is publicly available and may be utilized through an online tool[4] (Wenger et al., 2017).

Changing the method used to derive kinematic distances may have important implications. When applying kinematic distances to Galactic morphological or metallicity structure analyses, it is important to consider the kinematic distance uncertainties and inaccuracies in the KDAR techniques. For example, Koo et al. (2017) recently re-analyzed the Leiden/Argentine/Bonn H I 21 cm line all-sky survey (Hartmann & Burton, 1997; Arnal et al., 2000; Bajaja et al., 2005; Kalberla et al., 2005) to characterize the spiral structure in the outer Galaxy. They derived kinematic distances to their H I features to produce a face-on map of the H I distribution beyond the solar orbit. Even though there is no KDA in this part of the Galaxy, their kinematic distances will be affected by the uncertainties discussed here. Their results, determining the pitch angles of the spiral features for example, may change significantly if they use the Monte Carlo method to derive the kinematic distances of their H I features.

Monte Carlo kinematic distances will also affect the interpretation of Galactic metallicity structure. For example, Balser et al. (2015) recently discovered azimuthal variations in the radial metallicity gradient of the Milky Way inferred by the electron temperatures of Galactic H II regions. They used the Reid et al. (2014) rotation curve to derive their kinematic distances and the A12 kinematic distance uncertainty model to assign distance uncertainties. After resampling their H II region distances within the A12 uncertainties, they determined that the azimuthal metallicity gradient variations were statistically significant. The Balser et al. (2015) result may be affected by the results of this analysis. Not only will the kinematic distances for their sample of H II regions change slightly, the uncertainties will change as well. These changes will affect the statistical significance of their result.

This new kinematic distance method will affect all distance estimation techniques that rely, at least in part, on kinematic distances. For example, Reid et al. (2016) used a Bayesian distance estimation method to derive the distance to HMSFRs. The priors in their method included the parallax distance (if available), the kinematic

[4] `http://doi.org/10.5281/zenodo.1166001`

distance with equal weight given to both the near and far kinematic distance, the Galactic latitude, and a spiral arm model of the Galaxy. Instead of using a Gaussian kinematic distance PDF, future Bayesian analyses should use the full Monte Carlo kinematic distance PDF.

The difference between Method A and Method C kinematic distances is fairly large, whereas the difference between Method B and Method C is small. Figure 3.14 shows the difference between the Method A and C distances as well as the Method B and C distances for LSR velocities along $\ell = 30°$. We choose this line of sight because it crosses both the inner and outer Galaxy through most of the Galactic disk. The difference between Method A and C is $< 0.5\,\mathrm{kpc}$ within the solar orbit, and approaches $3\,\mathrm{kpc}$ at a distance of $20\,\mathrm{kpc}$. This discrepancy is caused by the variations in the GRMs used by each method. The difference between Method B and C, however, is small ($\lesssim 0.5\,\mathrm{kpc}$) across the Galaxy since both methods use the same GRM.

The largest distinction between the different kinematic distance methods is the magnitude of the uncertainties. In Figure 3.15 we show the ratio of the Method C kinematic distance uncertainty to those of Methods A and B (the A12 model) along $\ell = 30°$. Except near the tangent point, the Method C kinematic distance uncertainties are smaller than the A12 model uncertainties. At a distance of $15\,\mathrm{kpc}$, the Model C uncertainty is half of the A12 model uncertainty. The spikes near $5\,\mathrm{kpc}$ and $9\,\mathrm{kpc}$ are located at the boundaries of the "tangent point region" (within $20\,\mathrm{km\,s^{-1}}$ of the tangent point velocity). Here, the Method C kinematic distance uncertainties are much larger than the A12 model uncertainties.

Although kinematic distances are not as accurate as parallax distances in the solar neighborhood, their accuracy is much better in distant regions of the Milky Way. To demonstrate this point, we generate a face-on view of the typical parallax distance uncertainty in the Galaxy (Figure 3.16). We assume a characteristic parallax uncertainty of $0.02\,\mu$as (Reid & Honma, 2014) which corresponds to a typical parallax distance uncertainty of $\sigma_d/\mathrm{kpc} = 0.02(d/\mathrm{kpc})^2$. This figure uses the same color scale as the Method C Monte Carlo kinematic distance uncertainty map in Figure 3.8. By comparing these figures we see that large regions of Galactic quadrants I and IV ($-90° < \ell < 90°$) have Method C kinematic distance uncertainties much smaller than the typical parallax distance uncertainties. In Figure 3.17 we show the ratio of the Method C kinematic distance uncertainty to the typical parallax distance

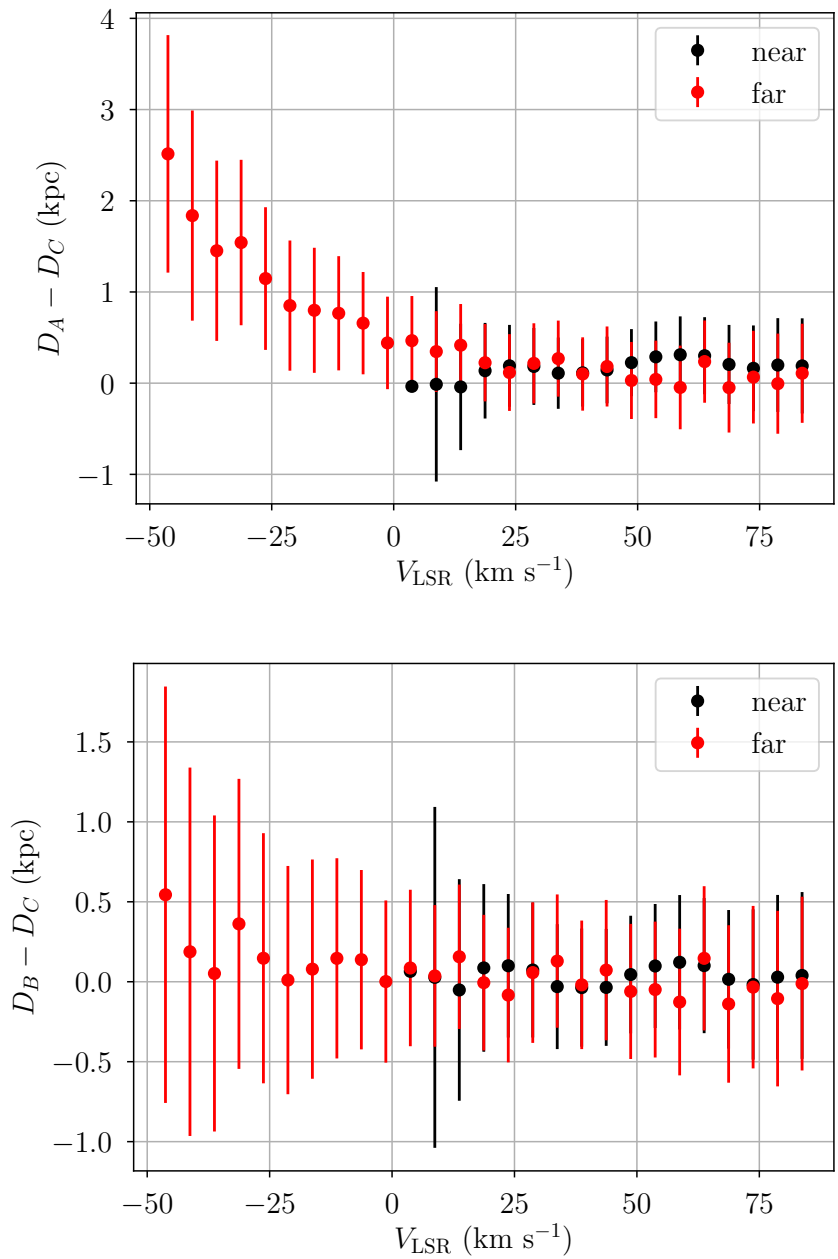

Figure 3.14: Difference between Method A and Method C kinematic distances (top) and Method B and Method C kinematic distances (bottom) as a function of LSR velocity in the direction $\ell = 30°$. The black points correspond to near kinematic distances and the red points correspond to far kinematic distances. The error bars are the combined uncertainties of both the A12 kinematic distance uncertainty model (Methods A and B) and the Method C Monte Carlo uncertainty. We exclude 20 km s^{-1} near the tangent point for clarity.

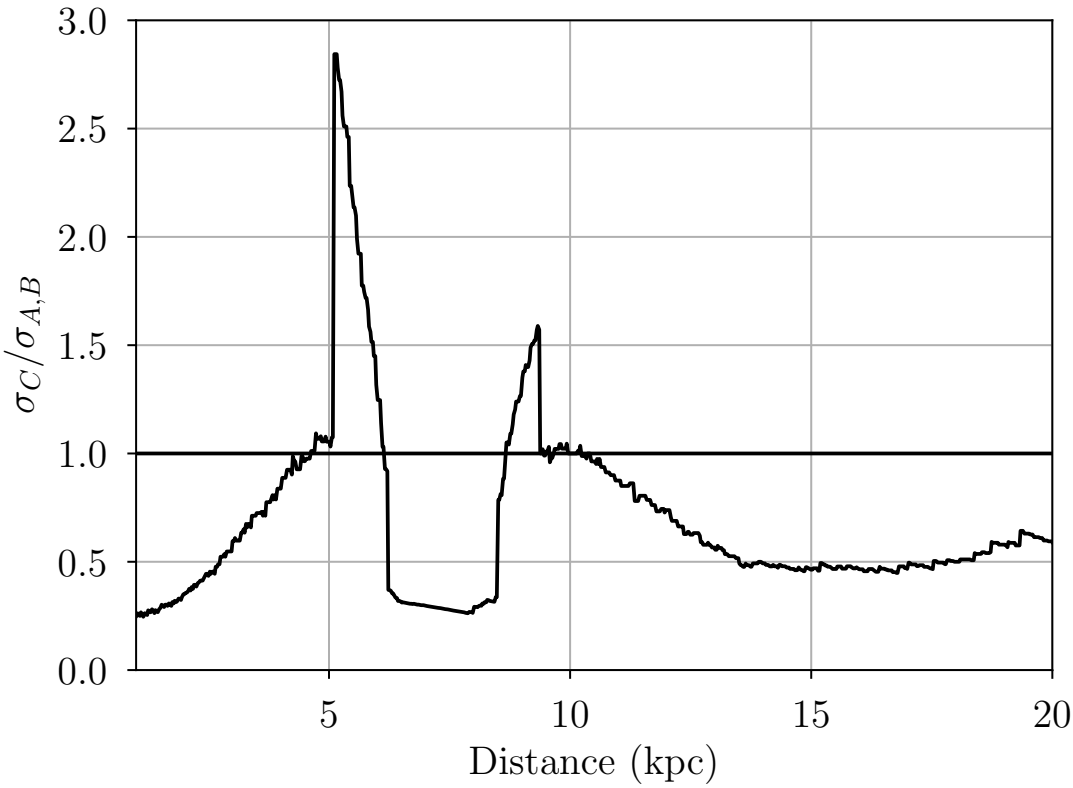

Figure 3.15: Ratio of the Method C Monte Carlo kinematic distance uncertainty to the A12 kinematic distance uncertainty model (Methods A and B) as a function of distance in the direction $\ell = 30°$. The solid vertical line indicates a ratio of one where $\sigma_C = \sigma_{A,B}$. The spikes near 5 kpc and 9 kpc are at the boundaries of the "tangent point region," defined where the LSR velocity is within 20 km s^{-1} of the tangent point velocity.

uncertainty along $\ell = 30°$. Beyond the tangent point at a distance of $\sim$8 kpc, the Method C kinematic distance uncertainties are smaller than the typical parallax distance uncertainty. This ratio reaches a minimum at about 14 kpc where the Method C kinematic distance uncertainty is less than 10% of the typical parallax distance uncertainty. The spikes near 5 kpc and 9 kpc are, again, located at the boundaries of the "tangent point region," where the Method C kinematic distance uncertainties are much larger.

The accuracy of the Method C kinematic distances is especially apparent when we consider that Galactic structure analyses are more interested in the Galactocentric positions of structure tracers $(R, \theta_{\rm Az}, z)$ than the heliocentric positions (ℓ, b, d). We derive the relationship between the distance uncertainty and uncertainties in R and $\theta_{\rm Az}$ in Appendix A. Figure 3.18 shows the face-on uncertainties in Galactocentric position given these uncertainties in parallax distance. The same analysis using the Monte Carlo kinematic distance uncertainties is shown in Figure 3.19. In large regions of Galactic quadrants I and IV ($-90° < \ell < 90°$), the Monte Carlo kinematic distances have smaller uncertainties in both R and $\theta_{\rm Az}$ than the parallax distances. Kinematic distances therefore determine not only the distance of objects, but also the *Galactocentric* position of objects more accurately than parallax distances when the object is far from the solar neighborhood.

Streaming motions will have a *systematic* effect on the accuracy of kinematic distances rather than a *random* effect as we have assumed in this analysis. With a much larger catalog of parallax observations of HMSFRs, we could compare kinematic and parallax distances and uncover any systematic differences. We may then be able to create a non-axisymmetric GRM that includes these non-circular motions. Such a task requires parallax observations uniformly across the entire Galactic disk.

3.8 Conclusions

We investigate the accuracy of kinematic distances by comparing the kinematic and parallax distances of 75 Galactic HMSFRs. We derive the kinematic distances using three different methods: the traditional method using the Brand & Blitz (1993) rotation curve and the IAU-defined solar motion parameters (Method A), the traditional method using the Reid et al. (2014) rotation curve and their revised solar motion parameters (Method B), and a new Monte Carlo method using the Reid et al. (2014) rotation curve and their revised solar motion parameters (Method C). The

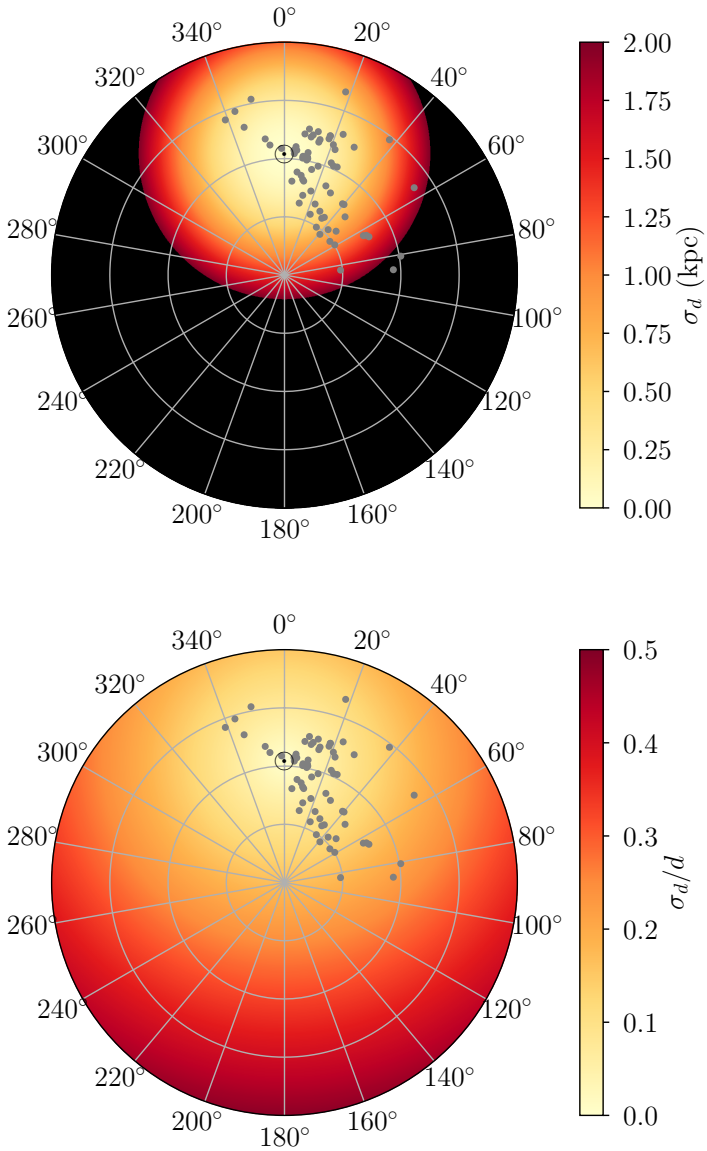

Figure 3.16: Face-on Galactic view of the parallax distance uncertainties assuming a typical parallax uncertainty of $0.02\,\mu$as. The top panel is the absolute distance uncertainty and the bottom panel is the fractional distance uncertainty. The Galactic Center is located at the origin and the sun is located 8.34 kpc in the direction $\theta_{\rm Az} = 0°$. The concentric circles are 4, 8, and 12 kpc in R and $\theta_{\rm Az}$ is given in degrees. The color represents the distance uncertainty. The black regions represent distance uncertainties greater than $\sigma_d = 2\,$kpc (top) or $\sigma_d/d = 0.5$ (bottom). The gray points are the HMSFRs in our sample.

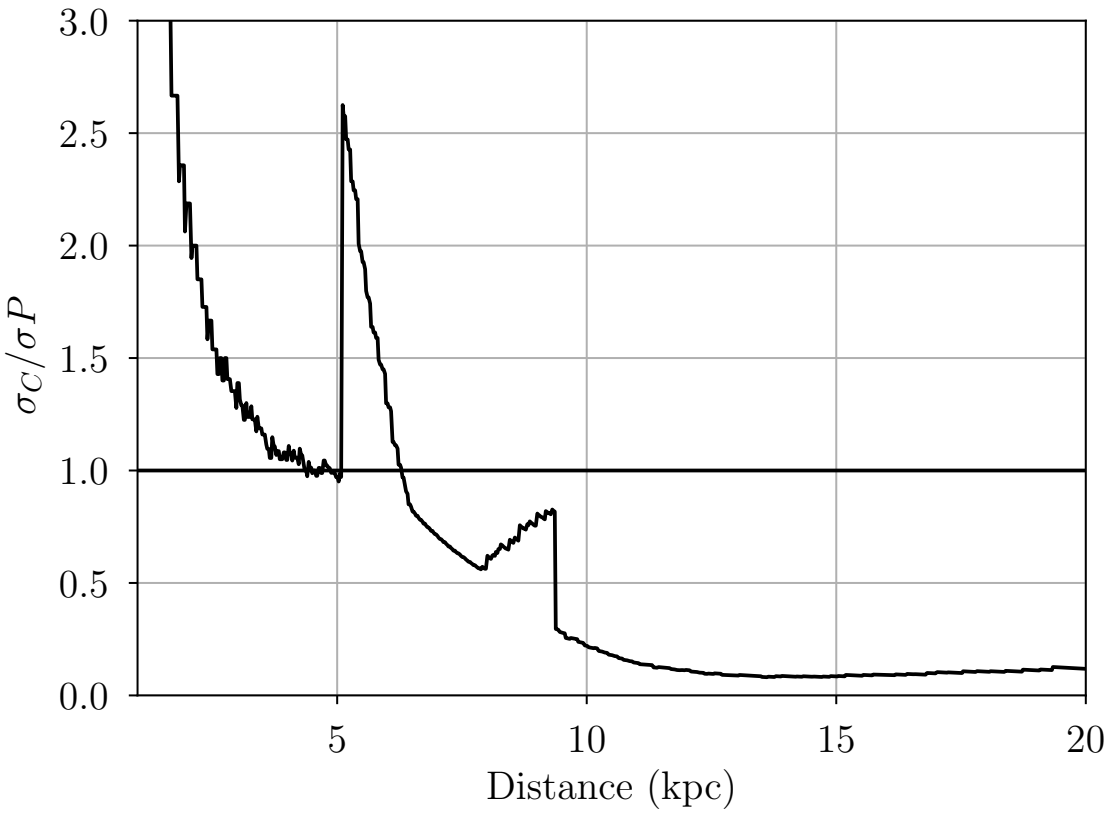

Figure 3.17: Ratio of the Method C Monte Carlo kinematic distance uncertainty to the typical parallax distance uncertainty as a function of distance in the direction $\ell = 30°$. The solid vertical line indicates a ratio of one where $\sigma_C = \sigma_P$. The spikes near 5 kpc and 9 kpc are at the boundaries of the "tangent point region," defined where the LSR velocity is within $20\,\mathrm{km\,s^{-1}}$ of the tangent point velocity.

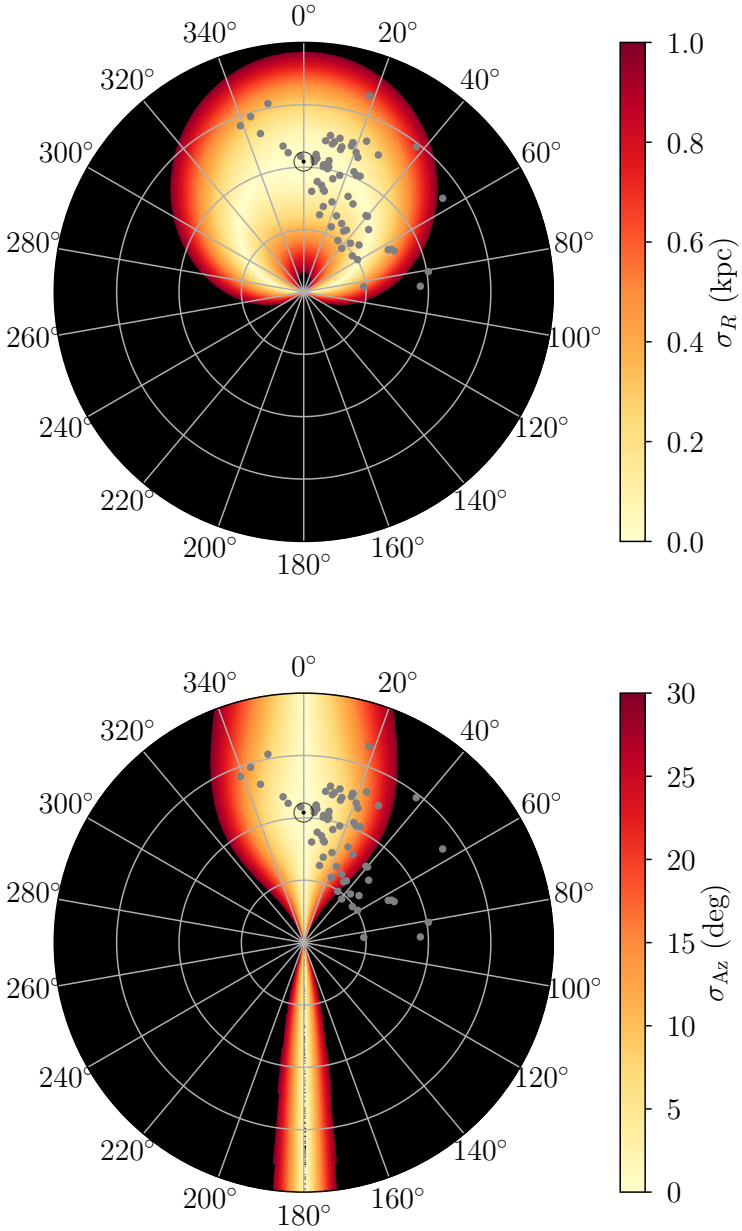

Figure 3.18: Face-on Galactic view of the typical parallax distance uncertainties converted to Galactocentric coordinates, R (top) and $\theta_{\rm Az}$ (bottom). The Galactic Center is located at the origin and the sun is located 8.34 kpc in the direction $\theta_{\rm Az} = 0°$. The concentric circles are 4, 8, and 12 kpc in R and $\theta_{\rm Az}$ is given in degrees. The color represents the distance uncertainty. The black regions have uncertainties larger than the maximum value shown in the color scale. The gray points are the HMSFRs in our sample.

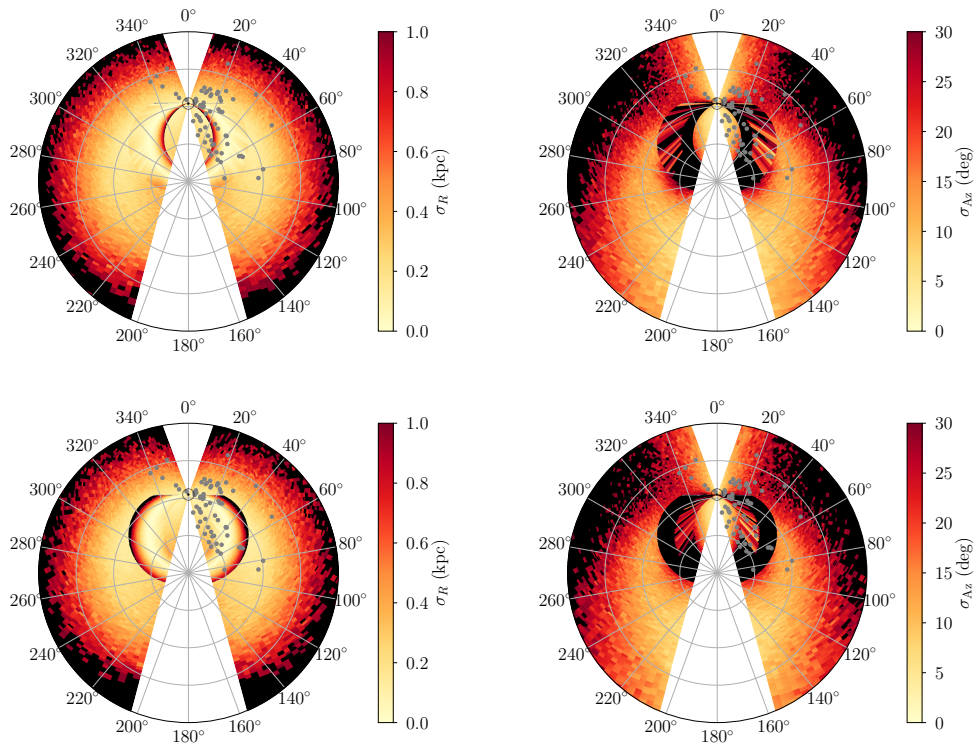

Figure 3.19: Face-on Galactic view of the Monte Carlo kinematic distance uncertainties converted to Galactocentric coordinates, R (left) and $\theta_{\rm Az}$ (right). The top figures are the distance uncertainties in the negative direction while the bottom figures are the distance uncertainties in the positive direction. The Galactic Center is located at the origin and the sun is located 8.34 kpc in the direction $\theta_{\rm Az} = 0°$. The concentric circles are 4, 8, and 12 kpc in R and $\theta_{\rm Az}$ is given in degrees. The color represents the distance uncertainty. The black regions have uncertainties larger than the maximum value shown in the color scale. The regions $-15° < \ell < 15°$ and $160° < \ell < 200°$ are masked in white since kinematic distances are very inaccurate toward the Galactic Center and Galactic Anti-center. The gray points are the HMSFRs in our sample.

best agreement between the kinematic and parallax distances is when we use Method C. In this case, the median absolute difference between the kinematic distances and parallax distances is 0.71 kpc with a standard deviation of 0.83 kpc. The Method C kinematic distance uncertainties are smaller than those of Methods A and B for most of the Galaxy, except near the tangent point. Along the line of sight with $\ell = 30°$, for example, the Method C kinematic distance uncertainty is 50% of the Method A and B uncertainties at a distance of 15 kpc. We test the accuracy of KDAR techniques using the KDARs derived in the literature for 9 of our inner Galaxy, non-tangent point HMSFRs. The KDAR is incorrect in 3 cases when using the *WISE* catalog KDARs to compare the parallax distances to our Monte Carlo kinematic distances, but each of these KDARs are low-quality determinations.

We recommend a new prescription for deriving and applying kinematic distances and their uncertainties: (1) correct the measured LSR velocity using the Reid et al. (2014) solar motion parameters and Equations 3.4 and 3.5; (2) use the corrected LSR velocity and the Monte Carlo method (Method C) to derive the kinematic distances and uncertainties; and (3) use only the highest quality KDARs from the *WISE* Catalog to resolve the kinematic distance ambiguity. Based on the typical parallax distance uncertainties, we show that, in a large region of Galactic quadrants I and IV ($-90° < \ell < 90°$), both the distances and the Galactocentric positions of HMSFRs are more accurately constrained by the Method C kinematic distances than parallax distances. In the direction $\ell = 30°$, for example, the Method C kinematic distance uncertainties are smaller than the parallax distance uncertainties everywhere beyond the tangent point, reaching a minimum of 10% of the parallax distance uncertainty at a distance of 14 kpc. The code to derive the Method C Monte Carlo kinematic distances and kinematic distance uncertainties is publicly available and may be utilized through an on-line tool. In a future paper, we will investigate the effects of using the Monte Carlo kinematic distances on the interpretation of Galactic morphological and metallicity structure.

Chapter 4

The Southern H II Region Discovery Survey

4.1 Introduction

Massive OB-type stars ionize the natal gas in their surroundings, creating H II regions. Since these nebulae have short lifetimes ($\lesssim$10 Myr) they are the locations of current high-mass star formation in the Galaxy. H II regions are the classic tracer of Galactic spiral structure, and their chemical abundances reveal the metallicity of the interstellar medium (ISM) in which they formed. A complete census of Galactic H II regions would inform models of both Galactic kinematics, as well as the formation and chemo-dynamical evolution of the Galaxy.

More than 60 years ago, Sharpless (1953, 1959) began surveys of Galactic H II regions. Starting with photographic plates from the 48" Schmidt telescope (now known as the Samuel Oschin Telescope) at the Palomar Observatory, Sharpless (1953) compiled a catalog of 142 "emission nebulae" and stars associated with those nebulae. Sharpless (1959) expanded upon his previous work using the newly completed National Geographic-Palomar Sky Atlas. Adopting the term "H II region" from Strömgren (1948), this second catalog contains 313 optical H II regions, covering the entire

This chapter previously appeared in the Astrophysical Journal Supplement Series. The original citation is as follows: T. V. Wenger, J. M. Dickey, C. H. Jordan, D. S. Balser, W. P. Armentrout, L. D. Anderson, T. M. Bania, J. R. Dawson, N. M. McClure-Griffiths, and J. Shea. "The Southern H II Region Discovery Survey. I. The Bright Catalog." *Astrophysical Journal Supplement Series*, 240:24, February 2019.

sky north of declination $-27°$. Gum (1955), and later Rodgers et al. (1960), expanded the H II region survey to the southern hemisphere using Hα photographic plates from the Mount Stromolo Observatory.

With the prediction of radio recombination lines (RRLs) by Kardashev (1959) and their subsequent discovery by Hoglund & Mezger (1965a,b), there was now an extinction-free spectroscopic tracer of optically obscured H II regions. The first generation of RRL H II region surveys was carried out by Reifenstein et al. (1970) and Wilson et al. (1970b). Using the National Radio Astronomy Observatory (NRAO, now the Green Bank Observatory) 140 Foot telescope, Reifenstein et al. (1970) detected the H109α RRL toward 82 Galactic H II regions. Wilson et al. (1970b) extended the survey to the southern sky using the NRAO 6 cm receiver on the 210 foot Parkes Telescope. They detected H109α RRL emission toward 130 Galactic H II regions, bringing the total census to 212 nebulae with RRL detections. These projects were successful despite the low spectral resolution ($\sim$6 km s^{-1}) and high system temperatures ($\sim$100 K) of their instruments.

Equipped with better telescopes, more sensitive receivers, and more advanced correlators, the second generation of surveys began with Downes et al. (1980) in the northern sky and Caswell & Haynes (1987) in the southern sky. Using the Effelsburg 100 m telescope, Downes et al. (1980) targeted 262 bright sources from the recently completed 5 GHz continuum survey by Altenhoff et al. (1979) in search of H110α RRL emission and H_2CO absorption. They detected RRL emission toward 171 nebulae. Caswell & Haynes (1987) used the updated 1024-channel digital correlator on the Parkes telescope to simultaneously observe two RRLs (H109α and H110α), as well as H_2CO. By averaging the two RRL transitions, they were able to detect RRL emission from 316 Galactic H II regions. Using the NRAO 140 Foot telescope, Lockman (1989) observed all remaining reasonably bright compact radio continuum sources ($\gtrsim$ 1 Jy beam^{-1}) in the Altenhoff et al. (1979) survey. This generation of RRL surveys was completed by Lockman et al. (1996), who observed faint and diffuse radio sources in search of angularly large H II regions. These 140 Foot telescope surveys discovered approximately 350 new Galactic H II regions, bringing the total census of known Galactic H II regions to $\sim$1000 nebulae.

With the completion of the Lockman (1989) and Lockman et al. (1996) surveys, all of the bright radio continuum sources in the Altenhoff et al. (1979) catalog were observed, and systematic searches for Galactic H II regions ceased. It was apparent,

however, that the census of H II regions was vastly incomplete; only a handful of H II regions were known in the outer Galaxy in the first and fourth Galactic quadrants, for example. A deeper RRL survey would discover fainter and more distant H II regions, allowing us to explore both the Galactic structure and the properties of high-mass star formation beyond the Galactic Center.

We are now completing the third generation of RRL surveys of H II regions. This generation is motivated by two great advancements in the field: (1) deep all-sky infrared surveys, which are sensitive to the thermal dust emission associated with H II regions across the Galactic disk, and (2) ultra-sensitive radio telescopes with wide-bandpass receivers and correlators, which can simultaneously observe many RRL transitions. The Green Bank Telescope H II Region Discovery survey (GBT HRDS; Bania et al., 2010; Anderson et al., 2011) used the largest fully steerable telescope in the world to discover 448 new Galactic H II regions in the first and second Galactic quadrants. Follow-up surveys with the GBT and the Arecibo Telescope (Bania et al., 2012; Anderson et al., 2015a, 2018) added another 439 H II regions, bringing the total number of HRDS discoveries to 887. These surveys more than doubled the number of known H II regions in the surveyed zone and completed the census of northern sky H II regions brighter than $\sim$100 mJy beam^{-1} at $\sim$9 GHz.

The Southern H II Region Discovery Survey (SHRDS) is an extension of the HRDS into the southern sky. Using the sensitive and wide-bandpass receivers on the Australia Telescope Compact Array (ATCA), we aim to complete the census of southern sky H II regions to nearly the same sensitivity limit as the HRDS ($\sim$100 mJy beam^{-1}). At the conclusion of the SHRDS, we will have a catalog of all Galactic H II regions ionized by at least a single O star. This catalog will reveal new insights into the current structure, formation, and evolutionary history of the Milky Way.

4.2 Target Sample

Our targets are selected from the *Wide-field Infrared Survey Explorer (WISE)* Catalog of Galactic H II Regions (Anderson et al., 2014). The *WISE* Catalog is the most complete census of known and candidate H II regions extant. Candidate H II regions are identified based on their spatially coincident 12 μm, 22 μm, and, if available, radio emission. The infrared data are taken from the *WISE* All-Sky data (Wright et al., 2010) and the radio data from the Multi-Array Galactic Plane Imaging Survey (MAGPIS; Becker et al., 1994; Helfand et al., 2006), the Very Large Array

(VLA) Galactic Plane Survey (VGPS; Stil et al., 2006), the Canadian Galactic Plane Survey (CGPS; Taylor et al., 2003), the NRAO VLA Sky Survey (NVSS; Condon et al., 1998), the Southern Galactic Plane Survey (SGPS; McClure-Griffiths et al., 2005), and the Sydney University Molonglo Sky Survey (SUMSS; Bock et al., 1999; Mauch et al., 2003). The 12 and 22 μm emission stems from the polycyclic aromatic hydrocarbons (PAHs) in the photodissociation region (PDR) surrounding the H II region and the warm dust associated with the H II region, respectively. The radio emission is caused by thermal (free-free) emission from the ionized gas. The *WISE* Catalog contains about 8000 objects: ∼2000 known H II regions, ∼2000 radio-loud H II region candidates, and ∼4000 radio-quiet H II region candidates. Radio-quiet H II region candidates are sources that have not been detected in existing radio continuum surveys. Figure 4.1 shows the *WISE* infrared image and SHRDS observed 7 GHz radio continuum contours for the H II region candidate, G309.176–00.028.

In this first data release, we target H II region candidates in the Galactic longitude range $259^\circ < \ell < 344^\circ$ with a predicted 6 GHz peak flux density greater than 60 mJy beam^{-1}. This longitude range contains the portion of the sky visible by the ATCA that could not be observed by the HRDS telescopes. We estimate the 6 GHz peak flux density by extrapolating from the measured SUMSS 843 MHz flux density assuming $S_{6\,\mathrm{GHz}}/S_{843\,\mathrm{MHz}} = (6\,\mathrm{GHz}/843\,\mathrm{MHz})^{\alpha}$ with an optically thin spectral index of $\alpha = -0.1$. We also observe several previously known H II regions from the GBT HRDS, Caswell & Haynes (1987), and Wilson et al. (1970b) catalogs. These observations allow us to test our data reduction and analysis procedure and to compare single-dish and interferometric results.

Our target list for the SHRDS Bright Catalog contains 257 H II region candidates and 25 previously known H II regions. In some cases, multiple targets are observable within one ATCA primary beam, so we group them into a single pointing, a "field," centered between the targets. We observe 282 individual fields that contain many more *WISE* Catalog sources than the 282 bright targets. In total, there are 632 H II region candidates and 149 previously known H II regions within our fields, but most of these will be too distant and faint or too large and diffuse to be detected in our survey. Table 4.1 lists information about the H II regions and H II region candidates in each field. The field name, center position, and observing epoch are listed for each field. Each field contains multiple sources, and for each source we list the *WISE* Catalog source name; the *WISE* Catalog designation (K for previously known H II region, C

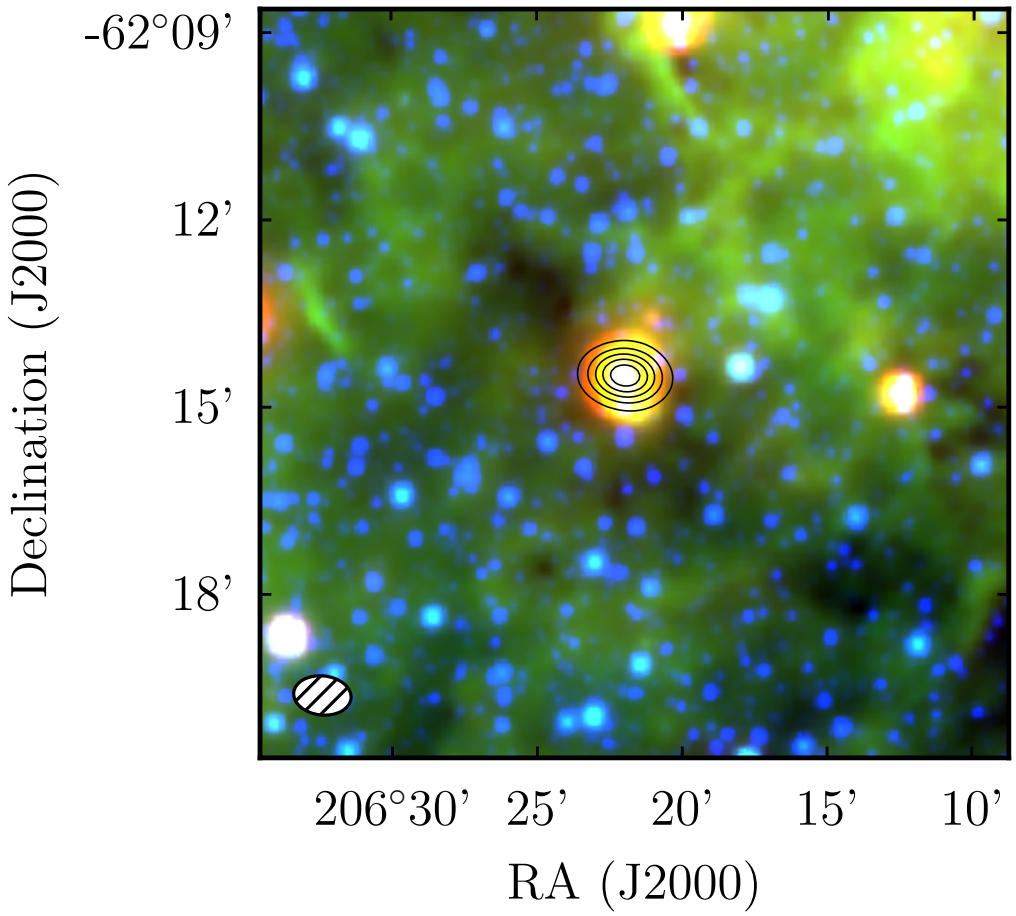

Figure 4.1: Infrared image of a typical H II region candidate from the *WISE* Catalog, G309.176–00.028. The image is a composite of *WISE* 22μm (red), 12μm (green), and 3.4μm (blue) data. The black contours are the SHRDS 7 GHz continuum emission (50 mJy beam^{-1} to 250 mJy beam^{-1} in 50 mJy beam^{-1} intervals). The hatched ellipse represents the ATCA half-power synthesized beam.

for H II region candidate, Q for radio-quiet H II region candidate, and G for H II region candidate associated with a group of H II regions); the *WISE* infrared position; the *WISE* infrared radius, $R_{\rm IR}$; the predicted 6 GHz peak continuum flux density, $S_{6\,\rm GHz}$; the separation between the position of the SUMSS continuum peak emission and the infrared position, $\Delta\theta$; and the reference to the previously known RRL detection, if any. A superscript "T" on the source name indicates that this object meets our "nominal" target criteria: a predicted 6 GHz peak continuum flux density brighter than 60 mJy beam^{-1} and a predicted radio diameter smaller than the maximum recoverable scale of the ATCA at 6 GHz, which is ∼265 arcseconds. We estimate that the radio diameter is half of the *WISE* Catalog infrared diameter (e.g. Bihr et al., 2016). There are 179 H II region candidates and 100 previously known H II regions in our fields that meet our nominal criteria. About 6% of our fields do not contain a nominal target due to a larger size criterion in our early observations. Figure 4.2 shows the positions of all *WISE* Catalog H II regions and H II region candidates with $259^\circ < \ell < 344^\circ$, as well as the subset of those observed in SHRDS fields.

4.3 OBSERVATIONS

We use the ATCA to observe radio continuum and hydrogen RRL emission in each field. The observing procedure and correlator configuration are similar to that used in the SHRDS pilot project (Brown et al., 2017). Data included here were observed 2015 June–October and 2016 July–September. In total, we observe 478 hr split nearly equally between the most compact H75 antenna configuration and the more extended H168 antenna configuration. A summary of the observing dates, hours observed, and antenna configurations is given in Table 4.2.

The *C*/*X*-band receiver on the ATCA covers 4–10 GHz with a ∼20 K system temperature. The Compact Array Broadband Backend (CABB) simultaneously measures both low spectral resolution, large-bandwidth radio continuum spectral windows (hereafter, continuum windows), as well as many high spectral resolution, small-bandwidth spectral windows (hereafter, spectral line windows). We use CABB in the 64 MHz mode, which allows us to simultaneously observe two 2 GHz bandwidth continuum windows (4.5–6.5 GHz and 7.5–9.5 GHz) and thirty-two 64 MHz bandwidth spectral line windows. The continuum windows have 33 channels (64 MHz/channel) and the spectral line windows have 2048 channels (31.25 kHz/channel). We tune the spectral line windows to 20 different hydrogen RRLs, as summarized in Table 4.3.

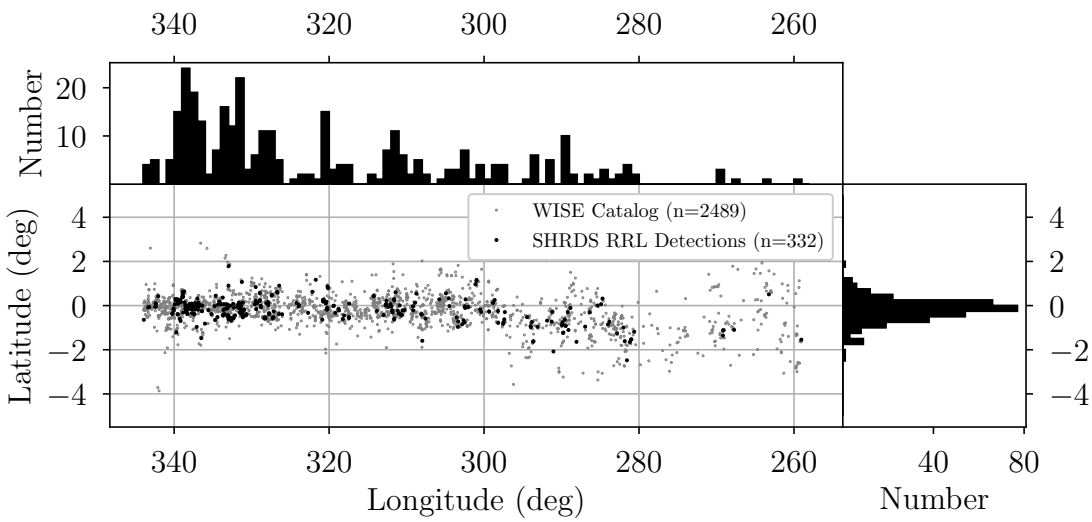

Figure 4.2: The Galactic positions of all *WISE* Catalog H II regions and H II region candidates with $259^\circ < \ell < 344^\circ$, $|b| < 4^\circ$ (gray points), as well as the subset of those observed in SHRDS fields (black points). The histograms show the Galactic distribution of the observed SHRDS targets.

Table 4.1: Bright Catalog Fields and Targets

Field	R.A. J2000 (hh:mm:ss)	Decl. J2000 (dd:mm:ss)	Epoch	Target[a]	Cat.[b]	R.A. J2000 (hh:mm:ss)	Decl. J2000 (dd:mm:ss)	$R_{\rm IR}$ (arcsec)	$S_{6\,\rm GHz}$ (mJy beam^{-1})	$\Delta\theta^c$ (arcsec)	Author
shrds030	08:26:18.8	−40:48:36.5	2016	G259.013−01.546	Q	08:26:13.5	−40:46:45.0	68.08	···	···	
				G259.057−01.544^T	C	08:26:22.1	−40:48:49.4	103.98	135.54	39.81	
				G259.086−01.612	C	08:26:09.9	−40:52:36.1	103.98	···	···	
shrds035	08:37:05.6	−39:44:51.8	2015	G259.359+00.820	C	08:37:17.6	−39:39:30.3	500.76	94.64	350.65	
				G259.771+00.541	C	08:37:25.8	−40:09:15.3	3361.35	···	···	
shrds060	08:48:40.9	−42:53:10.3	2015	G263.237+00.509^T	C	08:48:44.0	−42:54:01.6	204.56	168.93	61.36	
shrds063	08:49:49.2	−43:09:37.3	2015	G263.554+00.656	C	08:50:27.3	−43:03:08.8	1043.51	43.67	568.91	
shrds073	08:52:41.6	−44:13:27.4	2015	G264.220+00.216	C	08:50:54.8	−43:50:47.4	1824.13	42.02	526.47	
				G264.681+00.272	C	08:52:47.3	−44:09:56.9	557.96	37.64	220.29	
shrds075	08:50:35.2	−45:10:44.6	2015	G265.191−00.641	C	08:50:39.7	−45:08:27.9	124.22	54.54	145.97	
shrds078	08:58:03.7	−47:22:59.3	2016	G267.730−01.100^T	G	08:58:05.4	−47:22:43.9	200.97	315.42	23.69	
				G267.935−01.075	K	08:58:59.6	−47:31:03.8	557.50	···	···	CH87
shrds081	09:03:03.1	−47:51:18.3	2015	G268.618−00.739	C	09:03:10.3	−47:48:32.5	170.01	44.08	180.11	
shrds085	09:03:36.9	−48:28:13.1	2016	G269.068−01.114	K	09:03:17.1	−48:23:40.2	290.19	···	···	CH87
				G269.158−01.137	G	09:03:32.4	−48:28:38.5	64.13	···	···	
				G269.159−01.119^T	G	09:03:37.5	−48:27:57.9	64.13	443.35	15.84	
				G269.186−01.177	Q	09:03:28.3	−48:31:29.3	64.13	···	···	
shrds086	09:02:31.5	−48:38:04.8	2016	G269.167−01.357^T	G	09:02:35.2	−48:37:46.8	63.30	81.31	40.70	
				G269.174−01.436	K	09:02:15.2	−48:41:15.9	414.43	···	···	CH87
shrds111	09:58:22.9	−56:22:20.2	2015	G280.626−01.186^T	C	09:58:25.7	−56:22:19.3	207.05	75.22	22.91	
shrds113	10:02:28.7	−56:04:34.6	2015	G280.903−00.522	C	10:02:53.9	−56:00:34.4	441.52	70.03	317.71	
shrds1005	09:59:14.5	−56:54:33.8	2016	G280.989−01.527^T	K	09:59:00.6	−56:51:49.1	254.18	···	···	CH87
				G281.047−01.541^T	G	09:59:17.1	−56:54:35.6	116.87	511.36	21.70	
				G281.095−01.594	G	09:59:19.7	−56:58:51.6	116.87	···	···	
caswell1	09:59:32.0	−57:04:05.2	2016	G281.095−01.594	G	09:59:19.7	−56:58:51.6	116.87	···	···	
				G281.175−01.645^T	K	09:59:34.0	−57:04:13.2	189.51	···	···	CH87
shrds114	09:58:01.9	−57:57:49.3	2015	G281.560−02.478^T	C	09:58:03.7	−57:57:54.4	210.09	308.66	14.94	
shrds117	10:03:40.2	−57:26:42.3	2015	G281.840−01.609^T	C	10:03:39.4	−57:26:27.4	113.02	111.96	17.21	
				G281.865−01.649	Q	10:03:37.8	−57:29:16.2	78.60	···	···	
shrds1007	10:06:56.8	−57:02:13.4	2016	G282.015−00.997	G	10:07:22.3	−57:02:57.6	284.54	169.08	214.10	
				G282.027−01.182	K	10:06:38.5	−57:12:25.2	496.08	···	···	CH87
				G282.372−01.044	K	10:09:18.8	−57:17:42.1	1280.53	···	···	CH87
shrds1232	10:11:15.3	−57:44:02.4	2016	G282.788−01.321	C	10:10:39.3	−57:45:40.2	117.84	···	···	
				G282.842−01.252^T	C	10:11:17.0	−57:44:07.8	84.34	186.79	16.83	
shrds132	10:16:15.1	−57:10:21.0	2015	G283.098−00.400	C	10:16:26.0	−57:10:37.6	106.64	53.68	90.25	
				G283.140−00.490	C	10:16:19.2	−57:16:30.6	240.27	···	···	

Table 4.1 continued

Table 4.1: Bright Catalog Fields and Targets (continued)

Field	R.A. J2000 (hh:mm:ss)	Decl. J2000 (dd:mm:ss)	Epoch	Target[a]	Cat.[b]	R.A. J2000 (hh:mm:ss)	Decl. J2000 (dd:mm:ss)	$R_{\rm IR}$ (arcsec)	$S_{6\,\rm GHz}$ (mJy beam^{-1})	$\Delta\theta^c$ (arcsec)	Author
				G283.157−00.334	C	10:17:03.9	−57:09:18.8	172.57	···	···	
shrds1013	10:19:41.0	−57:51:29.6	2016	G283.729−00.774	G	10:18:48.2	−57:50:17.1	203.39	28.04	1.48	
				G283.832−00.730^T	G	10:19:37.9	−57:51:28.4	165.84	133.68	23.37	
				G283.895−00.956	K	10:19:05.8	−58:04:52.0	755.56	···	···	CH87
shrds1014	10:20:15.3	−58:03:50.8	2016	G283.895−00.956	K	10:19:05.8	−58:04:52.0	755.56	···	···	CH87
				G284.014−00.857^T	G	10:20:15.4	−58:03:50.2	66.62	603.55	0.65	
caswell2	10:29:29.1	−57:26:47.6	2016	G284.682+00.271	G	10:28:60.0	−57:27:49.4	92.52	22.72	1.75	
				G284.712+00.317^T	K	10:29:22.1	−57:26:23.1	201.20	···	···	CH87
shrds141	10:29:36.0	−57:45:21.5	2015	G284.902+00.060^T	C	10:29:35.3	−57:45:30.5	148.57	68.01	12.09	
shrds143	10:32:17.3	−58:02:15.3	2016	G285.260−00.051	K	10:31:28.4	−58:02:14.6	399.08	···	···	CH87
				G285.353+00.004^T	C	10:32:17.3	−58:02:14.9	134.94	60.49	0.43	
shrds1017	10:37:47.8	−58:47:27.5	2016	G286.260−00.155	K	10:37:40.5	−58:37:38.7	622.58	···	···	CH87
				G286.362−00.297^T	G	10:37:49.4	−58:48:03.9	131.94	66.63	39.19	
				G286.376−00.257	G	10:38:04.0	−58:46:24.6	86.59	43.33	1.43	
				G286.455−00.252	G	10:38:37.1	−58:48:27.9	180.64	13.22	1.22	
				G286.468−00.358	C	10:38:18.3	−58:54:24.4	314.11	20.00	81.25	
shrds158	10:39:21.0	−59:39:57.1	2015	G286.951−00.955^T	C	10:39:20.2	−59:39:46.0	71.10	376.49	13.51	
				G287.524−00.735	K	10:44:09.5	−59:44:36.2	2283.37	···	···	CH87
shrds162	10:44:40.2	−60:48:06.2	2016	G288.074−01.642^T	C	10:44:39.1	−60:48:06.5	99.09	99.26	7.83	
shrds1020	10:47:42.6	−60:25:03.6	2016	G288.230−01.153	Q	10:47:37.4	−60:26:26.0	81.41	···	···	
				G288.233−01.118^T	C	10:47:46.5	−60:24:39.5	95.40	60.18	36.92	
shrds167	10:55:48.5	−59:46:53.5	2016	G288.823−00.088	C	10:55:40.9	−59:45:00.1	43.34	···	···	
				G288.851−00.108^T	C	10:55:48.7	−59:46:49.9	95.85	84.50	5.09	
				G288.928−00.010	C	10:56:42.1	−59:43:27.2	214.89	24.26	71.19	
				G288.929−00.118	C	10:56:20.3	−59:49:22.9	102.60	···	···	
shrds173	10:54:12.5	−60:47:24.5	2016	G289.109−01.107^T	C	10:54:12.1	−60:47:31.5	87.86	63.47	7.99	
shrds1024	10:57:37.1	−60:05:27.4	2016	G289.077−00.346	K	10:56:37.8	−60:05:30.3	396.59	···	···	CH87
				G289.188−00.293^T	G	10:57:37.0	−60:05:28.5	87.50	141.64	1.28	
shrds181	10:57:38.1	−60:45:55.8	2016	G289.470−00.928^T	C	10:57:30.2	−60:47:08.2	88.92	87.00	91.47	
				G289.476−00.899^T	C	10:57:38.7	−60:45:45.9	112.41	87.00	12.03	
shrds184	10:59:19.6	−60:33:50.3	2016	G289.582−00.636^T	C	10:59:20.1	−60:34:07.2	103.50	97.60	16.95	
				G289.612−00.611	C	10:59:38.6	−60:33:28.9	217.89	···	···	
shrds1026	10:58:43.0	−61:10:38.8	2016	G289.769−01.220^T	G	10:58:43.1	−61:10:37.3	59.93	122.19	1.69	
				G289.806−01.242	K	10:58:55.2	−61:12:45.7	1088.92	···	···	CH87
shrds1028	11:01:04.3	−60:47:12.7	2016	G289.799−00.839	G	11:00:15.4	−60:50:37.1	225.36	32.20	0.66	
				G289.874−00.752^T	G	11:01:06.8	−60:47:41.3	151.30	107.43	34.51	

Table 4.1 continued

Table 4.1: Bright Catalog Fields and Targets (continued)

Field	R.A. J2000 (hh:mm:ss)	Decl. J2000 (dd:mm:ss)	Epoch	Target[a]	Cat.[b]	R.A. J2000 (hh:mm:ss)	Decl. J2000 (dd:mm:ss)	$R_{\rm IR}$ (arcsec)	$S_{6\,\rm GHz}$ (mJy beam^{-1})	$\Delta\theta^c$ (arcsec)	Author
				G289.880−00.801^T	K	11:00:59.5	−60:50:32.1	115.69	···	···	CH87
				G289.929−00.784	Q	11:01:24.9	−60:50:49.2	98.34	···	···	
shrds191	11:01:12.2	−60:56:44.0	2015	G289.911−00.859	Q	11:01:01.6	−60:54:29.4	67.53	···	···	
				G289.920−00.914	Q	11:00:54.4	−60:57:42.5	51.52	···	···	
				G289.944−00.889^T	C	11:01:10.3	−60:56:56.5	102.21	97.57	16.79	
				G289.966−00.962	C	11:01:05.4	−61:01:27.8	173.48	42.05	93.96	
				G290.012−00.867	C	11:01:45.4	−60:57:25.1	102.21	54.11	94.18	
shrds199	11:05:40.5	−62:29:14.1	2015	G291.046−02.079^T	C	11:05:37.0	−62:28:58.0	243.46	100.34	29.39	
shrds1032	11:12:33.5	−60:52:10.7	2016	G291.154−00.321	G	11:12:10.2	−60:54:04.8	90.88	46.61	0.02	
				G291.186−00.274^T	G	11:12:33.5	−60:52:12.0	90.88	193.48	1.39	
				G291.202−00.295^T	G	11:12:36.9	−60:53:44.9	90.88	231.55	0.80	
				G291.214−00.246^T	K	11:12:51.5	−60:51:14.8	245.72	···	···	CH87
shrds1034	11:11:31.8	−61:21:43.0	2016	G291.255−00.776^T	G	11:11:31.9	−61:21:42.1	83.67	264.74	0.96	
				G291.281−00.726	K	11:11:53.5	−61:19:28.1	446.49	···	···	CH87
caswell3	11:11:53.4	−61:19:00.5	2016	G291.255−00.776^T	G	11:11:31.9	−61:21:42.1	83.67	264.74	0.96	
				G291.281−00.726	K	11:11:53.5	−61:19:28.1	446.49	···	···	CH87
caswell4	11:16:33.7	−61:29:57.3	2016	G291.614−00.525	K	11:15:05.0	−61:15:40.9	1125.19	···	···	CH87
				G291.863−00.682^T	K	11:16:33.0	−61:29:50.0	155.35	···	···	CH87
				G291.947−00.910	K	11:16:31.4	−61:44:25.4	920.14	···	···	CH87
shrds207	11:25:41.9	−62:11:13.4	2015	G293.024−01.029^T	K	11:24:47.2	−62:13:19.7	162.84	···	···	CH87
				G293.113−00.961	C	11:25:42.1	−62:11:10.2	314.96	109.61	3.33	
				G293.232−00.659	C	11:27:29.6	−61:56:18.9	1397.56	···	···	
shrds210	11:28:20.7	−62:58:38.6	2016	G293.619−01.613^T	G	11:28:02.5	−62:57:59.4	35.39	63.23	41.46	
				G293.620−01.638	C	11:27:58.8	−62:59:27.2	274.30	···	···	
				G293.661−01.639^T	G	11:28:19.2	−63:00:16.2	73.72	154.41	16.66	
				G293.683−01.590	G	11:28:38.5	−62:57:52.6	38.56	58.02	21.62	
shrds215	11:32:03.7	−62:11:27.9	2015	G293.675−00.729	C	11:30:53.7	−62:08:37.9	390.94	19.81	280.43	
				G293.824−00.761^T	C	11:32:01.7	−62:13:10.6	64.68	125.21	63.57	
				G293.829−00.744^T	C	11:32:06.9	−62:12:16.6	64.68	143.35	52.76	
shrds219	11:32:37.2	−62:28:02.7	2015	G293.952−00.894^T	C	11:32:44.0	−62:23:07.9	75.25	155.57	101.23	
				G293.967−00.984^T	C	11:32:37.5	−62:28:30.3	120.38	151.65	27.01	
				G293.994−00.934^T	C	11:32:58.6	−62:26:08.6	69.31	230.16	53.76	
shrds226	11:37:47.8	−62:09:47.0	2015	G294.453−00.521^T	C	11:37:47.3	−62:10:23.7	205.47	130.53	36.68	
shrds242	12:02:14.6	−62:35:53.4	2015	G297.312−00.295^T	C	12:02:14.8	−62:37:41.5	212.36	116.70	108.27	
shrds243	12:02:24.4	−62:57:40.5	2015	G297.392−00.624^T	C	12:02:23.3	−62:58:00.2	232.66	261.08	20.65	
shrds244	12:04:24.3	−62:23:52.6	2015	G297.455−00.010	Q	12:03:55.3	−62:22:31.4	40.00	···	···	

Table 4.1 continued

Table 4.1: Bright Catalog Fields and Targets (continued)

Field	R.A. J2000 (hh:mm:ss)	Decl. J2000 (dd:mm:ss)	Epoch	Target[a]	Cat.[b]	R.A. J2000 (hh:mm:ss)	Decl. J2000 (dd:mm:ss)	$R_{\rm IR}$ (arcsec)	$S_{6\,\rm GHz}$ (mJy beam^{-1})	$\Delta\theta^c$ (arcsec)	Author
				G297.519−00.031	Q	12:04:25.9	−62:24:27.8	45.00	···	···	
				G297.570−00.036	C	12:04:51.5	−62:25:17.8	302.36	138.73	207.54	
shrds246	12:03:13.3	−63:10:53.3	2015	G297.464−00.784	Q	12:02:44.7	−63:08:15.0	45.62	···	···	
				G297.469−00.767	Q	12:02:49.1	−63:07:17.3	52.25	···	···	
				G297.497−00.758^T	K	12:03:04.6	−63:07:03.2	216.30	···	···	CH87
				G297.531−00.823^T	C	12:03:15.9	−63:11:15.2	29.18	157.89	29.32	
				G297.535−00.832^T	C	12:03:17.1	−63:11:52.1	26.43	91.53	38.96	
				G297.536−00.826^T	C	12:03:18.2	−63:11:30.9	26.43	157.89	51.18	
shrds249	12:08:26.2	−63:11:13.3	2015	G298.108−00.740^T	C	12:08:26.0	−63:12:26.5	182.35	170.74	72.54	
				G298.183−00.784^T	K	12:09:01.6	−63:15:47.2	174.60	···	···	CH87
caswell5	12:09:02.7	−63:16:06.4	2016	G298.108−00.740^T	C	12:08:26.0	−63:12:26.5	182.35	170.74	72.54	
				G298.183−00.784^T	K	12:09:01.6	−63:15:47.2	174.60	···	···	CH87
shrds1041	12:09:54.3	−62:44:10.4	2016	G298.196−00.247^T	G	12:09:54.3	−62:44:08.6	131.82	322.24	1.80	
				G298.205−00.142	G	12:10:07.8	−62:38:00.0	153.57	52.11	1.15	
				G298.224−00.334	K	12:10:01.5	−62:49:35.6	303.21	···	···	CH87
				G298.529−00.251	K	12:12:46.5	−62:47:29.5	974.83	···	···	CH87
shrds253	12:14:26.6	−62:16:34.9	2015	G298.630+00.253	C	12:14:17.0	−62:18:26.8	278.01	144.08	129.89	
shrds256	12:15:17.5	−62:23:36.4	2015	G298.630+00.253	C	12:14:17.0	−62:18:26.8	278.01	144.08	129.89	
				G298.756+00.059	Q	12:15:07.3	−62:31:03.3	204.69	···	···	
				G298.765+00.174^T	C	12:15:20.3	−62:24:15.9	232.88	102.61	45.51	
shrds258	12:15:50.6	−62:27:21.3	2015	G298.756+00.059	Q	12:15:07.3	−62:31:03.3	204.69	···	···	
				G298.765+00.174^T	C	12:15:20.3	−62:24:15.9	232.88	102.61	45.51	
				G298.833+00.117^T	C	12:15:51.2	−62:28:13.0	38.61	199.06	25.52	
				G298.834+00.127^T	C	12:15:52.4	−62:27:38.6	38.61	199.06	24.71	
				G298.846+00.121^T	C	12:15:58.1	−62:28:06.8	38.61	198.73	27.47	
				G298.878+00.192^T	C	12:16:19.6	−62:24:10.9	58.09	74.71	27.86	
shrds261	12:16:23.6	−62:23:49.5	2016	G298.765+00.174^T	C	12:15:20.3	−62:24:15.9	232.88	102.61	45.51	
				G298.878+00.192^T	C	12:16:19.6	−62:24:10.9	58.09	74.71	27.86	
				G298.899+00.187^T	C	12:16:30.0	−62:24:35.6	58.09	67.43	63.45	
				G298.903+00.218	Q	12:16:34.2	−62:22:50.4	27.81	···	···	
caswell6	12:19:56.6	−62:55:29.8	2016	G299.290−00.289	Q	12:19:20.4	−62:55:57.3	179.86	···	···	
				G299.326−00.311	Q	12:19:37.8	−62:57:32.7	54.08	···	···	
				G299.336−00.329	Q	12:19:41.9	−62:58:41.2	25.80	···	···	
				G299.349−00.267^T	K	12:19:52.7	−62:55:06.6	140.00	···	···	CH87
				G299.399−00.235^T	G	12:20:20.9	−62:53:33.5	102.39	87.65	43.16	
shrds1046	12:20:26.4	−62:53:54.9	2016	G299.349−00.267^T	K	12:19:52.7	−62:55:06.6	140.00	···	···	CH87

Table 4.1 continued

Table 4.1: Bright Catalog Fields and Targets (continued)

Field	R.A. J2000 (hh:mm:ss)	Decl. J2000 (dd:mm:ss)	Epoch	Target[a]	Cat.[b]	R.A. J2000 (hh:mm:ss)	Decl. J2000 (dd:mm:ss)	$R_{\rm IR}$ (arcsec)	$S_{6\,\rm GHz}$ (mJy beam^{-1})	$\Delta\theta^c$ (arcsec)	Author
				G299.399−00.235^T	G	12:20:20.9	−62:53:33.5	102.39	87.65	43.16	
shrds268	12:26:50.6	−62:48:53.0	2015	G300.134−00.100	C	12:26:53.1	−62:50:16.8	383.88	148.36	84.11	
shrds271	12:28:48.0	−63:02:09.7	2015	G300.084−00.485	C	12:26:07.1	−63:12:59.6	1199.89	73.57	563.27	
				G300.344−00.219	Q	12:28:37.5	−62:58:32.9	73.25	···	···	
				G300.369−00.288^T	C	12:28:47.5	−63:02:45.8	163.06	136.18	37.38	
				G300.420−00.302^T	C	12:29:13.8	−63:03:52.2	225.89	136.18	93.03	
shrds273	12:29:26.8	−62:55:04.6	2015	G300.424−00.153^T	C	12:29:22.6	−62:55:00.5	166.65	160.34	27.67	
				G300.427−00.180	C	12:29:23.0	−62:56:38.9	64.36	17.56	0.00	
				G300.455−00.190	C	12:29:37.2	−62:57:23.4	63.12	23.21	0.00	
				G300.470−00.103	Q	12:29:49.0	−62:52:15.5	79.25	···	···	
				G300.502−00.180^T	K	12:30:02.4	−62:57:01.4	132.59	···	···	CH87
caswell7	12:34:53.6	−61:39:16.8	2016	G300.965+01.162^T	K	12:34:51.8	−61:38:43.9	111.33	···	···	CH87
				G300.983+01.117^T	C	12:34:59.4	−61:41:31.6	88.54	360.38	86.50	
caswell8	12:36:05.6	−61:51:06.6	2016	G301.116+00.968^T	K	12:36:02.1	−61:50:57.3	180.98	···	···	CH87
caswell9	12:43:34.9	−62:55:16.0	2016	G302.024−00.113	Q	12:43:26.7	−62:58:13.6	88.01	···	···	
				G302.032−00.063^T	K	12:43:31.8	−62:55:12.7	118.92	···	···	CH87
				G302.076+00.029	C	12:43:56.3	−62:49:47.8	175.59	55.65	4.09	
shrds293	12:46:44.3	−62:35:26.9	2016	G302.384+00.294	Q	12:46:40.8	−62:34:21.4	31.52	···	···	
				G302.391+00.280^T	C	12:46:44.3	−62:35:10.7	89.41	94.68	14.49	
shrds294	12:47:02.2	−62:58:35.3	2016	G302.436−00.106^T	C	12:47:04.3	−62:58:23.8	119.22	95.00	19.63	
				G302.441−00.131	Q	12:47:06.8	−62:59:53.2	34.25	···	···	
				G302.481−00.035^T	C	12:47:28.7	−62:54:09.7	91.95	67.93	28.80	
				G302.582−00.083	K	12:48:21.6	−62:57:08.0	470.39	···	···	CH87
				G302.631+00.030	K	12:48:48.1	−62:50:24.6	860.88	···	···	CH87
shrds295	12:47:32.9	−62:54:12.3	2016	G302.436−00.106^T	C	12:47:04.3	−62:58:23.8	119.22	95.00	19.63	
				G302.460−00.031	Q	12:47:17.6	−62:53:55.5	42.80	···	···	
				G302.481−00.035^T	C	12:47:28.7	−62:54:09.7	91.95	67.93	28.80	
				G302.582−00.083	K	12:48:21.6	−62:57:08.0	470.39	···	···	CH87
				G302.631+00.030	K	12:48:48.1	−62:50:24.6	860.88	···	···	CH87
shrds296	12:47:34.0	−63:38:00.7	2015	G302.453−00.740	Q	12:47:07.7	−63:36:27.8	46.12	···	···	
				G302.503−00.762^T	K	12:47:34.5	−63:37:49.4	251.74	···	···	CH87
				G302.614−00.756	C	12:48:34.5	−63:37:33.1	847.45	45.00	589.65	
shrds297	12:48:46.9	−63:32:32.0	2016	G302.614−00.756	C	12:48:34.5	−63:37:33.1	847.45	45.00	589.65	
				G302.636−00.672^T	C	12:48:46.9	−63:32:29.3	159.77	250.00	2.72	
				G302.671−00.677	Q	12:49:05.7	−63:32:48.9	38.05	···	···	
shrds299	12:50:20.7	−63:43:03.0	2016	G302.614−00.756	C	12:48:34.5	−63:37:33.1	847.45	45.00	589.65	

Table 4.1 continued

Table 4.1: Bright Catalog Fields and Targets (continued)

Field	R.A. J2000 (hh:mm:ss)	Decl. J2000 (dd:mm:ss)	Epoch	Target[a]	Cat.[b]	R.A. J2000 (hh:mm:ss)	Decl. J2000 (dd:mm:ss)	$R_{\rm IR}$ (arcsec)	$S_{6\ \rm GHz}$ (mJy beam^{-1})	$\Delta\theta^c$ (arcsec)	Author
				G302.722−00.816	C	12:49:32.6	−63:41:10.9	250.19	46.06	107.80	
				G302.816−00.844^T	C	12:50:23.5	−63:42:52.5	82.94	69.42	21.65	
shrds303	12:55:06.4	−63:35:16.2	2015	G303.320−00.755	Q	12:54:55.9	−63:37:26.1	41.81	···	···	
				G303.342−00.718^T	C	12:55:07.5	−63:35:09.6	57.60	141.13	10.73	
				G303.445−00.745	K	12:56:03.3	−63:36:40.1	435.56	···	···	CH87
shrds305	12:55:33.4	−63:50:06.4	2016	G303.384−00.965^T	C	12:55:32.3	−63:49:57.5	81.00	75.72	11.01	
shrds308	12:57:01.9	−63:24:21.4	2016	G303.557−00.539^T	C	12:57:01.4	−63:24:12.8	107.56	77.95	9.04	
				G303.593−00.631	C	12:57:21.8	−63:29:41.4	142.57	45.92	49.42	
shrds336	13:04:52.9	−62:50:55.4	2015	G304.465−00.023^T	C	13:04:53.1	−62:51:14.2	143.75	109.74	17.94	
shrds338	13:05:31.3	−62:29:57.5	2016	G304.557+00.329^T	C	13:05:31.3	−62:29:53.5	71.13	74.52	5.47	
shrds344	13:08:36.5	−62:15:14.9	2015	G304.925+00.555^T	C	13:08:34.3	−62:14:58.9	174.35	344.78	21.17	
				G305.056+00.372	G	13:09:48.4	−62:25:23.5	558.38	93.90	624.47	
shrds350	13:16:12.5	−62:26:49.6	2016	G305.789+00.280^T	C	13:16:11.3	−62:27:15.4	128.28	83.03	26.44	
				G305.789+00.138	K	13:16:18.4	−62:35:43.6	321.19	···	···	CH87
caswell10	13:32:32.1	−63:05:33.7	2016	G307.559−00.585^T	K	13:32:30.1	−63:05:14.0	119.68	···	···	CH87
				G307.571−00.620	C	13:32:39.2	−63:07:09.2	72.79	41.78	79.77	
				G307.610−00.593	C	13:32:57.4	−63:05:12.4	67.81	52.86	15.44	
shrds373	13:37:41.4	−64:00:40.0	2016	G307.974−01.594^T	C	13:37:42.0	−64:00:41.7	128.84	65.55	5.35	
caswell11	13:36:46.9	−62:49:38.9	2016	G308.056−00.397	G	13:36:32.7	−62:49:07.5	34.19	···	···	
				G308.067−00.432	Q	13:36:41.0	−62:51:03.9	25.79	···	···	
				G308.069−00.439	Q	13:36:42.8	−62:51:29.7	19.86	···	···	
				G308.072−00.389	G	13:36:39.7	−62:48:28.3	47.63	···	···	
				G308.079−00.406^T	K	13:36:44.9	−62:49:23.3	131.95	···	···	CH87
				G308.096−00.326	G	13:36:46.4	−62:44:31.9	324.14	···	···	
shrds1091	13:40:54.1	−61:45:54.0	2016	G308.571+00.500	G	13:39:30.8	−61:50:39.2	474.66	···	···	
				G308.713+00.646	K	13:40:27.6	−61:40:27.2	477.49	···	···	CH87
				G308.747+00.547^T	G	13:40:54.1	−61:45:53.7	100.40	297.60	0.37	
shrds384	13:43:01.1	−62:09:03.5	2015	G308.916+00.124^T	C	13:43:00.6	−62:08:45.9	167.21	204.10	19.29	
				G309.075+00.172	K	13:44:15.6	−62:04:03.4	489.31	···	···	CH87
shrds385	13:45:19.4	−62:25:23.8	2016	G309.151−00.215^T	C	13:45:35.0	−62:25:50.7	191.04	63.51	112.47	
shrds386	13:45:26.7	−62:14:39.9	2015	G309.176−00.028^T	C	13:45:27.5	−62:14:32.9	72.27	226.24	8.52	
shrds403	13:54:48.3	−62:10:06.8	2016	G310.168−00.132^T	K	13:53:56.8	−62:07:18.6	244.78	···	···	CH87
				G310.182−00.247	C	13:54:17.9	−62:13:46.8	121.90	···	···	
				G310.220−00.134	Q	13:54:22.9	−62:06:39.0	38.22	···	···	
				G310.260−00.199^T	C	13:54:51.0	−62:09:53.4	150.76	63.68	23.30	
shrds407	13:57:01.8	−62:07:11.2	2015	G310.519−00.220^T	C	13:57:02.5	−62:07:15.5	95.54	331.76	5.27	

Table 4.1 continued

Table 4.1: Bright Catalog Fields and Targets (continued)

Field	R.A. J2000 (hh:mm:ss)	Decl. J2000 (dd:mm:ss)	Epoch	Target[a]	Cat.[b]	R.A. J2000 (hh:mm:ss)	Decl. J2000 (dd:mm:ss)	$R_{\rm IR}$ (arcsec)	$S_{6\,\rm GHz}$ (mJy beam^{-1})	$\Delta\theta^c$ (arcsec)	Author
				G310.560−00.194	C	13:57:19.4	−62:05:06.6	40.11	···	···	
shrds409	13:58:37.3	−62:17:39.7	2015	G310.578−00.456	Q	13:58:02.6	−62:20:02.2	38.73	···	···	
				G310.630−00.421^T	C	13:58:24.0	−62:17:14.3	111.39	126.20	20.41	
				G310.672−00.450^T	C	13:58:48.9	−62:18:17.7	107.06	104.02	26.57	
shrds411	13:58:39.3	−62:09:54.1	2015	G310.688−00.314^T	C	13:58:38.8	−62:10:09.3	59.66	628.85	14.15	
				G310.755−00.354	Q	13:59:17.3	−62:11:25.4	48.38	···	···	
shrds412	13:59:35.8	−61:48:07.0	2015	G310.887+00.009^T	C	13:59:34.2	−61:48:18.4	89.85	131.72	15.65	
shrds1096	14:00:32.4	−62:10:14.9	2016	G310.808−00.399	K	13:59:49.8	−62:13:13.0	266.89	···	···	CH87
				G310.901−00.373^T	G	14:00:32.4	−62:10:13.8	101.31	412.14	1.14	
				G310.961−00.384	Q	14:01:03.6	−62:09:55.6	25.39	···	···	
shrds413	14:01:20.0	−62:08:02.0	2016	G310.961−00.384	Q	14:01:03.6	−62:09:55.6	25.39	···	···	
				G311.003−00.355^T	C	14:01:20.4	−62:07:32.7	122.03	77.29	30.63	
				G311.138−00.278	K	14:02:16.5	−62:00:56.8	355.92	···	···	CH87
shrds418	14:02:05.6	−61:59:04.1	2015	G311.137−00.235^T	C	14:02:09.9	−61:58:26.3	38.58	117.36	47.74	
				G311.138−00.278	K	14:02:16.5	−62:00:56.8	355.92	···	···	CH87
shrds425	14:02:35.4	−61:05:42.5	2015	G311.386+00.649	Q	14:02:10.3	−61:03:19.6	42.78	···	···	
				G311.396+00.583	C	14:02:24.0	−61:07:01.2	641.84	···	···	
				G311.425+00.598^T	C	14:02:35.8	−61:05:39.9	62.23	117.77	3.61	
shrds428	14:04:33.4	−61:23:51.7	2016	G311.540+00.319	Q	14:04:09.1	−61:19:51.2	57.65	···	···	
				G311.563+00.239^T	C	14:04:31.4	−61:24:06.7	27.86	76.50	20.29	
				G311.575+00.239^T	C	14:04:37.2	−61:23:54.0	28.95	76.50	26.66	
				G311.598+00.272	Q	14:04:43.6	−61:21:35.5	21.67	···	···	
				G311.621+00.295^T	K	14:04:51.4	−61:19:52.5	32.39	···	···	CH87
				G311.629+00.277	Q	14:04:57.8	−61:20:47.1	15.65	···	···	
				G311.629+00.289^T	K	14:04:56.0	−61:20:04.7	29.94	···	···	CH87
shrds1101	14:06:41.8	−62:11:26.0	2016	G311.551−00.584	G	14:06:23.5	−62:11:38.7	82.97	52.14	25.70	
				G311.581−00.593^T	G	14:06:39.7	−62:11:39.2	67.83	133.12	20.12	
				G311.597−00.635	Q	14:06:53.7	−62:13:46.4	31.63	···	···	
				G311.606−00.638	Q	14:06:58.7	−62:13:49.6	24.47	···	···	
				G311.639−00.627^T	K	14:07:13.4	−62:12:38.3	262.25	···	···	CH87
caswell12	14:04:54.0	−61:19:53.5	2016	G311.575+00.239^T	C	14:04:37.2	−61:23:54.0	28.95	76.50	26.66	
				G311.598+00.272	Q	14:04:43.6	−61:21:35.5	21.67	···	···	
				G311.621+00.295^T	K	14:04:51.4	−61:19:52.5	32.39	···	···	CH87
				G311.629+00.277	Q	14:04:57.8	−61:20:47.1	15.65	···	···	
				G311.629+00.289^T	K	14:04:56.0	−61:20:04.7	29.94	···	···	CH87
				G311.638+00.301	Q	14:04:58.7	−61:19:15.7	31.72	···	···	

Table 4.1 continued

Table 4.1: Bright Catalog Fields and Targets (continued)

Field	R.A. J2000 (hh:mm:ss)	Decl. J2000 (dd:mm:ss)	Epoch	Target[a]	Cat.[b]	R.A. J2000 (hh:mm:ss)	Decl. J2000 (dd:mm:ss)	$R_{\rm IR}$ (arcsec)	$S_{6\,\rm GHz}$ (mJy beam^{-1})	$\Delta\theta^c$ (arcsec)	Author
shrds1103	14:07:50.4	−61:49:56.9	2016	G311.809−00.309^T	G	14:07:49.4	−61:51:23.4	253.20	100.94	87.19	
				G311.841−00.219^T	K	14:07:51.5	−61:45:38.7	58.85	···	···	CH87
				G311.843−00.261	Q	14:07:58.8	−61:48:02.3	27.33	···	···	
				G311.866−00.238^T	K	14:08:06.5	−61:46:18.4	61.57	···	···	CH87
				G311.908−00.279	G	14:08:33.0	−61:47:56.3	191.98	···	···	
shrds439	14:08:33.1	−61:34:05.6	2016	G311.932−00.107	Q	14:08:19.1	−61:37:38.3	17.61	···	···	
				G311.949−00.114	C	14:08:28.3	−61:37:44.0	50.38	45.15	19.84	
				G311.963−00.037^T	C	14:08:23.6	−61:33:04.2	212.94	85.04	90.18	
shrds440	14:08:29.3	−61:24:26.5	2015	G311.991+00.219	K	14:07:59.5	−61:17:53.4	363.99	···	···	CH87
				G312.091+00.069^T	C	14:09:09.4	−61:24:43.4	97.69	65.08	104.44	
shrds450	14:11:38.1	−61:26:02.2	2015	G312.388−00.057	C	14:11:50.7	−61:26:36.5	86.37	50.00	13.62	
shrds456	14:12:40.8	−61:06:35.1	2016	G312.591+00.210^T	C	14:12:46.1	−61:07:36.0	129.29	88.18	73.62	
				G312.620+00.280	Q	14:12:49.1	−61:03:04.9	34.68	···	···	
shrds458	14:13:14.4	−61:16:52.6	2016	G312.536+00.064	C	14:12:42.6	−61:16:58.4	46.95	···	···	
				G312.598+00.048^T	C	14:13:14.4	−61:16:42.3	47.17	87.45	10.04	
				G312.675+00.048^T	C	14:13:51.0	−61:15:16.6	109.78	79.66	51.11	
shrds462	14:14:10.1	−61:16:07.4	2015	G312.675+00.048^T	C	14:13:51.0	−61:15:16.6	109.78	79.66	51.11	
				G312.706+00.012^T	C	14:14:11.3	−61:16:43.5	95.87	125.85	37.12	
				G312.764+00.067	C	14:14:30.1	−61:12:31.1	80.22	31.11	26.01	
shrds465	14:17:20.5	−61:37:53.4	2016	G312.877−00.460	Q	14:16:48.5	−61:40:19.5	55.90	···	···	
				G312.888−00.447	C	14:16:51.6	−61:39:21.8	116.14	10.95	119.16	
				G312.979−00.432^T	C	14:17:32.7	−61:36:45.0	201.29	506.65	111.97	
shrds479	14:23:52.6	−61:08:18.0	2016	G313.851−00.243^T	C	14:23:51.7	−61:08:22.1	70.58	64.16	7.31	
shrds1111	14:25:16.8	−60:21:17.9	2016	G314.220+00.477	G	14:24:37.5	−60:20:10.1	315.97	21.04	0.68	
				G314.239+00.428^T	K	14:24:54.4	−60:22:28.4	130.62	···	···	CH87
				G314.257+00.379	Q	14:25:11.0	−60:24:50.8	21.12	···	···	
				G314.288+00.431^T	G	14:25:16.7	−60:21:16.4	20.41	250.09	1.58	
				G314.303+00.416	G	14:25:26.1	−60:21:48.2	13.19	···	···	
				G314.323+00.384	C	14:25:40.2	−60:23:11.5	74.62	···	···	
shrds1122	14:49:09.7	−59:25:07.2	2016	G317.030+00.028	K	14:46:43.4	−59:39:01.3	1463.64	···	···	CH87
				G317.405+00.091^T	G	14:49:10.3	−59:25:49.4	154.34	623.26	43.11	
shrds518	14:51:44.4	−59:57:50.6	2015	G317.426−00.561^T	C	14:51:36.4	−60:00:24.1	71.65	82.15	7.12	
				G317.431−00.522	C	14:51:30.2	−59:58:09.6	63.03	30.23	71.61	
				G317.458−00.533^T	C	14:51:44.1	−59:58:02.5	33.15	107.20	12.35	
				G317.466−00.524^T	C	14:51:45.6	−59:57:20.1	33.15	107.20	31.54	
				G317.475−00.586	Q	14:52:02.7	−60:00:24.0	19.40	···	···	

Table 4.1 continued

Table 4.1: Bright Catalog Fields and Targets (continued)

Field	R.A. J2000 (hh:mm:ss)	Decl. J2000 (dd:mm:ss)	Epoch	Target[a]	Cat.[b]	R.A. J2000 (hh:mm:ss)	Decl. J2000 (dd:mm:ss)	$R_{\rm IR}$ (arcsec)	$S_{6\,\rm GHz}$ (mJy beam^{-1})	$\Delta\theta^c$ (arcsec)	Author
				G317.487−00.564	Q	14:52:03.2	−59:58:54.9	21.81	···	···	
				G317.498−00.576	Q	14:52:10.4	−59:59:14.9	55.76	···	···	
				G317.517−00.629	C	14:52:30.0	−60:01:36.0	190.27	···	···	
				G317.528−00.535	Q	14:52:14.6	−59:56:16.7	14.92	···	···	
shrds521	14:51:26.3	−59:40:04.6	2015	G317.570−00.257	C	14:51:33.2	−59:40:12.7	419.51	190.56	53.65	
				G317.577−00.169	C	14:51:17.7	−59:35:18.2	103.19	···	···	
caswell13	14:55:41.9	−59:37:01.6	2016	G318.059−00.450^T	K	14:55:41.8	−59:37:16.5	100.16	···	···	CH87
shrds1126	14:57:29.3	−59:40:43.0	2016	G318.141−00.697	G	14:57:10.8	−59:48:09.7	522.52	23.39	0.52	
				G318.233−00.605^T	G	14:57:29.2	−59:40:42.7	131.16	63.72	0.36	
shrds535	14:59:30.0	−59:06:41.4	2016	G318.726−00.222^T	C	14:59:30.0	−59:06:33.3	71.19	99.42	9.31	
shrds536	14:59:35.1	−59:01:18.2	2015	G318.726−00.222^T	C	14:59:30.0	−59:06:33.3	71.19	99.42	9.31	
				G318.774−00.150^T	C	14:59:33.8	−59:01:22.1	61.84	266.55	10.80	
shrds1129	15:03:02.3	−58:55:23.3	2016	G319.188−00.329	G	15:03:03.2	−58:58:57.0	463.22	106.03	213.63	
				G319.293−00.426	G	15:04:07.7	−59:00:56.9	410.57	55.40	147.89	
shrds1131	15:03:41.5	−58:35:05.1	2016	G319.397−00.006^T	K	15:03:15.5	−58:35:55.5	128.64	···	···	CH87
				G319.453−00.022^T	G	15:03:41.6	−58:35:06.7	80.54	157.99	1.80	
shrds1137	15:05:22.3	−57:26:33.5	2016	G320.148+00.873	Q	15:04:59.2	−57:27:53.1	70.60	···	···	
				G320.163+00.797^T	K	15:05:21.3	−57:31:26.9	186.23	···	···	CH87
				G320.205+00.867^T	G	15:05:22.2	−57:26:32.4	64.41	75.55	1.26	
				G320.236+00.938	C	15:05:18.7	−57:21:54.2	233.29	14.07	76.53	
shrds1139	15:09:30.1	−58:19:44.5	2016	G320.190−00.172	G	15:09:09.6	−58:21:05.1	171.42	41.64	63.17	
				G320.236−00.099^T	G	15:09:11.0	−58:15:53.6	168.90	81.85	63.70	
				G320.240−00.176^T	G	15:09:30.2	−58:19:45.8	83.56	65.52	1.56	
				G320.278−00.217	G	15:09:54.8	−58:20:45.6	106.02	26.19	25.72	
				G320.278−00.157	G	15:09:41.0	−58:17:39.1	151.48	···	···	
				G320.311−00.176^T	K	15:09:58.3	−58:17:38.2	91.96	···	···	CH87
shrds1140	15:09:09.2	−58:14:53.4	2016	G320.190−00.172	G	15:09:09.6	−58:21:05.1	171.42	41.64	63.17	
				G320.236−00.099^T	G	15:09:11.0	−58:15:53.6	168.90	81.85	63.70	
				G320.249−00.043	Q	15:09:03.3	−58:12:37.3	14.34	···	···	
				G320.278−00.157	G	15:09:41.0	−58:17:39.1	151.48	···	···	
				G320.298−00.101	Q	15:09:35.9	−58:14:08.6	22.26	···	···	
shrds555	15:09:32.4	−57:59:25.2	2015	G320.354+00.114	Q	15:09:08.7	−58:01:18.2	23.67	···	···	
				G320.357+00.153^T	K	15:09:00.9	−57:59:10.2	69.99	···	···	CH87
				G320.376+00.172^T	K	15:09:04.0	−57:57:37.3	70.15	···	···	CH87
				G320.399+00.162^T	K	15:09:15.4	−57:57:28.0	50.48	···	···	CH87
				G320.407+00.134^T	K	15:09:24.8	−57:58:39.2	135.25	···	···	CH87

Table 4.1 continued

Table 4.1: Bright Catalog Fields and Targets (continued)

Field	R.A. J2000 (hh:mm:ss)	Decl. J2000 (dd:mm:ss)	Epoch	Target[a]	Cat.[b]	R.A. J2000 (hh:mm:ss)	Decl. J2000 (dd:mm:ss)	$R_{\rm IR}$ (arcsec)	$S_{6\,\rm GHz}$ (mJy beam^{-1})	$\Delta\theta^c$ (arcsec)	Author
				G320.419+00.114^T	C	15:09:34.0	−57:59:19.5	36.61	125.10	14.43	
				G320.423+00.101^T	C	15:09:38.6	−57:59:52.8	36.61	100.92	28.27	
				G320.431+00.114	Q	15:09:38.7	−57:58:56.8	20.62	···	···	
shrds559	15:10:49.2	−57:45:04.1	2015	G320.590+00.190	G	15:10:23.2	−57:50:10.9	435.24	22.03	339.37	
				G320.663+00.336	G	15:10:18.2	−57:40:24.8	138.30	44.71	20.73	
				G320.675+00.246^T	C	15:10:43.5	−57:44:44.0	42.28	103.97	48.93	
				G320.692+00.185	K	15:11:04.0	−57:47:20.8	341.06	···	···	CH87
				G320.782+00.258^T	G	15:11:22.1	−57:40:50.2	147.82	200.96	27.67	
				G320.799+00.187^T	G	15:11:44.9	−57:43:57.6	216.02	143.03	23.65	
shrds1146	15:11:22.2	−57:40:22.3	2016	G320.692+00.185	K	15:11:04.0	−57:47:20.8	341.06	···	···	CH87
				G320.778+00.241^T	G	15:11:24.5	−57:41:50.2	37.97	175.34	1.31	
				G320.782+00.258^T	G	15:11:22.1	−57:40:50.2	147.82	200.96	27.67	
				G320.799+00.187^T	G	15:11:44.9	−57:43:57.6	216.02	143.03	23.65	
shrds1147	15:11:46.1	−57:44:20.2	2016	G320.692+00.185	K	15:11:04.0	−57:47:20.8	341.06	···	···	CH87
				G320.778+00.241^T	G	15:11:24.5	−57:41:50.2	37.97	175.34	1.31	
				G320.782+00.258^T	G	15:11:22.1	−57:40:50.2	147.82	200.96	27.67	
				G320.799+00.187^T	G	15:11:44.9	−57:43:57.6	216.02	143.03	23.65	
shrds561	15:15:33.5	−58:23:30.4	2016	G320.884−00.641^T	C	15:15:32.3	−58:23:50.0	138.34	89.42	22.51	
				G321.061−00.763	C	15:17:10.7	−58:24:28.7	533.84	49.10	337.01	
caswell14	15:13:49.9	−56:24:48.0	2016	G321.725+01.169^T	K	15:13:52.3	−56:24:52.5	175.12	···	···	CH87
caswell15	15:18:39.2	−56:39:00.9	2016	G322.036+00.625	G	15:17:51.8	−56:42:51.3	386.37	49.80	189.52	
				G322.162+00.625^T	K	15:18:38.4	−56:38:50.1	174.22	···	···	CH87
				G322.220+00.504	G	15:19:28.2	−56:43:07.7	480.22	108.32	289.37	
shrds1151	15:18:54.7	−56:41:42.9	2016	G322.036+00.625	G	15:17:51.8	−56:42:51.3	386.37	49.80	189.52	
				G322.162+00.625^T	K	15:18:38.4	−56:38:50.1	174.22	···	···	CH87
				G322.220+00.504	G	15:19:28.2	−56:43:07.7	480.22	108.32	289.37	
shrds574	15:25:47.3	−57:08:54.6	2015	G322.706−00.330^T	C	15:25:47.5	−57:09:09.9	77.40	186.71	16.46	
shrds590	15:31:34.3	−56:10:12.1	2015	G323.895+00.116	C	15:31:06.5	−56:06:51.4	65.66	33.13	13.02	
				G323.915+00.026^T	C	15:31:35.9	−56:10:37.7	69.12	277.34	29.59	
				G323.936−00.038	C	15:31:59.0	−56:13:00.6	217.18	47.40	112.58	
				G323.942+00.042	Q	15:31:41.3	−56:08:52.4	20.48	···	···	
				G323.973+00.057^T	K	15:31:48.6	−56:07:05.0	48.91	···	···	CH87
				G324.025+00.089	C	15:31:59.1	−56:03:43.3	205.50	43.40	142.46	
caswell16	15:32:53.5	−55:56:17.2	2016	G324.135+00.236	K	15:32:01.5	−55:52:42.6	386.29	···	···	CH87
				G324.201+00.117^T	K	15:32:53.9	−55:56:16.6	156.60	···	···	CH87
shrds1161	15:45:59.0	−55:14:43.9	2016	G326.036−00.497	G	15:45:56.3	−55:20:18.2	251.91	20.17	1.56	

Table 4.1 continued

Table 4.1: Bright Catalog Fields and Targets (continued)

Field	R.A. J2000 (hh:mm:ss)	Decl. J2000 (dd:mm:ss)	Epoch	Target[a]	Cat.[b]	R.A. J2000 (hh:mm:ss)	Decl. J2000 (dd:mm:ss)	$R_{\rm IR}$ (arcsec)	$S_{6\,\rm GHz}$ (mJy beam^{-1})	$\Delta\theta^c$ (arcsec)	Author
				G326.065−00.393^T	G	15:45:39.1	−55:14:18.6	234.61	63.27	171.33	
				G326.474−00.292	K	15:47:28.1	−54:54:25.4	1252.65	···	···	CH87
caswell17	15:42:18.3	−53:58:25.8	2016	G326.270+00.783	K	15:41:49.8	−54:10:48.2	949.79	···	···	CH87
				G326.446+00.901^T	K	15:42:18.0	−53:58:46.2	178.99	···	···	CH87
shrds609	15:47:49.7	−54:58:44.7	2015	G326.467−00.382^T	C	15:47:49.1	−54:58:55.6	32.43	101.53	12.42	
				G326.473−00.378^T	C	15:47:50.0	−54:58:30.9	32.43	101.53	13.66	
				G326.474−00.292	K	15:47:28.1	−54:54:25.4	1252.65	···	···	CH87
shrds1163	15:44:44.2	−54:05:60.0	2016	G326.628+00.612	Q	15:44:28.9	−54:05:56.7	33.84	···	···	
				G326.643+00.514	K	15:44:58.2	−54:10:02.0	524.91	···	···	CH87
				G326.657+00.588^T	G	15:44:44.2	−54:06:00.3	118.28	3761.99	0.35	
				G326.728+00.616^T	G	15:45:00.3	−54:02:06.2	118.28	1185.90	0.84	
shrds1164	15:45:00.4	−54:02:06.9	2016	G326.643+00.514	K	15:44:58.2	−54:10:02.0	524.91	···	···	CH87
				G326.657+00.588^T	G	15:44:44.2	−54:06:00.3	118.28	3761.99	0.35	
				G326.728+00.616^T	G	15:45:00.3	−54:02:06.2	118.28	1185.90	0.84	
				G326.780+00.669	Q	15:45:03.7	−53:57:38.8	77.14	···	···	
shrds618	15:50:56.6	−54:28:23.6	2016	G326.900−00.347	K	15:50:01.1	−54:41:05.8	683.04	···	···	CH87
				G327.078+00.050	K	15:49:16.2	−54:15:49.7	1049.93	···	···	CH87
				G327.128−00.371	Q	15:51:21.2	−54:33:40.7	189.24	···	···	
				G327.139−00.261^T	C	15:50:56.1	−54:28:06.9	91.80	100.00	16.84	
shrds1167	15:52:33.1	−54:43:42.6	2016	G327.172−00.527	G	15:52:15.9	−54:39:14.4	546.34	222.40	305.84	
caswell18	15:53:02.8	−54:35:13.8	2016	G327.172−00.527	G	15:52:15.9	−54:39:14.4	546.34	222.40	305.84	
				G327.263−00.500	Q	15:52:38.1	−54:34:32.4	39.35	···	···	
				G327.267−00.557	Q	15:52:54.3	−54:37:02.3	24.74	···	···	
				G327.269−00.572	Q	15:52:59.1	−54:37:41.3	21.21	···	···	
				G327.273−00.578	Q	15:53:01.8	−54:37:47.8	21.21	···	···	
				G327.285−00.576^T	K	15:53:05.2	−54:37:15.0	45.22	···	···	CH87
				G327.287−00.589	Q	15:53:09.1	−54:37:45.7	21.21	···	···	
				G327.295−00.562	Q	15:53:04.8	−54:36:14.1	24.74	···	···	
				G327.296−00.595	Q	15:53:13.6	−54:37:41.5	21.21	···	···	
				G327.300−00.548	K	15:53:02.6	−54:35:22.3	276.04	···	···	CH87
				G327.454−00.633	G	15:54:14.3	−54:33:27.3	633.52	280.72	453.17	
shrds1168	15:53:24.1	−54:35:34.5	2016	G327.172−00.527	G	15:52:15.9	−54:39:14.4	546.34	222.40	305.84	
				G327.267−00.557	Q	15:52:54.3	−54:37:02.3	24.74	···	···	
				G327.269−00.572	Q	15:52:59.1	−54:37:41.3	21.21	···	···	
				G327.273−00.578	Q	15:53:01.8	−54:37:47.8	21.21	···	···	
				G327.285−00.576^T	K	15:53:05.2	−54:37:15.0	45.22	···	···	CH87
				G327.287−00.589	Q	15:53:09.1	−54:37:45.7	21.21	···	···	

Table 4.1 continued

Table 4.1: Bright Catalog Fields and Targets (continued)

Field	R.A. J2000 (hh:mm:ss)	Decl. J2000 (dd:mm:ss)	Epoch	Target[a]	Cat.[b]	R.A. J2000 (hh:mm:ss)	Decl. J2000 (dd:mm:ss)	$R_{\rm IR}$ (arcsec)	$S_{6\ \rm GHz}$ (mJy beam^{-1})	$\Delta\theta^c$ (arcsec)	Author
				G327.295−00.562	Q	15:53:04.8	−54:36:14.1	24.74	···	···	
				G327.296−00.595	Q	15:53:13.6	−54:37:41.5	21.21	···	···	
				G327.300−00.548	K	15:53:02.6	−54:35:22.3	276.04	···	···	CH87
				G327.454−00.633	G	15:54:14.3	−54:33:27.3	633.52	280.72	453.17	
shrds621	15:49:19.2	−53:45:46.0	2016	G327.400+00.444^T	C	15:49:18.7	−53:45:17.7	38.48	74.21	29.57	
				G327.401+00.483^T	C	15:49:09.2	−53:43:26.5	133.68	132.85	44.36	
shrds628	15:54:40.2	−54:11:34.6	2015	G327.651−00.334^T	K	15:53:58.4	−54:12:05.8	130.56	···	···	CH87
				G327.708−00.392^T	C	15:54:31.5	−54:12:35.1	48.00	119.08	57.61	
				G327.735−00.396^T	C	15:54:41.1	−54:11:44.1	70.14	497.36	13.33	
				G327.757−00.331	Q	15:54:31.2	−54:07:54.9	33.22	···	···	
				G327.770−00.346^T	K	15:54:39.1	−54:08:05.2	122.34	···	···	CH87
				G327.773−00.344	Q	15:54:39.4	−54:07:52.0	18.27	···	···	
shrds635	15:53:30.4	−53:48:13.2	2016	G327.824+00.117^T	K	15:52:56.0	−53:44:35.0	236.65	···	···	CH87
				G327.848+00.016^T	C	15:53:29.5	−53:48:20.4	31.11	67.37	10.89	
				G327.889−00.045	C	15:53:58.3	−53:49:38.0	358.62	43.54	120.48	
shrds639	15:53:14.4	−53:39:22.6	2016	G327.824+00.117^T	K	15:52:56.0	−53:44:35.0	236.65	···	···	CH87
				G327.852+00.189	Q	15:52:46.3	−53:40:09.8	14.49	···	···	
				G327.857+00.189	Q	15:52:48.0	−53:40:00.4	7.62	···	···	
				G327.867+00.173	Q	15:52:55.1	−53:40:20.2	43.33	···	···	
				G327.885+00.147	Q	15:53:07.4	−53:40:51.1	17.56	···	···	
				G327.916+00.154^T	C	15:53:15.3	−53:39:21.1	60.03	65.67	7.58	
shrds643	15:53:18.7	−53:27:40.4	2015	G328.043+00.298^T	C	15:53:18.1	−53:27:50.9	94.13	176.87	11.32	
				G328.118+00.374	Q	15:53:22.1	−53:21:29.2	313.54	···	···	
shrds647	15:54:31.1	−53:33:39.2	2015	G328.062+00.076	C	15:54:21.1	−53:37:24.6	48.00	43.98	16.43	
				G328.117+00.108^T	C	15:54:30.1	−53:33:51.1	106.92	141.56	15.32	
				G328.146+00.185	C	15:54:19.1	−53:29:08.5	48.00	36.84	36.77	
shrds652	15:57:49.8	−54:02:13.5	2015	G328.162−00.614^T	C	15:57:52.5	−54:05:17.9	175.83	95.59	59.45	
				G328.193−00.569^T	C	15:57:50.3	−54:02:01.9	116.42	555.89	13.25	
				G328.193−00.479	C	15:57:26.7	−53:57:56.0	142.02	53.99	28.87	
				G328.224−00.582^T	C	15:58:03.4	−54:01:26.1	92.84	324.71	102.62	
				G328.240−00.545	C	15:57:58.7	−53:59:07.9	15.89	···	···	
				G328.248−00.532	Q	15:57:57.6	−53:58:11.9	12.99	···	···	
				G328.253−00.531	Q	15:57:59.1	−53:57:59.5	18.54	···	···	
				G328.279−00.559^T	K	15:58:14.5	−53:58:15.5	98.15	···	···	CH87
shrds659	15:58:35.4	−53:55:39.6	2016	G328.277−00.530	Q	15:58:06.3	−53:57:00.7	20.19	···	···	
				G328.279−00.559^T	K	15:58:14.5	−53:58:15.5	98.15	···	···	CH87

Table 4.1 continued

Table 4.1: Bright Catalog Fields and Targets (continued)

Field	R.A. J2000 (hh:mm:ss)	Decl. J2000 (dd:mm:ss)	Epoch	Target[a]	Cat.[b]	R.A. J2000 (hh:mm:ss)	Decl. J2000 (dd:mm:ss)	$R_{\rm IR}$ (arcsec)	$S_{6\,\rm GHz}$ (mJy beam^{-1})	$\Delta\theta^c$ (arcsec)	Author
				G328.294−00.536	Q	15:58:12.9	−53:56:35.4	42.10	···	···	
				G328.315−00.594^T	K	15:58:34.8	−53:58:25.7	93.40	···	···	CH87
				G328.355−00.485	Q	15:58:18.4	−53:51:53.7	28.96	···	···	
				G328.356−00.559^T	C	15:58:38.3	−53:55:14.7	96.57	92.04	36.05	
shrds668	15:58:34.0	−53:11:45.8	2016	G328.807−00.078^T	K	15:58:50.9	−53:15:44.8	131.59	···	···	CH87
				G328.819−00.004^T	C	15:58:35.2	−53:11:52.3	72.03	96.70	12.14	
shrds669	15:56:47.5	−52:40:27.7	2015	G328.945+00.570^T	C	15:56:45.9	−52:40:43.9	118.31	281.48	21.67	
				G328.946+00.551	Q	15:56:51.1	−52:41:34.3	39.15	···	···	
				G328.982+00.572	Q	15:56:56.5	−52:39:11.9	20.84	···	···	
				G328.996+00.602	C	15:56:53.0	−52:37:15.8	113.16	14.65	9.59	
shrds670	15:58:12.1	−52:55:01.6	2015	G328.961+00.248^T	C	15:58:13.1	−52:54:50.0	79.82	120.06	14.82	
				G328.962+00.207^T	C	15:58:24.1	−52:56:40.6	88.35	76.92	21.60	
shrds677	16:00:19.9	−52:49:24.7	2015	G329.265+00.046	C	16:00:37.3	−52:52:10.2	63.90	56.53	10.99	
				G329.266+00.111^T	C	16:00:20.8	−52:49:11.9	120.72	122.30	15.69	
				G329.338+00.147^T	K	16:00:32.9	−52:44:42.5	77.26	···	···	CH87
				G329.340+00.121^T	K	16:00:40.3	−52:45:49.0	57.86	···	···	CH87
shrds684	16:02:17.4	−52:55:32.9	2015	G329.389−00.072	C	16:01:45.4	−52:52:39.5	296.56	26.05	135.82	
				G329.422−00.160^T	C	16:02:18.2	−52:55:18.9	82.84	243.13	16.25	
shrds686	16:01:02.3	−52:38:51.6	2015	G329.389+00.135	C	16:00:51.4	−52:43:15.9	56.06	42.70	11.03	
				G329.408+00.163	Q	16:00:49.9	−52:41:16.3	29.35	···	···	
				G329.454+00.236	Q	16:00:44.8	−52:36:09.2	24.37	···	···	
				G329.460+00.174^T	C	16:01:02.7	−52:38:43.9	66.34	192.19	8.28	
				G329.465+00.207^T	K	16:00:55.6	−52:37:01.8	16.53	···	···	CH87
				G329.465+00.235	Q	16:00:48.4	−52:35:46.1	19.91	···	···	
				G329.470+00.205^T	K	16:00:57.5	−52:36:54.4	18.04	···	···	CH87
				G329.472+00.214^T	K	16:00:55.7	−52:36:25.2	55.04	···	···	CH87
				G329.475+00.226	Q	16:00:53.6	−52:35:46.0	25.73	···	···	
				G329.567+00.242	C	16:01:17.0	−52:31:26.4	262.44	55.55	166.22	
shrds687	15:58:16.0	−52:07:44.6	2016	G329.474+00.839^T	C	15:58:16.2	−52:07:52.6	67.31	86.78	7.16	
shrds690	16:02:13.4	−52:38:37.6	2015	G329.530+00.093	Q	16:01:44.6	−52:39:38.6	19.52	···	···	
				G329.601+00.059^T	C	16:02:14.4	−52:38:21.2	86.30	247.86	19.44	
				G329.649+00.094	Q	16:02:19.7	−52:34:53.8	41.30	···	···	
shrds697	16:00:50.2	−51:42:50.2	2016	G329.804+00.917	C	15:59:34.4	−51:51:29.2	941.87	378.89	83.34	
				G330.049+00.899^T	C	16:00:50.9	−51:42:41.4	99.60	97.80	10.86	
				G330.121+00.687	C	16:02:06.0	−51:49:28.0	786.92	24.58	370.76	
shrds1171	16:09:50.8	−52:15:28.8	2016	G330.673−00.388^T	K	16:09:26.3	−52:15:23.7	113.85	···	···	CH87

Table 4.1 continued

Table 4.1: Bright Catalog Fields and Targets (continued)

Field	R.A. J2000 (hh:mm:ss)	Decl. J2000 (dd:mm:ss)	Epoch	Target[a]	Cat.[b]	R.A. J2000 (hh:mm:ss)	Decl. J2000 (dd:mm:ss)	$R_{\rm IR}$ (arcsec)	$S_{6\,\rm GHz}$ (mJy beam^{-1})	$\Delta\theta^c$ (arcsec)	Author
				G330.738−00.449^T	G	16:10:01.1	−52:15:25.3	148.18	100.86	94.74	
				G330.775−00.398	G	16:09:58.3	−52:11:41.1	358.22	68.91	109.96	
shrds1172	16:09:58.4	−52:09:50.3	2016	G330.738−00.449^T	G	16:10:01.1	−52:15:25.3	148.18	100.86	94.74	
				G330.775−00.398	G	16:09:58.3	−52:11:41.1	358.22	68.91	109.96	
				G330.873−00.369^T	K	16:10:18.8	−52:06:24.5	98.86	···	···	CH87
				G330.986−00.433	G	16:11:08.1	−52:04:36.2	572.96	···	···	
shrds709	16:09:52.7	−51:54:38.6	2015	G330.954−00.181^T	C	16:09:52.2	−51:54:49.5	66.43	119.71	12.32	
				G330.966−00.190	Q	16:09:58.1	−51:54:45.1	28.84	···	···	
				G331.020−00.143^T	K	16:10:01.2	−51:50:29.6	228.96	···	···	CH87
shrds710	16:11:27.7	−52:01:46.7	2016	G330.986−00.433	G	16:11:08.1	−52:04:36.2	572.96	···	···	
				G331.056−00.437^T	C	16:11:29.1	−52:01:55.1	75.67	65.14	14.16	
				G331.127−00.481^T	C	16:12:01.3	−52:00:58.6	64.02	240.12	74.72	
				G331.628−00.926	C	16:16:22.2	−51:59:36.5	2790.92	41.04	1160.96	
shrds711	16:10:37.5	−51:52:55.2	2015	G330.986−00.433	G	16:11:08.1	−52:04:36.2	572.96	···	···	
				G331.020−00.143^T	K	16:10:01.2	−51:50:29.6	228.96	···	···	CH87
				G331.057−00.229^T	C	16:10:34.3	−51:52:45.0	79.53	144.78	31.89	
				G331.120−00.248	C	16:10:57.3	−51:51:00.3	231.19	···	···	
				G331.121−00.169	C	16:10:36.7	−51:47:30.1	103.18	30.17	99.63	
				G331.129−00.243^T	C	16:10:58.5	−51:50:25.5	44.24	198.98	3.74	
shrds717	16:12:07.5	−52:01:43.9	2015	G330.986−00.433	G	16:11:08.1	−52:04:36.2	572.96	···	···	
				G331.087−00.518	Q	16:11:59.5	−52:04:12.2	26.40	···	···	
				G331.119−00.496^T	C	16:12:02.9	−52:01:57.0	28.63	178.71	27.51	
				G331.123−00.530^T	K	16:12:13.0	−52:03:15.4	143.49	···	···	CH87
				G331.127−00.481^T	C	16:12:01.3	−52:00:58.6	64.02	240.12	74.72	
				G331.146−00.480	Q	16:12:06.3	−52:00:08.1	37.79	···	···	
				G331.157−00.462	Q	16:12:04.6	−51:58:53.3	30.64	···	···	
				G331.172−00.460^T	C	16:12:08.5	−51:58:12.7	104.39	411.54	8.35	
				G331.182−00.541	Q	16:12:32.9	−52:01:20.0	56.22	···	···	
				G331.195−00.469	Q	16:12:17.4	−51:57:39.8	37.79	···	···	
				G331.256−00.480	C	16:12:37.7	−51:55:38.3	348.58	14.60	144.36	
				G331.628−00.926	C	16:16:22.2	−51:59:36.5	2790.92	41.04	1160.96	
shrds716	16:10:58.7	−51:50:22.0	2015	G331.057−00.229^T	C	16:10:34.3	−51:52:45.0	79.53	144.78	31.89	
				G331.120−00.248	C	16:10:57.3	−51:51:00.3	231.19	···	···	
				G331.121−00.169	C	16:10:36.7	−51:47:30.1	103.18	30.17	99.63	
				G331.129−00.243^T	C	16:10:58.5	−51:50:25.5	44.24	198.98	3.74	
shrds720	16:11:41.7	−51:55:59.7	2015	G330.986−00.433	G	16:11:08.1	−52:04:36.2	572.96	···	···	

Table 4.1 continued

Table 4.1: Bright Catalog Fields and Targets (continued)

Field	R.A. J2000 (hh:mm:ss)	Decl. J2000 (dd:mm:ss)	Epoch	Target[a]	Cat.[b]	R.A. J2000 (hh:mm:ss)	Decl. J2000 (dd:mm:ss)	$R_{\rm IR}$ (arcsec)	$S_{6\,\rm GHz}$ (mJy beam^{-1})	$\Delta\theta^c$ (arcsec)	Author
				G331.156−00.391^T	C	16:11:45.6	−51:55:50.4	141.66	148.82	36.52	
				G331.157−00.462	Q	16:12:04.6	−51:58:53.3	30.64	···	···	
				G331.172−00.460^T	C	16:12:08.5	−51:58:12.7	104.39	411.54	8.35	
				G331.256−00.480	C	16:12:37.7	−51:55:38.3	348.58	14.60	144.36	
				G331.628−00.926	C	16:16:22.2	−51:59:36.5	2790.92	41.04	1160.96	
shrds719	16:09:25.0	−51:33:09.0	2015	G331.127+00.127	Q	16:09:20.9	−51:34:13.2	15.86	···	···	
				G331.137+00.112	Q	16:09:27.6	−51:34:28.6	26.70	···	···	
				G331.145+00.133^T	C	16:09:24.2	−51:33:11.5	38.91	100.32	8.62	
				G331.150+00.115	Q	16:09:30.4	−51:33:48.1	27.54	···	···	
shrds721	16:12:08.2	−51:58:20.4	2015	G330.986−00.433	G	16:11:08.1	−52:04:36.2	572.96	···	···	
				G331.119−00.496^T	C	16:12:02.9	−52:01:57.0	28.63	178.71	27.51	
				G331.123−00.530^T	K	16:12:13.0	−52:03:15.4	143.49	···	···	CH87
				G331.127−00.481^T	C	16:12:01.3	−52:00:58.6	64.02	240.12	74.72	
				G331.146−00.480	Q	16:12:06.3	−52:00:08.1	37.79	···	···	
				G331.156−00.391^T	C	16:11:45.6	−51:55:50.4	141.66	148.82	36.52	
				G331.157−00.462	Q	16:12:04.6	−51:58:53.3	30.64	···	···	
				G331.172−00.460^T	C	16:12:08.5	−51:58:12.7	104.39	411.54	8.35	
				G331.182−00.541	Q	16:12:32.9	−52:01:20.0	56.22	···	···	
				G331.195−00.469	Q	16:12:17.4	−51:57:39.8	37.79	···	···	
				G331.256−00.480	C	16:12:37.7	−51:55:38.3	348.58	14.60	144.36	
				G331.628−00.926	C	16:16:22.2	−51:59:36.5	2790.92	41.04	1160.96	
shrds1174	16:05:52.9	−50:48:03.2	2016	G331.249+01.071^T	G	16:05:52.4	−50:47:20.9	209.94	151.89	43.11	
				G331.344+01.055^T	K	16:06:23.2	−50:44:14.1	251.85	···	···	CH87
shrds725	16:11:34.4	−51:39:34.2	2016	G331.259−00.188^T	K	16:11:20.9	−51:42:41.8	154.19	···	···	CH87
				G331.300−00.071	C	16:11:01.8	−51:35:54.1	174.29	18.53	71.87	
				G331.322−00.176^T	C	16:11:35.7	−51:39:36.4	89.77	70.00	12.36	
				G331.341−00.268	C	16:12:05.4	−51:42:52.0	164.41	24.35	50.19	
				G331.367−00.143	Q	16:11:39.6	−51:36:18.1	20.91	···	···	
				G331.398−00.182	C	16:11:58.6	−51:36:43.9	37.32	18.61	16.09	
				G331.628−00.926	C	16:16:22.2	−51:59:36.5	2790.92	41.04	1160.96	
shrds729	16:11:10.4	−51:27:27.9	2015	G331.352+00.023	Q	16:10:51.7	−51:29:37.4	35.97	···	···	
				G331.361−00.019^T	K	16:11:05.2	−51:31:05.3	151.43	···	···	CH87
				G331.382+00.004	G	16:11:05.3	−51:29:14.8	50.62	···	···	
				G331.412+00.011^T	C	16:11:11.9	−51:27:43.3	60.32	257.27	22.07	
				G331.580−00.022	G	16:12:07.9	−51:22:17.5	396.57	232.53	318.32	
shrds731	16:12:50.8	−51:43:36.4	2015	G331.338−00.365^T	K	16:12:30.3	−51:47:14.1	208.23	···	···	CH87

Table 4.1 continued

Table 4.1: Bright Catalog Fields and Targets (continued)

Field	R.A. J2000 (hh:mm:ss)	Decl. J2000 (dd:mm:ss)	Epoch	Target[a]	Cat.[b]	R.A. J2000 (hh:mm:ss)	Decl. J2000 (dd:mm:ss)	$R_{\rm IR}$ (arcsec)	$S_{6\,\rm GHz}$ (mJy beam^{-1})	$\Delta\theta^c$ (arcsec)	Author
				G331.378−00.386	Q	16:12:47.1	−51:46:30.1	35.02	···	···	
				G331.384−00.358^T	G	16:12:41.3	−51:45:01.6	58.81	335.64	1.70	
				G331.417−00.354^T	C	16:12:49.5	−51:43:29.1	43.64	121.00	15.04	
				G331.427−00.372^T	C	16:12:57.2	−51:43:52.0	35.35	67.53	44.17	
				G331.628−00.926	C	16:16:22.2	−51:59:36.5	2790.92	41.04	1160.96	
shrds735	16:13:11.1	−51:36:21.4	2015	G331.468−00.262	C	16:12:39.7	−51:37:23.6	62.68	29.18	13.69	
				G331.538−00.308^T	C	16:13:11.4	−51:36:30.2	53.77	135.67	7.90	
				G331.628−00.926	C	16:16:22.2	−51:59:36.5	2790.92	41.04	1160.96	
shrds736	16:12:27.2	−51:27:37.0	2015	G331.485−00.123	Q	16:12:07.7	−51:30:36.5	26.16	···	···	
				G331.491−00.116	C	16:12:07.5	−51:30:03.1	17.33	45.52	28.84	
				G331.520−00.076^T	K	16:12:05.1	−51:27:05.6	153.20	···	···	CH87
				G331.546−00.154	Q	16:12:33.0	−51:29:27.3	26.16	···	···	
				G331.559−00.128^T	C	16:12:29.7	−51:27:46.4	60.73	647.58	25.24	
				G331.580−00.022	G	16:12:07.9	−51:22:17.5	396.57	232.53	318.32	
				G331.604−00.110	C	16:12:37.6	−51:25:07.5	44.04	44.68	7.35	
				G331.628−00.926	C	16:16:22.2	−51:59:36.5	2790.92	41.04	1160.96	
shrds737	16:11:40.7	−51:18:48.1	2015	G331.560+00.091^T	C	16:11:32.4	−51:18:07.5	81.91	220.42	86.78	
				G331.580−00.022	G	16:12:07.9	−51:22:17.5	396.57	232.53	318.32	
shrds741	16:11:48.0	−51:12:28.4	2015	G331.580−00.022	G	16:12:07.9	−51:22:17.5	396.57	232.53	318.32	
				G331.653+00.128^T	C	16:11:49.0	−51:12:43.9	105.12	136.89	16.57	
				G331.689+00.162	Q	16:11:50.2	−51:09:46.0	52.54	···	···	
shrds743	16:13:06.7	−51:17:32.0	2015	G331.580−00.022	G	16:12:07.9	−51:22:17.5	396.57	232.53	318.32	
				G331.667−00.093	C	16:12:50.9	−51:21:49.7	99.01	20.72	60.42	
				G331.744−00.068^T	C	16:13:05.7	−51:17:32.4	74.29	210.00	9.98	
				G331.786−00.133	Q	16:13:34.6	−51:18:39.4	45.01	···	···	
				G331.797−00.148	C	16:13:41.8	−51:18:52.5	146.95	32.49	80.89	
				G331.834−00.002^T	C	16:13:13.5	−51:10:57.2	160.99	72.35	49.56	
shrds746	16:13:11.1	−51:11:41.8	2016	G331.760+00.064	C	16:12:35.7	−51:11:08.7	109.70	42.51	7.57	
				G331.834−00.002^T	C	16:13:13.5	−51:10:57.2	160.99	72.35	49.56	
				G331.864+00.059	C	16:13:06.0	−51:07:05.3	38.12	···	···	
shrds753	16:16:20.5	−51:18:15.7	2015	G331.628−00.926	C	16:16:22.2	−51:59:36.5	2790.92	41.04	1160.96	
				G332.092−00.422^T	C	16:16:16.1	−51:18:30.4	81.56	161.20	43.91	
				G332.145−00.452^T	K	16:16:38.8	−51:17:35.9	236.28	···	···	CH87
shrds756	16:15:45.9	−50:56:10.5	2015	G332.233−00.052	Q	16:15:17.2	−50:56:39.8	42.34	···	···	
				G332.275−00.004	C	16:15:16.0	−50:52:49.0	249.52	16.22	116.88	
				G332.291−00.092^T	C	16:15:43.7	−50:55:58.8	30.27	206.76	24.06	

Table 4.1 continued

Table 4.1: Bright Catalog Fields and Targets (continued)

Field	R.A. J2000 (hh:mm:ss)	Decl. J2000 (dd:mm:ss)	Epoch	Target[a]	Cat.[b]	R.A. J2000 (hh:mm:ss)	Decl. J2000 (dd:mm:ss)	$R_{\rm IR}$ (arcsec)	$S_{6\,\rm GHz}$ (mJy beam^{-1})	$\Delta\theta^c$ (arcsec)	Author
				G332.293−00.106^T	C	16:15:47.8	−50:56:29.5	44.35	206.76	26.55	
				G332.340−00.115	C	16:16:03.1	−50:54:55.8	39.68	10.59	25.25	
				G332.353−00.118	Q	16:16:07.4	−50:54:30.7	16.20	···	···	
				G332.356−00.122	Q	16:16:09.5	−50:54:35.5	16.20	···	···	
shrds759	16:17:57.9	−51:15:06.5	2015	G331.628−00.926	C	16:16:22.2	−51:59:36.5	2790.92	41.04	1160.96	
				G332.293−00.536	C	16:17:42.0	−51:15:02.6	52.55	···	···	
				G332.311−00.567^T	C	16:17:55.4	−51:15:39.3	112.54	105.76	40.59	
				G332.394−00.668	C	16:18:45.1	−51:16:29.3	437.84	23.63	160.23	
shrds763	16:15:32.1	−50:44:22.5	2015	G332.382+00.080^T	C	16:15:23.4	−50:44:45.0	93.10	135.97	85.95	
				G332.415+00.053^T	C	16:15:39.6	−50:44:33.5	228.79	449.24	127.50	
shrds766	16:15:52.6	−50:44:01.1	2015	G332.382+00.080^T	C	16:15:23.4	−50:44:45.0	93.10	135.97	85.95	
				G332.415+00.053^T	C	16:15:39.6	−50:44:33.5	228.79	449.24	127.50	
shrds771	16:19:10.1	−51:03:56.9	2015	G332.555−00.602	Q	16:19:11.5	−51:06:53.9	21.35	···	···	
				G332.585−00.561^T	C	16:19:08.6	−51:03:52.7	71.86	186.44	16.13	
				G332.620−00.570	Q	16:19:20.6	−51:02:47.5	62.23	···	···	
				G332.657−00.622^T	K	16:19:44.7	−51:03:29.0	218.84	···	···	CH87
				G332.762−00.595	K	16:20:06.0	−50:57:53.9	411.03	···	···	CH87
shrds1181	16:19:54.6	−51:07:06.0	2016	G332.601−00.727	C	16:19:57.5	−51:10:17.4	75.07	···	···	
				G332.633−00.683^T	G	16:19:54.5	−51:07:05.0	78.31	176.11	1.39	
				G332.657−00.622^T	K	16:19:44.7	−51:03:29.0	218.84	···	···	CH87
				G332.762−00.595	K	16:20:06.0	−50:57:53.9	411.03	···	···	CH87
shrds774	16:17:32.1	−50:32:17.0	2015	G332.718−00.053	Q	16:17:30.0	−50:36:30.3	25.20	···	···	
				G332.733−00.028	Q	16:17:27.3	−50:34:46.6	19.89	···	···	
				G332.766−00.006^T	C	16:17:30.7	−50:32:29.5	86.11	135.41	18.02	
shrds777	16:20:11.3	−50:53:32.3	2015	G332.762−00.595	K	16:20:06.0	−50:57:53.9	411.03	···	···	CH87
				G332.823−00.550^T	C	16:20:10.4	−50:53:23.5	44.76	519.39	11.64	
				G332.833−00.569^T	C	16:20:18.1	−50:53:46.6	44.76	200.85	6.81	
				G332.840−00.543^T	C	16:20:13.1	−50:52:22.4	44.76	505.18	46.21	
				G332.861−00.573^T	C	16:20:26.9	−50:52:47.0	74.41	166.99	76.27	
shrds782	16:10:37.4	−49:05:46.7	2016	G332.815+01.874	Q	16:09:42.9	−49:08:29.5	497.00	···	···	
				G332.957+01.793^T	C	16:10:41.4	−49:06:18.6	145.46	77.12	51.73	
				G333.053+01.748	C	16:11:18.3	−49:04:20.4	551.13	···	···	
				G333.093+01.966	K	16:10:34.7	−48:53:07.8	739.74	···	···	CH87
shrds784	16:14:33.4	−49:43:33.6	2016	G332.987+00.902^T	C	16:14:34.6	−49:44:01.1	92.86	79.99	28.43	
shrds785	16:21:14.8	−50:49:25.2	2015	G332.990−00.619^T	C	16:21:13.9	−50:49:16.2	167.80	292.24	11.92	
				G333.045−00.564	Q	16:21:13.9	−50:44:35.7	41.86	···	···	

Table 4.1 continued

Table 4.1: Bright Catalog Fields and Targets (continued)

Field	R.A. J2000 (hh:mm:ss)	Decl. J2000 (dd:mm:ss)	Epoch	Target[a]	Cat.[b]	R.A. J2000 (hh:mm:ss)	Decl. J2000 (dd:mm:ss)	$R_{\rm IR}$ (arcsec)	$S_{6\ \rm GHz}$ (mJy beam^{-1})	$\Delta\theta^c$ (arcsec)	Author
shrds788	16:18:37.4	−50:18:42.6	2015	G332.978−00.074	C	16:18:45.7	−50:26:30.5	258.54	21.52	25.53	
				G333.052+00.033^T	C	16:18:37.5	−50:18:48.7	118.05	222.73	4.94	
shrds789	16:21:00.8	−50:39:26.7	2015	G333.011−00.441^T	K	16:20:32.0	−50:40:49.3	137.51	···	···	W70
				G333.049−00.463	Q	16:20:48.1	−50:40:08.9	24.59	···	···	
				G333.067−00.447	G	16:20:48.7	−50:38:42.9	17.21	···	···	
				G333.068−00.443	G	16:20:47.8	−50:38:28.7	17.21	···	···	
				G333.074−00.482^T	C	16:20:59.7	−50:39:52.6	160.23	1139.89	27.98	
				G333.080−00.413	Q	16:20:43.2	−50:36:43.1	22.09	···	···	
				G333.085−00.479^T	G	16:21:02.0	−50:39:18.5	57.40	1138.95	0.80	
				G333.095−00.460	G	16:20:59.6	−50:38:03.8	52.76	···	···	
				G333.108−00.507^T	G	16:21:15.5	−50:39:29.6	72.40	345.87	0.10	
				G333.129−00.439^T	K	16:21:03.1	−50:35:44.4	112.55	···	···	CH87
shrds792	16:19:41.5	−50:21:46.4	2015	G333.113−00.141^T	C	16:19:39.6	−50:23:41.2	108.36	133.08	116.44	
				G333.164−00.100	Q	16:19:42.6	−50:19:48.9	26.22	···	···	
				G333.173−00.068	K	16:19:36.4	−50:18:02.2	279.46	···	···	CH87
shrds794	16:19:23.8	−50:09:03.9	2015	G333.255+00.065^T	C	16:19:23.5	−50:08:55.9	120.14	689.81	7.46	
				G333.265+00.041^T	C	16:19:32.5	−50:09:32.3	24.73	123.13	1284.09	
shrds799	16:21:19.3	−50:09:40.1	2015	G333.467−00.159^T	C	16:21:18.9	−50:09:31.3	93.89	762.10	10.03	
				G333.508−00.138	G	16:21:24.2	−50:06:52.9	203.31	···	···	
shrds800	16:22:03.6	−50:12:51.3	2015	G333.497−00.275^T	C	16:21:57.6	−50:13:10.1	110.65	259.08	60.48	
				G333.531−00.303	G	16:22:14.1	−50:12:55.6	85.86	···	···	
				G333.534−00.383^T	C	16:22:36.0	−50:16:09.9	238.34	127.75	18.76	
				G333.563−00.216^T	G	16:21:59.4	−50:07:52.0	52.26	328.97	1.49	
				G333.568−00.317	Q	16:22:27.7	−50:11:57.4	28.74	···	···	
				G333.594−00.291	G	16:22:27.5	−50:09:43.7	267.88	···	···	
				G333.627−00.199	K	16:22:11.8	−50:04:25.5	270.66	···	···	CH87
shrds801	16:22:36.0	−50:16:29.7	2015	G333.531−00.303	G	16:22:14.1	−50:12:55.6	85.86	···	···	
				G333.534−00.383^T	C	16:22:36.0	−50:16:09.9	238.34	127.75	18.76	
				G333.594−00.291	G	16:22:27.5	−50:09:43.7	267.88	···	···	
shrds802	16:20:45.2	−49:55:54.4	2016	G333.575+00.098	Q	16:20:39.7	−49:54:00.1	28.51	···	···	
				G333.580+00.058	C	16:20:51.6	−49:55:30.4	292.98	89.19	66.81	
				G333.586+00.071	Q	16:20:49.9	−49:54:43.2	28.51	···	···	
				G333.603−00.009	Q	16:21:15.3	−49:57:22.5	74.06	···	···	
caswell19	16:22:10.7	−50:05:56.3	2016	G333.508−00.138	G	16:21:24.2	−50:06:52.9	203.31	···	···	
				G333.563−00.216^T	G	16:21:59.4	−50:07:52.0	52.26	328.97	1.49	
				G333.593−00.090^T	K	16:21:34.1	−50:01:15.3	205.38	···	···	W70

Table 4.1 continued

Table 4.1: Bright Catalog Fields and Targets (continued)

Field	R.A. J2000 (hh:mm:ss)	Decl. J2000 (dd:mm:ss)	Epoch	Target[a]	Cat.[b]	R.A. J2000 (hh:mm:ss)	Decl. J2000 (dd:mm:ss)	$R_{\rm IR}$ (arcsec)	$S_{6\,\rm GHz}$ (mJy beam^{-1})	$\Delta\theta^c$ (arcsec)	Author
				G333.594−00.291	G	16:22:27.5	−50:09:43.7	267.88	···	···	
				G333.627−00.199	K	16:22:11.8	−50:04:25.5	270.66	···	···	CH87
				G333.668−00.122^T	G	16:22:02.2	−49:59:24.7	199.35	170.90	119.35	
shrds1200	16:21:53.5	−49:58:00.3	2016	G333.593−00.090^T	K	16:21:34.1	−50:01:15.3	205.38	···	···	W70
				G333.618−00.037	Q	16:21:26.6	−49:57:55.6	66.35	···	···	
				G333.627−00.199	K	16:22:11.8	−50:04:25.5	270.66	···	···	CH87
				G333.668−00.122^T	G	16:22:02.2	−49:59:24.7	199.35	170.90	119.35	
				G333.719−00.027	C	16:21:50.8	−49:53:14.7	45.71	21.48	0.00	
shrds803	16:20:09.0	−49:36:11.6	2015	G333.725+00.364^T	C	16:20:10.0	−49:36:21.7	100.75	266.64	15.01	
				G333.757+00.360	C	16:20:19.4	−49:35:09.9	61.03	···	···	
shrds804	16:23:41.0	−50:09:24.5	2015	G333.681−00.441^T	K	16:23:30.3	−50:12:21.1	65.97	···	···	CH87
				G333.683−00.512^T	K	16:23:49.7	−50:15:15.4	240.72	···	···	CH87
				G333.733−00.429^T	C	16:23:40.8	−50:09:37.4	59.53	180.81	13.65	
shrds806	16:22:30.4	−49:39:12.3	2015	G333.962+00.063^T	C	16:22:30.8	−49:39:06.1	67.49	153.90	7.22	
				G334.022+00.106^T	C	16:22:35.1	−49:34:42.5	119.37	65.52	64.55	
shrds807	16:22:28.8	−49:35:02.8	2016	G333.962+00.063^T	C	16:22:30.8	−49:39:06.1	67.49	153.90	7.22	
				G334.022+00.106^T	C	16:22:35.1	−49:34:42.5	119.37	65.52	64.55	
				G334.106+00.109	C	16:22:56.4	−49:31:02.5	130.21	43.85	50.05	
shrds811	16:22:59.9	−49:23:34.6	2015	G334.202+00.193^T	C	16:22:59.4	−49:23:23.8	83.82	193.76	13.15	
				G334.221+00.065	K	16:23:37.9	−49:27:59.8	293.86	···	···	CH87
shrds814	16:24:14.8	−49:23:32.9	2015	G334.221+00.065	K	16:23:37.9	−49:27:59.8	293.86	···	···	CH87
				G334.341+00.045^T	C	16:24:14.2	−49:23:42.3	52.80	309.22	11.06	
shrds815	16:27:00.5	−49:44:53.7	2016	G334.400−00.523^T	C	16:26:60.0	−49:44:58.9	61.63	61.32	7.21	
				G334.440−00.575	Q	16:27:24.2	−49:45:25.2	18.39	···	···	
				G334.444−00.504	C	16:27:06.1	−49:42:15.5	238.15	···	···	
shrds825	16:23:50.9	−48:54:05.4	2015	G334.571+00.471	C	16:23:22.1	−48:55:54.6	306.26	10.50	99.18	
				G334.646+00.442^T	C	16:23:48.9	−48:53:56.1	111.90	106.15	22.78	
caswell20	16:28:57.8	−49:36:29.5	2016	G334.721−00.653^T	K	16:28:57.1	−49:36:28.2	105.60	···	···	CH87
shrds828	16:26:26.5	−49:07:28.5	2015	G334.698−00.090^T	K	16:26:21.7	−49:14:03.8	157.89	···	···	CH87
				G334.774−00.023^T	C	16:26:23.3	−49:07:58.3	122.72	210.61	43.23	
shrds836	16:29:48.2	−49:04:53.0	2016	G335.195−00.385^T	C	16:29:45.8	−49:04:46.2	51.78	65.80	25.20	
				G335.223−00.345	Q	16:29:42.3	−49:01:54.1	35.82	···	···	
shrds841	16:30:34.2	−48:40:54.4	2016	G335.499−00.142	C	16:29:57.9	−48:41:30.7	355.16	21.34	167.03	
				G335.510−00.244	Q	16:30:27.7	−48:45:15.5	34.41	···	···	
				G335.579−00.209^T	C	16:30:35.5	−48:40:46.8	78.30	96.28	15.46	
shrds843	16:35:05.9	−48:45:57.4	2015	G336.026−00.817^T	C	16:35:08.3	−48:45:59.6	85.16	352.32	23.88	

Table 4.1 continued

Table 4.1: Bright Catalog Fields and Targets (continued)

Field	R.A. J2000 (hh:mm:ss)	Decl. J2000 (dd:mm:ss)	Epoch	Target[a]	Cat.[b]	R.A. J2000 (hh:mm:ss)	Decl. J2000 (dd:mm:ss)	$R_{\rm IR}$ (arcsec)	$S_{6\,\rm GHz}$ (mJy beam^{-1})	$\Delta\theta^c$ (arcsec)	Author
shrds852	16:32:52.1	−47:57:20.0	2015	G336.367−00.003^T	C	16:32:55.9	−47:57:50.8	34.76	244.95	49.56	
				G336.446−00.198	K	16:34:06.3	−48:02:17.8	623.89	···	···	CH87
				G336.455+00.042^T	K	16:33:05.4	−47:52:07.5	197.00	···	···	CH87
shrds853	16:34:13.1	−48:06:11.8	2016	G336.410−00.257^T	C	16:34:13.2	−48:06:18.0	22.51	934.98	5.01	
				G336.418−00.249^T	K	16:34:13.1	−48:05:38.0	105.60	···	···	CH87
				G336.446−00.198	K	16:34:06.3	−48:02:17.8	623.89	···	···	CH87
caswell21	16:40:00.3	−48:51:37.3	2016	G336.491−01.474^T	K	16:39:59.6	−48:51:40.6	93.15	···	···	CH87
				G336.524−01.466	Q	16:40:05.4	−48:49:52.8	49.50	···	···	
				G336.551−01.422	Q	16:39:59.9	−48:46:55.3	49.29	···	···	
				G336.789−01.726	G	16:42:20.5	−48:48:17.3	1540.11	···	···	
shrds854	16:33:06.5	−47:45:54.5	2015	G336.455+00.042^T	K	16:33:05.4	−47:52:07.5	197.00	···	···	CH87
				G336.518+00.119^T	C	16:33:00.7	−47:46:13.5	186.70	444.19	61.75	
				G336.585+00.019^T	C	16:33:43.2	−47:47:21.7	132.52	241.29	17.82	
shrds857	16:33:43.4	−47:47:04.5	2015	G336.518+00.119^T	C	16:33:00.7	−47:46:13.5	186.70	444.19	61.75	
				G336.585+00.019^T	C	16:33:43.2	−47:47:21.7	132.52	241.29	17.82	
				G336.753+00.097	K	16:34:03.4	−47:36:47.2	410.12	···	···	CH87
shrds1209	16:34:22.4	−47:28:38.3	2016	G336.753+00.097	K	16:34:03.4	−47:36:47.2	410.12	···	···	CH87
				G336.874+00.139^T	G	16:34:21.4	−47:29:42.6	143.62	146.98	63.53	
				G336.888+00.057^T	G	16:34:46.3	−47:32:25.7	105.60	460.94	17.39	
				G336.922+00.062^T	G	16:34:53.2	−47:30:44.4	89.08	205.70	183.61	
shrds1212	16:34:59.4	−47:33:38.5	2016	G336.753+00.097	K	16:34:03.4	−47:36:47.2	410.12	···	···	CH87
				G336.854−00.018^T	G	16:34:57.9	−47:36:59.8	146.00	794.48	68.70	
				G336.879+00.000	Q	16:34:59.0	−47:35:08.4	31.27	···	···	
				G336.888+00.057^T	G	16:34:46.3	−47:32:25.7	105.60	460.94	17.39	
				G336.900−00.033	C	16:35:12.9	−47:35:34.5	26.38	···	···	
				G336.915−00.026	Q	16:35:14.6	−47:34:36.8	21.44	···	···	
				G336.922+00.062^T	G	16:34:53.2	−47:30:44.4	89.08	205.70	183.61	
shrds862	16:35:25.7	−47:31:16.9	2015	G336.915−00.026	Q	16:35:14.6	−47:34:36.8	21.44	···	···	
				G336.922+00.062^T	G	16:34:53.2	−47:30:44.4	89.08	205.70	183.61	
				G336.969−00.013	Q	16:35:24.1	−47:31:41.2	17.32	···	···	
				G336.970−00.051	Q	16:35:34.5	−47:33:12.5	33.59	···	···	
				G336.978−00.007^T	C	16:35:24.8	−47:31:03.6	11.58	850.91	47.17	
				G336.986−00.006^T	C	16:35:26.3	−47:30:38.6	17.58	850.91	41.03	
				G336.990−00.021^T	C	16:35:31.4	−47:31:06.3	28.51	850.91	19.86	
				G336.994−00.028^T	C	16:35:34.0	−47:31:11.4	17.99	850.91	47.26	
				G337.001−00.030	Q	16:35:36.3	−47:30:57.9	22.86	···	···	

Table 4.1 continued

Table 4.1: Bright Catalog Fields and Targets (continued)

Field	R.A. J2000 (hh:mm:ss)	Decl. J2000 (dd:mm:ss)	Epoch	Target[a]	Cat.[b]	R.A. J2000 (hh:mm:ss)	Decl. J2000 (dd:mm:ss)	$R_{\rm IR}$ (arcsec)	$S_{6\,\rm GHz}$ (mJy beam^{-1})	$\Delta\theta^c$ (arcsec)	Author
				G337.046−00.001	Q	16:35:39.5	−47:27:48.8	27.56	···	···	
shrds864	16:36:09.3	−47:37:06.3	2015	G336.919−00.188^T	K	16:35:58.0	−47:40:58.7	191.21	···	···	W70
				G336.984−00.183^T	C	16:36:12.4	−47:37:54.5	45.19	442.86	59.12	
shrds865	16:34:01.1	−47:16:20.6	2015	G337.004+00.322^T	C	16:34:05.2	−47:16:34.0	53.15	127.23	43.67	
shrds867	16:40:02.7	−48:04:15.4	2015	G337.091−00.965^T	C	16:40:06.0	−48:04:30.0	159.35	104.67	36.07	
				G337.113−01.049	C	16:40:34.1	−48:06:48.8	104.74	12.47	26.45	
shrds869	16:36:19.5	−47:24:14.3	2015	G337.097−00.045	Q	16:36:03.2	−47:27:19.2	33.08	···	···	
				G337.138+00.008	Q	16:35:59.0	−47:23:20.6	33.77	···	···	
				G337.170−00.059^T	C	16:36:24.2	−47:24:37.8	35.25	574.45	51.30	
				G337.177−00.062^T	C	16:36:26.8	−47:24:28.1	28.86	262.35	0.00	
				G337.188−00.060	C	16:36:28.8	−47:23:52.8	28.86	···	···	
				G337.195−00.060	C	16:36:30.5	−47:23:34.6	28.86	···	···	
shrds870	16:37:07.3	−47:25:14.9	2015	G337.253−00.165^T	C	16:37:12.0	−47:25:14.6	59.25	872.51	46.78	
				G337.260−00.150	Q	16:37:09.6	−47:24:18.1	13.94	···	···	
				G337.281−00.163^T	C	16:37:18.1	−47:23:54.9	30.12	184.76	0.00	
				G337.285−00.113^T	C	16:37:05.9	−47:21:43.0	57.15	880.79	12.15	
				G337.304−00.142^T	C	16:37:17.9	−47:22:01.1	85.64	855.00	89.26	
shrds871	16:36:02.5	−47:12:36.5	2015	G337.286+00.113^T	C	16:36:07.0	−47:12:34.0	105.60	143.25	45.75	
				G337.327+00.053	Q	16:36:32.4	−47:13:10.3	57.30	···	···	
shrds875	16:38:51.0	−47:26:44.7	2015	G337.367−00.402	Q	16:38:41.6	−47:29:40.1	22.37	···	···	
				G337.377−00.389	Q	16:38:40.6	−47:28:42.6	22.37	···	···	
				G337.392−00.401	Q	16:38:47.2	−47:28:30.4	22.37	···	···	
				G337.404−00.404^T	C	16:38:50.9	−47:28:06.2	38.72	406.78	95.31	
				G337.412−00.401	Q	16:38:51.9	−47:27:36.8	22.37	···	···	
				G337.428−00.401^T	C	16:38:55.7	−47:26:53.4	58.62	406.78	9.26	
				G337.439−00.397	Q	16:38:57.3	−47:26:15.0	22.37	···	···	
				G337.453−00.363^T	C	16:38:51.6	−47:24:15.4	95.16	406.78	154.49	
				G337.496−00.258	K	16:38:33.9	−47:18:06.8	335.50	···	···	CH87
shrds880	16:38:08.0	−47:04:57.8	2015	G337.583−00.044^T	C	16:37:58.2	−47:05:38.8	95.77	742.48	107.07	
				G337.584−00.069	Q	16:38:05.2	−47:06:37.9	26.51	···	···	
				G337.608−00.047	Q	16:38:05.1	−47:04:40.7	29.22	···	···	
				G337.617−00.065^T	C	16:38:11.7	−47:04:58.6	49.58	378.88	0.00	
				G337.652−00.050^T	K	16:38:16.2	−47:02:50.0	197.83	···	···	CH87
shrds881	16:37:49.0	−46:58:30.3	2015	G337.593+00.096	Q	16:37:24.0	−46:59:35.3	22.03	···	···	
				G337.652−00.050^T	K	16:38:16.2	−47:02:50.0	197.83	···	···	CH87
				G337.664+00.049^T	C	16:37:53.1	−46:58:19.5	102.49	290.53	42.23	

Table 4.1 continued

Table 4.1: Bright Catalog Fields and Targets (continued)

Field	R.A. J2000 (hh:mm:ss)	Decl. J2000 (dd:mm:ss)	Epoch	Target[a]	Cat.[b]	R.A. J2000 (hh:mm:ss)	Decl. J2000 (dd:mm:ss)	$R_{\rm IR}$ (arcsec)	$S_{6\,\rm GHz}$ (mJy beam^{-1})	$\Delta\theta^c$ (arcsec)	Author
				G337.709+00.091^T	C	16:37:52.8	−46:54:38.5	68.90	481.51	31.45	
				G337.754+00.057^T	C	16:38:12.2	−46:53:59.3	203.32	420.54	127.29	
shrds883	16:38:50.0	−47:06:57.2	2015	G337.652−00.050^T	K	16:38:16.2	−47:02:50.0	197.83	···	···	CH87
				G337.653−00.180	Q	16:38:50.6	−47:08:00.5	19.92	···	···	
				G337.658−00.162^T	C	16:38:46.8	−47:07:01.8	93.26	454.69	25.05	
				G337.660−00.183	Q	16:38:53.0	−47:07:48.0	19.92	···	···	
				G337.665−00.176^T	C	16:38:52.4	−47:07:18.4	19.92	354.19	33.53	
				G337.671−00.195	Q	16:38:58.7	−47:07:47.4	19.92	···	···	
shrds884	16:39:38.9	−47:12:36.1	2015	G337.684−00.343^T	C	16:39:40.7	−47:13:06.7	162.52	408.07	35.56	
shrds885	16:38:25.5	−47:00:33.2	2015	G337.652−00.050^T	K	16:38:16.2	−47:02:50.0	197.83	···	···	CH87
				G337.696−00.070	Q	16:38:31.6	−47:01:38.7	28.34	···	···	
				G337.705−00.059^T	C	16:38:31.0	−47:00:49.2	67.52	600.02	56.46	
				G337.754+00.057^T	C	16:38:12.2	−46:53:59.3	203.32	420.54	127.29	
shrds886	16:37:57.9	−46:55:01.6	2015	G337.664+00.049^T	C	16:37:53.1	−46:58:19.5	102.49	290.53	42.23	
				G337.709+00.091^T	C	16:37:52.8	−46:54:38.5	68.90	481.51	31.45	
				G337.754+00.057^T	C	16:38:12.2	−46:53:59.3	203.32	420.54	127.29	
shrds888	16:38:23.4	−46:53:03.2	2015	G337.754+00.057^T	C	16:38:12.2	−46:53:59.3	203.32	420.54	127.29	
				G337.827+00.056^T	C	16:38:29.6	−46:50:46.4	135.53	195.06	150.27	
shrds1233	16:39:33.8	−46:55:26.4	2016	G337.876−00.133^T	C	16:39:30.4	−46:56:07.4	137.56	70.08	53.59	
				G337.920−00.158	Q	16:39:47.4	−46:55:09.8	35.87	···	···	
				G337.926−00.133	Q	16:39:42.2	−46:53:53.7	16.13	···	···	
				G338.003−00.121	K	16:39:57.0	−46:49:58.3	276.32	···	···	CH87
shrds890	16:38:58.4	−46:42:18.8	2015	G337.996+00.081^T	C	16:39:02.6	−46:42:13.2	67.80	267.20	42.21	
				G338.009+00.016^T	C	16:39:22.4	−46:44:13.1	101.02	757.99	19.67	
shrds891	16:40:02.0	−46:51:07.3	2015	G337.920−00.158	Q	16:39:47.4	−46:55:09.8	35.87	···	···	
				G337.926−00.133	Q	16:39:42.2	−46:53:53.7	16.13	···	···	
				G337.986−00.144	Q	16:39:59.0	−46:51:37.9	19.35	···	···	
				G338.002−00.149^T	C	16:40:04.1	−46:51:07.3	19.35	651.66	20.88	
				G338.003−00.121	K	16:39:57.0	−46:49:58.3	276.32	···	···	CH87
				G338.114−00.193	K	16:40:41.8	−46:47:51.7	271.53	···	···	CH87
shrds892	16:39:21.1	−46:44:00.4	2015	G337.996+00.081^T	C	16:39:02.6	−46:42:13.2	67.80	267.20	42.21	
				G338.003−00.121	K	16:39:57.0	−46:49:58.3	276.32	···	···	CH87
				G338.009+00.016^T	C	16:39:22.4	−46:44:13.1	101.02	757.99	19.67	
				G338.075+00.016^T	K	16:39:38.0	−46:41:17.4	75.12	···	···	CH87
shrds1219	16:39:58.1	−46:45:05.0	2016	G338.003−00.121	K	16:39:57.0	−46:49:58.3	276.32	···	···	CH87
				G338.066−00.069^T	C	16:39:58.1	−46:45:04.3	35.88	213.51	0.00	

Table 4.1 continued

Table 4.1: Bright Catalog Fields and Targets (continued)

Field	R.A. J2000 (hh:mm:ss)	Decl. J2000 (dd:mm:ss)	Epoch	Target[a]	Cat.[b]	R.A. J2000 (hh:mm:ss)	Decl. J2000 (dd:mm:ss)	$R_{\rm IR}$ (arcsec)	$S_{6\,\rm GHz}$ (mJy beam^{-1})	$\Delta\theta^c$ (arcsec)	Author
				G338.075+00.016^T	K	16:39:38.0	−46:41:17.4	75.12	···	···	CH87
				G338.080−00.028	Q	16:39:50.6	−46:42:48.7	34.89	···	···	
				G338.114−00.193	K	16:40:41.8	−46:47:51.7	271.53	···	···	CH87
shrds893	16:39:38.7	−46:39:37.6	2015	G338.009+00.016^T	C	16:39:22.4	−46:44:13.1	101.02	757.99	19.67	
				G338.075+00.016^T	K	16:39:38.0	−46:41:17.4	75.12	···	···	CH87
				G338.080−00.028	Q	16:39:50.6	−46:42:48.7	34.89	···	···	
				G338.106+00.020^T	C	16:39:44.1	−46:39:43.5	50.45	497.15	14.47	
shrds894	16:42:01.7	−46:47:02.3	2015	G338.263−00.364^T	C	16:42:01.2	−46:47:54.6	35.26	175.40	52.52	
				G338.271−00.293	Q	16:41:44.4	−46:44:45.2	25.86	···	···	
				G338.289−00.373^T	C	16:42:09.5	−46:47:04.9	59.11	175.40	54.51	
				G338.328−00.291	Q	16:41:57.1	−46:42:06.7	54.93	···	···	
shrds896	16:41:06.8	−46:32:35.6	2015	G338.360−00.095^T	C	16:41:12.8	−46:32:52.2	94.24	803.94	65.72	
				G338.364−00.020^T	C	16:40:54.3	−46:29:44.5	54.03	416.34	0.00	
				G338.374−00.152^T	C	16:41:31.1	−46:34:31.1	34.37	131.02	0.00	
				G338.430+00.048	K	16:40:51.8	−46:24:04.3	346.56	···	···	CH87
caswell22	16:41:51.7	−46:35:04.5	2016	G338.344−00.159	Q	16:41:26.0	−46:36:08.9	34.37	···	···	
				G338.374−00.152^T	C	16:41:31.1	−46:34:31.1	34.37	131.02	0.00	
				G338.405−00.203^T	K	16:41:51.7	−46:35:09.4	63.49	···	···	CH87
				G338.430−00.214	Q	16:42:00.2	−46:34:26.4	38.72	···	···	
				G338.446−00.261	Q	16:42:16.3	−46:35:34.9	21.21	···	···	
				G338.450−00.250	Q	16:42:14.3	−46:34:57.8	21.21	···	···	
				G338.461−00.217	Q	16:42:08.1	−46:33:09.7	43.86	···	···	
				G338.462−00.262^T	C	16:42:20.3	−46:34:54.6	138.65	508.64	43.03	
shrds898	16:42:16.2	−46:35:05.8	2015	G338.405−00.203^T	K	16:41:51.7	−46:35:09.4	63.49	···	···	CH87
				G338.430−00.214	Q	16:42:00.2	−46:34:26.4	38.72	···	···	
				G338.446−00.261	Q	16:42:16.3	−46:35:34.9	21.21	···	···	
				G338.450−00.250	Q	16:42:14.3	−46:34:57.8	21.21	···	···	
				G338.461−00.217	Q	16:42:08.1	−46:33:09.7	43.86	···	···	
				G338.462−00.262^T	C	16:42:20.3	−46:34:54.6	138.65	508.64	43.03	
shrds899	16:42:09.7	−46:25:15.8	2015	G338.565−00.151^T	C	16:42:14.7	−46:25:50.9	155.02	167.65	61.41	
shrds900	16:41:28.9	−46:18:11.8	2015	G338.430+00.048	K	16:40:51.8	−46:24:04.3	346.56	···	···	CH87
				G338.576+00.020^T	C	16:41:32.7	−46:18:36.6	135.11	775.32	47.37	
				G338.596−00.007	Q	16:41:44.3	−46:18:46.6	31.74	···	···	
shrds901	16:41:09.7	−46:10:52.9	2015	G338.628+00.145^T	C	16:41:12.1	−46:11:19.0	88.43	648.66	36.57	
shrds1223	16:39:42.0	−45:47:21.8	2016	G338.706+00.645^T	K	16:39:20.5	−45:47:52.8	181.86	···	···	CH87
				G338.861+00.597	G	16:40:08.4	−45:42:52.2	460.33	80.67	387.70	

Table 4.1 continued

Table 4.1: Bright Catalog Fields and Targets (continued)

Field	R.A. J2000 (hh:mm:ss)	Decl. J2000 (dd:mm:ss)	Epoch	Target[a]	Cat.[b]	R.A. J2000 (hh:mm:ss)	Decl. J2000 (dd:mm:ss)	$R_{\rm IR}$ (arcsec)	$S_{6\,\rm GHz}$ (mJy beam^{-1})	$\Delta\theta^c$ (arcsec)	Author
shrds904	16:43:56.7	−46:20:15.1	2015	G338.837−00.318^T	C	16:44:00.9	−46:20:09.4	118.21	107.97	42.09	
shrds905	16:40:51.7	−45:51:18.6	2015	G338.816+00.403^T	C	16:40:48.2	−45:52:36.9	135.03	106.39	86.61	
				G338.848+00.412	Q	16:40:53.1	−45:50:48.6	18.21	···	···	
				G338.851+00.405	C	16:40:55.5	−45:50:56.0	18.21	31.13	0.00	
				G338.861+00.597	G	16:40:08.4	−45:42:52.2	460.33	80.67	387.70	
				G338.896+00.384	Q	16:41:11.2	−45:49:44.6	18.61	···	···	
				G338.901+00.348	Q	16:41:21.7	−45:50:57.5	67.95	···	···	
				G338.904+00.393	Q	16:41:10.7	−45:49:02.3	18.61	···	···	
				G338.926+00.392^T	C	16:41:16.1	−45:48:05.9	80.90	539.24	40.70	
shrds1225	16:40:29.0	−45:44:17.0	2016	G338.861+00.597	G	16:40:08.4	−45:42:52.2	460.33	80.67	387.70	
				G338.883+00.537^T	G	16:40:28.9	−45:44:16.1	82.68	90.74	1.45	
				G338.906+00.557	Q	16:40:28.9	−45:42:26.1	25.33	···	···	
				G338.911+00.615^T	K	16:40:15.1	−45:39:53.3	226.25	···	···	CH87
				G338.915+00.547	Q	16:40:33.6	−45:42:25.8	25.33	···	···	
				G338.921+00.549	Q	16:40:34.3	−45:42:03.7	27.09	···	···	
				G338.925+00.563	Q	16:40:31.6	−45:41:19.5	25.33	···	···	
shrds906	16:41:12.3	−45:48:14.3	2015	G338.816+00.403^T	C	16:40:48.2	−45:52:36.9	135.03	106.39	86.61	
				G338.848+00.412	Q	16:40:53.1	−45:50:48.6	18.21	···	···	
				G338.851+00.405	C	16:40:55.5	−45:50:56.0	18.21	31.13	0.00	
				G338.896+00.384	Q	16:41:11.2	−45:49:44.6	18.61	···	···	
				G338.901+00.348	Q	16:41:21.7	−45:50:57.5	67.95	···	···	
				G338.904+00.393	Q	16:41:10.7	−45:49:02.3	18.61	···	···	
				G338.917+00.382	Q	16:41:16.6	−45:48:53.5	23.22	···	···	
				G338.926+00.392^T	C	16:41:16.1	−45:48:05.9	80.90	539.24	40.70	
shrds909	16:42:55.3	−45:48:58.4	2015	G339.094+00.208	Q	16:42:41.8	−45:47:47.4	36.60	···	···	
				G339.106+00.152^T	C	16:42:59.1	−45:49:28.5	52.91	181.21	51.10	
				G339.233+00.243	K	16:43:04.1	−45:40:07.0	484.34	···	···	CH87
shrds910	16:47:00.5	−46:24:45.9	2015	G339.169−00.698	C	16:46:56.1	−46:19:52.2	584.29	123.46	298.61	
shrds913	16:42:59.8	−45:39:56.8	2015	G339.216+00.263^T	C	16:42:55.2	−45:40:07.4	52.80	154.27	49.45	
				G339.233+00.243	K	16:43:04.1	−45:40:07.0	484.34	···	···	CH87
shrds915	16:46:50.3	−46:11:50.5	2015	G339.147−00.600	C	16:46:25.2	−46:17:03.1	284.17	89.94	119.41	
				G339.169−00.698	C	16:46:56.1	−46:19:52.2	584.29	123.46	298.61	
				G339.275−00.607^T	C	16:46:55.9	−46:11:28.9	117.65	123.46	61.08	
shrds917	16:44:11.8	−45:31:34.3	2015	G339.478+00.181^T	C	16:44:15.2	−45:31:26.9	73.00	183.83	37.00	
shrds918	16:44:37.1	−45:34:31.5	2015	G339.478+00.181^T	C	16:44:15.2	−45:31:26.9	73.00	183.83	37.00	
				G339.486+00.087^T	C	16:44:41.5	−45:34:47.6	88.04	286.33	48.05	
shrds919	16:46:59.2	−45:50:33.7	2015	G339.531−00.417	Q	16:47:03.3	−45:52:20.3	46.76	···	···	

Table 4.1 continued

Table 4.1: Bright Catalog Fields and Targets (continued)

Field	R.A. J2000 (hh:mm:ss)	Decl. J2000 (dd:mm:ss)	Epoch	Target[a]	Cat.[b]	R.A. J2000 (hh:mm:ss)	Decl. J2000 (dd:mm:ss)	$R_{\rm IR}$ (arcsec)	$S_{6\,\rm GHz}$ (mJy beam^{-1})	$\Delta\theta^c$ (arcsec)	Author
				G339.548−00.385	C	16:46:58.7	−45:50:23.9	52.32	···	···	
				G339.553−00.401^T	C	16:47:03.9	−45:50:47.1	191.03	307.21	51.79	
shrds920	16:44:05.6	−45:23:39.2	2015	G339.556+00.282^T	C	16:44:06.7	−45:23:58.5	82.94	244.44	22.44	
shrds921	16:44:59.2	−45:30:01.5	2015	G339.584+00.084^T	C	16:45:04.0	−45:30:26.0	98.68	195.12	55.08	
				G339.590+00.083	Q	16:45:05.8	−45:30:13.2	20.23	···	···	
				G339.596+00.079	Q	16:45:08.1	−45:30:05.6	18.41	···	···	
shrds922	16:44:30.2	−45:18:39.6	2016	G339.676+00.283^T	C	16:44:33.1	−45:18:28.2	57.87	61.35	32.87	
				G339.699+00.302	Q	16:44:33.3	−45:16:40.7	21.20	···	···	
shrds925	16:51:15.0	−46:14:23.3	2015	G339.494−01.308	C	16:50:51.3	−46:28:27.2	648.70	61.64	626.35	
				G339.717−01.211^T	C	16:51:15.0	−46:14:27.8	141.60	125.29	4.09	
fa642	16:45:03.4	−45:14:54.5	2015	G339.781+00.243^T	C	16:45:07.0	−45:15:17.0	119.86	125.00	42.51	
				G339.845+00.299^T	K	16:45:06.5	−45:10:09.4	97.83	···	···	CH87
shrds928	16:45:03.4	−45:14:54.5	2015	G339.781+00.243^T	C	16:45:07.0	−45:15:17.0	119.86	125.00	42.51	
				G339.845+00.299^T	K	16:45:06.5	−45:10:09.4	97.83	···	···	CH87
shrds1234	16:46:34.5	−45:14:38.8	2016	G339.952+00.052^T	C	16:46:34.1	−45:14:54.9	82.98	88.04	16.38	
				G340.002+00.159^T	K	16:46:17.7	−45:08:29.8	164.85	···	···	GBT HRDS
shrds1236	16:48:01.3	−45:17:13.4	2016	G340.029−00.158	C	16:47:45.8	−45:19:33.0	101.45	···	···	
				G340.051−00.231^T	K	16:48:09.8	−45:21:23.8	74.22	···	···	CH87
				G340.059−00.138^T	C	16:47:47.4	−45:17:25.7	105.16	155.94	56.21	
				G340.068−00.075	C	16:47:32.7	−45:14:32.6	107.10	···	···	
				G340.097−00.174^T	C	16:48:04.9	−45:17:03.0	113.14	128.49	38.57	
				G340.118−00.142	Q	16:48:01.4	−45:14:52.8	26.86	···	···	
shrds1237	16:49:14.3	−45:18:22.4	2016	G340.106−00.354	K	16:48:54.0	−45:23:36.5	309.80	···	···	GBT HRDS
				G340.211−00.318^T	K	16:49:07.6	−45:17:23.8	192.06	···	···	GBT HRDS
				G340.234−00.368	Q	16:49:25.7	−45:18:15.8	35.86	···	···	
				G340.247−00.373	C	16:49:29.8	−45:17:50.8	35.86	···	···	
shrds930	16:54:03.6	−45:23:08.7	2016	G340.678−01.049	G	16:54:01.6	−45:23:43.0	324.38	63.65	39.81	
				G340.780−01.022^T	K	16:54:16.5	−45:17:57.7	128.22	···	···	CH87
caswell23	16:52:33.0	−43:23:38.0	2016	G341.962+00.437^T	K	16:52:08.3	−43:27:37.9	131.28	···	···	GBT HRDS
				G342.062+00.417^T	K	16:52:34.4	−43:23:45.8	175.01	···	···	CH87
				G342.139+00.430	C	16:52:47.2	−43:19:41.0	78.90	···	···	
shrds1238	16:55:11.2	−43:21:30.1	2016	G342.349+00.100	Q	16:54:55.3	−43:22:24.8	20.78	···	···	
				G342.360+00.107^T	K	16:54:55.9	−43:21:38.3	66.77	···	···	GBT HRDS
				G342.363+00.124	Q	16:54:52.1	−43:20:51.4	20.78	···	···	
				G342.377+00.133	Q	16:54:52.8	−43:19:52.8	15.69	···	···	
				G342.384+00.122	C	16:54:57.1	−43:19:58.3	20.78	···	···	

Table 4.1 continued

Table 4.1: Bright Catalog Fields and Targets (continued)

Field	R.A. J2000 (hh:mm:ss)	Decl. J2000 (dd:mm:ss)	Epoch	Target[a]	Cat.[b]	R.A. J2000 (hh:mm:ss)	Decl. J2000 (dd:mm:ss)	$R_{\rm IR}$ (arcsec)	$S_{6\,\rm GHz}$ (mJy beam^{-1})	$\Delta\theta^c$ (arcsec)	Author
				G342.388+00.074^T	C	16:55:10.1	−43:21:34.6	68.94	61.14	12.67	
				G342.389+00.125	C	16:54:57.4	−43:19:37.8	20.78	···	···	
shrds1239	16:55:55.5	−43:24:03.1	2016	G342.354−00.047^T	K	16:55:34.2	−43:27:43.5	123.51	···	···	CH87
				G342.429−00.046^T	K	16:55:49.4	−43:24:10.4	61.54	···	···	GBT HRDS
				G342.438−00.061^T	C	16:55:55.2	−43:24:19.0	43.80	80.23	16.16	
shrds1240	16:58:38.4	−42:46:45.4	2016	G343.224−00.065^T	C	16:58:37.3	−42:47:35.6	97.50	64.16	50.39	
				G343.234−00.078	C	16:58:42.6	−42:47:36.4	21.37	···	···	
				G343.328+00.009	G	16:58:39.6	−42:39:58.6	586.12	···	···	
shrds1241	16:59:04.2	−42:41:24.8	2016	G343.328+00.009	G	16:58:39.6	−42:39:58.6	586.12	···	···	
				G343.352−00.081^T	C	16:59:07.3	−42:42:09.9	56.50	173.69	57.48	
				G343.353−00.068	C	16:59:04.2	−42:41:38.1	29.71	···	···	
				G343.355−00.101	Q	16:59:13.1	−42:42:46.3	35.96	···	···	
				G343.480−00.043	K	16:59:23.5	−42:34:43.8	277.42	···	···	CH87
caswell24	17:03:31.3	−42:37:07.7	2016	G343.914−00.646^T	K	17:03:25.5	−42:36:22.9	229.35	···	···	CH87
caswell25	17:02:10.3	−41:46:32.2	2016	G344.424+00.044^T	K	17:02:09.4	−41:46:52.4	95.52	···	···	CH87
fa644	17:16:59.8	−38:19:28.6	2015	G348.855−00.165	Q	17:16:49.7	−38:20:43.2	20.62	···	···	
				G348.858−00.167	Q	17:16:50.9	−38:20:39.6	71.33	···	···	
				G348.881−00.174	Q	17:16:56.6	−38:19:45.8	27.14	···	···	
				G348.890−00.190	Q	17:17:02.3	−38:19:53.4	20.99	···	···	
				G348.892−00.179^T	K	17:16:59.9	−38:19:24.7	28.14	362.22	4.01	GBT HRDS
gs038	17:17:27.3	−37:51:05.9	2015	G349.293+00.019	Q	17:17:21.4	−37:52:55.2	21.76	···	···	
				G349.297+00.088	Q	17:17:05.0	−37:50:19.6	22.35	···	···	
				G349.328+00.020^T	K	17:17:27.2	−37:51:09.6	83.62	···	···	GBT HRDS
fa016	17:27:47.6	−35:39:14.4	2015	G352.251−00.442	Q	17:27:37.9	−35:42:23.6	99.21	···	···	
				G352.313−00.442^T	K	17:27:48.0	−35:39:17.5	79.13	264.45	5.54	GBT HRDS
				G352.333−00.455	Q	17:27:54.5	−35:38:43.8	16.95	···	···	
				G352.337−00.451	Q	17:27:54.1	−35:38:23.2	37.86	···	···	
fa032	17:33:29.6	−32:48:02.3	2015	G355.244+00.109	K	17:33:22.6	−32:54:14.0	405.64	···	···	L89
				G355.344+00.145^T	K	17:33:29.6	−32:48:02.3	42.50	540.89	0.00	GBT HRDS
gs108	17:42:28.2	−30:09:30.7	2015	G358.541−00.076	Q	17:42:24.0	−30:13:06.7	55.85	···	···	
				G358.552−00.026^T	K	17:42:13.7	−30:10:56.9	42.50	···	···	GBT HRDS
				G358.561−00.096	Q	17:42:31.5	−30:12:42.5	21.04	···	···	
				G358.563−00.067	Q	17:42:25.0	−30:11:41.4	15.41	···	···	
				G358.586−00.076	Q	17:42:30.5	−30:10:48.0	15.86	···	···	
				G358.599−00.086	Q	17:42:34.7	−30:10:27.2	19.41	···	···	
				G358.600−00.058^T	K	17:42:28.3	−30:09:30.9	47.54	···	···	GBT HRDS

Table 4.1 continued

Table 4.1: Bright Catalog Fields and Targets (continued)

Field	R.A. J2000 (hh:mm:ss)	Decl. J2000 (dd:mm:ss)	Epoch	Target[a]	Cat.[b]	R.A. J2000 (hh:mm:ss)	Decl. J2000 (dd:mm:ss)	$R_{\rm IR}$ (arcsec)	$S_{6\,\rm GHz}$ (mJy beam^{-1})	$\Delta\theta^c$ (arcsec)	Author
				G358.616−00.077^T	K	17:42:35.1	−30:09:17.8	42.50	···	···	GBT HRDS
				G358.618−00.060	C	17:42:31.4	−30:08:39.5	21.70	···	···	
				G358.635−00.067	Q	17:42:35.6	−30:08:01.7	11.73	···	···	
				G358.641−00.070	Q	17:42:37.1	−30:07:48.6	14.14	···	···	
				G358.643−00.035^T	K	17:42:29.1	−30:06:35.7	55.30	···	···	GBT HRDS
				G358.646−00.065	Q	17:42:36.8	−30:07:25.1	13.03	···	···	
				G358.652−00.079^T	K	17:42:40.8	−30:07:31.4	42.50	···	···	GBT HRDS
fa054	17:42:05.0	−30:04:03.9	2015	G358.633+00.062^T	K	17:42:05.0	−30:04:04.0	42.50	377.74	0.00	GBT HRDS
fa489	17:45:01.1	−29:28:50.3	2015	G359.436−00.091^T	K	17:44:37.5	−29:27:52.1	98.55	···	···	CH87
				G359.464−00.094	C	17:44:42.3	−29:26:32.5	40.82	···	···	
				G359.467−00.173^T	K	17:45:01.1	−29:28:50.3	42.50	228.59	0.00	GBT HRDS
				G359.504−00.108	Q	17:44:51.3	−29:24:55.3	22.08	···	···	

[a] "T" indicates that this source is a "nominal" target (see the text)

[b] The *WISE* Catalog designation: "K" is a known H II region, "C" is an H II region candidate, "Q" is a radio-quiet H II region candidate, and "G" is an H II candidate associated with an H II region group.

[c] The separation between the *WISE* Catalog infrared position and the position of the SUMSS continuum peak.

References — GBT HRDS (Anderson et al., 2011, 2015a, 2018); CH87 (Caswell & Haynes, 1987); L89 (Lockman, 1989); W70 (Wilson et al., 1970b)

Table 4.2: Observation Summary

Parameters	Epoch: 2015	Epoch: 2016
H75 Observing Dates	2015 Jul 24 to 2015 Aug 23	2016 Jul 23 to 2016 Aug 15
H75 Observing Time (hr)	121	150
H168 Observing Dates	2015 Sep 18 to 2015 Oct 14	2016 Sep 03 to 2016 Sep 29
H168 Observing Time (hr)	63	144
Total Observing Time (hr)	184	294
Primary Calibrators	0823−500, 1934−638	0823−500, 1934−638
Secondary Calibrators	0906−47, 1036−52, 1613−586, 1714−336, 1714−397, J1322−6532	1036−52, 1613−586, J1322−6532

For each spectral window, we list the center frequency, $\nu_{\rm center}$; the bandwidth; the number of channels; and the channel width, $\Delta\nu$. For the spectral line windows, we also identify the targeted RRL and RRL rest frequency, $\nu_{\rm RRL}$. The data are observed in two circular polarizations, LL and RR, thus yielding 40 independent RRL spectra.

Our spectral window configuration is a compromise between the two setups used in the pilot survey. At lower frequencies, the RRLs are more tightly spaced in frequency, and we can observe more of them within a given bandwidth, but these RRLs are fainter and contaminated with more radio frequency interference (RFI). At higher frequencies, the RRLs are brighter, but they are more spaced out in frequency, and thus we observe fewer of them within a given bandwidth.

We use a two-phase observing strategy for the SHRDS: a first-pass "snapshot" survey in the H75 antenna configuration to measure the continuum brightness of each target, and then a second-pass "deep" survey split between the H75 and H168 antenna configurations to measure the RRLs. In the "snapshot" survey, we observe each target for a total of ∼20 minutes in ∼2–3 minute integrations spread over ∼9 hr in hour angle. We reduce these data and measure the continuum flux density of each target. Assuming an RRL-to-continuum intensity ratio of 0.10, which is typical for an optically thin H II region in local thermodynamic equilibrium (LTE) at 6 GHz (e.g. Wilson et al., 1970b; Lockman & Brown, 1975), we estimate the integration time required to detect the RRL after averaging the 20 observed RRL transitions. We also take note of the level of confusion in each field, and we give confused fields priority in the H168 antenna configuration. In the "deep" survey, we re-observe each target for this estimated integration time split between the H75 and H168 antenna configurations.

Unlike the pilot survey, we aim to create high dynamic range images of our targets. Therefore, we require longer integrations and good coverage in the *uv*-plane. Total integration times on our targets range from ∼30 minutes to ∼60 minutes spread over ∼9 hr in hour angle depending on the predicted RRL intensity. Figure 4.3 shows an example of the typical *uv*-coverage for our observations. Our observing strategy nearly fills the *uv*-plane and yields high-fidelity, high dynamic range images. Due to the nature of an interferometer, however, we are not sensitive to any emission on spatial scales larger than the maximum recoverable scale of our most compact antenna configuration, which is ∼265 arcsec at 6 GHz. Since over 95% of the sources in the *WISE* Catalog have predicted radio sizes smaller than 265 arcsec, the ATCA

is optimized for the SHRDS.

4.4 Data Reduction and Analysis

We developed a publicly available, modular data calibration, reduction, and analysis pipeline for the SHRDS: the Wenger Interferometry Software Package (WISP; Wenger, 2018)[1]. The pipeline is written in *Python* and is implemented through the Common Astronomy Software Applications (CASA) package (McMullin et al., 2007). These tools are generic and may be used to reduce and analyze any continuum or spectral line interferometric data set. They benefit from a balance of automation and user-input with tunable parameters to handle multiple use cases. For example, the calibration pipeline uses built-in CASA automatic bad-data flagging algorithms, but also generates many data quality diagnostics used for manual flagging. Here, we briefly describe the specific calibration, reduction, and analysis steps used for the SHRDS. A more complete discussion of WISP and our data reduction process is in Appendix B.

4.4.1 Calibration

We observe at least one "primary" calibrator and several "secondary" calibrators each day. The primary calibrators, 0823–500 and 1934–638, are used to calibrate the absolute flux and delays and to remove instrumental bandpass structure. The secondary calibrators are point sources located close to our science targets on the sky and are used to calibrate the complex gains (phases and amplitudes) of our data. We typically observe a primary calibrator twice during a single observing session and a secondary calibrator every 10–20 minutes. Table 4.2 lists the calibrators we used in the Bright Catalog.

The calibration pipeline uses calibrator data to iteratively compute calibration solutions, to automatically flag bad data, to apply calibration solutions, and to manually flag bad data. We typically repeat this process two or three times for each observing session before the data are clear of all obvious RFI (or otherwise bad data) and the calibration solutions converge. The most common features we flag in the SHRDS data are (1) persistent RFI missed by the automatic flagging algorithms, (2) off-source antennas at the beginning of each scan, and (3) the first and last ∼200 channels of each spectral line window. Spectral window 17 (8060 MHz, see Table 4.3),

[1] https://doi.org/10.5281/zenodo.2225273

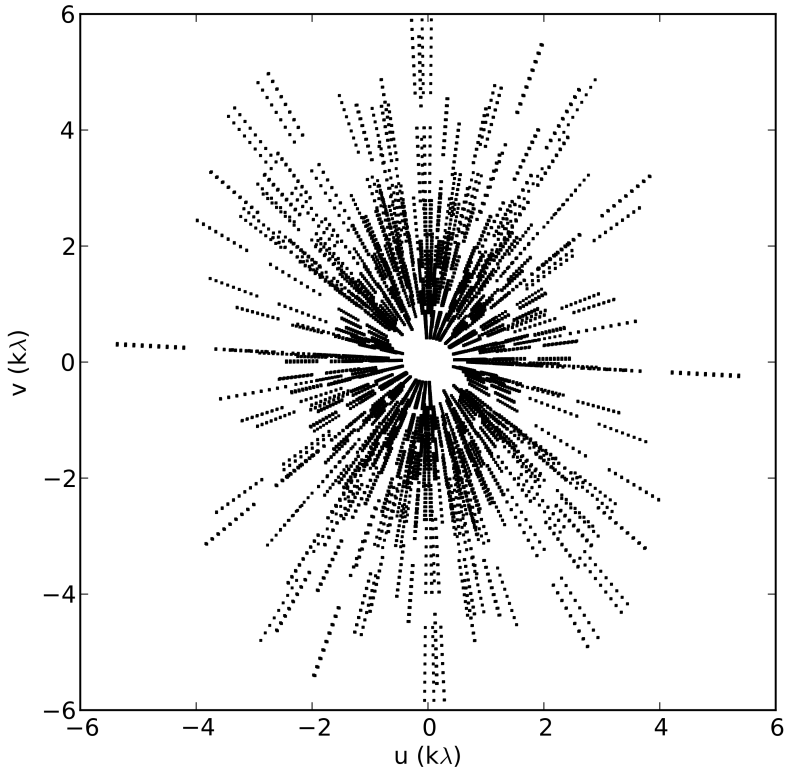

Figure 4.3: Representative example of the *uv*-coverage obtained for each SHRDS field. For clarity, only 9 of the 66 observed continuum window channels are shown. These data are the combination of 30 ∼2 minute snapshots split equally between the H75 and H168 antenna configurations.

Table 4.3: Correlator Setup

Window	$\nu_{\rm center}$ (MHz)	Bandwidth (MHz)	Channels	$\Delta\nu$ (kHz)	RRL	$\nu_{\rm RRL}$ (MHz)
0	5505	2112	33	64000	...	...
1	4609	64	2049	31.25	H112α	4618.790
2	4737	64	2049	32.25	H111α	4744.184
3	4865	64	2049	31.25	H110α	4874.158
4	4993	64	2049	31.25	H109α	5008.924
5	5153	64	2049	31.25	H108α	5148.704
6	5281	64	2049	31.25	H107α	5293.733
7	5441	64	2049	31.25	H106α	5444.262
8	5601	64	2049	31.25	H105α	5600.551
9	5761	64	2049	31.25	H104α	5762.881
10	5921	64	2049	31.25	H103α	5931.546
11	6113	64	2049	31.25	H102α	6106.857
12	6305	64	2049	31.25	H101α	6289.145
13	6465	64	2049	31.25	H100α	6478.761
14	8540	2112	33	64000	...	...
15	7548	64	2049	31.25	H95α	7550.616
16	7804	64	2049	31.25	H94α	7792.872
17	8060	64	2049	31.25	H93α	8045.604
18	8316	64	2049	31.25	H92α	8309.384
19	8572	64	2049	31.25	H91α	8584.823
20	9180	64	2049	31.25	H89α	9173.323
21	9500	64	2049	31.25	H88α	9487.823

covering H93α, is nearly always flagged due to persistent, broad-frequency RFI.

4.4.2 Imaging

Once the data from each observing session are fully calibrated, we create a single data set for each field, from which we generate images. The imaging part of our data reduction and analysis pipeline is nearly fully automated (see Appendix B). We first regrid all of the visibilities to a common kinematic local standard of rest (LSR or LSRK[2]) velocity frame with a channel width $\Delta v_{\rm LSR} = 2.5\,{\rm km\ s^{-1}}$. For each field, we then use the *CLEAN* algorithm to generate the following images and data cubes: (1) a multiscale, multi-frequency synthesis (MS-MFS) image produced by combining the two 2 GHz continuum windows, (2) an MS-MFS image of each 2 GHz continuum window, (3) an MS-MFS image of each 64 MHz bandwidth spectral line window, and (4) a multiscale data cube of each spectral line window.

The emission mechanisms of H II regions allow us to take some shortcuts in our imaging process. The thermal radio continuum emission and RRL emission originate within the same volume of ionized gas. Thus, the morphology of the H II region should not change from channel to channel within a spectral line window. Therefore, to minimize computation time, we use the *CLEAN* masks from the MS-MFS images of each spectral line window to *CLEAN* that entire data cube. We also do not perform any continuum subtraction.

For resolved sources, we can increase the surface brightness sensitivity by *uv*-tapering our data. By giving less weight to the longer baselines when generating an image, *uv*-tapering increases the synthesized beam size and surface brightness sensitivity. Some fraction of our sources will be unresolved and/or in confused fields. In these cases, *uv*-tapering will worsen our point-source sensitivity and spatial resolution. Therefore, we generate two sets of images: one with no *uv*-tapering and a second with a *uv*-taper to a synthesized half-power beam width (HPBW) of 100 arcsec, which is approximately the synthesized HPBW of our lowest frequency spectral line window. Depending on the morphology of the source, the level of confusion within the field, and the scientific use, one of these methods may be more useful than the other.

[2]LSRK is defined by a solar motion of $20\,{\rm km\,s^{-1}}$ in the direction (R.A., Decl.) = ($18^{\rm h}$, $+30°$) at epoch 1900.

4.4.3 Continuum Data Products

The radio continuum image provides several measurable quantities for each detected continuum source: the position, peak continuum flux density, total continuum flux density, and continuum spectral index. In this first data release, we only extract the positions and peak continuum flux densities of our continuum detections associated with *WISE* Catalog H II regions and H II region candidates. In a future data release, we will publish the total continuum flux densities and continuum spectral indicies as well.

We use the 8–10 GHz MS-MFS continuum band image to identify continuum sources within our primary beam. Although the full 4 GHz bandwidth continuum image has better sensitivity, the 8–10 GHz image has better spatial resolution. This higher-frequency image will reveal more structure in confused fields. In each field, we identify distinct continuum emission peaks by visual inspection. Each distinct continuum peak is what we call a "continuum source." In this data release, we only identify continuum sources associated with *WISE* Catalog H II regions or H II region candidates. To be a continuum source in our Bright Catalog, we require that the continuum peak be within a circle centered on the *WISE* Catalog position with a radius equal to the infrared radius.

4.4.4 RRL Data Products

Our goal here is to create a catalog of H II region positions and RRL LSR velocities. We maximize our spectral sensitivity by averaging every H$n\alpha$ RRL transition and both polarizations to create a stacked H$n\alpha$ spectrum, denoted by <H$n\alpha$>. Upon the completion of the entire SHRDS, we will publish the spectra for each detected individual RRL transition.

We extract and average spectra from our data in two ways, depending on whether the data cube is *uv*-tapered or not. For non-tapered data cubes, we extract spectra from each of our spectral windows at the location of the peak continuum source brightness. We remove all poor-quality spectra, usually caused by unflagged RFI or a very poor baseline structure, then we use a weighted average to create the <H$n\alpha$> spectrum. The weights for the ith spectral line window are given by $w_i = S_{C,i}/\mathrm{rms}_i^2$, where $S_{C,i}$ is the continuum brightness, and rms_i is the spectral noise of the ith spectral line window. Both the continuum brightness and rms noise are estimated from the line-free regions of the spectrum. For *uv*-tapered data cubes, we first smooth

each of the spectral window cubes to a common beam size that is slightly larger than the *uv*-tapered beam size (typically 110 arcsec). After removing spectral windows with poor-quality spectra, we average the remaining cubes to create the <H$n\alpha$> cube using the same weighting scheme as with the non-tapered data. We extract the <H$n\alpha$> spectrum at the location of the peak continuum source brightness.

For each <H$n\alpha$> spectrum, we identify the line-free regions and use those to estimate the spectral rms noise and to fit and subtract a third-order polynomial baseline. We then fit a single Gaussian line profile to the spectrum to measure the RRL brightness, the FWHM line width, the LSR velocity, and the signal-to-noise ratio (S/N). We estimate the S/N following the Lenz & Ayres (1992) method:

$$\mathrm{S/N} = 0.7 \left(\frac{S_L}{\mathrm{rms}}\right) \left(\frac{\Delta V}{\Delta v}\right)^{0.5} \tag{4.1}$$

where S_L is the peak line intensity, rms is the spectral noise, ΔV is the FWHM line width, and Δv is the channel width ($2.5\,\mathrm{km\,s^{-1}}$). In cases where multiple RRL components are visible, we fit multiple Gaussian profiles.

4.5 SHRDS: The Bright Catalog

The SHRDS Bright Catalog contains the radio continuum and <H$n\alpha$> RRL properties of the brightest H II regions in the survey. We observe 282 fields containing 149 previously known H II regions and 632 H II region candidates in the Galactic longitude range of $259° < \ell < 344°$. The majority of these objects are too faint or too large to be detected by the ATCA. They are serendipitously observed because they are close to bright H II regions and H II region candidates on the sky. We detect at least 1 radio continuum source in 275 fields (97.5%) and at least 1 <H$n\alpha$> RRL in 258 fields (91.5%). We find radio continuum and <H$n\alpha$> RRL emission toward 80 and 76 previously known H II regions, respectively, and toward 298 and 256 H II region candidates, respectively. If instead we consider our "nominal" targets (H II region candidates with predicted 6 GHz peak continuum flux densities brighter than $60\,\mathrm{mJy\,beam^{-1}}$ and predicted radio diameters less than 265 arcsec, or known H II regions with predicted radio diameters less than 265 arcsec), there are only 100 previously known H II regions and 279 H II region candidates in our fields. Of these, we detect radio continuum emission toward 72 (72%) previously known H II regions and 246 (88%) H II region candidates. We also find RRL emission toward 76 (76%)

previously known H II regions and 230 (82%) H II region candidates. Many of these sources lie near the edge of our primary beam, which further decreases our detection rates.

In this catalog, we also include data from the SHRDS pilot survey (Brown et al., 2017). We attempt to reprocess these data using WISP with mixed success. The fields observed in the SHRDS pilot survey did not typically have adequate *uv*-coverage to create high-fidelity images. Rather, Brown et al. (2017) extracted spectra directly from the *uv* data and averaged them to create the <H$n\alpha$> spectra. They report detections of <H$n\alpha$> RRL emission from 7 previously known H II regions and 36 out of 53 H II region candidates. In our reprocessed pilot survey data, we find continuum emission from 7 previously known H II regions and 46 H II region candidates, and <H$n\alpha$> RRL emission from 7 previously known H II regions and 26 H II region candidates. Nearly all of our detections are from the first epoch (2013) of the SHRDS pilot survey, simply due to the better *uv*-coverage of the first epoch observations. Our reprocessing discovers <H$n\alpha$> RRL emission from four previously known H II regions and one H II region candidate not in the pilot survey catalog. These sources are not in the center of the field and thus were missed by the *uv*-spectra averaging method used by Brown et al. (2017). In the following catalogs, we list our re-analyzed products, if available; otherwise, we give the values from Brown et al. (2017). Data taken directly from Brown et al. (2017) have an asterisk (*) appended to the epoch. Three of the pilot survey "previously known" H II regions (G290.323–02.984, G295.748–00.207, and G323.464+00.079) did not have previous detections of Hα or RRL emission, so they are listed as candidate H II regions in the *WISE* Catalog. These sources are new SHRDS H II region discoveries.

4.5.1 Continuum Catalog

Our continuum source detections are listed in Table 4.4 (non-tapered) and Table 4.5 (*uv*-tapered). For each source, we list the *WISE* Catalog name; the position of the peak radio continuum emission; the field containing the source; the epoch; the synthesized beam area in the continuum image; the separation between the observed continuum peak position and infrared position, $\Delta\theta$; the MFS-synthesized frequency of the continuum image, ν_C; the peak continuum flux density, S_C; the rms noise, rms_C; and a "quality factor". The peak continuum flux density and position are measured at the location of the brightest pixel of the continuum source in the 4 GHz

bandwidth MS-MFS continuum image. The rms noise is estimated as the rms across the entire residual image divided by the primary beam response at the continuum source position. The quality factor, QF, is a qualitative assessment of the accuracy of the peak continuum flux density. QF A means the source is unresolved, unconfused, and located near the center of the primary beam; QF B means the source is slightly resolved, slightly confused, and/or located off-center; and QF C means the source is very resolved, very confused, and/or located near the edge of the primary beam. The primary beam shape is not modeled accurately by CASA beyond ∼300 arcsec from the field center, so continuum sources near the primary beam edge may have flux density errors of $\gtrsim 10\%$ (see Appendix B). Figure 4.4 shows representative 8–10 GHz continuum band images for each QF: G333.725+00.364 (QF A), G312.706+00.012 and G312.675+00.048 (QF B), and G312.764+00.067 (QF C).

A given *WISE* Catalog source may appear in multiple fields. These cases, which we call "multiple detections," nonetheless have only a single entry in Tables 4.4 and 4.5. The data for these targets have the highest continuum QF and/or the largest peak continuum flux-to-rms ratio. Every field is an independent observation of the source, however, so we give the continuum properties as measured in each field in Appendix C. In the next data release, we will combine the data from each field to improve our sensitivity and to measure the continuum properties of these sources more accurately.

4.5.2 Radio Recombination Line Catalog

We list the RRL emission properties for detected sources in Table 4.6 (non-tapered <H$n\alpha$>) and Table 4.7 (uv-tapered <H$n\alpha$>). For each source, we give the *WISE* Catalog name; the field; the epoch; the weighted-average frequency of the <H$n\alpha$> RRL, ν_L; the Gaussian fits to the peak line intensity, S_L; the LSR velocity, $V_{\rm LSR}$; and the FWHM line width, ΔV; the rms spectral noise in the line-free region of the spectrum, rms$_L$; the signal-to-noise ratio calculated using Equation 4.1, S/N; and a quality factor, QF. Like those assigned in the continuum catalog, the QFs are qualitative assessments of the accuracy of the Gaussian fits. Some of the <H$n\alpha$> spectra show multiple RRL components. These components may be distinct in velocity but they are often spectrally blended. QF A means the RRL is unblended with $S/N > 15$. QF B means the RRL is partially blended but has distinct peaks and/or has $15 > S/N > 10$. QF C means the RRL is very blended with no distinct

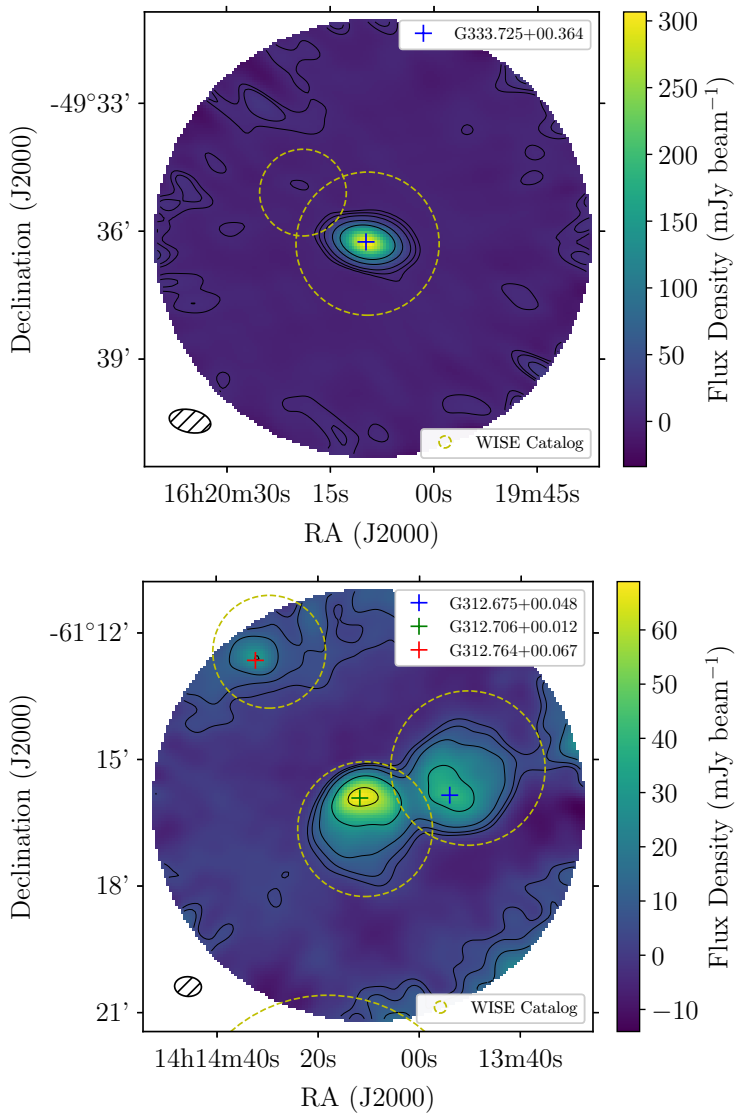

Figure 4.4: Representative 8–10 GHz continuum band images for each continuum quality factor (QF). The top panel is field "shrds803" (non-tapered), which contains a continuum QF A target, G333.725+00.364 (unresolved, unconfused, and centered). The bottom panel is field "shrds462" (non-tapered), which contains two continuum QF B targets, G312.706+00.012 and G312.675+00.048 (resolved and spatially confused), as well as a QF C target, G312.764+00.067 (resolved and far off-center). The black contours are at 5, 10, 20, 50, and 100 times the field center rms noise. The yellow dashed circles represent infrared positions and sizes of the objects in the *WISE* Catalog, the crosses are the locations of the peak continuum emission, and the hatched ellipse represents the ATCA half-power synthesized beam at 7 GHz.

Table 4.4: Non-tapered Image Continuum Properties

Target	R.A. J2000 (hh:mm:ss)	Decl. J2000 (dd:mm:ss)	Field	Epoch[a]	Beam Area (arcsec^2)	$\Delta\theta^b$ (arcsec)	ν_C (MHz)	S_C (mJy beam^{-1})	rms$_C$ (mJy beam^{-1})	QF
G213.833+00.618	06:55:16.9	+0:31:12.3	g213.833+00.618	2014*	···	2.5	···	···	···	···
G230.354−00.597	07:21:49.5	−15:44:09.9	g230.354-00.597	2014*	···	2.2	···	···	···	···
G259.057−01.544	08:26:18.1	−40:48:36.0	shrds030	2016	1353	47.4	7022	69.76	0.31	B
G259.359+00.820	08:37:05.3	−39:44:47.8	shrds035	2015	2501	347.8	7022	19.62	0.06	A
G263.237+00.509	08:48:37.6	−42:53:54.1	shrds060	2015	3077	70.1	7022	67.53	0.43	B
G264.681+00.272	08:52:55.7	−44:16:11.3	shrds073	2015	1382	385.2	7022	2.94	0.23	C
G265.191−00.641	08:50:38.3	−45:08:20.4	shrds075	2015	2479	17.1	7022	56.13	0.31	B
G267.730−01.100	08:58:04.5	−47:22:51.2	shrds078	2016	1627	12.2	7023	226.76	8.29	A
G268.618−00.739	09:03:09.4	−47:48:26.3	shrds081	2015	2435	10.6	7022	24.69	3.25	B
G269.068−01.114	09:03:23.2	−48:26:33.0	shrds085	2016	1677	183.3	7023	578.98	7.01	B
G269.159−01.119	09:03:38.1	−48:27:52.9	shrds085	2016	1677	7.8	7023	236.22	4.59	B
G269.167−01.357	09:02:30.7	−48:38:24.8	shrds086	2016	1317	58.4	7022	48.32	3.72	C
G280.626−01.186	09:58:23.4	−56:22:11.9	shrds111	2015	2566	20.6	7023	88.95	0.21	A
G280.903−00.522	10:02:27.8	−56:04:42.3	shrds113	2015	1366	330.5	7022	16.45	0.11	B
G280.989−01.527	09:58:58.9	−56:52:05.7	shrds1005	2016	1784	21.5	7023	184.19	6.09	B
G281.047−01.541	09:59:16.0	−56:54:37.4	shrds1005	2016	1784	9.2	7023	456.01	3.43	B
G281.175−01.645	09:59:32.0	−57:03:49.1	caswell1	2016	2330	29.1	7023	711.97	1.96	A
G281.560−02.478	09:58:02.9	−57:57:45.1	shrds114	2015	2997	11.2	7023	645.40	1.54	A
G281.840−01.609	10:03:40.7	−57:26:38.2	shrds117	2015	3287	15.3	7023	151.88	0.53	A
G282.015−00.997	10:06:57.3	−57:02:05.4	shrds1007	2016	1600	210.3	7023	72.27	1.99	B
G282.842−01.252	10:11:16.8	−57:44:02.3	shrds1232	2016	1703	5.8	7023	146.11	0.52	B
G283.098−00.400	10:16:15.6	−57:10:16.8	shrds132	2015	1327	87.0	7022	17.12	0.17	B
G283.832−00.730	10:19:41.0	−57:51:05.5	shrds1013	2016	1673	33.8	7023	87.06	2.08	B
G284.014−00.857	10:20:15.9	−58:03:50.8	shrds1014	2016	1822	4.0	7023	628.14	4.01	B
G284.712+00.317	10:29:30.6	−57:26:43.5	caswell2	2016	2224	71.6	7023	719.54	3.56	B
G284.902+00.060	10:29:36.0	−57:45:09.3	shrds141	2015	2343	21.9	7023	75.24	0.41	A
G285.353+00.004	10:32:14.3	−58:02:11.0	shrds143	2016	1857	24.6	7023	61.94	6.06	A

Table 4.4 continued

Table 4.4: Non-tapered Image Continuum Properties (continued)

Target	R.A. J2000 (hh:mm:ss)	Decl. J2000 (dd:mm:ss)	Field	Epoch[a]	Beam Area (arcsec^2)	$\Delta\theta^b$ (arcsec)	ν_C (MHz)	S_C (mJy beam^{-1})	rms$_C$ (mJy beam^{-1})	QF
G286.362−00.297	10:37:45.8	−58:47:27.6	shrds1017	2016	1388	46.2	7023	48.70	1.17	B
G286.376−00.257	10:38:04.8	−58:46:23.3	shrds1017	2016	1388	6.0	7023	40.74	1.61	B
G286.951−00.955	10:39:19.9	−59:39:53.0	shrds158	2015	2097	7.3	7023	449.22	2.08	A
G288.074−01.642	10:44:38.6	−60:48:10.0	shrds162	2016	1382	4.9	7023	90.30	0.18	A
G288.230−01.153	10:47:38.3	−60:26:11.6	shrds1020	2016	1959	15.8	7023	9.68	0.53	B
G288.233−01.118	10:47:43.2	−60:24:51.5	shrds1020	2016	1959	27.2	7023	15.25	0.48	B
G288.851−00.108	10:55:49.6	−59:47:01.3	shrds167	2016	1465	13.1	7023	74.15	0.32	B
G289.109−01.107	10:54:10.9	−60:47:28.2	shrds173	2016	1278	9.1	7023	88.96	0.26	A
G289.188−00.293	10:57:37.6	−60:05:35.2	shrds1024	2016	1364	8.2	7023	122.64	0.79	A
G289.470−00.928	10:57:31.0	−60:46:51.5	shrds181	2016	1384	17.6	7023	38.75	0.42	B
G289.476−00.899	10:57:39.8	−60:45:43.5	shrds181	2016	1384	8.1	7023	61.40	0.38	B
G289.582−00.636	10:59:20.1	−60:33:58.1	shrds184	2016	1339	9.0	7023	81.74	0.25	A
G289.769−01.220	10:58:43.6	−61:11:58.7	shrds1026	2016	1445	81.5	7023	70.63	1.80	B
G289.806−01.242	10:58:47.5	−61:07:42.9	shrds1026	2016	1445	308.0	7023	147.83	2.64	B
G289.874−00.752	11:01:01.6	−60:46:52.4	shrds1028	2016	1849	62.3	7023	98.57	2.07	B
G289.880−00.801	11:00:59.4	−60:50:24.4	shrds1028	2016	1849	7.8	7023	1179.80	3.62	B
G289.944−00.889	11:01:11.1	−60:56:48.0	shrds191	2015	2502	10.2	7023	123.68	1.47	A
G289.966−00.962	11:01:03.4	−60:59:23.8	shrds191	2015	2502	124.8	7023	29.42	2.29	C
G290.012−00.867	11:01:59.2	−60:56:48.8	g290.012-00.867	2014	5394	106.4	6050	200.17	3.66	B
G290.321−03.024	10:56:10.6	−62:59:52.2	g290.323-02.984	2014	5453	199.0	6050	14.40	0.49	B
G290.323−02.984	10:56:33.0	−63:00:43.9	g290.323-02.984	2014	5453	26.8	6050	28.85	0.34	A
G290.385−01.042	11:03:59.6	−61:16:04.4	g290.385-01.042	2014	5384	2.0	6050	23.30	0.87	A
G290.674−00.133	11:08:43.9	−60:31:29.3	g290.674-00.133	2014	5351	187.1	6050	-0.73	0.88	C
G291.046−02.079	11:05:39.4	−62:29:21.9	shrds199	2015	2476	29.1	7023	114.32	0.56	B
G291.154−00.321	11:12:08.9	−60:54:02.5	shrds1032	2016	1808	10.3	7023	50.95	5.36	B
G291.186−00.274	11:12:35.2	−60:52:22.6	shrds1032	2016	1808	16.5	7023	178.42	2.75	B
G291.202−00.295	11:12:36.3	−60:53:46.6	shrds1032	2016	1808	4.5	7023	205.59	3.18	B

Table 4.4 continued

Table 4.4: Non-tapered Image Continuum Properties (continued)

Target	R.A. J2000 (hh:mm:ss)	Decl. J2000 (dd:mm:ss)	Field	Epoch[a]	Beam Area (arcsec^2)	$\Delta\theta^b$ (arcsec)	ν_C (MHz)	S_C (mJy beam^{-1})	rms$_C$ (mJy beam^{-1})	QF
G291.281−00.726	11:11:52.3	−61:18:48.4	caswell3	2016	2238	40.6	7023	38233.32	102.06	B
G291.596−00.239	11:15:49.4	−60:59:20.4	g291.596-00.239	2014	5376	9.7	6050	32.12	13.76	A
G291.863−00.682	11:16:33.2	−61:29:57.2	caswell4	2016	2185	7.3	7023	1021.23	6.74	A
G292.722+00.157	11:25:35.0	−60:59:58.7	g292.722+00.157	2014	5340	30.4	6050	3.21	0.12	B
G292.889−00.831	11:24:08.6	−61:58:27.7	g292.889-00.831	2014	5402	74.7	6050	4.43	0.62	C
G293.113−00.961	11:25:31.0	−62:10:53.3	shrds207	2015	1248	78.9	7023	13.97	0.38	B
G293.483−00.903	11:28:50.4	−62:14:31.5	g293.483-00.903	2014	5477	31.6	6050	10.12	0.29	B
G293.619−01.613	11:28:02.5	−62:57:14.2	shrds210	2016	1948	45.2	7023	35.43	2.06	B
G293.661−01.639	11:28:20.1	−63:00:18.6	shrds210	2016	1948	6.2	7023	133.62	1.70	B
G293.683−01.590	11:28:34.7	−62:57:38.5	shrds210	2016	1948	29.2	7023	31.67	1.78	B
G293.824−00.761	11:32:01.9	−62:13:15.9	shrds215	2015	1576	5.6	7023	23.03	0.55	B
G293.829−00.744	11:32:06.6	−62:12:19.7	shrds215	2015	1576	3.8	7023	204.29	0.48	B
G293.936−00.873	11:32:38.8	−62:21:31.7	g293.936-00.873	2014	5536	6.8	6050	112.29	1.91	B
G293.952−00.894	11:32:43.9	−62:23:12.0	g293.936-00.873	2014	5536	4.0	6050	127.21	2.15	B
G293.967−00.984	11:32:36.0	−62:28:14.3	shrds219	2015	2584	19.2	7023	174.35	0.62	B
G293.994−00.934	11:32:58.5	−62:26:02.4	shrds219	2015	2584	6.2	7023	256.90	1.07	B
G294.453−00.521	11:37:48.4	−62:10:42.8	shrds226	2015	2365	20.5	7023	139.75	0.27	A
G294.656−00.438	11:39:46.2	−62:09:36.0	g294.656-00.438	2014	6703	59.3	6050	17.36	0.19	B
G294.988−00.538	11:42:10.3	−62:20:09.5	g294.988-00.538	2014	6672	0.9	6050	157.84	0.92	A
G295.275−00.255	11:44:54.8	−62:08:08.9	g295.275-00.255	2014	8350	112.5	6050	20.75	1.14	C
G295.748−00.207	11:49:12.7	−62:12:25.1	g295.748-00.207	2014	8361	1.2	6050	82.13	0.62	A
G297.248−00.754	12:00:55.4	−63:04:09.4	g297.248-00.754	2014	8311	10.1	6050	304.13	1.45	A
G297.312−00.295	12:02:21.0	−62:36:45.0	shrds242	2015	2437	71.1	7023	65.88	0.33	B
G297.392−00.624	12:02:24.4	−62:58:32.4	shrds243	2015	1748	33.1	7023	94.47	0.58	B
G297.497−00.758	12:03:10.4	−63:08:09.1	shrds246	2015	2368	76.7	7023	354.63	1.36	B
G297.519−00.031	12:04:24.3	−62:24:24.3	shrds244	2015	1365	12.2	7023	11.83	0.21	C
G297.536−00.826	12:03:16.9	−63:11:21.1	shrds246	2015	2368	13.3	7023	170.77	0.92	A

Table 4.4 continued

Table 4.4: Non-tapered Image Continuum Properties (continued)

Target	R.A. J2000 (hh:mm:ss)	Decl. J2000 (dd:mm:ss)	Field	Epoch[a]	Beam Area (arcsec^2)	$\Delta\theta^b$ (arcsec)	ν_C (MHz)	S_C (mJy beam^{-1})	rms$_C$ (mJy beam^{-1})	QF
G297.626−00.906	12:03:58.2	−63:17:09.2	g297.626-00.906	2014	8396	6.3	6050	169.81	2.30	A
G297.651−00.973	12:04:05.3	−63:21:52.9	g297.626-00.906	2014	8396	26.8	6050	752.87	5.80	C
G298.183−00.784	12:09:01.6	−63:15:58.8	caswell5	2016	2068	11.6	7023	1952.65	2.84	A
G298.196−00.247	12:09:56.1	−62:44:26.2	shrds1041	2016	1898	21.3	7023	243.48	11.66	A
G298.473+00.104	12:12:50.5	−62:25:59.1	g298.473+00.104	2014	8329	36.6	6050	113.65	1.85	A
G298.630+00.253	12:14:24.3	−62:16:46.5	shrds253	2015	1615	112.6	7023	29.80	0.28	C
G298.669+00.064	12:14:22.9	−62:30:02.3	g298.669+00.064	2014*	···	2.7	···	···	···	···
G298.765+00.174	12:15:21.5	−62:24:24.2	shrds256	2015	1359	11.6	7023	5.39	0.47	C
G298.846+00.121	12:15:57.0	−62:27:57.2	shrds258	2015	2520	12.5	7023	231.78	0.75	A
G298.878+00.192	12:16:19.6	−62:23:57.3	shrds261	2016	1780	13.6	7023	21.70	0.62	B
G298.899+00.187	12:16:30.0	−62:24:45.5	shrds261	2016	1780	9.9	7023	19.33	0.67	B
G299.349−00.267	12:19:54.2	−62:55:25.7	caswell6	2016	2031	21.7	7023	179.70	0.65	B
G299.399−00.235	12:20:25.2	−62:53:46.7	shrds1046	2016	1683	32.3	7023	19.97	0.36	A
G299.505+00.025	12:21:25.2	−62:38:16.5	g299.505+00.025	2014	8343	59.3	6050	1.99	0.39	C
G300.134−00.100	12:27:01.0	−62:50:45.0	shrds268	2015	1348	61.2	7023	10.52	0.32	B
G300.369−00.288	12:28:51.5	−63:02:41.5	shrds271	2015	2392	27.4	7023	46.43	0.46	B
G300.420−00.302	12:29:10.9	−63:03:13.5	shrds271	2015	2392	43.3	7023	15.27	0.69	B
G300.424−00.153	12:29:37.3	−62:56:16.4	shrds273	2015	1322	126.0	7023	12.93	0.46	C
G300.455−00.190	12:29:36.2	−62:57:16.4	shrds273	2015	1322	10.1	7023	12.88	0.55	C
G300.502−00.180	12:30:04.3	−62:56:40.1	shrds273	2015	1322	25.0	7023	89.57	1.19	C
G300.965+01.162	12:34:53.3	−61:39:26.8	g300.983+01.117	2014	8253	44.2	6050	1463.12	4.83	B
G300.972+00.994	12:34:49.9	−61:48:52.3	g300.972+00.994	2014*	···	1.2	···	···	···	···
G300.983+01.117	12:34:52.5	−61:39:32.6	caswell7	2016	2049	129.0	7023	809.67	2.55	B
G301.116+00.968	12:36:02.2	−61:51:10.5	caswell8	2016	2054	13.2	7023	1543.18	2.91	A
G302.032−00.063	12:43:32.0	−62:55:08.1	caswell9	2016	2132	4.9	7023	1066.05	1.46	A
G302.391+00.280	12:46:43.7	−62:35:14.6	shrds293	2016	1502	5.7	7023	160.47	0.24	A
G302.436−00.106	12:47:03.4	−62:58:39.2	shrds294	2016	1398	16.7	7023	69.55	0.29	B

Table 4.4 continued

Table 4.4: Non-tapered Image Continuum Properties (continued)

Target	R.A. J2000 (hh:mm:ss)	Decl. J2000 (dd:mm:ss)	Field	Epoch[a]	Beam Area (arcsec^2)	$\Delta\theta^b$ (arcsec)	ν_C (MHz)	S_C (mJy beam^{-1})	rms$_C$ (mJy beam^{-1})	QF
G302.481−00.035	12:47:32.3	−62:53:60.0	shrds295	2016	1464	26.9	7023	64.39	0.43	B
G302.503−00.762	12:47:34.0	−63:38:16.4	shrds296	2015	1365	27.3	7023	59.40	0.49	B
G302.636−00.672	12:48:47.4	−63:32:27.8	shrds297	2016	1761	4.0	7023	167.68	0.55	B
G302.816−00.844	12:50:20.2	−63:42:58.8	shrds299	2016	1275	22.5	7023	42.19	0.28	B
G303.342−00.718	12:55:05.8	−63:35:08.0	shrds303	2015	2890	11.3	7023	159.33	0.77	B
G303.384−00.965	12:55:32.2	−63:50:02.2	shrds305	2016	1674	4.7	7023	78.05	0.19	A
G303.557−00.539	12:57:01.4	−63:24:09.2	shrds308	2016	1593	3.6	7023	63.78	0.41	B
G304.465−00.023	13:04:54.1	−62:50:55.2	shrds336	2015	2782	20.3	7023	122.55	0.52	B
G304.557+00.329	13:05:30.7	−62:29:57.5	shrds338	2016	1599	5.6	7023	107.92	0.23	A
G304.925+00.555	13:08:36.5	−62:15:06.9	shrds344	2015	2331	17.6	7023	373.50	0.75	A
G305.789+00.280	13:16:12.5	−62:26:37.4	shrds350	2016	1577	38.9	7023	66.24	0.75	B
G307.559−00.585	13:32:31.0	−63:05:21.3	caswell10	2016	2225	9.6	7023	865.16	1.35	A
G307.571−00.620	13:32:45.7	−63:07:01.7	caswell10	2016	2225	44.7	7023	28.83	1.72	B
G307.610−00.593	13:32:55.8	−63:05:41.4	caswell10	2016	2225	31.1	7023	53.51	1.99	B
G307.974−01.594	13:37:41.5	−64:00:39.9	shrds373	2016	1804	4.2	7023	65.20	0.12	A
G308.056−00.397	13:36:32.3	−62:49:06.5	caswell11	2016	2205	3.1	7023	125.80	1.23	B
G308.072−00.389	13:36:41.0	−62:48:38.8	caswell11	2016	2205	13.9	7023	45.28	1.12	B
G308.079−00.406	13:36:46.9	−62:49:42.6	caswell11	2016	2205	23.8	7023	321.88	1.04	B
G308.747+00.547	13:40:52.4	−61:45:45.9	shrds1091	2016	1708	14.0	7023	231.66	2.81	B
G308.916+00.124	13:43:01.7	−62:08:55.4	shrds384	2015	2324	12.3	7023	467.24	1.32	A
G309.151−00.215	13:45:18.8	−62:25:31.4	shrds385	2016	1387	114.1	7023	46.63	0.57	B
G309.176−00.028	13:45:28.4	−62:14:31.6	shrds386	2015	2362	6.5	7023	295.18	0.55	A
G310.260−00.199	13:54:49.4	−62:10:06.5	shrds403	2016	1385	17.2	7023	38.70	0.40	B
G310.519−00.220	13:57:01.2	−62:07:10.9	shrds407	2015	2252	9.9	7023	387.96	0.65	A
G310.630−00.421	13:58:25.2	−62:17:47.5	shrds409	2015	1554	34.3	7023	94.23	0.66	B
G310.672−00.450	13:58:51.0	−62:17:59.4	shrds409	2015	1554	23.7	7023	90.47	0.68	B
G310.688−00.314	13:58:40.4	−62:09:53.7	shrds411	2015	1493	19.3	7023	108.66	0.89	A

Table 4.4 continued

Table 4.4: Non-tapered Image Continuum Properties (continued)

Target	R.A. J2000 (hh:mm:ss)	Decl. J2000 (dd:mm:ss)	Field	Epoch[a]	Beam Area (arcsec^2)	$\Delta\theta^b$ (arcsec)	ν_C (MHz)	S_C (mJy beam^{-1})	rms$_C$ (mJy beam^{-1})	QF
G310.887+00.009	13:59:35.3	−61:48:18.8	shrds412	2015	2676	7.7	7023	150.60	0.36	A
G310.901−00.373	14:00:33.6	−62:10:38.8	shrds1096	2016	1762	26.4	7023	507.30	1.37	B
G311.003−00.355	14:01:20.6	−62:07:42.0	shrds413	2016	1652	9.4	7023	68.78	0.75	B
G311.137−00.235	14:02:07.3	−61:58:55.9	shrds418	2015	1378	35.1	7023	53.66	0.70	C
G311.425+00.598	14:02:36.0	−61:05:42.5	shrds425	2015	2302	2.8	7023	132.93	0.90	A
G311.551−00.584	14:06:20.6	−62:11:33.8	shrds1101	2016	1385	21.1	7023	36.48	1.01	B
G311.575+00.239	14:04:32.3	−61:24:15.4	shrds428	2016	1679	40.8	7023	66.21	1.54	A
G311.581−00.593	14:06:41.2	−62:11:25.8	shrds1101	2016	1385	17.3	7023	106.03	0.72	B
G311.606−00.638	14:06:58.4	−62:13:45.8	shrds1101	2016	1385	4.4	7023	40.01	1.19	C
G311.629+00.289	14:04:55.1	−61:20:05.4	caswell12	2016	2248	6.7	7023	2274.81	4.88	A
G311.809−00.309	14:07:47.6	−61:50:12.5	shrds1103	2016	1539	72.0	7023	75.62	1.12	B
G311.841−00.219	14:07:51.6	−61:45:32.7	shrds1103	2016	1539	6.0	7023	100.12	3.11	C
G311.866−00.238	14:08:06.8	−61:46:16.6	shrds1103	2016	1539	2.6	7023	159.13	2.77	C
G311.949−00.114	14:08:28.1	−61:37:41.5	shrds439	2016	1482	2.8	7023	44.21	1.89	B
G311.963−00.037	14:08:37.6	−61:33:41.2	shrds439	2016	1482	106.6	7023	47.90	0.94	B
G312.091+00.069	14:08:46.1	−61:24:46.3	shrds440	2015	1444	167.5	7023	44.58	1.68	C
G312.388−00.057	14:11:49.8	−61:26:26.0	shrds450	2015	1373	12.3	7023	33.98	0.29	B
G312.591+00.210	14:12:39.6	−61:06:38.9	shrds456	2016	1432	73.9	7023	49.07	0.58	B
G312.598+00.048	14:13:13.9	−61:16:48.2	shrds458	2016	1483	7.2	7023	136.91	0.50	B
G312.675+00.048	14:13:54.0	−61:15:51.2	shrds462	2015	1614	40.9	7023	55.22	0.59	B
G312.706+00.012	14:14:11.8	−61:15:55.2	shrds462	2015	1614	48.4	7023	95.29	0.48	B
G312.764+00.067	14:14:32.3	−61:12:39.4	shrds462	2015	1614	17.7	7023	33.50	1.33	C
G312.979−00.432	14:17:18.8	−61:38:05.1	shrds465	2016	1548	127.3	7023	93.03	0.49	B
G313.671−00.105	14:22:02.3	−61:04:16.0	atca348	2013	4257	13.4	8450	69.25	0.32	B
G313.790+00.705	14:20:41.3	−60:15:55.8	atca352	2013	4231	24.7	8450	275.24	0.95	A
G313.851−00.243	14:23:52.6	−61:08:22.0	shrds479	2016	1639	6.2	7023	49.92	0.28	A
G314.219+00.343	14:25:02.2	−60:27:44.8	atca361	2013	4132	17.0	8450	270.48	3.50	B

Table 4.4 continued

Table 4.4: Non-tapered Image Continuum Properties (continued)

Target	R.A. J2000 (hh:mm:ss)	Decl. J2000 (dd:mm:ss)	Field	Epoch[a]	Beam Area (arcsec^2)	$\Delta\theta^b$ (arcsec)	ν_C (MHz)	S_C (mJy beam^{-1})	rms$_C$ (mJy beam^{-1})	QF
G314.239+00.428	14:24:57.3	−60:22:57.6	shrds1111	2016	1708	36.4	7023	744.91	3.00	B
G314.288+00.431	14:25:15.2	−60:21:25.8	shrds1111	2016	1708	14.7	7023	190.95	1.89	B
G315.312−00.272	14:35:09.7	−60:37:38.1	ch87.1	2013	4158	22.5	8450	149.80	1.34	A
G316.516−00.600	14:45:05.2	−60:26:30.8	atca382	2013	4075	29.3	8450	75.30	0.42	A
G317.405+00.091	14:49:09.7	−59:24:55.1	shrds1122	2016	1711	54.5	7023	689.99	1.56	A
G317.426−00.561	14:51:37.5	−60:00:22.6	shrds518	2015	2316	8.2	7023	114.74	0.90	B
G317.431−00.522	14:51:32.2	−59:57:46.4	shrds518	2015	2316	27.7	7023	29.69	0.69	B
G317.458−00.533	14:51:45.5	−59:57:26.8	shrds518	2015	2316	37.1	7023	115.47	0.61	B
G317.570−00.257	14:51:26.3	−59:40:08.5	shrds521	2015	1582	52.8	7023	19.75	0.49	A
G317.861+00.160	14:52:04.9	−59:10:09.8	atca402	2013	3989	27.4	8450	340.89	2.42	B
G318.059−00.450	14:55:41.9	−59:37:09.5	caswell13	2016	2075	7.0	7023	207.22	1.02	B
G318.233−00.605	14:57:33.0	−59:41:30.8	shrds1126	2016	1236	55.8	7023	32.27	0.36	C
G318.248+00.150	14:55:04.9	−59:00:39.8	atca406	2013	4015	109.0	8450	38.43	1.69	C
G318.726−00.222	14:59:30.0	−59:06:37.1	shrds535	2016	1662	3.8	7023	160.53	0.42	A
G318.774−00.150	14:59:34.6	−59:01:22.1	shrds536	2015	1938	6.3	7023	328.80	1.64	A
G319.188−00.329	15:02:56.1	−58:54:47.2	shrds1129	2016	1525	255.7	7023	52.83	2.26	C
G319.229+00.225	15:01:21.6	−58:26:59.7	atca412	2013	4105	104.0	8450	54.52	0.87	B
G319.397−00.006	15:03:16.9	−58:36:12.9	shrds1131	2016	1768	20.3	7023	1129.76	7.60	B
G319.453−00.022	15:03:41.5	−58:35:09.1	shrds1131	2016	1768	2.5	7023	236.33	4.09	A
G320.163+00.797	15:05:18.9	−57:30:25.2	shrds1137	2016	1509	64.8	7023	932.30	5.33	C
G320.205+00.867	15:05:22.8	−57:26:45.4	shrds1137	2016	1509	13.8	7023	98.89	2.37	A
G320.236−00.099	15:09:09.2	−58:14:45.4	shrds1140	2016	1955	69.7	7023	71.99	1.74	B
G320.240−00.176	15:09:28.6	−58:19:52.4	shrds1139	2016	1581	14.3	7023	47.97	2.29	A
G320.311−00.176	15:10:00.6	−58:17:32.2	shrds1139	2016	1581	18.9	7023	1511.02	6.95	C
G320.376+00.172	15:09:04.2	−57:57:28.8	shrds555	2015	2033	8.6	7023	295.44	6.12	C
G320.399+00.162	15:09:16.8	−57:57:41.2	shrds555	2015	2033	17.4	7023	61.74	3.54	B
G320.419+00.114	15:09:32.3	−57:59:17.3	shrds555	2015	2033	13.5	7023	133.69	2.38	C

Table 4.4 continued

Table 4.4: Non-tapered Image Continuum Properties (continued)

Target	R.A. J2000 (hh:mm:ss)	Decl. J2000 (dd:mm:ss)	Field	Epoch[a]	Beam Area (arcsec^2)	$\Delta\theta^b$ (arcsec)	ν_C (MHz)	S_C (mJy beam^{-1})	rms$_C$ (mJy beam^{-1})	QF
G320.423+00.101	15:09:38.4	−57:59:45.2	shrds555	2015	2033	7.8	7023	88.05	2.48	C
G320.675+00.246	15:10:50.2	−57:45:44.0	shrds559	2015	1274	80.4	7023	35.65	1.18	C
G320.692+00.185	15:11:20.7	−57:46:31.8	shrds559	2015	1274	142.4	7023	62.75	3.33	C
G320.778+00.241	15:11:24.2	−57:41:50.1	shrds1146	2016	1680	2.6	7023	109.30	3.09	B
G320.782+00.258	15:11:21.7	−57:40:14.0	shrds1146	2016	1680	36.4	7023	143.93	2.73	B
G320.799+00.187	15:11:45.6	−57:44:24.2	shrds1147	2016	1681	27.1	7023	77.99	2.24	B
G320.884−00.641	15:15:32.5	−58:23:06.2	shrds561	2016	1501	43.9	7023	51.36	0.56	B
G321.725+01.169	15:13:49.9	−56:24:47.8	caswell14	2016	2098	19.9	7023	1829.92	3.10	A
G322.162+00.625	15:18:39.3	−56:38:52.6	caswell15	2016	2062	7.5	7023	6041.97	19.36	A
G322.706−00.330	15:25:47.8	−57:09:02.3	shrds574	2015	2385	8.1	7023	192.13	0.38	A
G323.449+00.095	15:28:32.5	−56:22:57.8	atca449	2013	4209	9.2	8450	85.45	0.78	A
G323.464−00.079	15:29:19.6	−56:31:19.6	atca450	2013	4077	15.0	8450	672.79	1.46	A
G323.743−00.249	15:31:43.9	−56:30:14.7	atca456	2013	4090	14.0	8450	136.29	0.42	A
G323.806+00.020	15:31:05.7	−56:14:21.0	atca459	2013	4083	61.6	8450	205.68	1.10	B
G323.915+00.026	15:31:34.3	−56:10:20.0	shrds590	2015	2550	22.1	7023	304.76	1.21	A
G323.936−00.038	15:31:37.2	−56:11:44.0	shrds590	2015	2550	197.0	7023	36.85	1.39	B
G324.201+00.117	15:32:53.0	−55:56:13.1	caswell16	2016	2046	9.0	7023	2768.51	6.63	A
G324.642−00.321	15:37:23.7	−56:01:49.9	atca466	2013	4148	58.5	8450	275.18	1.12	A
G324.924−00.569	15:39:57.2	−56:04:09.1	ch87.2	2013	4575	8.0	8450	543.79	3.87	B
G325.108+00.053	15:38:35.7	−55:28:10.9	atca472	2013	4125	111.7	8450	72.62	0.74	B
G325.354−00.036	15:40:11.4	−55:23:08.8	atca475	2013	3999	18.3	8450	158.27	0.80	A
G326.065−00.393	15:45:58.1	−55:14:47.9	shrds1161	2016	1366	164.9	7023	29.29	0.84	C
G326.446+00.901	15:42:17.4	−53:58:29.8	caswell17	2016	2025	17.2	7023	3041.30	8.42	B
G326.467−00.382	15:47:49.7	−54:58:32.7	shrds609	2015	2395	23.5	7023	405.36	1.55	A
G326.657+00.588	15:44:43.3	−54:05:51.9	shrds1163	2016	1609	11.6	7023	6421.29	20.52	A
G326.721+00.773	15:44:14.9	−53:54:45.8	atca484	2013	4118	36.5	8450	116.41	4.18	B
G326.728+00.616	15:44:59.5	−54:02:14.6	shrds1164	2016	1588	11.2	7023	3633.95	9.90	A

Table 4.4 continued

Table 4.4: Non-tapered Image Continuum Properties (continued)

Target	R.A. J2000 (hh:mm:ss)	Decl. J2000 (dd:mm:ss)	Field	Epoch[a]	Beam Area (arcsec^2)	$\Delta\theta^b$ (arcsec)	ν_C (MHz)	S_C (mJy beam^{-1})	rms$_C$ (mJy beam^{-1})	QF
G326.890−00.277	15:49:39.1	−54:38:18.1	atca486	2013	3904	8.5	8450	378.29	2.62	A
G326.916−01.100	15:53:26.9	−55:15:15.9	atca487	2013	4023	26.4	8450	88.72	0.80	A
G327.139−00.261	15:50:54.7	−54:28:31.5	shrds618	2016	1306	27.3	7023	82.87	1.24	A
G327.172−00.527	15:52:27.1	−54:43:22.4	shrds1167	2016	1980	266.3	7023	73.22	11.65	B
G327.285−00.576	15:53:06.5	−54:37:13.6	caswell18	2016	2005	11.9	7023	1070.51	41.84	B
G327.300−00.548	15:53:03.3	−54:35:25.5	caswell18	2016	2005	7.1	7023	17063.66	33.10	B
G327.400+00.444	15:49:19.7	−53:45:13.8	shrds621	2016	2009	9.3	7023	123.26	1.00	A
G327.401+00.483	15:49:09.0	−53:44:14.8	atca492	2013	3904	48.3	8450	99.12	1.47	B
G327.555−00.829	15:55:46.3	−54:38:57.6	atca495	2013	3818	72.0	8450	98.22	1.99	B
G327.714+00.576	15:50:16.9	−53:27:43.7	atca498	2013	4075	71.7	8450	58.96	0.46	B
G327.735−00.396	15:54:40.2	−54:11:42.6	shrds628	2015	2378	7.9	7023	555.96	3.07	A
G327.763+00.163	15:52:28.2	−53:44:54.9	atca501	2013	3782	27.9	8450	126.83	2.23	B
G327.770−00.346	15:54:37.0	−54:08:42.5	shrds628	2015	2378	41.6	7023	1049.60	4.85	B
G327.824+00.117	15:52:45.3	−53:46:06.9	atca501	2013	3782	132.2	8450	140.69	5.01	C
G327.848+00.016	15:53:29.5	−53:48:17.4	shrds635	2016	1500	3.0	7023	47.68	0.97	C
G327.916+00.154	15:53:14.8	−53:39:18.4	shrds639	2016	1512	4.8	7023	38.11	0.61	B
G328.043+00.298	15:53:19.2	−53:27:56.4	shrds643	2015	1278	10.8	7023	28.54	0.64	C
G328.062+00.076	15:54:20.4	−53:37:26.9	shrds647	2015	2322	6.9	7023	67.00	4.24	C
G328.117+00.108	15:54:31.1	−53:33:15.0	shrds647	2015	2322	37.2	7023	123.09	1.72	B
G328.193−00.569	15:57:50.7	−54:02:21.2	shrds652	2015	2341	19.7	7023	584.63	3.56	B
G328.279−00.559	15:58:15.0	−53:57:47.2	shrds659	2016	1412	28.6	7023	83.62	1.66	C
G328.294−00.536	15:58:12.8	−53:56:47.2	shrds659	2016	1412	11.9	7023	52.75	1.57	C
G328.315−00.594	15:58:32.7	−53:58:11.2	shrds659	2016	1412	23.8	7023	112.44	1.15	B
G328.356−00.559	15:58:35.9	−53:55:27.3	shrds659	2016	1412	25.3	7023	67.90	0.81	B
G328.807−00.078	15:58:50.1	−53:14:41.5	shrds668	2016	1291	63.8	7023	130.77	0.86	C
G328.819−00.004	15:58:34.5	−53:11:49.4	shrds668	2016	1291	6.8	7023	92.71	0.40	A
G328.825−00.081	15:58:56.3	−53:15:13.6	shrds668	2016	1291	8.0	7023	391.74	1.36	C

Table 4.4 continued

Table 4.4: Non-tapered Image Continuum Properties (continued)

Target	R.A. J2000 (hh:mm:ss)	Decl. J2000 (dd:mm:ss)	Field	Epoch[a]	Beam Area (arcsec^2)	$\Delta\theta^b$ (arcsec)	ν_C (MHz)	S_C (mJy beam^{-1})	rms$_C$ (mJy beam^{-1})	QF
G328.945+00.570	15:56:47.9	−52:40:31.3	shrds669	2015	2430	22.3	7023	307.26	1.56	B
G328.961+00.248	15:58:12.6	−52:54:41.1	shrds670	2015	1884	10.1	7023	110.04	0.97	B
G328.962+00.207	15:58:25.8	−52:56:33.4	shrds670	2015	1884	17.5	7023	69.19	1.39	B
G329.266+00.111	16:00:20.8	−52:48:56.5	shrds677	2015	1916	15.4	7023	79.74	2.55	B
G329.422−00.160	16:02:18.8	−52:55:28.7	shrds684	2015	2958	11.1	7023	321.75	0.73	A
G329.460+00.174	16:01:02.3	−52:38:43.4	shrds686	2015	3067	3.3	7023	225.97	2.37	A
G329.472+00.214	16:00:55.8	−52:36:23.6	shrds686	2015	3067	1.6	7023	873.30	3.49	B
G329.474+00.839	15:58:16.5	−52:07:40.6	shrds687	2016	1303	12.2	7023	77.23	0.24	B
G329.601+00.059	16:02:14.7	−52:38:29.4	shrds690	2015	2674	8.6	7023	285.56	0.97	A
G330.049+00.899	16:00:50.6	−51:42:46.3	shrds697	2016	1572	5.5	7023	64.66	0.27	A
G330.673−00.388	16:09:29.9	−52:15:44.4	shrds1171	2016	1284	38.9	7023	466.22	2.12	B
G330.738−00.449	16:09:50.8	−52:15:08.8	shrds1171	2016	1284	96.2	7023	45.93	1.22	B
G330.954−00.181	16:09:52.7	−51:54:54.4	shrds709	2015	2315	6.9	7023	1852.67	6.11	A
G331.056−00.437	16:11:28.2	−52:01:38.5	shrds710	2016	1476	18.8	7023	42.81	1.19	A
G331.057−00.229	16:10:36.6	−51:53:03.1	shrds711	2015	1749	27.7	7023	82.37	4.54	A
G331.123−00.530	16:12:14.0	−52:02:39.7	shrds717	2015	2302	36.8	7023	577.16	6.28	B
G331.127−00.481	16:12:01.4	−52:00:55.6	shrds717	2015	2302	3.2	7023	94.51	6.16	B
G331.129−00.243	16:10:59.1	−51:50:25.8	shrds716	2015	1346	5.7	7023	352.22	1.82	A
G331.145+00.133	16:09:24.6	−51:33:08.9	shrds719	2015	2470	4.6	7023	129.13	0.81	B
G331.156−00.391	16:11:41.7	−51:55:55.1	shrds720	2015	2176	35.9	7023	103.79	3.41	B
G331.172−00.460	16:12:07.8	−51:58:16.3	shrds721	2015	2268	7.6	7023	408.98	4.33	A
G331.249+01.071	16:05:52.0	−50:48:06.8	shrds1174	2016	1453	46.1	7023	111.07	1.31	B
G331.259−00.188	16:11:27.1	−51:41:58.0	shrds725	2016	1425	72.3	7023	872.02	3.01	B
G331.322−00.176	16:11:35.7	−51:39:22.1	shrds725	2016	1425	14.3	7023	42.08	2.06	A
G331.361−00.019	16:11:06.5	−51:30:51.8	shrds729	2015	2632	18.4	7023	595.08	14.39	B
G331.384−00.358	16:12:42.2	−51:45:00.1	shrds731	2015	1453	8.1	7023	325.54	3.47	B
G331.412+00.011	16:11:11.7	−51:27:35.8	shrds729	2015	2632	7.9	7023	310.31	7.60	A

Table 4.4 continued

Table 4.4: Non-tapered Image Continuum Properties (continued)

Target	R.A. J2000 (hh:mm:ss)	Decl. J2000 (dd:mm:ss)	Field	Epoch[a]	Beam Area (arcsec^2)	$\Delta\theta^b$ (arcsec)	ν_C (MHz)	S_C (mJy beam^{-1})	rms$_C$ (mJy beam^{-1})	QF
G331.417−00.354	16:12:50.3	−51:43:32.1	shrds731	2015	1453	8.1	7023	202.75	2.82	A
G331.520−00.076	16:12:09.3	−51:27:52.9	shrds736	2015	1396	61.4	7023	1963.45	21.83	C
G331.538−00.308	16:13:11.5	−51:36:28.9	shrds735	2015	3463	1.5	7023	151.77	1.78	B
G331.559−00.128	16:12:27.7	−51:27:28.9	shrds736	2015	1396	26.2	7023	565.15	14.21	A
G331.560+00.091	16:11:42.8	−51:18:32.1	shrds737	2015	1382	100.4	7023	89.38	2.83	C
G331.653+00.128	16:11:47.6	−51:12:24.4	shrds741	2015	1459	23.6	7023	108.19	1.91	B
G331.744−00.068	16:13:06.3	−51:17:47.9	shrds743	2015	2551	16.5	7023	223.18	3.25	A
G331.834−00.002	16:13:11.1	−51:11:37.8	shrds746	2016	1401	46.4	7023	48.38	0.74	B
G332.145−00.452	16:16:41.4	−51:17:03.4	shrds753	2015	2493	40.7	7023	5770.89	25.82	B
G332.291−00.092	16:15:45.5	−50:56:06.6	shrds756	2015	2936	19.0	7023	277.93	1.17	A
G332.311−00.567	16:17:57.1	−51:14:58.5	shrds759	2015	3041	43.7	7023	134.37	2.47	B
G332.382+00.080	16:15:30.9	−50:44:30.5	shrds763	2015	1448	72.7	7023	49.94	1.00	B
G332.415+00.053	16:16:00.6	−50:43:28.8	shrds766	2015	1605	209.9	7023	155.10	1.12	C
G332.585−00.561	16:19:09.3	−51:04:00.7	shrds771	2015	2190	10.1	7023	202.53	6.55	A
G332.633−00.683	16:19:54.2	−51:06:41.8	shrds1181	2016	1967	23.3	7023	140.07	7.06	B
G332.657−00.622	16:19:39.0	−51:03:12.6	shrds771	2015	2190	56.4	7023	2236.41	20.17	C
G332.766−00.006	16:17:31.6	−50:32:32.9	shrds774	2015	3271	9.4	7023	189.21	0.86	A
G332.823−00.550	16:20:11.3	−50:53:16.3	shrds777	2015	2690	11.4	7023	3912.12	13.41	B
G332.957+01.793	16:10:38.2	−49:05:34.4	shrds782	2016	1237	54.2	7023	41.59	0.29	B
G332.987+00.902	16:14:33.9	−49:43:37.5	shrds784	2016	1379	24.7	7023	60.76	0.50	B
G332.990−00.619	16:21:15.3	−50:49:25.1	shrds785	2015	1349	15.8	7023	130.68	3.70	B
G333.011−00.441	16:20:36.4	−50:41:17.9	shrds789	2015	1375	50.3	7023	955.16	44.18	C
G333.052+00.033	16:18:37.8	−50:18:50.5	shrds788	2015	2612	3.4	7022	235.86	3.68	A
G333.085−00.479	16:21:00.8	−50:39:18.5	shrds789	2015	1375	12.2	7023	614.81	16.49	C
G333.095−00.460	16:20:57.8	−50:38:18.5	shrds789	2015	1375	22.3	7023	429.81	17.90	B
G333.113−00.141	16:19:41.6	−50:20:42.3	shrds792	2015	2424	179.8	7023	173.66	7.21	C
G333.129−00.439	16:21:00.4	−50:35:10.5	shrds789	2015	1375	43.1	7023	5854.38	43.66	B

Table 4.4 continued

Table 4.4: Non-tapered Image Continuum Properties (continued)

Target	R.A. J2000 (hh:mm:ss)	Decl. J2000 (dd:mm:ss)	Field	Epoch[a]	Beam Area (arcsec^2)	$\Delta\theta^b$ (arcsec)	ν_C (MHz)	S_C (mJy beam^{-1})	rms$_C$ (mJy beam^{-1})	QF
G333.164−00.100	16:19:42.8	−50:19:50.2	shrds792	2015	2424	1.8	7023	287.99	8.34	C
G333.255+00.065	16:19:23.8	−50:09:19.8	shrds794	2015	2682	24.0	7022	837.11	3.87	A
G333.467−00.159	16:21:19.7	−50:09:43.9	shrds799	2015	2454	14.9	7023	947.50	24.98	A
G333.534−00.383	16:22:32.2	−50:16:33.5	shrds801	2015	1216	43.4	7023	54.80	4.91	A
G333.580+00.058	16:20:40.6	−49:55:46.3	shrds802	2016	1529	107.4	7023	4.69	6.11	C
G333.627−00.199	16:22:09.5	−50:06:00.1	caswell19	2016	1586	97.2	7023	37263.74	218.24	A
G333.681−00.441	16:23:28.1	−50:12:16.3	shrds804	2015	1356	21.5	7023	206.61	15.06	B
G333.725+00.364	16:20:09.8	−49:36:15.3	shrds803	2015	2591	6.7	7022	324.71	1.23	A
G333.733−00.429	16:23:40.6	−50:09:32.6	shrds804	2015	1356	5.1	7023	215.82	7.70	A
G333.962+00.063	16:22:30.4	−49:39:00.3	shrds806	2015	3681	7.1	7022	149.25	1.27	A
G334.022+00.106	16:22:29.6	−49:34:14.9	shrds807	2016	1501	59.8	7023	17.77	1.11	B
G334.202+00.193	16:22:59.5	−49:23:38.8	shrds811	2015	2909	15.0	7022	226.48	1.42	A
G334.341+00.045	16:24:14.4	−49:23:40.8	shrds814	2015	2719	2.6	7022	371.46	1.06	A
G334.400−00.523	16:27:00.9	−49:44:49.7	shrds815	2016	1500	13.0	7023	48.79	0.29	A
G334.646+00.442	16:23:50.1	−48:54:09.4	shrds825	2015	3404	17.7	7022	127.28	0.53	B
G334.721−00.653	16:28:57.8	−49:36:25.2	caswell20	2016	1847	7.4	7023	889.01	2.47	A
G334.774−00.023	16:26:25.7	−49:07:16.3	shrds828	2015	2714	48.0	7022	237.73	2.37	A
G335.195−00.385	16:29:47.0	−49:04:48.9	shrds836	2016	1503	11.3	7023	67.05	0.33	A
G335.579−00.209	16:30:35.1	−48:40:46.2	shrds841	2016	1178	4.6	7023	118.91	0.34	B
G336.026−00.817	16:35:07.9	−48:46:17.1	shrds843	2015	2741	17.8	7022	371.00	1.06	A
G336.367−00.003	16:32:56.5	−47:57:56.0	shrds852	2015	2967	7.8	7022	653.29	5.90	A
G336.410−00.257	16:34:11.9	−48:06:07.9	shrds853	2016	1589	16.7	7022	289.79	5.40	C
G336.418−00.249	16:34:20.7	−48:05:07.6	shrds853	2016	1589	81.5	7022	215.86	6.27	C
G336.491−01.474	16:39:59.9	−48:51:41.2	caswell21	2016	1781	3.2	7023	5446.49	11.56	A
G336.518+00.119	16:33:16.9	−47:45:58.6	shrds854	2015	1404	163.8	7022	35.18	1.03	C
G336.585+00.019	16:33:51.0	−47:46:44.2	shrds857	2015	1301	87.3	7022	159.49	1.36	B
G336.854−00.018	16:34:56.2	−47:35:50.5	shrds1212	2016	1972	71.3	7022	716.89	13.05	B

Table 4.4 continued

Table 4.4: Non-tapered Image Continuum Properties (continued)

Target	R.A. J2000 (hh:mm:ss)	Decl. J2000 (dd:mm:ss)	Field	Epoch[a]	Beam Area (arcsec^2)	$\Delta\theta^b$ (arcsec)	ν_C (MHz)	S_C (mJy beam^{-1})	rms$_C$ (mJy beam^{-1})	QF
G336.874+00.139	16:34:22.0	−47:28:50.3	shrds1209	2016	1428	52.7	7022	86.26	2.98	B
G336.888+00.057	16:34:48.7	−47:32:46.4	shrds1212	2016	1972	32.2	7022	322.76	12.27	B
G336.900−00.033	16:35:12.2	−47:35:32.8	shrds862	2015	1279	7.0	7022	172.60	10.45	C
G336.919−00.188	16:35:58.2	−47:38:58.1	shrds864	2015	1443	120.7	7023	105.33	8.27	B
G336.984−00.183	16:36:12.5	−47:37:50.3	shrds864	2015	1443	4.3	7023	41.50	5.91	B
G336.986−00.006	16:35:26.1	−47:30:36.8	shrds862	2015	1279	2.8	7022	52.10	3.09	B
G336.990−00.021	16:35:32.4	−47:31:12.8	shrds862	2015	1279	12.3	7022	261.97	3.24	B
G337.004+00.322	16:34:04.7	−47:16:28.4	shrds865	2015	2305	7.6	7022	262.11	1.20	A
G337.091−00.965	16:40:08.3	−48:04:19.1	shrds867	2015	1509	25.5	7023	17.35	0.43	B
G337.138+00.008	16:35:58.7	−47:23:18.3	shrds869	2015	1205	3.9	7023	53.78	4.68	B
G337.170−00.059	16:36:25.1	−47:24:30.3	shrds869	2015	1205	11.5	7023	163.34	2.41	B
G337.188−00.060	16:36:28.2	−47:23:58.3	shrds869	2015	1205	8.3	7023	134.28	2.58	B
G337.253−00.165	16:37:12.8	−47:25:14.5	shrds870	2015	2002	8.2	7023	327.36	9.01	A
G337.281−00.163	16:37:17.5	−47:23:46.6	shrds870	2015	2002	10.4	7023	130.86	11.41	B
G337.285−00.113	16:37:05.3	−47:21:34.5	shrds870	2015	2002	10.1	7023	282.38	17.78	B
G337.286+00.113	16:36:05.7	−47:12:40.4	shrds871	2015	2314	14.8	7023	130.42	1.24	B
G337.404−00.404	16:38:50.6	−47:28:04.7	shrds875	2015	1328	3.9	7023	133.05	0.77	B
G337.428−00.401	16:38:51.8	−47:26:24.6	shrds875	2015	1328	48.7	7023	95.35	0.71	B
G337.453−00.363	16:38:52.2	−47:24:36.7	shrds875	2015	1328	22.2	7023	22.90	0.90	B
G337.617−00.065	16:38:11.1	−47:04:57.9	shrds880	2015	2118	6.6	7023	396.58	4.89	B
G337.652−00.050	16:38:18.1	−47:02:13.1	shrds885	2015	1505	41.7	7023	13.75	5.64	B
G337.664+00.049	16:37:54.4	−46:58:01.8	shrds886	2015	2094	22.2	7023	51.18	5.27	B
G337.665−00.176	16:38:52.0	−47:07:16.8	shrds883	2015	2136	3.9	7023	565.30	5.19	A
G337.684−00.343	16:39:46.0	−47:13:23.7	shrds884	2015	1207	56.4	7023	79.57	1.61	B
G337.705−00.059	16:38:30.2	−47:00:37.0	shrds885	2015	1505	14.3	7023	362.76	4.58	A
G337.709+00.091	16:37:52.4	−46:54:33.3	shrds886	2015	2094	6.1	7023	348.35	3.37	A
G337.754+00.057	16:38:26.1	−46:54:51.1	shrds888	2015	1416	152.2	7023	36.73	1.23	B

Table 4.4 continued

Table 4.4: Non-tapered Image Continuum Properties (continued)

Target	R.A. J2000 (hh:mm:ss)	Decl. J2000 (dd:mm:ss)	Field	Epoch[a]	Beam Area (arcsec^2)	$\Delta\theta^b$ (arcsec)	ν_C (MHz)	S_C (mJy beam^{-1})	rms$_C$ (mJy beam^{-1})	QF
G337.827+00.056	16:38:32.0	−46:51:59.2	shrds888	2015	1416	76.9	7023	32.79	1.22	B
G337.876−00.133	16:39:34.2	−46:55:22.2	shrds1233	2016	2549	59.9	7023	19.88	4.72	C
G337.996+00.081	16:39:03.5	−46:42:22.9	shrds890	2015	1447	13.5	7023	111.64	3.20	A
G338.002−00.149	16:40:04.3	−46:51:15.2	shrds891	2015	1311	8.4	7023	59.84	2.49	B
G338.003−00.121	16:39:58.1	−46:52:27.2	shrds891	2015	1311	149.3	7023	88.59	2.79	B
G338.009+00.016	16:39:21.5	−46:44:12.3	shrds892	2015	1340	10.0	7023	148.25	2.61	B
G338.066−00.069	16:39:57.4	−46:45:08.7	shrds1219	2016	1480	8.2	7022	206.62	3.35	A
G338.075+00.016	16:39:39.0	−46:41:24.2	shrds892	2015	1340	11.9	7023	1818.34	6.19	B
G338.106+00.020	16:39:43.8	−46:39:37.3	shrds893	2015	2084	7.1	7023	153.98	5.87	B
G338.263−00.364	16:42:01.0	−46:47:50.3	shrds894	2015	2666	4.6	7023	72.26	1.38	B
G338.271−00.293	16:41:44.3	−46:44:38.2	shrds894	2015	2666	7.2	7023	45.32	2.95	B
G338.289−00.373	16:42:09.1	−46:47:02.2	shrds894	2015	2666	4.4	7023	135.98	1.46	B
G338.360−00.095	16:41:13.4	−46:32:47.3	shrds896	2015	1779	7.5	7023	156.30	5.53	B
G338.364−00.020	16:40:55.2	−46:29:43.4	shrds896	2015	1779	8.6	7023	258.65	9.93	B
G338.374−00.152	16:41:30.8	−46:34:32.4	caswell22	2016	1718	3.5	7022	263.24	12.01	B
G338.405−00.203	16:41:51.7	−46:35:08.2	caswell22	2016	1718	1.2	7022	1974.80	5.90	A
G338.462−00.262	16:42:19.3	−46:34:53.5	shrds898	2015	2221	9.8	7023	175.23	4.14	B
G338.565−00.151	16:42:14.0	−46:25:27.8	shrds899	2015	2316	24.0	7023	326.13	2.23	A
G338.576+00.020	16:41:35.8	−46:17:55.8	shrds900	2015	2247	52.5	7023	327.52	4.07	B
G338.628+00.145	16:41:13.6	−46:11:24.8	shrds901	2015	1804	17.0	7023	345.14	4.24	A
G338.706+00.645	16:39:23.7	−45:48:53.7	shrds1223	2016	1359	69.3	7023	55.60	2.27	C
G338.837−00.318	16:44:02.5	−46:20:31.1	shrds904	2015	2625	27.8	7023	66.19	0.45	B
G338.851+00.405	16:40:55.2	−45:50:54.5	shrds905	2015	1187	3.7	7022	41.26	0.53	A
G338.861+00.597	16:39:42.0	−45:47:29.7	shrds1223	2016	1359	391.6	7023	35.22	1.15	C
G338.883+00.537	16:40:28.6	−45:44:24.9	shrds1225	2016	1168	9.1	7022	46.95	1.74	A
G338.911+00.615	16:40:25.9	−45:41:28.9	shrds1225	2016	1168	148.5	7022	162.29	2.70	B
G338.917+00.382	16:41:16.1	−45:48:50.3	shrds906	2015	1838	5.4	7023	281.16	1.63	C

Table 4.4 continued

Table 4.4: Non-tapered Image Continuum Properties (continued)

Target	R.A. J2000 (hh:mm:ss)	Decl. J2000 (dd:mm:ss)	Field	Epoch[a]	Beam Area (arcsec^2)	$\Delta\theta^b$ (arcsec)	ν_C (MHz)	S_C (mJy beam^{-1})	rms$_C$ (mJy beam^{-1})	QF
G338.926+00.392	16:41:16.9	−45:48:06.2	shrds906	2015	1838	8.5	7023	229.90	1.62	C
G339.106+00.152	16:42:59.1	−45:49:38.0	shrds909	2015	2516	9.5	7023	217.75	0.62	A
G339.169−00.698	16:46:52.0	−46:25:09.8	shrds910	2015	1193	320.5	7023	4.64	0.14	C
G339.216+00.263	16:42:56.0	−45:40:04.6	shrds913	2015	1173	8.6	7022	20.66	0.37	A
G339.233+00.243	16:43:23.4	−45:37:56.5	shrds913	2015	1173	241.5	7022	34.21	1.13	C
G339.275−00.607	16:46:54.9	−46:11:58.1	shrds915	2015	2443	30.8	7023	59.32	0.59	B
G339.478+00.181	16:44:14.1	−45:31:26.2	shrds917	2015	2624	11.3	7023	209.82	0.60	A
G339.486+00.087	16:44:41.3	−45:34:35.2	shrds918	2015	1850	12.6	7023	183.74	0.89	A
G339.548−00.385	16:46:59.6	−45:50:33.8	shrds919	2015	2035	14.2	7023	86.71	0.67	B
G339.553−00.401	16:47:05.4	−45:50:33.5	shrds919	2015	2035	20.4	7023	278.01	0.71	B
G339.556+00.282	16:44:06.0	−45:24:07.0	shrds920	2015	2598	11.2	7023	115.05	0.57	B
G339.584+00.084	16:45:03.0	−45:30:29.5	shrds921	2015	2641	11.0	7023	219.21	0.57	A
G339.676+00.283	16:44:34.7	−45:18:27.4	shrds922	2016	1383	17.2	7023	16.81	0.26	C
G339.699+00.302	16:44:32.5	−45:16:31.5	shrds922	2016	1383	12.8	7023	6.14	0.33	C
G339.717−01.211	16:51:13.8	−46:14:23.1	shrds925	2015	2434	12.7	7023	149.37	0.36	A
G339.781+00.243	16:45:04.6	−45:15:02.1	shrds928	2015	1202	28.9	7022	12.30	0.52	B
G339.845+00.299	16:45:07.2	−45:10:14.4	shrds928	2015	1202	8.4	7022	199.44	1.70	C
G339.952+00.052	16:46:34.1	−45:14:38.8	shrds1234	2016	1179	16.1	7022	65.24	0.27	B
G340.051−00.231	16:48:10.4	−45:21:29.1	shrds1236	2016	1442	8.1	7022	459.87	4.78	C
G340.053−00.244	16:48:14.2	−45:21:41.3	shrds1236	2016	1442	8.9	7022	493.54	5.96	C
G340.059−00.138	16:47:50.7	−45:16:33.3	shrds1236	2016	1442	63.2	7022	76.59	1.96	C
G340.097−00.174	16:47:58.7	−45:18:05.1	shrds1236	2016	1442	90.5	7022	51.92	1.66	C
G340.234−00.368	16:49:26.0	−45:18:10.4	shrds1237	2016	1315	6.0	7022	33.70	1.74	B
G340.247−00.373	16:49:30.2	−45:17:46.2	shrds1237	2016	1315	6.0	7022	177.13	2.15	B
G340.296−00.276	16:49:13.1	−45:19:01.9	shrds1237	2016	1315	431.5	7022	25.62	1.41	B
G342.062+00.417	16:52:33.1	−43:23:41.8	caswell23	2016	1719	15.5	7022	1129.99	5.13	B
G342.354−00.047	16:55:36.0	−43:27:30.7	shrds1239	2016	2498	23.3	7022	248.32	2.36	C

Table 4.4 continued

Table 4.4: Non-tapered Image Continuum Properties (continued)

Target	R.A. J2000 (hh:mm:ss)	Decl. J2000 (dd:mm:ss)	Field	Epoch[a]	Beam Area (arcsec^2)	$\Delta\theta^b$ (arcsec)	ν_C (MHz)	S_C (mJy beam^{-1})	rms$_C$ (mJy beam^{-1})	QF
G342.360+00.107	16:54:56.2	−43:21:37.9	shrds1238	2016	1379	3.5	7022	73.30	0.62	B
G342.384+00.122	16:54:56.9	−43:19:53.8	shrds1238	2016	1379	5.1	7022	17.86	0.68	B
G342.388+00.074	16:55:09.7	−43:21:34.0	shrds1238	2016	1379	4.3	7022	40.84	0.41	A
G342.438−00.061	16:55:54.4	−43:24:18.6	shrds1239	2016	2498	8.9	7022	75.06	0.65	B
G343.224−00.065	16:58:37.3	−42:46:57.3	shrds1240	2016	1169	38.3	7022	25.96	0.34	C
G343.234−00.078	16:58:42.4	−42:47:33.3	shrds1240	2016	1169	4.2	7022	43.96	0.36	C
G343.352−00.081	16:59:03.9	−42:41:36.6	shrds1241	2016	1420	50.3	7022	173.14	1.12	A
G343.914−00.646	17:03:29.1	−42:37:43.4	caswell24	2016	1177	89.9	7022	36.62	0.44	B
G344.424+00.044	17:02:09.6	−41:46:44.1	caswell25	2016	1772	8.4	7022	2325.68	6.35	A
G348.892−00.179	17:16:59.8	−38:19:24.6	fa644	2015	1155	0.7	7022	347.68	0.78	A
G349.328+00.020	17:17:27.0	−37:51:09.7	gs038	2015	1157	3.1	7022	162.59	0.47	A
G352.313−00.442	17:27:48.7	−35:39:10.6	fa016	2015	1170	10.4	7022	236.53	0.55	A
G355.344+00.145	17:33:29.0	−32:47:58.1	fa032	2015	1178	9.0	7022	538.03	1.47	A
G358.552−00.026	17:42:14.1	−30:11:06.5	gs108	2015	1159	10.9	7022	39.36	2.54	B
G358.600−00.058	17:42:27.6	−30:09:14.6	gs108	2015	1159	18.3	7022	167.36	1.34	B
G358.616−00.077	17:42:35.0	−30:09:14.6	gs108	2015	1159	3.2	7022	41.45	1.51	B
G358.633+00.062	17:42:04.7	−30:04:03.8	fa054	2015	1151	3.9	7022	312.28	0.98	A
G358.643−00.035	17:42:29.2	−30:06:30.6	gs108	2015	1159	5.2	7022	123.42	2.18	B
G358.652−00.079	17:42:40.9	−30:07:30.8	gs108	2015	1159	1.3	7022	44.22	2.47	B
G359.436−00.091	17:44:40.0	−29:28:26.2	fa489	2015	1120	47.2	7022	194.49	6.59	C
G359.467−00.173	17:45:00.8	−29:28:46.1	fa489	2015	1120	5.9	7022	128.42	2.11	A

[a] Rows with epochs with an asterisk (*) are copied directly from Brown et al. (2017). They did not give the continuum fluxes for their detections.

[b] The separation between the *WISE* Catalog infrared position and the position of the SHRDS continuum peak.

Table 4.5: *uv*-tapered Image Continuum Properties

Target	R.A. J2000 (hh:mm:ss)	Decl. J2000 (dd:mm:ss)	Field	Epoch[a]	Beam Area (arcsec^2)	$\Delta\theta^b$ (arcsec)	ν_C (MHz)	S_C (mJy beam^{-1})	rms$_C$ (mJy beam^{-1})	QF
G213.833+00.618	06:55:16.9	+0:31:12.3	g213.833+00.618	2014*	···	2.5	···	···	···	···
G230.354−00.597	07:21:49.5	−15:44:09.9	g230.354-00.597	2014*	···	2.2	···	···	···	···
G259.057−01.544	08:26:19.2	−40:48:32.2	shrds030	2016	9022	37.8	7022	192.46	0.98	B
G259.359+00.820	08:37:05.6	−39:44:47.7	shrds035	2015	9230	346.0	7022	20.98	0.13	A
G263.237+00.509	08:48:38.4	−42:53:58.1	shrds060	2015	9205	61.8	7022	149.64	0.89	A
G264.681+00.272	08:52:50.5	−44:13:51.4	shrds073	2015	8244	237.1	7022	4.91	1.88	C
G265.191−00.641	08:50:38.6	−45:08:12.4	shrds075	2015	9233	19.1	7022	61.11	0.73	B
G267.730−01.100	08:58:04.4	−47:22:55.2	shrds078	2016	8498	15.1	7023	404.28	32.87	A
G268.618−00.739	09:03:10.6	−47:48:22.1	shrds081	2015	9443	10.9	7022	24.99	4.65	C
G269.068−01.114	09:03:24.4	−48:26:20.9	shrds085	2016	8522	176.5	7023	1829.82	31.02	B
G269.159−01.119	09:03:37.7	−48:28:16.7	shrds085	2016	8522	19.0	7023	534.39	20.35	A
G269.167−01.357	09:02:31.1	−48:38:08.3	shrds086	2016	7559	45.9	7022	167.63	35.02	B
G280.626−01.186	09:58:23.3	−56:22:12.4	shrds111	2015	9545	20.6	7023	100.57	0.50	A
G280.903−00.522	10:02:28.3	−56:04:30.6	shrds113	2015	8357	319.0	7022	23.33	0.67	B
G280.989−01.527	09:59:00.3	−56:51:41.5	shrds1005	2016	8830	7.8	7023	572.49	31.73	B
G281.047−01.541	09:59:16.0	−56:54:33.5	shrds1005	2016	8830	9.3	7023	736.50	16.71	A
G281.175−01.645	09:59:32.0	−57:03:57.1	caswell1	2016	9323	23.1	7023	1168.26	4.02	A
G281.560−02.478	09:58:02.9	−57:57:45.1	shrds114	2015	9446	11.1	7023	653.29	2.14	A
G281.840−01.609	10:03:40.7	−57:26:38.0	shrds117	2015	9455	15.2	7023	167.49	1.35	A
G282.015−00.997	10:06:59.3	−57:02:25.4	shrds1007	2016	8702	190.5	7023	270.92	11.82	B
G282.842−01.252	10:11:15.9	−57:44:02.4	shrds1232	2016	9204	10.9	7023	333.64	1.55	A
G283.098−00.400	10:16:26.9	−57:10:37.0	shrds132	2015	8142	7.6	7022	19.43	1.38	B
G283.832−00.730	10:19:40.0	−57:51:21.4	shrds1013	2016	8945	18.4	7023	276.99	10.10	A
G284.014−00.857	10:20:15.3	−58:03:30.6	shrds1014	2016	9128	19.6	7023	1137.90	22.20	B
G284.712+00.317	10:29:29.1	−57:26:47.5	caswell2	2016	9096	61.9	7023	1417.71	10.07	A
G284.902+00.060	10:29:36.0	−57:45:13.3	shrds141	2015	9185	18.0	7023	104.79	1.19	A
G285.353+00.004	10:32:13.8	−58:02:07.2	shrds143	2016	8521	29.2	7023	53.51	21.79	A

Table 4.5 continued

Table 4.5: *uv*-tapered Image Continuum Properties (continued)

Target	R.A. J2000 (hh:mm:ss)	Decl. J2000 (dd:mm:ss)	Field	Epoch[a]	Beam Area (arcsec^2)	$\Delta\theta^b$ (arcsec)	ν_C (MHz)	S_C (mJy beam^{-1})	rms$_C$ (mJy beam^{-1})	QF
G286.362−00.297	10:37:47.8	−58:47:23.4	shrds1017	2016	8163	42.4	7023	191.48	6.18	B
G286.951−00.955	10:39:19.9	−59:39:53.0	shrds158	2015	8246	7.2	7023	505.49	7.33	A
G288.074−01.642	10:44:39.2	−60:48:09.9	shrds162	2016	8383	3.4	7023	161.87	0.75	A
G288.233−01.118	10:47:36.1	−60:25:39.3	shrds1020	2016	8814	97.2	7023	24.65	2.03	B
G288.851−00.108	10:55:48.5	−59:46:53.5	shrds167	2016	8085	4.0	7023	151.71	1.80	B
G289.109−01.107	10:54:10.9	−60:47:28.2	shrds173	2016	7855	9.3	7023	108.60	0.87	A
G289.188−00.293	10:57:37.6	−60:05:35.2	shrds1024	2016	8583	8.0	7023	192.98	4.68	B
G289.476−00.899	10:57:38.6	−60:45:51.7	shrds181	2016	8411	5.8	7023	198.57	1.44	B
G289.582−00.636	10:59:20.1	−60:34:06.1	shrds184	2016	8075	1.1	7023	141.78	1.01	A
G289.769−01.220	10:58:43.6	−61:11:46.7	shrds1026	2016	8944	69.5	7023	202.73	10.09	A
G289.806−01.242	10:58:44.7	−61:07:22.5	shrds1026	2016	8944	332.0	7023	467.70	16.75	B
G289.874−00.752	11:01:05.4	−60:46:52.6	shrds1028	2016	9758	49.8	7023	281.82	6.34	B
G289.880−00.801	11:00:59.4	−60:50:36.5	shrds1028	2016	9758	4.5	7023	1455.44	11.95	B
G289.944−00.889	11:01:11.1	−60:56:48.0	shrds191	2015	9232	10.1	7023	145.89	3.69	A
G290.012−00.867	11:01:59.1	−60:56:49.2	g290.012-00.867	2014	7104	105.8	6050	196.21	5.43	B
G290.321−03.024	10:56:10.6	−62:59:48.3	g290.323-02.984	2014	7202	202.3	6050	12.38	0.67	B
G290.323−02.984	10:56:33.0	−63:00:44.2	g290.323-02.984	2014	7202	27.2	6050	29.11	0.46	A
G290.385−01.042	11:03:59.5	−61:16:04.9	g290.385-01.042	2014	7084	1.4	6050	24.97	1.35	A
G290.674−00.133	11:09:07.0	−60:32:47.0	g290.674-00.133	2014*	···	2.0	···	···	···	···
G291.046−02.079	11:05:38.2	−62:29:06.0	shrds199	2015	9054	11.7	7023	306.76	1.32	A
G291.202−00.295	11:12:36.3	−60:53:46.6	shrds1032	2016	9644	4.6	7023	430.09	12.63	B
G291.281−00.726	11:11:52.9	−61:18:48.3	caswell3	2016	9253	40.1	7023	60503.27	235.80	A
G291.596−00.239	11:15:49.9	−60:59:20.6	g291.596-00.239	2014	7121	13.1	6050	37.46	25.11	C
G291.863−00.682	11:16:32.6	−61:29:53.3	caswell4	2016	8767	4.5	7023	1841.72	24.58	A
G292.722+00.157	11:25:35.0	−60:59:58.2	g292.722+00.157	2014	6950	30.2	6050	3.45	0.23	B
G292.889−00.831	11:24:15.3	−61:59:26.9	g292.889-00.831	2014*	···	2.0	···	···	···	···
G293.113−00.961	11:25:57.9	−62:12:21.2	shrds207	2015	7205	131.7	7023	34.22	2.88	C

Table 4.5 continued

Table 4.5: *uv*-tapered Image Continuum Properties (continued)

Target	R.A. J2000 (hh:mm:ss)	Decl. J2000 (dd:mm:ss)	Field	Epoch[a]	Beam Area (arcsec^2)	$\Delta\theta^b$ (arcsec)	ν_C (MHz)	S_C (mJy beam^{-1})	rms$_C$ (mJy beam^{-1})	QF
G293.483−00.903	11:28:51.0	−62:14:35.5	g293.483-00.903	2014	7170	26.5	6050	11.19	0.44	B
G293.619−01.613	11:28:03.7	−62:57:26.3	shrds210	2016	8800	34.0	7023	80.65	6.36	B
G293.661−01.639	11:28:19.5	−63:00:30.3	shrds210	2016	8800	14.2	7023	241.77	5.81	B
G293.683−01.590	11:28:37.1	−62:57:34.4	shrds210	2016	8800	20.5	7023	70.32	6.17	B
G293.829−00.744	11:32:06.6	−62:12:23.9	shrds215	2015	8524	7.6	7023	220.13	0.67	B
G293.936−00.873	11:32:38.8	−62:21:31.8	g293.936-00.873	2014	7287	6.8	6050	121.99	2.82	B
G293.952−00.894	11:32:43.4	−62:23:11.8	g293.936-00.873	2014	7287	5.7	6050	127.53	3.16	B
G293.967−00.984	11:32:36.6	−62:28:22.4	shrds219	2015	9356	10.3	7023	224.20	1.04	A
G293.994−00.934	11:32:59.7	−62:25:58.4	shrds219	2015	9356	12.5	7023	302.07	1.88	B
G294.453−00.521	11:37:49.0	−62:10:46.9	shrds226	2015	9169	25.9	7023	174.88	0.44	A
G294.656−00.438	11:39:46.2	−62:09:31.8	g294.656-00.438	2014	9512	57.1	6050	18.30	0.26	A
G294.988−00.538	11:42:10.3	−62:20:09.5	g294.988-00.538	2014	9367	0.9	6050	163.76	1.64	A
G295.275−00.255	11:44:54.8	−62:08:05.1	g295.275-00.255	2014	10997	112.4	6050	23.73	1.98	B
G295.748−00.207	11:49:12.1	−62:12:25.3	g295.748-00.207	2014	11002	3.2	6050	83.80	1.08	A
G297.248−00.754	12:00:55.5	−63:04:05.6	g297.248-00.754	2014	10913	6.3	6050	316.90	2.12	A
G297.312−00.295	12:02:19.8	−62:36:45.2	shrds242	2015	8985	66.2	7023	123.07	1.08	A
G297.392−00.624	12:02:24.4	−62:58:24.5	shrds243	2015	8722	25.4	7023	253.72	2.18	A
G297.497−00.758	12:03:09.8	−63:07:45.1	shrds246	2015	9109	54.8	7023	770.10	4.09	B
G297.519−00.031	12:04:25.4	−62:24:24.5	shrds244	2015	7666	5.2	7023	49.16	1.71	B
G297.536−00.826	12:03:16.8	−63:11:25.3	shrds246	2015	9109	10.9	7023	195.45	2.44	A
G297.626−00.906	12:03:58.2	−63:17:09.1	g297.626-00.906	2014	11074	6.5	6050	174.48	3.49	A
G297.651−00.973	12:04:04.7	−63:21:56.9	g297.626-00.906	2014	11074	29.8	6050	837.43	8.98	C
G298.183−00.784	12:09:01.5	−63:15:54.3	caswell5	2016	9135	7.0	7023	2155.71	5.58	A
G298.196−00.247	12:09:54.2	−62:44:18.1	shrds1041	2016	9315	9.5	7023	465.59	34.80	A
G298.473+00.104	12:12:49.9	−62:25:54.9	g298.473+00.104	2014	11055	32.3	6050	121.93	3.60	A
G298.630+00.253	12:14:24.3	−62:16:42.9	shrds253	2015	8085	115.8	7023	83.21	1.83	B
G298.669+00.064	12:14:22.9	−62:30:02.3	g298.669+00.064	2014*	...	2.7	...	...	...	...

Table 4.5 continued

Table 4.5: *uv*-tapered Image Continuum Properties (continued)

Target	R.A. J2000 (hh:mm:ss)	Decl. J2000 (dd:mm:ss)	Field	Epoch[a]	Beam Area (arcsec^2)	$\Delta\theta^b$ (arcsec)	ν_C (MHz)	S_C (mJy beam^{-1})	rms$_C$ (mJy beam^{-1})	QF
G298.765+00.174	12:15:22.1	−62:24:24.6	shrds256	2015	7611	14.8	7023	20.62	5.65	A
G298.846+00.121	12:15:55.8	−62:27:53.0	shrds258	2015	8995	21.0	7023	319.95	1.71	A
G298.878+00.192	12:16:17.9	−62:24:09.4	shrds261	2016	8898	11.7	7023	60.02	3.82	C
G298.899+00.187	12:16:26.0	−62:24:41.2	shrds261	2016	8898	29.0	7023	49.78	3.87	C
G299.349−00.267	12:19:53.0	−62:55:13.6	caswell6	2016	8956	7.3	7023	371.53	1.81	B
G299.399−00.235	12:20:24.6	−62:53:38.8	shrds1046	2016	8725	25.9	7023	22.05	1.33	A
G299.505+00.025	12:21:25.2	−62:38:16.4	g299.505+00.025	2014	10971	59.4	6050	1.83	0.58	C
G300.369−00.288	12:28:51.5	−63:02:41.3	shrds271	2015	8854	27.6	7023	102.48	1.88	A
G300.502−00.180	12:30:02.0	−62:57:32.2	shrds273	2015	7469	30.9	7023	281.09	14.38	C
G300.965+01.162	12:34:53.4	−61:39:22.9	g300.983+01.117	2014	10927	40.5	6050	1689.33	5.53	B
G300.972+00.994	12:34:49.9	−61:48:52.3	g300.972+00.994	2014*	...	1.2	...	...	...	...
G300.983+01.117	12:34:53.0	−61:39:20.6	caswell7	2016	9123	138.7	7023	1600.66	5.87	B
G301.116+00.968	12:36:02.2	−61:51:06.8	caswell8	2016	9158	9.6	7023	2606.67	6.50	A
G302.032−00.063	12:43:31.4	−62:55:07.7	caswell9	2016	9243	5.7	7023	1087.56	1.77	A
G302.391+00.280	12:46:43.7	−62:35:14.9	shrds293	2016	8623	6.0	7023	167.55	0.63	A
G302.436−00.106	12:47:04.0	−62:58:27.3	shrds294	2016	8444	4.3	7023	192.37	1.34	A
G302.481−00.035	12:47:32.9	−62:54:11.9	shrds295	2016	8249	28.8	7023	124.98	2.50	B
G302.503−00.762	12:47:35.7	−63:38:08.4	shrds296	2015	7397	20.7	7023	120.28	4.19	B
G302.636−00.672	12:48:45.7	−63:32:19.9	shrds297	2016	9270	12.2	7023	474.87	1.82	A
G302.816−00.844	12:50:20.7	−63:42:54.8	shrds299	2016	7675	18.1	7023	98.10	1.96	B
G303.342−00.718	12:55:06.5	−63:35:07.9	shrds303	2015	9103	7.0	7023	220.46	2.90	B
G303.384−00.965	12:55:32.2	−63:49:54.2	shrds305	2016	8557	3.3	7023	130.40	0.63	A
G303.557−00.539	12:57:02.5	−63:24:21.3	shrds308	2016	8382	11.5	7023	156.05	2.06	A
G304.465−00.023	13:04:55.3	−62:50:59.3	shrds336	2015	9062	21.2	7023	275.49	1.51	A
G304.557+00.329	13:05:30.7	−62:29:57.4	shrds338	2016	8272	5.6	7023	111.98	0.79	A
G304.925+00.555	13:08:35.9	−62:15:02.6	shrds344	2015	8981	12.1	7023	507.95	1.85	A
G305.789+00.280	13:16:12.4	−62:26:53.5	shrds350	2016	8515	23.4	7023	182.86	2.69	A

Table 4.5 continued

Table 4.5: *uv*-tapered Image Continuum Properties (continued)

Target	R.A. J2000 (hh:mm:ss)	Decl. J2000 (dd:mm:ss)	Field	Epoch[a]	Beam Area (arcsec^2)	$\Delta\theta^b$ (arcsec)	ν_C (MHz)	S_C (mJy beam^{-1})	rms$_C$ (mJy beam^{-1})	QF
G307.559−00.585	13:32:31.0	−63:05:21.3	caswell10	2016	8979	9.5	7023	882.58	3.64	B
G307.571−00.620	13:32:43.4	−63:07:13.6	caswell10	2016	8979	28.4	7023	69.00	4.62	B
G307.610−00.593	13:32:57.5	−63:05:25.8	caswell10	2016	8979	13.4	7023	79.87	5.68	B
G307.974−01.594	13:37:40.9	−64:00:39.8	shrds373	2016	8731	8.1	7023	83.57	0.30	A
G308.079−00.406	13:36:47.4	−62:49:42.6	caswell11	2016	8997	26.1	7023	506.36	2.53	B
G308.747+00.547	13:40:53.5	−61:45:46.0	shrds1091	2016	8890	8.6	7023	515.20	19.45	B
G308.916+00.124	13:43:01.7	−62:08:55.2	shrds384	2015	9029	11.9	7023	472.72	2.85	A
G309.151−00.215	13:45:22.8	−62:25:23.5	shrds385	2016	8162	89.0	7023	151.13	3.01	B
G309.176−00.028	13:45:28.4	−62:14:31.8	shrds386	2015	9019	6.0	7023	323.66	0.97	A
G310.260−00.199	13:54:48.8	−62:09:58.5	shrds403	2016	7640	15.7	7023	118.38	2.52	A
G310.519−00.220	13:57:01.2	−62:07:11.3	shrds407	2015	8975	9.8	7023	426.23	1.51	A
G310.630−00.421	13:58:24.1	−62:17:35.4	shrds409	2015	8204	21.2	7023	229.09	4.08	B
G310.672−00.450	13:58:49.9	−62:17:55.3	shrds409	2015	8204	23.5	7023	230.01	4.05	B
G310.688−00.314	13:58:40.4	−62:09:53.7	shrds411	2015	7877	19.3	7023	98.66	5.90	A
G310.887+00.009	13:59:35.3	−61:48:18.7	shrds412	2015	9282	7.8	7023	171.04	0.90	B
G310.901−00.373	14:00:33.0	−62:10:34.5	shrds1096	2016	9145	21.1	7023	630.16	4.58	B
G311.003−00.355	14:01:19.4	−62:07:49.7	shrds413	2016	8935	18.4	7023	143.16	3.15	B
G311.137−00.235	14:02:03.9	−61:59:07.9	shrds418	2015	7577	59.6	7023	197.56	4.67	B
G311.425+00.598	14:02:36.0	−61:05:46.2	shrds425	2015	8958	6.4	7023	139.81	2.69	B
G311.551−00.584	14:06:20.7	−62:11:29.8	shrds1101	2016	8258	22.0	7023	101.04	5.28	B
G311.575+00.239	14:04:32.3	−61:24:07.6	shrds428	2016	8625	37.3	7023	132.95	4.09	A
G311.581−00.593	14:06:41.3	−62:11:29.8	shrds1101	2016	8258	14.5	7023	150.54	3.78	B
G311.606−00.638	14:06:59.0	−62:13:45.8	shrds1101	2016	8258	4.3	7023	88.16	6.30	C
G311.629+00.289	14:04:54.6	−61:20:05.5	caswell12	2016	9111	10.6	7023	2461.56	10.74	A
G311.809−00.309	14:07:49.9	−61:50:04.8	shrds1103	2016	8518	78.7	7023	215.48	4.08	B
G311.841−00.219	14:07:51.5	−61:45:12.7	shrds1103	2016	8518	26.1	7023	163.87	13.47	C
G311.866−00.238	14:08:07.3	−61:46:04.9	shrds1103	2016	8518	14.7	7023	210.81	11.24	C

Table 4.5 continued

Table 4.5: *uv*-tapered Image Continuum Properties (continued)

Target	R.A. J2000 (hh:mm:ss)	Decl. J2000 (dd:mm:ss)	Field	Epoch[a]	Beam Area (arcsec^2)	$\Delta\theta^b$ (arcsec)	ν_C (MHz)	S_C (mJy beam^{-1})	rms$_C$ (mJy beam^{-1})	QF
G311.963−00.037	14:08:33.2	−61:33:53.6	shrds439	2016	8331	84.0	7023	197.24	6.33	B
G312.091+00.069	14:08:52.8	−61:25:26.3	shrds440	2015	8050	127.0	7023	139.50	12.45	B
G312.388−00.057	14:11:50.9	−61:26:37.8	shrds450	2015	7712	2.0	7023	66.65	1.38	B
G312.591+00.210	14:12:40.8	−61:06:47.2	shrds456	2016	8562	62.3	7023	183.20	3.19	B
G312.598+00.048	14:13:14.4	−61:16:48.2	shrds458	2016	8415	5.9	7023	151.32	2.93	A
G312.675+00.048	14:13:53.5	−61:15:39.1	shrds462	2015	8444	28.7	7023	195.67	2.29	B
G312.706+00.012	14:14:10.7	−61:16:07.4	shrds462	2015	8444	36.3	7023	253.18	1.81	B
G312.979−00.432	14:17:21.0	−61:37:53.1	shrds465	2016	8893	107.3	7023	197.16	1.96	B
G313.671−00.105	14:22:04.0	−61:04:19.8	atca348	2013	8829	0.8	8450	102.68	0.58	A
G313.790+00.705	14:20:41.9	−60:15:51.9	atca352	2013	9016	24.8	8450	361.87	1.69	A
G313.851−00.243	14:23:52.1	−61:08:21.9	shrds479	2016	8477	2.2	7023	86.15	0.99	A
G314.219+00.343	14:25:01.6	−60:27:52.8	atca361	2013	8689	16.9	8450	382.92	7.50	A
G314.239+00.428	14:24:56.2	−60:23:01.8	shrds1111	2016	9286	36.0	7023	1516.16	14.17	B
G314.288+00.431	14:25:16.2	−60:21:29.6	shrds1111	2016	9286	13.7	7023	391.45	8.53	B
G315.312−00.272	14:35:07.0	−60:37:29.7	ch87.1	2013	8758	6.2	8450	264.75	2.92	A
G316.516−00.600	14:45:05.7	−60:26:18.6	atca382	2013	8604	21.4	8450	116.46	0.64	A
G317.405+00.091	14:49:09.7	−59:25:03.1	shrds1122	2016	9029	46.5	7023	1064.80	4.94	A
G317.426−00.561	14:51:35.3	−60:00:30.4	shrds518	2015	9292	10.2	7023	197.17	3.15	B
G317.458−00.533	14:51:45.0	−59:57:34.4	shrds518	2015	9292	28.8	7023	168.93	2.01	B
G317.570−00.257	14:51:26.9	−59:40:12.5	shrds521	2015	8261	48.3	7023	18.76	2.11	A
G317.861+00.160	14:52:05.9	−59:10:09.8	atca402	2013	8615	19.7	8450	458.63	4.18	B
G318.059−00.450	14:55:42.5	−59:37:01.1	caswell13	2016	8900	16.0	7023	325.17	3.89	B
G318.233−00.605	14:57:31.4	−59:41:26.7	shrds1126	2016	7566	46.9	7023	102.62	2.75	B
G318.248+00.150	14:55:05.0	−59:00:55.9	atca406	2013	8603	115.7	8450	57.09	5.74	B
G318.726−00.222	14:59:30.0	−59:06:37.3	shrds535	2016	8971	4.0	7023	170.26	1.05	A
G318.774−00.150	14:59:34.6	−59:01:22.2	shrds536	2015	9224	6.0	7023	382.82	2.94	A
G319.188−00.329	15:03:00.7	−58:54:59.4	shrds1129	2016	8737	238.4	7023	213.72	13.08	B

Table 4.5 continued

Table 4.5: *uv*-tapered Image Continuum Properties (continued)

Target	R.A. J2000 (hh:mm:ss)	Decl. J2000 (dd:mm:ss)	Field	Epoch[a]	Beam Area (arcsec^2)	$\Delta\theta^b$ (arcsec)	ν_C (MHz)	S_C (mJy beam^{-1})	rms$_C$ (mJy beam^{-1})	QF
G319.229+00.225	15:01:21.1	−58:27:15.9	atca412	2013	8934	87.6	8450	96.09	1.61	B
G319.397−00.006	15:03:14.8	−58:36:16.8	shrds1131	2016	9433	22.0	7023	1880.41	34.37	B
G319.453−00.022	15:03:41.5	−58:35:00.8	shrds1131	2016	9433	5.9	7023	334.48	16.69	A
G320.163+00.797	15:05:18.4	−57:30:57.2	shrds1137	2016	8433	38.1	7023	2805.87	31.16	C
G320.205+00.867	15:05:23.3	−57:26:45.1	shrds1137	2016	8433	15.4	7023	106.43	10.94	A
G320.236−00.099	15:09:10.2	−58:14:49.0	shrds1140	2016	8748	64.9	7023	190.09	4.65	B
G320.240−00.176	15:09:28.6	−58:19:44.1	shrds1139	2016	8440	12.8	7023	61.36	11.49	A
G320.311−00.176	15:10:02.1	−58:17:28.2	shrds1139	2016	8440	31.5	7023	2671.87	38.58	C
G320.376+00.172	15:09:02.7	−57:57:32.6	shrds555	2015	9173	11.2	7023	549.36	26.69	A
G320.419+00.114	15:09:34.4	−57:59:24.9	shrds555	2015	9173	6.1	7023	245.51	9.72	C
G320.675+00.246	15:10:48.7	−57:45:35.8	shrds559	2015	7244	66.2	7023	115.66	9.06	B
G320.782+00.258	15:11:21.7	−57:40:34.3	shrds1146	2016	8993	16.2	7023	351.85	17.92	B
G320.799+00.187	15:11:48.1	−57:44:31.9	shrds1147	2016	8951	42.7	7023	252.70	12.17	B
G320.884−00.641	15:15:31.5	−58:23:30.1	shrds561	2016	8580	21.0	7023	214.50	2.91	A
G321.725+01.169	15:13:49.9	−56:24:47.8	caswell14	2016	9099	20.1	7023	2037.63	6.40	A
G322.162+00.625	15:18:38.8	−56:38:52.8	caswell15	2016	9149	3.9	7023	8280.75	47.65	A
G322.706−00.330	15:25:47.8	−57:09:06.6	shrds574	2015	9468	4.2	7023	218.24	0.64	A
G323.449+00.095	15:28:32.0	−56:22:57.8	atca449	2013	9069	11.8	8450	95.96	1.91	A
G323.464−00.079	15:29:19.1	−56:31:23.8	atca450	2013	9153	20.6	8450	677.85	2.51	A
G323.743−00.249	15:31:44.0	−56:30:14.9	atca456	2013	9097	14.2	8450	146.61	0.81	A
G323.806+00.020	15:31:05.2	−56:14:29.0	atca459	2013	9034	56.2	8450	291.92	1.97	A
G323.915+00.026	15:31:34.8	−56:10:19.8	shrds590	2015	9086	20.2	7023	354.25	2.64	A
G323.936−00.038	15:31:56.6	−56:11:04.9	atca462	2013	9085	117.3	8450	41.94	4.57	B
G324.201+00.117	15:32:53.5	−55:56:13.0	caswell16	2016	8971	5.4	7023	3128.12	16.61	A
G324.642−00.321	15:37:23.2	−56:01:50.1	atca466	2013	9060	54.6	8450	317.76	2.08	A
G324.924−00.569	15:39:56.3	−56:04:13.3	ch87.2	2013	9852	16.2	8450	535.56	6.89	B
G325.108+00.053	15:38:35.7	−55:28:23.0	atca472	2013	8900	115.9	8450	97.88	1.57	B

Table 4.5 continued

Table 4.5: *uv*-tapered Image Continuum Properties (continued)

Target	R.A. J2000 (hh:mm:ss)	Decl. J2000 (dd:mm:ss)	Field	Epoch[a]	Beam Area (arcsec^2)	$\Delta\theta^b$ (arcsec)	ν_C (MHz)	S_C (mJy beam^{-1})	rms$_C$ (mJy beam^{-1})	QF
G325.354−00.036	15:40:11.4	−55:23:05.1	atca475	2013	8825	17.9	8450	198.02	1.71	A
G326.065−00.393	15:45:56.6	−55:15:03.4	shrds1161	2016	7792	156.5	7023	108.26	7.41	B
G326.446+00.901	15:42:17.8	−53:58:29.7	caswell17	2016	9021	16.6	7023	4466.02	21.96	A
G326.467−00.382	15:47:49.7	−54:58:32.5	shrds609	2015	9147	23.7	7023	441.75	4.69	A
G326.657+00.588	15:44:43.2	−54:05:55.8	shrds1163	2016	9201	9.4	7023	10592.22	86.86	A
G326.721+00.773	15:44:16.8	−53:54:34.0	atca484	2013	8945	27.4	8450	193.77	7.41	A
G326.728+00.616	15:44:59.5	−54:02:14.7	shrds1164	2016	8874	11.2	7023	3975.21	41.68	A
G326.890−00.277	15:49:39.1	−54:38:18.1	atca486	2013	8685	8.5	8450	408.89	7.41	A
G326.916−01.100	15:53:25.5	−55:15:15.9	atca487	2013	8763	21.0	8450	135.18	1.54	A
G327.139−00.261	15:50:54.7	−54:28:23.3	shrds618	2016	8153	20.2	7023	137.65	6.09	A
G327.172−00.527	15:52:30.8	−54:43:38.4	shrds1167	2016	9723	293.9	7023	378.66	29.66	B
G327.300−00.548	15:53:03.3	−54:35:21.6	caswell18	2016	8991	6.4	7023	26594.54	85.78	A
G327.400+00.444	15:49:19.6	−53:45:13.9	shrds621	2016	8563	9.0	7023	138.57	4.51	B
G327.401+00.483	15:49:08.6	−53:43:58.8	atca492	2013	8493	32.8	8450	149.56	5.88	B
G327.555−00.829	15:55:46.3	−54:39:05.9	atca495	2013	8320	74.5	8450	143.61	4.46	B
G327.714+00.576	15:50:17.3	−53:27:51.9	atca498	2013	8768	71.6	8450	90.89	0.91	A
G327.735−00.396	15:54:40.2	−54:11:46.6	shrds628	2015	9578	8.5	7023	711.91	9.19	A
G327.763+00.163	15:52:27.7	−53:44:46.6	atca501	2013	8494	22.7	8450	197.40	5.52	A
G327.770−00.346	15:54:37.5	−54:08:26.4	shrds628	2015	9578	25.4	7023	1715.46	15.73	B
G327.824+00.117	15:52:48.5	−53:46:02.9	atca501	2013	8494	110.6	8450	215.76	15.57	C
G327.848+00.016	15:53:30.0	−53:48:29.2	shrds635	2016	7984	9.8	7023	98.53	5.96	B
G327.916+00.154	15:53:14.8	−53:39:22.5	shrds639	2016	8096	4.4	7023	66.26	3.48	B
G328.043+00.298	15:53:20.5	−53:27:48.1	shrds643	2015	7488	21.8	7023	48.72	4.01	A
G328.117+00.108	15:54:30.2	−53:33:26.8	shrds647	2015	9289	24.3	7023	335.81	6.76	A
G328.193−00.569	15:57:50.2	−54:02:17.4	shrds652	2015	9364	15.5	7023	981.93	13.68	B
G328.279−00.559	15:58:14.1	−53:57:51.1	shrds659	2016	8220	24.7	7023	301.21	11.02	B
G328.315−00.594	15:58:33.1	−53:58:31.4	shrds659	2016	8220	15.9	7023	304.08	7.90	B

Table 4.5 continued

Table 4.5: *uv*-tapered Image Continuum Properties (continued)

Target	R.A. J2000 (hh:mm:ss)	Decl. J2000 (dd:mm:ss)	Field	Epoch[a]	Beam Area (arcsec^2)	$\Delta\theta^b$ (arcsec)	ν_C (MHz)	S_C (mJy beam^{-1})	rms$_C$ (mJy beam^{-1})	QF
G328.356−00.559	15:58:37.2	−53:55:19.5	shrds659	2016	8220	11.0	7023	187.21	5.07	A
G328.819−00.004	15:58:34.0	−53:11:53.8	shrds668	2016	8162	10.4	7023	124.27	2.27	A
G328.825−00.081	15:58:55.9	−53:15:21.4	shrds668	2016	8162	16.1	7023	620.91	7.97	C
G328.945+00.570	15:56:47.5	−52:40:35.7	shrds669	2015	9225	16.7	7023	515.90	3.48	A
G328.961+00.248	15:58:13.5	−52:54:53.5	shrds670	2015	8977	4.6	7023	235.00	3.08	B
G328.962+00.207	15:58:25.8	−52:56:25.6	shrds670	2015	8977	22.0	7023	174.99	4.32	B
G329.266+00.111	16:00:22.6	−52:49:12.7	shrds677	2015	9002	16.1	7023	207.89	5.82	A
G329.422−00.160	16:02:18.8	−52:55:28.9	shrds684	2015	9225	11.2	7023	344.22	1.34	A
G329.460+00.174	16:01:01.9	−52:38:39.5	shrds686	2015	9639	8.2	7023	279.96	4.87	B
G329.472+00.214	16:00:55.3	−52:36:15.3	shrds686	2015	9639	10.6	7023	947.45	7.48	B
G329.474+00.839	15:58:16.9	−52:07:40.4	shrds687	2016	7860	13.5	7023	121.23	1.56	B
G329.601+00.059	16:02:14.7	−52:38:29.2	shrds690	2015	9242	8.3	7023	318.22	2.54	A
G330.049+00.899	16:00:50.6	−51:42:46.1	shrds697	2016	8317	5.4	7023	66.03	1.91	A
G330.673−00.388	16:09:27.7	−52:15:36.5	shrds1171	2016	8581	18.1	7023	1166.84	11.61	B
G330.738−00.449	16:09:51.2	−52:15:32.6	shrds1171	2016	8581	91.1	7023	198.75	5.93	A
G330.954−00.181	16:09:52.7	−51:54:54.4	shrds709	2015	8971	6.7	7023	1875.15	25.98	A
G331.056−00.437	16:11:28.6	−52:01:46.3	shrds710	2016	7826	10.1	7023	81.27	6.42	A
G331.123−00.530	16:12:12.7	−52:02:39.6	shrds717	2015	8983	35.9	7023	1265.81	18.02	B
G331.129−00.243	16:10:59.2	−51:50:25.9	shrds716	2015	7636	5.8	7023	415.27	16.04	A
G331.145+00.133	16:09:24.6	−51:33:08.6	shrds719	2015	8826	4.6	7023	155.04	3.08	A
G331.156−00.391	16:11:42.6	−51:55:51.4	shrds720	2015	8907	27.8	7023	317.54	18.12	A
G331.172−00.460	16:12:07.8	−51:58:12.3	shrds721	2015	8878	6.6	7023	548.35	15.69	A
G331.249+01.071	16:05:52.4	−50:47:54.8	shrds1174	2016	8826	34.0	7023	256.87	7.21	B
G331.259−00.188	16:11:26.2	−51:42:06.0	shrds725	2016	8248	60.8	7023	1890.06	13.54	B
G331.322−00.176	16:11:35.7	−51:39:25.9	shrds725	2016	8248	10.5	7023	109.98	8.77	A
G331.361−00.019	16:11:04.8	−51:31:15.8	shrds729	2015	8620	11.1	7023	1439.56	63.06	B
G331.384−00.358	16:12:41.3	−51:45:04.3	shrds731	2015	8050	2.6	7023	461.98	22.22	B

Table 4.5 continued

Table 4.5: *uv*-tapered Image Continuum Properties (continued)

Target	R.A. J2000 (hh:mm:ss)	Decl. J2000 (dd:mm:ss)	Field	Epoch[a]	Beam Area (arcsec^2)	$\Delta\theta^b$ (arcsec)	ν_C (MHz)	S_C (mJy beam^{-1})	rms$_C$ (mJy beam^{-1})	QF
G331.412+00.011	16:11:11.7	−51:27:35.6	shrds729	2015	8620	8.1	7023	407.12	28.02	A
G331.417−00.354	16:12:50.0	−51:43:28.0	shrds731	2015	8050	4.1	7023	187.06	17.55	A
G331.520−00.076	16:12:07.5	−51:27:24.8	shrds736	2015	7843	29.9	7023	6106.29	176.45	B
G331.538−00.308	16:13:12.0	−51:36:33.1	shrds735	2015	9219	5.6	7023	168.58	5.73	B
G331.560+00.091	16:11:40.7	−51:18:55.9	shrds737	2015	7568	91.1	7023	333.67	20.19	B
G331.653+00.128	16:11:48.0	−51:12:28.2	shrds741	2015	7855	18.4	7023	274.87	12.61	A
G331.744−00.068	16:13:06.3	−51:17:43.8	shrds743	2015	8616	12.7	7023	311.01	12.80	A
G331.834−00.002	16:13:12.8	−51:11:25.7	shrds746	2016	7738	29.1	7023	157.43	4.54	A
G332.145−00.452	16:16:41.4	−51:17:07.7	shrds753	2015	9064	37.2	7023	8189.93	84.12	B
G332.291−00.092	16:15:45.5	−50:56:06.4	shrds756	2015	9050	19.0	7023	302.40	3.20	A
G332.311−00.567	16:17:57.1	−51:15:06.3	shrds759	2015	9417	36.4	7023	200.98	6.08	A
G332.382+00.080	16:15:30.5	−50:44:46.4	shrds763	2015	7907	67.2	7023	127.97	6.23	B
G332.415+00.053	16:16:01.0	−50:43:12.6	shrds766	2015	8428	218.9	7023	388.46	6.03	B
G332.585−00.561	16:19:09.7	−51:04:00.5	shrds771	2015	8704	12.8	7023	208.56	21.13	A
G332.657−00.622	16:19:41.6	−51:03:16.5	shrds771	2015	8704	32.5	7023	4278.39	78.67	C
G332.766−00.006	16:17:31.7	−50:32:32.7	shrds774	2015	9274	9.6	7023	207.34	3.26	A
G332.823−00.550	16:20:11.3	−50:53:16.2	shrds777	2015	9046	11.4	7023	4130.44	37.99	A
G332.957+01.793	16:10:38.2	−49:05:42.6	shrds782	2016	7783	47.8	7023	119.06	2.30	B
G332.987+00.902	16:14:33.9	−49:43:45.4	shrds784	2016	7559	17.3	7023	140.86	2.51	A
G332.990−00.619	16:21:15.3	−50:49:21.1	shrds785	2015	7644	13.9	7023	511.53	23.31	A
G333.011−00.441	16:20:34.2	−50:41:18.4	shrds789	2015	7894	35.8	7023	2951.43	332.60	C
G333.052+00.033	16:18:37.4	−50:18:54.4	shrds788	2015	8617	5.7	7022	326.25	16.29	A
G333.085−00.479	16:21:02.0	−50:39:10.5	shrds789	2015	7894	8.0	7023	1456.36	108.39	A
G333.129−00.439	16:21:00.3	−50:35:02.8	shrds789	2015	7894	49.5	7023	9756.36	303.36	C
G333.164−00.100	16:19:42.8	−50:19:50.0	shrds792	2015	8802	1.6	7023	602.67	33.97	B
G333.255+00.065	16:19:23.8	−50:09:15.8	shrds794	2015	9043	20.0	7022	1220.19	9.25	A
G333.467−00.159	16:21:20.1	−50:09:39.8	shrds799	2015	8662	14.5	7023	1168.84	56.35	A

Table 4.5 continued

Table 4.5: *uv*-tapered Image Continuum Properties (continued)

Target	R.A. J2000 (hh:mm:ss)	Decl. J2000 (dd:mm:ss)	Field	Epoch[a]	Beam Area (arcsec^2)	$\Delta\theta^b$ (arcsec)	ν_C (MHz)	S_C (mJy beam^{-1})	rms$_C$ (mJy beam^{-1})	QF
G333.534−00.383	16:22:34.3	−50:16:33.8	shrds801	2015	7315	28.9	7023	277.12	20.98	C
G333.580+00.058	16:20:42.7	−49:56:02.2	shrds802	2016	8115	92.2	7023	17.41	27.89	A
G333.627−00.199	16:22:09.9	−50:06:04.1	caswell19	2016	8018	100.4	7023	49414.95	509.22	A
G333.681−00.441	16:23:30.2	−50:12:12.1	shrds804	2015	7773	9.1	7023	318.33	97.56	B
G333.725+00.364	16:20:09.8	−49:36:19.6	shrds803	2015	8845	3.0	7022	364.34	4.06	A
G333.733−00.429	16:23:40.6	−50:09:32.2	shrds804	2015	7773	5.4	7023	214.16	54.41	A
G333.962+00.063	16:22:30.5	−49:39:00.0	shrds806	2015	9436	7.1	7022	176.02	2.84	A
G334.022+00.106	16:22:29.6	−49:34:22.5	shrds807	2016	8219	56.9	7023	60.55	4.29	B
G334.202+00.193	16:22:59.5	−49:23:34.4	shrds811	2015	9053	10.8	7022	332.81	2.92	A
G334.341+00.045	16:24:14.0	−49:23:41.0	shrds814	2015	8842	2.4	7022	451.08	2.34	A
G334.400−00.523	16:27:00.5	−49:44:49.7	shrds815	2016	8179	10.4	7023	74.12	1.63	B
G334.646+00.442	16:23:49.7	−48:54:05.3	shrds825	2015	9230	12.2	7022	218.19	1.31	A
G334.721−00.653	16:28:57.7	−49:36:25.4	caswell20	2016	8168	7.0	7023	1119.33	4.23	A
G334.774−00.023	16:26:26.1	−49:07:24.2	shrds828	2015	9079	43.8	7022	401.45	7.86	A
G335.195−00.385	16:29:46.9	−49:04:44.9	shrds836	2016	8182	10.9	7023	80.45	2.30	A
G335.579−00.209	16:30:35.5	−48:40:50.3	shrds841	2016	7545	3.5	7023	154.99	2.07	A
G336.026−00.817	16:35:07.9	−48:46:17.1	shrds843	2015	9218	17.9	7022	452.28	1.43	A
G336.367−00.003	16:32:56.4	−47:57:55.7	shrds852	2015	8769	7.5	7022	634.99	33.56	A
G336.418−00.249	16:34:13.1	−48:05:43.8	shrds853	2016	8254	5.8	7022	708.24	29.26	B
G336.491−01.474	16:40:00.3	−48:51:41.0	caswell21	2016	8199	7.0	7023	6384.39	21.55	A
G336.518+00.119	16:33:12.9	−47:46:06.4	shrds854	2015	8078	123.0	7022	99.16	9.41	B
G336.585+00.019	16:33:50.2	−47:46:52.4	shrds857	2015	7417	76.3	7022	261.86	12.81	A
G336.854−00.018	16:34:55.8	−47:36:02.5	shrds1212	2016	9622	60.9	7022	1348.37	50.08	B
G336.874+00.139	16:34:21.2	−47:28:42.3	shrds1209	2016	8691	60.4	7022	260.85	28.34	B
G336.888+00.057	16:34:47.9	−47:32:18.3	shrds1212	2016	9622	18.3	7022	727.67	48.48	B
G336.990−00.021	16:35:32.4	−47:31:12.7	shrds862	2015	7332	12.2	7022	455.18	39.02	B
G337.004+00.322	16:34:05.1	−47:16:28.6	shrds865	2015	7921	5.5	7022	256.11	4.24	A

Table 4.5 continued

Table 4.5: *uv*-tapered Image Continuum Properties (continued)

Target	R.A. J2000 (hh:mm:ss)	Decl. J2000 (dd:mm:ss)	Field	Epoch[a]	Beam Area (arcsec^2)	$\Delta\theta^b$ (arcsec)	ν_C (MHz)	S_C (mJy beam^{-1})	rms$_C$ (mJy beam^{-1})	QF
G337.091−00.965	16:40:07.1	−48:04:19.2	shrds867	2015	7130	15.7	7023	56.27	2.00	A
G337.170−00.059	16:36:26.2	−47:24:14.4	shrds869	2015	6930	31.3	7023	357.66	10.88	B
G337.253−00.165	16:37:12.8	−47:25:14.8	shrds870	2015	8695	8.0	7023	552.61	32.03	B
G337.286+00.113	16:36:06.5	−47:12:36.3	shrds871	2015	8604	5.9	7023	214.61	4.80	A
G337.404−00.404	16:38:50.6	−47:28:00.8	shrds875	2015	7642	6.4	7023	182.33	4.08	B
G337.428−00.401	16:38:54.1	−47:26:24.5	shrds875	2015	7642	32.9	7023	264.37	3.81	B
G337.617−00.065	16:38:11.9	−47:04:57.6	shrds880	2015	8671	1.8	7023	535.55	24.86	B
G337.664+00.049	16:37:52.8	−46:58:33.5	shrds886	2015	8825	14.3	7023	147.85	21.21	B
G337.665−00.176	16:38:52.0	−47:07:17.0	shrds883	2015	8705	4.0	7023	648.31	23.47	A
G337.684−00.343	16:39:44.4	−47:13:11.7	shrds884	2015	6886	38.1	7023	293.84	10.68	A
G337.705−00.059	16:38:31.0	−47:00:41.1	shrds885	2015	6968	8.1	7023	506.41	32.45	A
G337.709+00.091	16:37:52.8	−46:54:37.4	shrds886	2015	8825	1.3	7023	418.78	10.95	A
G337.754+00.057	16:38:26.1	−46:54:50.9	shrds888	2015	8176	152.4	7023	90.72	6.89	B
G337.827+00.056	16:38:31.6	−46:51:39.2	shrds888	2015	8176	56.9	7023	91.82	7.07	B
G338.003−00.121	16:39:58.5	−46:52:19.2	shrds891	2015	7987	141.7	7023	297.39	21.62	B
G338.009+00.016	16:39:22.2	−46:44:00.1	shrds892	2015	8013	13.1	7023	397.37	11.55	A
G338.066−00.069	16:39:57.4	−46:45:09.3	shrds1219	2016	9061	8.6	7022	221.65	17.46	B
G338.075+00.016	16:39:38.7	−46:41:29.3	shrds893	2015	8991	13.9	7023	2122.57	19.69	B
G338.106+00.020	16:39:43.0	−46:39:49.4	shrds893	2015	8991	12.8	7023	236.11	16.76	B
G338.263−00.364	16:42:02.1	−46:47:50.4	shrds894	2015	9034	10.7	7023	99.19	4.26	C
G338.289−00.373	16:42:09.2	−46:47:02.1	shrds894	2015	9034	4.3	7023	161.58	4.49	C
G338.360−00.095	16:41:13.0	−46:32:55.5	shrds896	2015	8128	3.7	7023	391.30	32.90	B
G338.364−00.020	16:40:54.0	−46:29:31.4	shrds896	2015	8128	13.6	7023	530.10	65.97	B
G338.405−00.203	16:41:52.1	−46:35:08.4	caswell22	2016	8110	4.1	7022	2508.80	17.22	A
G338.462−00.262	16:42:19.7	−46:35:01.8	shrds898	2015	8631	9.2	7023	381.92	9.26	A
G338.565−00.151	16:42:14.0	−46:25:27.9	shrds899	2015	8350	24.0	7023	343.26	5.42	A
G338.576+00.020	16:41:36.2	−46:18:03.6	shrds900	2015	8333	49.4	7023	524.08	19.39	B

Table 4.5 continued

Table 4.5: *uv*-tapered Image Continuum Properties (continued)

Target	R.A. J2000 (hh:mm:ss)	Decl. J2000 (dd:mm:ss)	Field	Epoch[a]	Beam Area (arcsec^2)	$\Delta\theta^b$ (arcsec)	ν_C (MHz)	S_C (mJy beam^{-1})	rms$_C$ (mJy beam^{-1})	QF
G338.628+00.145	16:41:13.6	−46:11:16.8	shrds901	2015	8079	16.0	7023	598.34	19.35	A
G338.706+00.645	16:39:22.5	−45:48:49.7	shrds1223	2016	7604	60.6	7023	160.10	15.93	B
G338.837−00.318	16:44:02.1	−46:20:22.9	shrds904	2015	8938	19.0	7023	126.96	1.33	A
G338.851+00.405	16:40:55.1	−45:50:50.1	shrds905	2015	6350	6.8	7022	37.14	3.76	A
G338.861+00.597	16:39:41.6	−45:47:13.6	shrds1223	2016	7604	383.3	7023	63.99	7.64	B
G338.883+00.537	16:40:28.6	−45:44:16.7	shrds1225	2016	7524	3.0	7022	111.96	14.99	A
G338.911+00.615	16:40:25.2	−45:41:12.8	shrds1225	2016	7524	132.4	7022	661.95	25.53	B
G338.926+00.392	16:41:16.9	−45:48:30.2	shrds906	2015	8249	25.7	7023	583.57	6.77	A
G339.106+00.152	16:42:59.5	−45:49:38.3	shrds909	2015	8727	10.6	7023	256.19	1.86	A
G339.169−00.698	16:46:52.8	−46:25:01.8	shrds910	2015	6523	311.5	7023	7.64	0.79	C
G339.216+00.263	16:42:55.6	−45:40:12.9	shrds913	2015	6294	6.9	7022	33.49	2.13	A
G339.233+00.243	16:43:21.5	−45:37:56.6	shrds913	2015	6294	224.9	7022	70.27	5.53	C
G339.275−00.607	16:46:55.3	−46:11:54.6	shrds915	2015	8778	26.5	7023	111.39	2.12	B
G339.478+00.181	16:44:14.4	−45:31:30.1	shrds917	2015	8797	8.2	7023	260.09	1.72	A
G339.486+00.087	16:44:41.3	−45:34:43.3	shrds918	2015	8787	4.8	7023	286.96	2.81	A
G339.553−00.401	16:47:05.3	−45:50:41.3	shrds919	2015	8837	15.8	7023	397.41	1.82	B
G339.556+00.282	16:44:06.8	−45:23:58.9	shrds920	2015	8739	0.9	7023	225.89	1.75	A
G339.584+00.084	16:45:03.4	−45:30:29.6	shrds921	2015	8814	7.4	7023	282.57	1.43	A
G339.676+00.283	16:44:34.4	−45:18:19.5	shrds922	2016	7778	16.0	7023	48.56	2.17	B
G339.717−01.211	16:51:13.9	−46:14:23.3	shrds925	2015	9072	12.5	7023	178.15	0.74	A
G339.952+00.052	16:46:34.9	−45:14:38.4	shrds1234	2016	7648	18.1	7022	128.44	2.06	A
G340.059−00.138	16:47:51.4	−45:17:01.1	shrds1236	2016	9065	49.7	7022	282.80	7.41	B
G340.247−00.373	16:49:30.2	−45:17:46.0	shrds1237	2016	7786	6.3	7022	168.91	15.30	B
G340.296−00.276	16:49:13.5	−45:18:42.0	shrds1237	2016	7786	411.4	7022	83.59	9.86	B
G342.062+00.417	16:52:33.4	−43:23:41.8	caswell23	2016	7933	11.7	7022	1828.89	14.89	A
G342.360+00.107	16:54:56.2	−43:21:34.1	shrds1238	2016	7795	5.6	7022	108.47	3.55	B
G342.388+00.074	16:55:09.4	−43:21:34.1	shrds1238	2016	7795	8.2	7022	61.41	2.38	A

Table 4.5 continued

Table 4.5: *uv*-tapered Image Continuum Properties (continued)

Target	R.A. J2000 (hh:mm:ss)	Decl. J2000 (dd:mm:ss)	Field	Epoch[a]	Beam Area (arcsec^2)	$\Delta\theta^b$ (arcsec)	ν_C (MHz)	S_C (mJy beam^{-1})	rms$_C$ (mJy beam^{-1})	QF
G342.438−00.061	16:55:54.0	−43:24:18.7	shrds1239	2016	7978	12.6	7022	107.38	2.47	A
G343.224−00.065	16:58:39.8	−42:47:21.2	shrds1240	2016	7429	31.5	7022	110.00	2.24	B
G343.352−00.081	16:59:03.9	−42:41:40.8	shrds1241	2016	8592	47.6	7022	202.60	6.36	A
G343.914−00.646	17:03:31.0	−42:37:15.5	caswell24	2016	7284	79.9	7022	142.40	3.37	B
G344.424+00.044	17:02:09.6	−41:46:48.2	caswell25	2016	8086	4.5	7022	2534.09	14.53	A
G348.892−00.179	17:16:59.8	−38:19:24.6	fa644	2015	6722	0.6	7022	377.72	2.22	A
G349.328+00.020	17:17:27.0	−37:51:09.8	gs038	2015	6773	3.1	7022	229.43	2.02	A
G352.313−00.442	17:27:48.6	−35:39:10.3	fa016	2015	6928	10.3	7022	275.03	1.23	A
G355.344+00.145	17:33:29.0	−32:47:58.3	fa032	2015	7135	8.8	7022	533.88	4.98	A
G358.600−00.058	17:42:28.6	−30:09:18.4	gs108	2015	7357	13.0	7022	457.33	5.94	A
G358.633+00.062	17:42:04.7	−30:04:07.7	fa054	2015	6938	5.5	7022	381.14	9.92	A
G359.467−00.173	17:45:01.1	−29:28:50.3	fa489	2015	6208	0.2	7022	181.71	15.52	A

[a] Rows with epochs with an asterisk (*) are copied directly from Brown et al. (2017). They did not give the continuum fluxes for their detections.

[b] The separation between the *WISE* Catalog infrared position and the position of the SHRDS continuum peak.

peaks and/or has $S/N < 10$. Finally, QF D is assigned to spectra with no visible RRL. Figure 4.5 shows example <H$n\alpha$> spectra for each QF: G333.129–00.439 (QF A), G312.979–00.432 (QF B), and G311.866–00.238 and G332.823–00.550 (QF C). Sources with multiple RRL components have multiple rows in the tables, and the *WISE* Catalog name is appended by a letter, with "a" being the brightest RRL component, "b" being the second brightest, and so on.

We have multiple detections of RRLs for sources observed in separate fields. Tables 4.6 and 4.7 only contain the <H$n\alpha$> Gaussian fits with the highest RRL QF and/or S/N. The data for these sources, as measured in each independent field, are listed in Appendix C. In the next data release, we will combine the <H$n\alpha$> spectra from each field to increase our spectral sensitivity.

4.6 Properties of Bright Catalog Nebulae

For the longitude range $259° < \ell < 344°$, the SHRDS Bright Catalog increases the number of known Galactic H II regions to 568 nebulae, an 82% increase in the H II region census of this Galactic zone. With such a large sample of H II regions in the third and fourth Galactic quadrants, we can begin to get a global view of star formation and Galactic structure across the entire disk.

To assess the validity of our data reduction and analysis pipeline, we compare our measured RRL properties with those in the *WISE* Catalog for 76 previously known H II regions, 25 of which were re-observed by the SHRDS for this purpose. Figure 4.6 shows the difference between the SHRDS and previously measured <H$n\alpha$> LSR velocities and FWHM line widths as a function of the SHRDS-measured values, for both the non-tapered and *uv*-tapered SHRDS data. These figures exclude six non-tapered and five *uv*-tapered SHRDS detections with LSR velocities more than $15\,\mathrm{km\,s^{-1}}$ different from the Caswell & Haynes (1987) velocities. These sources are: G289.806–01.242, G300.502–00.180 (non-tapered only), G311.841–00.219, G311.866–00.238, G324.924–00.569, and G333.681–00.441. Each of these nebulae are near an extended H II region or an H II region complex with many other nebulae. We suspect that the Caswell & Haynes (1987) single-dish survey is more sensitive to the larger H II regions, and thus some LSR velocities are incorrectly assigned to these smaller, nearby H II regions in the *WISE* Catalog.

The SHRDS LSR velocities match previous measurements fairly well. The LSR velocity differences are clustered around $0\,\mathrm{km\,s^{-1}}$ with slightly more scatter toward

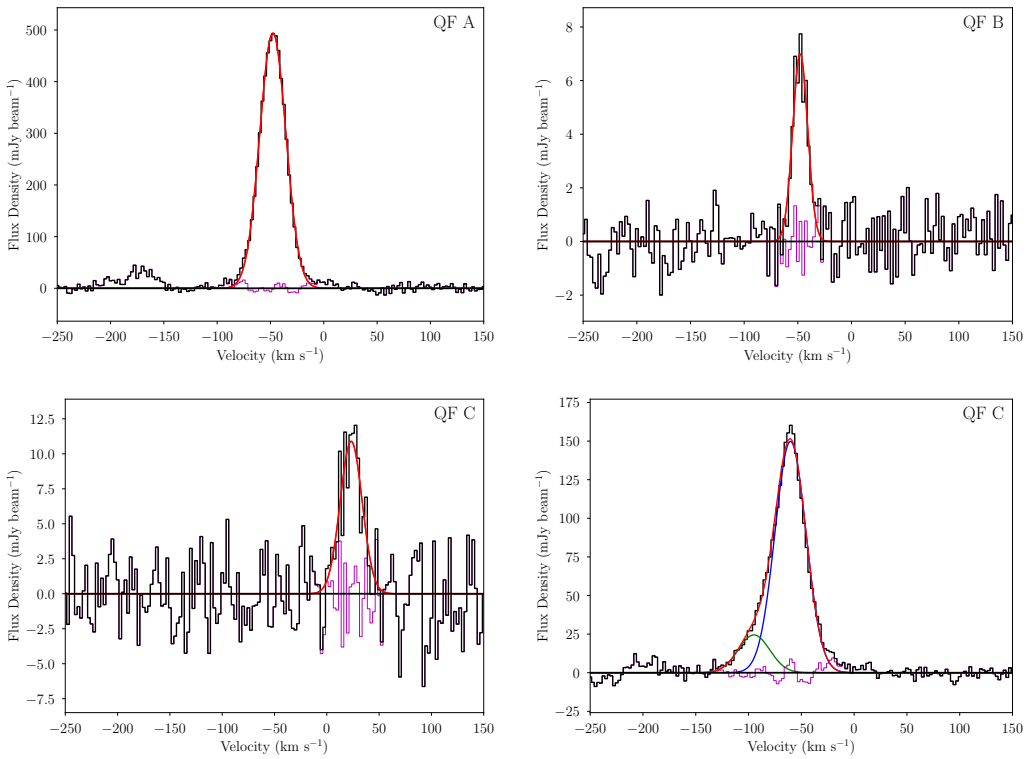

Figure 4.5: Representative <H$n\alpha$> spectra for each spectral quality factor (QF). The top left panel is G333.129–00.439 and is a QF A spectrum (S/N> 15, unblended), the top right is G312.979–00.432 and is a QF B spectrum (15 > S/N > 10), the bottom left panel is G311.866–00.238 and is a QF C spectrum (S/N < 10), and the bottom right is G332.823–00.550 and is a QF C spectrum (spectrally blended). The red curves are Gaussian fits to the data (or the sum of the two Gaussian components in G332.823–00.550), and the magenta curves are the fit residuals.

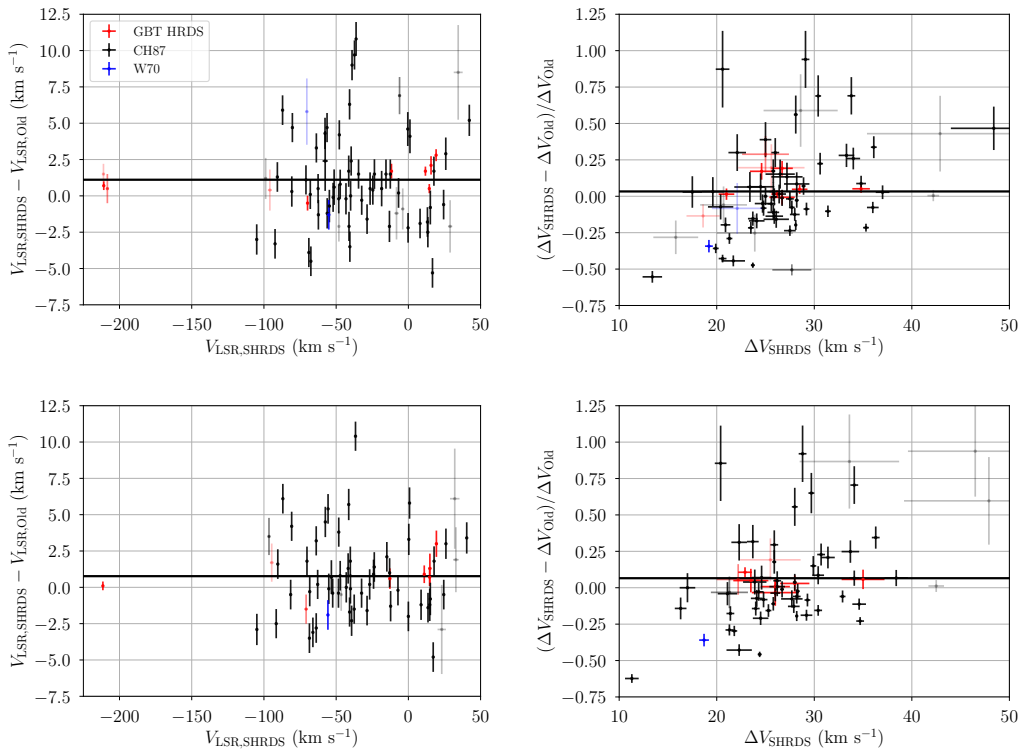

Figure 4.6: Differences between SHRDS and previously measured <H$n\alpha$> LSR velocities, $V_{\rm LSR}$ (left), and fractional differences between SHRDS and previously measured FWHM line widths, ΔV (right). The top two panels use the non-tapered data and the bottom two panels use the *uv*-tapered data. Previous RRL measurements are from the GBT HRDS (red; $n = 10$ non-tapered; $n = 8$ tapered), Caswell & Haynes (1987) (CH87; black; $n = 63$ non-tapered; $n = 56$ tapered), and Wilson et al. (1970b) (W70; blue; $n = 2$ non-tapered; $n = 1$ tapered). The transparency of the points represents the quality factor of the SHRDS RRL detection: QF A (not transparent), QF B (partially transparent), and QF C (mostly transparent). Six non-tapered SHRDS detections and five *uv*-tapered detections with LSR velocities more than 15 km s^{-1} different from the Caswell & Haynes (1987) velocities are excluded. The mean of each sample is indicated by the horizontal solid line.

Table 4.6: Non-tapered Image RRL Properties

Target	Field	Epoch[a]	ν_L[b] (MHz)	S_L (mJy beam^{-1})	$V_{\rm LSR}$ (km s^{-1})	ΔV (km s^{-1})	rms$_L$ (mJy beam^{-1})	S/N	QF
G213.833+00.618	g213.833+00.618	2014*	···	1.90 ± 2.30	53.20 ± 20.20	33.50 ± 20.90	1.40	3.5	C
G230.354−00.597	g230.354-00.597	2014*	···	2.10 ± 2.00	69.00 ± 16.10	35.00 ± 16.70	1.50	3.7	C
G259.057−01.544	shrds030	2016	6474	5.20 ± 0.40	59.20 ± 1.10	26.80 ± 2.60	1.10	10.9	B
G263.237+00.509	shrds060	2015	6338	8.10 ± 1.10	10.40 ± 1.20	17.50 ± 2.70	1.90	7.8	C
G267.730−01.100	shrds078	2016	6928	26.50 ± 0.70	7.30 ± 0.30	21.50 ± 0.60	1.50	36.6	A
G269.068−01.114	shrds085	2016	6028	75.70 ± 1.50	13.20 ± 0.20	25.00 ± 0.60	3.40	49.4	A
G269.159−01.119	shrds085	2016	6513	28.80 ± 0.70	10.70 ± 0.30	25.90 ± 0.80	1.80	36.3	A
G269.167−01.357	shrds086	2016	6445	7.30 ± 0.50	2.80 ± 0.80	23.90 ± 1.90	1.00	16.1	A
G280.626−01.186	shrds111	2015	7029	6.50 ± 1.00	33.70 ± 1.60	21.90 ± 4.10	1.80	7.6	C
G280.989−01.527	shrds1005	2016	5704	25.90 ± 1.30	-0.40 ± 0.60	26.50 ± 1.50	2.70	21.6	A
G281.047−01.541	shrds1005	2016	6697	45.50 ± 0.50	-9.30 ± 0.10	24.50 ± 0.30	1.50	64.4	A
G281.175−01.645	caswell1	2016	6560	50.00 ± 0.60	-6.80 ± 0.20	27.50 ± 0.40	2.30	50.4	A
G281.560−02.478	shrds114	2015	6998	46.70 ± 0.90	-2.20 ± 0.20	25.80 ± 0.60	1.80	59.8	A
G281.840−01.609	shrds117	2015	7022	10.80 ± 0.60	-9.10 ± 0.80	28.30 ± 1.90	1.40	18.7	A
G282.015−00.997	shrds1007	2016	6092	11.80 ± 0.60	0.00 ± 0.50	21.50 ± 1.30	1.60	14.7	B
G282.842−01.252	shrds1232	2016	6485	12.60 ± 0.50	-3.70 ± 0.50	29.10 ± 1.20	1.30	23.1	A
G283.832−00.730	shrds1013	2016	6327	9.70 ± 0.60	5.80 ± 0.70	22.60 ± 1.70	1.40	14.6	B
G284.014−00.857	shrds1014	2016	6830	41.60 ± 1.30	9.00 ± 0.40	26.50 ± 1.00	1.80	51.5	A
G284.712+00.317	caswell2	2016	6277	53.20 ± 1.00	8.10 ± 0.20	27.50 ± 0.60	2.20	55.7	A
G284.902+00.060	shrds141	2015	6826	6.00 ± 0.90	2.40 ± 1.90	25.40 ± 4.90	1.80	7.3	C
G285.353+00.004	shrds143	2016	6591	6.60 ± 1.10	-5.20 ± 1.50	18.20 ± 3.80	1.90	6.7	C
G286.362−00.297	shrds1017	2016	5980	6.70 ± 0.80	-33.10 ± 1.30	23.50 ± 3.10	1.50	9.9	C
G286.951−00.955	shrds158	2015	6580	23.10 ± 0.60	36.70 ± 0.40	30.20 ± 0.80	1.50	36.4	A
G288.074−01.642	shrds162	2016	6462	7.20 ± 0.60	9.40 ± 1.00	22.60 ± 2.30	1.10	13.5	B
G288.851−00.108	shrds167	2016	6675	5.30 ± 0.40	19.90 ± 0.90	24.10 ± 2.10	0.90	12.2	B
G289.109−01.107	shrds173	2016	6507	5.80 ± 0.40	23.60 ± 1.00	27.80 ± 2.40	0.90	15.4	A
G289.188−00.293	shrds1024	2016	6778	8.40 ± 0.50	35.30 ± 0.80	25.00 ± 1.80	1.00	19.1	A
G289.470−00.928	shrds181	2016	6201	5.40 ± 0.50	14.90 ± 0.90	18.10 ± 2.10	1.20	8.6	C

Table 4.6 continued

Table 4.6: Non-tapered Image RRL Properties (continued)

Target	Field	Epoch[a]	ν_L[b] (MHz)	S_L (mJy beam^{-1})	$V_{\rm LSR}$ (km s^{-1})	ΔV (km s^{-1})	rms$_L$ (mJy beam^{-1})	S/N	QF
G289.476−00.899	shrds181	2016	6175	6.00 ± 0.50	18.70 ± 1.00	23.30 ± 2.40	1.10	11.5	B
G289.582−00.636	shrds184	2016	6531	6.40 ± 0.40	20.60 ± 0.90	25.60 ± 2.10	1.00	14.1	B
G289.769−01.220	shrds1026	2016	6470	5.40 ± 0.50	24.50 ± 1.30	31.50 ± 3.50	1.30	10.5	B
G289.806−01.242	shrds1026	2016	5947	11.20 ± 0.80	4.10 ± 0.90	27.80 ± 2.20	1.80	14.7	B
G289.874−00.752	shrds1028	2016	6483	10.00 ± 0.50	18.30 ± 0.70	28.50 ± 1.70	1.50	15.3	A
G289.880−00.801	shrds1028	2016	6091	90.80 ± 1.20	16.70 ± 0.20	25.60 ± 0.40	2.40	85.3	A
G289.944−00.889	shrds191	2015	6800	8.60 ± 0.50	31.50 ± 0.70	23.60 ± 1.70	1.40	13.6	B
G290.012−00.867	g290.012-00.867	2014*	···	3.60 ± 2.50	14.70 ± 8.30	24.90 ± 8.60	1.80	4.5	C
G290.323−02.984	g290.323-02.984	2014*	···	3.50 ± 2.10	-17.70 ± 8.00	28.30 ± 8.30	1.50	5.6	C
G290.385−01.042	g290.385-01.042	2014*	···	4.00 ± 2.90	9.91 ± 4.60	13.20 ± 4.70	1.90	3.4	C
G290.674−00.133	g290.674-00.133	2014*	···	5.20 ± 2.40	19.30 ± 5.20	23.20 ± 5.30	1.40	8.0	C
G291.046−02.079	shrds199	2015	6106	9.30 ± 0.60	-18.70 ± 0.80	24.70 ± 2.00	1.50	13.3	B
G291.186−00.274	shrds1032	2016	6554	15.40 ± 0.60	12.90 ± 0.50	25.10 ± 1.10	1.50	22.8	A
G291.202−00.295	shrds1032	2016	6303	21.50 ± 0.70	8.10 ± 0.30	21.60 ± 0.80	1.70	26.0	A
G291.281−00.726	caswell3	2016	5468	2534.20 ± 27.10	-24.10 ± 0.20	33.20 ± 0.40	59.80	108.1	A
G291.596−00.239	g291.596-00.239	2014*	···	15.30 ± 3.70	11.40 ± 5.10	44.20 ± 5.40	2.50	18.0	A
G291.863−00.682	caswell4	2016	6216	84.80 ± 1.00	24.40 ± 0.20	25.80 ± 0.40	2.90	66.1	A
G292.889−00.831	g292.889-00.831	2014*	···	4.80 ± 2.30	21.80 ± 7.10	30.00 ± 7.30	1.40	8.4	C
G293.661−01.639	shrds210	2016	6041	15.70 ± 1.50	-21.00 ± 0.90	19.10 ± 2.10	2.90	10.3	B
G293.829−00.744	shrds215	2015	6705	14.20 ± 0.40	38.40 ± 0.30	23.60 ± 0.80	0.90	32.6	A
G293.936−00.873	g293.936-00.873	2014*	···	16.40 ± 2.20	36.60 ± 1.40	22.30 ± 1.50	2.00	17.0	A
G293.967−00.984	shrds219	2015	6710	10.60 ± 0.50	27.80 ± 0.70	30.50 ± 1.60	1.30	20.2	A
G293.994−00.934	g293.994-00.934	2014*	···	18.60 ± 2.60	46.50 ± 1.70	25.60 ± 1.80	1.30	32.0	A
G294.453−00.521	shrds226	2015	6622	11.70 ± 0.60	-12.00 ± 0.60	22.30 ± 1.40	1.50	16.5	A
G294.988−00.538	g294.988-00.538	2014*	···	9.70 ± 1.40	39.80 ± 1.90	27.40 ± 2.00	1.20	19.0	A
G295.275−00.255	g295.275-00.255	2014*	···	5.60 ± 2.30	30.10 ± 6.20	30.60 ± 6.30	1.60	8.7	C
G295.748−00.207	g295.748-00.207	2014*	···	7.20 ± 2.10	23.30 ± 3.50	23.90 ± 3.50	1.60	9.8	C
G297.248−00.754	g297.248-00.754	2014*	···	22.60 ± 2.90	22.60 ± 1.50	24.40 ± 1.60	1.90	26.0	A

Table 4.6 continued

Table 4.6: Non-tapered Image RRL Properties (continued)

Target	Field	Epoch[a]	ν_L[b] (MHz)	S_L (mJy beam^{-1})	$V_{\rm LSR}$ (km s^{-1})	ΔV (km s^{-1})	rms$_L$ (mJy beam^{-1})	S/N	QF
G297.312−00.295	shrds242	2015	6422	5.70 ± 0.80	16.30 ± 1.20	17.70 ± 3.00	1.50	7.3	C
G297.392−00.624	shrds243	2015	6313	8.20 ± 0.80	22.70 ± 1.40	28.50 ± 3.50	1.90	10.2	B
G297.497−00.758	shrds246	2015	6032	26.70 ± 1.10	25.90 ± 0.50	26.10 ± 1.30	2.30	25.9	A
G297.536−00.826	shrds246	2015	6820	10.90 ± 0.70	39.40 ± 0.80	25.30 ± 1.90	1.40	16.7	A
G297.626−00.906	g297.626-00.906	2014*	···	16.10 ± 2.50	31.30 ± 2.10	28.40 ± 2.20	1.50	26.0	A
G297.651−00.973	g297.626-00.906	2014	5383	22.20 ± 3.20	34.50 ± 3.10	42.90 ± 7.50	9.30	6.9	C
G298.183−00.784	caswell5	2016	6444	101.80 ± 0.70	17.70 ± 0.10	36.10 ± 0.30	1.40	188.6	A
G298.196−00.247	shrds1041	2016	6737	19.10 ± 0.60	31.90 ± 0.40	27.30 ± 1.00	1.60	28.3	A
G298.473+00.104	g298.473+00.104	2014*	···	12.20 ± 2.20	32.90 ± 2.00	23.50 ± 2.10	2.00	13.0	B
G298.630+00.253	shrds253	2015	6131	3.90 ± 0.50	33.30 ± 1.30	19.50 ± 3.10	1.10	6.8	C
G298.669+00.064	g298.669+00.064	2014*	···	11.40 ± 3.90	24.10 ± 2.40	14.10 ± 2.40	2.20	8.7	C
G298.846+00.121	shrds258	2015	6668	15.10 ± 0.60	22.00 ± 0.50	28.50 ± 1.30	1.60	21.8	A
G299.349−00.267	caswell6	2016	6535	19.40 ± 0.60	-40.50 ± 0.30	20.60 ± 0.70	1.30	29.5	A
G300.369−00.288	shrds271	2015	6324	4.20 ± 1.10	29.80 ± 2.60	20.00 ± 7.60	1.30	6.3	C
G300.502−00.180	shrds273	2015	5480	7.60 ± 1.20	5.60 ± 1.60	22.00 ± 3.90	3.40	4.7	C
G300.965+01.162	g300.983+01.117	2014	5912	90.30 ± 2.20	-40.70 ± 0.30	26.40 ± 0.70	5.60	36.5	A
G300.972+00.994	g300.972+00.994	2014*	···	3.80 ± 1.40	-34.50 ± 7.20	39.10 ± 7.50	1.70	6.3	C
G300.983+01.117	caswell7	2016	6611	67.40 ± 0.80	-38.60 ± 0.10	25.50 ± 0.30	3.00	50.3	A
G301.116+00.968	caswell8	2016	6110	126.10 ± 1.30	-39.60 ± 0.10	29.20 ± 0.30	2.90	104.1	A
G302.032−00.063	caswell9	2016	7091	80.40 ± 1.00	-28.60 ± 0.20	29.10 ± 0.40	1.50	131.9	A
G302.391+00.280	shrds293	2016	6605	15.20 ± 0.30	-40.50 ± 0.20	22.90 ± 0.60	1.00	32.0	A
G302.436−00.106	shrds294	2016	6302	8.30 ± 0.60	-41.40 ± 0.90	25.20 ± 2.10	1.00	19.2	A
G302.481−00.035	shrds295	2016	6515	6.00 ± 0.60	-40.20 ± 1.20	25.20 ± 2.90	1.10	12.0	B
G302.503−00.762	shrds296	2015	6396	3.80 ± 0.40	28.90 ± 1.50	28.60 ± 3.80	1.00	8.8	C
G302.636−00.672	shrds297	2016	6495	15.50 ± 0.40	31.20 ± 0.30	25.70 ± 0.70	1.10	32.2	A
G302.816−00.844	shrds299	2016	6162	3.50 ± 0.40	35.30 ± 1.00	19.70 ± 2.30	0.80	8.3	C
G303.342−00.718	shrds303	2015	6652	8.80 ± 0.50	28.00 ± 0.80	30.30 ± 2.20	1.40	14.9	B
G303.384−00.965	shrds305	2016	6739	6.20 ± 0.40	47.90 ± 0.70	23.30 ± 1.60	0.80	16.3	A

Table 4.6 continued

Table 4.6: Non-tapered Image RRL Properties (continued)

Target	Field	Epoch[a]	ν_L[b] (MHz)	S_L (mJy beam^{-1})	$V_{\rm LSR}$ (km s^{-1})	ΔV (km s^{-1})	rms$_L$ (mJy beam^{-1})	S/N	QF
G303.557−00.539	shrds308	2016	6660	6.40 ± 0.50	33.20 ± 0.90	20.40 ± 2.00	0.90	14.0	B
G304.465−00.023	shrds336	2015	6289	16.20 ± 0.60	-14.20 ± 0.40	22.00 ± 0.90	1.20	27.0	A
G304.557+00.329	shrds338	2016	7050	10.10 ± 0.30	-39.80 ± 0.40	26.20 ± 1.00	0.70	32.7	A
G304.925+00.555	shrds344	2015	6489	15.10 ± 0.60	-37.20 ± 0.90	41.50 ± 2.10	1.60	26.5	A
G305.789+00.280	shrds350	2016	6578	7.90 ± 0.30	-38.20 ± 0.60	26.40 ± 1.30	0.90	20.1	A
G307.559−00.585	caswell10	2016	7018	72.40 ± 1.00	-40.00 ± 0.20	28.00 ± 0.50	1.50	114.5	A
G307.974−01.594	shrds373	2016	6240	5.30 ± 0.70	37.80 ± 1.60	25.60 ± 4.00	1.70	6.8	C
G308.056−00.397	caswell11	2016	6921	3.90 ± 0.40	-6.50 ± 2.00	41.20 ± 5.00	1.40	7.9	C
G308.072−00.389	caswell11	2016	6317	6.30 ± 0.50	-13.90 ± 1.20	28.30 ± 3.00	1.50	9.7	C
G308.079−00.406	caswell11	2016	6688	34.90 ± 0.40	-15.50 ± 0.10	21.30 ± 0.30	1.50	46.8	A
G308.747+00.547	shrds1091	2016	6609	31.80 ± 0.60	-40.30 ± 0.20	21.10 ± 0.50	1.20	52.2	A
G308.916+00.124	shrds384	2015	6966	29.90 ± 0.80	-41.80 ± 0.40	32.40 ± 1.00	1.40	53.0	A
G309.151−00.215	shrds385	2016	6273	5.60 ± 0.60	-11.00 ± 1.30	24.80 ± 3.00	1.20	10.6	B
G309.176−00.028	shrds386	2015	6819	24.70 ± 0.50	-17.20 ± 0.30	26.50 ± 0.70	1.30	44.1	A
G310.260−00.199	shrds403	2016	5998	3.40 ± 0.50	10.60 ± 2.10	27.40 ± 5.40	1.00	8.0	C
G310.519−00.220	shrds407	2015	6753	23.40 ± 0.70	24.20 ± 0.50	30.50 ± 1.10	1.50	39.3	A
G310.630−00.421	shrds409	2015	6155	13.10 ± 0.40	-29.10 ± 0.40	22.70 ± 0.90	1.20	23.9	A
G310.672−00.450	shrds409	2015	6178	10.80 ± 0.40	-25.20 ± 0.40	22.40 ± 1.00	1.10	20.4	A
G310.887+00.009	shrds412	2015	6848	17.80 ± 0.60	-55.20 ± 0.30	20.30 ± 0.70	1.30	26.4	A
G310.901−00.373	shrds1096	2016	6945	38.10 ± 0.40	28.60 ± 0.10	25.90 ± 0.30	1.10	80.7	A
G311.003−00.355	shrds413	2016	6705	6.30 ± 0.40	34.40 ± 0.80	26.00 ± 2.00	0.90	15.4	A
G311.137−00.235	shrds418	2015	6357	5.20 ± 0.70	43.40 ± 1.80	28.40 ± 4.60	1.40	9.1	C
G311.425+00.598	shrds425	2015	7195	11.30 ± 0.70	-43.80 ± 0.80	28.80 ± 1.90	1.90	14.5	B
G311.575+00.239	shrds428	2016	6546	9.00 ± 0.30	2.40 ± 0.40	20.70 ± 0.90	0.70	24.5	A
G311.581−00.593	shrds1101	2016	6721	5.20 ± 0.40	34.70 ± 1.10	33.30 ± 2.90	1.00	13.2	B
G311.629+00.289	caswell12	2016	6807	133.50 ± 1.10	-56.30 ± 0.10	35.30 ± 0.30	2.60	136.9	A
G311.809−00.309	shrds1103	2016	6263	10.10 ± 0.40	-36.70 ± 0.50	27.90 ± 1.30	1.10	21.1	A
G311.841−00.219	shrds1103	2016	5577	5.50 ± 0.90	27.50 ± 3.30	34.80 ± 12.60	2.60	5.6	C

Table 4.6 continued

Table 4.6: Non-tapered Image RRL Properties (continued)

Target	Field	Epoch[a]	ν_L[b] (MHz)	S_L (mJy beam^{-1})	$V_{\rm LSR}$ (km s^{-1})	ΔV (km s^{-1})	rms$_L$ (mJy beam^{-1})	S/N	QF
G311.866−00.238	shrds1103	2016	5694	10.90 ± 1.00	23.30 ± 1.10	24.70 ± 2.80	2.50	9.8	C
G311.963−00.037	shrds439	2016	6064	9.50 ± 0.50	-54.10 ± 0.60	20.80 ± 1.30	1.00	18.7	A
G312.091+00.069	shrds440	2015	6138	4.00 ± 0.60	-61.40 ± 2.40	30.80 ± 6.30	1.50	6.3	C
G312.388−00.057	shrds450	2015	6491	4.90 ± 0.60	-60.80 ± 0.90	15.50 ± 2.10	1.20	7.0	C
G312.591+00.210a	shrds456	2016	6165	8.20 ± 0.40	-62.50 ± 0.50	18.10 ± 1.20	1.00	16.0	B
G312.591+00.210b	shrds456	2016	6165	2.50 ± 0.30	-30.70 ± 2.40	33.10 ± 6.50	1.00	6.6	C
G312.598+00.048	shrds458	2016	6801	14.10 ± 0.40	-67.10 ± 0.30	23.90 ± 0.70	1.00	30.4	A
G312.675+00.048	shrds462	2015	5945	9.90 ± 0.60	-61.60 ± 0.60	21.20 ± 1.50	1.30	15.4	A
G312.706+00.012	shrds462	2015	6253	11.40 ± 0.50	-67.90 ± 0.50	25.60 ± 1.20	1.10	23.6	A
G312.979−00.432	shrds465	2016	6489	7.00 ± 0.50	-47.80 ± 0.60	16.40 ± 1.40	0.90	14.7	B
G313.671−00.105	atca348	2013*	···	12.00 ± 1.40	-54.60 ± 1.40	24.60 ± 1.50	1.60	17.0	A
G313.790+00.705	atca352	2013*	···	38.70 ± 3.00	-57.20 ± 0.90	22.60 ± 0.90	2.60	32.0	A
G314.219+00.343	atca361	2013*	···	66.40 ± 3.10	-62.50 ± 0.40	20.00 ± 0.50	3.50	38.0	A
G314.239+00.428	shrds1111	2016	6043	88.60 ± 1.00	-62.50 ± 0.10	23.50 ± 0.30	1.90	100.7	A
G314.288+00.431	shrds1111	2016	6573	27.60 ± 0.40	-58.50 ± 0.20	19.90 ± 0.40	1.00	54.1	A
G315.312−00.272	ch87.1	2013	7878	20.10 ± 1.00	15.20 ± 0.60	24.50 ± 1.40	2.30	19.5	A
G316.516−00.600	atca382	2013*	···	19.00 ± 1.70	-45.60 ± 0.90	19.90 ± 0.90	1.70	22.0	A
G317.405+00.091	shrds1122	2016	6610	78.80 ± 0.50	-39.70 ± 0.10	21.70 ± 0.20	1.60	103.4	A
G317.426−00.561	shrds518	2015	6214	7.80 ± 0.80	28.70 ± 1.00	20.70 ± 2.50	2.00	8.1	C
G317.431−00.522	shrds518	2015	6137	3.80 ± 0.60	25.60 ± 1.70	22.40 ± 4.00	1.60	4.9	C
G317.458−00.533	shrds518	2015	6761	8.40 ± 0.60	25.70 ± 0.90	26.80 ± 2.40	1.40	13.7	B
G317.861+00.160	atca402	2013*	···	55.60 ± 4.60	1.53 ± 0.90	22.90 ± 0.90	2.70	44.0	A
G318.059−00.450	caswell13	2016	6742	13.30 ± 0.40	42.20 ± 0.40	25.90 ± 0.90	1.10	28.3	A
G318.233−00.605	shrds1126	2016	6107	6.10 ± 0.50	-40.90 ± 0.50	14.20 ± 1.20	1.00	10.4	B
G318.248+00.150	atca406	2013*	···	17.00 ± 3.70	-39.90 ± 2.00	19.00 ± 2.00	2.80	12.0	B
G318.726−00.222	shrds535	2016	6663	11.70 ± 0.40	-11.90 ± 0.40	26.40 ± 1.00	1.20	22.4	A
G318.774−00.150	shrds536	2015	6778	37.50 ± 0.80	-39.60 ± 0.20	21.40 ± 0.50	1.40	55.4	A
G319.188−00.329	shrds1129	2016	6101	12.10 ± 0.70	-27.30 ± 0.60	18.90 ± 1.30	1.30	18.1	A

Table 4.6 continued

Table 4.6: Non-tapered Image RRL Properties (continued)

Target	Field	Epoch[a]	ν_L[b] (MHz)	S_L (mJy beam^{-1})	$V_{\rm LSR}$ (km s^{-1})	ΔV (km s^{-1})	rms$_L$ (mJy beam^{-1})	S/N	QF
G319.229+00.225	atca412	2013*	···	12.90 ± 2.20	-66.10 ± 1.80	20.90 ± 1.80	1.90	14.0	B
G319.397−00.006	shrds1131	2016	5907	92.20 ± 0.90	-12.50 ± 0.10	30.40 ± 0.30	2.80	79.2	A
G319.453−00.022	shrds1131	2016	6638	17.50 ± 0.60	-22.60 ± 0.50	32.50 ± 1.20	1.40	31.0	A
G320.163+00.797	shrds1137	2016	5759	106.00 ± 1.00	-34.50 ± 0.10	25.90 ± 0.30	2.00	119.1	A
G320.205+00.867	shrds1137	2016	6927	12.00 ± 0.30	-39.30 ± 0.30	21.10 ± 0.60	0.70	35.4	A
G320.236−00.099	shrds1140	2016	6448	14.50 ± 0.60	-6.10 ± 0.40	18.90 ± 0.90	1.00	27.2	A
G320.240−00.176	shrds1139	2016	6255	5.10 ± 1.00	-7.80 ± 1.20	12.80 ± 2.90	1.70	4.7	C
G320.311−00.176	shrds1139	2016	5364	112.00 ± 2.40	-13.10 ± 0.40	33.30 ± 0.80	4.90	58.0	A
G320.376+00.172	shrds555	2015	5576	35.70 ± 2.00	1.10 ± 0.60	20.40 ± 1.30	4.00	17.7	A
G320.399+00.162	shrds555	2015	5790	13.40 ± 1.70	-3.90 ± 1.00	15.80 ± 2.30	2.60	9.1	C
G320.419+00.114	shrds555	2015	6651	14.90 ± 0.50	-7.10 ± 0.40	23.30 ± 0.90	1.70	19.2	A
G320.423+00.101	shrds555	2015	6585	10.00 ± 0.60	-7.70 ± 0.70	23.40 ± 1.70	1.80	12.0	B
G320.692+00.185	shrds559	2015	5512	9.30 ± 1.20	-8.20 ± 1.50	23.90 ± 3.90	3.00	6.8	C
G320.778+00.241	shrds1146	2016	6095	14.10 ± 0.70	-5.60 ± 0.60	26.00 ± 1.50	1.70	18.5	A
G320.782+00.258	shrds1146	2016	6353	22.30 ± 0.80	-13.30 ± 0.40	21.10 ± 0.90	1.60	27.5	A
G320.799+00.187	shrds1147	2016	6067	9.60 ± 0.70	-12.40 ± 0.90	25.20 ± 2.10	1.50	14.4	B
G320.884−00.641	shrds561	2016	6043	5.50 ± 0.50	9.70 ± 1.10	25.60 ± 2.80	1.10	11.0	B
G321.725+01.169	caswell14	2016	6552	150.10 ± 0.80	-32.30 ± 0.10	25.80 ± 0.20	1.30	253.9	A
G322.162+00.625	caswell15	2016	5966	501.90 ± 1.70	-52.10 ± 0.00	28.10 ± 0.10	4.10	287.7	A
G322.706−00.330	shrds574	2015	6930	15.60 ± 0.60	-13.90 ± 0.40	24.20 ± 1.00	1.20	27.7	A
G323.449+00.095	atca449	2013	8183	11.70 ± 0.80	-75.00 ± 0.80	22.10 ± 1.80	1.30	18.3	A
G323.464−00.079a	atca450	2013	8285	30.40 ± 0.80	-67.50 ± 0.60	29.90 ± 1.40	1.20	61.3	C
G323.464−00.079b	atca450	2013	8285	5.40 ± 0.90	-105.10 ± 3.20	27.40 ± 7.90	1.20	10.5	C
G323.743−00.249	atca456	2013	8234	21.90 ± 0.50	-47.90 ± 0.20	17.40 ± 0.40	1.40	28.2	A
G323.806+00.020	atca459	2013	7902	22.40 ± 0.50	-60.80 ± 0.30	25.30 ± 0.70	1.90	26.8	A
G323.915+00.026	shrds590	2015	6941	26.00 ± 0.60	-53.40 ± 0.30	25.00 ± 0.70	1.50	38.7	A
G323.936−00.038	atca462	2013*	···	13.80 ± 5.20	-57.30 ± 4.50	24.50 ± 4.60	2.40	12.7	B
G324.201+00.117	caswell16	2016	6407	157.90 ± 1.80	-90.70 ± 0.20	34.80 ± 0.50	1.70	236.0	A

Table 4.6 continued

Table 4.6: Non-tapered Image RRL Properties (continued)

Target	Field	Epoch[a]	ν_L[b] (MHz)	S_L (mJy beam^{-1})	$V_{\rm LSR}$ (km s^{-1})	ΔV (km s^{-1})	rms$_L$ (mJy beam^{-1})	S/N	QF
G324.642−00.321	atca466	2013	8084	31.20 ± 1.30	-47.00 ± 0.40	21.90 ± 1.00	2.30	28.3	A
G324.924−00.569	ch87.2	2013	7472	51.70 ± 1.80	-79.30 ± 0.50	27.80 ± 1.10	4.10	29.2	A
G325.108+00.053	atca472	2013	7770	11.20 ± 0.70	-61.20 ± 0.70	21.10 ± 1.60	1.70	13.1	B
G325.354−00.036	atca475	2013*	···	15.00 ± 1.50	-63.80 ± 0.60	34.40 ± 1.50	1.40	26.0	A
G326.065−00.393	shrds1161	2016	6033	6.70 ± 0.50	-63.90 ± 0.60	18.50 ± 1.50	1.00	12.8	B
G326.446+00.901	caswell17	2016	6211	278.30 ± 1.70	-41.10 ± 0.10	26.70 ± 0.20	3.80	166.0	A
G326.467−00.382	shrds609	2015	6880	28.30 ± 0.60	-52.90 ± 0.40	34.50 ± 0.80	1.50	47.7	A
G326.657+00.588	shrds1163	2016	5998	630.20 ± 1.60	-44.10 ± 0.00	26.00 ± 0.10	7.20	197.4	A
G326.721+00.773	atca484	2013*	···	45.50 ± 3.70	-40.60 ± 0.90	22.60 ± 0.90	4.90	20.0	A
G326.728+00.616	shrds1164	2016	6426	236.70 ± 1.60	-41.00 ± 0.10	33.70 ± 0.30	1.80	340.7	A
G326.890−00.277	atca486	2013	8168	59.50 ± 0.90	-44.40 ± 0.10	19.20 ± 0.40	1.90	60.5	A
G326.916−01.100	atca487	2013	7797	14.50 ± 1.20	-51.40 ± 0.90	20.30 ± 2.00	2.10	13.8	B
G327.139−00.261	shrds618	2016	6796	12.10 ± 0.50	-65.50 ± 0.40	17.80 ± 0.90	0.90	26.2	A
G327.172−00.527	shrds1167	2016	6112	18.30 ± 1.40	-52.60 ± 0.80	20.80 ± 1.90	2.40	15.6	A
G327.285−00.576	caswell18	2016	5742	106.20 ± 3.00	-39.00 ± 0.30	24.10 ± 0.80	5.20	44.6	A
G327.300−00.548	caswell18	2016	5795	1508.20 ± 8.60	-48.30 ± 0.10	29.40 ± 0.20	15.60	231.6	A
G327.400+00.444	shrds621	2016	7127	2.30 ± 0.20	-80.10 ± 5.10	102.90 ± 16.40	0.90	12.0	C
G327.401+00.483	atca492	2013*	···	31.50 ± 6.10	-76.30 ± 1.70	17.70 ± 1.70	2.60	23.0	A
G327.555−00.829	atca495	2013	7827	11.80 ± 1.00	-38.40 ± 1.10	26.50 ± 2.80	2.20	12.1	B
G327.714+00.576	atca498	2013	7691	8.10 ± 0.50	-52.10 ± 0.80	25.10 ± 1.90	1.30	13.9	B
G327.735−00.396	shrds628	2015	6602	56.30 ± 1.20	-71.80 ± 0.30	24.30 ± 0.60	1.80	66.8	A
G327.763+00.163	atca501	2013*	···	30.10 ± 3.40	-92.80 ± 1.20	21.60 ± 1.20	2.60	24.0	A
G327.770−00.346	shrds628	2015	6126	104.90 ± 1.10	-70.90 ± 0.10	24.80 ± 0.30	3.40	67.6	A
G327.824+00.117	atca501	2013	7227	17.30 ± 1.70	-98.80 ± 1.00	20.70 ± 2.40	3.80	9.3	C
G327.848+00.016	shrds635	2016	6012	4.50 ± 0.90	-57.80 ± 4.40	40.40 ± 14.60	1.60	7.7	C
G327.916+00.154	shrds639	2016	6137	6.80 ± 1.00	-97.70 ± 1.40	19.30 ± 3.40	1.80	7.3	C
G328.117+00.108	shrds647	2015	6387	14.60 ± 0.80	-104.70 ± 0.60	24.80 ± 1.50	1.70	18.6	A
G328.193−00.569	shrds652	2015	6479	82.90 ± 1.20	-44.60 ± 0.20	22.70 ± 0.40	2.20	78.8	A

Table 4.6 continued

Table 4.6: Non-tapered Image RRL Properties (continued)

Target	Field	Epoch[a]	ν_L[b] (MHz)	S_L (mJy beam^{-1})	$V_{\rm LSR}$ (km s^{-1})	ΔV (km s^{-1})	rms$_L$ (mJy beam^{-1})	S/N	QF
G328.279−00.559	shrds659	2016	5483	27.10 ± 1.30	-43.20 ± 0.40	17.50 ± 1.00	2.00	25.1	A
G328.294−00.536	shrds659	2016	5703	10.50 ± 1.20	-39.90 ± 0.90	16.60 ± 2.20	1.80	10.3	B
G328.315−00.594	shrds659	2016	5971	20.90 ± 0.80	-41.30 ± 0.40	22.10 ± 0.90	1.40	30.5	A
G328.356−00.559	shrds659	2016	6279	14.20 ± 0.50	-48.50 ± 0.30	18.60 ± 0.80	1.00	26.6	A
G328.807−00.078	shrds668	2016	5570	16.50 ± 0.70	-36.20 ± 0.60	28.20 ± 1.30	1.70	23.2	A
G328.819−00.004	shrds668	2016	6719	8.40 ± 0.40	-30.80 ± 0.50	22.80 ± 1.20	0.80	21.6	A
G328.825−00.081	shrds668	2016	5421	31.70 ± 0.90	-37.90 ± 0.40	28.60 ± 1.00	2.30	32.3	A
G328.945+00.570	shrds669	2015	6436	31.10 ± 0.90	-93.80 ± 0.30	24.40 ± 0.80	1.70	40.8	A
G328.961+00.248	shrds670	2015	6469	20.30 ± 1.10	-90.10 ± 0.40	15.00 ± 0.90	2.10	16.9	A
G328.962+00.207	shrds670	2015	5973	13.50 ± 1.30	-85.50 ± 0.80	17.10 ± 1.80	2.70	9.0	C
G329.266+00.111	shrds677	2015	6313	11.10 ± 0.80	-71.40 ± 0.90	23.60 ± 2.00	2.10	11.2	B
G329.422−00.160	shrds684	2015	6906	31.50 ± 0.60	-71.60 ± 0.20	23.70 ± 0.50	1.30	51.5	A
G329.460+00.174	shrds686	2015	6681	22.30 ± 0.50	-107.60 ± 0.30	23.00 ± 0.60	1.20	41.2	A
G329.472+00.214	shrds686	2015	6278	54.40 ± 1.00	-105.00 ± 0.30	34.00 ± 0.70	2.00	70.5	A
G329.474+00.839	shrds687	2016	6817	9.40 ± 0.40	-89.70 ± 0.40	21.80 ± 1.00	0.70	29.0	A
G329.601+00.059	shrds690	2015	6773	28.30 ± 0.70	-102.00 ± 0.30	22.60 ± 0.70	1.50	39.4	A
G330.673−00.388	shrds1171	2016	5832	58.20 ± 1.20	-62.30 ± 0.20	23.70 ± 0.50	2.00	62.3	A
G330.738−00.449	shrds1171	2016	6072	11.20 ± 0.60	-59.50 ± 0.50	18.00 ± 1.10	1.10	18.9	A
G330.954−00.181a	shrds709	2015	7066	54.40 ± 1.50	-88.50 ± 0.20	25.10 ± 0.70	2.00	60.7	C
G330.954−00.181b	shrds709	2015	7066	12.60 ± 1.40	-88.70 ± 1.60	83.40 ± 5.80	2.00	25.7	C
G331.056−00.437	shrds710	2016	6134	7.90 ± 0.90	-63.70 ± 1.40	24.10 ± 3.40	1.80	9.7	C
G331.057−00.229	shrds716	2015	5518	11.00 ± 1.20	-90.50 ± 0.90	16.60 ± 2.10	2.60	7.7	C
G331.123−00.530	shrds717	2015	6247	84.00 ± 1.20	-67.90 ± 0.10	19.90 ± 0.30	2.90	57.3	A
G331.127−00.481	shrds717	2015	6523	11.50 ± 1.00	-66.20 ± 0.80	18.30 ± 1.90	1.90	11.6	B
G331.129−00.243a	shrds716	2015	6997	35.20 ± 0.50	-84.30 ± 0.20	23.10 ± 0.60	0.90	79.4	C
G331.129−00.243b	shrds716	2015	6997	5.80 ± 0.60	-58.40 ± 1.20	16.60 ± 2.60	0.90	11.1	C
G331.145+00.133	shrds719	2015	6930	13.60 ± 0.50	-73.70 ± 0.40	22.20 ± 1.00	1.30	21.6	A
G331.156−00.391	shrds720	2015	6273	21.20 ± 0.90	-62.40 ± 0.40	18.90 ± 0.90	2.00	20.1	A

Table 4.6 continued

Table 4.6: Non-tapered Image RRL Properties (continued)

Target	Field	Epoch[a]	ν_L[b] (MHz)	S_L (mJy beam^{-1})	$V_{\rm LSR}$ (km s^{-1})	ΔV (km s^{-1})	rms$_L$ (mJy beam^{-1})	S/N	QF
G331.172−00.460	shrds721	2015	6534	49.20 ± 0.90	-70.90 ± 0.20	22.20 ± 0.40	2.00	52.4	A
G331.249+01.071	shrds1174	2016	6324	12.60 ± 0.60	-83.00 ± 0.70	26.70 ± 1.50	1.50	18.9	A
G331.259−00.188	shrds725	2016	6063	103.40 ± 0.80	-80.30 ± 0.10	23.70 ± 0.20	1.30	165.7	A
G331.322−00.176	shrds725	2016	6779	9.20 ± 0.30	-47.40 ± 0.30	18.30 ± 0.80	0.70	24.2	A
G331.361−00.019	shrds729	2015	5783	78.00 ± 2.20	-80.70 ± 0.30	24.70 ± 0.80	3.90	43.5	A
G331.384−00.358	shrds731	2015	6585	38.70 ± 0.60	-69.40 ± 0.20	23.10 ± 0.40	1.30	65.2	A
G331.412+00.011	shrds729	2015	6842	18.80 ± 0.90	0.00 ± 0.70	28.00 ± 1.60	2.00	21.6	A
G331.417−00.354	shrds731	2015	7028	22.90 ± 0.50	-67.70 ± 0.20	22.70 ± 0.50	1.10	45.3	A
G331.520−00.076	shrds736	2015	5448	299.60 ± 5.70	-92.30 ± 0.20	25.80 ± 0.60	7.30	92.3	A
G331.538−00.308	shrds735	2015	6897	14.50 ± 0.80	-97.10 ± 0.60	22.60 ± 1.40	1.20	26.4	A
G331.559−00.128	shrds736	2015	5784	57.70 ± 1.10	-106.00 ± 0.30	26.90 ± 0.60	2.70	49.2	A
G331.560+00.091	shrds737	2015	6188	37.70 ± 1.00	-87.40 ± 0.20	13.00 ± 0.40	1.50	39.4	A
G331.653+00.128	shrds741	2015	6267	20.00 ± 0.70	-91.30 ± 0.30	17.90 ± 0.70	1.10	34.7	A
G331.744−00.068	shrds743	2015	6469	21.20 ± 1.00	-88.70 ± 0.60	26.90 ± 1.50	1.80	27.8	A
G331.834−00.002	shrds746	2016	6335	7.80 ± 0.40	-81.30 ± 0.70	25.10 ± 1.60	0.70	24.0	A
G332.145−00.452	shrds753	2015	5511	320.80 ± 4.60	-56.20 ± 0.30	36.00 ± 0.60	7.40	115.8	A
G332.291−00.092	shrds756	2015	6713	29.90 ± 0.60	-48.60 ± 0.20	23.80 ± 0.50	1.60	41.0	A
G332.311−00.567	shrds759	2015	6553	20.20 ± 0.80	-56.00 ± 0.40	18.20 ± 0.90	1.50	25.5	A
G332.382+00.080	shrds763	2015	6299	7.10 ± 0.50	-41.50 ± 0.70	20.10 ± 1.70	1.00	13.6	B
G332.585−00.561	shrds771	2015	6603	27.70 ± 1.40	-51.60 ± 0.50	20.80 ± 1.20	2.40	23.0	A
G332.633−00.683	shrds1181	2016	6041	26.20 ± 1.20	-50.00 ± 0.50	21.20 ± 1.20	2.60	20.6	A
G332.657−00.622	shrds1181	2016	5343	255.40 ± 2.00	-47.20 ± 0.10	25.00 ± 0.20	7.10	80.0	A
G332.766−00.006	shrds774	2015	6784	21.00 ± 0.80	-96.90 ± 0.50	24.90 ± 1.10	1.20	38.9	A
G332.823−00.550a	shrds777	2015	6288	149.80 ± 3.80	-60.30 ± 0.80	34.60 ± 1.20	3.00	128.0	C
G332.823−00.550b	shrds777	2015	6288	24.50 ± 3.60	-94.90 ± 4.90	35.10 ± 7.50	3.00	21.1	C
G332.957+01.793	shrds782	2016	6446	3.70 ± 0.30	-27.90 ± 1.20	28.00 ± 2.90	0.70	12.8	B
G332.987+00.902	shrds784	2016	6788	9.70 ± 0.30	-45.40 ± 0.30	20.30 ± 0.70	0.70	27.4	A
G332.990−00.619	shrds785	2015	6156	33.00 ± 0.90	-49.00 ± 0.20	17.60 ± 0.50	1.30	46.5	A

Table 4.6 continued

Table 4.6: Non-tapered Image RRL Properties (continued)

Target	Field	Epoch[a]	ν_L[b] (MHz)	S_L (mJy beam^{-1})	$V_{\rm LSR}$ (km s^{-1})	ΔV (km s^{-1})	rms$_L$ (mJy beam^{-1})	S/N	QF
G333.011−00.441	shrds789	2015	5479	162.50 ± 2.60	-55.10 ± 0.20	19.20 ± 0.40	6.20	50.6	A
G333.052+00.033	shrds788	2015	6415	25.90 ± 0.90	-37.30 ± 0.40	24.30 ± 1.00	1.90	30.0	A
G333.085−00.479	shrds789	2015	6705	79.60 ± 1.00	-54.80 ± 0.10	25.10 ± 0.40	2.60	66.9	A
G333.095−00.460	shrds789	2015	6488	63.70 ± 0.90	-51.20 ± 0.10	18.30 ± 0.30	2.70	44.6	A
G333.113−00.141	shrds792	2015	6119	29.70 ± 1.00	-90.30 ± 0.40	24.60 ± 1.00	2.60	25.1	A
G333.129−00.439	shrds789	2015	5463	494.00 ± 3.50	-47.80 ± 0.10	28.90 ± 0.20	6.30	186.5	A
G333.164−00.100	shrds792	2015	5997	41.50 ± 1.10	-94.10 ± 0.30	24.90 ± 0.80	2.70	34.2	A
G333.255+00.065	shrds794	2015	6030	84.10 ± 1.40	-52.40 ± 0.20	26.00 ± 0.50	2.20	84.8	A
G333.467−00.159	shrds799	2015	6021	102.40 ± 1.20	-42.10 ± 0.10	22.10 ± 0.30	2.90	72.6	A
G333.534−00.383	shrds801	2015	5901	14.40 ± 0.80	-57.10 ± 0.50	18.10 ± 1.20	1.40	20.0	A
G333.580+00.058	shrds802	2016	6765	4.40 ± 0.60	-87.20 ± 1.50	20.30 ± 3.50	1.30	6.5	C
G333.627−00.199a	caswell19	2016	5929	1512.50 ± 9.60	-48.10 ± 0.30	42.20 ± 0.60	19.10	227.1	C
G333.627−00.199b	caswell19	2016	5929	225.50 ± 22.10	-82.40 ± 1.50	29.50 ± 2.40	19.10	28.3	C
G333.681−00.441	shrds804	2015	5941	9.80 ± 0.60	-11.00 ± 0.60	20.80 ± 1.60	2.50	7.8	C
G333.725+00.364	shrds803	2015	6579	33.60 ± 0.90	-27.20 ± 0.30	23.00 ± 0.70	1.90	37.0	A
G333.733−00.429	shrds804	2015	7228	14.50 ± 0.60	-5.80 ± 0.50	24.10 ± 1.10	1.20	26.6	A
G333.962+00.063	shrds806	2015	6683	14.50 ± 0.50	-64.10 ± 0.30	21.10 ± 0.80	1.40	21.8	A
G334.202+00.193	shrds811	2015	6318	23.50 ± 1.00	-94.70 ± 0.60	26.90 ± 1.30	2.10	26.2	A
G334.341+00.045	shrds814	2015	6479	32.90 ± 0.90	-65.90 ± 0.30	26.10 ± 0.80	2.10	36.0	A
G334.400−00.523	shrds815	2016	6073	4.30 ± 0.60	-9.90 ± 1.30	19.10 ± 3.10	1.80	4.7	C
G334.646+00.442	shrds825	2015	6300	15.10 ± 1.10	-66.20 ± 0.80	23.60 ± 1.90	1.80	17.8	A
G334.721−00.653	caswell20	2016	6432	37.20 ± 0.60	13.50 ± 0.30	37.00 ± 0.70	1.90	53.3	A
G334.774−00.023	shrds828	2015	6376	23.00 ± 0.80	-25.70 ± 0.40	22.40 ± 0.90	2.20	22.2	A
G335.195−00.385	shrds836	2016	6266	5.10 ± 0.50	-2.60 ± 1.50	30.10 ± 4.50	1.60	7.6	C
G335.579−00.209	shrds841	2016	6726	11.50 ± 0.40	-80.20 ± 0.60	32.90 ± 1.40	0.80	36.4	A
G336.026−00.817	shrds843	2015	6471	45.30 ± 0.70	-45.80 ± 0.20	20.90 ± 0.40	2.00	46.5	A
G336.367−00.003	shrds852	2015	6542	57.90 ± 1.30	-130.40 ± 0.30	25.80 ± 0.60	2.40	54.9	A
G336.410−00.257	shrds853	2016	6430	32.40 ± 0.70	-87.80 ± 0.30	32.10 ± 0.80	1.40	59.1	A

Table 4.6 continued

Table 4.6: Non-tapered Image RRL Properties (continued)

Target	Field	Epoch[a]	ν_L[b] (MHz)	S_L (mJy beam^{-1})	$V_{\rm LSR}$ (km s^{-1})	ΔV (km s^{-1})	rms$_L$ (mJy beam^{-1})	S/N	QF
G336.418−00.249	shrds853	2016	6117	46.40 ± 0.80	-87.10 ± 0.20	20.60 ± 0.40	1.60	58.0	A
G336.491−01.474	caswell21	2016	5943	378.60 ± 4.70	-23.50 ± 0.20	26.00 ± 0.40	4.70	180.7	A
G336.854−00.018	shrds1212	2016	6060	78.00 ± 2.00	-71.90 ± 0.30	25.90 ± 0.80	3.90	44.6	A
G336.874+00.139	shrds1209	2016	6137	21.20 ± 0.70	-79.80 ± 0.30	17.40 ± 0.70	1.50	25.6	A
G336.888+00.057	shrds1212	2016	6151	53.30 ± 1.40	-121.80 ± 0.30	24.70 ± 0.70	3.20	36.2	C
G336.900−00.033	shrds862	2015	5611	7.90 ± 1.50	-119.50 ± 2.10	23.30 ± 4.90	2.60	6.6	C
G336.919−00.188	shrds864	2015	6306	14.70 ± 1.50	-70.30 ± 1.10	22.10 ± 2.60	3.20	9.6	C
G336.986−00.006a	shrds862	2015	6508	6.40 ± 0.70	-119.70 ± 1.20	21.10 ± 2.80	1.10	12.0	B
G336.986−00.006b	shrds862	2015	6508	3.30 ± 0.70	-84.20 ± 2.10	19.10 ± 5.20	1.10	5.8	C
G336.990−00.021a	shrds862	2015	6713	25.30 ± 0.70	-113.00 ± 0.40	28.10 ± 1.10	1.20	49.2	C
G336.990−00.021b	shrds862	2015	6713	3.50 ± 0.90	-81.90 ± 2.10	14.50 ± 5.00	1.20	4.9	C
G337.004+00.322	shrds865	2015	6409	20.20 ± 1.30	-60.80 ± 0.80	26.80 ± 2.00	2.60	18.0	A
G337.170−00.059a	shrds869	2015	6495	16.10 ± 0.50	-114.00 ± 0.40	25.90 ± 0.90	1.10	32.6	B
G337.170−00.059b	shrds869	2015	6495	8.90 ± 0.60	-69.10 ± 0.60	16.50 ± 1.30	1.10	14.3	B
G337.188−00.060	shrds869	2015	6375	20.40 ± 0.50	-69.50 ± 0.30	21.70 ± 0.60	1.10	37.0	A
G337.253−00.165	shrds870	2015	6634	31.10 ± 0.90	-39.30 ± 0.40	26.40 ± 0.90	2.00	36.3	A
G337.281−00.163	shrds870	2015	6204	20.00 ± 1.30	-52.80 ± 0.80	24.30 ± 1.80	2.60	16.8	A
G337.285−00.113	shrds870	2015	5790	23.10 ± 1.90	-41.20 ± 1.20	30.20 ± 2.90	3.80	14.9	B
G337.286+00.113	shrds871	2015	6438	21.10 ± 0.60	-107.90 ± 0.30	19.20 ± 0.60	1.40	28.7	A
G337.404−00.404	shrds875	2015	6999	6.30 ± 0.40	-33.70 ± 1.20	37.10 ± 2.90	1.00	16.3	A
G337.453−00.363	shrds875	2015	6185	5.10 ± 0.80	-46.00 ± 1.00	13.00 ± 2.30	1.20	6.8	C
G337.617−00.065	shrds880	2015	6702	50.20 ± 1.10	-50.90 ± 0.20	21.20 ± 0.50	2.00	50.5	A
G337.664+00.049	shrds886	2015	5831	12.80 ± 1.50	-48.80 ± 1.10	19.50 ± 2.70	2.70	9.2	C
G337.665−00.176	shrds883	2015	6705	44.70 ± 1.00	-50.60 ± 0.30	28.80 ± 0.80	1.90	55.0	A
G337.684−00.343	shrds884	2015	5967	12.60 ± 0.70	-36.50 ± 0.70	24.30 ± 1.60	1.30	21.7	A
G337.705−00.059	shrds885	2015	6627	31.50 ± 1.30	-46.30 ± 0.40	22.40 ± 1.00	2.60	25.5	A
G337.709+00.091	shrds886	2015	6602	27.60 ± 0.70	-78.30 ± 0.40	30.90 ± 1.00	1.80	38.7	A
G337.754+00.057	shrds886	2015	6153	13.10 ± 1.00	-46.00 ± 0.60	16.30 ± 1.50	1.90	12.2	B

Table 4.6 continued

Table 4.6: Non-tapered Image RRL Properties (continued)

Target	Field	Epoch[a]	ν_L[b] (MHz)	S_L (mJy beam^{-1})	$V_{\rm LSR}$ (km s^{-1})	ΔV (km s^{-1})	rms$_L$ (mJy beam^{-1})	S/N	QF
G337.827+00.056	shrds888	2015	6295	6.00 ± 0.50	-127.90 ± 0.90	21.80 ± 2.20	1.20	10.5	B
G337.996+00.081	shrds892	2015	5945	15.40 ± 0.90	-130.20 ± 0.60	21.60 ± 1.50	1.80	17.4	A
G338.002−00.149	shrds891	2015	6411	5.80 ± 0.40	-66.30 ± 0.90	26.10 ± 2.20	1.20	11.2	B
G338.003−00.121	shrds891	2015	6189	14.60 ± 0.70	-54.70 ± 0.50	21.70 ± 1.20	1.30	23.0	A
G338.009+00.016	shrds892	2015	6363	23.40 ± 0.60	-59.00 ± 0.30	22.60 ± 0.70	1.20	40.6	A
G338.066−00.069	shrds1219	2016	6817	19.00 ± 0.90	-34.90 ± 0.60	26.20 ± 1.40	1.30	31.9	A
G338.075+00.016	shrds893	2015	6129	134.50 ± 1.30	-37.30 ± 0.10	30.60 ± 0.30	2.60	124.9	A
G338.106+00.020	shrds893	2015	6507	21.10 ± 0.90	-44.90 ± 0.40	19.90 ± 1.00	2.10	20.2	A
G338.263−00.364	shrds894	2015	6638	8.60 ± 0.80	-13.80 ± 0.70	15.90 ± 1.70	1.40	10.8	B
G338.289−00.373	shrds894	2015	6732	11.10 ± 0.50	-7.10 ± 0.60	26.40 ± 1.50	1.40	18.0	A
G338.360−00.095	shrds896	2015	6275	19.10 ± 1.10	-38.30 ± 0.60	19.70 ± 1.40	2.40	15.9	A
G338.364−00.020	shrds896	2015	5809	32.80 ± 1.40	-58.70 ± 0.50	21.50 ± 1.10	3.70	18.1	A
G338.374−00.152	caswell22	2016	6056	13.10 ± 0.90	8.40 ± 1.10	31.70 ± 2.80	3.00	10.9	B
G338.405−00.203	caswell22	2016	6265	110.90 ± 1.10	-0.20 ± 0.20	33.80 ± 0.40	1.90	148.3	A
G338.462−00.262	shrds898	2015	6434	23.10 ± 1.00	-57.70 ± 0.50	25.90 ± 1.30	1.60	33.1	A
G338.565−00.151	shrds899	2015	6658	35.90 ± 0.70	-114.40 ± 0.20	24.80 ± 0.60	1.60	48.9	A
G338.576+00.020	shrds900	2015	6606	51.40 ± 1.00	-25.00 ± 0.20	20.60 ± 0.50	1.90	53.3	A
G338.628+00.145a	shrds901	2015	6287	8.00 ± 1.40	-26.20 ± 5.70	75.00 ± 10.10	1.80	17.1	C
G338.628+00.145b	shrds901	2015	6287	4.30 ± 0.40	-124.10 ± 17.50	120.90 ± 44.10	1.80	11.8	C
G338.706+00.645	shrds1223	2016	5728	17.00 ± 1.10	-57.70 ± 0.40	13.40 ± 1.00	1.40	19.2	A
G338.837−00.318	shrds904	2015	6421	13.30 ± 0.70	-123.50 ± 0.40	17.80 ± 1.00	1.40	17.3	A
G338.851+00.405	shrds905	2015	6708	6.70 ± 0.50	-50.10 ± 0.80	21.80 ± 1.80	1.10	12.3	B
G338.861+00.597	shrds1223	2016	6705	10.30 ± 0.40	-68.90 ± 0.30	13.30 ± 0.60	0.80	21.6	A
G338.883+00.537	shrds1225	2016	6312	8.50 ± 0.40	-59.40 ± 0.50	21.60 ± 1.30	0.80	20.7	A
G338.911+00.615	shrds1225	2016	5780	35.20 ± 0.70	-67.50 ± 0.20	20.90 ± 0.50	1.70	42.9	A
G338.917+00.382	shrds906	2015	6604	19.20 ± 0.70	-24.70 ± 0.60	30.50 ± 1.40	1.90	24.6	A
G338.926+00.392	shrds906	2015	6348	28.80 ± 0.90	-27.70 ± 0.30	21.90 ± 0.80	1.70	35.2	A
G339.106+00.152	shrds909	2015	6727	25.00 ± 0.60	-86.70 ± 0.30	23.40 ± 0.60	1.70	32.0	A

Table 4.6 continued

Table 4.6: Non-tapered Image RRL Properties (continued)

Target	Field	Epoch[a]	ν_L[b] (MHz)	S_L (mJy beam^{-1})	$V_{\rm LSR}$ (km s^{-1})	ΔV (km s^{-1})	rms$_L$ (mJy beam^{-1})	S/N	QF
G339.169−00.698	shrds910	2015	6340	4.60 ± 0.70	-50.60 ± 0.60	8.50 ± 1.50	1.10	5.4	C
G339.216+00.263	shrds913	2015	6562	3.50 ± 0.60	-73.10 ± 1.20	14.90 ± 2.90	1.10	5.2	C
G339.275−00.607	shrds915	2015	6301	10.40 ± 0.90	-39.10 ± 0.90	21.00 ± 2.00	1.40	15.2	A
G339.478+00.181	shrds917	2015	6857	29.20 ± 0.70	-84.40 ± 0.20	20.00 ± 0.60	1.30	45.7	A
G339.486+00.087	shrds918	2015	6594	24.70 ± 0.90	-116.90 ± 0.40	21.80 ± 0.90	1.80	27.7	A
G339.548−00.385	shrds919	2015	6330	4.30 ± 0.60	-49.10 ± 2.30	32.70 ± 5.50	1.70	6.6	C
G339.553−00.401	shrds919	2015	6624	13.00 ± 0.70	-50.60 ± 1.00	40.70 ± 2.50	1.80	20.2	A
G339.556+00.282	shrds920	2015	6539	15.70 ± 1.10	-42.40 ± 0.70	20.00 ± 1.60	1.40	22.5	A
G339.584+00.084	shrds921	2015	6740	30.90 ± 0.70	-114.40 ± 0.20	20.80 ± 0.60	1.30	48.1	A
G339.676+00.283	shrds922	2016	5898	5.70 ± 1.00	-91.00 ± 1.40	17.00 ± 3.30	2.30	4.6	C
G339.717−01.211	shrds925	2015	6751	21.70 ± 0.60	-33.40 ± 0.30	19.70 ± 0.70	1.40	30.9	A
G339.781+00.243	shrds928	2015	5989	2.80 ± 0.50	-30.20 ± 1.70	19.40 ± 4.10	1.30	4.0	C
G339.845+00.299	shrds928	2015	5359	31.60 ± 1.90	-18.50 ± 0.70	23.40 ± 1.60	3.70	18.4	A
G339.952+00.052	shrds1234	2016	6363	8.60 ± 0.40	-121.90 ± 0.50	23.30 ± 1.20	0.80	22.6	A
G340.051−00.231	shrds1236	2016	5477	45.50 ± 2.40	-51.40 ± 0.70	27.20 ± 1.60	3.50	30.4	A
G340.053−00.244	shrds1236	2016	5378	47.90 ± 1.80	-49.40 ± 0.50	26.80 ± 1.20	4.30	25.6	A
G340.059−00.138	shrds1236	2016	5823	16.20 ± 0.90	-52.00 ± 0.60	20.90 ± 1.40	1.70	19.3	A
G340.097−00.174	shrds1236	2016	5895	14.30 ± 0.70	-51.00 ± 0.50	21.20 ± 1.30	1.40	20.2	A
G340.234−00.368	shrds1237	2016	5972	5.10 ± 0.50	-61.30 ± 0.70	14.60 ± 1.60	1.60	5.4	C
G340.247−00.373	shrds1237	2016	6301	9.00 ± 0.80	-61.50 ± 1.30	28.90 ± 3.20	1.70	12.3	B
G340.296−00.276	shrds1237	2016	6058	7.00 ± 0.50	-45.70 ± 0.60	17.90 ± 1.50	1.30	9.9	C
G342.062+00.417	caswell23	2016	6301	109.10 ± 1.10	-68.90 ± 0.10	27.70 ± 0.30	2.50	103.1	A
G342.354−00.047	shrds1239	2016	5343	21.50 ± 1.30	-6.10 ± 0.80	27.70 ± 2.00	3.90	12.9	B
G342.360+00.107	shrds1238	2016	5726	8.70 ± 1.00	-95.90 ± 1.40	25.60 ± 3.40	2.80	7.0	C
G342.388+00.074	shrds1238	2016	6097	6.20 ± 0.80	-121.00 ± 0.90	14.70 ± 2.10	2.00	5.3	C
G342.438−00.061	shrds1239	2016	6772	7.10 ± 0.50	-2.70 ± 0.70	19.80 ± 1.60	1.20	11.6	B
G343.224−00.065	shrds1240	2016	5959	5.30 ± 0.40	1.30 ± 0.60	16.30 ± 1.40	0.90	10.1	B
G343.234−00.078	shrds1240	2016	6306	4.10 ± 0.50	-0.90 ± 1.10	19.50 ± 2.60	0.90	8.5	C

Table 4.6 continued

Table 4.6: Non-tapered Image RRL Properties (continued)

Target	Field	Epoch[a]	ν_L[b] (MHz)	S_L (mJy beam^{-1})	$V_{\rm LSR}$ (km s^{-1})	ΔV (km s^{-1})	rms$_L$ (mJy beam^{-1})	S/N	QF
G343.352−00.081	shrds1241	2016	6904	19.80 ± 0.70	-130.20 ± 0.40	23.60 ± 1.00	1.40	31.4	A
G343.914−00.646	caswell24	2016	6376	8.70 ± 0.40	-26.50 ± 0.50	19.60 ± 1.10	0.90	19.1	A
G344.424+00.044	caswell25	2016	6612	203.40 ± 1.60	-63.70 ± 0.10	28.10 ± 0.20	1.60	299.8	A
G348.892−00.179	fa644	2015	6891	21.90 ± 0.50	11.80 ± 0.30	28.50 ± 0.80	1.30	40.9	A
G349.328+00.020	gs038	2015	6786	12.40 ± 0.50	15.70 ± 0.60	26.70 ± 1.30	1.30	22.6	A
G352.313−00.442	fa016	2015	6709	16.70 ± 0.60	-11.70 ± 0.50	26.70 ± 1.10	1.40	27.9	A
G355.344+00.145	fa032	2015	6715	27.00 ± 0.60	19.20 ± 0.40	34.80 ± 0.90	1.40	49.1	A
G358.600−00.058	gs108	2015	6340	23.70 ± 0.80	-210.90 ± 0.30	21.00 ± 0.80	1.50	31.1	A
G358.616−00.077	gs108	2015	6180	6.50 ± 0.50	-211.10 ± 0.70	18.60 ± 1.70	1.70	7.5	C
G358.633+00.062	fa054	2015	6754	24.40 ± 0.50	14.50 ± 0.30	26.20 ± 0.60	1.50	38.1	A
G358.643−00.035	gs108	2015	6219	11.90 ± 1.00	-208.40 ± 1.00	25.00 ± 2.40	2.40	11.1	B
G359.436−00.091	fa489	2015	5380	26.00 ± 1.90	-57.60 ± 1.80	48.40 ± 4.40	4.20	18.9	A
G359.467−00.173	fa489	2015	6848	14.30 ± 0.60	-69.80 ± 0.50	24.60 ± 1.20	1.30	24.3	A

[a] Rows with epochs with an asterisk (*) are copied directly from Brown et al. (2017). They did not give the weigted-average frequency of their H$n\alpha$ RRL spectra.

[b] This is the weighted-average frequency of the <H$n\alpha$> spectrum.

Table 4.7: *uv*-tapered Image RRL Properties

Target	Field	Epoch[a]	ν_L[b] (MHz)	S_L (mJy beam^{-1})	$V_{\rm LSR}$ (km s^{-1})	ΔV (km s^{-1})	rms$_L$ (mJy beam^{-1})	S/N	QF
G213.833+00.618	g213.833+00.618	2014*	···	1.90 ± 2.30	53.20 ± 20.20	33.50 ± 20.90	1.40	3.5	C
G230.354−00.597	g230.354-00.597	2014*	···	2.10 ± 2.00	69.00 ± 16.10	35.00 ± 16.70	1.50	3.7	C
G259.057−01.544	shrds030	2016	6295	10.80 ± 0.80	58.00 ± 0.90	24.50 ± 2.10	2.10	11.3	B
G263.237+00.509	shrds060	2015	6196	16.90 ± 1.30	11.10 ± 0.60	17.20 ± 1.50	2.30	13.5	B
G267.730−01.100	shrds078	2016	6447	32.40 ± 1.30	7.70 ± 0.40	22.70 ± 1.00	2.30	29.6	A
G269.068−01.114	shrds085	2016	6127	149.70 ± 3.20	13.60 ± 0.20	23.70 ± 0.60	6.10	52.8	A
G269.159−01.119	shrds085	2016	6411	53.40 ± 1.50	11.00 ± 0.30	23.60 ± 0.80	3.10	37.1	A
G269.167−01.357	shrds086	2016	6515	22.00 ± 1.00	3.20 ± 0.50	22.10 ± 1.20	2.10	22.3	A
G280.626−01.186	shrds111	2015	6542	7.20 ± 1.20	32.60 ± 1.70	20.80 ± 4.20	2.10	6.9	C
G280.989−01.527	shrds1005	2016	5894	48.40 ± 1.70	0.80 ± 0.40	24.60 ± 1.00	4.10	25.8	A
G281.047−01.541	shrds1005	2016	6944	61.10 ± 1.10	-10.30 ± 0.20	24.20 ± 0.50	2.50	53.2	A
G281.175−01.645	caswell1	2016	6314	70.20 ± 1.30	-7.20 ± 0.30	30.40 ± 0.60	3.00	57.9	A
G281.560−02.478	shrds114	2015	6692	44.40 ± 1.00	-2.20 ± 0.30	27.00 ± 0.70	2.00	51.1	A
G281.840−01.609	shrds117	2015	6507	11.00 ± 0.90	-8.60 ± 1.00	25.50 ± 2.40	1.60	15.8	A
G282.015−00.997	shrds1007	2016	5995	32.20 ± 1.20	1.50 ± 0.40	22.50 ± 1.00	2.20	30.2	A
G282.842−01.252	shrds1232	2016	6320	25.00 ± 0.70	-3.30 ± 0.40	26.30 ± 0.90	1.90	30.2	A
G283.832−00.730	shrds1013	2016	6314	24.30 ± 0.70	6.30 ± 0.30	21.50 ± 0.70	2.10	23.8	A
G284.014−00.857	shrds1014	2016	6912	77.40 ± 1.20	9.00 ± 0.20	25.20 ± 0.40	3.60	47.3	A
G284.712+00.317	caswell2	2016	6175	84.70 ± 1.60	8.80 ± 0.30	29.20 ± 0.60	3.50	57.8	A
G284.902+00.060	shrds141	2015	6588	8.20 ± 0.90	3.40 ± 1.20	22.30 ± 2.90	2.10	8.2	C
G285.353+00.004	shrds143	2016	6830	7.90 ± 1.10	-6.90 ± 1.30	18.40 ± 3.30	2.40	6.2	C
G286.362−00.297	shrds1017	2016	6129	17.90 ± 1.20	-33.50 ± 0.70	23.20 ± 1.80	2.40	15.9	A
G286.951−00.955	shrds158	2015	6364	24.50 ± 0.80	36.10 ± 0.50	30.90 ± 1.20	2.00	29.8	A
G288.074−01.642	shrds162	2016	6457	9.30 ± 0.80	10.40 ± 1.10	26.20 ± 2.50	1.60	13.0	B
G288.851−00.108	shrds167	2016	6460	9.60 ± 0.70	18.20 ± 0.80	23.00 ± 2.00	1.60	13.0	B
G289.109−01.107	shrds173	2016	6349	6.50 ± 0.60	24.20 ± 1.30	29.50 ± 3.20	1.50	10.8	B
G289.188−00.293	shrds1024	2016	6757	11.70 ± 0.60	34.50 ± 0.50	23.40 ± 1.30	1.60	15.6	A
G289.476−00.899	shrds181	2016	6195	12.30 ± 0.70	19.30 ± 0.80	27.80 ± 1.90	1.80	16.3	A

Table 4.7 continued

Table 4.7: *uv*-tapered Image RRL Properties (continued)

Target	Field	Epoch[a]	ν_L[b] (MHz)	S_L (mJy beam^{-1})	$V_{\rm LSR}$ (km s^{-1})	ΔV (km s^{-1})	rms$_L$ (mJy beam^{-1})	S/N	QF
G289.582−00.636	shrds184	2016	6543	9.10 ± 0.50	20.60 ± 0.70	27.90 ± 1.80	1.50	13.7	B
G289.769−01.220	shrds1026	2016	6241	11.30 ± 0.60	27.00 ± 0.90	31.60 ± 2.20	2.10	13.6	B
G289.806−01.242	shrds1026	2016	5746	26.30 ± 1.20	5.80 ± 0.70	31.20 ± 1.60	3.40	19.2	A
G289.874−00.752	shrds1028	2016	6179	22.30 ± 0.90	15.60 ± 0.50	26.70 ± 1.20	2.10	24.3	A
G289.880−00.801	shrds1028	2016	5982	100.00 ± 1.70	17.20 ± 0.20	26.00 ± 0.50	3.20	71.3	A
G289.944−00.889	shrds191	2015	6429	8.90 ± 0.80	32.30 ± 0.90	21.40 ± 2.10	1.70	11.0	B
G290.012−00.867	g290.012-00.867	2014*	···	3.60 ± 2.50	14.70 ± 8.30	24.90 ± 8.60	1.80	4.5	C
G290.323−02.984	g290.323-02.984	2014*	···	3.50 ± 2.10	-17.70 ± 8.00	28.30 ± 8.30	1.50	5.6	C
G290.385−01.042	g290.385-01.042	2014*	···	4.00 ± 2.90	9.91 ± 4.60	13.20 ± 4.70	1.90	3.4	C
G290.674−00.133	g290.674-00.133	2014*	···	5.20 ± 2.40	19.30 ± 5.20	23.20 ± 5.30	1.40	8.0	C
G291.046−02.079	shrds199	2015	5924	19.30 ± 0.90	-18.80 ± 0.60	26.00 ± 1.40	2.30	18.9	A
G291.202−00.295	shrds1032	2016	6491	34.90 ± 1.00	9.50 ± 0.30	20.70 ± 0.70	2.40	28.8	A
G291.281−00.726	caswell3	2016	5492	3208.30 ± 38.10	-24.10 ± 0.20	33.90 ± 0.50	74.70	110.7	A
G291.596−00.239	g291.596-00.239	2014*	···	15.30 ± 3.70	11.40 ± 5.10	44.20 ± 5.40	2.50	18.0	A
G291.863−00.682	caswell4	2016	6374	124.90 ± 1.60	24.50 ± 0.20	26.20 ± 0.40	3.30	85.6	A
G292.889−00.831	g292.889-00.831	2014*	···	4.80 ± 2.30	21.80 ± 7.10	30.00 ± 7.30	1.40	8.4	C
G293.113−00.961	shrds207	2015	5763	4.90 ± 0.60	-29.10 ± 1.50	26.30 ± 3.60	2.60	4.3	C
G293.619−01.613	shrds210	2016	5998	12.00 ± 1.60	-13.90 ± 1.10	15.80 ± 2.50	4.10	5.2	C
G293.661−01.639	shrds210	2016	6066	23.30 ± 1.50	-20.70 ± 0.60	17.70 ± 1.30	3.20	13.7	B
G293.829−00.744	shrds215	2015	6201	13.60 ± 0.60	37.60 ± 0.60	26.50 ± 1.40	1.50	20.8	A
G293.936−00.873	g293.936-00.873	2014*	···	16.40 ± 2.20	36.60 ± 1.40	22.30 ± 1.50	2.00	17.0	A
G293.967−00.984	shrds219	2015	6348	12.90 ± 0.60	27.20 ± 0.70	30.40 ± 1.70	1.60	19.9	A
G293.994−00.934	g293.994-00.934	2014*	···	18.60 ± 2.60	46.50 ± 1.70	25.60 ± 1.80	1.30	32.0	A
G294.453−00.521	shrds226	2015	6305	13.70 ± 0.90	-10.70 ± 0.60	20.20 ± 1.50	1.80	15.5	A
G294.988−00.538	g294.988-00.538	2014*	···	9.70 ± 1.40	39.80 ± 1.90	27.40 ± 2.00	1.20	19.0	A
G295.275−00.255	g295.275-00.255	2014*	···	5.60 ± 2.30	30.10 ± 6.20	30.60 ± 6.30	1.60	8.7	C
G295.748−00.207	g295.748-00.207	2014*	···	7.20 ± 2.10	23.30 ± 3.50	23.90 ± 3.50	1.60	9.8	C
G297.248−00.754	g297.248-00.754	2014*	···	22.60 ± 2.90	22.60 ± 1.50	24.40 ± 1.60	1.90	26.0	A

Table 4.7 continued

Table 4.7: *uv*-tapered Image RRL Properties (continued)

Target	Field	Epoch[a]	ν_L[b] (MHz)	S_L (mJy beam^{-1})	$V_{\rm LSR}$ (km s^{-1})	ΔV (km s^{-1})	rms$_L$ (mJy beam^{-1})	S/N	QF
G297.312−00.295	shrds242	2015	6048	8.20 ± 1.30	14.90 ± 1.50	19.90 ± 3.90	2.00	7.9	C
G297.392−00.624	shrds243	2015	6063	17.20 ± 1.20	24.50 ± 1.00	29.40 ± 2.50	3.20	12.8	B
G297.497−00.758	shrds246	2015	5575	49.30 ± 1.40	26.00 ± 0.30	24.50 ± 0.80	3.10	35.3	A
G297.536−00.826	shrds246	2015	6604	12.00 ± 0.80	37.80 ± 0.80	25.40 ± 2.10	1.60	16.7	A
G297.626−00.906	g297.626-00.906	2014*	···	16.10 ± 2.50	31.30 ± 2.10	28.40 ± 2.20	1.50	26.0	A
G297.651−00.973	g297.626-00.906	2014	5327	23.20 ± 3.20	32.10 ± 3.30	47.90 ± 8.70	9.70	7.3	C
G298.183−00.784	caswell5	2016	6372	106.90 ± 0.90	17.80 ± 0.20	36.30 ± 0.40	2.00	142.6	A
G298.196−00.247	shrds1041	2016	6827	29.50 ± 0.80	31.50 ± 0.40	27.10 ± 0.90	1.90	34.9	A
G298.473+00.104	g298.473+00.104	2014*	···	12.20 ± 2.20	32.90 ± 2.00	23.50 ± 2.10	2.00	13.0	B
G298.630+00.253	shrds253	2015	5938	7.80 ± 0.60	34.30 ± 0.90	22.30 ± 2.10	1.70	9.6	C
G298.669+00.064	g298.669+00.064	2014*	···	11.40 ± 3.90	24.10 ± 2.40	14.10 ± 2.40	2.20	8.7	C
G298.846+00.121	shrds258	2015	6387	20.60 ± 0.70	20.70 ± 0.40	25.30 ± 1.00	2.00	23.4	A
G299.349−00.267	caswell6	2016	6254	33.40 ± 0.90	-39.30 ± 0.30	20.40 ± 0.60	1.90	35.7	A
G300.369−00.288	shrds271	2015	6117	7.60 ± 0.90	31.40 ± 1.80	30.50 ± 4.60	2.00	9.3	C
G300.502−00.180	shrds273	2015	5268	13.20 ± 1.70	23.10 ± 2.90	46.50 ± 6.90	5.50	7.3	C
G300.965+01.162	g300.983+01.117	2014	5933	97.70 ± 2.70	-41.30 ± 0.40	26.20 ± 0.80	7.00	31.5	A
G300.972+00.994	g300.972+00.994	2014*	···	3.80 ± 1.40	-34.50 ± 7.20	39.10 ± 7.50	1.70	6.3	C
G300.983+01.117	caswell7	2016	6060	118.40 ± 1.00	-43.00 ± 0.10	26.20 ± 0.20	2.50	106.6	A
G301.116+00.968	caswell8	2016	6245	177.40 ± 1.50	-40.20 ± 0.10	29.30 ± 0.30	2.20	193.4	A
G302.032−00.063	caswell9	2016	6703	76.50 ± 1.00	-28.60 ± 0.20	28.80 ± 0.40	2.20	82.8	A
G302.391+00.280	shrds293	2016	6609	16.40 ± 0.40	-40.20 ± 0.30	22.00 ± 0.70	1.20	28.5	A
G302.436−00.106	shrds294	2016	6258	15.10 ± 0.70	-39.40 ± 0.60	24.40 ± 1.40	1.50	22.4	A
G302.481−00.035	shrds295	2016	6397	11.60 ± 0.60	-43.20 ± 0.50	21.40 ± 1.30	1.60	14.9	B
G302.503−00.762	shrds296	2015	5690	7.30 ± 0.90	32.90 ± 2.00	33.60 ± 5.10	2.20	8.5	C
G302.636−00.672	shrds297	2016	6364	30.90 ± 0.60	30.40 ± 0.20	24.80 ± 0.50	1.40	49.2	A
G302.816−00.844	shrds299	2016	6175	6.90 ± 0.60	35.30 ± 0.80	18.70 ± 1.80	1.20	11.4	B
G303.342−00.718	shrds303	2015	6293	10.20 ± 0.50	28.30 ± 0.90	34.60 ± 2.30	1.40	18.9	A
G303.384−00.965	shrds305	2016	6459	9.10 ± 0.40	47.30 ± 0.50	22.50 ± 1.30	1.20	15.5	A

Table 4.7 continued

Table 4.7: *uv*-tapered Image RRL Properties (continued)

Target	Field	Epoch[a]	ν_L[b] (MHz)	S_L (mJy beam^{-1})	$V_{\rm LSR}$ (km s^{-1})	ΔV (km s^{-1})	rms$_L$ (mJy beam^{-1})	S/N	QF
G303.557−00.539	shrds308	2016	6267	12.20 ± 1.10	33.10 ± 0.90	20.80 ± 2.10	1.30	18.5	A
G304.465−00.023	shrds336	2015	5940	29.10 ± 0.70	-13.80 ± 0.20	22.10 ± 0.60	1.70	36.2	A
G304.557+00.329	shrds338	2016	6648	9.50 ± 0.40	-40.10 ± 0.60	26.60 ± 1.30	1.10	19.4	A
G304.925+00.555	shrds344	2015	6068	21.20 ± 1.20	-37.20 ± 1.00	37.20 ± 2.50	2.70	20.9	A
G305.789+00.280	shrds350	2016	6355	15.40 ± 0.60	-36.80 ± 0.50	25.10 ± 1.10	1.50	22.7	A
G307.559−00.585	caswell10	2016	6606	71.20 ± 1.30	-40.10 ± 0.20	27.90 ± 0.60	1.70	98.8	A
G307.974−01.594	shrds373	2016	6503	7.90 ± 0.80	39.60 ± 1.00	21.30 ± 2.40	1.70	9.7	C
G308.079−00.406	caswell11	2016	6107	48.10 ± 0.80	-14.90 ± 0.20	21.30 ± 0.40	2.20	45.0	A
G308.747+00.547	shrds1091	2016	6343	49.90 ± 1.20	-40.30 ± 0.30	22.30 ± 0.60	1.90	54.0	A
G308.916+00.124	shrds384	2015	6585	30.40 ± 1.10	-42.40 ± 0.60	33.00 ± 1.40	2.00	38.9	A
G309.151−00.215	shrds385	2016	6080	18.40 ± 1.00	-10.90 ± 0.50	20.10 ± 1.30	1.80	20.3	A
G309.176−00.028	shrds386	2015	6449	25.50 ± 0.70	-17.10 ± 0.40	26.90 ± 0.90	1.70	34.7	A
G310.260−00.199	shrds403	2016	6153	7.50 ± 0.40	8.90 ± 0.80	28.70 ± 1.90	1.50	12.2	B
G310.519−00.220	shrds407	2015	6581	25.30 ± 0.80	23.80 ± 0.50	29.80 ± 1.10	1.80	33.2	A
G310.630−00.421	shrds409	2015	6042	24.20 ± 0.80	-28.30 ± 0.30	21.60 ± 0.80	1.90	26.0	A
G310.672−00.450	shrds409	2015	6013	22.60 ± 0.70	-25.80 ± 0.30	20.50 ± 0.80	1.90	24.5	A
G310.887+00.009	shrds412	2015	6343	18.20 ± 0.70	-54.60 ± 0.40	20.10 ± 0.90	1.60	22.1	A
G310.901−00.373	shrds1096	2016	6727	45.60 ± 0.60	28.70 ± 0.20	25.60 ± 0.40	1.50	68.9	A
G311.003−00.355	shrds413	2016	6421	10.10 ± 0.50	33.20 ± 0.70	28.60 ± 1.80	1.40	17.2	A
G311.137−00.235	shrds418	2015	5915	12.80 ± 1.40	44.20 ± 1.90	35.20 ± 5.00	2.90	11.6	B
G311.425+00.598	shrds425	2015	6654	10.40 ± 1.30	-46.00 ± 1.50	24.80 ± 3.60	3.00	7.5	C
G311.575+00.239	shrds428	2016	6378	13.90 ± 0.50	1.50 ± 0.30	19.90 ± 0.80	1.10	25.4	A
G311.581−00.593	shrds1101	2016	6625	5.50 ± 0.50	35.10 ± 1.70	39.10 ± 4.50	1.20	12.5	B
G311.606−00.638	shrds1101	2016	5881	7.40 ± 1.60	33.70 ± 1.90	18.00 ± 4.80	2.20	6.2	C
G311.629+00.289	caswell12	2016	6514	137.40 ± 1.50	-55.60 ± 0.20	34.70 ± 0.40	3.10	114.8	A
G311.809−00.309	shrds1103	2016	6164	23.70 ± 0.60	-37.10 ± 0.30	25.70 ± 0.80	1.60	33.0	A
G311.841−00.219	shrds1103	2016	5531	10.30 ± 1.50	24.80 ± 1.90	26.50 ± 5.40	3.80	6.2	C
G311.866−00.238	shrds1103	2016	5627	12.70 ± 1.70	25.20 ± 1.70	25.60 ± 4.10	3.40	8.4	C

Table 4.7 continued

Table 4.7: *uv*-tapered Image RRL Properties (continued)

Target	Field	Epoch[a]	ν_L[b] (MHz)	S_L (mJy beam^{-1})	$V_{\rm LSR}$ (km s^{-1})	ΔV (km s^{-1})	rms$_L$ (mJy beam^{-1})	S/N	QF
G311.963−00.037	shrds439	2016	6193	26.70 ± 0.80	-54.50 ± 0.30	19.70 ± 0.70	1.50	35.4	A
G312.091+00.069	shrds440	2015	5725	12.40 ± 1.30	-68.30 ± 0.90	16.70 ± 2.10	3.10	7.3	C
G312.388−00.057	shrds450	2015	6136	7.10 ± 1.20	-63.00 ± 1.60	18.50 ± 3.70	2.10	6.4	C
G312.591+00.210a	shrds456	2016	6140	18.60 ± 0.50	-63.20 ± 0.30	19.00 ± 0.70	1.50	23.4	B
G312.591+00.210b	shrds456	2016	6140	5.40 ± 0.50	-32.10 ± 1.10	22.80 ± 2.90	1.50	7.5	C
G312.598+00.048	shrds458	2016	6611	14.80 ± 0.50	-66.60 ± 0.40	22.70 ± 0.90	1.30	24.6	A
G312.675+00.048	shrds462	2015	5618	21.80 ± 0.90	-62.70 ± 0.40	20.80 ± 1.00	2.00	21.8	A
G312.706+00.012	shrds462	2015	5861	23.30 ± 0.70	-68.60 ± 0.40	24.10 ± 0.90	1.90	26.9	A
G312.979−00.432	shrds465	2016	5964	19.70 ± 0.60	-48.30 ± 0.30	17.80 ± 0.70	1.40	26.9	A
G313.671−00.105	atca348	2013*	···	12.00 ± 1.40	-54.60 ± 1.40	24.60 ± 1.50	1.60	17.0	A
G313.790+00.705	atca352	2013*	···	38.70 ± 3.00	-57.20 ± 0.90	22.60 ± 0.90	2.60	32.0	A
G313.851−00.243	shrds479	2016	6276	4.10 ± 0.70	34.50 ± 2.60	31.80 ± 6.40	1.70	5.9	C
G314.219+00.343	atca361	2013*	···	66.40 ± 3.10	-62.50 ± 0.40	20.00 ± 0.50	3.50	38.0	A
G314.239+00.428	shrds1111	2016	5824	130.00 ± 1.30	-62.80 ± 0.10	25.30 ± 0.30	3.00	97.7	A
G314.288+00.431	shrds1111	2016	6351	44.00 ± 0.60	-59.00 ± 0.10	20.90 ± 0.30	1.60	57.0	A
G315.312−00.272	ch87.1	2013	7762	30.10 ± 1.40	15.20 ± 0.50	23.90 ± 1.20	2.70	23.9	A
G316.516−00.600	atca382	2013*	···	19.00 ± 1.70	-45.60 ± 0.90	19.90 ± 0.90	1.70	22.0	A
G317.405+00.091	shrds1122	2016	6456	103.00 ± 0.60	-39.40 ± 0.10	22.30 ± 0.20	1.90	110.9	A
G317.426−00.561	shrds518	2015	5792	12.60 ± 1.20	27.80 ± 0.90	18.90 ± 2.10	2.70	9.1	C
G317.458−00.533	shrds518	2015	6349	12.10 ± 0.80	27.70 ± 0.90	25.70 ± 2.10	1.70	15.7	A
G317.861+00.160	atca402	2013*	···	55.60 ± 4.60	1.53 ± 0.90	22.90 ± 0.90	2.70	44.0	A
G318.059−00.450	caswell13	2016	6254	17.70 ± 0.60	40.40 ± 0.40	27.70 ± 1.10	1.50	28.3	A
G318.233−00.605	shrds1126	2016	5969	14.50 ± 0.80	-41.40 ± 0.40	14.70 ± 0.90	1.40	17.9	A
G318.248+00.150	atca406	2013*	···	17.00 ± 3.70	-39.90 ± 2.00	19.00 ± 2.00	2.80	12.0	B
G318.726−00.222	shrds535	2016	6599	12.40 ± 0.60	-11.90 ± 0.60	27.60 ± 1.50	1.60	18.4	A
G318.774−00.150	shrds536	2015	6433	41.30 ± 0.80	-39.30 ± 0.20	21.80 ± 0.50	1.80	48.4	A
G319.188−00.329	shrds1129	2016	6197	28.10 ± 0.80	-26.30 ± 0.30	19.30 ± 0.60	1.90	29.2	A
G319.229+00.225	atca412	2013*	···	12.90 ± 2.20	-66.10 ± 1.80	20.90 ± 1.80	1.90	14.0	B

Table 4.7 continued

Table 4.7: *uv*-tapered Image RRL Properties (continued)

Target	Field	Epoch[a]	ν_L[b] (MHz)	S_L (mJy beam^{-1})	$V_{\rm LSR}$ (km s^{-1})	ΔV (km s^{-1})	rms$_L$ (mJy beam^{-1})	S/N	QF
G319.397−00.006	shrds1131	2016	5842	136.90 ± 1.40	-13.00 ± 0.10	29.70 ± 0.30	4.10	81.0	A
G319.453−00.022	shrds1131	2016	6626	25.70 ± 0.90	-20.80 ± 0.50	28.70 ± 1.20	1.90	32.9	A
G320.163+00.797	shrds1137	2016	5368	185.60 ± 1.50	-37.50 ± 0.10	29.90 ± 0.30	3.80	119.5	A
G320.205+00.867	shrds1137	2016	6467	12.50 ± 0.60	-39.00 ± 0.50	19.10 ± 1.10	1.10	21.8	A
G320.236−00.099	shrds1140	2016	6113	29.00 ± 0.90	-6.60 ± 0.30	16.80 ± 0.60	1.50	34.9	A
G320.240−00.176	shrds1139	2016	6589	7.20 ± 1.00	-5.30 ± 0.90	13.40 ± 2.10	1.90	6.3	C
G320.311−00.176	shrds1139	2016	5311	165.50 ± 3.00	-12.30 ± 0.30	31.40 ± 0.70	5.30	77.7	A
G320.376+00.172	shrds555	2015	5441	55.60 ± 2.20	0.30 ± 0.40	21.10 ± 1.00	5.00	22.9	A
G320.419+00.114	shrds555	2015	6190	26.00 ± 1.00	-6.80 ± 0.40	22.40 ± 1.00	2.30	23.9	A
G320.675+00.246	shrds559	2015	5934	9.70 ± 0.80	-56.00 ± 0.90	23.40 ± 2.20	2.10	10.0	B
G320.782+00.258	shrds1146	2016	6347	41.70 ± 1.10	-10.90 ± 0.30	21.80 ± 0.70	2.00	42.6	A
G320.799+00.187	shrds1147	2016	6246	15.20 ± 1.00	-9.50 ± 1.00	32.40 ± 2.40	1.80	21.4	A
G320.884−00.641	shrds561	2016	6130	15.10 ± 0.60	7.80 ± 0.50	24.90 ± 1.20	1.50	22.7	A
G321.725+01.169	caswell14	2016	6445	158.80 ± 1.10	-32.40 ± 0.10	25.90 ± 0.20	2.10	169.4	A
G322.162+00.625	caswell15	2016	6042	622.00 ± 2.20	-52.40 ± 0.00	28.20 ± 0.10	4.40	334.6	A
G322.706−00.330	shrds574	2015	6475	15.70 ± 0.60	-13.70 ± 0.50	24.20 ± 1.10	1.60	21.9	A
G323.449+00.095	atca449	2013	7885	12.80 ± 0.90	-75.10 ± 0.70	21.00 ± 1.70	1.60	15.8	A
G323.464−00.079a	atca450	2013	8010	29.40 ± 0.70	-67.50 ± 0.40	29.20 ± 1.00	1.30	52.7	B
G323.464−00.079b	atca450	2013	8010	5.20 ± 0.80	-105.40 ± 1.80	20.50 ± 4.60	1.30	7.8	C
G323.743−00.249	atca456	2013	7881	22.50 ± 0.60	-48.10 ± 0.20	16.70 ± 0.50	1.70	24.7	A
G323.806+00.020	atca459	2013	7617	29.90 ± 0.80	-60.30 ± 0.30	23.70 ± 0.80	2.10	30.7	A
G323.915+00.026	shrds590	2015	6499	27.60 ± 0.80	-53.80 ± 0.40	25.10 ± 0.80	1.80	33.6	A
G323.936−00.038	atca462	2013*	···	13.80 ± 5.20	-57.30 ± 4.50	24.50 ± 4.60	2.40	12.7	B
G324.201+00.117	caswell16	2016	6334	173.20 ± 2.10	-90.40 ± 0.20	34.10 ± 0.50	2.30	196.5	A
G324.642−00.321	atca466	2013	7822	35.00 ± 1.70	-47.50 ± 0.50	21.60 ± 1.20	2.70	26.2	A
G324.924−00.569	ch87.2	2013	7618	55.30 ± 1.80	-79.30 ± 0.40	26.40 ± 1.00	5.20	24.1	A
G325.108+00.053	atca472	2013	7455	15.30 ± 1.00	-62.80 ± 0.70	22.10 ± 1.70	2.20	14.7	B
G325.354−00.036	atca475	2013*	···	15.00 ± 1.50	-63.80 ± 0.60	34.40 ± 1.50	1.40	26.0	A

Table 4.7 continued

Table 4.7: *uv*-tapered Image RRL Properties (continued)

Target	Field	Epoch[a]	ν_L[b] (MHz)	S_L (mJy beam^{-1})	$V_{\rm LSR}$ (km s^{-1})	ΔV (km s^{-1})	rms$_L$ (mJy beam^{-1})	S/N	QF
G326.065−00.393	shrds1161	2016	6030	16.70 ± 0.50	-63.10 ± 0.30	20.70 ± 0.70	1.30	25.8	A
G326.446+00.901	caswell17	2016	6000	353.20 ± 2.20	-40.70 ± 0.10	26.70 ± 0.20	3.40	237.8	A
G326.467−00.382	shrds609	2015	6522	28.70 ± 0.70	-53.40 ± 0.40	35.50 ± 1.00	2.00	38.3	A
G326.657+00.588	shrds1163	2016	6062	837.90 ± 3.00	-43.70 ± 0.00	26.20 ± 0.10	7.30	259.3	A
G326.721+00.773	atca484	2013	7670	30.10 ± 1.30	-38.50 ± 0.50	22.50 ± 1.10	3.10	20.6	A
G326.728+00.616	shrds1164	2016	6661	258.10 ± 1.90	-40.70 ± 0.10	33.90 ± 0.30	2.80	234.2	A
G326.890−00.277	atca486	2013	7832	60.00 ± 1.30	-44.50 ± 0.20	19.90 ± 0.50	2.50	48.1	A
G326.916−01.100	atca487	2013	7594	19.80 ± 1.40	-51.80 ± 0.70	21.40 ± 1.80	2.50	16.0	A
G327.139−00.261	shrds618	2016	6766	18.60 ± 1.00	-66.40 ± 0.50	17.30 ± 1.10	1.50	23.0	A
G327.172−00.527	shrds1167	2016	6268	44.10 ± 1.50	-51.70 ± 0.30	19.80 ± 0.80	2.70	31.7	A
G327.300−00.548	caswell18	2016	5772	1999.60 ± 13.20	-48.60 ± 0.10	29.30 ± 0.20	20.40	235.2	A
G327.400+00.444	shrds621	2016	6511	2.80 ± 0.30	-83.70 ± 5.40	90.60 ± 15.70	1.40	8.6	C
G327.401+00.483	shrds621	2016	6099	24.10 ± 0.80	-76.70 ± 0.30	17.20 ± 0.70	1.80	25.1	A
G327.555−00.829	atca495	2013	7459	15.30 ± 1.30	-40.10 ± 1.20	28.50 ± 2.80	2.70	13.2	B
G327.714+00.576	atca498	2013	7438	10.80 ± 0.70	-50.60 ± 0.80	25.70 ± 1.80	1.70	14.1	B
G327.735−00.396	shrds628	2015	6449	70.50 ± 1.30	-71.50 ± 0.20	24.00 ± 0.50	2.40	64.2	A
G327.763+00.163	atca501	2013*	···	30.10 ± 3.40	-92.80 ± 1.20	21.60 ± 1.20	2.60	24.0	A
G327.770−00.346	shrds628	2015	5808	146.20 ± 1.80	-70.20 ± 0.10	24.80 ± 0.40	4.60	70.4	A
G327.824+00.117	atca501	2013	7206	23.10 ± 1.80	-96.50 ± 0.80	21.30 ± 1.90	4.40	10.7	B
G327.848+00.016a	shrds635	2016	5965	6.50 ± 0.90	-54.20 ± 2.10	29.50 ± 5.00	2.00	7.9	C
G327.848+00.016b	shrds635	2016	5965	6.30 ± 1.10	-105.90 ± 1.90	23.00 ± 4.50	2.00	6.8	C
G327.916+00.154	shrds639	2016	6137	9.70 ± 1.10	-96.50 ± 1.00	19.40 ± 2.50	2.00	9.5	C
G328.117+00.108	shrds647	2015	6261	32.90 ± 0.90	-104.10 ± 0.30	21.70 ± 0.70	2.00	34.6	A
G328.193−00.569	shrds652	2015	6403	121.90 ± 1.50	-43.80 ± 0.10	23.80 ± 0.30	2.40	110.1	A
G328.279−00.559	shrds659	2016	5524	51.30 ± 2.10	-43.00 ± 0.30	17.00 ± 0.80	2.80	33.3	A
G328.315−00.594	shrds659	2016	6038	32.90 ± 1.00	-41.70 ± 0.30	22.30 ± 0.80	2.10	32.6	A
G328.356−00.559	shrds659	2016	6208	25.60 ± 0.70	-49.10 ± 0.20	17.90 ± 0.50	1.40	34.1	A
G328.819−00.004	shrds668	2016	6349	10.40 ± 0.60	-31.70 ± 0.60	21.20 ± 1.30	1.30	16.5	A

Table 4.7 continued

Table 4.7: *uv*-tapered Image RRL Properties (continued)

Target	Field	Epoch[a]	ν_L[b] (MHz)	S_L (mJy beam^{-1})	$V_{\rm LSR}$ (km s^{-1})	ΔV (km s^{-1})	rms$_L$ (mJy beam^{-1})	S/N	QF
G328.825−00.081	shrds668	2016	5301	44.10 ± 1.50	-38.20 ± 0.50	28.10 ± 1.10	3.40	30.5	A
G328.945+00.570	shrds669	2015	6362	48.50 ± 1.10	-92.30 ± 0.30	24.10 ± 0.60	2.20	48.7	A
G328.961+00.248	shrds670	2015	6127	35.50 ± 1.80	-90.60 ± 0.40	16.00 ± 0.90	2.80	22.0	A
G328.962+00.207	shrds670	2015	5922	25.00 ± 1.40	-85.30 ± 0.50	17.60 ± 1.20	3.40	13.6	B
G329.266+00.111	shrds677	2015	6252	24.10 ± 1.70	-72.40 ± 0.70	21.70 ± 1.70	2.80	18.0	A
G329.422−00.160	shrds684	2015	6612	32.60 ± 0.50	-71.20 ± 0.20	22.90 ± 0.40	1.60	42.7	A
G329.460+00.174	shrds686	2015	6399	26.70 ± 0.70	-107.30 ± 0.30	23.00 ± 0.70	1.50	39.0	A
G329.472+00.214	shrds686	2015	5943	54.10 ± 1.20	-104.90 ± 0.40	33.70 ± 0.90	2.60	54.4	A
G329.474+00.839	shrds687	2016	6432	13.30 ± 0.60	-88.50 ± 0.50	22.00 ± 1.20	1.20	23.5	A
G329.601+00.059	shrds690	2015	6451	28.20 ± 0.80	-101.50 ± 0.30	23.80 ± 0.80	1.90	32.2	A
G330.673−00.388	shrds1171	2016	5680	109.50 ± 1.70	-63.80 ± 0.20	24.00 ± 0.40	3.70	63.8	A
G330.738−00.449	shrds1171	2016	6221	25.70 ± 0.80	-60.90 ± 0.30	21.20 ± 0.80	1.80	28.8	A
G330.954−00.181a	shrds709	2015	6884	50.90 ± 2.20	-89.30 ± 0.30	26.80 ± 1.10	2.80	40.9	C
G330.954−00.181b	shrds709	2015	6884	10.50 ± 2.20	-92.90 ± 2.70	82.40 ± 9.80	2.80	14.9	C
G331.056−00.437	shrds710	2016	6203	12.50 ± 0.80	-66.00 ± 0.70	23.20 ± 1.70	2.40	11.1	B
G331.123−00.530	shrds717	2015	6068	147.20 ± 1.70	-68.30 ± 0.10	21.80 ± 0.30	3.50	87.6	A
G331.129−00.243a	shrds716	2015	6471	34.90 ± 1.00	-84.40 ± 0.40	23.30 ± 1.00	1.80	41.3	B
G331.129−00.243b	shrds716	2015	6471	20.50 ± 1.30	-59.30 ± 0.50	13.90 ± 1.20	1.80	18.7	B
G331.145+00.133	shrds719	2015	6404	14.80 ± 0.50	-74.60 ± 0.40	25.70 ± 1.00	1.70	19.2	A
G331.156−00.391	shrds720	2015	6221	48.40 ± 1.20	-63.00 ± 0.20	20.10 ± 0.60	2.60	36.7	A
G331.172−00.460	shrds721	2015	6372	60.40 ± 1.20	-71.00 ± 0.20	22.00 ± 0.50	2.50	50.2	A
G331.249+01.071	shrds1174	2016	6288	29.00 ± 0.70	-82.00 ± 0.30	24.20 ± 0.70	2.10	30.7	A
G331.259−00.188	shrds725	2016	5797	164.00 ± 1.00	-80.80 ± 0.10	24.40 ± 0.20	2.80	130.3	A
G331.322−00.176	shrds725	2016	6614	16.40 ± 0.40	-47.60 ± 0.20	17.10 ± 0.50	1.20	25.2	A
G331.361−00.019	shrds729	2015	5659	151.20 ± 3.10	-81.50 ± 0.20	24.10 ± 0.60	7.60	43.3	A
G331.384−00.358	shrds731	2015	6287	51.20 ± 1.20	-68.20 ± 0.30	23.60 ± 0.60	3.00	36.8	A
G331.412+00.011	shrds729	2015	6195	21.80 ± 1.20	0.10 ± 0.70	27.00 ± 1.70	2.70	18.4	A
G331.417−00.354	shrds731	2015	6643	22.50 ± 0.60	-67.60 ± 0.30	23.70 ± 0.70	1.80	27.2	A

Table 4.7 continued

Table 4.7: *uv*-tapered Image RRL Properties (continued)

Target	Field	Epoch[a]	ν_L[b] (MHz)	S_L (mJy beam^{-1})	$V_{\rm LSR}$ (km s^{-1})	ΔV (km s^{-1})	rms$_L$ (mJy beam^{-1})	S/N	QF
G331.520−00.076	shrds736	2015	5333	671.80 ± 5.30	-91.50 ± 0.10	25.80 ± 0.20	14.80	102.2	A
G331.538−00.308a	shrds735	2015	6435	14.00 ± 0.90	-96.30 ± 0.60	20.60 ± 1.50	1.50	19.1	B
G331.538−00.308b	shrds735	2015	6435	5.10 ± 0.90	-60.20 ± 1.70	19.60 ± 4.10	1.50	6.8	B
G331.560+00.091	shrds737	2015	5974	76.00 ± 1.90	-88.30 ± 0.20	14.50 ± 0.40	2.60	50.1	A
G331.653+00.128	shrds741	2015	5995	41.60 ± 1.20	-91.10 ± 0.30	18.40 ± 0.60	2.10	38.5	A
G331.744−00.068	shrds743	2015	6382	26.20 ± 1.10	-89.40 ± 0.50	25.70 ± 1.20	2.70	21.8	A
G331.834−00.002	shrds746	2016	5970	17.60 ± 0.90	-81.40 ± 0.60	24.30 ± 1.40	1.40	27.4	A
G332.145−00.452	shrds753	2015	5396	420.20 ± 7.70	-55.10 ± 0.30	34.60 ± 0.70	12.50	87.4	A
G332.291−00.092	shrds756	2015	6494	31.80 ± 0.80	-48.20 ± 0.30	22.50 ± 0.70	1.90	35.3	A
G332.311−00.567	shrds759	2015	6340	29.30 ± 1.00	-56.30 ± 0.30	17.30 ± 0.70	1.80	30.5	A
G332.382+00.080	shrds763	2015	5935	15.00 ± 1.10	-42.20 ± 0.70	18.40 ± 1.60	2.00	14.5	B
G332.585−00.561	shrds771	2015	6582	18.80 ± 1.30	-51.40 ± 0.70	21.40 ± 1.70	2.80	13.7	B
G332.657−00.622	shrds771	2015	5380	355.60 ± 5.90	-47.20 ± 0.20	24.30 ± 0.50	13.10	59.4	A
G332.766−00.006	shrds774	2015	6428	22.90 ± 1.00	-97.00 ± 0.50	24.10 ± 1.20	1.70	30.0	A
G332.823−00.550a	shrds777	2015	6044	151.40 ± 2.10	-60.00 ± 0.40	33.30 ± 0.90	4.90	79.1	C
G332.823−00.550b	shrds777	2015	6044	26.40 ± 2.70	-94.70 ± 1.80	24.00 ± 3.90	4.90	11.7	C
G332.957+01.793	shrds782	2016	6032	8.20 ± 0.50	-27.50 ± 1.00	29.50 ± 2.30	1.30	15.0	A
G332.987+00.902	shrds784	2016	6083	17.60 ± 0.70	-45.40 ± 0.40	20.00 ± 1.00	1.20	28.7	A
G332.990−00.619	shrds785	2015	5978	75.30 ± 2.00	-49.20 ± 0.30	18.90 ± 0.60	2.70	53.1	A
G333.011−00.441	shrds789	2015	5384	301.30 ± 6.50	-55.70 ± 0.20	18.70 ± 0.50	12.50	46.0	A
G333.052+00.033	shrds788	2015	6240	30.70 ± 1.40	-39.60 ± 0.60	28.50 ± 1.50	2.90	25.2	A
G333.085−00.479	shrds789	2015	6289	157.40 ± 2.20	-53.70 ± 0.20	22.90 ± 0.40	8.00	41.9	A
G333.129−00.439	shrds789	2015	5341	676.40 ± 5.00	-48.20 ± 0.10	28.00 ± 0.20	15.00	105.7	A
G333.164−00.100	shrds792	2015	5899	80.80 ± 1.80	-93.40 ± 0.30	24.80 ± 0.60	3.90	45.3	A
G333.255+00.065	shrds794	2015	5970	110.60 ± 1.20	-52.20 ± 0.10	25.50 ± 0.30	3.20	77.9	A
G333.467−00.159	shrds799	2015	6179	121.60 ± 1.70	-41.70 ± 0.10	21.40 ± 0.30	3.90	63.6	A
G333.534−00.383	shrds801	2015	5956	39.80 ± 1.60	-56.00 ± 0.40	19.10 ± 0.90	2.80	27.7	A
G333.580+00.058	shrds802	2016	7078	6.20 ± 0.60	-84.00 ± 1.60	31.10 ± 4.10	1.80	8.6	C

Table 4.7 continued

Table 4.7: *uv*-tapered Image RRL Properties (continued)

Target	Field	Epoch[a]	ν_L[b] (MHz)	S_L (mJy beam^{-1})	$V_{\rm LSR}$ (km s^{-1})	ΔV (km s^{-1})	rms$_L$ (mJy beam^{-1})	S/N	QF
G333.627−00.199a	caswell19	2016	5676	1853.30 ± 15.50	-46.50 ± 0.50	42.50 ± 0.80	35.20	152.1	C
G333.627−00.199b	caswell19	2016	5676	281.10 ± 31.30	-83.00 ± 2.10	31.60 ± 3.30	35.20	19.9	C
G333.681−00.441	shrds804	2015	5663	17.70 ± 1.60	-1.60 ± 1.40	32.90 ± 3.40	4.10	10.9	B
G333.725+00.364	shrds803	2015	6335	35.50 ± 1.20	-27.10 ± 0.40	23.70 ± 0.90	2.40	31.4	A
G333.733−00.429	shrds804	2015	6439	13.80 ± 1.00	-6.90 ± 1.20	31.00 ± 2.90	2.50	13.7	B
G333.962+00.063	shrds806	2015	6368	14.80 ± 0.80	-64.50 ± 0.60	22.20 ± 1.40	1.80	17.2	A
G334.022+00.106	shrds807	2016	6183	7.10 ± 1.00	-64.60 ± 1.40	20.70 ± 3.40	1.90	7.4	C
G334.202+00.193	shrds811	2015	6286	31.50 ± 1.20	-95.10 ± 0.50	26.00 ± 1.10	2.70	26.2	A
G334.341+00.045	shrds814	2015	6299	38.80 ± 1.00	-66.90 ± 0.30	25.70 ± 0.80	2.40	36.2	A
G334.400−00.523	shrds815	2016	6069	4.90 ± 0.90	-10.70 ± 1.80	21.30 ± 4.30	2.30	4.4	C
G334.646+00.442	shrds825	2015	6117	22.10 ± 1.00	-64.90 ± 0.50	25.20 ± 1.30	2.20	22.6	A
G334.721−00.653	caswell20	2016	6152	40.70 ± 1.10	14.80 ± 0.50	38.40 ± 1.20	2.70	41.9	A
G334.774−00.023	shrds828	2015	6433	34.70 ± 1.20	-26.40 ± 0.40	24.00 ± 1.00	3.20	23.6	A
G335.195−00.385	shrds836	2016	6065	5.30 ± 1.00	-4.60 ± 2.40	25.80 ± 5.60	2.10	5.8	C
G335.579−00.209	shrds841	2016	6529	13.80 ± 0.70	-79.60 ± 0.80	32.10 ± 1.80	1.40	24.9	A
G336.026−00.817	shrds843	2015	6042	49.80 ± 1.20	-46.00 ± 0.20	21.00 ± 0.60	2.60	38.4	A
G336.367−00.003	shrds852	2015	6351	60.40 ± 1.70	-130.70 ± 0.30	24.50 ± 0.80	3.20	41.3	A
G336.418−00.249	shrds853	2016	5982	71.10 ± 0.80	-86.90 ± 0.20	30.40 ± 0.40	2.50	69.2	A
G336.491−01.474	caswell21	2016	6069	426.40 ± 5.10	-23.60 ± 0.20	25.90 ± 0.40	6.10	158.6	A
G336.585+00.019	shrds857	2015	6039	10.00 ± 1.70	-80.50 ± 1.20	14.70 ± 2.90	2.10	8.1	C
G336.854−00.018	shrds1212	2016	6048	125.10 ± 2.90	-70.70 ± 0.30	27.60 ± 0.70	4.70	62.2	A
G336.874+00.139	shrds1209	2016	6303	52.60 ± 1.20	-80.00 ± 0.20	18.50 ± 0.50	2.10	48.2	A
G336.888+00.057	shrds1212	2016	6308	90.70 ± 2.10	-122.90 ± 0.30	26.30 ± 0.70	4.40	46.8	C
G336.990−00.021a	shrds862	2015	6123	31.30 ± 1.20	-116.80 ± 0.90	34.10 ± 2.30	2.80	29.2	C
G336.990−00.021b	shrds862	2015	6123	11.10 ± 1.70	-83.80 ± 1.80	19.20 ± 4.00	2.80	7.8	C
G337.004+00.322	shrds865	2015	6482	19.00 ± 1.80	-59.20 ± 1.20	26.50 ± 2.90	3.70	11.7	B
G337.091−00.965	shrds867	2015	5981	11.20 ± 2.10	-47.40 ± 1.60	17.80 ± 3.80	3.60	5.8	C
G337.170−00.059a	shrds869	2015	6073	30.50 ± 1.20	-69.60 ± 0.40	21.40 ± 1.00	2.30	26.9	B

Table 4.7 continued

Table 4.7: *uv*-tapered Image RRL Properties (continued)

Target	Field	Epoch[a]	ν_L[b] (MHz)	S_L (mJy beam^{-1})	$V_{\rm LSR}$ (km s^{-1})	ΔV (km s^{-1})	rms$_L$ (mJy beam^{-1})	S/N	QF
G337.170−00.059b	shrds869	2015	6073	14.70 ± 1.10	-113.60 ± 1.00	26.60 ± 2.40	2.30	14.5	B
G337.253−00.165	shrds870	2015	6188	45.60 ± 1.10	-38.30 ± 0.30	28.20 ± 0.80	3.10	34.3	A
G337.286+00.113	shrds871	2015	6136	29.10 ± 1.10	-107.80 ± 0.40	20.10 ± 0.80	1.90	30.2	A
G337.404−00.404	shrds875	2015	6273	5.60 ± 0.60	-33.00 ± 2.40	44.50 ± 5.70	1.80	9.1	C
G337.617−00.065	shrds880	2015	6510	64.20 ± 1.30	-51.50 ± 0.20	23.00 ± 0.50	3.10	43.5	A
G337.664+00.049	shrds886	2015	5660	20.60 ± 1.80	-51.80 ± 0.80	18.90 ± 1.90	3.90	10.2	B
G337.665−00.176	shrds883	2015	6184	45.30 ± 1.20	-50.30 ± 0.40	28.40 ± 0.90	2.80	38.3	A
G337.684−00.343	shrds884	2015	5689	32.40 ± 1.50	-39.30 ± 0.60	27.30 ± 1.50	2.60	29.4	A
G337.705−00.059	shrds885	2015	6332	43.70 ± 2.70	-45.40 ± 0.60	20.80 ± 1.50	4.40	19.8	A
G337.709+00.091	shrds886	2015	6184	33.60 ± 1.60	-78.80 ± 0.70	28.60 ± 1.60	2.70	29.0	A
G337.754+00.057a	shrds888	2015	6020	12.10 ± 0.90	-49.60 ± 0.60	17.40 ± 1.50	1.70	13.2	B
G337.754+00.057b	shrds888	2015	6020	5.40 ± 0.80	-124.20 ± 1.80	25.70 ± 4.20	1.70	7.1	C
G337.827+00.056	shrds888	2015	5896	17.20 ± 1.00	-127.40 ± 0.50	19.50 ± 1.30	1.80	19.1	A
G338.003−00.121	shrds891	2015	6130	31.60 ± 1.60	-53.30 ± 0.60	22.30 ± 1.30	2.60	24.9	A
G338.009+00.016	shrds892	2015	6192	56.70 ± 1.50	-59.40 ± 0.30	22.50 ± 0.70	2.30	52.8	A
G338.066−00.069	shrds1219	2016	6534	27.80 ± 2.40	-33.70 ± 1.00	22.90 ± 2.20	2.00	28.9	A
G338.075+00.016	shrds893	2015	5996	142.60 ± 1.80	-37.10 ± 0.20	30.20 ± 0.40	3.40	102.4	A
G338.106+00.020	shrds893	2015	6072	32.50 ± 1.10	-43.80 ± 0.40	21.20 ± 0.90	2.80	23.5	A
G338.263−00.364	shrds894	2015	6191	11.70 ± 1.00	-13.00 ± 0.60	15.50 ± 1.50	1.80	11.2	B
G338.289−00.373	shrds894	2015	6305	13.70 ± 0.90	-7.20 ± 0.80	27.00 ± 2.00	1.90	16.4	A
G338.360−00.095	shrds896	2015	6279	29.10 ± 1.40	-39.10 ± 0.50	22.20 ± 1.20	3.50	17.4	A
G338.364−00.020	shrds896	2015	5709	57.70 ± 2.80	-58.30 ± 0.50	21.40 ± 1.20	7.20	16.4	A
G338.405−00.203	caswell22	2016	6235	126.70 ± 1.20	0.00 ± 0.20	34.10 ± 0.40	2.70	119.4	A
G338.462−00.262	shrds898	2015	6397	45.30 ± 1.30	-57.60 ± 0.40	25.20 ± 0.90	2.60	38.3	A
G338.565−00.151	shrds899	2015	6317	35.70 ± 0.70	-115.10 ± 0.20	25.90 ± 0.60	2.10	37.5	A
G338.576+00.020	shrds900	2015	6485	70.50 ± 1.00	-24.20 ± 0.10	20.10 ± 0.30	2.70	52.3	A
G338.628+00.145a	shrds901	2015	6222	10.20 ± 0.90	-37.00 ± 6.30	84.20 ± 16.50	3.10	13.4	C
G338.628+00.145b	shrds901	2015	6222	3.10 ± 1.40	-116.10 ± 14.30	51.10 ± 35.00	3.10	3.2	C

Table 4.7 continued

Table 4.7: *uv*-tapered Image RRL Properties (continued)

Target	Field	Epoch[a]	ν_L[b] (MHz)	S_L (mJy beam^{-1})	$V_{\rm LSR}$ (km s^{-1})	ΔV (km s^{-1})	rms$_L$ (mJy beam^{-1})	S/N	QF
G338.706+00.645	shrds1223	2016	5620	30.40 ± 1.70	-57.50 ± 0.30	11.30 ± 0.70	2.20	21.1	A
G338.837−00.318	shrds904	2015	6086	20.40 ± 0.90	-122.40 ± 0.40	19.00 ± 0.90	1.90	20.6	A
G338.851+00.405	shrds905	2015	5961	7.20 ± 0.80	-51.50 ± 1.10	21.40 ± 2.70	2.00	7.3	C
G338.861+00.597	shrds1223	2016	6207	16.90 ± 1.00	-69.40 ± 0.30	11.60 ± 0.80	1.00	25.0	A
G338.883+00.537	shrds1225	2016	6066	12.50 ± 0.80	-59.00 ± 0.60	21.00 ± 1.50	1.20	20.9	A
G338.911+00.615	shrds1225	2016	5649	91.50 ± 1.30	-66.10 ± 0.20	21.40 ± 0.40	3.10	60.3	A
G338.926+00.392	shrds906	2015	6169	50.10 ± 1.50	-26.80 ± 0.40	24.00 ± 0.80	2.60	41.2	A
G339.106+00.152	shrds909	2015	6282	28.00 ± 1.00	-86.80 ± 0.40	22.70 ± 0.90	1.70	35.3	A
G339.169−00.698	shrds910	2015	6259	8.10 ± 1.50	-50.50 ± 0.80	8.90 ± 1.90	1.80	6.1	C
G339.275−00.607	shrds915	2015	6110	16.60 ± 1.00	-40.10 ± 0.60	22.50 ± 1.50	1.80	19.2	A
G339.478+00.181	shrds917	2015	6284	33.80 ± 0.80	-84.10 ± 0.20	19.00 ± 0.50	1.80	36.7	A
G339.486+00.087	shrds918	2015	6180	33.80 ± 1.60	-116.70 ± 0.50	22.00 ± 1.20	2.80	24.8	A
G339.553−00.401	shrds919	2015	5934	13.70 ± 0.90	-51.70 ± 1.40	42.00 ± 3.50	2.90	13.5	B
G339.556+00.282	shrds920	2015	6055	23.50 ± 1.00	-43.90 ± 0.50	22.30 ± 1.10	2.10	23.9	A
G339.584+00.084	shrds921	2015	6227	35.70 ± 0.80	-113.90 ± 0.20	20.80 ± 0.60	2.00	36.9	A
G339.676+00.283	shrds922	2016	5977	5.90 ± 1.20	-92.80 ± 2.30	22.80 ± 5.40	2.60	4.8	C
G339.717−01.211	shrds925	2015	6402	23.80 ± 0.80	-33.40 ± 0.30	20.80 ± 0.80	1.80	26.7	A
G339.952+00.052	shrds1234	2016	6205	12.20 ± 0.60	-123.00 ± 0.50	23.80 ± 1.30	1.50	17.4	A
G340.059−00.138	shrds1236	2016	5903	45.60 ± 1.00	-51.70 ± 0.20	19.70 ± 0.50	2.30	38.7	A
G340.296−00.276	shrds1237	2016	6473	13.90 ± 0.80	-44.90 ± 0.50	17.60 ± 1.10	1.40	18.8	A
G342.062+00.417	caswell23	2016	6067	154.90 ± 1.70	-68.50 ± 0.20	28.20 ± 0.40	4.40	82.6	A
G342.360+00.107	shrds1238	2016	5496	11.30 ± 1.20	-94.60 ± 1.30	25.50 ± 3.10	3.20	7.9	C
G342.388+00.074	shrds1238	2016	5775	8.00 ± 1.40	-118.80 ± 1.50	17.70 ± 3.50	2.30	6.4	C
G342.438−00.061	shrds1239	2016	6430	8.50 ± 0.90	-2.40 ± 1.10	20.50 ± 2.50	1.70	10.2	B
G343.224−00.065	shrds1240	2016	6041	9.20 ± 0.70	1.20 ± 0.70	17.70 ± 1.70	1.50	11.7	B
G343.352−00.081	shrds1241	2016	6664	20.10 ± 0.90	-130.50 ± 0.50	24.40 ± 1.20	1.80	24.6	A
G343.914−00.646	caswell24	2016	6074	27.50 ± 0.90	-26.80 ± 0.30	16.30 ± 0.60	1.70	29.4	A
G344.424+00.044	caswell25	2016	6295	206.60 ± 1.70	-63.80 ± 0.10	28.00 ± 0.30	2.30	214.6	A

Table 4.7 continued

Table 4.7: *uv*-tapered Image RRL Properties (continued)

Target	Field	Epoch[a]	ν_L[b] (MHz)	S_L (mJy beam^{-1})	$V_{\rm LSR}$ (km s^{-1})	ΔV (km s^{-1})	rms$_L$ (mJy beam^{-1})	S/N	QF
G348.892−00.179	fa644	2015	6413	21.40 ± 1.00	11.00 ± 0.60	28.00 ± 1.50	2.30	21.6	A
G349.328+00.020	gs038	2015	6358	16.60 ± 1.30	14.90 ± 1.00	26.00 ± 2.40	2.50	15.2	A
G352.313−00.442	fa016	2015	6237	20.00 ± 1.30	-12.80 ± 0.70	23.50 ± 1.80	2.80	15.5	A
G355.344+00.145	fa032	2015	6320	24.10 ± 1.30	19.40 ± 0.90	35.00 ± 2.20	2.50	25.0	A
G358.600−00.058	gs108	2015	6076	44.80 ± 1.10	-211.50 ± 0.30	22.90 ± 0.70	2.80	33.6	A
G358.633+00.062	fa054	2015	6263	27.20 ± 1.30	14.70 ± 0.60	26.00 ± 1.50	2.60	24.0	A
G359.467−00.173	fa489	2015	5943	15.30 ± 1.30	-70.80 ± 1.00	22.20 ± 2.20	2.40	13.0	B

[a] Rows with epochs with an asterisk (*) are copied directly from Brown et al. (2017). They did not give the weigted-average frequency of their H$n\alpha$ RRL spectra.

[b] This is the weighted-average frequency of the <H$n\alpha$> spectrum.

larger SHRDS velocities. The mean velocity difference is $1.1\pm0.4\,\mathrm{km\,s^{-1}}$ with a standard deviation of 3.2 $\mathrm{km\,s^{-1}}$ for the non-tapered sample. For the *uv*-tapered sample, the mean difference is $0.8\pm0.3\,\mathrm{km\,s^{-1}}$ with a standard deviation of $2.8\,\mathrm{km\,s^{-1}}$. This scatter is comparable to the spectral resolution of the SHRDS and the Caswell & Haynes (1987) survey ($\sim$2.5 $\mathrm{km\,s^{-1}}$).

Similarly, the FWHM line width differences are centered around zero with more scatter toward larger SHRDS line widths, some of which are nearly a factor of two larger than previous measurements. We compute the fractional difference between the SHRDS-measured FWHM line width, $\Delta\nu_{\mathrm{SHRDS}}$, and the previously measured value, $\Delta\nu_{\mathrm{Old}}$, as $(\Delta\nu_{\mathrm{SHRDS}} - \Delta\nu_{\mathrm{Old}})/\Delta\nu_{\mathrm{Old}}$. The mean FWHM line width fractional difference is $3\pm3\%$ with a standard deviation of 30% for the non-tapered sample and is $7\pm8\%$ with a standard deviation of 32% for the *uv*-tapered sample. The large scatter in the line widths is probably an artifact of the different spatial scales probed by an interferometer and a single-dish telescope.

There is no difference in the distribution of <H$n\alpha$> RRL FWHM line widths in the SHRDS and those in the *WISE* Catalog, nor a difference between the non-tapered and *uv*-tapered FWHM line width distributions. Figure 4.7 shows the RRL line widths of all known H II regions with RRL measurements in the *WISE* Catalog and all of the RRL line widths measured in the SHRDS, both non-tapered and *uv*-tapered. Each distribution peaks near $\sim$23 km s^{-1} and has a long tail toward large FWHMs. The mean FWHM line widths are 25 km s^{-1} in each sample. The similarity of the SHRDS and *WISE* Catalog line width distributions implies that the physical conditions (e.g., internal turbulence) of H II regions are comparable between the SHRDS survey zone and the rest of the Galaxy.

The Galactic longitude–velocity (ℓ-v) diagram that includes the nebulae discovered here shows interesting structure in the fourth Galactic quadrant. Figure 4.8 is the ℓ-v diagram of all previously known and SHRDS-discovered H II regions with LSR velocities $|V_{\mathrm{LSR}}| < 150\,\mathrm{km\ s^{-1}}$, and Figure 4.9 is zoomed-in on the fourth Galactic quadrant. The SHRDS nebulae are constrained to $V_{\mathrm{LSR}} < 50\,\mathrm{km\,s^{-1}}$ in the fourth quadrant, which is likely due to a lack of sensitivity. In the next data release, we will target fainter and, perhaps more distant, H II regions, which may fill in this region of the ℓ-v diagram.

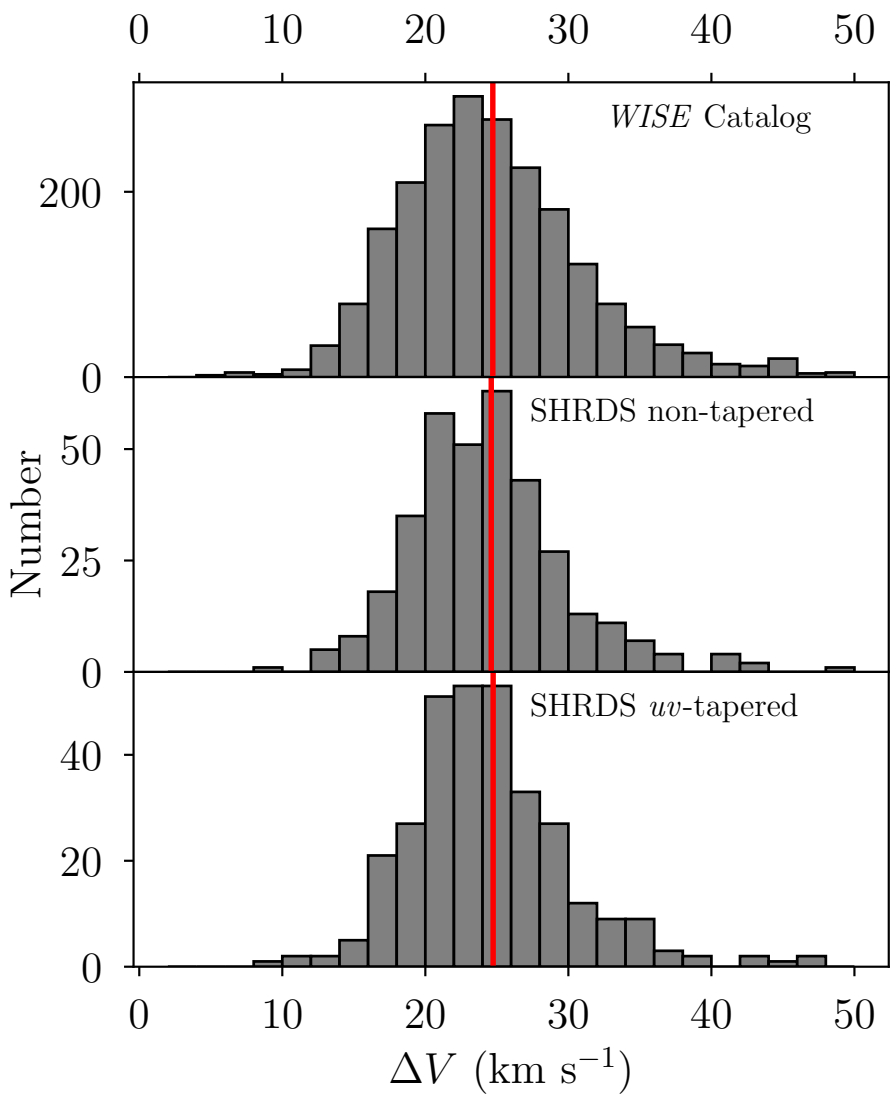

Figure 4.7: Distribution of <H$n\alpha$> RRL FWHM line widths, ΔV, for all previously known H II regions in the *WISE* Catalog (top; $n = 2148$), SHRDS non-tapered detections (middle; $n = 353$), and SHRDS *uv*-tapered detections (bottom; $n = 317$), excluding 16 sources from the *WISE* Catalog and 2 sources from the SHRDS with $\Delta V > 50\,\mathrm{km\,s^{-1}}$. The mean of each sample is indicated by the vertical red line: $24.7\,\mathrm{km\,s^{-1}}$ for the *WISE* Catalog, $24.6\,\mathrm{km\,s^{-1}}$ for the non-tapered SHRDS, and $24.7\,\mathrm{km\,s^{-1}}$ for the *uv*-tapered SHRDS.

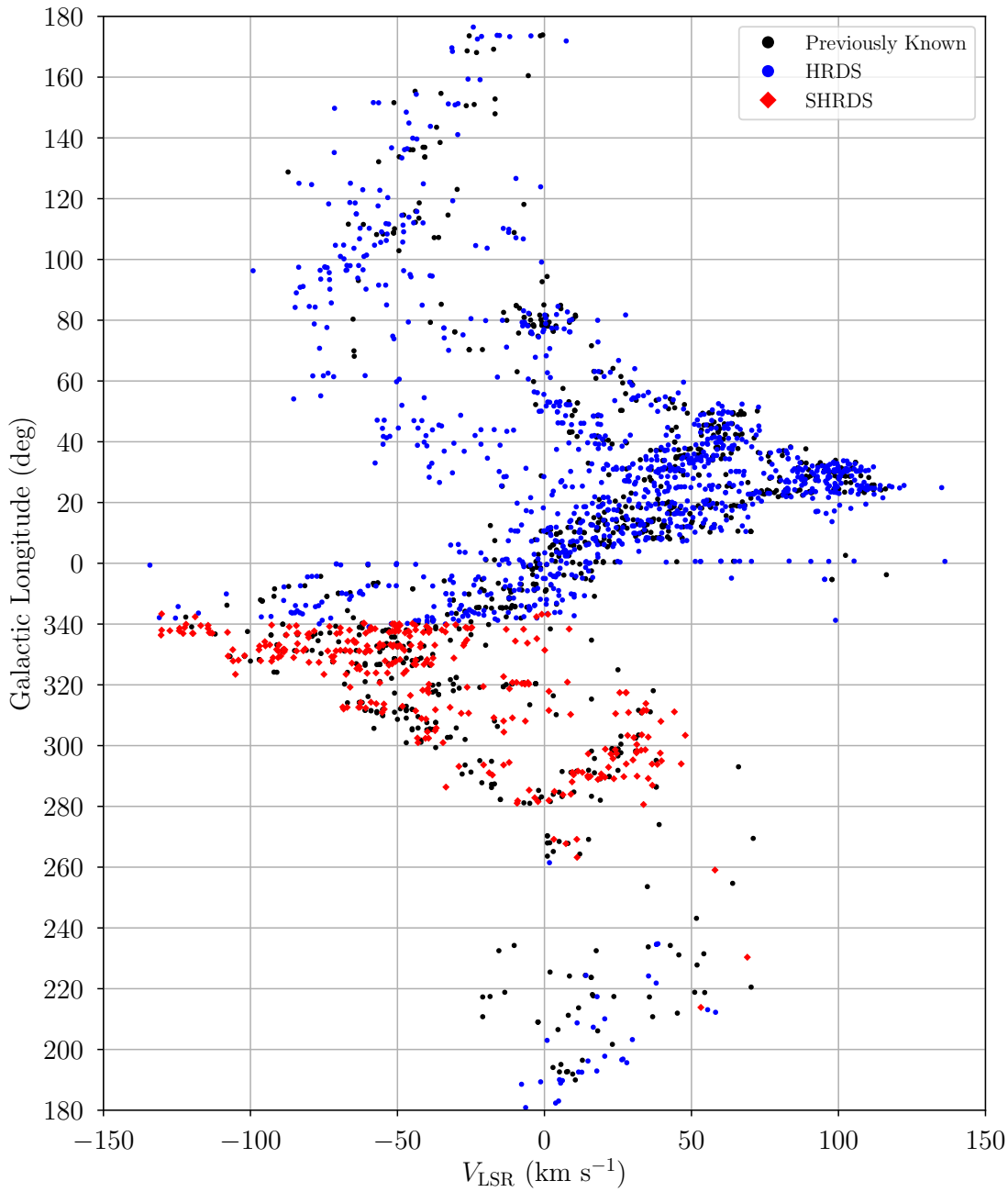

Figure 4.8: Galactic longitude, ℓ, as a function of LSR velocity, $V_{\rm LSR}$, for all known Galactic H II regions with $|V_{\rm LSR}| < 150\,{\rm km\,s^{-1}}$. Black points are H II regions known prior to the GBT HRDS, blue points are H II regions discovered by the GBT and Arecibo HRDS and their extensions, and red diamonds are H II regions in the SHRDS Bright Catalog.

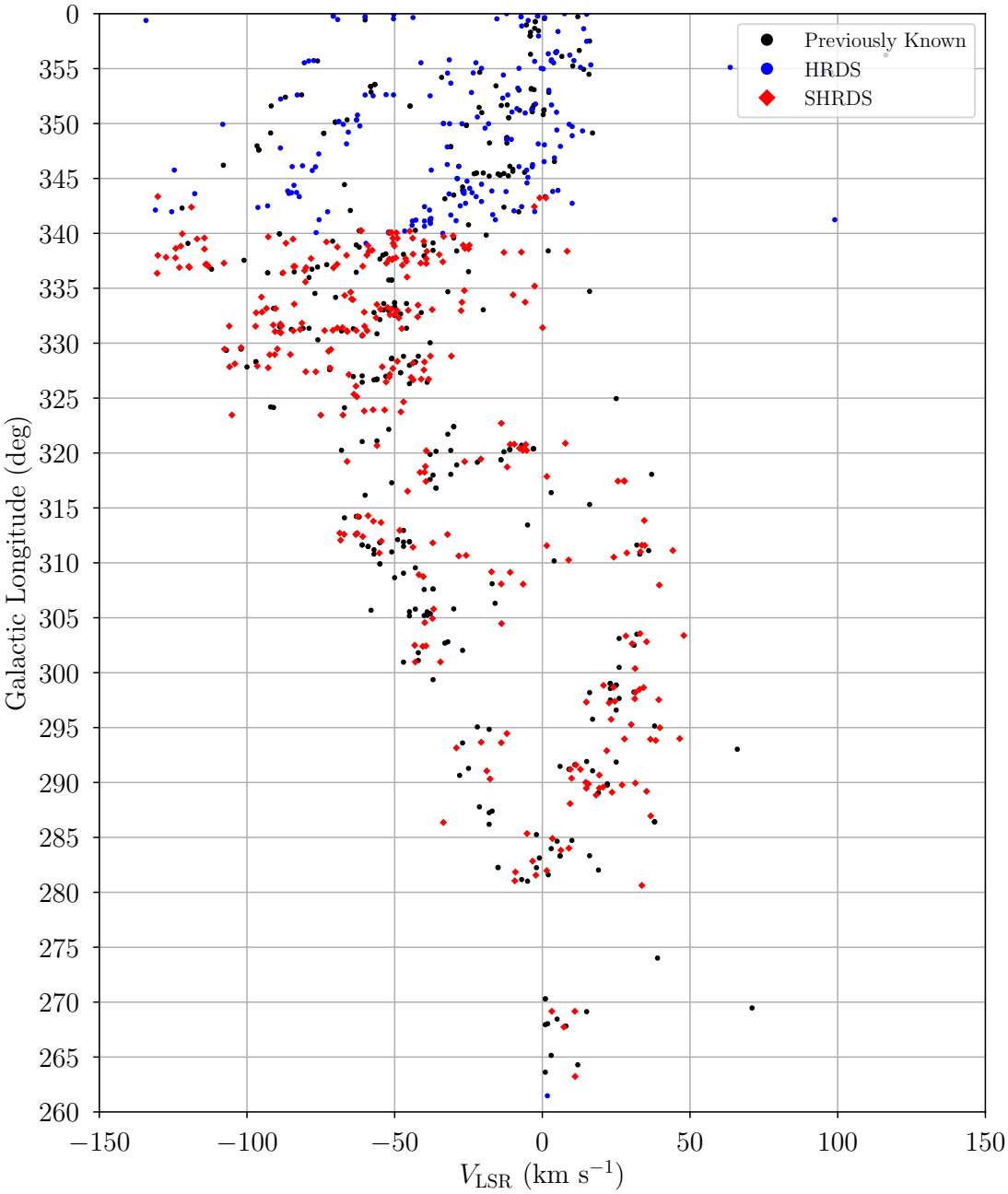

Figure 4.9: Same as Figure 4.8, but zoomed-in on the fourth Galactic quadrant.

4.6.1 Survey Completeness

Following the strategy of Anderson et al. (2011), we estimate the completeness of the Bright Catalog to be the point at which the flux density distribution of SHRDS nebulae begins to deviate from a power law. Assuming that the Galactic H II region luminosity function is a power law (e.g. Smith & Kennicutt, 1989; McKee & Williams, 1997) and that the distribution of nebulae is relatively smooth across the disk, the distribution of H II region flux densities should be a power law as well. In this data release, we only measure peak flux densities. These flux densities will underestimate the total flux densities of resolved sources and, therefore, this analysis is not a representation of the true H II region luminosity function. In the next data release, we will measure the total flux densities of all SHRDS nebulae and reassess the SHRDS completeness limit.

Figure 4.10 shows the distribution of SHRDS peak continuum flux densities in both the non-tapered and *uv*-tapered data. Both distributions follow a power law at the brighter end. We estimate the completeness of the continuum catalog as the point when these distributions begin to deviate from a power law: $\sim$125 mJy beam^{-1} in the non-tapered catalog and $\sim$200 mJy beam^{-1} in the *uv*-tapered catalog. Similar distributions are shown in Figure 4.11 for the distribution of <H$n\alpha$> RRL flux densities. The completeness of the RRL catalog as inferred from these distributions is ten times lower than that of the continuum catalog, as expected for a typical RRL-to-continuum intensity ratio of 0.1 at these frequencies.

Our non-tapered completeness limit ($\sim$125 mJy beam^{-1}) is more than twice our target selection criterion (60 mJy beam^{-1}). This difference is likely due to the uncertainty in extrapolating H II region flux densities from SUMSS 843 MHz to 6 GHz. Figure 4.12 shows the fractional difference between the measured and predicted peak continuum flux densities for both our non-tapered and *uv*-tapered catalogs. Here, the SHRDS continuum fluxes are scaled from their observed frequencies to 6 GHz assuming a spectral index of $\alpha = -0.1$. The mean difference for the non-tapered data is -6% (overpredicted) and for the *uv*-tapered data is 54% (underpredicted). In both cases, the standard deviation is $\sim$100%. Anderson et al. (2011) found a similar scatter when extrapolating from $\sim$1.4 GHz to 10 GHz. This suggests that many H II regions are optically thick at and below 1.4 GHz.

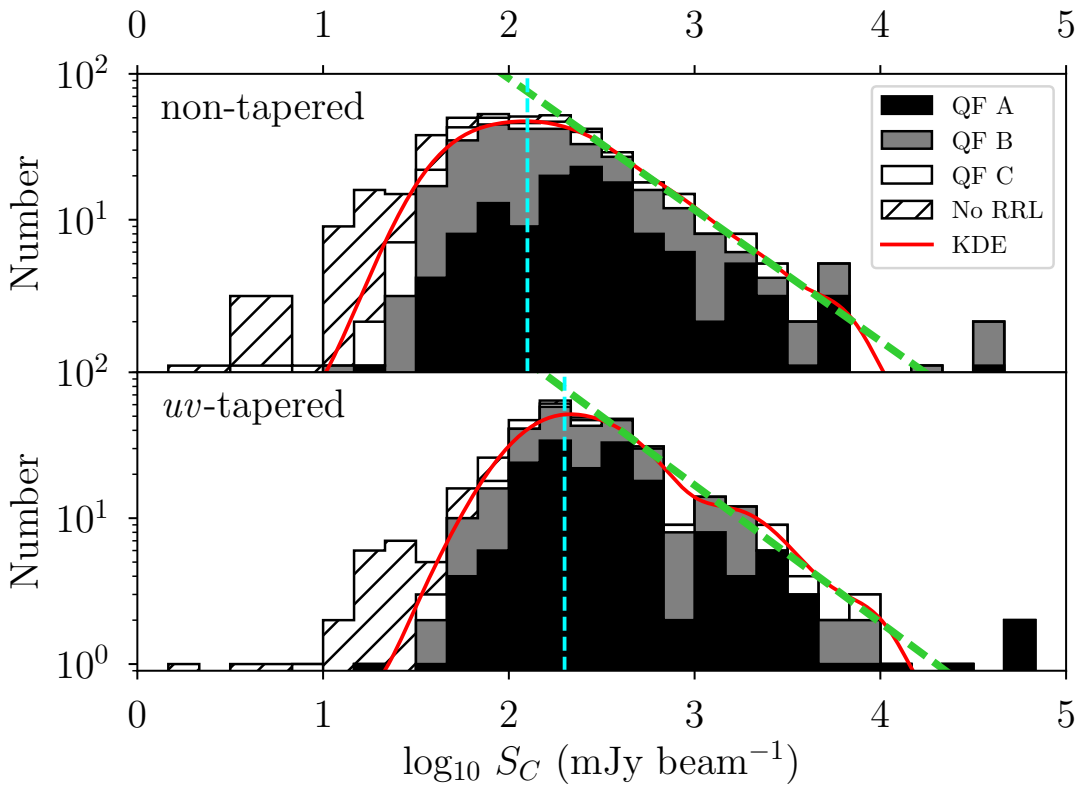

Figure 4.10: Distribution of peak continuum flux densities for the non-tapered (top) and *uv*-tapered (bottom) SHRDS data. The shaded regions represent the contribution from sources of each continuum QF with a detected RRL (QF A in black, QF B in gray, and QF C in white), and the hatched regions represent the contribution from sources without a detected RRL. The red curves are the Gaussian kernel density estimator (KDE) fits to the distributions, and the green dashed curves are the power laws fit to a subset of the KDEs. The vertical cyan dashed lines represent the estimated continuum completeness limit of the SHRDS: 125 mJy beam^{-1} (non-tapered) and 200 mJy beam^{-1} (tapered) at $\sim$7 GHz.

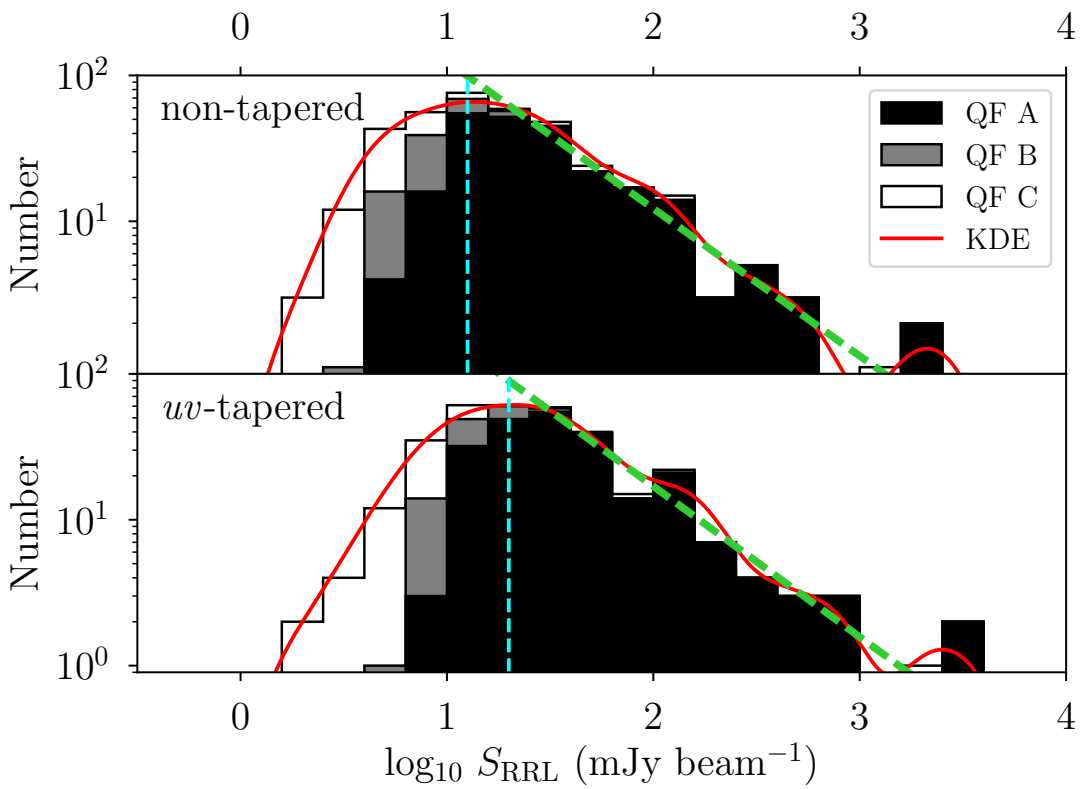

Figure 4.11: Distribution of <H$n\alpha$> RRL flux densities (see Figure 4.10). We estimate the ∼7 GHz RRL completeness to be 12.5 mJy beam^{-1} in the non-tapered data and 20 mJy beam^{-1} in the *uv*-tapered data.

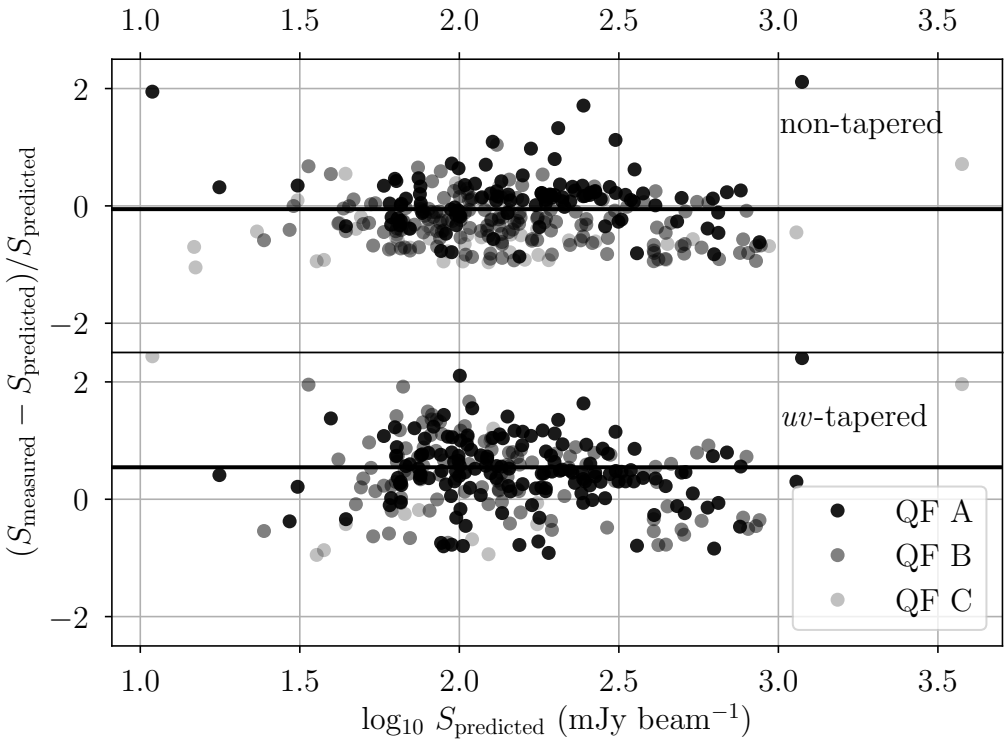

Figure 4.12: Fractional difference between the measured 6 GHz peak continuum flux densities and predicted flux densities, as extrapolated from SUMSS. There are 313 non-tapered continuum detections (top) and 278 *uv*-tapered continuum detections (bottom) with SUMSS predicted fluxes in the *WISE* Catalog. Five sources with differences > 250% are excluded from each sample for clarity. The SHRDS peak continuum flux densities are extrapolated from their measured frequencies to 6 GHz assuming a spectral index of $\alpha = -0.1$. The transparency of the points represents the continuum quality factor of the detection: QF A (opaque), QF B (slightly transparent), and QF C (mostly transparent). The horizontal solid lines indicate the mean fractional difference: -6% (non-tapered) and 54% (*uv*-tapered).

4.7 Summary and Future Work

The SHRDS has already nearly doubled the number of known Galactic H II regions in the longitude range $259° < \ell < 344°$. In this first data release, the Bright Catalog, we report the detection of 256 new nebulae. We observe 282 fields and find continuum emission toward H II regions or H II region candidates in 275 (97.5%) and RRL emission in 258 (91.5%) of them. We estimate that the SHRDS Bright Catalog is complete for all H II regions with 7GHz peak continuum flux densities brighter than 125 mJy beam^{-1} in the surveyed zone.

We detect RRL emission from 76 previously known H II regions and find that the SHRDS RRL properties are similar to previous measurements. The mean LSR velocity difference between our measurements and those in the *WISE* Catalog is 1.1 km s^{-1} with a standard deviation of 3.2 km s^{-1}. This scatter is likely due to the velocity resolution of the SHRDS and previous observations. The mean FWHM line width difference is 3% with a standard deviation of 30%. All previous H II region surveys used single-dish telescopes, thus the scatter in FWHM line width differences is likely to be a consequence of the different spatial scales probed by the ATCA.

The distribution of SHRDS line widths is nearly identical to that of all previously known H II regions in the *WISE* Catalog. The physical conditions, such as internal turbulence, of SHRDS H II regions are thus similar to those of the Galactic population of H II regions as a whole.

In this data release, we provide only the positions, continuum flux densities, and stacked $<$H$n\alpha>$ RRL properties for our sample of bright H II regions. Much more insight will be gained by looking at the intermediate data products, such as the continuum spectral energy distributions, RRL spectral energy distributions, RRL-to-continuum intensity ratio distributions, etc. The next SHRDS data release will add ∼200 more H II regions to the SHRDS catalog, bringing the total number of newly discovered nebulae to ∼500. We will also publish the intermediate data products that will allow for a more detailed analysis of individual H II regions.

A complete catalog of Galactic H II regions in the third and fourth Galactic quadrants will drastically improve our understanding of Galactic high-mass star formation, spiral structure, and metallicity structure. With H I emission/absorption observations toward these newly discovered H II regions, we will resolve the kinematic distance ambiguity of a subset of our sample and create the most complete face-on map of Galactic

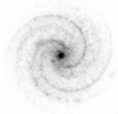

H ii regions to date.

Chapter 5

Metallicity Structure in the Milky Way Disk

5.1 Introduction

The present day chemical structure of the Milky Way disk is among the most important constraints on models of Galactic chemodynamical evolution (e.g., Chiappini et al., 2003; Minchev et al., 2014; Snaith et al., 2015; Minchev et al., 2018). Radial metallicity gradients, for example, are observed in both the Milky Way and other spiral galaxies using collisionally excited lines in ionized star forming regions (e.g., Searle, 1971; Shaver et al., 1983) and stellar abundances (e.g., Hayden et al., 2014; Bovy et al., 2014). These gradients reveal the complex history of star formation, stellar migration, and chemical enrichment by stars across galactic disks (Minchev et al., 2018). Stellar and gaseous tracers provide complementary information about the chemodynamical history of the Galaxy. The chemical abundances of stars represent the enrichment of the interstellar medium (ISM) when the stars were born, whereas the abundances of gaseous tracers represent the end product of billions of years of stellar evolution and ISM enrichment.

Evidence for azimuthal variations in galactic radial metallicity gradients has been observed in both the Milky Way (e.g., Balser et al., 2015, hereafter, B15) and other galaxies (e.g., Ho et al., 2017). Such variations are not expected in an old and well-mixed galaxy (Balser et al., 2011), and chemodynamical models of galaxies typically assume axisymmetric metallcitiy gradients (e.g., Chiappini et al., 2003). Azimuthal variations may be caused by streaming motions and radial migration induced by

galactic bars (Di Matteo et al., 2013), spiral arms (Grand et al., 2016; Ho et al., 2017), and/or perturbations from minor galaxy interactions (Bird et al., 2012).

Here we expand the Galactic H II region metallicity surveys of Quireza et al. (2006b), Balser et al. (2011), and B15 to create a more complete map of metallicity structure in the Milky Way disk and to search for evidence of azimuthal variations in the Galactic radial metallicity gradient. H II regions are the sites of recent high-mass star formation. These nebulae are an ideal tracer of Galactic metallicity structure because (1) they live for $\lesssim$10 Myr, and they therefore reveal the current enrichment of the ISM; (2) their distances are derived accurately using maser parallax measurements (e.g., Reid et al., 2014) or kinematic techniques (e.g., Wenger et al., 2018a, Chapter 3); and (3) their metallicities are either derived using optical and infrared collisionally excited lines or inferred from the nebular electron temperatures. The radio recombination line (RRL) and radio continuum emission from H II regions are an extinction-free diagnostic of the nebular electron temperature, which is empirically related to the H II region metallcitiy (Shaver et al., 1983). Radio wavelength observations of H II regions can reveal metallicity structure across the Milky Way disk.

The local thermodynamic equilibrium electron temperature of an ionized gas is derived from the RRL-to-continuum brightness ratio when the nebula is optically thin (B15). The electron temperature surveys of Galactic H II regions by B15, Balser et al. (2011), and Quireza et al. (2006b) used single dish telescopes. Although these instruments are extremely sensitive to faint RRL emission, they are not ideal for measuring accurate RRL-to-continuum brightness ratios. We measure the single dish continuum brightness of an H II region by scanning across the source in multiple directions. Then, we remove a baseline fit to the diffuse background continuum emission. The accuracy of the radio continuum brightness is limited by our ability to accurately remove this diffuse component.

An interferometer is the ideal tool for measuring the RRL-to-continuum brightness ratio of Galactic H II regions. By their nature, interferometers are not sensitive to large scale, diffuse emission, such as the non-thermal radio continuum emission that permeates the Galactic plane. We measure the total continuum flux density of nebulae more accurately with an interferometer than with a single dish telescope if the angular size of the source is smaller than the largest angular scale of the telescope. Too, interferometer data can be constructed as a high spatial resolution image or data

cube. These images and cubes reduce source confusion. Finally, interferometers like the National Radio Astronomy Observatory (NRAO) Karl G. Jansky Very Large Array (VLA) simultaneously measure both radio continuum and RRL emission. Any systematic calibration or weather issues affecting the data will be removed in the RRL-to-continuum flux ratio.

We use the VLA to derive the nebular electron temperatures and metallicities of Galactic H II regions across the Milky Way disk. A subset of these nebulae overlap with previous single dish surveys, which allows us to compare the interferometer-derived electron temperatures with those derived from single dish observations. We create the most complete map of Galactic metallicity structure as traced by H II regions to date and we place constraints on the level of azimuthal variations in the Milky Way's radial metallicity gradient.

5.2 Target Sample

Recent RRL surveys have more than doubled the number of known Galactic H II regions (Bania et al., 2010, 2012; Anderson et al., 2014, 2015a,b, 2018; Wenger et al., 2019, Chapter 4). The *Widefield Infrared Survey Explorer (WISE)* Catalog of Galactic H II Regions contains the infrared and radio properties of more than 2000 known nebulae (Anderson et al., 2014). To derive accurate electron temperatures, we require the subset of *WISE* Catalog nebulae observable by the VLA. Our selection criteria are nebulae with 1) a single RRL velocity component, 2) a maser parallax measurement or an accurate kinematic distance, and 3) a predicted RRL flux density $> 1.8\,\mathrm{mJy\ beam^{-1}}$.

When this survey began, the *WISE* Catalog contained RRL measurements of $\sim$1200 unique Galactic H II regions. Many of these nebulae are clustered in H II region groups or complexes, and a single dish observation will see the combined emission from multiple discrete sources. These star forming complexes are the source of ionizing photons, which may leak out into and ionize the diffuse ISM. In these cases, the RRL spectrum of the H II region will show multiple velocity components from either multiple discrete H II regions or a mix of H II regions and diffuse ionized gas. The presence of spectrally confused, or blended, RRL components will limit our ability to derive the nebular RRL flux density accurately. Therefore, we remove $\sim$100 nebulae with multiple velocity component RRLs in the *WISE* Catalog.

Accurate distances are a necessary characteristic of Galactic metallicity structure

tracers. We further limit the *WISE* Catalog sample to those nebulae with published maser parallax measurements and/or accurate kinematic distances. We adopt the kinematic distance uncertainty model of Anderson et al. (2012) to estimate the accuracy of kinematic distances in the *WISE* Catalog. Because we aim to generate a Galactocentric map of the Milky Way metallicity structure, we require kinematic distance accuracies such that the uncertainty in the Galactocentric radius is $\sigma_R < 2\,\mathrm{kpc}$ and the uncertainty in Galactocentric azimuth is $\sigma_\theta < 20°$. Out of our sample of ∼1100 single velocity RRL component nebulae, 107 have an associated maser parallax measurement and 364 have a kinematic distance meeting these accuracy thresholds. This brings our total sample of H II regions to 471 nebulae.

Finally, we identify the subset of this sample with previously measured RRL flux densities bright enough to be detected by the VLA in a 10 minute observation. The point source sensitivity of the VLA with this integration time is ∼2 mJy beam^{-1} per 31.25 kHz channel at ∼9 GHz. By smoothing the spectra to 5 km s^{-1} and averaging 7 hydrogen RRL transitions, we estimate a spectral rms noise of ∼0.3 mJy beam^{-1} per channel. We require our sample of H II regions to have a predicted 9 GHz RRL flux density greater than 5 times this sensitivity limit, ∼1.7 mJy beam^{-1}.

All previously measured RRL flux densities of northern sky H II regions in the *WISE* catalog were made with single dish telescopes around ∼9 GHz. We first scale the observed RRL brightness temperatures to 9 GHz assuming the RRL brightness temperature is proportional to the RRL frequency (B15). We convert these scaled RRL brightness temperatures to point source flux densities assuming telescope gains of ∼2 K Jy^{-1} for the Green Bank Observatory (GBO) Green Bank Telescope (GBT; Balser et al., 2011), ∼0.27 K Jy^{-1} for the NRAO 140 Foot Telescope (hereafter, 140 Foot; Balser et al., 2016), and ∼5 K Jy^{-1} for the Arecibo Observatory (Bania et al., 2012). Any source with a predicted ∼9 GHz RRL flux density $S_{L,9\mathrm{GHz}} > 1.7\,\mathrm{mJy\ beam^{-1}}$ fulfills the criterion. This threshold removes only 10 nebulae from our sample, bringing the total number of observable H II regions to 461.

The VLA is not sensitive to emission on scales largest than ∼145 arcsec in the D (most compact) configuration at ∼9 GHz. If we assume that the radio size of an H II is approximately half of the infrared size (e.g., Bihr et al., 2016), then 30% of the H II regions in our sample have radio diameters greater than this largest angular scale. Our observations will not be sensitive to these angularly large nebulae if their emission is uniform on such large spatial scales. We expect to detect clumpy emission

within these large H II regions, however, so we do not use any size restriction when defining our sample.

Finally, we select our observing targets from this sample of 461 nebulae to maximize our coverage of the Galactic disk. We divide the Galaxy into 120 bins of size 12° in Galactocentric azimuth, over the azimuth range −30° to 150°, and 2 kpc in Galactocentric radius, up to 18 kpc. Using the maser parallax distance, when available, or the *WISE* Catalog kinematic distance to compute the Galactocentric radii and azimuths of the nebulae, we identify the two brightest and most compact H II regions in each bin. Some bins only have one (or zero) nebulae that meet our distance accuracy and predicted RRL flux density requirements. Figure 5.1 shows the Galactocentric positions of the 128 H II regions we select using these criteria as well as the 20 nebulae observed in the pilot survey. One H II region, G032.272−0.226, is observed in both the pilot survey and main survey. Of the 120 position bins, 78 (65%) contain at least one H II region that meets our selection criteria.

Our final H II region target catalog contains 147 unique nebulae. Table 5.1 lists the information about these H II regions: the *WISE* Catalog name; the VLA project in which it was observed (13A−030 is the pilot survey and 15B−178 is the main survey); the *WISE* infrared position; the *WISE* infrared radius, $R_{\rm IR}$; the estimated 9 GHz RRL flux density, $S_{9{\rm GHz},\,L}$; the telescope and reference for the previous RRL detection; the previously measured RRL-to-continuum brightness ratio, S_L/S_C, and derived electron temperature, T_e; and the reference for the RRL-to-continuum brightness ratio and electron temperature.

5.3 Observations and Data Reduction

We used the VLA to simultaneously observe radio continuum and RRL emission toward our sample of 147 Galactic H II regions. The data were acquired in the most compact (D) antenna configuration as part of two projects: the pilot survey (13A-030; 5 hours) in Feb and Apr 2013, and the main survey (15B-178; 30 hours) in Oct and Nov 2015. A summary of the observations is in Table 5.2.

The VLA X-band receiver covers the frequency range ∼8–12 GHz. We used the Wideband Interferometric Digital ARchitecture (WIDAR) correlator in the 8-bit sampler mode to simultaneously measure ∼8–10 GHz radio continuum emission and 8 hydrogen RRL transitions in both linear polarizations. The continuum data were measured by 16 low spectral resolution spectral windows (hereafter, continuum win-

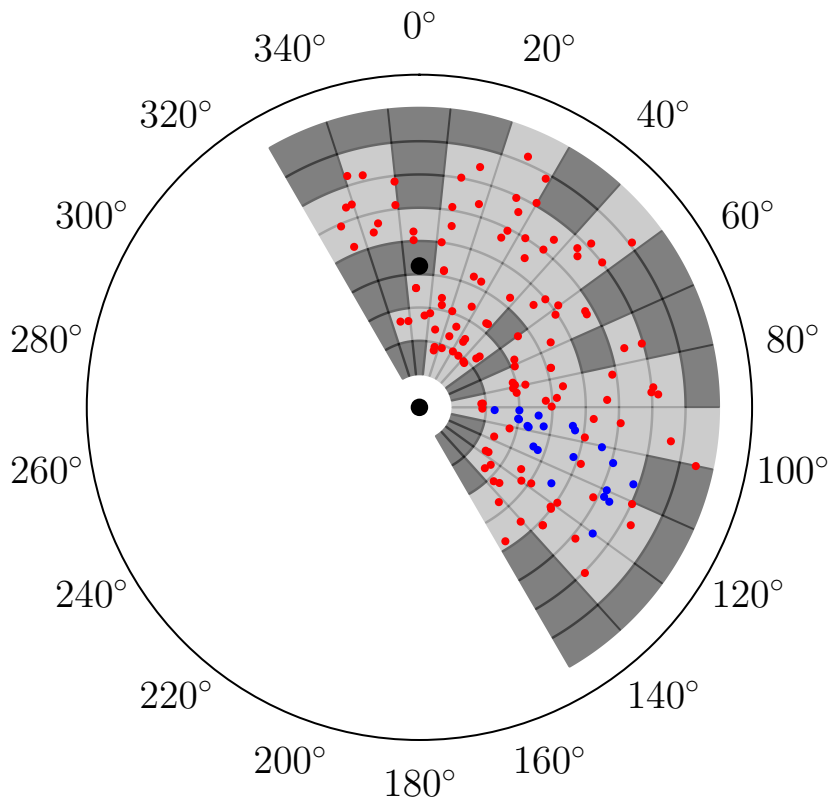

Figure 5.1: Galactocentric positions and Milky Way disk coverage of the VLA survey H II regions. The Galactic Center is the black point at the origin and the Sun is the black point 8.34 kpc in the direction $\theta = 0°$. The colored points are the H II regions in the pilot survey (blue) and main survey (red). The Galactic disk is divided into 120 bins of size 12° in Galactocentric azimuth, over the azimuth range −30° to 150°, and 2 kpc in Galactocentric radius, up to 18 kpc. Bins that contain at least one nebulae are colored light gray, whereas empty bins are dark gray.

Table 5.1: VLA Electron Temperature Survey Targets

Field	Project	R.A. J2000 (hh:mm:ss)	Decl. J2000 (dd:mm:ss)	$R_{\rm IR}$ (arcsec)	$S_{9{\rm GHz},\,L}$ (mJy beam^{-1})	Telescope[a]	RRL Author[b]	S_L/S_C	T_e (K)	T_e Author[c]
G005.883−0.399	15B-178	18:00:31.5	−24:04:18.9	22.35	844.15 ± 5.77	140 Foot	Q06	···	···	···
G009.598+0.199	15B-178	18:06:11.1	−20:32:36.5	34.09	226.92 ± 20.00	140 Foot	L89	···	···	···
G010.596−0.381	15B-178	18:10:24.6	−19:57:08.4	60.00	586.69 ± 4.23	140 Foot	Q06	0.0686 ± 0.0006	9810 ± 90	Q06b;B15
G012.804−0.207	15B-178	18:14:15.0	−17:55:56.4	21.15	3034.62 ± 23.85	140 Foot	Q06	0.0808 ± 0.0007	7620 ± 100	Q06b;B15
G013.880+0.285	15B-178	18:14:35.7	−16:45:09.7	144.31	587.42 ± 5.00	140 Foot	Q06	0.1210 ± 0.0012	6960 ± 80	Q06b;B15
G015.212+0.167	15B-178	18:17:40.0	−15:38:13.8	176.72	10.95 ± 0.11	GBT	A15b	···	···	···
G017.336−0.146	15B-178	18:22:57.2	−13:54:41.0	102.77	6.70 ± 0.18	GBT	A11	···	···	···
G017.928−0.677	15B-178	18:26:01.7	−13:38:14.6	164.84	13.00 ± 0.30	GBT	A11	···	···	···
G018.584+0.344	15B-178	18:23:34.9	−12:34:48.7	42.50	14.00 ± 0.28	GBT	A11	···	···	···
G019.030+0.423	15B-178	18:24:09.0	−12:08:53.0	77.79	4.05 ± 0.38	GBT	A11	···	···	···
G019.716−0.261	15B-178	18:27:56.0	−11:51:39.4	58.90	14.80 ± 0.27	GBT	A15b	···	···	···
G019.728−0.113	15B-178	18:27:25.2	−11:46:55.1	42.50	7.70 ± 0.20	GBT	A11	···	···	···
G020.227+0.110	15B-178	18:27:33.8	−11:14:11.4	71.07	5.25 ± 0.12	GBT	A11	···	···	···
G020.363−0.014	15B-178	18:28:16.1	−11:10:25.6	42.50	10.90 ± 0.24	GBT	A11	···	···	···
G021.386−0.255	15B-178	18:31:04.0	−10:22:43.4	57.60	15.65 ± 0.14	GBT	A11	···	···	···
G021.603−0.169	15B-178	18:31:10.0	−10:08:48.4	31.87	4.10 ± 0.20	GBT	A15b	···	···	···
G023.041−0.399	15B-178	18:34:41.3	−8:58:37.1	151.85	65.35 ± 0.66	GBT	A11	···	···	···
G023.423−0.216	15B-178	18:34:44.5	−8:33:10.9	96.79	816.54 ± 3.65	140 Foot	Q06	0.1162 ± 0.0008	6500 ± 55	Q06b;B15
G023.661−0.252	15B-178	18:35:18.9	−8:21:34.2	56.59	24.30 ± 0.23	GBT	A11	···	···	···
G023.787+0.223	15B-178	18:33:50.6	−8:01:42.3	189.71	146.15 ± 22.69	140 Foot	L89	···	···	···
G024.185+0.211	15B-178	18:34:37.6	−7:40:51.3	178.07	176.92 ± 16.15	140 Foot	L89	···	···	···
G024.724−0.084	15B-178	18:36:41.1	−7:20:16.7	254.14	253.85 ± 26.92	140 Foot	L89	···	···	···
G024.728+0.159	15B-178	18:35:49.5	−7:13:20.1	75.57	42.20 ± 0.25	GBT	A11	···	···	···
G024.734+0.087	15B-178	18:36:05.6	−7:15:01.3	85.58	93.95 ± 0.50	GBT	A11	···	···	···
G025.397+0.033	15B-178	18:37:30.8	−6:41:08.8	39.69	88.46 ± 10.38	140 Foot	L89	···	···	···
G025.398+0.562	15B-178	18:35:37.4	−6:26:34.0	42.50	23.25 ± 0.15	GBT	A11	···	···	···
G025.477+0.040	15B-178	18:37:38.2	−6:36:45.1	42.50	4.60 ± 0.20	GBT	A11	···	···	···
G026.597−0.024	15B-178	18:39:55.9	−5:38:45.0	26.61	16.65 ± 0.25	GBT	A15a	···	···	···
G027.210+0.282	15B-178	18:39:58.0	−4:57:39.4	42.50	6.00 ± 0.17	GBT	A15b	···	···	···
G027.562+0.084	13A-030	18:41:19.3	−4:44:21.4	42.50	22.60 ± 0.15	GBT	A11	0.1601 ± 0.0021	5827 ± 94	B11;B15
G028.320+1.243	15B-178	18:38:34.9	−3:32:04.8	60.00	2.25 ± 0.10	GBT	A15b	···	···	···
G028.451+0.001	15B-178	18:43:14.9	−3:59:11.0	28.70	9.20 ± 0.20	GBT	A15b	···	···	···
G028.581+0.145	15B-178	18:42:58.4	−3:48:18.8	42.50	6.75 ± 0.10	GBT	A11	···	···	···
G029.019+0.165	15B-178	18:43:42.1	−3:24:19.3	106.80	14.35 ± 0.19	GBT	A11	···	···	···
G029.770+0.219	15B-178	18:44:53.2	−2:42:49.6	42.50	7.60 ± 0.10	GBT	A11	···	···	···
G029.816+2.225	15B-178	18:37:49.6	−1:45:17.9	168.83	9.25 ± 0.16	GBT	A15b	···	···	···
G029.956−0.020	15B-178	18:46:04.5	−2:39:25.2	94.36	896.81 ± 3.69	140 Foot	Q06	0.0992 ± 0.0064	6510 ± 90	Q06b;B15

Table 5.1 continued

Table 5.1: VLA Electron Temperature Survey Targets (continued)

Field	Project	R.A. J2000 (hh:mm:ss)	Decl. J2000 (dd:mm:ss)	$R_{\rm IR}$ (arcsec)	$S_{9{\rm GHz},\,L}$ (mJy beam^{-1})	Telescope[a]	RRL Author[b]	S_L/S_C	T_e (K)	T_e Author[c]
G030.211+0.428	15B-178	18:44:56.7	−2:13:30.7	37.11	2.75 ± 0.20	GBT	A15b	···	···	···
G031.269+0.064	15B-178	18:48:10.6	−1:27:00.7	24.84	92.31 ± 10.38	140 Foot	L89	···	···	···
G031.274+0.485	13A-030	18:46:41.9	−1:15:43.8	83.38	4.15 ± 0.10	GBT	A11	0.0944 ± 0.0042	8690 ± 462	B11;B15
G031.577+0.103	15B-178	18:48:35.9	−1:09:28.0	117.27	80.77 ± 8.46	140 Foot	L89	···	···	···
G032.030+0.048	15B-178	18:49:37.2	+0:46:47.7	42.50	6.35 ± 0.13	GBT	A11	···	···	···
G032.272−0.226	13A-030	18:51:02.3	+0:41:25.4	42.50	32.90 ± 0.14	GBT	A11	0.0889 ± 0.0008	8238 ± 104	B11;B15
G032.272−0.226	15B-178	18:51:02.3	+0:41:25.4	42.50	32.90 ± 0.14	GBT	A11	0.0889 ± 0.0008	8238 ± 104	B11;B15
G032.733+0.209	13A-030	18:50:19.9	+0:04:54.3	42.50	11.95 ± 0.27	GBT	A11	0.1638 ± 0.0037	5856 ± 156	B11;B15
G032.876−0.423	13A-030	18:52:50.7	+0:14:57.6	126.62	15.20 ± 0.32	GBT	A11	0.1817 ± 0.0043	6074 ± 176	B11;B15
G032.928+0.607	13A-030	18:49:16.4	+0:16:22.3	65.68	25.60 ± 0.09	GBT	A11	0.0680 ± 0.0006	9843 ± 170	B11;B15
G032.976−0.334	13A-030	18:52:44.0	+0:06:31.4	131.80	12.50 ± 0.20	GBT	A11	0.1485 ± 0.0040	6411 ± 207	B11;B15
G033.643−0.229	15B-178	18:53:32.9	+0:31:44.7	42.50	3.35 ± 0.16	GBT	A11	···	···	···
G034.041+0.053	13A-030	18:53:16.4	+1:00:40.2	42.50	19.45 ± 0.20	GBT	A11	0.1384 ± 0.0021	6105 ± 120	B11;B15
G034.133+0.471	13A-030	18:51:57.1	+1:17:01.3	42.50	58.55 ± 0.18	GBT	A11	0.1021 ± 0.0005	7655 ± 63	B11;B15
G034.686+0.068	13A-030	18:54:23.8	+1:35:31.5	42.50	21.75 ± 0.15	GBT	A11	0.1492 ± 0.0026	5335 ± 112	B11;B15
G035.126−0.755	15B-178	18:58:07.6	+1:36:30.0	169.39	36.85 ± 0.26	GBT	A15b	···	···	···
G035.948−0.149	15B-178	18:57:28.4	+2:37:01.0	42.50	3.35 ± 0.21	GBT	A11	···	···	···
G036.918+0.482	15B-178	18:56:59.9	+3:46:04.5	29.02	6.25 ± 0.17	GBT	A11	···	···	···
G037.445−0.212	15B-178	19:00:26.2	+3:55:11.2	124.08	17.35 ± 0.15	GBT	A11	···	···	···
G037.469−0.105	15B-178	19:00:05.9	+3:59:22.0	41.03	5.14 ± 0.10	Arecibo	B12	···	···	···
G038.550+0.163	13A-030	19:01:07.7	+5:04:22.6	42.50	15.50 ± 0.20	GBT	A11	0.1008 ± 0.0016	8216 ± 167	B11;B15
G038.643−0.227	15B-178	19:02:41.5	+4:58:37.5	42.50	5.30 ± 0.09	GBT	A11	···	···	···
G038.651+0.087	13A-030	19:01:35.3	+5:07:43.9	42.50	8.70 ± 0.07	GBT	A11	0.0738 ± 0.0015	9428 ± 245	B11;B15
G038.738−0.140	15B-178	19:02:33.4	+5:06:05.0	105.52	9.75 ± 0.10	GBT	A11	···	···	···
G038.840+0.497	13A-030	19:00:28.5	+5:28:58.5	84.39	7.45 ± 0.07	GBT	A11	0.0734 ± 0.0020	9221 ± 317	B11;B15
G038.875+0.308	13A-030	19:01:12.5	+5:25:41.8	42.50	27.05 ± 0.12	GBT	A11	0.0822 ± 0.0008	8384 ± 116	B11;B15
G039.183−1.422	15B-178	19:07:56.9	+4:54:31.2	60.00	4.95 ± 0.16	GBT	A15b	···	···	···
G039.196+0.224	15B-178	19:02:05.8	+5:40:32.2	60.00	2.32 ± 0.10	Arecibo	B12	···	···	···
G039.869+0.645	13A-030	19:01:49.3	+6:27:45.5	68.19	10.80 ± 0.09	GBT	A11	0.0708 ± 0.0013	9373 ± 214	B11;B15
G041.750+0.034	15B-178	19:07:29.9	+7:51:27.3	121.00	2.90 ± 0.10	GBT	A15b	···	···	···
G041.762+1.479	15B-178	19:02:19.9	+8:31:54.0	268.99	2.35 ± 0.09	GBT	A15b	···	···	···
G043.149+0.028	15B-178	19:10:07.7	+9:05:47.0	35.18	3129.19 ± 10.23	140 Foot	Q06	···	···	···
G043.240+0.131	15B-178	19:09:55.7	+9:13:28.1	42.50	5.40 ± 0.17	GBT	A11	···	···	···
G043.432+0.521	13A-030	19:08:54.1	+9:34:22.2	74.33	11.25 ± 0.15	GBT	A11	0.1021 ± 0.0019	8338 ± 198	B11;B15
G043.523−0.648	15B-178	19:13:15.5	+9:06:54.0	88.57	2.20 ± 0.18	GBT	A11	···	···	···
G043.818+0.393	13A-030	19:10:03.7	+9:51:31.6	108.26	14.80 ± 0.09	GBT	A11	0.0781 ± 0.0013	8802 ± 196	B11;B15
G043.818+0.395	15B-178	19:10:03.7	+9:51:31.6	108.26	14.80 ± 0.09	GBT	A11	0.0781 ± 0.0013	8802 ± 196	B11;B15

Table 5.1 continued

Table 5.1: VLA Electron Temperature Survey Targets (continued)

Field	Project	R.A. J2000 (hh:mm:ss)	Decl. J2000 (dd:mm:ss)	$R_{\rm IR}$ (arcsec)	$S_{9{\rm GHz},\,L}$ (mJy beam^{-1})	Telescope[a]	RRL Author[b]	S_L/S_C	T_e (K)	T_e Author[c]
G043.968+0.993	15B-178	19:08:11.3	+10:16:04.7	50.84	5.55 ± 0.25	GBT	A15b	···	···	···
G044.417+0.536	13A-030	19:10:41.0	+10:27:22.6	84.69	6.55 ± 0.08	GBT	A11	0.0926 ± 0.0026	8492 ± 299	B11;B15
G044.501+0.335	13A-030	19:11:34.3	+10:26:07.5	50.65	24.25 ± 0.12	GBT	A11	0.1017 ± 0.0017	8350 ± 153	B11;B15
G045.197+0.738	13A-030	19:11:24.5	+11:14:28.3	80.49	9.35 ± 0.10	GBT	A11	0.0556 ± 0.0010	10841 ± 245	B11;B15
G045.391−0.725	15B-178	19:17:03.7	+10:43:57.9	191.48	26.50 ± 0.26	GBT	A11	···	···	···
G046.173+0.533	15B-178	19:14:00.4	+12:00:39.7	60.00	2.04 ± 0.04	Arecibo	B12	···	···	···
G048.719+1.147	15B-178	19:16:38.2	+14:32:58.9	82.92	6.30 ± 0.32	GBT	A15b	···	···	···
G049.399−0.490	15B-178	19:23:55.6	+14:22:54.6	51.68	68.15 ± 0.23	GBT	A11	···	···	···
G049.690−0.166	15B-178	19:23:19.0	+14:47:29.5	178.62	76.92 ± 7.69	140 Foot	L96	···	···	···
G050.032+0.605	15B-178	19:21:09.8	+15:27:24.2	139.55	5.50 ± 0.20	GBT	A15b	···	···	···
G052.001+1.602	15B-178	19:21:21.4	+17:39:45.1	49.60	2.00 ± 0.07	GBT	A15b	···	···	···
G052.098+1.042	15B-178	19:23:37.1	+17:29:01.8	122.52	38.40 ± 0.17	GBT	A11	···	···	···
G052.160+0.708	15B-178	19:24:58.5	+17:22:49.6	67.26	7.00 ± 0.20	GBT	A11	···	···	···
G052.256+0.702	15B-178	19:25:11.2	+17:27:43.9	120.73	5.30 ± 0.08	Arecibo	B12	···	···	···
G054.093+1.748	15B-178	19:24:58.5	+19:34:32.6	81.06	2.60 ± 0.10	GBT	A15b	···	···	···
G054.490+0.930	15B-178	19:28:49.9	+19:32:08.0	245.76	4.95 ± 0.09	GBT	A11	···	···	···
G054.490+1.579	15B-178	19:26:24.4	+19:50:41.1	87.52	3.50 ± 0.10	GBT	A15b	···	···	···
G055.114+2.422	15B-178	19:24:29.9	+20:47:33.2	146.16	28.75 ± 0.17	GBT	A15b	0.0423 ± 0.0003	13126 ± 144	B11;B15
G059.796+0.241	15B-178	19:42:32.9	+23:50:02.4	159.46	53.38 ± 0.41	GBT	B11	0.0975 ± 0.0008	9068 ± 120	B11;B15
G060.592+1.572	15B-178	19:39:11.2	+25:10:59.4	126.28	13.05 ± 0.13	GBT	A15b	···	···	···
G061.431+2.081	15B-178	19:39:02.7	+26:09:52.0	143.57	3.65 ± 0.17	GBT	A15b	···	···	···
G061.720+0.863	15B-178	19:44:23.6	+25:48:44.2	72.00	9.30 ± 0.10	GBT	A11	···	···	···
G062.577+2.389	15B-178	19:40:21.9	+27:18:45.9	141.52	31.60 ± 0.18	GBT	A15b	···	···	···
G068.144+0.915	15B-178	19:59:09.7	+31:21:32.3	160.08	23.91 ± 0.27	GBT	B11	0.0697 ± 0.0009	10834 ± 207	B11;B15
G070.280+1.583	15B-178	20:01:47.8	+33:31:33.4	53.06	328.08 ± 1.75	GBT	B11	···	···	···
G070.673+1.190	15B-178	20:04:24.0	+33:38:59.2	120.63	2.65 ± 0.13	GBT	A15b	···	···	···
G070.765+1.820	15B-178	20:02:03.9	+34:03:47.8	86.97	12.10 ± 0.14	GBT	A15b	···	···	···
G071.150+0.397	15B-178	20:08:50.5	+33:37:30.8	144.06	33.75 ± 0.10	GBT	A15b	···	···	···
G073.878+1.023	15B-178	20:13:34.7	+36:15:00.4	71.21	7.80 ± 0.10	GBT	A15b	···	···	···
G074.155+1.646	15B-178	20:11:45.0	+36:49:26.5	95.39	3.70 ± 0.11	GBT	A15b	···	···	···
G074.753+0.912	15B-178	20:16:27.5	+36:54:57.7	91.43	6.40 ± 0.12	GBT	A15b	···	···	···
G075.175−0.593	15B-178	20:23:50.1	+36:24:39.5	306.78	8.80 ± 0.14	GBT	A15b	···	···	···
G075.768+0.344	15B-178	20:21:41.2	+37:26:02.9	197.80	273.60 ± 0.56	GBT	B11	0.0790 ± 0.0004	8590 ± 47	B11;B15
G078.174−0.550	15B-178	20:32:30.2	+38:52:15.1	160.63	10.20 ± 0.15	GBT	A15b	···	···	···
G078.886+0.709	15B-178	20:29:24.7	+40:11:18.7	174.84	9.75 ± 0.23	GBT	A15b	···	···	···
G080.191+0.534	15B-178	20:34:13.7	+41:08:14.5	53.88	4.85 ± 0.12	GBT	A15b	···	···	···
G091.113+1.580	15B-178	21:09:36.0	+50:13:22.5	278.16	37.75 ± 0.17	GBT	A15b	···	···	···

Table 5.1 continued

Table 5.1: VLA Electron Temperature Survey Targets (continued)

Field	Project	R.A. J2000 (hh:mm:ss)	Decl. J2000 (dd:mm:ss)	$R_{\rm IR}$ (arcsec)	$S_{9{\rm GHz},\,L}$ (mJy beam^{-1})	Telescope[a]	RRL Author[b]	S_L/S_C	T_e (K)	T_e Author[c]
G093.518+2.611	15B-178	21:15:22.5	+52:40:39.6	107.51	4.45 ± 0.16	GBT	A15b	···	···	···
G094.263−0.414	15B-178	21:32:32.7	+51:02:19.3	100.14	2.10 ± 0.10	GBT	A15b	···	···	···
G096.289+2.593	15B-178	21:28:42.4	+54:37:05.8	193.20	23.60 ± 0.11	GBT	A15b	0.0570 ± 0.0009	11039 ± 314	B11;B15
G096.434+1.324	15B-178	21:35:20.3	+53:47:14.1	91.59	5.05 ± 0.14	GBT	A15b	···	···	···
G097.444+3.083	15B-178	21:32:14.7	+55:45:52.4	95.94	2.00 ± 0.18	GBT	A15b	···	···	···
G097.515+3.173	15B-178	21:32:10.8	+55:52:44.6	122.86	33.60 ± 0.18	GBT	A15b	···	···	···
G101.016+2.590	15B-178	21:54:19.5	+57:43:06.4	101.64	3.40 ± 0.18	GBT	A15b	···	···	···
G104.700+2.784	15B-178	22:16:25.9	+60:03:01.8	102.78	6.25 ± 0.18	GBT	A15b	···	···	···
G109.104−0.347	15B-178	22:59:09.0	+59:28:36.7	95.34	6.00 ± 0.12	GBT	A15b	···	···	···
G111.802+0.526	15B-178	23:16:32.4	+61:19:49.6	96.95	5.10 ± 0.20	GBT	A15b	···	···	···
G118.276+2.490	15B-178	00:07:14.9	+64:57:44.9	239.84	2.35 ± 0.17	GBT	A15b	···	···	···
G118.592+2.828	15B-178	00:09:40.8	+65:20:50.2	161.64	3.30 ± 0.18	GBT	A15b	···	···	···
G124.637+2.535	15B-178	01:07:47.3	+65:21:12.5	165.16	18.30 ± 0.21	GBT	A15b	0.0576 ± 0.0012	10758 ± 288	B11;B15
G125.092+0.778	15B-178	01:10:51.9	+63:34:06.7	136.99	2.85 ± 0.17	GBT	A15b	···	···	···
G135.188+2.701	15B-178	02:42:24.6	+62:54:07.3	142.05	6.05 ± 0.12	GBT	A15b	···	···	···
G136.119+2.118	15B-178	02:47:33.7	+61:58:48.1	127.23	3.30 ± 0.13	GBT	A15b	···	···	···
G136.884+0.911	15B-178	02:48:55.9	+60:33:38.8	805.95	69.23 ± 8.08	140 Foot	L89	0.0995 ± 0.0025	8204 ± 257	B11;B15
G141.084−1.063	15B-178	03:10:16.0	+56:50:04.3	249.15	7.80 ± 0.12	GBT	A15b	···	···	···
G148.474+1.982	15B-178	04:05:41.7	+54:54:55.2	104.17	2.55 ± 0.14	GBT	A15b	···	···	···
G150.859−1.115	15B-178	04:03:50.6	+51:00:57.9	123.28	2.85 ± 0.13	GBT	A15b	···	···	···
G154.646+2.438	15B-178	04:36:48.8	+50:52:42.5	370.38	25.02 ± 0.33	GBT	B11	0.0673 ± 0.0009	9734 ± 175	B11;B15
G189.830+0.417	15B-178	06:08:58.1	+20:38:29.2	199.15	82.62 ± 1.35	140 Foot	Q06	···	···	···
G192.638−0.008	15B-178	06:13:07.5	+17:58:33.5	174.27	52.91 ± 0.44	GBT	B11	0.0971 ± 0.0010	8833 ± 107	B11;B15
G196.448−1.673	15B-178	06:14:37.3	+13:50:02.6	302.50	30.80 ± 0.37	GBT	B11	0.0773 ± 0.0010	9945 ± 164	B11;B15
G201.535+1.597	15B-178	06:36:11.8	+10:51:56.8	790.64	12.79 ± 0.26	GBT	B11	0.0713 ± 0.0015	10063 ± 283	B11;B15
G212.021−1.309	15B-178	06:45:07.1	+0:12:49.8	1075.77	50.00 ± 5.38	140 Foot	L96	···	···	···
G218.737+1.850	15B-178	07:08:39.2	−4:18:55.1	215.23	35.22 ± 0.28	GBT	B11	0.0509 ± 0.0005	14578 ± 195	B11;B15
G224.158+1.213	15B-178	07:16:29.0	−9:24:51.3	558.98	8.35 ± 0.12	GBT	A15b	···	···	···
G227.760−0.127	15B-178	07:18:30.6	−13:13:29.4	324.34	7.54 ± 0.09	GBT	B11	0.0485 ± 0.0007	12495 ± 249	B11;B15
G231.481−4.401	15B-178	07:09:54.3	−18:29:53.7	511.74	21.11 ± 0.49	GBT	B11	0.1011 ± 0.0024	9098 ± 286	B11;B15
G233.753−0.193	15B-178	07:30:04.6	−18:32:03.8	311.06	27.16 ± 0.41	GBT	B11	0.0822 ± 0.0015	9482 ± 209	B11;B15
G243.244+0.406	15B-178	07:52:42.5	−26:29:00.1	941.61	49.06 ± 0.47	GBT	B11	0.0764 ± 0.0012	10220 ± 110	Q06b;B15
G253.694−0.414	15B-178	08:15:34.9	−35:45:30.3	1540.80	42.31 ± 4.23	140 Foot	L89	···	···	···
G341.207−0.232	15B-178	16:52:20.7	−44:28:06.8	58.11	90.60 ± 0.45	GBT	A15b	···	···	···
G348.691−0.826	15B-178	17:19:06.6	−38:51:37.7	1328.28	3132.27 ± 13.38	140 Foot	Q06	···	···	···
G351.246+0.673	15B-178	17:20:17.7	−35:54:29.2	131.55	2251.35 ± 7.73	140 Foot	Q06	0.0896 ± 0.0006	8560 ± 70	Q06b;B15
G351.311+0.663	15B-178	17:20:31.2	−35:51:37.7	119.03	3356.38 ± 10.69	140 Foot	Q06	···	···	···

Table 5.1 continued

Table 5.1: VLA Electron Temperature Survey Targets (continued)

Field	Project	R.A. J2000 (hh:mm:ss)	Decl. J2000 (dd:mm:ss)	$R_{\rm IR}$ (arcsec)	$S_{9{\rm GHz},\,L}$ (mJy beam^{-1})	Telescope[a]	RRL Author[b]	S_L/S_C	T_e (K)	T_e Author[c]

[a] The telescope used for the original RRL detection
[b] The reference for the original RRL detection
[c] The reference for the RRL-to-continuum flux ratio measurement and electron temperature derivation

References — (L89) Lockman (1989); (L96) Lockman et al. (1996); (Q06a) Quireza et al. (2006a); (Q06b) Quireza et al. (2006b); (A11) Anderson et al. (2011); (B11) Balser et al. (2011); (B12) Bania et al. (2012); (A15a) Anderson et al. (2015a); (A15b) Anderson et al. (2015b); (B15) Balser et al. (2015)

Table 5.2: VLA Observation Summary

	13A-030	15B-178
Dates	2013 Feb and Apr	2015 Oct and Nov
Observing Time (hr)	5	30
H II Region Targets	20	128
Primary Calibrators	3C286	3C286, 3C48
Secondary Calibrators	J1733−1304, J1822−0938	J0019+7327, J0102+5824
	J1824+1044, J1922+1530	J0244+6228, J0349+4609
		J0358+5606, J0625+1440
		J0653−0625, J0735−1735
		J0804−2749, J1604−4441
		J1744−3116, J1820−2528
		J1822−0938, J1824+1044
		J1922+1530, J1924+3329
		J1925+2106, J2007+4029
		J2025+3343, J2137+5101
		J2137+5101
		J2148+6107

dows) covering 7.8–8.9 GHz and 9–10 GHz continuously. The RRL spectra were measured by 8 high spectral resolution (31.25 kHz) spectral windows (hereafter, spectral line windows), each with 16 MHz of frequency coverage. There are only 7 Hα RRL transitions in this frequency range (H87α to H93α), so we tuned one of the spectral line windows to H109β. The native velocity resolution ranges from 0.9 km s^{-1} at H87α to 1.2 km s^{-1} at H93α, with a velocity coverage ranging from 488 km s^{-1} to 600 km s^{-1} for these transitions, respectively. In one observing session of the pilot survey, the spectral line window for H88α was mistuned, so we exclude that spectral window from these analyses. Table 5.3 lists the following properties for each spectral window: the center frequency, $\nu_{\rm center}$; the bandwidth, the number of channels; the channel width, $\Delta\nu$; the targeted RRL transition; and the RRL rest frequency, $\nu_{\rm RRL}$.

Our targets are clustered into 12 observing sessions based on position, with ∼10 H II regions per group. Every observing session begins with a ∼15 minute integration on a primary calibrator, which is used for the absolute flux, delay, and bandpass calibration, followed by a ∼10 minute integration on a secondary calibrator located near the H II region science targets, which is used for the complex gain calibration. We observe each science target for 10–15 minutes to reach the necessary spectral sensitivity, then we return to the secondary calibrator for ∼5 more minutes. We repeat this process for each science target and each observing session.

We use the Wenger Interferometry Software Package (WISP) calibration, reduction, and analysis software package to reduce and analyze these data (Wenger, 2018). WISP is a *Python* wrapper for the Common Astronomy Software Applications package (CASA; McMullin et al., 2007). Although WISP was developed to reduce Australia Telescope Compact Array data for the Southern H II Region Discovery Survey (Wenger et al., 2019, Chapter 4), its modular framework can be applied to any radio interferometric dataset. We follow nearly the exact same data reduction process as Wenger et al. (2019, Chapter 4), which we briefly describe here.

5.3.1 Calibration

Each observing session contains one primary calibrator and one or more secondary calibrators. The primary calibrator data are used to determine the absolute flux, delay, and bandpass calibration solutions. The secondary calibrators set the complex gain (phases and amplitude) calibration solutions for the science targets. We use the VLA calibrator database to identify secondary calibrators close to the science targets

Table 5.3: VLA Correlator Setup

Window	$\nu_{\rm center}$ (MHz)	Bandwidth (MHz)	Channels	$\Delta\nu$ (kHz)	RRL	$\nu_{\rm RRL}$ (MHz)
0	7949.3	128	128	1000	···	···
1	8049.1	128	128	1000	···	···
2	8049.1	16	512	31.25	H93α	8045.605
3	8205.3	128	128	1000	···	···
4	8333.3	128	128	1000	···	···
5	8313.0	16	512	31.25	H92α	8309.385
6	8461.3	128	128	1000	···	···
7	8589.3	128	128	1000	···	···
8	8588.5	16	512	31.25	H91α	8584.823
9	8717.3	128	128	1000	···	···
10	8845.3	128	128	1000	···	···
11	8876.4	16	512	31.25	H90α	8872.571
12	9082.3	128	128	1000	···	···
13	9210.3	128	128	1000	···	···
14	9177.3	16	512	1000	H89α	9173.323
15	9338.3	128	128	1000	···	···
16	9466.3	128	128	1000	···	···
17	9491.9	16	512	31.25	H88α	9487.824
18	9594.3	128	128	1000	···	···
19	9722.3	128	128	1000	···	···
20	9850.3	128	128	1000	···	···
21[a]	9821.1	16	512	31.25	H87α	9816.867
22	9887.3	16	512	31.25	H109β	9883.083
23	9978.3	128	128	1000	···	···

[a] Spectral window 21 was mistuned for one observing session in 13A-030.

on the sky. These calibrators are listed in Table 5.2.

The WISP calibration pipeline uses the calibrator data to iteratively derive calibration solution tables, flags radio frequency interference (RFI) and other bad data, and applies the calibration solutions to the science target data. We inspect both the calibration solutions and calibrated data to assess the quality of the calibration pipeline and to manually flag bad data that was missed by the WISP automatic flagging routines. The most common issues we flag are (1) antennas with poor calibration solutions, (2) broad frequency RFI that contaminates an entire spectral window, and (3) shadowed antennas. In rare cases, RFI will compromise nearly half of our spectral windows.

5.3.2 Imaging

We use the WISP imaging pipeline to automatically generate and clean images from the calibrated visibility data. We begin by regridding all of the data to a common kinematic local standard of rest (LSR or LSRK) velocity frame with a channel width $\Delta v_{\rm LSR} = 1.2\,{\rm km\,s^{-1}}$. Using the *TCLEAN* task in *CASA*, we generate several images and data cubes: (1) a multiscale, multi-frequency synthesis (MS-MFS) continuum image of the combined continuum spectral windows, (2) an MS-MFS image of each continuum and spectral line window, and (3) a multiscale data cube of each spectral line window. Following the strategy of Wenger et al. (2019, Chapter 4), we use *CLEAN* masks from each spectral line window MS-MFS image to *CLEAN* the data cube for that spectral window.

Many of our observed H II regions are spatially resolved. We increase our surface brightness sensitivity to resolved emission by *uv*-tapering our visibilities when generating images. This process, however, reduces our point source sensitivity and worsens our spatial resolution. Therefore, we generate both non-tapered and *uv*-tapered images/data cubes for each field. The latter are tapered to a synthesized half-power beam width (HPBW) of 15 arcsec.

5.4 Data Reduction and Analysis

The data analysis process for this survey closely follows the Wenger et al. (2019, Chapter 4) strategy. Because multiple nebulae may be observed in a single VLA pointing, we first identify unique *WISE* Catalog sources in each 8–10 GHzMS-MFS continuum image. Emission is associated with the *WISE* Catalog nebulae as long as

the peak continuum brightness pixel is within a circle centered on the *WISE* Catalog position with a radius equal to the *WISE* Catalog infrared radius. We manually locate these peak continuum brightness pixels for each nebula with detected radio continuum emission.

Unlike Wenger et al. (2019, Chapter 4), we wish to derive the total fluxes of extended sources in addition to their peak fluxes. We use a watershed segmentation algorithm (hereafter, watershed algorithm) to identify the pixels associated with the manually identified continuum peaks in our images and data cubes. The watershed algorithm considers an image as a three dimensional topological surface, where the image brightness corresponds to the "depth" of the surface. The algorithm identifies the basins that would be filled by flooding the surface from a given starting point (see Bertrand, 2005). In cases where multiple starting points will flood the same basin (i.e., in confused fields), the algorithm divides the basin into separate regions for each flooding source.

We set the manually identified continuum brightness peak locations as the flooding sources for the watershed algorithm. Using the MS-MFS images clipped at 7.5 times the spatial rms noise, we run the watershed algorithm to identify the pixels associated with each continuum source. Figure 5.2 shows an example region identified by this algorithm.

We measure the peak continuum brightness and total continuum flux of each continuum source at the location of the peak continuum brightness and within the watershed algorithm region, respectively. The uncertainty on the peak continuum brightness is measured as the spatial rms of the *CLEAN* residual image divided by the VLA primary beam response at the peak continuum brightness position. To compute the uncertainty on the total continuum flux, we add in quadrature the spatial rms divided by the primary beam response of each pixel within the watershed algorithm region.

We maximize our sensitivity to the faint RRL emission by averaging each observed Hnα RRL transition and both polarizations. This average spectrum is denoted by <Hnα>. For non-tapered images, we extract spectra from each line spectral window data cube at the location of the peak continuum brightness. The <Hnα> spectrum is computed as the weighted average of the individual RRL transitions. The weights are given by $w_i = S_{C,i}/\mathrm{rms}_i^2$ where $S_{C,i}$ is the continuum brightness and rms_i is the spectral rms noise of the ith spectral window, both measured in the line-free region

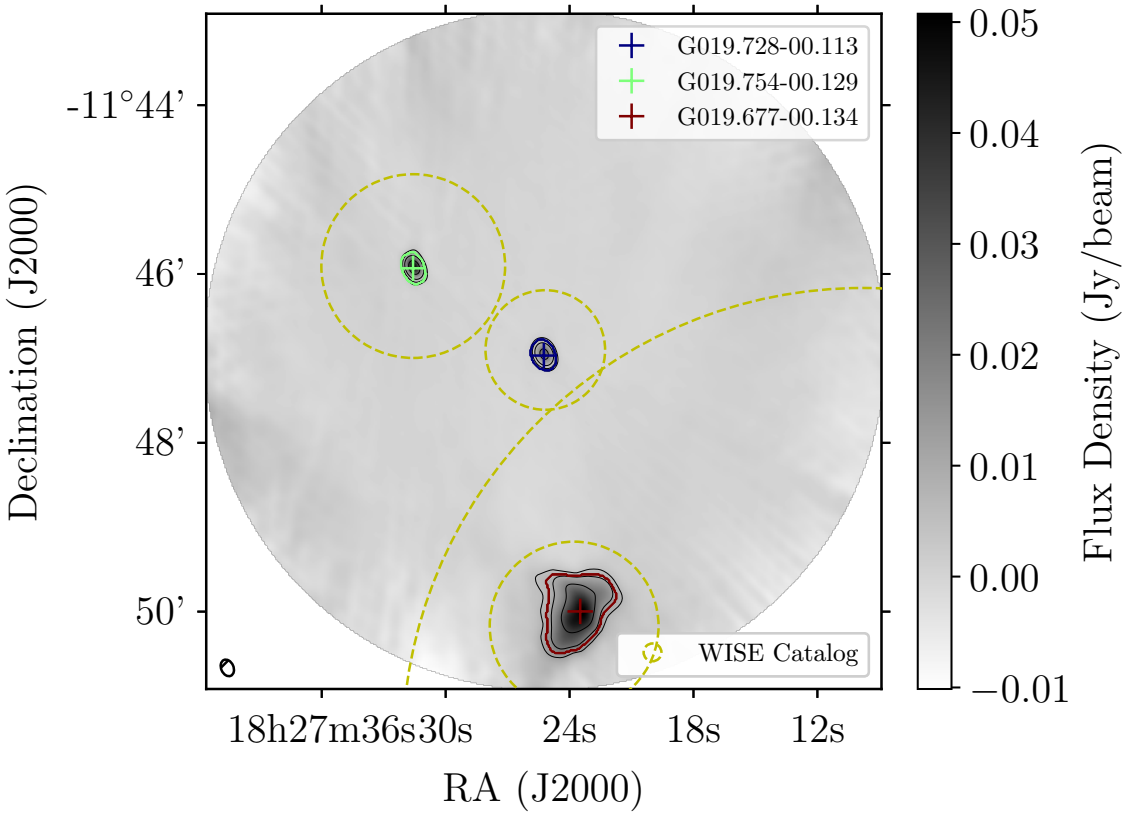

Figure 5.2: Watershed segmentation regions in a ∼2GHz combined MS-MFS continuum image. This field is centered on G019.728−0.113 and contains three *WISE* Catalog H II regions. The black contours are at 5, 10, 20, and 50 times the spatial rms noise (∼0.6 mJy beam^{-1} at the field center), and the yellow dashed circles represent the position and infrared radii of the *WISE* Catalog nebulae. The manually identified peak continuum brightness pixels are indicated by the colored plus symbols, and the watershed algorithm regions by the colored contours. These regions were created using the MS-MFS image clipped at 7.5 times the spatial rms noise.

of the spectrum. For *uv*-tapered images, we spatially smooth the data cubes to a common beam size, then extract the spectra and compute the <Hnα> spectrum in the same fashion.

The total RRL emission within the watershed algorithm regions is extracted from the data cubes differently than for the peak position. For each pixel in the region, we measure the median continuum brightness in the line-free region of the spectrum, $S_{C,i}$. Then, we sum each pixel's spectrum, $S_{L,i}$, weighted by the median continuum brightness in that pixel. The final extracted spectrum for this spectral window is normalized by the ratio of the median non-weighted sum and median weighted sum:

$$S_L(\nu) = \left(\sum_i S_{L,i}(\nu) S_{C,i}\right) \frac{\text{median}\left(\sum_i S_{L,i}\right)}{\text{median}\left(\sum_i S_{L,i}(\nu) S_{C,i}\right)}. \tag{5.1}$$

This complicated procedure correctly weights the final spectrum by the continuum level in each pixels' spectra while also ensuring that the final spectrum has the correct flux density. The watershed algorithm region <Hnα> spectrum is then computed using the same weighted average of the individual RRL transitions as for the peak positions.

Finally, we measure the <Hnα> RRL properties. We first identify the line-free regions of the spectrum to estimate the spectral rms noise and to fit and remove a third-order polynomial baseline. Then, we fit a Gaussian to the baseline-subtracted spectrum and measure the RRL brightness, the FWHM line width, and the LSR velocity.

5.5 RESULTS

5.5.1 VLA Data Products

Our goal is to derive an accurate nebular electron temperature for as many of the observed Galactic H II regions as possible. Given that some of these nebulae will be extremely faint, spatially resolved, and/or in confusing fields, no single data analysis method will work for each nebula. We pick the combination of non-tapered or *uv*-tapered images and peak position <Hnα> or watershed region <Hnα> spectra that maximizes our RRL sensitivity and minimizes our electron temperature uncertainty.

We detect radio continuum emission in 88 (69%) of the 128 observed fields. This low detection rate is a result of the relatively poor surface brightness sensitivity of

Table 5.4: VLA Continuum Data Products

Name	ν_C (MHz)	$S_C^{\rm P}$ (mJy beam^{-1})	$\rm QF_C^P$	$\rm Taper^{P\,a}$	$S_C^{\rm T}$ (mJy)	$\rm QF_C^T$	$\rm Taper^{T\,a}$
G005.885−00.393	8962.2	4516.01 ± 13.31	A	N	5182.11 ± 1.46	A	Y
G010.596−00.381	8962.2	395.02 ± 6.66	A	Y	843.64 ± 0.67	A	Y
G013.880+00.285	8962.2	1696.64 ± 3.26	A	Y	3408.35 ± 0.43	A	Y
G017.336−00.146	8962.1	10.91 ± 0.29	C	Y	54.58 ± 0.04	C	Y
G017.928−00.677	8962.1	14.48 ± 0.37	C	Y	69.06 ± 0.05	C	Y
G018.584+00.344	8962.1	22.53 ± 0.82	A	Y	45.66 ± 0.07	A	Y
G018.630+00.309	8962.1	13.01 ± 4.37	C	Y	0.02 ± 0.01	C	Y
G019.677−00.134	8962.1	163.19 ± 3.36	C	Y	492.33 ± 0.40	C	Y
G019.728−00.113	8962.1	24.23 ± 0.40	A	N	26.13 ± 0.06	A	N
G019.754−00.129	8962.1	46.45 ± 0.59	B	N	44.16 ± 0.08	B	N
G020.227+00.110	8962.1	8.61 ± 0.13	B	Y	41.01 ± 0.02	B	Y
G020.363−00.014	8962.1	50.30 ± 0.09	A	N	57.56 ± 0.02	A	N
G020.387−00.018	8962.1	2.61 ± 0.11	B	N	23.25 ± 0.04	B	N
G021.386−00.255	8962.1	122.94 ± 0.12	A	N	130.96 ± 0.03	A	N
G021.596−00.161	8962.2	5.70 ± 0.16	A	N	6.25 ± 0.02	A	N
G021.603−00.169	8962.2	19.32 ± 0.15	A	N	26.88 ± 0.03	B	Y
G023.661−00.252	8962.2	30.11 ± 0.46	B	Y	148.31 ± 0.09	B	Y
G024.153+00.163	8962.2	10.94 ± 1.62	C	N	0.12 ± 0.02	C	N
G024.166+00.250	8962.2	16.56 ± 0.79	B	N	14.74 ± 0.10	B	N
G024.195+00.242	8962.2	9.77 ± 0.57	B	N	34.19 ± 0.12	B	Y
G024.713−00.125	8962.2	32.51 ± 2.11	C	N	101.56 ± 0.41	C	Y
G025.397+00.033	8962.2	229.49 ± 0.56	C	N	481.85 ± 0.25	C	N
G025.398+00.562	8962.1	203.74 ± 0.36	A	Y	227.01 ± 0.05	A	Y
G025.401+00.021	8962.2	54.54 ± 0.60	C	N	145.61 ± 0.18	C	N
G027.562+00.084	8898.2	47.71 ± 0.23	A	N	114.43 ± 0.06	A	Y
G028.320+01.243	8962.1	21.17 ± 0.04	A	N	29.91 ± 0.01	A	N
G028.438+00.014	8962.2	4.01 ± 0.35	A	N	4.75 ± 0.04	A	Y
G028.451+00.001	8962.2	36.09 ± 0.30	A	N	81.21 ± 0.11	A	Y
G028.581+00.145	8962.2	25.87 ± 0.18	A	N	36.38 ± 0.04	A	Y
G029.770+00.219	8962.2	35.40 ± 0.16	A	N	71.63 ± 0.04	A	Y
G029.956−00.020	8962.2	1770.38 ± 4.48	A	N	4066.72 ± 1.74	A	Y
G030.211+00.428	8962.2	15.61 ± 0.04	A	N	25.88 ± 0.01	A	Y
G031.269+00.064	8962.2	2.70 ± 0.34	A	N	0.39 ± 0.02	A	N
G031.279+00.061	8962.2	125.29 ± 0.35	A	N	300.59 ± 0.09	A	Y
G031.580+00.074	8962.2	13.41 ± 0.21	B	N	14.19 ± 0.04	B	N
G032.030+00.048	8962.2	17.10 ± 0.19	A	N	24.52 ± 0.03	A	Y
G032.057+00.077	8962.2	13.36 ± 1.03	C	Y	123.82 ± 0.15	C	Y
G032.272−00.226	8962.2	147.87 ± 0.18	A	N	337.97 ± 0.06	A	Y
G032.928+00.606	8898.2	173.86 ± 0.27	A	N	335.51 ± 0.07	A	Y
G033.643−00.229	8962.2	6.37 ± 0.09	A	Y	11.45 ± 0.01	A	Y
G034.041+00.052	8962.2	25.97 ± 0.48	A	Y	93.62 ± 0.08	A	Y
G034.089+00.438	8962.2	34.42 ± 2.87	C	N	83.68 ± 0.37	C	Y
G034.133+00.471	8962.2	378.58 ± 1.10	A	Y	530.87 ± 0.15	A	Y
G034.686+00.068	8962.2	55.42 ± 0.60	A	Y	111.21 ± 0.08	A	Y
G035.126−00.755	8962.2	123.85 ± 0.43	A	Y	240.60 ± 0.06	A	Y
G035.948−00.149	8962.2	12.05 ± 0.03	A	N	27.19 ± 0.01	A	Y
G036.870+00.462	8962.2	3.03 ± 0.31	C	N	5.76 ± 0.04	C	Y
G036.877+00.498	8962.2	1.22 ± 0.17	C	N	0.02 ± 0.00	C	N
G036.918+00.482	8962.2	6.21 ± 0.08	A	N	7.27 ± 0.02	A	N
G038.550+00.163	8962.2	54.11 ± 0.25	A	N	122.68 ± 0.06	A	Y
G038.643−00.227	8962.3	18.70 ± 0.05	A	N	25.99 ± 0.02	A	Y
G038.652+00.087	8962.2	19.77 ± 0.24	A	N	64.23 ± 0.10	A	Y
G038.840+00.495	8962.2	4.49 ± 0.09	B	N	88.72 ± 0.05	B	Y
G038.875+00.308	8962.2	279.04 ± 0.43	A	N	317.69 ± 0.07	A	Y
G039.183−01.422	8962.3	20.75 ± 0.15	A	Y	57.00 ± 0.02	A	Y
G039.196+00.224	8962.3	62.54 ± 0.06	A	N	67.56 ± 0.02	A	Y

Table 5.4 continued

Table 5.4: VLA Continuum Data Products (continued)

Name	ν_C (MHz)	$S_C^{\rm P}$ (mJy beam^{-1})	$\rm QF_C^P$	$\rm Taper^{P\,a}$	$S_C^{\rm T}$ (mJy)	$\rm QF_C^T$	$\rm Taper^{T\,a}$
G039.213+00.202	8962.3	5.13 ± 0.09	B	N	5.60 ± 0.01	B	Y
G039.864+00.645	8962.3	67.52 ± 0.51	A	Y	114.15 ± 0.07	A	Y
G043.146+00.013	8962.3	1434.45 ± 126.49	C	Y	712.04 ± 5.36	C	Y
G043.165−00.031	8962.3	2330.17 ± 78.58	C	N	2903.33 ± 15.09	C	N
G043.168+00.019	8962.3	332.86 ± 17.06	B	N	473.62 ± 3.16	B	N
G043.170−00.004	8962.3	4331.44 ± 149.88	C	Y	9281.33 ± 17.33	C	Y
G043.432+00.516	8962.3	11.08 ± 0.35	B	Y	88.42 ± 0.08	B	Y
G043.523−00.648	8962.3	5.84 ± 0.04	A	Y	13.43 ± 0.01	A	Y
G043.818+00.395	8962.3	21.54 ± 0.97	B	Y	121.42 ± 0.19	B	Y
G043.968+00.993	8962.2	47.26 ± 0.07	A	N	48.65 ± 0.02	A	N
G043.999+00.978	8962.2	22.23 ± 0.22	C	N	24.36 ± 0.05	C	N
G044.501+00.332	8962.3	21.92 ± 1.24	A	Y	144.10 ± 0.23	A	Y
G044.503+00.349	8962.3	7.16 ± 0.36	A	N	8.58 ± 0.06	A	N
G045.197+00.740	8962.3	7.76 ± 0.18	B	N	143.23 ± 0.14	B	Y
G048.719+01.147	8962.4	37.12 ± 0.10	A	Y	69.58 ± 0.01	A	Y
G049.399−00.490	8962.4	166.98 ± 7.12	A	Y	252.72 ± 0.49	A	Y
G052.098+01.042	8962.3	287.77 ± 0.50	A	Y	428.14 ± 0.06	A	Y
G052.232+00.735	8962.4	68.65 ± 4.32	A	Y	158.05 ± 0.37	A	Y
G054.093+01.748	8962.3	18.84 ± 0.03	A	Y	34.47 ± 0.00	A	Y
G054.490+01.579	8962.3	24.30 ± 0.06	A	Y	44.30 ± 0.01	A	Y
G054.543+01.560	8962.3	3.73 ± 0.26	C	Y	3.12 ± 0.01	C	Y
G055.114+02.422	8962.3	138.55 ± 1.25	A	Y	606.48 ± 0.23	A	Y
G060.592+01.572	8962.3	55.66 ± 0.22	A	Y	164.62 ± 0.04	A	Y
G061.720+00.863	8962.7	90.28 ± 0.16	A	N	100.23 ± 0.02	A	Y
G062.577+02.389	8962.7	51.31 ± 0.28	B	N	368.60 ± 0.13	A	Y
G068.144+00.915	8962.7	42.25 ± 1.61	B	Y	319.23 ± 0.29	B	Y
G070.280+01.583	8962.6	542.61 ± 15.70	A	Y	2365.79 ± 2.34	A	Y
G070.293+01.599	8962.6	3550.27 ± 9.03	A	N	5075.85 ± 3.18	A	N
G070.304+01.595	8962.6	245.05 ± 9.37	B	N	1547.41 ± 3.85	B	N
G070.329+01.589	8962.6	1067.39 ± 23.78	C	N	2737.57 ± 4.34	C	Y
G070.673+01.190	8962.6	260.40 ± 0.72	A	Y	407.52 ± 0.10	A	Y
G070.765+01.820	8962.6	28.79 ± 0.52	A	Y	175.23 ± 0.10	A	Y
G071.150+00.397	8962.7	208.43 ± 0.25	A	N	386.71 ± 0.06	A	Y
G073.878+01.023	8962.6	75.77 ± 0.09	A	N	122.77 ± 0.02	A	Y
G074.155+01.646	8962.6	10.25 ± 0.04	A	N	39.01 ± 0.02	A	Y
G074.753+00.912	8962.6	55.70 ± 0.07	A	N	72.48 ± 0.02	A	Y
G075.768+00.344	8962.6	1059.58 ± 10.20	A	Y	4180.43 ± 1.84	A	Y
G078.114−00.550	8962.6	14.17 ± 3.03	C	Y	0.04 ± 0.01	C	Y
G078.174−00.550	8962.6	4.21 ± 0.19	B	N	16.80 ± 0.06	B	Y
G078.886+00.709	8962.6	83.02 ± 0.08	A	N	117.58 ± 0.03	A	Y
G080.191+00.534	8962.6	5.14 ± 0.09	B	N	40.25 ± 0.04	A	Y
G094.263−00.414	8963.1	4.40 ± 0.04	B	Y	26.26 ± 0.01	B	Y
G096.289+02.593	8963.1	27.93 ± 0.32	B	N	417.07 ± 0.25	B	Y
G096.434+01.324	8963.1	23.34 ± 0.10	A	N	36.55 ± 0.03	A	N
G097.515+03.173	8963.1	131.05 ± 0.65	B	Y	504.28 ± 0.11	B	Y
G097.528+03.184	8963.1	41.23 ± 0.29	A	N	48.71 ± 0.06	A	N
G101.016+02.590	8963.0	17.71 ± 0.06	A	Y	21.19 ± 0.01	A	Y
G104.700+02.784	8963.0	9.00 ± 0.17	A	Y	39.05 ± 0.03	A	Y
G109.104−00.347	8963.0	7.10 ± 0.07	A	N	17.70 ± 0.02	A	Y
G124.637+02.535	8963.4	252.56 ± 0.20	A	N	287.82 ± 0.03	A	Y
G125.092+00.778	8963.5	6.70 ± 0.02	A	Y	20.82 ± 0.00	A	Y
G135.188+02.701	8963.4	19.82 ± 0.09	A	Y	65.14 ± 0.01	A	Y
G141.084−01.063	8963.8	12.17 ± 0.19	A	Y	66.06 ± 0.04	A	Y
G150.859−01.115	8963.8	11.73 ± 0.10	A	Y	17.96 ± 0.01	A	Y
G196.448−01.673	8964.0	10.93 ± 0.47	B	N	235.36 ± 0.37	B	N
G218.737+01.850	8964.1	202.41 ± 0.69	A	Y	554.51 ± 0.11	A	Y

Table 5.4 continued

Table 5.4: VLA Continuum Data Products (continued)

Name	ν_C (MHz)	$S_C^{\rm P}$ (mJy beam^{-1})	$\rm QF_C^P$	$\rm Taper^{P\,a}$	$S_C^{\rm T}$ (mJy)	$\rm QF_C^T$	$\rm Taper^{T\,a}$
G351.246+00.673	8962.2	6536.22 ± 235.09	A	Y	13098.28 ± 16.58	A	Y
G351.311+00.663	8962.2	2200.65 ± 119.99	A	Y	3726.42 ± 6.79	A	Y

[a] "N" if measured in the non-tapered images, "Y" if measured in the *uv*-tapered images

the VLA. Many of the fields contain multiple *WISE* Catalog H II regions, however. We detect radio continuum emission toward 114 known H II regions. Table 5.4 lists the measured radio continuum properties of these nebulae: the *WISE* Catalog source name; the MS-MFS synthesized frequency of the combined continuum spectral windows, ν_C; the peak continuum flux density, S_C^P; a quality factor for the peak flux density, QF_C^P; a column indicating whether the peak flux density was measured using the non-tapered (N) or *uv*-tapered (Y) image; the total flux density within the watershed segmentation region, S_C^T; a quality factor for the total flux density, QF_C^T; and a column indicating whether the peak flux density was measured using the non-tapered or *uv*-tapered image. The MS-MFS synthesized frequency varies slightly for each field due to differences in data flagging. We select either non-tapered or *uv*-tapered based on which gives the smallest fractional uncertainty in the final electron temperature derivation (if the source also has a RRL detection), or which has the smallest fractional uncertainty in the continuum flux density. The *uv*-tapered images typically have a smaller fractional electron temperature or continuum flux density uncertainty for resolved nebulae. The quality factor (QF) is a qualitative assessment of the accuracy of the continuum flux measurement. QF A detections are isolated, unresolved, and near the center of the primary beam, QF B detections are slightly resolved, in crowded fields, and/or are located off-center in the primary beam, QF C detections are very resolved, in very crowded fields, and/or are located near the edge of the primary beam. Any continuum sources that are confused/blended are assigned QF D; these nebulae are excluded from the tables and all subsequent analysis since we are unable to measure their continuum fluxes accurately. The three nebulae in Figure 5.2 are examples of each continuum QF. G019.728−00.113 is a QF A detection, G019.754−00.129 is a QF B detection because it is off-center, and G019.677−00.134 is a QF C detection because it is resolved and near the edge of the primary beam.

We detect <Hnα> RRL emission toward 82 (72%) of our 114 continuum sources. Figure 5.3 shows representative <Hnα> RRL detections of different signal-to-noise ratios. Our typical spectral rms noise is $\sim$1 mJy beam^{-1}, about three times greater than what we estimated using the VLA sensitivity calculator. This decease in sensitivity is likely due to RFI that compromised entire spectral line spectral windows. We may be able to further increase our spectral line sensitivity by self-calibration.

Table 5.5 lists the measured <Hnα> RRL properties of our detections: the *WISE* Catalog source name; the weighted-average frequency of the <Hnα> spectrum, ν_L;

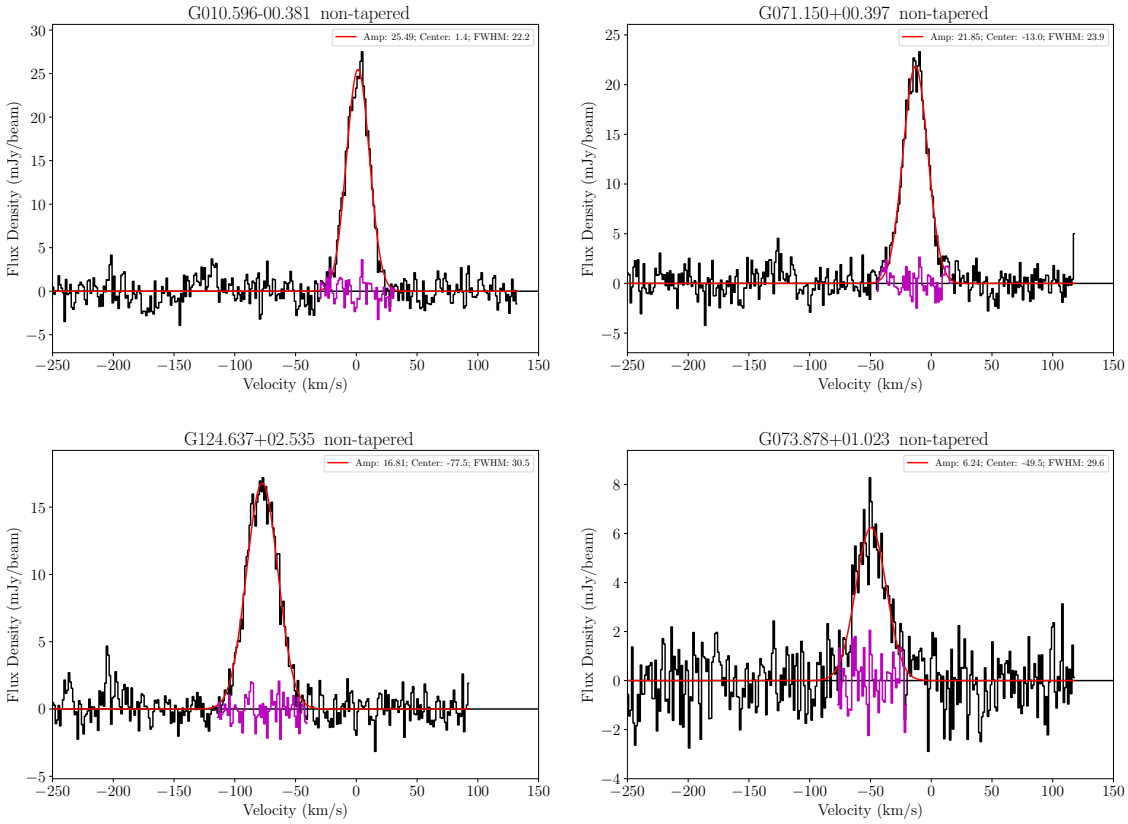

Figure 5.3: Representative <Hnα> stacked spectra. The spectra for G010.596−00.381 (top-left), G071.150+00.397 (top-right), G124.637+02.535 (bottom-left), and G073.878+01.023 (bottom-right) span the range of typical RRL detection signal-to-noise ratios. The black histogram is the data, the red curve is the Gaussian fit with parameters listed in the legend, and the magenta curve is the fit residuals. These spectra were extracted from the non-tapered data cubes at the location of the peak continuum brightness.

the amplitude of the Gaussian fit to the spectrum extracted from the location of peak continuum brightness, S_L^P; the spectral rms at this position, rms^P; the center LSR velocity of the fitted Gaussian, v_{LSR}^P; the FWHM line width of the fitted Gaussian, ΔV^P; a column indicating whether the spectrum was extracted from the non-tapered (N) or *uv*-tapered (Y) image; the amplitude of the Gaussian fit to the spectrum summed within the watershed segmentation region, S_L^T; the spectral rms in this region, rms^T; the center LSR velocity of the fitted Gaussian, v_{LSR}^T; the FWHM line width of the fitted Gaussian, ΔV^T; and a column indicating whether the spectrum was extracted from the non-tapered or *uv*-tapered image. As before, we use either the non-tapered or *uv*-tapered image depending on which gives the smallest fractional uncertainty in the derive electron temperature. Unlike B15, we do not assign quality factors to our RRL detections. Our spectral baselines are always extremely flat, therefore no qualitative assessment is necessary. Two nebulae, G005.885−00.393 and G070.293+01.599, are excluded from Table 5.5 because they have blended, non-Gaussian line profiles.

5.5.2 Electron Temperatures

Thermal bremsstrahlung (free-free) emission is the primary source of H II radio continuum emission, and its intensity depends on the plasma electron temperature, the plasma electron density, and the stellar ionizing photon rate. The free-free opacity of an H II region in local thermodynamic equilibrium (LTE) is well-approximated by

$$\tau_C \simeq 3.28 \times 10^{-7} \left(\frac{T_e}{10^4\,\mathrm{K}}\right)^{-1.35} \left(\frac{\nu}{\mathrm{GHz}}\right)^{-2.1} \left(\frac{\mathrm{EM}}{\mathrm{pc\ cm^{-6}}}\right) \tag{5.2}$$

where T_e is the plasma electron temperature, EM is the emission measure, and ν is the frequency (Mezger & Henderson, 1967). The emission measure is the integral of the squared electron density, n_e^2, along the line of sight, $\mathrm{EM} = \int n_e^2\, dl$. Without an independent determination of the emission measure, we are unable to use the continuum emission alone to derive the nebular electron temperature.

The RRL intensity and line width reveal the physical characteristics of an H II region. The line center opacity of an H II region in LTE is approximated by

$$\tau_L \simeq 1.92 \times 10^3 \left(\frac{T_e}{\mathrm{K}}\right)^{-2.5} \left(\frac{\mathrm{EM}}{\mathrm{pc\ cm^{-6}}}\right) \left(\frac{\Delta\nu}{\mathrm{kHz}}\right)^{-1} \tag{5.3}$$

where $\Delta\nu$ is the full-width half-maximum (FWHM) line width in frequency units

Table 5.5: VLA RRL Data Products

Name	ν_L (MHz)	$S_L^{\rm P}$ (mJy beam^{-1})	rms$^{\rm P}$ (mJy beam^{-1})	$v_{\rm LSR}^{\rm P}$ (km s^{-1})	$\Delta V^{\rm P}$ (km s^{-1})	Taper$^{{\rm P}\,a}$	$S_L^{\rm T}$ (mJy)	rms$^{\rm T}$ (mJy)	$v_{\rm LSR}^{\rm T}$ (km s^{-1})	$\Delta V^{\rm T}$ (km s^{-1})	Taper$^{{\rm T}\,a}$
G009.612+00.205	8862.2	5.53 ± 0.40	1.19	2.5 ± 0.8	22.2 ± 1.9	N	12.68 ± 0.38	1.10	2.6 ± 0.3	20.4 ± 0.7	N
G009.613+00.200	8786.3	81.07 ± 0.65	1.97	4.0 ± 0.1	20.4 ± 0.2	Y	152.45 ± 1.29	3.92	3.8 ± 0.1	20.4 ± 0.2	Y
G010.596−00.381	8816.4	59.07 ± 0.85	1.87	1.1 ± 0.2	23.3 ± 0.4	Y	2.23 ± 0.03	0.08	1.3 ± 0.1	23.0 ± 0.3	N
G010.621−00.380	8789.6	80.22 ± 0.52	1.67	-0.5 ± 0.1	24.8 ± 0.2	N	4.13 ± 0.03	0.10	-0.7 ± 0.1	24.9 ± 0.2	N
G010.623−00.385	8718.4	112.00 ± 0.98	2.81	0.8 ± 0.2	38.7 ± 0.4	N	233.45 ± 2.25	5.27	0.9 ± 0.2	33.0 ± 0.4	Y
G012.805−00.196	8779.1	1097.15 ± 7.39	11.78	36.3 ± 0.1	36.4 ± 0.3	Y	2036.19 ± 13.32	21.56	36.7 ± 0.1	34.5 ± 0.3	Y
G012.813−00.200	8767.2	199.79 ± 1.67	4.85	30.2 ± 0.1	27.2 ± 0.3	N	87.62 ± 0.81	2.58	30.5 ± 0.1	27.8 ± 0.3	N
G013.880+00.285	8806.2	267.42 ± 0.93	1.90	52.4 ± 0.0	21.5 ± 0.1	Y	493.34 ± 1.83	3.82	52.2 ± 0.0	21.4 ± 0.1	N
G017.928−00.677	8740.2	...	...	...	...	...	8.89 ± 0.97	2.57	38.8 ± 1.1	20.8 ± 2.7	Y
G018.584+00.344	8806.1	3.57 ± 0.41	1.09	14.4 ± 1.4	24.1 ± 3.5	Y	5.66 ± 0.56	1.42	14.7 ± 1.1	23.3 ± 2.8	Y
G019.677−00.134	8595.3	18.57 ± 1.19	4.14	54.7 ± 0.8	27.0 ± 2.2	Y	53.70 ± 2.50	8.96	55.8 ± 0.6	26.5 ± 1.5	Y
G019.728−00.113	8883.1	4.09 ± 0.36	1.08	53.6 ± 1.1	25.3 ± 2.6	Y	2.91 ± 0.22	0.73	52.9 ± 0.9	24.6 ± 2.2	N
G020.363−00.014	8832.6	7.16 ± 0.35	0.98	55.1 ± 0.5	22.3 ± 1.2	N	7.77 ± 0.31	1.03	55.5 ± 0.4	22.5 ± 1.0	N
G021.603−00.169	8886.8	2.67 ± 0.30	0.87	-4.9 ± 1.3	23.0 ± 3.8	Y	...	...	...	...	...
G023.661−00.252	8885.9	5.28 ± 0.29	1.03	66.5 ± 0.6	22.2 ± 1.4	Y	23.69 ± 0.69	2.80	67.3 ± 0.3	20.7 ± 0.7	Y
G024.195+00.242	8819.2	3.38 ± 0.47	1.53	33.0 ± 1.7	24.3 ± 4.5	Y	1.70 ± 0.24	0.75	32.3 ± 1.8	25.7 ± 5.1	Y
G025.397+00.033	8826.1	20.71 ± 0.29	0.94	-14.0 ± 0.2	28.0 ± 0.5	N	33.83 ± 0.48	1.77	-14.0 ± 0.2	27.3 ± 0.5	N
G025.398+00.562	8775.9	15.47 ± 0.32	0.98	11.7 ± 0.3	32.0 ± 0.8	Y	15.38 ± 0.31	1.04	11.5 ± 0.3	31.3 ± 0.7	N
G025.401+00.021	8867.2	10.30 ± 0.48	1.73	-10.7 ± 0.6	24.3 ± 1.3	Y	10.84 ± 0.42	1.34	-10.3 ± 0.4	22.4 ± 1.0	N
G026.597−00.024	8841.1	8.61 ± 0.28	1.00	18.0 ± 0.5	32.3 ± 1.3	Y	9.15 ± 0.30	1.04	18.1 ± 0.5	32.4 ± 1.3	N
G027.562+00.084	8542.6	15.65 ± 0.49	1.55	88.2 ± 0.3	20.4 ± 0.7	Y	18.08 ± 0.54	1.74	88.2 ± 0.3	20.8 ± 0.7	N
G028.320+01.243	8893.2	1.77 ± 0.24	0.65	-40.5 ± 1.0	15.0 ± 2.5	N	1.73 ± 0.28	0.84	-39.6 ± 4.2	33.5 ± 20.2	N
G028.451+00.001	8857.2	3.70 ± 0.23	0.87	-6.3 ± 0.9	28.9 ± 2.2	N	5.37 ± 0.33	1.10	-6.8 ± 0.8	26.9 ± 2.0	N
G028.581+00.145	8860.3	2.84 ± 0.29	0.76	-13.1 ± 1.2	24.4 ± 3.0	N	3.45 ± 0.32	0.90	-12.9 ± 1.2	26.8 ± 3.1	N
G029.770+00.219	8778.8	5.85 ± 0.47	1.15	-30.9 ± 0.8	21.6 ± 2.0	Y	6.91 ± 0.49	1.35	-30.9 ± 0.7	21.4 ± 1.8	N
G030.211+00.428	8715.8	2.83 ± 0.32	0.97	-10.8 ± 0.9	16.6 ± 2.3	Y	2.91 ± 0.33	0.99	-11.5 ± 1.0	17.6 ± 2.4	N
G031.580+00.074	8793.6	3.98 ± 0.56	1.41	100.7 ± 0.9	13.8 ± 2.2	Y	2.86 ± 0.34	0.80	100.8 ± 0.8	13.3 ± 1.8	N
G032.030+00.048	8848.2	5.13 ± 0.42	0.99	89.8 ± 0.6	15.3 ± 1.4	Y	3.51 ± 0.26	0.69	89.6 ± 0.6	16.2 ± 1.4	Y
G032.272−00.226	8819.0	21.61 ± 0.30	1.32	22.9 ± 0.2	26.5 ± 0.4	Y	26.46 ± 0.33	1.59	22.9 ± 0.2	26.9 ± 0.4	N
G032.928+00.606	8590.7	13.70 ± 0.27	1.00	-37.9 ± 0.3	28.9 ± 0.7	N	20.89 ± 0.43	1.63	-38.2 ± 0.3	26.9 ± 0.7	N
G034.041+00.052	8776.4	4.10 ± 0.36	1.26	36.9 ± 1.0	23.6 ± 2.4	Y	10.17 ± 0.66	2.38	36.7 ± 0.7	22.1 ± 1.7	N
G034.133+00.471	8801.3	42.46 ± 0.42	1.41	36.1 ± 0.1	24.6 ± 0.3	Y	56.32 ± 0.53	1.86	36.1 ± 0.1	24.6 ± 0.3	N
G034.686+00.068	8724.2	7.06 ± 0.33	1.15	50.5 ± 0.5	23.8 ± 1.3	Y	14.29 ± 0.53	1.94	50.4 ± 0.4	22.4 ± 1.0	Y
G035.126−00.755	8814.3	17.99 ± 0.38	1.17	35.0 ± 0.2	20.0 ± 0.5	Y	34.63 ± 0.67	2.12	35.6 ± 0.2	19.4 ± 0.4	Y
G035.948−00.149	8863.9	2.80 ± 0.35	1.03	48.6 ± 1.2	19.2 ± 3.0	Y	3.05 ± 0.33	1.15	49.4 ± 1.1	21.0 ± 2.9	N
G038.550+00.163	8758.9	11.79 ± 0.27	1.18	27.6 ± 0.3	23.7 ± 0.6	Y	14.88 ± 0.36	1.46	27.7 ± 0.3	23.8 ± 0.7	N
G038.643−00.227	8762.5	2.70 ± 0.43	1.12	69.4 ± 1.5	18.5 ± 3.7	Y	2.07 ± 0.24	0.98	69.2 ± 1.2	21.1 ± 3.6	N

Table 5.5 continued

Table 5.5: VLA RRL Data Products (continued)

Name	ν_L (MHz)	$S_L^{\rm P}$ (mJy beam^{-1})	rms$^{\rm P}$ (mJy beam^{-1})	$v_{\rm LSR}^{\rm P}$ (km s^{-1})	$\Delta V^{\rm P}$ (km s^{-1})	Taper$^{{\rm P}\,a}$	$S_L^{\rm T}$ (mJy)	rms$^{\rm T}$ (mJy)	$v_{\rm LSR}^{\rm T}$ (km s^{-1})	$\Delta V^{\rm T}$ (km s^{-1})	Taper$^{{\rm T}\,a}$
G038.840+00.495	8764.1	···	···	···	···	···	7.57 ± 0.94	2.80	-42.8 ± 1.2	20.3 ± 3.1	Y
G038.875+00.308	8808.9	25.36 ± 0.23	0.89	-13.4 ± 0.1	27.8 ± 0.3	N	27.91 ± 0.27	1.07	-13.8 ± 0.1	28.3 ± 0.3	N
G039.196+00.224	8780.7	4.85 ± 0.19	1.04	-21.1 ± 0.6	30.8 ± 1.5	Y	4.83 ± 0.23	0.94	-21.1 ± 0.7	29.2 ± 1.6	N
G039.864+00.645	8738.8	5.21 ± 0.31	1.14	-41.3 ± 0.8	27.3 ± 1.9	Y	8.57 ± 0.40	1.72	-42.0 ± 0.6	27.6 ± 1.5	N
G043.146+00.013	8708.1	134.45 ± 1.04	2.67	8.7 ± 0.1	30.2 ± 0.3	Y	16.45 ± 0.13	0.32	8.7 ± 0.1	30.6 ± 0.3	Y
G043.151+00.011	8695.6	62.31 ± 0.83	1.84	5.8 ± 0.2	31.8 ± 0.5	N	33.01 ± 0.40	0.87	5.9 ± 0.2	31.9 ± 0.4	N
G043.162+00.005	8768.7	42.28 ± 0.59	2.22	6.5 ± 0.2	27.0 ± 0.4	N	0.52 ± 0.01	0.03	6.5 ± 0.2	27.0 ± 0.4	N
G043.165−00.031	8665.8	154.87 ± 2.77	8.99	6.8 ± 0.3	38.8 ± 0.8	N	62.41 ± 1.03	3.35	7.1 ± 0.3	39.2 ± 0.8	N
G043.168+00.019	8762.5	46.09 ± 0.60	1.69	9.9 ± 0.2	24.1 ± 0.4	N	0.56 ± 0.01	0.02	9.9 ± 0.2	24.1 ± 0.4	N
G043.170−00.004	8670.2	223.40 ± 2.39	3.38	7.8 ± 0.2	36.0 ± 0.4	Y	688.55 ± 4.66	8.39	4.4 ± 0.1	30.8 ± 0.2	Y
G043.175+00.025	8739.0	40.65 ± 0.64	2.02	14.9 ± 0.2	28.7 ± 0.5	N	0.77 ± 0.01	0.04	14.9 ± 0.2	28.7 ± 0.5	N
G043.432+00.516	8896.0	···	···	···	···	···	6.81 ± 1.01	2.92	-11.8 ± 1.9	25.1 ± 5.8	Y
G043.818+00.395	8881.8	···	···	···	···	···	8.70 ± 0.63	2.11	-8.5 ± 1.1	31.0 ± 2.8	Y
G043.968+00.993	8789.7	3.87 ± 0.27	0.87	-25.5 ± 1.1	31.9 ± 2.8	N	3.92 ± 0.30	0.92	-25.2 ± 1.1	30.3 ± 2.9	N
G044.501+00.332	8806.0	2.80 ± 0.29	0.85	-41.6 ± 1.1	22.0 ± 2.8	Y	6.46 ± 0.46	1.05	-43.4 ± 0.7	19.7 ± 1.6	Y
G048.719+01.147	8828.4	3.70 ± 0.28	1.05	-25.6 ± 1.0	26.5 ± 2.4	Y	6.21 ± 0.48	1.72	-26.0 ± 1.0	26.8 ± 2.5	N
G049.399−00.490	8880.6	21.50 ± 0.46	1.34	62.7 ± 0.2	22.7 ± 0.6	Y	0.29 ± 0.01	0.02	62.0 ± 0.2	23.2 ± 0.5	Y
G052.098+01.042	8835.7	24.43 ± 0.37	1.15	37.5 ± 0.2	29.3 ± 0.5	Y	36.30 ± 0.53	1.61	37.3 ± 0.2	28.7 ± 0.5	N
G052.232+00.735	8756.0	5.54 ± 0.95	2.72	-1.1 ± 2.3	26.2 ± 7.3	Y	12.60 ± 1.15	3.07	-2.0 ± 1.0	21.4 ± 2.3	Y
G055.114+02.422	8859.8	6.60 ± 0.27	1.08	-73.6 ± 0.6	32.8 ± 1.6	Y	28.15 ± 0.57	2.73	-74.8 ± 0.3	32.7 ± 0.8	Y
G060.592+01.572	8864.6	3.93 ± 0.38	1.05	-50.2 ± 1.3	27.2 ± 3.3	Y	10.40 ± 0.64	2.35	-48.5 ± 0.8	26.4 ± 2.0	N
G061.720+00.863	8808.8	7.00 ± 0.66	2.11	-69.6 ± 1.2	25.9 ± 3.2	N	7.19 ± 0.73	2.37	-68.7 ± 1.3	25.4 ± 3.2	N
G062.577+02.389	8747.3	8.53 ± 0.93	2.95	-71.2 ± 1.2	22.3 ± 3.0	Y	23.96 ± 2.72	7.16	-72.1 ± 1.2	21.8 ± 3.0	Y
G070.280+01.583	8782.7	49.01 ± 0.97	2.68	-23.6 ± 0.2	23.4 ± 0.5	Y	126.24 ± 1.44	4.27	-25.2 ± 0.1	25.1 ± 0.3	Y
G070.304+01.595	8763.0	72.95 ± 0.93	3.53	-18.2 ± 0.2	24.5 ± 0.4	Y	8.67 ± 0.11	0.37	-18.6 ± 0.2	24.7 ± 0.4	Y
G070.329+01.589	8694.4	157.24 ± 2.94	8.96	-18.4 ± 0.3	30.4 ± 0.7	Y	132.53 ± 2.30	7.29	-18.7 ± 0.3	29.9 ± 0.6	Y
G070.765+01.820	8840.9	···	···	···	···	···	11.19 ± 1.28	4.14	-78.3 ± 1.4	25.7 ± 3.8	N
G071.150+00.397	8783.3	34.14 ± 0.53	1.56	-12.2 ± 0.2	24.2 ± 0.4	Y	37.25 ± 0.56	1.93	-12.4 ± 0.2	24.0 ± 0.4	N
G073.878+01.023	8815.2	6.24 ± 0.30	1.12	-49.5 ± 0.7	29.6 ± 1.7	N	8.40 ± 0.40	1.45	-50.3 ± 0.7	30.8 ± 1.7	N
G074.155+01.646	8798.0	4.15 ± 0.45	1.18	-32.2 ± 0.9	15.9 ± 2.0	Y	5.64 ± 0.63	1.80	-31.7 ± 0.9	15.8 ± 2.1	Y
G074.753+00.912	8785.4	6.53 ± 0.33	1.39	-48.4 ± 0.6	25.6 ± 1.6	Y	6.32 ± 0.32	1.23	-49.6 ± 0.7	27.9 ± 1.7	N
G075.768+00.344	8789.4	100.01 ± 0.66	2.09	-8.6 ± 0.1	25.5 ± 0.2	Y	308.82 ± 1.55	6.24	-9.4 ± 0.1	26.4 ± 0.1	N
G078.886+00.709	8821.1	12.24 ± 0.42	1.04	-1.9 ± 0.3	19.1 ± 0.8	N	15.69 ± 0.54	1.29	-1.9 ± 0.3	19.5 ± 0.8	N
G096.289+02.593	8873.2	4.36 ± 0.29	0.97	-87.5 ± 0.9	26.8 ± 2.1	Y	25.10 ± 0.90	2.94	-97.7 ± 0.5	28.4 ± 1.2	Y
G096.434+01.324	8876.4	2.75 ± 0.21	0.70	-78.7 ± 0.9	22.6 ± 2.1	N	3.98 ± 0.30	0.86	-77.9 ± 0.8	21.8 ± 1.9	N
G097.515+03.173	8865.1	9.56 ± 0.32	1.00	-76.8 ± 0.5	28.0 ± 1.1	Y	34.23 ± 0.79	2.66	-74.4 ± 0.3	28.2 ± 0.8	Y
G097.528+03.184	8865.1	4.81 ± 0.27	1.03	-71.7 ± 0.7	25.4 ± 1.8	Y	4.33 ± 0.23	0.75	-71.9 ± 0.6	23.8 ± 1.5	N

Table 5.5 continued

Table 5.5: VLA RRL Data Products (continued)

Name	ν_L (MHz)	$S_L^{\rm P}$ (mJy beam^{-1})	rms$^{\rm P}$ (mJy beam^{-1})	$v_{\rm LSR}^{\rm P}$ (km s^{-1})	$\Delta V^{\rm P}$ (km s^{-1})	Taper$^{\rm P}$ [a]	$S_L^{\rm T}$ (mJy)	rms$^{\rm T}$ (mJy)	$v_{\rm LSR}^{\rm T}$ (km s^{-1})	$\Delta V^{\rm T}$ (km s^{-1})	Taper$^{\rm T}$ [a]
G101.016+02.590	8896.8	2.57 ± 0.46	0.92	-70.2 ± 1.4	16.3 ± 3.5	Y	2.74 ± 0.37	0.95	-70.3 ± 1.1	16.6 ± 2.7	N
G109.104−00.347	8852.5	2.98 ± 0.30	0.90	-44.1 ± 1.1	22.7 ± 2.7	Y	4.04 ± 0.42	1.11	-44.5 ± 1.0	20.1 ± 2.5	Y
G124.637+02.535	8817.1	16.81 ± 0.28	0.96	-77.5 ± 0.2	30.5 ± 0.6	N	18.19 ± 0.31	1.17	-77.6 ± 0.3	30.7 ± 0.6	N
G135.188+02.701	8974.4	2.61 ± 0.35	1.06	-73.2 ± 1.3	19.9 ± 3.1	Y	6.35 ± 0.65	2.53	-72.1 ± 2.0	31.4 ± 9.0	Y
G141.084−01.063	8844.0	...	...	...	...	...	7.77 ± 0.99	2.85	-25.2 ± 1.2	18.6 ± 3.0	Y
G196.448−01.673	8872.6	4.71 ± 0.36	1.08	10.9 ± 0.8	20.8 ± 1.9	Y	15.97 ± 0.66	1.97	12.2 ± 0.5	23.1 ± 1.1	Y
G351.246+00.673	8789.9	851.65 ± 3.29	8.64	-0.4 ± 0.0	24.7 ± 0.1	Y	1390.99 ± 3.99	11.32	-0.1 ± 0.0	25.1 ± 0.1	Y
G351.311+00.663	8839.3	356.60 ± 1.68	5.76	-6.9 ± 0.1	24.2 ± 0.1	Y	693.17 ± 2.58	7.22	-6.2 ± 0.0	24.1 ± 0.1	Y

[a] "N" if measured in the non-tapered images, "Y" if measured in the *uv*-tapered images

(Kardashev, 1959; Mezger & Hoglund, 1967). Similar to the continuum, we need an independent measurement of the emission measure in order to use the RRL properties to derive the electron temperature. There are three physical effects that set the RRL FWHM line width: (1) intrinsic broadening, due to the uncertainty principle; (2) collisional broadening, due to the collisions of the emitting atoms; and (3) Doppler broadening, due to the Maxwellian velocity distribution of emitting atoms in the plasma. Of these, Doppler broadening is the most significant contribution to the width of RRLs, and the typical hydrogen RRL line width is $\sim$25 km s^{-1} (Wenger et al., 2019, Chapter 4). RRLs of different atoms are necessary to constrain the non-thermal (i.e., turbulent) component of the line width, since atoms with different masses have different Maxwellian velocity distributions.

We derive the nebular electron temperature by measuring the RRL-to-continuum brightness ratio. For an optically thin H II region in LTE, the ratio of the radio continuum brightness temperature to the RRL peak brightness temperature is equal to the ratio of the continuum opacity to the line center opacity. This ratio is independent of the emission measure. A complete derivation of the electron temperature equation is in Appendix D. For RRLs near H90α, assuming the continuum and RRL emission originate in the same volume of gas, we find

$$\frac{T_e}{\mathrm{K}} \simeq \left[7.100 \times 10^3 \left(\frac{\nu_L}{\mathrm{GHz}}\right)^{1.1} \left(\frac{S_C}{S_L}\right) \left(\frac{\Delta V}{\mathrm{km\ s^{-1}}}\right)^{-1} (1+y)^{-1}\right]^{0.87} \tag{5.4}$$

where ν_L is the RRL frequency, S_C is the continuum flux density, S_L is the RRL center flux density, ΔV is the RRL FWHM line width in velocity units, and y is the ratio of the number density of singly ionized helium to hydrogen. This is the same equation used in B15 within $\sim$0.04%.

We use Equation 5.4 to derive the electron temperatures of the 72 nebulae in our sample with a VLA <Hnα> RRL detection and a continuum quality factor A, B, or C. We only detect helium RRLs in a few, bright sources, so we assume $y = 0.08$ for all VLA detections, following Balser et al. (2011) and B15. Furthermore, we assume non-LTE effects and pressure broadening are negligible at these frequencies (see Balser et al., 1999). The RRL flux density, RRL FWHM line width, and continuum flux density are measured in the <Hnα> stacked spectra, and the RRL frequency is the weighted average frequency of the individual RRL transitions. In Appendix D, we

show that this strategy produces accurate electron temperatures.

Table 5.6 lists the measured RRL-to-continuum flux ratios, the RRL FWHM line widths, and the derived electron temperatures for the B15 single dish catalog and our VLA catalog. This table only lists the highest quality electron temperature derivations; we remove all QF D sources from the B15 catalog and our sample. The electron temperature uncertainties are computed by propagating the RRL-to-continuum flux ratio and FWHM line width uncertainties through Equation 5.4. For the VLA sources, we use the "Type" column to indicate if the position of peak continuum brightness (P) or watershed algorithm region (T) is used to measure the RRL-to-continuum flux ratio, and the "Taper" column to indicate if the non-tapered (N) or *uv*-tapered (Y) data cube is used. We select the combination of "Type" and "Taper" that minimizes the fractional uncertainty in the derived electron temperature. In cases where the same source is detected in multiple surveys, we only list the VLA values, if available. If the source is not observed or detected in the VLA survey, we list the GBT values. If the source is not in the VLA survey nor the GBT survey, we list the 140 Foot values.

In total, there are now 189 Galactic H II regions with accurate electron temperature determinations. This is an increase of 99 nebulae (110%) over the B15 single dish catalog. A fraction of these nebulae have inaccurate distances, however, and can not be used to investigate Galactic metallicity structure (see Section 5.5.4).

5.5.3 Comparison with Single Dish

Our sample combines measurements from three different telescopes: the 140 Foot, the GBT, and the VLA. Each of these telescopes may be affected by systematics that lead to differences in the derived electron temperatures. For example, diffuse foreground and background emission may affect the single dish observations, but such extended emission is filtered out by the VLA. In principle, there may be differences between the different single dish measurements as well. Balser et al. (2011) find no difference between the derived electron temperatures for 16 nebulae observed by both the 140 Foot and the GBT. Here we compare the single dish and VLA observations of 22 nebulae in common between the B15 single dish catalog and our VLA catalog.

We first compare the fitted LSR velocity of these nebulae. The top panel of Figure 5.4 shows the difference between the single dish RRL LSR velocity and that measured by the VLA for the 22 nebulae observed by the VLA and either the GBT

Table 5.6: H II Region Distances and Properties

Name	Telescope	S_L/S_C	ΔV (km s^{-1})	T_e (K)	Type[a]	Taper[b]	d (kpc)	R (kpc)	Distance[c] Method	Distance Reference
G000.666−00.036	140 Foot	0.0569 ± 0.0033	40.5 ± 0.4	8170 ± 180	···	···	$7.72\,^{+0.72}_{-0.78}$	$0.23\,^{+0.87}_{-0.13}$	P	R09c
G001.125−00.106	140 Foot	0.1070 ± 0.0018	24.5 ± 0.2	7130 ± 70	···	···	··· [d]	··· [d]	K	···
G003.266−00.061	140 Foot	0.0978 ± 0.0100	25.3 ± 0.4	7440 ± 280	···	···	··· [d]	··· [d]	K	···
G005.900−00.431	140 Foot	0.0691 ± 0.0006	22.5 ± 0.2	11130 ± 170	···	···	$2.94\,^{+0.24}_{-0.15}$	$5.43\,^{+0.13}_{-0.23}$	P	S14
G005.987−01.191	140 Foot	0.0840 ± 0.0008	26.5 ± 0.2	8180 ± 70	···	···	··· [d]	··· [d]	K	···
G008.137+00.232	140 Foot	0.1019 ± 0.0007	25.4 ± 0.1	7090 ± 60	···	···	··· [d]	··· [d]	K	···
G010.160−00.350	140 Foot	0.0911 ± 0.0005	31.2 ± 0.2	6830 ± 30	···	···	··· [d]	··· [d]	K	···
G010.308−00.150	140 Foot	0.0874 ± 0.0005	31.6 ± 0.2	6800 ± 40	···	···	··· [d]	··· [d]	K	···
G010.596−00.381	VLA	0.1517 ± 0.0022	23.0 ± 0.3	6224 ± 113	T	N	$4.86\,^{+0.53}_{-0.42}$	$3.67\,^{+0.38}_{-0.50}$	P	Sa14
G012.804−00.207	140 Foot	0.0808 ± 0.0007	30.7 ± 0.3	7620 ± 100	···	···	$2.90\,^{+0.31}_{-0.33}$	$5.54\,^{+0.31}_{-0.29}$	P	I13
G013.880+00.285	VLA	0.1568 ± 0.0006	21.5 ± 0.1	5848 ± 27	P	Y	$3.96\,^{+0.33}_{-0.45}$	$4.59\,^{+0.41}_{-0.29}$	P	S14
G015.097−00.729	140 Foot	0.0938 ± 0.0008	35.3 ± 0.3	5720 ± 60	···	···	$1.97\,^{+0.13}_{-0.13}$	$6.46\,^{+0.13}_{-0.13}$	P	X11
G016.993+00.873	140 Foot	0.0928 ± 0.0006	23.6 ± 0.1	6890 ± 60	···	···	$2.39\,^{+0.28}_{-0.24}$	$6.08\,^{+0.24}_{-0.26}$	K	···
G017.928−00.677	VLA	0.1527 ± 0.0180	20.8 ± 2.7	6104 ± 922	T	Y	$12.67\,^{+0.36}_{-0.43}$	$5.39\,^{+0.25}_{-0.30}$	K	···
G018.144−00.281	140 Foot	0.1052 ± 0.0008	25.2 ± 0.2	7180 ± 70	···	···	$4.03\,^{+0.34}_{-0.34}$	$4.69\,^{+0.25}_{-0.29}$	K	···
G018.584+00.344	VLA	0.1507 ± 0.0160	23.3 ± 2.8	5598 ± 779	T	Y	$14.32\,^{+0.43}_{-0.34}$	$7.00\,^{+0.26}_{-0.30}$	K	···
G018.669+01.965	140 Foot	0.0907 ± 0.0006	28.4 ± 0.2	7210 ± 60	···	···	$2.43\,^{+0.23}_{-0.27}$	$6.06\,^{+0.29}_{-0.25}$	K	···
G019.064−00.282	140 Foot	0.2916 ± 0.0052	25.2 ± 0.3	5440 ± 70	···	···	$4.42\,^{+0.42}_{-0.30}$	$4.37\,^{+0.27}_{-0.30}$	K	···
G019.677−00.134	VLA	0.1195 ± 0.0060	26.5 ± 1.5	6029 ± 392	T	Y	$11.64\,^{+0.45}_{-0.35}$	$4.77\,^{+0.26}_{-0.28}$	K	···
G019.728−00.113	VLA	0.1345 ± 0.0112	24.6 ± 2.2	5963 ± 642	T	N	$11.82\,^{+0.42}_{-0.36}$	$4.88\,^{+0.29}_{-0.24}$	K	···
G020.363−00.014	VLA	0.1417 ± 0.0062	22.5 ± 1.0	6157 ± 340	T	N	$11.71\,^{+0.38}_{-0.41}$	$4.90\,^{+0.21}_{-0.32}$	K	···
G020.728−00.105	140 Foot	0.1249 ± 0.0035	26.5 ± 0.1	5590 ± 90	···	···	$11.71\,^{+0.33}_{-0.43}$	$4.90\,^{+0.25}_{-0.29}$	K	···
G021.603−00.169	VLA	0.1039 ± 0.0121	23.0 ± 3.8	7959 ± 1395	P	Y	$15.93\,^{+0.58}_{-0.42}$	$8.77\,^{+0.44}_{-0.37}$	K	···
G023.423−00.216	140 Foot	0.1162 ± 0.0008	24.3 ± 0.1	6500 ± 55	···	···	$5.66\,^{+1.21}_{-1.09}$	$3.42\,^{+0.75}_{-0.11}$	P	B09
G023.661−00.252	VLA	0.1757 ± 0.0063	20.7 ± 0.7	5499 ± 234	T	Y	$10.95\,^{+0.45}_{-0.40}$	$4.72\,^{+0.29}_{-0.24}$	K	···
G023.713+00.175	140 Foot	0.1027 ± 0.0015	26.8 ± 0.4	6840 ± 110	···	···	$7.61\,^{+0.18}_{-0.14}$	$3.74\,^{+0.15}_{-0.30}$	K	···
G024.195+00.242	VLA	0.1190 ± 0.0177	24.3 ± 4.5	6692 ± 1384	P	Y	··· [d]	$6.22\,^{+0.24}_{-0.28}$	K	···
G024.456+00.489	140 Foot	0.1020 ± 0.0008	29.2 ± 0.5	6370 ± 80	···	···	$7.60\,^{+0.15}_{-0.15}$	$3.86\,^{+0.23}_{-0.25}$	K	···
G024.844+00.093	140 Foot	0.1326 ± 0.0012	24.9 ± 0.2	5860 ± 90	···	···	$7.58\,^{+0.14}_{-0.16}$	$3.68\,^{+0.25}_{-0.14}$	K	···
G025.382−00.151	140 Foot	0.0974 ± 0.0027	25.6 ± 0.1	7460 ± 70	···	···	$3.71\,^{+0.41}_{-0.26}$	$5.16\,^{+0.27}_{-0.24}$	K	···

Table 5.6 continued

Table 5.6: H II Region Distances and Properties (continued)

Name	Telescope	S_L/S_C	ΔV (km s^{-1})	T_e (K)	Type[a]	Taper[b]	d (kpc)	R (kpc)	Distance[c] Method	Distance Reference
G025.397+00.033	VLA	0.0853 ± 0.0013	28.0 ± 0.5	7893 ± 150	P	N	$16.37^{+0.65}_{-0.46}$	$9.51^{+0.56}_{-0.36}$	K	···
G025.398+00.562	VLA	0.0765 ± 0.0016	31.3 ± 0.7	7861 ± 214	T	N	$14.15^{+0.34}_{-0.43}$	$7.49^{+0.28}_{-0.28}$	K	···
G025.401+00.021	VLA	0.1078 ± 0.0044	22.4 ± 1.0	7861 ± 416	T	N	$16.08^{+0.49}_{-0.57}$	$9.28^{+0.38}_{-0.47}$	K	···
G025.867+00.118	140 Foot	0.1189 ± 0.0016	27.3 ± 0.4	6120 ± 100	···	···	$7.52^{+0.13}_{-0.17}$	$3.78^{+0.18}_{-0.15}$	K	···
G027.562+00.084	VLA	0.1594 ± 0.0054	20.8 ± 0.7	5765 ± 242	T	N	$9.66^{+0.48}_{-0.61}$	$4.45^{+0.23}_{-0.28}$	K	···
G028.320+01.243	VLA	0.0819 ± 0.0114	15.0 ± 2.5	14189 ± 2666	P	N	$19.43^{+1.12}_{-0.96}$	$12.66^{+1.10}_{-0.80}$	K	···
G028.451+00.001	VLA	0.0926 ± 0.0059	26.9 ± 2.0	7623 ± 642	T	N	$15.23^{+0.51}_{-0.51}$	$8.78^{+0.47}_{-0.32}$	K	···
G028.581+00.145	VLA	0.0949 ± 0.0092	26.8 ± 3.1	7487 ± 978	T	N	$15.79^{+0.56}_{-0.56}$	$9.36^{+0.46}_{-0.46}$	K	···
G028.746+03.458	GBT	0.1106 ± 0.0007	21.0 ± 0.1	8399 ± 73	···	···	$14.72^{+0.43}_{-0.46}$	$8.44^{+0.30}_{-0.37}$	K	···
G029.770+00.219	VLA	0.1029 ± 0.0075	21.4 ± 1.8	8458 ± 808	T	N	$17.64^{+0.75}_{-0.75}$	$11.31^{+0.52}_{-0.78}$	K	···
G029.956−00.020	140 Foot	0.0992 ± 0.0064	29.8 ± 0.1	6510 ± 90	···	···	$5.19^{+0.56}_{-0.51}$	$4.61^{+0.22}_{-0.24}$	P	Z14
G030.211+00.428	VLA	0.1262 ± 0.0153	17.6 ± 2.4	8346 ± 1306	T	N	$15.39^{+0.52}_{-0.52}$	$9.19^{+0.43}_{-0.40}$	K	···
G030.758−00.047	GBT	0.0908 ± 0.0003	33.5 ± 0.1	6567 ± 30	···	···	$7.20^{+0.11}_{-0.18}$	$4.67^{+0.19}_{-0.25}$	K	···
G031.268+00.478	GBT	0.0944 ± 0.0042	23.2 ± 1.0	8690 ± 462	···	···	$14.82^{+0.43}_{-0.51}$	$8.83^{+0.35}_{-0.42}$	K	···
G031.580+00.074	VLA	0.2546 ± 0.0350	13.3 ± 1.8	5808 ± 976	T	N	$4.82^{+0.76}_{-0.68}$	$4.88^{+0.31}_{-0.32}$	P	Z14
G032.030+00.048	VLA	0.2262 ± 0.0195	16.2 ± 1.4	5416 ± 569	T	Y	$5.19^{+0.20}_{-0.24}$	$4.80^{+0.10}_{-0.08}$	P	S14
G032.272−00.226	VLA	0.0850 ± 0.0011	26.9 ± 0.4	8207 ± 140	T	N	$12.53^{+0.39}_{-0.33}$	$7.05^{+0.28}_{-0.21}$	K	···
G032.733+00.209	GBT	0.1638 ± 0.0037	21.0 ± 0.4	5856 ± 156	···	···	$12.90^{+0.40}_{-0.35}$	$7.44^{+0.25}_{-0.27}$	K	···
G032.800+00.190	GBT	0.0750 ± 0.0004	29.5 ± 0.1	8625 ± 49	···	···	$12.93^{+0.40}_{-0.35}$	$7.52^{+0.23}_{-0.30}$	K	···
G032.870−00.427	GBT	0.1817 ± 0.0043	18.2 ± 0.4	6074 ± 176	···	···	$10.96^{+0.36}_{-0.43}$	$6.01^{+0.22}_{-0.26}$	K	···
G032.928+00.606	VLA	0.0723 ± 0.0015	28.9 ± 0.7	8641 ± 230	P	N	$17.72^{+0.82}_{-0.82}$	$11.68^{+0.74}_{-0.74}$	K	···
G032.982−00.338	GBT	0.1485 ± 0.0040	20.9 ± 0.5	6411 ± 207	···	···	$10.87^{+0.44}_{-0.31}$	$5.96^{+0.28}_{-0.19}$	K	···
G034.041+00.052	VLA	0.1532 ± 0.0113	22.1 ± 1.7	5821 ± 532	T	N	$11.51^{+0.34}_{-0.40}$	$6.54^{+0.24}_{-0.24}$	K	···
G034.133+00.471	VLA	0.1140 ± 0.0012	24.6 ± 0.3	6858 ± 88	T	N	$11.52^{+0.33}_{-0.39}$	$6.55^{+0.27}_{-0.21}$	K	···
G034.256+00.136	GBT	0.0999 ± 0.0006	24.4 ± 0.1	8084 ± 55	···	···	$3.14^{+0.44}_{-0.22}$	$5.93^{+0.25}_{-0.25}$	K	···
G034.686+00.068	VLA	0.1232 ± 0.0050	22.4 ± 1.0	6876 ± 353	T	Y	$10.54^{+0.45}_{-0.32}$	$6.01^{+0.28}_{-0.21}$	K	···
G035.126−00.755	VLA	0.1478 ± 0.0032	19.4 ± 0.4	6745 ± 181	T	Y	$2.28^{+0.28}_{-0.30}$	$6.60^{+0.26}_{-0.22}$	K	···
G035.197−01.756	GBT	0.0947 ± 0.0005	23.6 ± 0.0	8603 ± 40	···	···	$3.14^{+0.61}_{-0.39}$	$6.06^{+0.21}_{-0.37}$	P	Z09
G035.948−00.149	VLA	0.1229 ± 0.0145	21.0 ± 2.9	7419 ± 1172	T	N	$3.03^{+0.34}_{-0.34}$	$6.13^{+0.23}_{-0.23}$	K	···
G037.754+00.560	GBT	0.1170 ± 0.0028	23.4 ± 0.8	7163 ± 246	···	···	$11.99^{+0.40}_{-0.37}$	$7.42^{+0.29}_{-0.23}$	K	···

Table 5.6 continued

Table 5.6: H II Region Distances and Properties (continued)

Name	Telescope	S_L/S_C	ΔV (km s^{-1})	T_e (K)	Type[a]	Taper[b]	d (kpc)	R (kpc)	Distance[c] Method	Distance Reference
G038.550+00.163	VLA	0.1126 ± 0.0029	23.7 ± 0.6	7134 ± 232	P	Y	$11.31^{+0.33}_{-0.42}$	$7.05^{+0.24}_{-0.26}$	K	···
G038.643−00.227	VLA	0.1020 ± 0.0129	21.1 ± 3.6	8634 ± 1604	T	N	$6.51^{+0.13}_{-0.12}$	$5.65^{+0.22}_{-0.24}$	K	···
G038.652+00.087	GBT	0.0738 ± 0.0015	27.0 ± 0.6	9428 ± 245	···	···	$16.76^{+0.69}_{-0.93}$	$11.28^{+0.81}_{-0.56}$	K	···
G038.840+00.495	VLA	0.0900 ± 0.0116	20.3 ± 3.1	9919 ± 1725	T	Y	$16.75^{+0.93}_{-0.74}$	$11.52^{+0.79}_{-0.63}$	K	···
G038.875+00.308	VLA	0.0882 ± 0.0009	27.8 ± 0.3	7719 ± 97	P	N	$14.07^{+0.42}_{-0.59}$	$9.21^{+0.34}_{-0.45}$	K	···
G039.196+00.224	VLA	0.0745 ± 0.0031	30.8 ± 1.5	8145 ± 459	P	Y	$14.58^{+0.56}_{-0.60}$	$9.71^{+0.42}_{-0.52}$	K	···
G039.728−00.396	GBT	0.0874 ± 0.0020	25.7 ± 0.7	8503 ± 255	···	···	$9.30^{+0.40}_{-0.56}$	$6.05^{+0.20}_{-0.26}$	K	···
G039.864+00.645	VLA	0.0780 ± 0.0038	27.6 ± 1.5	8606 ± 553	T	N	$16.51^{+0.82}_{-0.82}$	$11.40^{+0.71}_{-0.71}$	K	···
G040.503+02.537	GBT	0.1074 ± 0.0006	22.4 ± 0.1	8223 ± 55	···	···	$1.35^{+0.39}_{-0.24}$	$7.33^{+0.25}_{-0.27}$	K	···
G043.146+00.013	VLA	0.0889 ± 0.0007	30.2 ± 0.3	7043 ± 73	P	Y	$11.58^{+0.46}_{-0.40}$	$7.91^{+0.31}_{-0.27}$	K	···
G043.165−00.031	VLA	0.0557 ± 0.0009	39.2 ± 0.8	8674 ± 191	T	N	$11.02^{+1.02}_{-0.83}$	$7.47^{+0.70}_{-0.48}$	P	Z13
G043.168+00.019	VLA	0.1274 ± 0.0018	24.1 ± 0.4	6250 ± 111	T	N	$10.93^{+0.97}_{-0.76}$	$7.43^{+0.68}_{-0.44}$	P	Z13
G043.170−00.004	VLA	0.0760 ± 0.0005	30.8 ± 0.2	7920 ± 71	T	Y	$11.05^{+0.91}_{-0.91}$	$7.41^{+0.75}_{-0.43}$	P	Z13
G043.432+00.516	VLA	0.0930 ± 0.0143	25.1 ± 5.8	8119 ± 1963	T	Y	$12.91^{+0.60}_{-0.43}$	$8.94^{+0.47}_{-0.33}$	K	···
G043.818+00.395	VLA	0.0788 ± 0.0059	31.0 ± 2.8	7806 ± 791	T	Y	$12.69^{+0.42}_{-0.54}$	$8.82^{+0.31}_{-0.40}$	K	···
G043.968+00.993	VLA	0.0822 ± 0.0060	31.9 ± 2.8	7255 ± 718	P	N	$13.83^{+0.72}_{-0.54}$	$9.74^{+0.57}_{-0.39}$	K	···
G044.418+00.535	GBT	0.0926 ± 0.0026	24.3 ± 0.7	8492 ± 299	···	···	$16.80^{+1.09}_{-0.86}$	$12.27^{+1.01}_{-0.74}$	K	···
G044.501+00.332	VLA	0.1064 ± 0.0078	19.7 ± 1.6	9044 ± 866	T	Y	$15.49^{+0.81}_{-0.81}$	$11.15^{+0.68}_{-0.63}$	K	···
G045.197+00.740	GBT	0.0556 ± 0.0010	30.5 ± 0.6	10841 ± 245	···	···	$14.46^{+0.87}_{-0.53}$	$10.39^{+0.71}_{-0.39}$	K	···
G045.453+00.044	GBT	0.0871 ± 0.0007	27.6 ± 0.1	8026 ± 63	···	···	$8.07^{+1.48}_{-0.99}$	$6.25^{+0.61}_{-0.30}$	P	W14
G046.495−00.241	140 Foot	0.1989 ± 0.0071	20.1 ± 0.2	4860 ± 80	···	···	$5.74^{+0.11}_{-0.12}$	$6.30^{+0.18}_{-0.22}$	K	···
G048.719+01.147	VLA	0.0987 ± 0.0080	26.5 ± 2.4	7310 ± 776	P	Y	$12.93^{+0.59}_{-0.63}$	$9.71^{+0.49}_{-0.49}$	K	···
G048.922−00.285	140 Foot	0.0805 ± 0.0005	26.7 ± 0.2	8440 ± 60	···	···	$5.26^{+0.22}_{-0.18}$	$6.29^{+0.01}_{-0.00}$	P	W14
G049.002−00.303	140 Foot	0.1859 ± 0.0017	24.4 ± 0.2	8170 ± 50	···	···	$5.27^{+0.22}_{-0.18}$	$6.30^{+0.01}_{-0.00}$	P	W14
G049.201−00.365	140 Foot	0.0650 ± 0.0003	30.3 ± 0.1	9070 ± 70	···	···	$5.27^{+0.23}_{-0.18}$	$6.31^{+0.01}_{-0.00}$	P	W14
G049.384−00.298	140 Foot	0.0786 ± 0.0006	31.6 ± 0.3	8585 ± 65	···	···	$5.43^{+0.11}_{-0.11}$	$6.36^{+0.18}_{-0.10}$	K	···
G049.399−00.490	VLA	0.1190 ± 0.0022	23.2 ± 0.5	6578 ± 156	T	Y	$5.35^{+0.34}_{-0.26}$	$6.33^{+0.01}_{-0.00}$	P	W14
G049.489−00.378	GBT	0.0903 ± 0.0003	30.2 ± 0.0	7166 ± 25	···	···	$4.47^{+2.24}_{-1.68}$	$6.53^{+3.64}_{-0.19}$	P	S10b
G052.098+01.042	VLA	0.0854 ± 0.0013	28.7 ± 0.5	7725 ± 153	T	N	$3.70^{+1.31}_{-0.79}$	$6.58^{+0.35}_{-0.14}$	P	O10
G052.232+00.735	VLA	0.1062 ± 0.0101	21.4 ± 2.3	8193 ± 1018	T	Y	$10.30^{+0.58}_{-0.43}$	$8.41^{+0.37}_{-0.32}$	K	···

Table 5.6 continued

Table 5.6: H II Region Distances and Properties (continued)

Name	Telescope	S_L/S_C	ΔV (km s^{-1})	T_e (K)	Type[a]	Taper[b]	d (kpc)	R (kpc)	Distance[c] Method	Distance Reference
G052.766+00.333	GBT	0.0841 ± 0.0011	25.4 ± 0.4	8970 ± 186	···	···	$9.39\,^{+0.38}_{-0.55}$	$7.89\,^{+0.29}_{-0.29}$	K	···
G055.114+02.422	VLA	0.0483 ± 0.0010	32.7 ± 0.8	11352 ± 313	T	Y	$16.18\,^{+1.25}_{-1.07}$	$13.21\,^{+1.15}_{-0.85}$	K	···
G059.796+00.241	GBT	0.0975 ± 0.0008	21.8 ± 0.2	9068 ± 120	···	···	$8.74\,^{+0.52}_{-0.60}$	$8.53\,^{+0.30}_{-0.37}$	K	···
G060.592+01.572	VLA	0.0732 ± 0.0046	26.4 ± 2.0	9587 ± 816	T	N	$11.94\,^{+0.95}_{-0.67}$	$10.70\,^{+0.73}_{-0.51}$	K	···
G060.881−00.135	GBT	0.1229 ± 0.0010	21.2 ± 0.2	7463 ± 77	···	···	$4.05\,^{+0.09}_{-0.07}$	$7.73\,^{+0.24}_{-0.27}$	K	···
G061.473+00.094	GBT	0.0846 ± 0.0004	26.0 ± 0.1	8857 ± 43	···	···	$3.99\,^{+0.08}_{-0.08}$	$7.50\,^{+0.21}_{-0.20}$	K	···
G061.720+00.863	VLA	0.0777 ± 0.0075	25.9 ± 3.2	9170 ± 1265	P	N	$13.75\,^{+1.28}_{-0.85}$	$12.26\,^{+0.99}_{-0.75}$	K	···
G062.577+02.389	VLA	0.0711 ± 0.0079	22.3 ± 3.0	11197 ± 1694	P	Y	$13.60\,^{+1.25}_{-0.86}$	$12.26\,^{+1.02}_{-0.70}$	K	···
G063.164+00.449	GBT	0.0994 ± 0.0011	25.1 ± 0.1	7760 ± 90	···	···	$3.77\,^{+0.07}_{-0.08}$	$7.76\,^{+0.25}_{-0.25}$	K	···
G064.130−00.475	GBT	0.0973 ± 0.0005	23.9 ± 0.1	8452 ± 58	···	···	$3.63\,^{+0.08}_{-0.06}$	$7.64\,^{+0.23}_{-0.18}$	K	···
G068.144+00.915	GBT	0.0697 ± 0.0009	24.7 ± 0.3	10834 ± 207	···	···	$11.84\,^{+0.95}_{-0.95}$	$11.68\,^{+0.75}_{-0.75}$	K	···
G069.922+01.511	GBT	0.0712 ± 0.0003	27.0 ± 0.1	9703 ± 50	···	···	$11.46\,^{+1.02}_{-0.89}$	$11.66\,^{+0.73}_{-0.73}$	K	···
G070.280+01.583	VLA	0.0901 ± 0.0011	25.1 ± 0.3	8318 ± 127	T	Y	$7.86\,^{+0.79}_{-0.59}$	$9.38\,^{+0.41}_{-0.41}$	K	···
G070.293+01.599	GBT	0.0505 ± 0.0005	37.0 ± 0.2	10297 ± 121	···	···	$8.00\,^{+0.69}_{-0.74}$	$9.45\,^{+0.38}_{-0.47}$	K	···
G070.304+01.595	VLA	0.0970 ± 0.0025	21.6 ± 0.6	9398 ± 316	T	N	$7.25\,^{+0.74}_{-0.62}$	$9.07\,^{+0.35}_{-0.41}$	K	···
G070.329+01.589	VLA	0.0784 ± 0.0014	29.9 ± 0.6	8021 ± 188	T	Y	$7.43\,^{+0.68}_{-0.74}$	$9.03\,^{+0.42}_{-0.34}$	K	···
G070.765+01.820	VLA	0.0950 ± 0.0114	25.7 ± 3.8	7760 ± 1279	T	N	$12.51\,^{+1.32}_{-0.93}$	$12.51\,^{+1.01}_{-0.75}$	K	···
G071.150+00.397	VLA	0.1020 ± 0.0016	24.0 ± 0.4	7686 ± 157	T	N	$6.72\,^{+0.65}_{-0.77}$	$8.83\,^{+0.36}_{-0.34}$	K	···
G073.878+01.023	VLA	0.0745 ± 0.0037	30.8 ± 1.7	8170 ± 532	T	N	$9.24\,^{+0.85}_{-0.79}$	$10.58\,^{+0.61}_{-0.53}$	K	···
G074.155+01.646	VLA	0.1929 ± 0.0236	15.9 ± 2.0	6327 ± 970	P	Y	$7.77\,^{+0.65}_{-0.83}$	$9.65\,^{+0.48}_{-0.42}$	K	···
G074.753+00.912	VLA	0.0923 ± 0.0049	27.9 ± 1.7	7391 ± 515	T	N	$9.10\,^{+0.82}_{-0.82}$	$10.54\,^{+0.63}_{-0.51}$	K	···
G075.768+00.344	VLA	0.0903 ± 0.0005	26.4 ± 0.1	7904 ± 54	T	N	$3.49\,^{+0.28}_{-0.28}$	$8.21\,^{+0.05}_{-0.05}$	P	A11
G075.842+00.404	GBT	0.0751 ± 0.0003	30.5 ± 0.1	8363 ± 32	···	···	$3.67\,^{+0.59}_{-0.31}$	$8.25\,^{+0.12}_{-0.07}$	P	R12
G076.155−00.286	GBT	0.0651 ± 0.0005	30.9 ± 0.2	9498 ± 119	···	···	$7.15\,^{+0.78}_{-0.72}$	$9.55\,^{+0.48}_{-0.41}$	K	···
G076.384−00.621	GBT	0.0407 ± 0.0002	42.0 ± 0.2	11245 ± 92	···	···	$1.30\,^{+0.08}_{-0.10}$	$8.13\,^{+0.01}_{-0.01}$	P	X13
G078.032+00.606	GBT	0.0832 ± 0.0005	27.2 ± 0.2	8567 ± 86	···	···	$1.49\,^{+0.09}_{-0.08}$	$8.16\,^{+0.00}_{-0.00}$	P	R12
G078.147+01.820	GBT	0.0910 ± 0.0008	24.6 ± 0.2	8596 ± 107	···	···	$1.49\,^{+0.09}_{-0.08}$	$8.16\,^{+0.00}_{-0.00}$	P	R12
G078.886+00.709	VLA	0.1483 ± 0.0054	19.1 ± 0.8	6816 ± 317	P	N	$3.29\,^{+0.30}_{-0.26}$	$8.34\,^{+0.07}_{-0.05}$	P	R12
G079.270+02.488	GBT	0.1161 ± 0.0021	20.8 ± 0.6	7977 ± 222	···	···	$1.49\,^{+0.08}_{-0.08}$	$8.20\,^{+0.00}_{-0.00}$	P	R12
G079.293+01.296	GBT	0.0729 ± 0.0007	30.0 ± 0.1	8693 ± 86	···	···	$7.26\,^{+0.79}_{-0.79}$	$9.95\,^{+0.52}_{-0.48}$	K	···

Table 5.6 continued

Table 5.6: H II Region Distances and Properties (continued)

Name	Telescope	S_L/S_C	ΔV (km s^{-1})	T_e (K)	Type[a]	Taper[b]	d (kpc)	R (kpc)	Distance[c] Method	Distance Reference
G080.350+00.718	GBT	0.0699 ± 0.0007	26.5 ± 0.3	10250 ± 155	···	···	$9.30^{+1.09}_{-0.90}$	$11.31^{+0.84}_{-0.54}$	K	···
G080.362+01.212	GBT	0.1058 ± 0.0030	23.0 ± 0.7	7921 ± 294	···	···	$1.60^{+0.08}_{-0.07}$	$8.21^{+0.00}_{-0.00}$	P	R12
G080.938−00.129	GBT	0.0774 ± 0.0004	28.7 ± 0.1	8853 ± 62	···	···	$1.48^{+0.10}_{-0.07}$	$8.24^{+0.00}_{-0.00}$	P	R12
G081.681+00.540	GBT	0.0608 ± 0.0002	35.9 ± 0.1	8829 ± 36	···	···	$1.49^{+0.09}_{-0.07}$	$8.26^{+0.00}_{-0.00}$	P	R12
G082.566+00.362	GBT	0.1038 ± 0.0011	23.4 ± 0.2	8030 ± 128	···	···	$1.49^{+0.09}_{-0.07}$	$8.28^{+0.00}_{-0.00}$	P	R12
G083.792+03.269	GBT	0.0943 ± 0.0012	23.1 ± 0.3	8643 ± 184	···	···	$1.51^{+0.08}_{-0.09}$	$8.31^{+0.01}_{-0.00}$	P	R12
G085.241+00.021	GBT	0.0799 ± 0.0011	26.9 ± 0.3	8824 ± 177	···	···	$5.84^{+0.79}_{-0.79}$	$9.68^{+0.53}_{-0.37}$	K	···
G092.920+02.823	140 Foot	0.1308 ± 0.0028	24.8 ± 0.5	10840 ± 270	···	···	$7.00^{+1.07}_{-0.84}$	$11.24^{+0.67}_{-0.67}$	K	···
G096.289+02.593	VLA	0.0637 ± 0.0023	28.4 ± 1.2	10125 ± 486	T	Y	$10.30^{+1.47}_{-1.26}$	$13.90^{+1.24}_{-1.06}$	K	···
G096.434+01.324	VLA	0.1124 ± 0.0088	21.8 ± 1.9	7747 ± 795	T	N	$8.12^{+1.13}_{-1.06}$	$12.23^{+0.92}_{-0.76}$	K	···
G097.515+03.173	VLA	0.0710 ± 0.0017	28.2 ± 0.8	9231 ± 287	T	Y	$7.26^{+1.09}_{-0.84}$	$11.71^{+0.84}_{-0.58}$	P	H15
G097.528+03.184	VLA	0.1032 ± 0.0058	23.8 ± 1.5	7799 ± 572	T	N	$7.33^{+1.06}_{-0.87}$	$11.82^{+0.76}_{-0.61}$	P	H15
G101.016+02.590	VLA	0.1527 ± 0.0222	16.6 ± 2.7	7560 ± 1436	T	N	$6.98^{+1.03}_{-1.03}$	$11.70^{+0.90}_{-0.63}$	K	···
G108.191+00.586	GBT	0.0759 ± 0.0004	25.8 ± 0.1	9590 ± 59	···	···	$4.26^{+0.56}_{-0.51}$	$10.49^{+0.40}_{-0.32}$	P	C14
G108.375−01.056	GBT	0.0806 ± 0.0009	26.1 ± 0.3	8992 ± 131	···	···	$4.90^{+0.87}_{-0.81}$	$10.83^{+0.71}_{-0.50}$	K	···
G108.764−00.952	GBT	0.0706 ± 0.0004	29.6 ± 0.2	9404 ± 81	···	···	$4.62^{+0.76}_{-0.81}$	$10.74^{+0.56}_{-0.60}$	K	···
G109.104−00.347	VLA	0.2091 ± 0.0249	22.7 ± 2.7	4360 ± 636	P	Y	$3.92^{+0.84}_{-0.73}$	$10.23^{+0.66}_{-0.41}$	K	···
G110.099+00.042	GBT	0.0543 ± 0.0003	38.0 ± 0.2	9240 ± 75	···	···	$4.52^{+0.78}_{-0.78}$	$10.77^{+0.55}_{-0.59}$	K	···
G111.558+00.804	GBT	0.0829 ± 0.0005	27.1 ± 0.1	8483 ± 51	···	···	$2.62^{+0.15}_{-0.10}$	$9.62^{+0.09}_{-0.06}$	P	M09
G111.612+00.371	GBT	0.0885 ± 0.0005	26.8 ± 0.1	8428 ± 68	···	···	$5.77^{+0.98}_{-0.85}$	$11.71^{+0.85}_{-0.65}$	K	···
G112.212+00.229	GBT	0.0777 ± 0.0008	28.8 ± 0.2	8641 ± 118	···	···	$3.72^{+0.80}_{-0.68}$	$10.28^{+0.66}_{-0.45}$	K	···
G115.785−01.561	GBT	0.0806 ± 0.0017	26.8 ± 0.6	8794 ± 242	···	···	$3.65^{+0.72}_{-0.72}$	$10.38^{+0.63}_{-0.50}$	K	···
G118.345+04.856	140 Foot	0.0911 ± 0.0193	20.7 ± 0.3	9540 ± 1050	···	···	$0.68^{+0.44}_{-0.49}$	$8.63^{+0.37}_{-0.25}$	K	···
G124.637+02.535	VLA	0.0659 ± 0.0011	30.5 ± 0.6	9181 ± 204	P	N	$6.94^{+1.27}_{-1.09}$	$13.53^{+1.10}_{-1.02}$	K	···
G124.894+00.323	GBT	0.0781 ± 0.0031	27.0 ± 1.2	8975 ± 460	···	···	$3.30^{+0.63}_{-0.73}$	$10.59^{+0.50}_{-0.58}$	K	···
G128.772+02.009	GBT	0.0854 ± 0.0028	20.9 ± 0.7	10361 ± 427	···	···	$8.85^{+1.49}_{-1.61}$	$15.45^{+1.49}_{-1.39}$	K	···
G132.156−00.729	GBT	0.0769 ± 0.0006	24.9 ± 0.2	9785 ± 123	···	···	$4.90^{+0.83}_{-0.96}$	$12.19^{+0.74}_{-0.85}$	K	···
G133.712+01.221	GBT	0.0760 ± 0.0003	27.7 ± 0.0	8977 ± 38	···	···	$1.94^{+0.05}_{-0.03}$	$9.79^{+0.04}_{-0.03}$	P	X06;H06
G133.781+01.428	GBT	0.0785 ± 0.0005	27.5 ± 0.1	8752 ± 74	···	···	$1.95^{+0.04}_{-0.04}$	$9.79^{+0.04}_{-0.03}$	P	X06;H06
G135.188+02.701	VLA	0.1347 ± 0.0195	19.9 ± 3.1	7259 ± 1349	P	Y	$7.30^{+1.41}_{-1.31}$	$14.44^{+1.34}_{-1.15}$	K	···

Table 5.6 continued

Table 5.6: H II Region Distances and Properties (continued)

Name	Telescope	S_L/S_C	ΔV (km s^{-1})	T_e (K)	Type[a]	Taper[b]	d (kpc)	R (kpc)	Distance[c] Method	Distance Reference
G136.884+00.911	GBT	0.0995 ± 0.0025	23.5 ± 0.6	8204 ± 257	···	···	$1.96\,^{+0.03}_{-0.05}$	$9.86\,^{+0.03}_{-0.04}$	P	X06;H06
G138.494+01.634	GBT	0.0969 ± 0.0014	23.8 ± 0.3	8302 ± 131	···	···	$2.91\,^{+0.62}_{-0.66}$	$10.67\,^{+0.59}_{-0.55}$	K	···
G141.084−01.063	VLA	0.1416 ± 0.0195	18.6 ± 3.0	7258 ± 1338	T	Y	$2.10\,^{+0.48}_{-0.61}$	$9.95\,^{+0.56}_{-0.45}$	K	···
G150.596−00.955	GBT	0.0671 ± 0.0005	27.8 ± 0.1	10016 ± 83	···	···	$2.65\,^{+0.64}_{-0.59}$	$10.76\,^{+0.61}_{-0.61}$	K	···
G151.609−00.233	GBT	0.0543 ± 0.0004	31.7 ± 0.2	10795 ± 98	···	···	$6.86\,^{+1.63}_{-1.15}$	$14.79\,^{+1.60}_{-1.13}$	K	···
G154.646+02.438	GBT	0.0673 ± 0.0009	28.6 ± 0.4	9734 ± 175	···	···	$4.59\,^{+0.89}_{-1.02}$	$12.64\,^{+0.90}_{-0.96}$	K	···
G155.372+02.613	GBT	0.0703 ± 0.0013	25.6 ± 0.5	10253 ± 309	···	···	$6.69\,^{+1.41}_{-1.21}$	$14.62\,^{+1.49}_{-1.09}$	K	···
G169.180−00.905	GBT	0.0872 ± 0.0013	23.1 ± 0.4	9345 ± 179	···	···	··· [d]	··· [d]	K	···
G173.599+02.803	GBT	0.1060 ± 0.0013	20.9 ± 0.3	8612 ± 137	···	···	··· [d]	··· [d]	K	···
G173.937+00.298	GBT	0.0935 ± 0.0014	23.0 ± 0.3	8829 ± 158	···	···	··· [d]	··· [d]	K	···
G192.638−00.008	GBT	0.0971 ± 0.0010	22.1 ± 0.2	8833 ± 107	···	···	$1.59\,^{+0.08}_{-0.07}$	$9.90\,^{+0.08}_{-0.07}$	P	R10
G196.448−01.673	VLA	0.0892 ± 0.0038	23.1 ± 1.1	9024 ± 508	T	Y	$5.31\,^{+0.33}_{-0.38}$	$13.51\,^{+0.32}_{-0.37}$	P	H07
G209.037−19.377	GBT	0.0878 ± 0.0007	26.1 ± 0.0	8322 ± 55	···	···	$0.42\,^{+0.00}_{-0.01}$	$8.71\,^{+0.00}_{-0.01}$	P	S07;M07;K08
G213.076−02.213	GBT	0.0564 ± 0.0006	28.6 ± 0.3	11343 ± 162	···	···	$6.50\,^{+1.19}_{-1.19}$	$14.23\,^{+1.19}_{-1.19}$	K	···
G213.703−12.601	GBT	0.0750 ± 0.0004	29.8 ± 0.1	8986 ± 65	···	···	$0.83\,^{+0.40}_{-0.40}$	$9.10\,^{+0.36}_{-0.41}$	K	···
G218.737+01.850	GBT	0.0702 ± 0.0007	24.6 ± 0.3	10671 ± 143	···	···	$5.46\,^{+0.94}_{-1.09}$	$13.05\,^{+0.84}_{-1.04}$	K	···
G220.524−02.759	GBT	0.0473 ± 0.0021	31.8 ± 1.7	12037 ± 725	···	···	$7.59\,^{+1.35}_{-1.35}$	$14.92\,^{+1.29}_{-1.29}$	K	···
G225.470−02.587	GBT	0.1141 ± 0.0020	22.6 ± 0.4	7537 ± 158	···	···	$0.15\,^{+0.36}_{-0.14}$	$8.50\,^{+0.34}_{-0.20}$	K	···
G227.760−00.127	GBT	0.0485 ± 0.0007	28.9 ± 0.4	12495 ± 249	···	···	$4.26\,^{+0.89}_{-0.72}$	$11.68\,^{+0.76}_{-0.71}$	K	···
G231.481−04.401	GBT	0.1011 ± 0.0024	20.5 ± 0.6	9098 ± 286	···	···	$4.28\,^{+0.98}_{-0.66}$	$11.51\,^{+0.84}_{-0.59}$	K	···
G233.753−00.193	GBT	0.0822 ± 0.0015	24.1 ± 0.4	9482 ± 209	···	···	$2.60\,^{+0.75}_{-0.51}$	$10.08\,^{+0.62}_{-0.42}$	K	···
G243.244+00.406	GBT	0.0793 ± 0.0014	22.3 ± 0.2	10477 ± 214	···	···	$4.32\,^{+0.82}_{-0.82}$	$10.80\,^{+0.79}_{-0.44}$	K	···
G345.284+01.463	140 Foot	0.0891 ± 0.0006	24.1 ± 0.2	8530 ± 640	···	···	··· [d]	··· [d]	K	···
G345.410−00.953	140 Foot	0.1036 ± 0.0004	26.3 ± 0.1	6960 ± 50	···	···	··· [d]	··· [d]	K	···
G348.249−00.971	140 Foot	0.0918 ± 0.0005	28.2 ± 0.2	6610 ± 100	···	···	··· [d]	··· [d]	K	···
G348.710−01.044	140 Foot	0.1067 ± 0.0008	24.6 ± 0.2	7150 ± 90	···	···	$3.30\,^{+0.35}_{-0.27}$	$5.14\,^{+0.25}_{-0.33}$	P	W12
G351.130+00.449	140 Foot	0.1272 ± 0.0015	22.1 ± 0.2	6650 ± 70	···	···	··· [d]	··· [d]	K	···
G351.170+00.704	140 Foot	0.1283 ± 0.0009	25.9 ± 0.1	5610 ± 20	···	···	··· [d]	··· [d]	K	···
G351.246+00.673	VLA	0.1131 ± 0.0003	25.1 ± 0.1	6772 ± 26	T	Y	$1.32\,^{+0.16}_{-0.13}$	$7.04\,^{+0.12}_{-0.16}$	P	W14
G351.311+00.663	VLA	0.1301 ± 0.0005	24.1 ± 0.1	6210 ± 31	T	Y	$1.34\,^{+0.13}_{-0.14}$	$7.02\,^{+0.14}_{-0.13}$	P	W14

Table 5.6 continued

Table 5.6: H II Region Distances and Properties (continued)

Name	Telescope	S_L/S_C	ΔV (km s^{-1})	T_e (K)	Type[a]	Taper[b]	d (kpc)	R (kpc)	Distance[c] Method	Distance Reference
G351.367+00.640	140 Foot	0.1151 ± 0.0012	23.9 ± 0.1	6840 ± 40	···	···	$1.33\,^{+0.15}_{-0.13}$	$7.02\,^{+0.14}_{-0.13}$	P	W14
G351.472−00.458	140 Foot	0.1067 ± 0.0012	23.3 ± 0.5	7460 ± 120	···	···	··· [d]	··· [d]	K	···
G351.646−01.252	140 Foot	0.0848 ± 0.0005	28.1 ± 0.1	7620 ± 30	···	···	··· [d]	··· [d]	K	···
G351.688−01.169	140 Foot	0.1029 ± 0.0006	23.6 ± 0.1	7560 ± 90	···	···	··· [d]	··· [d]	K	···
G352.597−00.188	140 Foot	0.1172 ± 0.0025	20.9 ± 0.9	7560 ± 240	···	···	··· [d]	··· [d]	K	···
G353.038+00.581	140 Foot	0.1040 ± 0.0012	28.6 ± 0.1	6250 ± 30	···	···	··· [d]	··· [d]	K	···
G353.092+00.857	140 Foot	0.2296 ± 0.0024	28.7 ± 0.1	5630 ± 40	···	···	··· [d]	··· [d]	K	···
G353.195+00.910	140 Foot	0.0826 ± 0.0006	30.8 ± 0.2	7100 ± 40	···	···	··· [d]	··· [d]	K	···
G353.408−00.381	140 Foot	0.0912 ± 0.0008	24.0 ± 0.2	8480 ± 60	···	···	··· [d]	··· [d]	K	···

[a] "P" if measured at the location of peak continuum brightness, "T" if measured within the watershed segmentation region

[b] "N" if measured in the non-tapered images, "Y" if measured in the uv-tapered images

[c] "K" for Monte Carlo kinematic distance, "P" for parallax distance

[d] Kinematic distances are unreliable in the direction of the Galactic center and anti-center

References — (A11) Ando et al. (2011); (B09) Brunthaler et al. (2009); (C14) Choi et al. (2014); (H06) Hachisuka et al. (2006); (H07) Honma et al. (2007); (H15) Hachisuka et al. (2015);(I13) Immer et al. (2013); (K08) Kim et al. (2008); (M07) Menten et al. (2007); (M09) Moscadelli et al. (2009); (O10) Oh et al. (2010); (RD09) Roman-Duval et al. (2009); (R09a) Reid et al. (2009a); (R09c) Reid et al. (2009b); (R10) Rygl et al. (2010); (R12) Rygl et al. (2012); (S07) Sandstrom et al. (2007); (S10) Sato et al. (2010); (S14) Sato et al. (2014); (Sa14) Sanna et al. (2014); (U12) Urquhart et al. (2012); (W12) Wu et al. (2012); (W14) Wu et al. (2014); (X06) Xu et al. (2006); (X11) Xu et al. (2011); (X13) Xu et al. (2013); (Z09) Zhang et al. (2009); (Z13) Zhang et al. (2013); (Z14) Zhang et al. (2014)

or the 140 Foot. Here and in all subsequent analyses, we use the "best" combination of non-tapered or *uv*-tapered data cubes and continuum peak brightness location or watershed algorithm region for spectral extraction. "Best" means the combination of tapering and spectral extraction technique that minimizes the fractional uncertainty in the derived electron temperature. The single dish and VLA LSR velocities are in good agreement, with a weighted mean difference of $0.15 \pm 0.35\,\mathrm{km\,s^{-1}}$ and a standard deviation of $1.64\,\mathrm{km\,s^{-1}}$.

The RRL FWHM line width probes the thermal Doppler broadening and non-thermal kinematics (e.g., turbulence) within an H II region. The bottom panel of Figure 5.4 shows the ratio of the single dish RRL line width to that measured by the VLA for the overlapping nebulae. The weighted mean of the line width ratios is 1.00 ± 0.02 with a standard deviation of 0.10. For the narrowest RRLs, the VLA line widths are ∼5-10% smaller than those measured by the single dish telescopes. This trend is likely due to the fact that the VLA is probing a denser and less turbulent component of the nebulae in some cases.

Next we compare the measured RRL-to-continuum brightness ratios and derived electron temperatures between the single dish and VLA surveys. We can not directly compare the total continuum flux or RRL flux between these different telescopes because each is sampling a different volume of gas within and surrounding the H II regions. Figure 5.5 shows the ratio of the single dish and VLA measured RRL-to-continuum flux ratios (top) and electron temperatures (bottom). The single dish RRL-to-continuum brightness ratios are systematically ∼10% less than the VLA brightness ratios. The weighted mean of these ratios is 0.86 ± 0.03 with a median of 0.90 and a standard deviation of 0.12. Consequently, the single dish electron temperatures are ∼10% greater than the VLA electron temperatures. The weighted mean of the electron temperature ratios is 1.12 ± 0.03 with a median of 1.10 and a standard deviation of 0.12.

The cause of the systematic difference between the single dish and VLA RRL-to-continuum brightness ratios and electron temperatures is unclear. The difference is either due to a problem with the derivation of the RRL-to-continuum brightness ratio or due to a fundamental difference in the RRL and/or continuum emission measured by the different telescopes. We know that there are a few issues with how the single dish RRL-to-continuum ratios are derived. B15 measured the continuum flux densities of their nebulae at $\nu_C = 8556\,\mathrm{MHz}$, whereas the average frequency of their observed

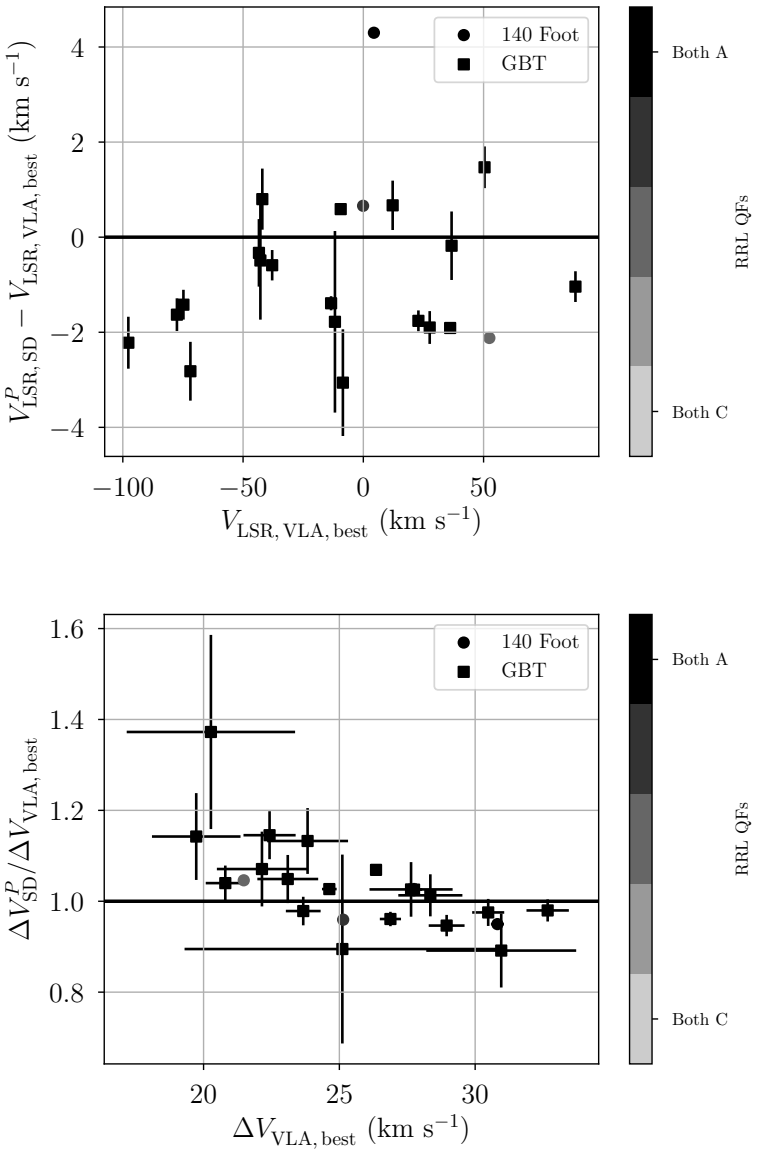

Figure 5.4: Difference between single dish and VLA RRL LSR velocities (top) and ratio of single dish to VLA RRL FWHM line widths (bottom) as a function of the VLA values for 22 nebulae also observed by the GBT (squares) or 140 Foot (circles). The color of the points represents the combined RRL quality factors (QFs) of the single dish and VLA surveys (all RRLs have QF A in the VLA survey). We use the "best" VLA images and spectral extraction technique, which minimizes the fractional uncertainty of the derived electron temperature. The weighted mean LSR velocity difference is $0.15 \pm 0.35\,\mathrm{km\,s^{-1}}$ and the weighted mean FWHM line width ratio is 1.00 ± 0.02.

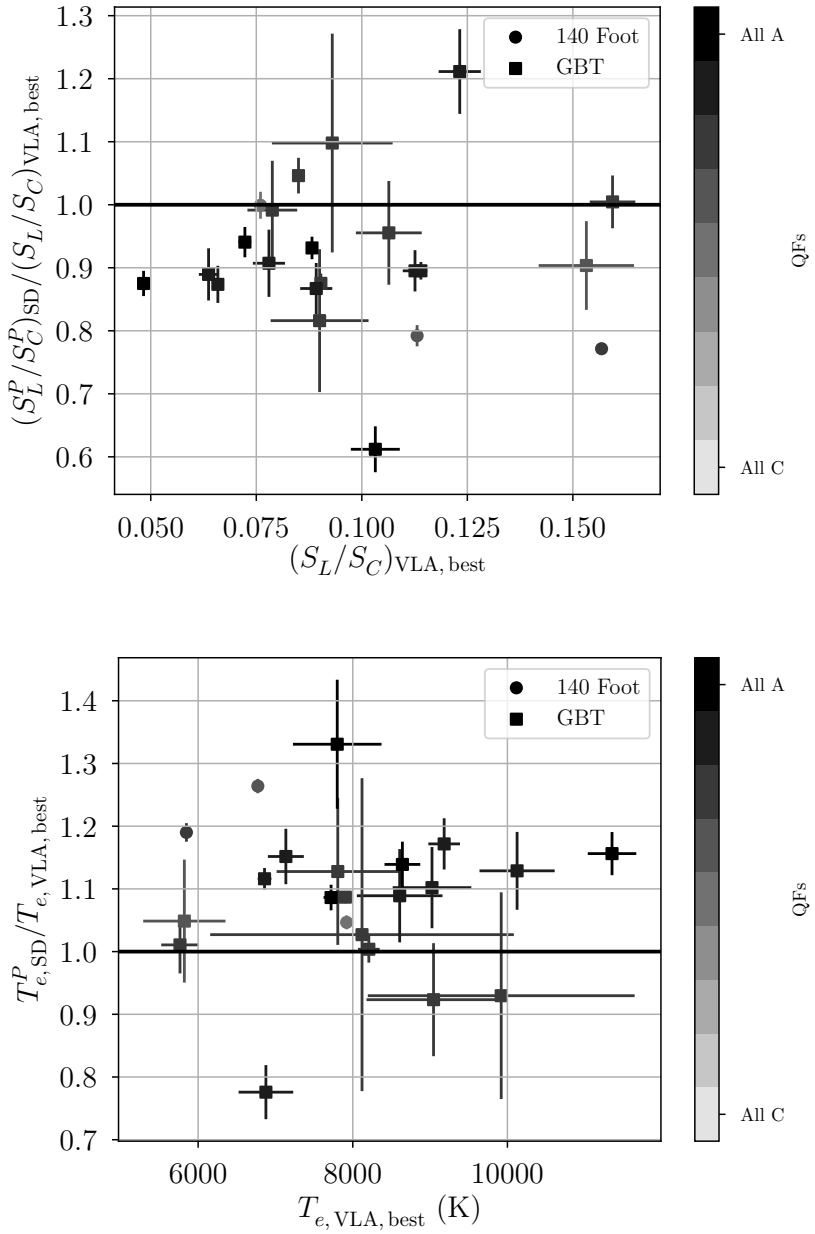

Figure 5.5: Ratio of single dish to VLA RRL-to-continuum brightness ratios (top) and ratio of single dish to VLA electron temperatures (bottom) as a function of the VLA values for the same nebulae as in Figure 5.4. The color of the points represents the combined continuum and RRL QFs of the single dish and VLA surveys. The weighted mean ratio of the single dish and VLA RRL-to-continuum brightness ratios is 0.86 ± 0.03 and the weighted mean electron temperature ratio is 1.12 ± 0.03.

RRL transitions is $\langle \nu_L \rangle = 8902\,\mathrm{MHz}$. In Appendix D, we show that the B15 strategy overestimates the true electron temperature by ∼6%. Furthermore, we do not scale the single dish and VLA RRL-to-continuum brightness ratios to a common frequency because each survey observed similar RRL transitions. The typical VLA <Hnα> weighted frequency is within 2% of the B15 average RRL frequency. Neither of these two effects can fully explain the observed 10% difference between the single dish and VLA RRL-to-continuum brightness ratios.

There are several factors that might affect the measured continuum and/or RRL flux densities: (1) the single dish continuum flux densities are inaccurate due to poor continuum background subtraction; (2) the single dish telescopes are not pointed at the center of the continuum source during the RRL observation; (3) the VLA is not sensitive to extended emission associated with the H II region; and/or (4) the VLA is seeing optically thick gas. The continuum flux densities are the largest source of uncertainty in the single dish electron temperature derivation (see B15). If the continuum background level is poorly constrained, then the single dish continuum flux densities will be inaccurate. We limit our analysis to high continuum QF single dish nebulae, however, so these problems should be minimal. The single dish RRL spectra must be measured at the location of the peak continuum brightness. If the telescope is not pointed properly, then the RRL flux densities will be underestimated. This is also not a likely explanation for the discrepency, because B15 peaked on source for their RRL observations. The VLA is not sensitive to diffuse emission. If the source of such emission has a different density and/or temperature, the VLA electron temperatures will differ from the single dish values. Finally, the nebulae may be optically thick. Optical depth effects would lead to an underestimation of the VLA continuum flux densities and electron temperatures. Some or all of these issues may be contributing to the remaining 4% discrepancy between the single dish and VLA RRL-to-continuum brightness ratios.

We wish to use as much data as possible to constrain the metallicity structure of the Galactic disk. Therefore, in subsequent analyses that combine the single dish and VLA electron temperatures, we scale the single dish electron temperatures by 90% to accommodate the systematic offset between the VLA and single dish data.

5.5.4 Distances

Distances to Galactic H II regions are derived in three ways: (1) spectrophotometrically, (2) geometrically, and (3) kinematically. Spectrophotometric distances are only available for optically unobscured nebulae. Since most of the nebulae in our sample are very distant through the Galactic plane, we do not consider spectrophotometric distances in this analysis. The extremely fine spatial resolution provided by very long baseline interferometry (VLBI) is used to measure the parallaxes and proper motions of masers associated with high-mass star forming regions (e.g., Reid & Honma, 2014). Several hundred maser parallax measurements have been made as part of the Bar and Spiral Structure Legacy (BeSSeL) Survey, the Japanese VLBI Exploration of Radio Astrometry (VERA), and various European VLBI Network (EVN) projects (see Wenger et al., 2018a, Chapter 3). The vast majority of Galactic H II regions, however, lack parallax measurements. Therefore, we rely on kinematic techniques to derive the distances to nebulae without a geometric distance determination.

Of the 189 Galactic H II regions in our sample with accurate electron temperature determinations, 47 (25%) have a maser parallax measurement. As in Wenger et al. (2018a, Chapter 3), we derive the parallax distance and distance uncertainties by Monte Carlo resampling the measured parallax within its uncertainties. We generate 5000 samples of the parallax distance, then we fit a kernel density estimator (KDE) to the distance distribution to estimate the probability distribution function (PDF). The peak of the PDF is the derived parallax distance, and the width of the PDF characterizes the parallax distance uncertainty (see Wenger et al., 2018a, Chapter 3). Figure 5.6 shows the parallax distance and Galactocentric radius PDFs for a representative source, G043.170−00.004.

Kinematic distances are computed by measuring the line of sight velocity of an object and assuming that object follows some Galactic rotation model (GRM). This technique uniquely identifies the object's Galactocentric radius, R. If the source is interior to the solar orbit, then the kinematic distance suffers from a kinematic distance ambiguity (KDA); two distances, a "near" distance and a "far" distance, have the same LSR velocity. Beyond the solar orbit, however, the kinematic distance is single valued. See Wenger et al. (2018a, Chapter 3) for more details about kinematic distance techniques.

We use the Wenger et al. (2018a, Chapter 3) Monte Carlo kinematic distance

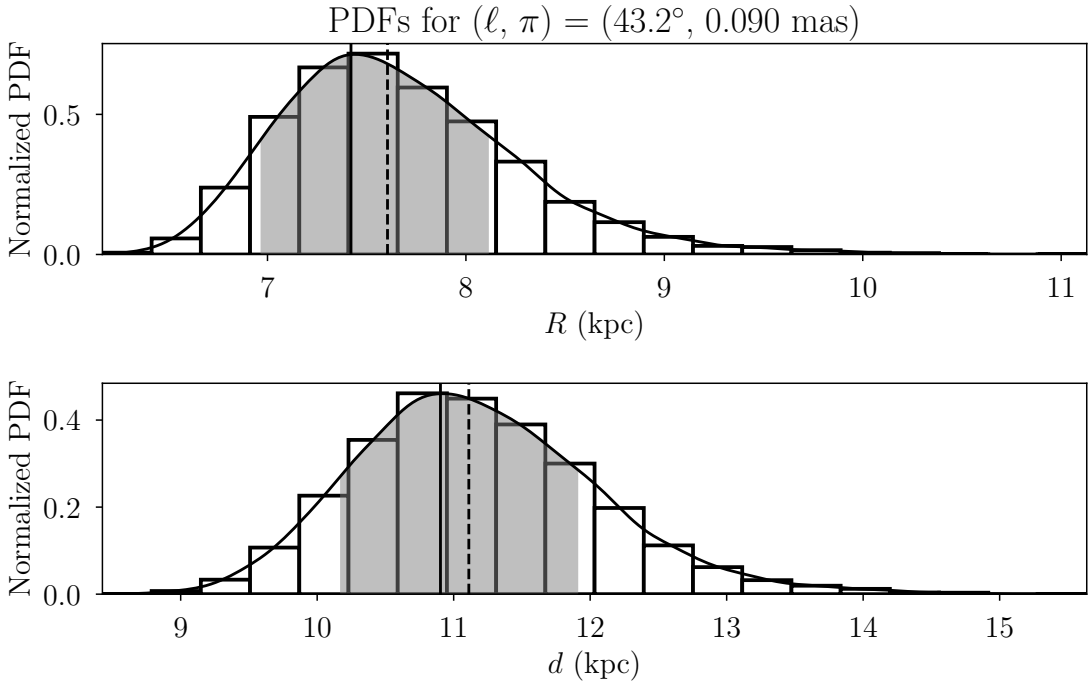

Figure 5.6: Monte Carlo parallax distance probability distribution functions for G043.170−00.004. The top panel is the PDF of Galactocentric radius, R, and the bottom panel is the PDF of distance, d. We Monte Carlo resample the parallax measurement within its uncertainty 5000 times to generate the data represented by the histogram. The solid curve is a kernel density estimator (KDE) fit to the data. The vertical dashed line is the "nominal" parallax distance (i.e., by inverting the parallax) and the solid line is the peak of the KDE and the derived Monte Carlo parallax distance. The shaded region represents the $\pm 1\sigma$ confidence interval (see Wenger et al., 2018a, Chapter 3).

method and the Reid et al. (2014) GRM to derive the kinematic distances to our sample of Galactic H II regions. This method computes the distances and distance uncertainties by resampling the observed LSR velocities, the solar motion parameters, which define the LSR, and the GRM parameters to determine the kinematic distance PDFs. We generate 5000 Monte Carlo realizations of the kinematic distances for each nebula. The peak locations of the PDFs are the derived Monte Carlo kinematic distances, and the PDF widths characterize the asymmetric kinematic distance uncertainties. Wenger et al. (2018a, Chapter 3) find that the Monte Carlo kinematic distances are quite accurate when compared to the parallax distances for a sample of 75 Galactic high-mass star forming regions. The median absolute difference between the kinematic and parallax distances is 0.71 kpc with a standard deviation of 0.83 kpc. Figure 5.7 shows an example of the kinematic distance PDFs for G043.170−00.004. This H II region has a far kinematic distance of $11.68^{+0.43}_{-0.43}$ kpc and a parallax distance of $11.00^{+0.96}_{-0.81}$ kpc.

The *WISE* Catalog lists the KDA resolutions (KDAR) for a subset of the known Galactic H II regions. These KDARs are determined by H I emission/absorption and self-absorption techniques (e.g., Anderson & Bania, 2009; Anderson et al., 2012), H I self-absorption based on molecular spectral line velocities (e.g., Urquhart et al., 2012), and H_2CO absorption experiments (e.g., Araya et al., 2002). As in Wenger et al. (2018a, Chapter 3), we use the *WISE* Catalog KDARs for nebulae with LSR velocities more than $20\,\mathrm{km\,s^{-1}}$ from the tangent point velocity. All nebulae within $20\,\mathrm{km\,s^{-1}}$ of the tangent point velocity are assigned to the tangent point distance.

Due to line of sight velocity crowding, kinematic distances are inaccurate in the direction of the Galactic center and anti-center. Following Wenger et al. (2018a, Chapter 3), we remove all kinematic distance nebulae with $-15^\circ < \ell < 15^\circ$ and $160^\circ < \ell < 200^\circ$. After removing nebulae in these directions, we are left with 120 Galactic H II regions with kinematic distances. Our final catalog contains 167 nebulae with accurate electron temperatures and either a parallax (47) or kinematic (120) distance. Table 5.6 lists the relevant distance parameters for each nebulae: the distance d; the Galactocentric radius, R; the distance method ("P" for parallax and "K" for kinematic); and the maser parallax observation reference, if any. Nebulae with accurate electron temperatures, without a parallax measurement, and in the direction of the Galactic center/anti-center are included in this table for completion. These nebulae are excluded from all subsequent analyses.

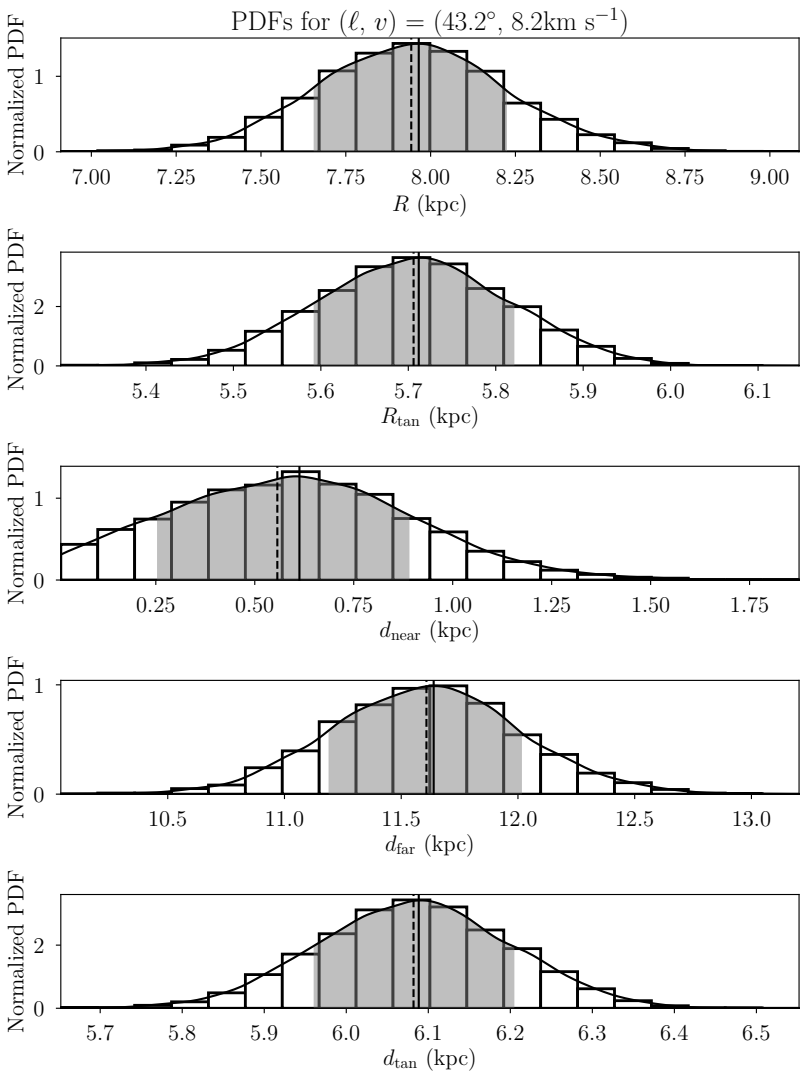

Figure 5.7: Monte Carlo kinematic distance probability distribution functions for G043.170−00.004. From top to bottom are the PDFs for the Galactocentric radius, R, the Galactocentric radius of the tangent point, $R_{\rm tan}$, the near kinematic distance, $d_{\rm near}$, the far kinematic distance, $d_{\rm far}$, and the tangent point distance, $d_{\rm tan}$. We Monte Carlo resample the kinematic distances 5000 times to generate the data represented by the histogram. The solid curve is a kernel density estimator (KDE) fit to the data. The vertical dashed line is the "nominal" kinematic distance (i.e., not using the Monte Carlo method) and the solid line is the peak of the KDE and the derived Monte Carlo kinematic distance. The shaded region represents the $\pm 1\sigma$ confidence interval (see Wenger et al., 2018a, Chapter 3).

5.5.5 Electron Temperature and Metallicity Structure

H II region electron temperatures are a proxy for their nebular metallicities (e.g., Churchwell & Walmsley, 1975). Shaver et al. (1983) derived an empirical relationship between H II region metallicities, determined using optical collisionally excited lines, and electron temperatures, determined from RRLs:

$$12 + \log_{10}(\mathrm{O/H}) = (9.82 \pm 0.02) - (1.49 \pm 0.11)\,\frac{T_e}{10^4\,\mathrm{K}} \tag{5.5}$$

where T_e is the nebular electron temperature. The H II region electron temperature structure across the Galactic disk also reveals structure in metallicity.

We begin our investigation of Galactic chemical structure by measuring the radial electron temperature and metallicity gradients. Figure 5.8 shows the nebular electron temperature and metallicity gradients using the electron temperatures and Galactocentric radii from Table 5.6 and metallicities derived using Equation 5.5. The metallicity uncertainties are determined by propogating the electron tememperature uncertainties through Equation 5.5. We use a robust least-squares routine to fit a linear model to both distributions. This routine does not consider the uncertainties of the data, because (1) there are uncertainties in both the dependent and independent variables, and (2) the Galactocentric radius uncertainties are asymmetric. Nonetheless, the best fit linear model to the nebular electron temperature distribution is $T_e/\mathrm{K} = (4579 \pm 214) + (348 \pm 30)\,R/\mathrm{kpc}$, and the best fit for the nebular metallicity distribution is $12 + \log_{10}(\mathrm{O/H}) = (9.139 \pm 0.038) - (0.054 \pm 0.004)\,R/\mathrm{kpc}$. Within the errors, these gradients are consistent with the gradients found by B15 using their "Best" distances and Green Bank sample: $T_e/\mathrm{K} \propto (402 \pm 33)\,R/\mathrm{kpc}$ and $12 + \log_{10}(\mathrm{O/H}) \propto (-0.058 \pm 0.004)\,R/\mathrm{kpc}$.

Our least-squares fitting method does not account for the data uncertainties in electron temperature and Galactocentric radius. We estimate the true variance of the linear model by Monte Carlo resampling the data 1000 times. The electron temperatures are drawn from a Gaussian distribution centered at the derived electron temperature and with a width equal to the derived electron temperature uncertainty. The Galactocentric radii are drawn from the parallax or kinematic distance PDFs. For each realization of the data, we fit a robust least-squares linear model. Similar to the Monte Carlo kinematic distance method in Wenger et al. (2018a, Chapter 3),

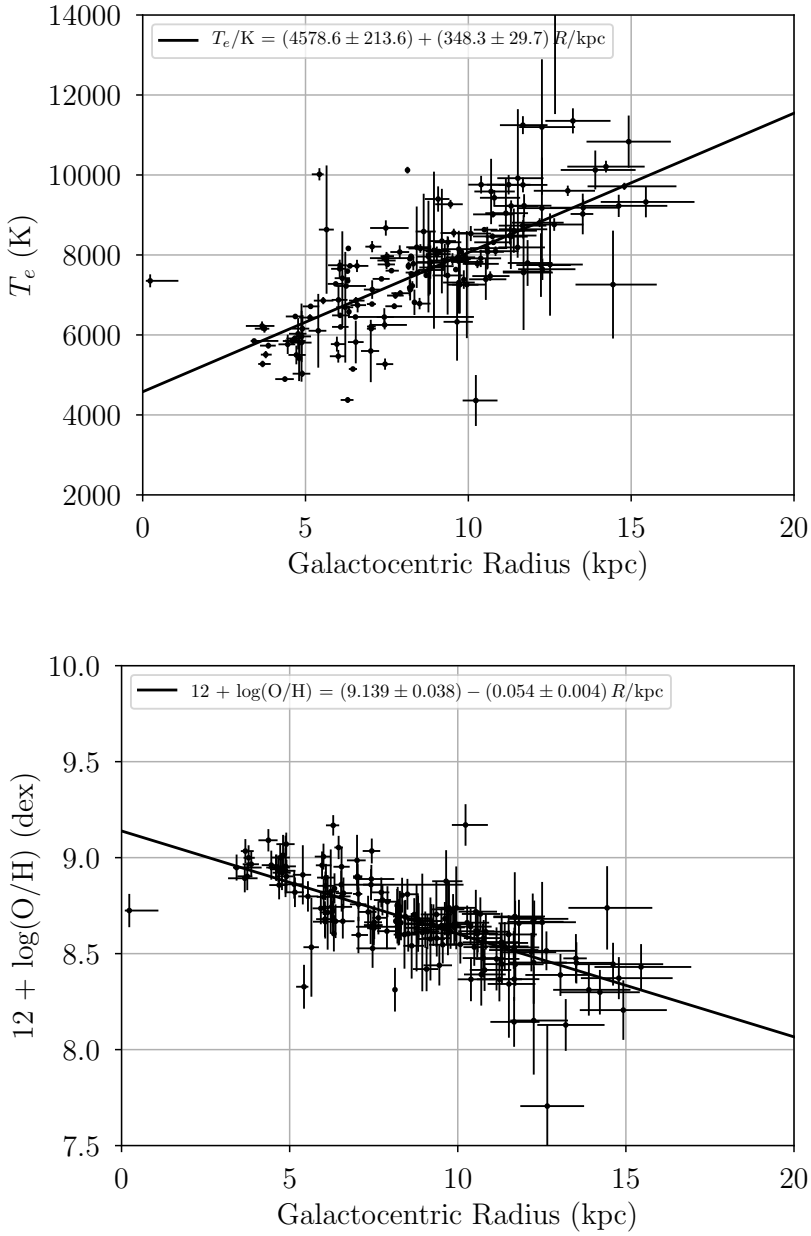

Figure 5.8: The nominal radial electron temperature (top) and metallicity (bottom) gradients. The lines are the robust least squares linear model fits to the data: $T_e/\mathrm{K} = (4579 \pm 214) + (348 \pm 30)\, R/\mathrm{kpc}$ and $12 + \log_{10}(\mathrm{O/H}) = (9.139 \pm 0.038) - (0.054 \pm 0.004)\, R/\mathrm{kpc}$.

we estimate the most likely linear model parameters by fitting a KDE to the PDFs of each model parameter. The peak of this KDE is the most likely parameter, and the 1σ confidence interval is derived as the bounds of the PDF such that (1) the PDF evaluated at the lower bound is equal to the PDF evaluated at the upper bound and (2) the integral of the normalized PDF between the bounds is 68.3%. Figures 5.9 and 5.10 shows the most likely linear model parameters derived by this Monte Carlo method and the covariance between the model parameters for the electron temperature and metallicity gradients, respectively. The most likely fit to the electron temperature data is $T_e/\mathrm{K} = 4539^{+221}_{-143} + 354^{+17}_{-25})\, R/\mathrm{kpc}$, and for the metallicity data is $12 + \log_{10}(\mathrm{O/H}) = 9.123^{+0.030}_{-0.030} - 0.052^{+0.004}_{-0.003}\, R/\mathrm{kpc}$. These gradients and uncertainties are nearly the same as the nominal least-squares values, but they are more accurate given the uncertainties in the derived electron temperatures and distances.

To visualize the variations in nebular electron temperature in the Galactic disk, we use Kriging to spatially interpolate between discrete nebulae (see also B15). The Kriging method computes the average semivariance of the data as a function of the spatial separation between the data points. The average semivariance is measured in many separation bins, known as "lags," and the semivariogram (average semivariance as a function of lag) is fitted with a model. The expected value of the data at any position is derived from this semivariogram model (see Feigelson & Babu, 2012).

We compute the nominal Kriging map of nebular electron temperatures using the electron temperatures and distances in Table 5.6. Figure 5.11 shows this nominal electron temperature map, where we use a linear semivariogram model to interpolate between the discrete H II region positions. The top panel is the Kriging result and the bottom panel is the standard deviation of the Kriging interpolation. This standard deviation map characterizes the intrinsic scatter of the data across the Galactic disk. The H II region points are colored by their electron temperature to highlight the differences between the actual nebular electron temperature and the interpolated value at that position. Figure 5.12 shows the same Kriging results with a linear semivariogram model for the H II region metallicities. Qualitatively, these figures are similar to the electron temperature and metallicity maps in B15. It is clear from these figures that the radial gradients have a strong dependence on Galactocentric azimuth.

These Kriging results consider neither the uncertainties in the nebular electron temperatures and metallicities nor the H II region distance uncertainties. We estimate

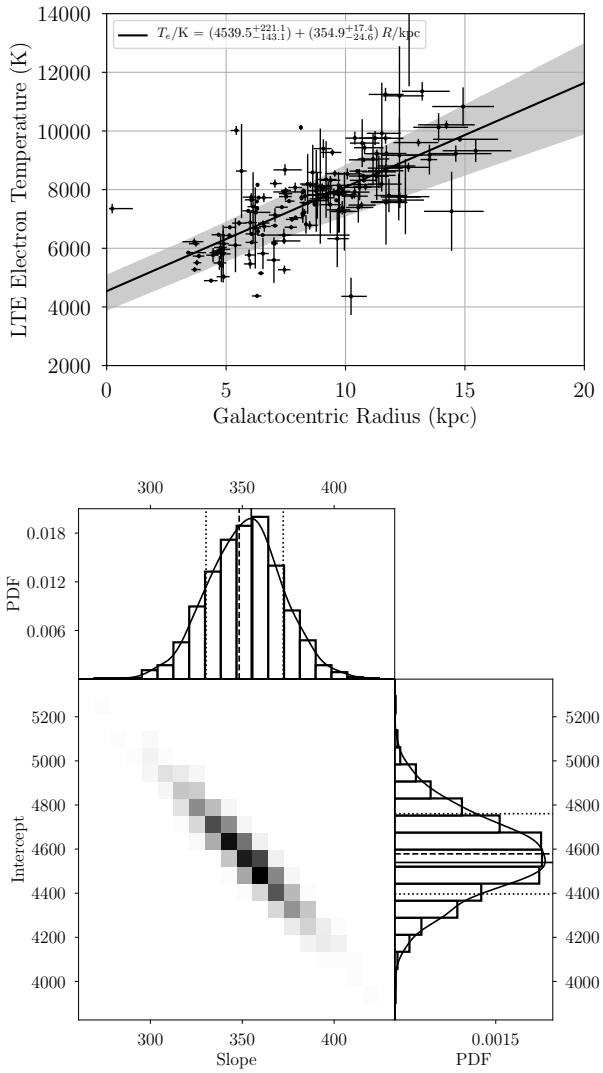

Figure 5.9: The most likely electron temperature gradient determined by Monte Carlo resampling the derived electron temperatures and Galactocentric radii. The top panel shows the data and the most likely linear model (black line). The shaded region represents the range of fits over 1000 Monte Carlo realizations of the data. The most likely linear model is $T_e/\mathrm{K} = 4556^{+198}_{-188} + 353^{+22}_{-20})\,R/\mathrm{kpc}$. The bottom panel shows the covariances between the linear model parameters (slope, with units of K kpc^{-1}, and intercept, with units of K). The histograms are the PDFs of the Monte Carlo fit parameters, and the black curves are KDE fits to the PDFs. The solid lines are the peaks of the PDFs and the most likely fit parameters, and the dotted lines represent the 1σ confidence intervals. The dashed lines are the nominal values of the fit parameters derived from the robust least squares fit to the data (i.e. without Monte Carlo resampling).

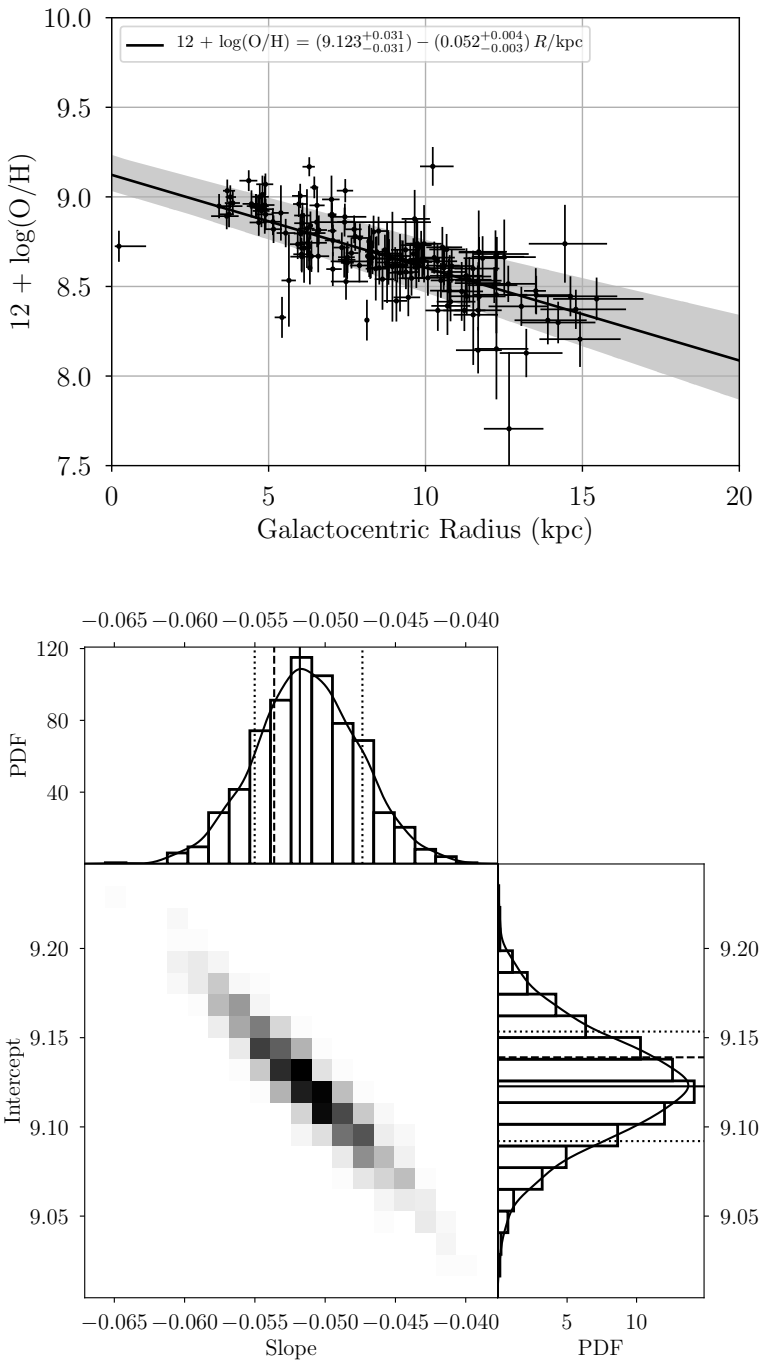

Figure 5.10: Same as Figure 5.9 for the radial metallicity gradient. The most likely linear model is $12 + \log_{10}(\mathrm{O/H}) = 9.128^{+0.023}_{-0.038} - 0.052^{+0.005}_{-0.003}\, R/\mathrm{kpc}$. The covariance slope has units of dex kpc^{-1} and the intercept has units of dex.

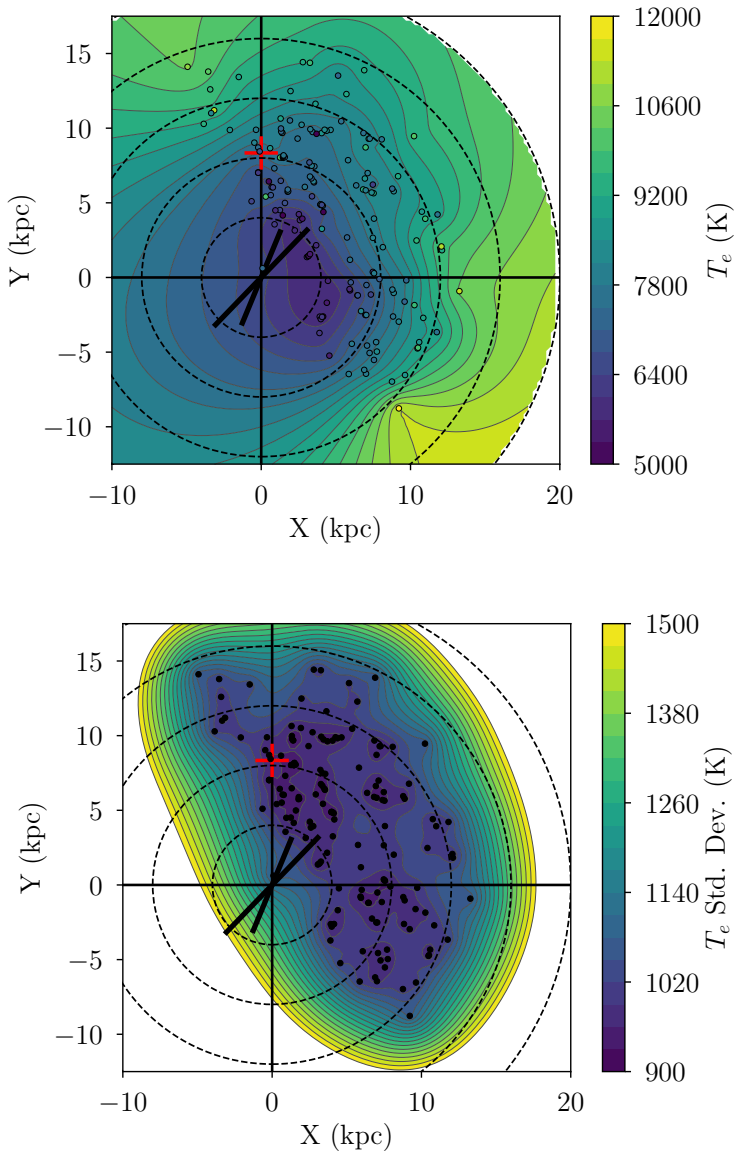

Figure 5.11: Kriging map of nebular electron temperatures. The top panel shows the Kriging interpolation in a face-on view of the Galactic disk. The points are the H II regions in our sample, colored by their derived electron temperatures. The bottom panel shows the Kriging standard deviation. The Galactic Center is located at the origin and the Sun is located at the red cross. The solid black lines represent the long and short Galactic bars (Benjamin et al., 2005). The dashed circles are 4, 8, 12, 16, and 20 kpc in radius. White areas are outside $R = 20$ kpc or have data values beyond the colorbar range.

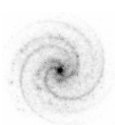

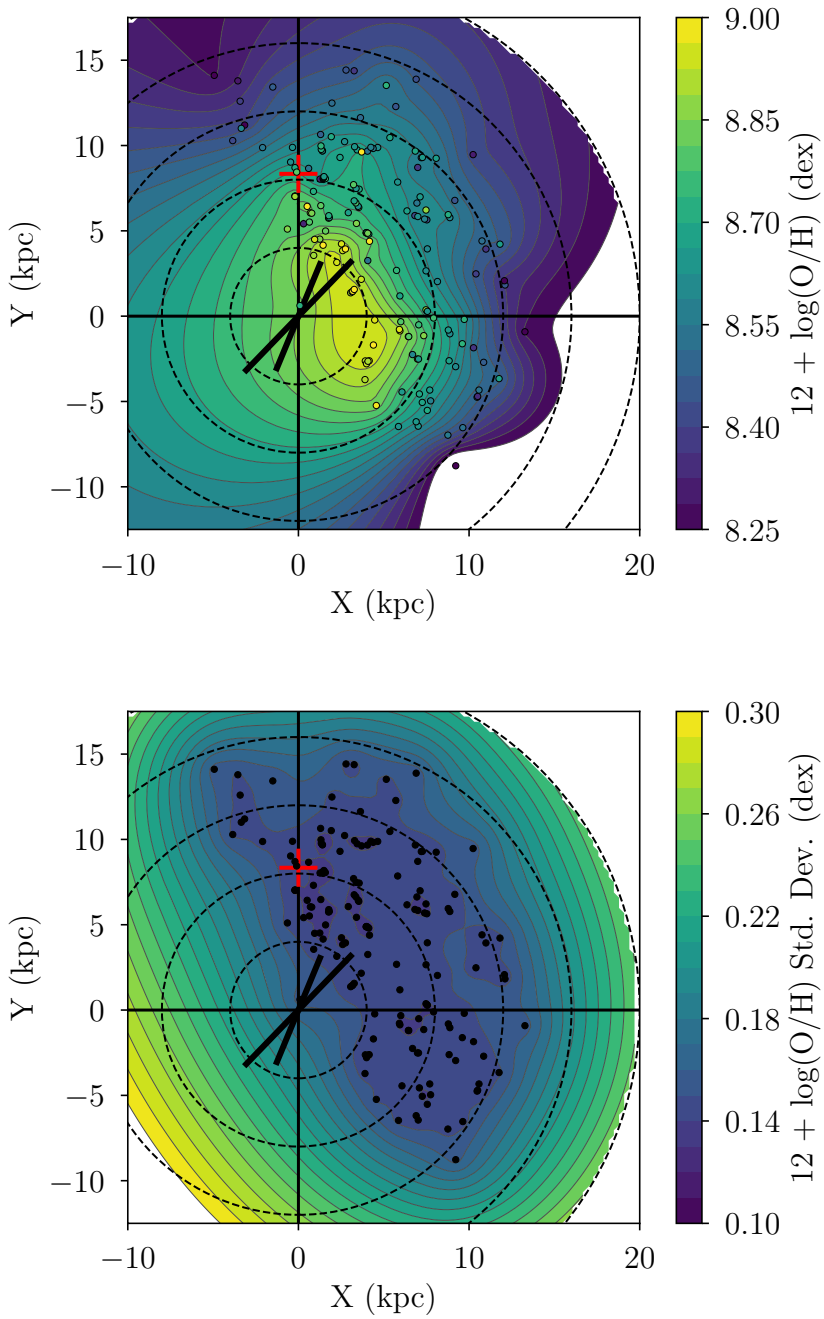

Figure 5.12: Same as Figure 5.11 for the nebular metallicities.

the most likely Kriging map of nebular electron temperatures and metallicities using a Monte Carlo technique in the same way as we determined the most likely radial gradients. We Monte Carlo resample the data within their uncertainties 1000 times, and, for each realization of the data, we generate a Kriging map. At each pixel of the Kriging map, we construct a PDF of the interpolation values, fit a KDE, and locate the peak and bounds of the KDE. The peak is the most likely Kriging value at that position, and the bounds represent the 1σ confidence interval, as before.

Figures 5.13 and 5.14 shows the most likely Kriging interpolation map, most likely standard deviation map, and the upper and lower 1σ confidence interval bound maps for the nebular electron temperatures and metallicities, respectively. The qualitative structure in the Monte Carlo Kriging interpolation maps is similar to that in the nominal Kriging maps, though the 1σ confidence interval bound maps reveal where the Kriging interpolation is ill constrained. For most of the Galactic disk, the most likely Kriging values have 1σ bounds $\lesssim 500\,\mathrm{K}$ in electron temperature and $\lesssim 0.8\,\mathrm{dex}$ in metallicity. These uncertainties are significantly less than the most likely Kriging standard deviations of $\sim$1000 K and $\sim$0.25 dex, which suggests that the intrinsic scatter in the nebular electron temperatures and metallicities exceeds the formal uncertainties.

5.6 Discussion

The radial gradient is the most prominent feature in the metallicity structure of the Galactic disk. Our Monte Carlo analysis of nebular metallicities results in an oxygen gradient of $-0.052^{+0.005}_{-0.003}\,\mathrm{dex\ kpc^{-1}}$. This gradient is listed in Table 5.7 along with the iron or oxygen from other studies that used a variety of tracers (see Mollá et al., 2019, for a thorough review of Galactic oxygen abundance gradients). Our gradient is most consistent with those found using young stellar populations close to the Galactic midplane.

The large variance in the measured radial metallicity gradients is likely due to two primary effects: (1) changes in the metallicity gradient with time and (2) dynamical evolution of stellar populations. The radial gradient as traced by stars is flatter at larger heights above the Galactic midplane (Cheng et al., 2012; Anders et al., 2017). There is evidence that the stellar metallicity gradient also flattens in the inner galaxy (Hayden et al., 2015). These stellar populations are likely older, and thus their metallicity gradient reflects that of a younger Galaxy. Radial migra-

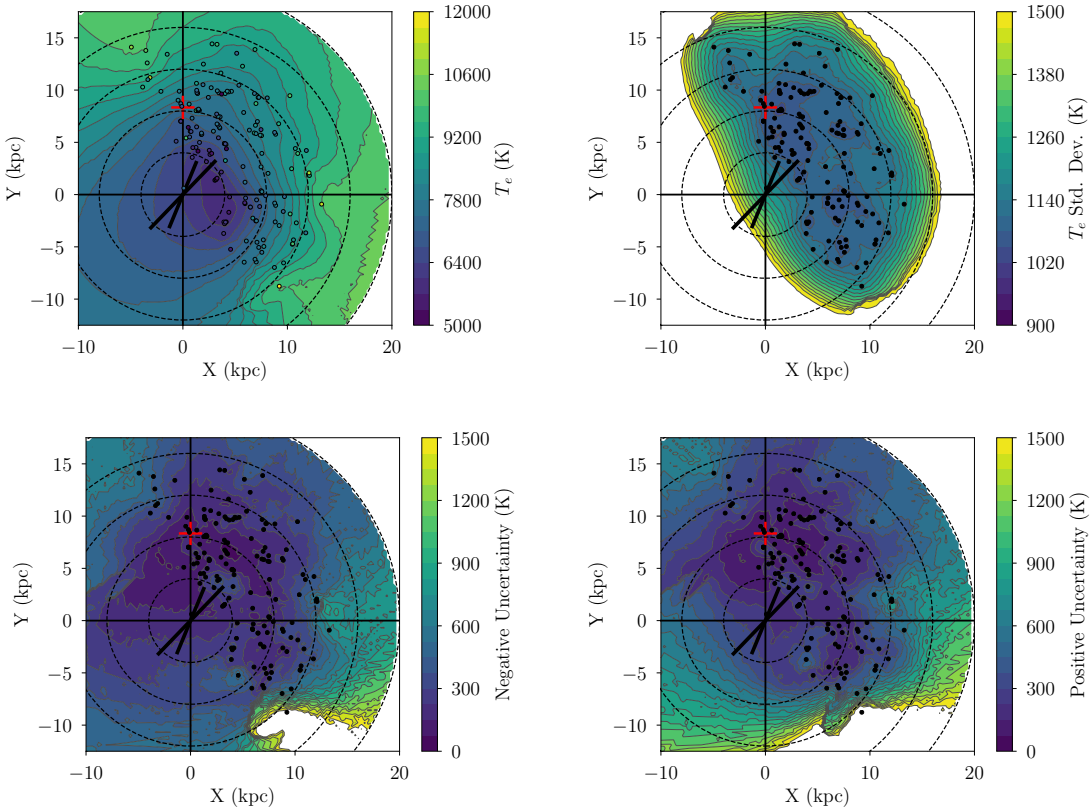

Figure 5.13: Most likely Kriging map of nebular electron temperatures determined by Monte Carlo resampling the derived electron temperatures and distances. Shown are the most likely Kriging interpolation values (top left), most likely Kriging standard deviation values (top right), lower 1σ bounds (bottom left), and upper 1σ bounds (bottom right) on the Kriging interpolation confidence intervals. The features in each plot are the same as in Figure 5.11.

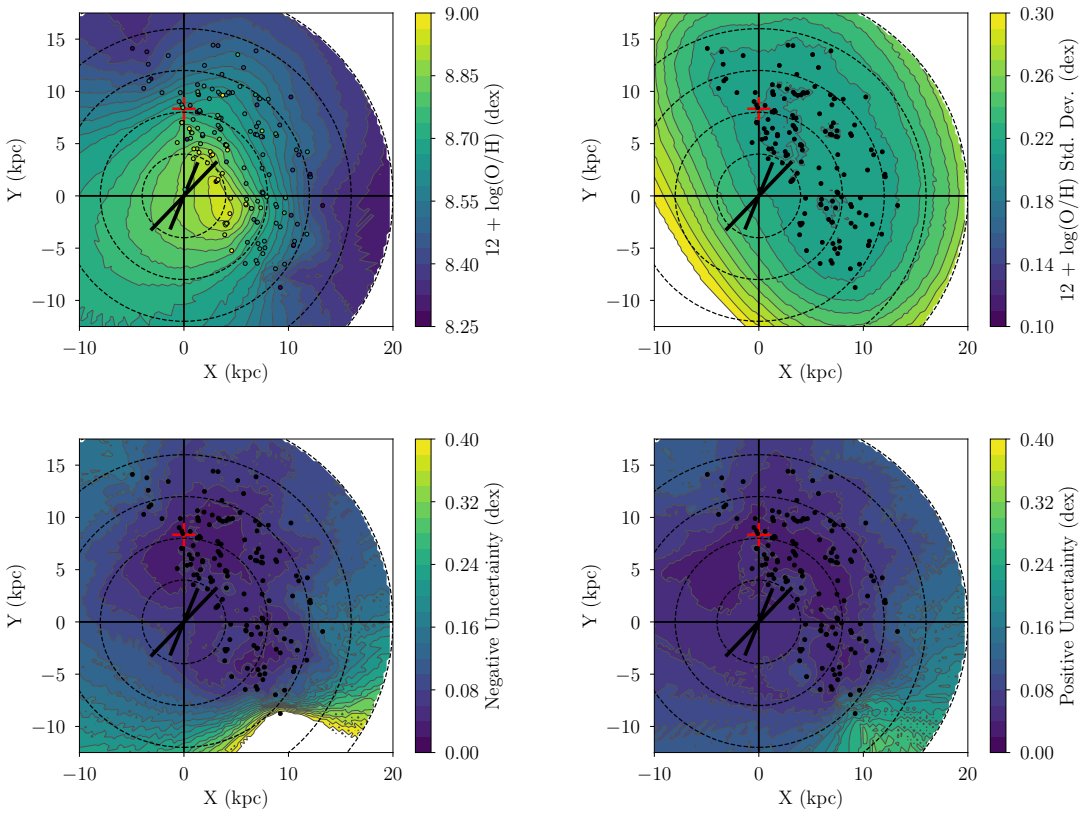

Figure 5.14: Same as Figure 5.13 for the nebular metallicities.

Table 5.7: Radial Metallicity Gradients

Tracer	Survey	Gradient (dex kpc^{-1})	Reference
H II Regions	Various	$-0.052^{+0.005}_{-0.003}$	This Work
Young Red Giants	CoRoGEE[a]	-0.058 ± 0.009	Anders et al. (2017)
Intermediate Age Red Giants	CoRoGEE[a]	-0.066 ± 0.007	Anders et al. (2017)
H II Regions	Various	-0.0573 ± 0.0043	Balser et al. (2015)
FKG Stars	*Gaia*-ESO Large Stellar Survey	-0.068 ± 0.014	Bergemann et al. (2014)
Main Sequence Turnoff Stars	SEGUE[b]	$-0.066^{+0.030}_{-0.044}$	Cheng et al. (2012)
Planetary Nebulae	Various	-0.023 ± 0.006	Stanghellini & Haywood (2010)
Cepheids	Various	-0.068 ± 0.003	Luck et al. (2006)
Open Clusters	Various	-0.06 ± 0.01	Friel et al. (2002)

[a] *Convection, Rotation et Transits planétaires* (CoRoT) + Apache Point Galactic Evolution Experiment (APOGEE)
[b] Sloan Extension for Galactic Understanding and Exploration

tion also plays an important role in stellar metallicity gradients (Sellwood & Binney, 2002). The dynamical influence of non-axisymmetric features, like spiral arms and bars, causes stars to migrate from their birth locations. Some studies have found that radial migration significantly affects the observed stellar metallicity gradients (e.g., Minchev et al., 2013, 2014), whereas others find only an increase in the stellar metallicity dispersion at all Galactocentric radii (e.g., Grand et al., 2014). These effects should have little impact on the H II region metallicity gradient, because these nebulae are very young ($\lesssim 10$ Myr) compared to the dynamical timescale of the Galaxy ($\sim$250 Myr). For example, Grand et al. (2014) use a chemodynamical simulation of a Milky Way-size galaxy to show that, over time, the gas metallicity maintains a low dispersion at all radii, whereas the dispersion of the stellar metallicity increases due to radial migration.

Evidence for azimuthal variations in the radial electron temperature and metallicity gradients has been found in the Milky Way (e.g., B15) and other galaxies (e.g., Ho et al., 2017). Here we expand upon the B15 analysis using a larger sample of Galactic H II regions and a more accurate kinematic distance technique. Evidence for azimuthal structure is already apparent in Figures 5.11–5.14, and here we test the statistical significance of these azimuthal variations.

To quantify the azimuthal structure in the nebular electron temperature and metallicity radial gradients, we divide the Galaxy into several azimuthal bins and compute the radial gradients within each bin. Following B15, we use bins of size 30° in Galactocentric azimuth centered every 5° from −50° to 200°. We make a robust least squares linear fit to the derived electron temperatures and metallicities as a function of Galactocentric radii for the nebulae in each bin. Figure 5.15 shows the best fit linear model parameters as a function of Galactocentric azimuth for the nebular electron temperature and metallicity gradients. Unlike B15, we do not exclude bins with only a few nebulae, nor those with nebulae spanning a small range of Galactocentric radii. The uncertainties in these bins will be correctly determined in the subsequent Monte Carlo analysis. In this simple least squares analysis, however, the best fit parameters and their uncertainties are unreliable in sparsely populated bins, such as those below ∼0° and above ∼120°. Nonetheless, we find a similar structure in the electron temperature and metallicity gradient slopes as found by B15. The electron temperature and metallicity slopes vary by a factor of 2 and 3, respectively, between Galactocentric azimuths of ∼20° and ∼100°. These variations are slightly

less in magnitude than those found by B15, probably because of our much larger sample size near 100° in Galactocentric azimuth.

Multiple sources of uncertainty affect the apparent azimuthal variations shown in Figure 5.15. These sources include the derived electron temperature uncertainties and the distance uncertainties, which affect both the derived Galactocentric radii and azimuths of the nebulae. To better quantify these sources of uncertainty and to test the statistical significance of the apparent azimuthal variations, we perform yet another Monte Carlo analysis. We Monte Carlo resample the nebular electron temperatures, metallicities, and distances to generate 1000 realizations of the data. As before, the electron temperatures and metallacities are drawn from a Gaussian distribution, whereas the distances are drawn from the parallax or kinematic distance PDFs. For each realization of the data, we fit the radial gradients in each of the several Galactocentric azimuth bins. Finally, we fit a KDE to the linear model parameter PDFs to estimate the most likely parameters and their confidence intervals.

Figure 5.16 shows the most likely electron temperature and metallicity gradients from our Monte Carlo analysis. The most obvious difference between this and the nominal gradients in Figure 5.15 is the larger error bars. This Monte Carlo analysis properly accounts for the uncertainties in both the nebular electron temperatures/metallicities and distances, so these error bars more accurately reflect the uncertainties in the gradients within each azimuth bin. Despite the larger uncertainties, the azimuthal variations in the radial gradients remain statistically significant. The electron temperature gradient ranges from $\sim$250 K kpc^{-1} at $\sim$30° to $\sim$500 K kpc^{-1} at $\sim$100°, a factor of $\sim$2 increase, and the metallicity gradient ranges from about -0.035 dex kpc^{-1} to about -0.075 dex kpc^{-1} over the same range, a factor of $\sim$2 decrease.

The derived electron temperatures and metallicities are the largest source of error in the radial gradient determinations. Figure 5.17 shows the radial metallicity gradients in each Galactocentric azimuth bin where we Monte Carlo resample only the metallicity (top) or distances (bottom). The gradient uncertainties are a factor of $\sim$2 larger when we resample only the metallicities.

The azimuthal variations in the metallicity gradient are predicted by some simulations (Di Matteo et al., 2013; Grand et al., 2016). Grand et al. (2016), for example, find azimuthal metallicity structure in the young, thin disk stellar population of a cosmological simulation of a Milky Way analogue. The azimuthal variations are in-

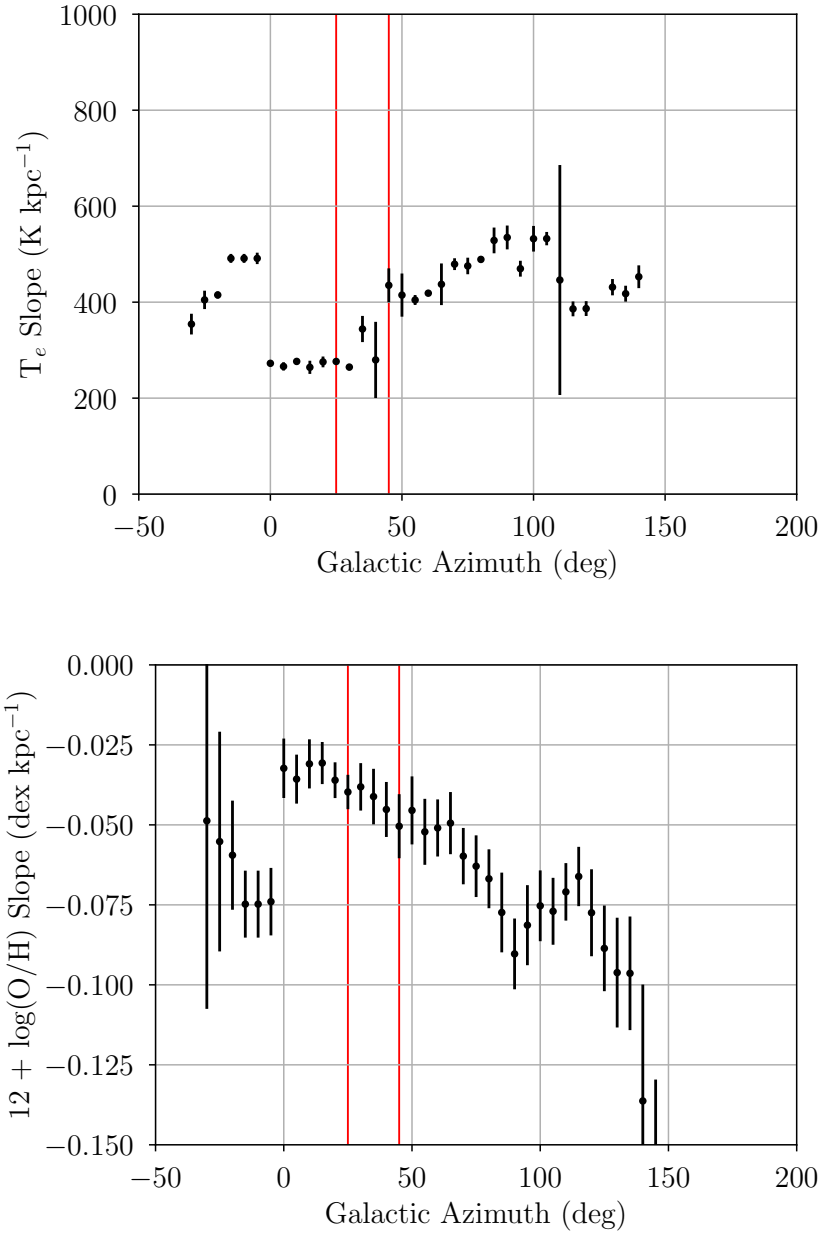

Figure 5.15: Nominal variations in the radial electron temperature (top) and metallcity (bottom) gradients as a function of Galactocentric azimuth. The Galaxy is divided into 30° bins spaced every 5° in Galactocentric azimuth. The points are the slopes of the robust least squares linear model fit to the data in each bin. The vertical red lines represent the Galactocentric azimuths of the long and short Galactic bars (Benjamin et al., 2005). Bins below ∼0° and above ∼120° are sparsely populated and their slopes are unreliable.

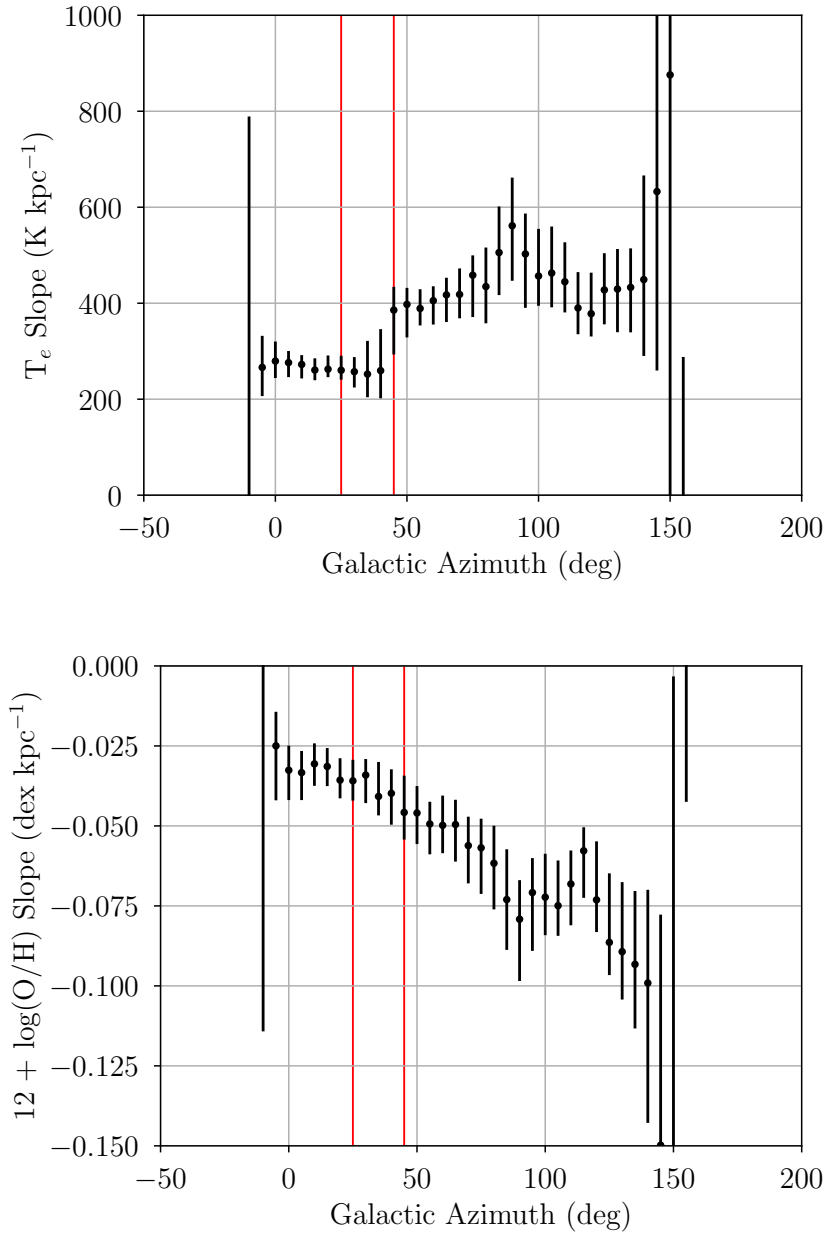

Figure 5.16: Same as Figure 5.15 for the most like gradients derived from our Monte Carlo analysis. The error bars are the 1σ confidence intervals on the most likely slopes.

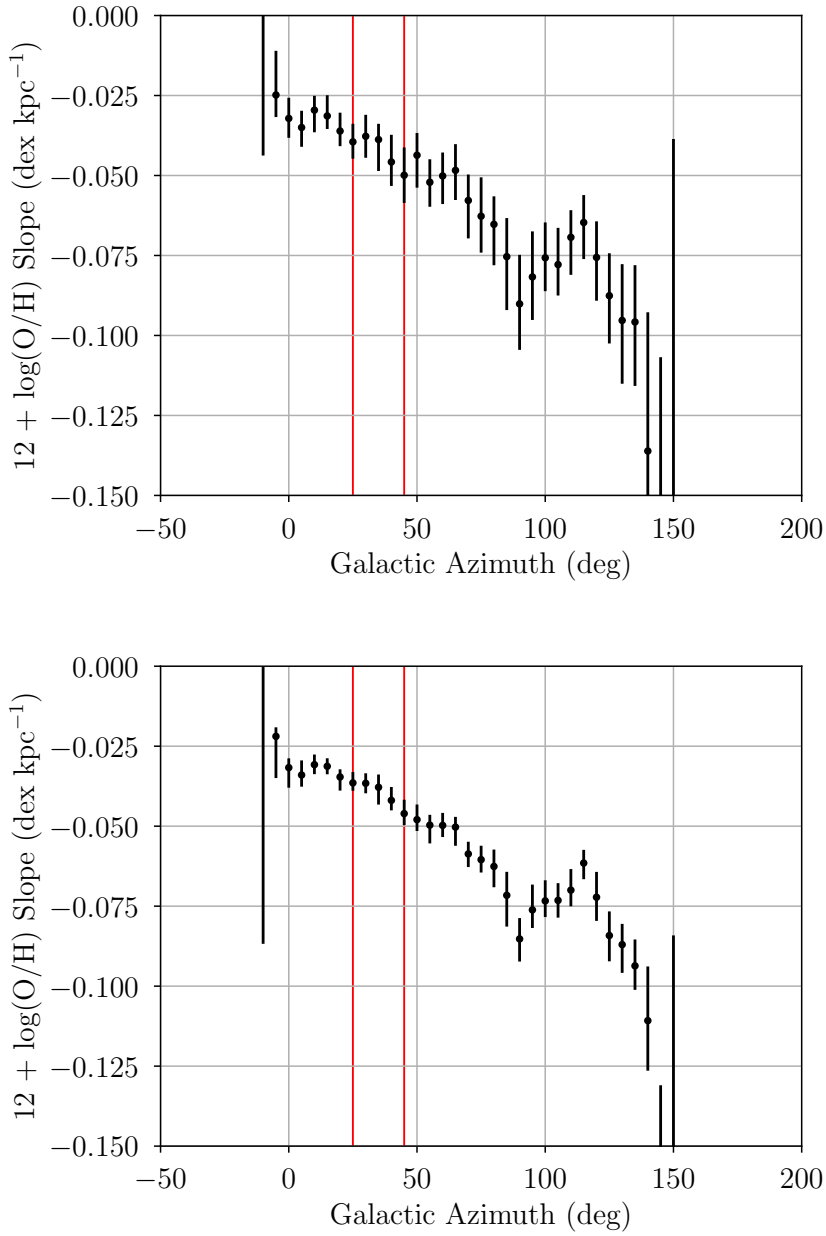

Figure 5.17: Same as the metallicity gradients in Figure 5.16, except we only Monte Carlo resample the derived metallicities (top) or distances (bottom).

duced by the non-axisymmetric peculiar motions near spiral arms, which drives radial migration and a redistribution of metals. The magnitude of the azimuthal variations is $\sim$0.1 dex in their simulation. Di Matteo et al. (2013) find a similar magnitude of variation in metallicities as traced by old stars in an N-body simulation. In Figure 5.18 we show the residuals of the electron temperature and metallicity Monte Carlo Kriging maps after subtracting the most likely radial gradients. Excluding the Galactic center and edge of the map, the magnitude of variation in the metallicity residual map is $\sim$0.1 dex, which is consistent with the Grand et al. (2016) simulation. In the first quadrant, the residual structure between $R\sim$6 kpc and $\sim$12 kpc is similar to the simulated residuals in Grand et al. (2016) and may be evidence for spiral arm induced radial migration in the Milky Way.

5.7 Summary and Future Work

We use the VLA to measure the $\sim$8–10 GHz RRL and radio continuum flux densities of 82 Galactic H II regions. We derive the RRL-to-continuum brightness ratio, electron temperature, and metallicity of these nebulae. Including previous single dish observations, the catalog of Galactic H II regions with accurate electron temperatures and distances now contains 167 nebulae spanning Galactocentric radii $4-16$ kpc and azimuths $-20^\circ - 140^\circ$.

The derived VLA RRL-to-continuum brightness ratios are consistently 10% larger than the single dish values. This systematic offset is partially due to the inaccurate RRL averaging techniques used by previous studies. The offset may also be due to fundamental differences between single dish and interferometric observations, such as optical depth effects. In the future, we will test the optically thin assumption be measuring the radio continuum spectral indicies of our nebulae. In this analysis, however, we simply scale the single dish electron temperatures by 90% to offset this systematic difference.

The distances to Galactic H II regions are the largest source of uncertainty in previous studies using these nebulae to trace Galactic metallicity structure (e.g., B15). Maser parallax distances have been determined for 47 of our nebulae. For the remainder, we use a novel Monte Carlo kinematic distance technique to determine distances (Wenger et al., 2018a, Chapter 3). Both the kinematic distances and distance uncertainties to the nebulae in our sample are more accurate than the B15 study. The largest source of uncertainty in this work is the RRL-to-continuum brightness ratio,

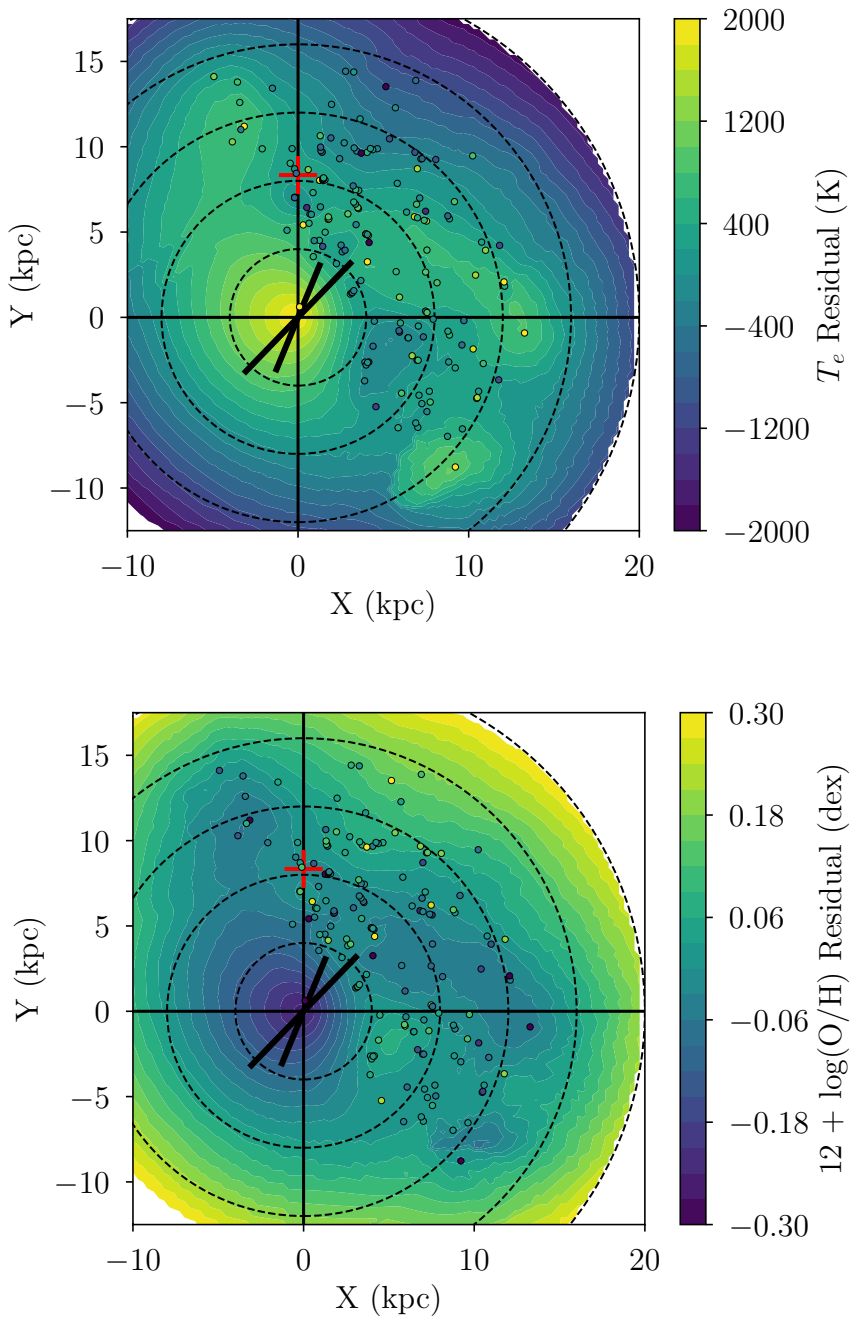

Figure 5.18: Most likely electron temperature (top) and metallicity (bottom) Kriging map residuals. The residuals are determined by subtracting the most likely gradient from the Monte Carlo kriging maps. The features in each plot are the same as in Figure 5.11.

not the distances.

We derive the most likely radial electron temperature and metallicity gradient of the Milky Way as $T_e/\mathrm{K} = 4539^{+221}_{-143} + 354^{+17}_{-25})\,R/\mathrm{kpc}$ and $12 + \log_{10}(\mathrm{O/H}) = 9.123^{+0.030}_{-0.030} - 0.052^{+0.004}_{-0.003}\,R/\mathrm{kpc}$, respectively, using a Monte Carlo analysis. This metallicity gradient is consistent with previous H II region studies (e.g., B15) and studies using young stars close to the Galactic midplane Mollá et al. (e.g., 2019). We generate maps of the electron temperature and metallicity structure of the Galactic disk using a Monte Carlo Kriging analysis. These maps reveal significant azimuthal variations in the Galaxy's metallicity structure.

The radial metallicity gradient varies by a factor of $\sim$2 ($\sim$0.04 dex kpc^{-1}) between Galactocentric azimuths of $\sim$30° and $\sim$100°. We find non-axisymmetric spatial metallicity variations on the order of $\sim$0.1 dex, which is consistent with the Grand et al. (2016) chemodynamical simulation. These variations may be evidence for radial migration and metal mixing induced by the Milky Way's spiral arms.

Chapter 6

Galactic Morphological Structure

6.1 Introduction

The morphological structure of the Milky Way remains an open question in astronomy, despite more than three centuries of research. The Sun is deeply embedded within the Galactic plane. Extinction by dust limits our ability to discern Galactic structure with optical tracers, such as stars, at distances of more than ∼4 kpc through the Galactic midplane (e.g., Gaia Collaboration et al., 2018). The discovery of cosmic radio waves (Jansky, 1933) and radio spectral lines (Ewen & Purcell, 1951) revolutionized our understanding of the Galaxy, since such emission is unaffected by extinction. Nonetheless, the vastness of the Galaxy means that determining the distances of Galactic structure tracers is a challenge, and the quest to create an accurate map of Galactic structure is ongoing.

The spiral nature of the Galaxy is well documented with a variety of tracers (e.g., Morgan et al., 1952; van de Hulst et al., 1954; Schmidt, 1957; Westerhout, 1957; Georgelin & Georgelin, 1976). Many theories and models have been developed to explain spiral structure in external galaxies, including stationary spiral density waves (Lin & Shu, 1964) and transient spiral theories (e.g., Sellwood & Carlberg, 1984). There is evidence to support both of these prominent theories (e.g., Burton, 1971; Dobbs & Baba, 2014; Shu, 2016). A better understanding of the detailed morphology of the Milky Way's spiral structure may allow us to determine the formation and evolution mechanisms of Galactic spiral arms.

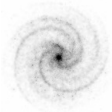

Modern optical and infrared surveys are revolutionizing our understanding of structure in the Galaxy. The accurate distances obtained by satellite-based stellar parallax observations, such as those from *Gaia*, reveal interesting kinematic structure across the Galactic disk (Gaia Collaboration et al., 2018) and place constraints on the warp of the Galactic plane (Poggio et al., 2018). The Apache Point Observatory Galactic Evolution Experiment (APOGEE) is precisely deriving the chemical abundances of hundreds of thousands of red giant stars across the Galaxy (Allende Prieto et al., 2008; Majewski et al., 2016). With accurate distances from parallaxes or other techniques (e.g., Nidever et al., 2014), APOGEE is mapping the morphological, kinematic, and chemical structure of the Galaxy.

Recent radio surveys have made some important discoveries, as well. Dame & Thaddeus (2011) found a new molecular spiral arm of the Milky Way. This arm, which they call the "Outer Scutum-Centaurus (OSC)" arm, is warped out of the Galactic midplane by several degrees, and thus it is not seen in most Galactic plane surveys. The Bar and Spiral Structure Legacy (BeSSeL) survey and related projects are measuring the parallaxes of masers associated with star forming regions using very long baseline interferometry (Brunthaler et al., 2011). From these data, we can derive more accurate Galactic rotation models and constrain the spiral structure of the Milky Way (e.g., Reid et al., 2014). The H II Region Discovery Surveys (HRDS) are finding thousands of new high-mass star forming regions (HMSFRs), a classic tracer of Galactic structure, across the Galactic disk (Bania et al., 2010, 2012; Wenger et al., 2013; Anderson et al., 2014, 2015a,b, 2018; Wenger et al., 2019, Chapter 4).

Here, we explore the spiral structure of the Milky Way using a simple morphological model of neutral gas, molecular gas, and HMSFRs. We only use these three structure tracers because they are bright at unextincted radio wavelengths and because they are associated with Galactic spiral arms. The model does not attempt to explain the physics of the interstellar medium (ISM), star formation, or galaxy evolution. Unlike previous Galactic structure studies (e.g. Hou & Han, 2014; Reid et al., 2014; Koo et al., 2017), we do not rely on distances. Instead, we aim to construct a model that can accurately reproduce the observed Galactic longitude, latitude, and local standard of rest (LSR) velocity ($\ell, b, V_{\rm LSR}$) distributions of recent H I, ^{12}CO, and Galactic H II region surveys.

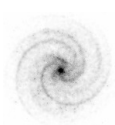

6.2 Structure Tracers

We model the morphological structure of neutral gas, molecular gas, and H II regions in the Galaxy. The ISM is a complicated, multi-phase medium, which includes the cold neutral medium (CNM; densities $n \gtrsim 10^3\,\mathrm{cm}^{-3}$, and temperatures $T \lesssim 100\,\mathrm{K}$), the warm neutral medium (WNM) and warm ionized medium (WIM; $n \sim 1\,\mathrm{cm}^{-3}$, $T \sim 5000\,\mathrm{K}$), the hot ionized medium (HIM; $n \lesssim 0.01\,\mathrm{cm}^{-3}$, $T \gtrsim 10^5\,\mathrm{K}$), and dense molecular clouds (e.g., Cox, 2005). Thermal and non-thermal pressures, heating and cooling physics (e.g., feedback from star formation), and interactions between the phases are just some of the complications that are important in the ISM. We are only interested in modeling Galactic spiral structure, so we ignore these complexities as well as some of the ISM phases, such as the HIM and the WIM. The HIM is most prevalent above and below the Galactic disk (e.g., Spitzer, 1956), and the WIM is affected by dust extinction in Hα surveys (e.g., Haffner et al., 1999) or is associated with HMSFRs in radio recombination line (RRL) surveys (Luisi et al., 2017). Here we motivate and provide historical context for the ISM tracers of Galactic structure in our model.

6.2.1 Neutral Gas

Since the discovery of Galactic 21 cm H I emission (Ewen & Purcell, 1951), H I has been used to trace the morphological and kinematic structure of the Galaxy. For example, van de Hulst et al. (1954) created the first face-on map of the Galactic H I distribution using a kinematic method to estimate the distances to the H I clouds. These early H I studies found strong evidence for spiral structure in the Milky Way (e.g., Oort et al., 1958). It was quickly realized, however, that the observed radial velocities of H I emission are affected by non-circular "streaming" motions, which complicate distance determinations (e.g., Burton, 1966, 1971, 1972). Nonetheless, neutral gas remains an important tool for mapping Galactic structure.

The Leiden/Argentine/Bonn (LAB) H I survey (Kalberla et al., 2005) was, until recently, the most sensitive H I survey of the entire sky. Dame & Thaddeus (2011) use LAB data to identify the OSC, and Koo et al. (2017) to trace out Galactic spiral arms by identifying peaks in the (ℓ, V_{LSR}) distribution of the LAB H I emission. They determine the kinematic distances to these traces and fit those traces with logarithmic spiral arms. Since kinematic distances are double valued in the inner Galaxy, they

are only able to map the outer Galaxy, beyond the solar orbit, in their face-on view of H I emission.

We use the latest and most sensitive all-sky H I data from the H I 4π (HI4PI) survey to probe Galactic structure (HI4PI Collaboration et al., 2016). HI4PI is a combination of the Effelsburg-Bonn H I Survey (EBHIS; Kerp et al., 2011; Winkel et al., 2016) in the northern sky and the Galactic All-Sky Survey (GASS; McClure-Griffiths et al., 2009; Kalberla et al., 2010; Kalberla & Haud, 2015) in the southern sky. The combined data have a native angular resolution of 16.2 arcmin, velocity resolution of $1.49\,\mathrm{km\,s^{-1}}$ covering $|V_{\mathrm{LSR}}| < 600\,\mathrm{km\,s^{-1}}$, and brightness temperature sensitivity $\sim$43 mK. Since we are only interested in the morphological structure of the Galactic disk, we use the $|b| < 7.5^\circ$ and $|V_{\mathrm{LSR}}| < 150\,\mathrm{km\,s^{-1}}$ subset of these data. Furthermore, we smooth and grid these data to a spatial resolution of 3° in ℓ, 1.5° in b, and $3\,\mathrm{km\,s^{-1}}$ in V_{LSR} to save computation time in our modeling. Figure 6.1 shows the ℓ-V_{LSR} diagram for these smoothed and gridded data, integrated over the full latitude range. We do not attempt to model the Galactic bar(s) or local gas, so we mask the Galactic center ($|\ell| < 15^\circ$) and low-velocity ($|V_{\mathrm{LSR}}| < 10\,\mathrm{km\,s^{-1}}$) regions of these data.

6.2.2 Molecular Gas

Unlike H I, which is ubiquitous throughout the Galaxy, molecular gas is only found in dense environments, such as star forming spiral arms (e.g., Young & Scoville, 1991). Molecular hydrogen, H_2, is the most common molecule in the Universe, but it lacks a permanent electric dipole moment and is thus unobservable in rotational transition spectroscopy. Carbon monoxide, ^{12}CO, is a common proxy for H_2 due to its low critical density ($\sim 10^3\,\mathrm{cm^{-3}}$) and abundance (e.g., Wilson et al., 1970a; Bania, 1977). The ^{12}CO ($J = 1 \rightarrow 0$) spectral line is a popular tool for studies of Galactic structure and star formation.

Early ^{12}CO maps of the Galaxy reveal important structural features, especially in the inner Galaxy, such as the "near" 3-kpc arm and the nuclear disk (Bania, 1977). ^{12}CO emission from giant molecular clouds (GMCs) traces out Galactic spiral arms (e.g., Dame et al., 1986; García et al., 2014) and is used to discover and characterize new spiral features, such as the "far" 3-kpc arm (Dame & Thaddeus, 2008) and the OSC (Dame & Thaddeus, 2011). Dame et al. (2001) compile data from several surveys to create the most sensitive and complete ^{12}CO survey of the Galaxy. Ongoing

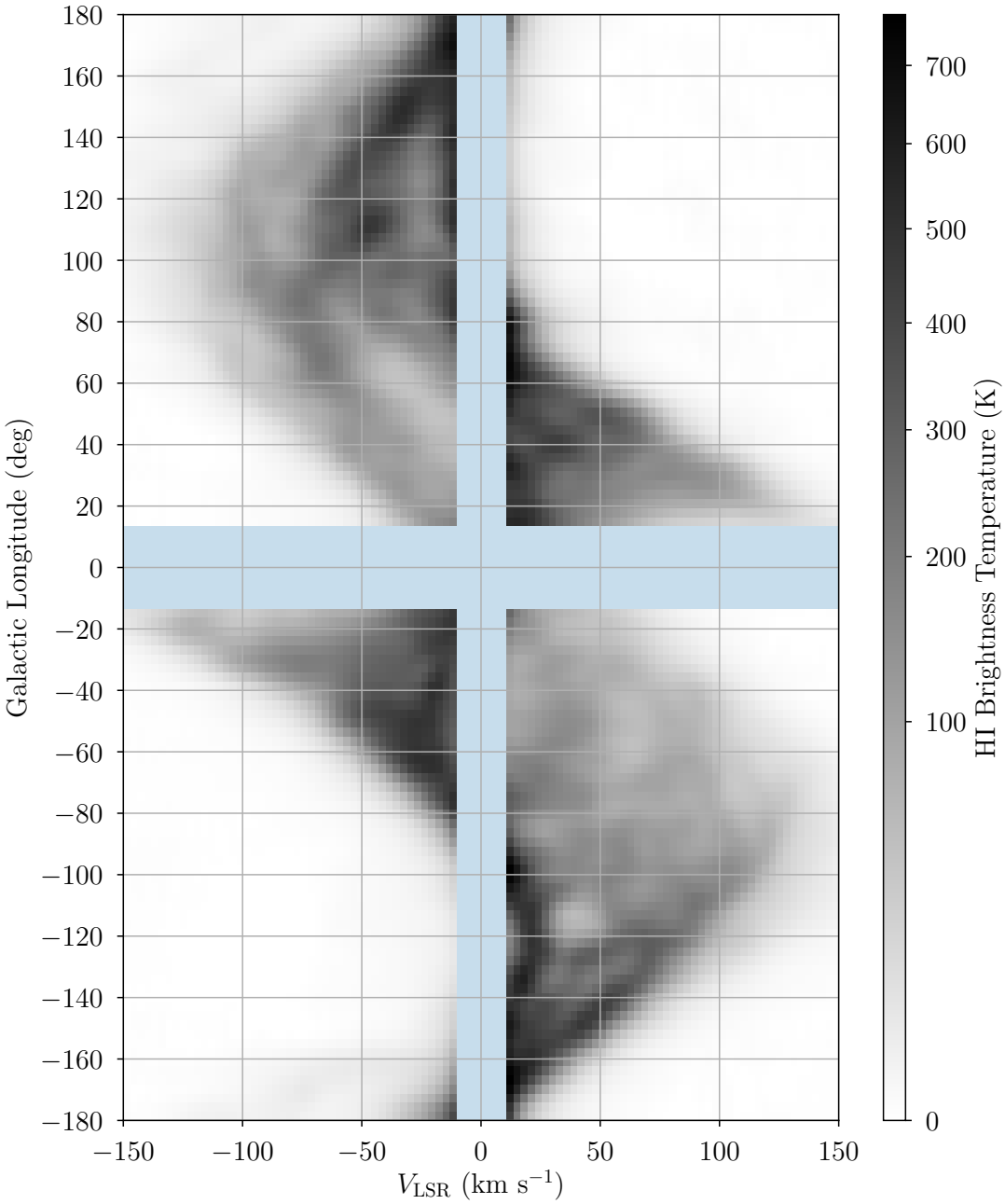

Figure 6.1: HI4PI H I brightness temperature, $T_{B,\rm HI}$, integrated over Galactic latitude as a function of Galactic longitude and LSR velocity, $V_{\rm LSR}$. We use the $|b| < 7.5°$ and $|V_{\rm LSR}| < 150\,{\rm km\,s^{-1}}$ subset of the HI4PI data, smoothed and gridded to 3° in ℓ, 1.5° in b, and $3\,{\rm km\,s^{-1}}$ in $V_{\rm LSR}$. We mask in light blue the Galactic center ($|\ell| < 15°$) and low-velocity ($|V_{\rm LSR}| < 10\,{\rm km\,s^{-1}}$) regions of these data.

surveys, such as the Milky Way Imaging Scroll Project (MWISP Su et al., 2019), are mapping the Galactic plane in ^{12}CO and its isotopologues with larger telescopes and more sensitivity, and they will soon supersede the Dame et al. (2001) survey for Galactic studies.

We use the Dame et al. (2001) ^{12}CO ($J = 1 \rightarrow 0$) survey in our analysis. The combined data are interpolated to a regular grid, with voxels of size 0.125° in ℓ and b and 1.3 km s^{-1} in $V_{\rm LSR}$. The brightness temperature sensitivity ranges from ∼0.1 K to ∼0.4 K. To match the neutral gas data, we smooth and grid the Dame et al. (2001) composite data to the same $(\ell, b, V_{\rm LSR})$ resolution and grid as the smoothed and gridded H I data. Figure 6.2 shows the ℓ-$V_{\rm LSR}$ diagram for the smoothed and gridded ^{12}CO data, integrated over the full latitude range. The Dame et al. (2001) composite data latitude coverage varies among the compiled surveys, so the latitude integration in Figure 6.2 is not uniform.

6.2.3 H II Regions

The archetypal tracers of Galactic spiral structure are HMSFRs, such as H II regions, due to their association with high-mass stars in spiral arms and their bright spectral line emission (e.g., Rosse & Parsons, 1880; Morgan et al., 1952). Optical observations of H II regions with spectroscopic parallax distance determinations reveal evidence for spiral structure (e.g., Morgan et al., 1952). Georgelin & Georgelin (1976) combine optical and radio observations of nebulae to create a "map" of the Galactic spiral arms, though they use a fairly small sample and unreliable distance techniques.

Most Galactic H II regions are optically obscured due to dust extinction, but they are among the brightest objects in the sky at radio wavelengths. RRL emission is used to locate these nebulae across the Galactic disk (e.g., Bania et al., 2010; Wenger et al., 2019, Chapter 4). The HRDS is now completing the catalog of all O star Galactic H II regions (e.g., Wenger et al., 2019, Chapter 4), which, when combined with accurate maser parallax distances (e.g., Reid et al., 2014) and kinematic distance techniques (e.g., Wenger et al., 2018a, Chapter 3), will reveal new insight into the structure of the Galaxy.

Here we use the latest compilation of all known Galactic H II regions, the *Widefield Infrared Survey Explorer (WISE)* Catalog of Galactic H II Regions (Anderson et al., 2014). The *WISE* Catalog contains the positions and LSR velocities of 2208 nebulae, including the 256 nebulae recently discovered by the Southern H II Region Discovery

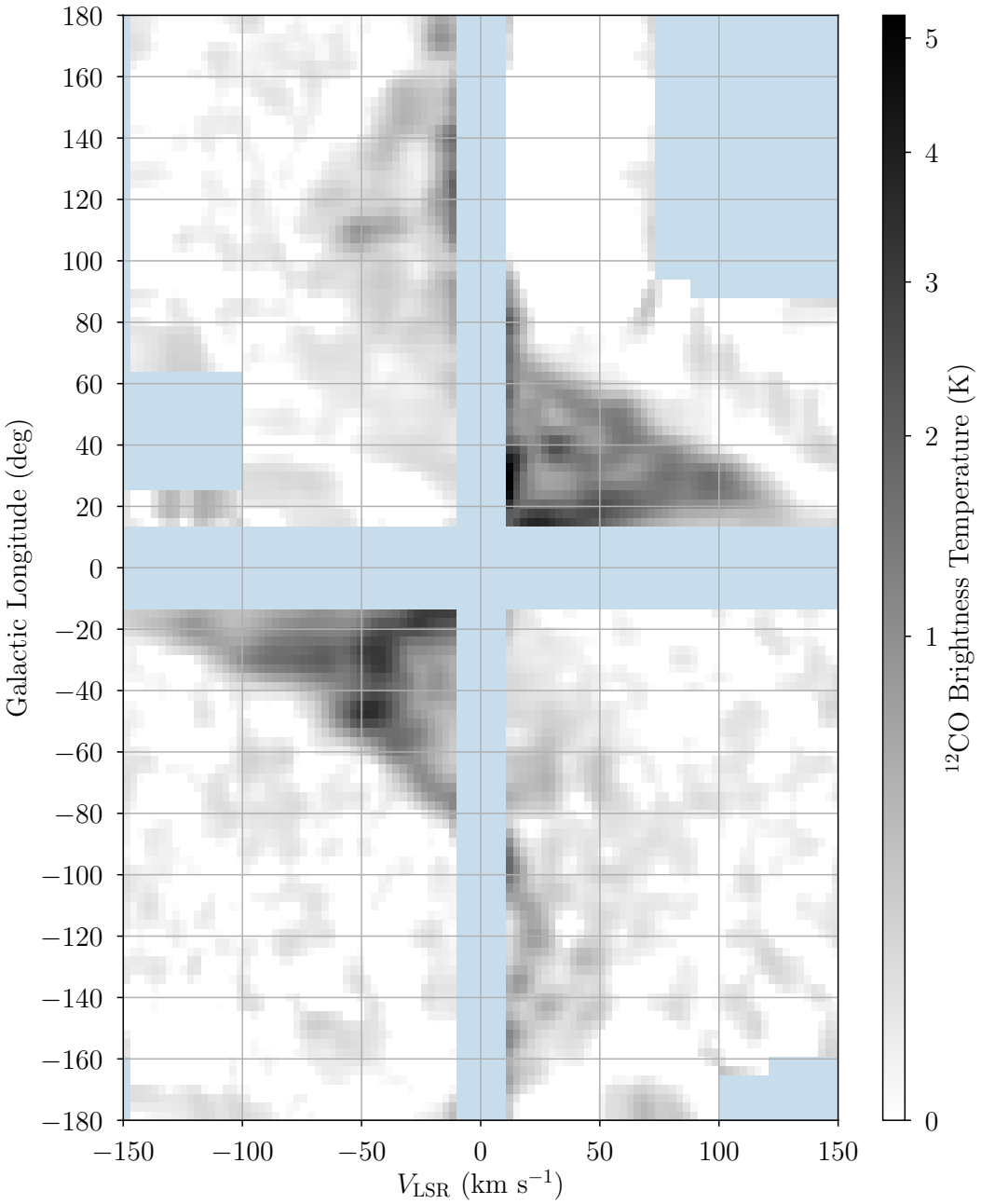

Figure 6.2: Same as Figure 6.1 for the Dame et al. (2001) ^{12}CO brightness temperature.

Survey (SHRDS; Wenger et al., 2019, Chapter 4). We count the number of nebulae in each $(\ell, b, V_{\rm LSR})$ bin using the same binning that we used to grid the H I and ^{12}CO data. Figure 6.3 shows the number of *WISE* Catalog H II regions in ℓ-$V_{\rm LSR}$ space, summed over the Galactic latitude range.

6.3 Model

We develop a simple model of the H I 21 cm hyperfine emission (hereafter, H I) distribution, ^{12}CO($J = 1 \rightarrow 0$; hereafter, ^{12}CO) emission distribution, and H II region number distribution in the Galaxy. The model is not predicated on the physics of galaxy formation and evolution, the ISM, star formation, nor theories of Galactic spiral structure. This is a simple proof of concept study to determine if the spiral structure of the Galaxy can be revealed by the $(\ell, b, V_{\rm LSR})$ distributions of common Galactic structure tracers.

Our model uses empirical formulae and scaling relations to analytically define the various bulk components of the ISM. For example, we use an empirical radial H I surface density profile determined from observations of many different galaxies, and we derive the ^{12}CO and H II region densities as a simple multiplicative factor of the H I densities. Every parameter in these empirical and scaling functions is tunable. These simplifications are approximations for the real physics. Our model is not able to reproduce small scale features of the ISM, such as individual clouds or star forming regions. We are only interested in modeling the large scale distributions of the ISM components. Small scale, stochastic features may skew our results, and some or all of our parametrizations may be too simplified to reproduce the observed $(\ell, b, V_{\rm LSR})$ distributions of our tracers. In these cases, we must reassess and redefine the failing aspects of the model.

The many free parameters of our model are listed and defined in Table 6.1. We also give the initial values, uncertainties, and references for those parameters that have been measured or derived in other studies. Here, we discuss these parameters in more detail, and we motivate and define the empirical and scaling relations we use to derive the neutral gas, molecular gas, and H II region distributions in the model Galaxy.

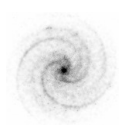

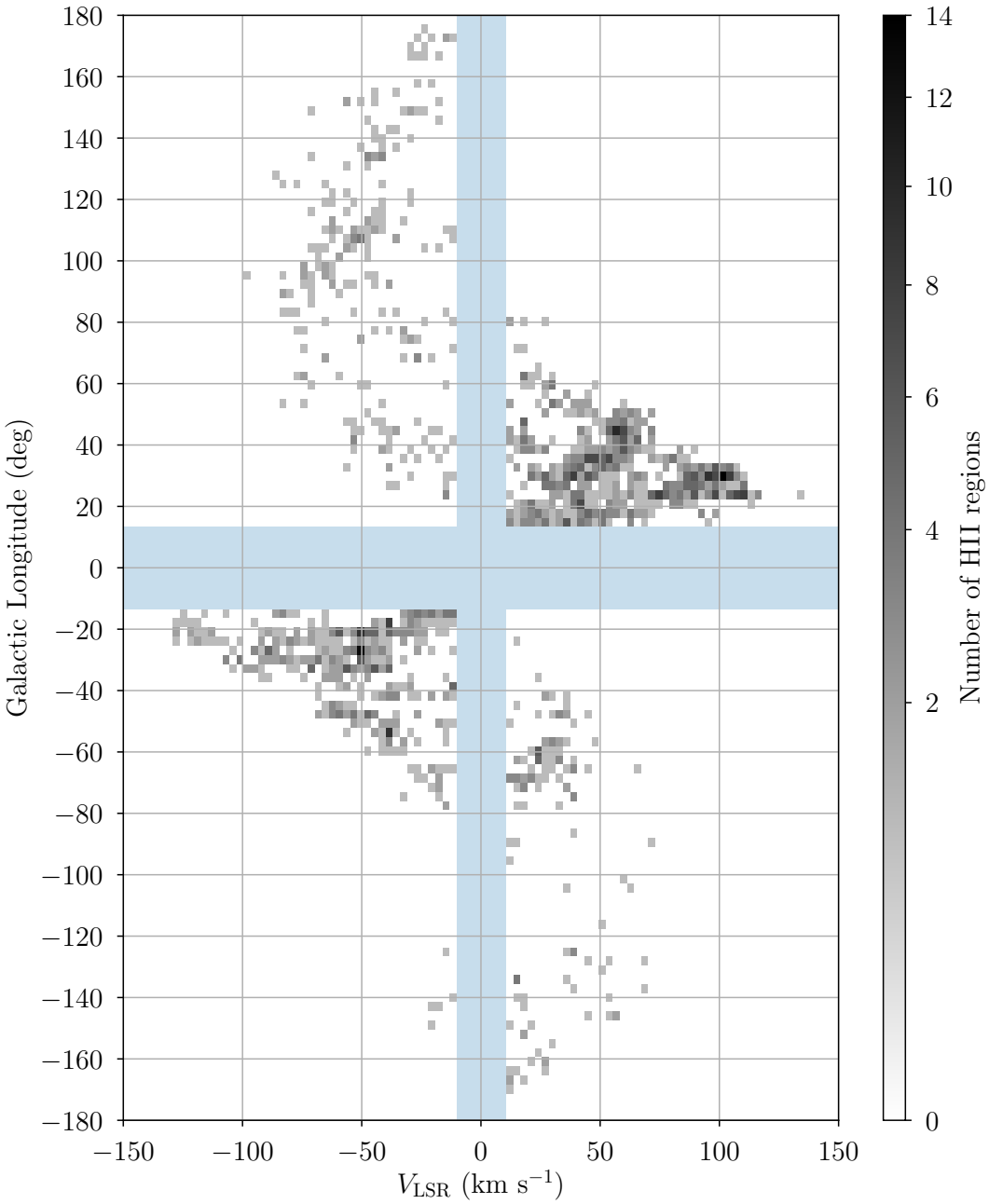

Figure 6.3: Same as Figure 6.1 for the number of *WISE* Catalog H II regions in each $(\ell, V_{\rm LSR})$ bin, summed over Galactic latitude.

Table 6.1: Model Parameters

Parameter	Definition	Initial Value	Reference
R_0	Galactocentric radius of the Sun	8.34 ± 0.16 kpc	Reid et al. (2014)
a_1	Galactic rotational velocity at R_0	241 ± 8 km s^{-1}	Reid et al. (2014)
a_2	Rotation curve parameter	0.90 ± 0.06	Reid et al. (2014)
a_3	Rotation cuve parameter	1.46 ± 0.16	Reid et al. (2014)
$U_\odot^{\rm rev}$	Solar non-circular motion	10.5 ± 1.7 km s^{-1}	Reid et al. (2014)
$V_\odot^{\rm rev}$	Solar non-circular motion	14.4 ± 6.8 km s^{-1}	Reid et al. (2014)
$W_\odot^{\rm rev}$	Solar non-circular motion	8.9 ± 0.9 km s^{-1}	Reid et al. (2014)
I_1	H I disk surface density	$50\,M_\odot$ pc^{-2}	
I_2	H I disk surface density	35	
r_s	H I disk scale length	4.5 kpc	
r_c	H I disk scale length	2.75 kpc	
h_0	H I disk scale height	0.1 kpc	
r_0	H I disk scale height	12.0 kpc	
$T_{D,\rm WNM}$	WNM Doppler temperature	6000 K	
$T_{S,\rm WNM}$	WNM spin temperature	1000 K	
$n_{\rm arm}$	Number of spiral arms	4	
$\theta_{0,i}$	Reference azimuth of ith arm	72°, 252°, 317°, 137°	Koo et al. (2017)
ϕ_i	Pitch angle of ith arm	$14 \pm 1.4°$	Koo et al. (2017)
Δ_i	FWHM of ith arm	1 kpc	
$n_{i,\rm CNM}/n_{i,\rm WNM}$	CNM density enhancement of ith arm	5	
$T_{D,\rm CNM}$	CNM Doppler temperature	500 K	
$T_{S,\rm CNM}$	CNM spin temperature	100 K	
$n_{\rm HI}^{\rm COmin}$	Minimum H I density for ^{12}CO presence	1 cm^{-3}	
$n_{\rm CO}/n_{\rm HI}$	^{12}CO density factor	$10^{-5.5}$	

Table 6.1 continued

Table 6.1: Model Parameters (continued)

Parameter	Definition	Initial Value	Reference
$T_{D,\mathrm{CO}}$	^{12}CO Doppler temperature	20 K	
$T_{X,\mathrm{CO}}$	^{12}CO excitation temperature	20 K	
$n_{\mathrm{HII\,Regions}}/n_{\mathrm{HI}}$	H II region density factor	-1	
$n_{\mathrm{HII\,Regions}}/n_{\mathrm{CO}}$	H II region density factor	$10^{7.5}$	
$\sigma_{V,\mathrm{HII\,Regions}}$	H II region velocity width	5 km s^{-1}	
n_{warp}	Number of warp modes	3	
W_i	Amplitude of ith warp mode at $R = 0\,\mathrm{kpc}$	-2.5, -1.5, -1.5 kpc	
dW_i/dR	Slope of ith warp mode amplitude	0.167, 0.15, 0.05	
$\theta_{w,i}$	Azimuth of ith warp mode at $R = 0\,\mathrm{kpc}$[a]	90°, 90°	
$d\theta_{w,i}/dR$	Slope of ith warp mode azimuth[a]	0, 0 deg kpc^{-1}	

[a] Warp mode 0 does not have an azimuthal component. The initial values of $\theta_{w,i}$ are incorrectly set as 180° in our Markov Chain Monte Carlo analysis.

6.3.1 Solar Galactocentric Radius

The first parameter in our model is the solar Galactocentric radius, R_0. This value is used to compute the Galactic rotation curve and to define the morphology of the spiral arms. Although published values of R_0 range from $\sim 7 - 10\,\mathrm{kpc}$, we adopt an initial value $R_0 = 8.34 \pm 0.16\,\mathrm{kpc}$ based on recent maser parallax and proper motion measurements (Reid et al., 2014).

6.3.2 Kinematics

The observed $(\ell, b, V_{\mathrm{LSR}})$ distribution of Galactic structure tracers depends on both the spatial and kinematic distributions of the emitters. The most important of these kinematics are the Galactic rotation model (GRM) and the deviation of the Sun from this GRM. The dominant component of the GRM is axisymmetric circular rotation. Streaming motions, or non-circular motions, are important near non-axisymmetric features, such as spiral arms and the Galactic bar (e.g., Burton, 1971; Gómez, 2006; Moisés et al., 2011). We do not consider streaming motions in our simple morphological model of the Galaxy.

The Galactic rotation curve is flat beyond $R \simeq 1\,\mathrm{kpc}$, with only small deviations of order $5 - 10\,\mathrm{km\,s^{-1}}$ (e.g., Brand & Blitz, 1993; Reid et al., 2014). We parameterize the axisymmetric Galactic rotation curve following Persic et al. (1996):

$$\Theta(R) = a_1 \left[\frac{1.97\beta x^{1.22}}{(x^2 + 0.78^2)^{1.43}} + (1-\beta)x^2 \left(\frac{1 + a_3^2}{x^2 + a_3^2} \right) \right]^{1/2} \tag{6.1}$$

where $x = R/(a_2 R_0)$ and $\beta = 0.72 + 0.44 \log_{10}[(a_3/1.5)^5]$. The first term in this equation is the contribution from the stellar disk, and the second term is the contribution from the dark matter halo. The parameters a_1, a_2, and a_3 are free in our model. The initial values are the Reid et al. (2014) best fit parameters based on maser parallax and proper motion measurements.

The non-circular motion of the Sun directly affects the definition of the LSR. The LSR is defined by the International Astronomical Union Commission 33 as $220\,\mathrm{km\,s^{-1}}$ in the direction $(\ell, b) = (90°, 0°)$ and a solar non-circular motion of $20\,\mathrm{km\,s^{-1}}$ in the direction (R.A., decl.)= $(18^{\mathrm{h}}, +30°; B1900)$ (Kerr & Lynden-Bell, 1986). In the modern epoch, the Cartesian components of this non-circular motion are $U_\odot^{\mathrm{Std}} = 10\,\mathrm{km\,s^{-1}}$ in the direction of the Galactic center, $V_\odot^{\mathrm{Std}} = 15\,\mathrm{km\,s^{-1}}$ in the direction of

Galactic rotation, and $W_{\odot}^{\rm Std} = 7\,{\rm km\,s^{-1}}$ in the direction of the North Galactic pole. Three parameters in our model, $U_{\odot}^{\rm rev}$, $V_{\odot}^{\rm rev}$, and $W_{\odot}^{\rm rev}$, are the revised values for the solar non-circular motion, with initial values from Reid et al. (2014). We derive the corrected LSR velocities following Wenger et al. (2018a, Chapter 3).

6.3.3 Warm Neutral Medium (WNM)

We adopt the simplistic model of a two phase neutral atomic ISM, which consists of the WNM and the CNM. The WNM is characterized by a thick, exponential disk of warm hydrogen. The H I surface density profile of external galaxies is typically constant within the stellar disk, or sometimes it has a slight depression near the galactic center, whereas the H I surface density in the outskirts of the galaxy falls off exponentially (e.g. Bigiel & Blitz, 2012; Wang et al., 2014). We use the Wang et al. (2014) "universal" H I surface density profile to parameterize the WNM surface density in our model:

$$\Sigma_{WNM}(R) = \frac{I_1 \exp(-R/r_s)}{1 + I_2 \exp(-R/r_c)} \tag{6.2}$$

where r_s is roughly the scale length of the outer disk, r_c is roughly the radius at which the profile transitions from inner flat to outer exponential, and I_1 and I_2 define the magnitude of the surface density. As noted by Wang et al. (2014), I_1 is likely related to the total (neutral and molecular) gas density profile of the galaxy, and I_1/I_2 is likely related to the atomic-to-molecular gas density ratio (Leroy et al., 2008). Each of these values, I_1, I_2, r_s, and r_c, are free parameters in our model.

To select initial values for the WNM surface density parameters, we look to the Kalberla & Kerp (2009) review of H I in the Milky Way. The surface density of H I in the inner Galaxy is $5 - 10\,{\rm M_{\odot}\ pc^2}$ (Dickey & Lockman, 1990; Binney & Merrifield, 1998; Wolfire et al., 2003), with an exponential scale length of $r_s \sim 3.75\,{\rm kpc}$ in the outer Galaxy (Wouterloot et al., 1990; Diplas & Savage, 1991; Kalberla & Dedes, 2008). The top panel in Figure 6.4 shows the radial profile of the WNM surface density using the initial parameters in Table 6.1. This radial profile is qualitatively similar in shape to the Kalberla & Kerp (2009) compilation of several different studies. The magnitude of the WNM surface density profile is less than the Kalberla & Kerp (2009) compilation because we have not yet included the CNM phase.

The vertical distribution of the Galactic WNM is typically modeled as a flaring

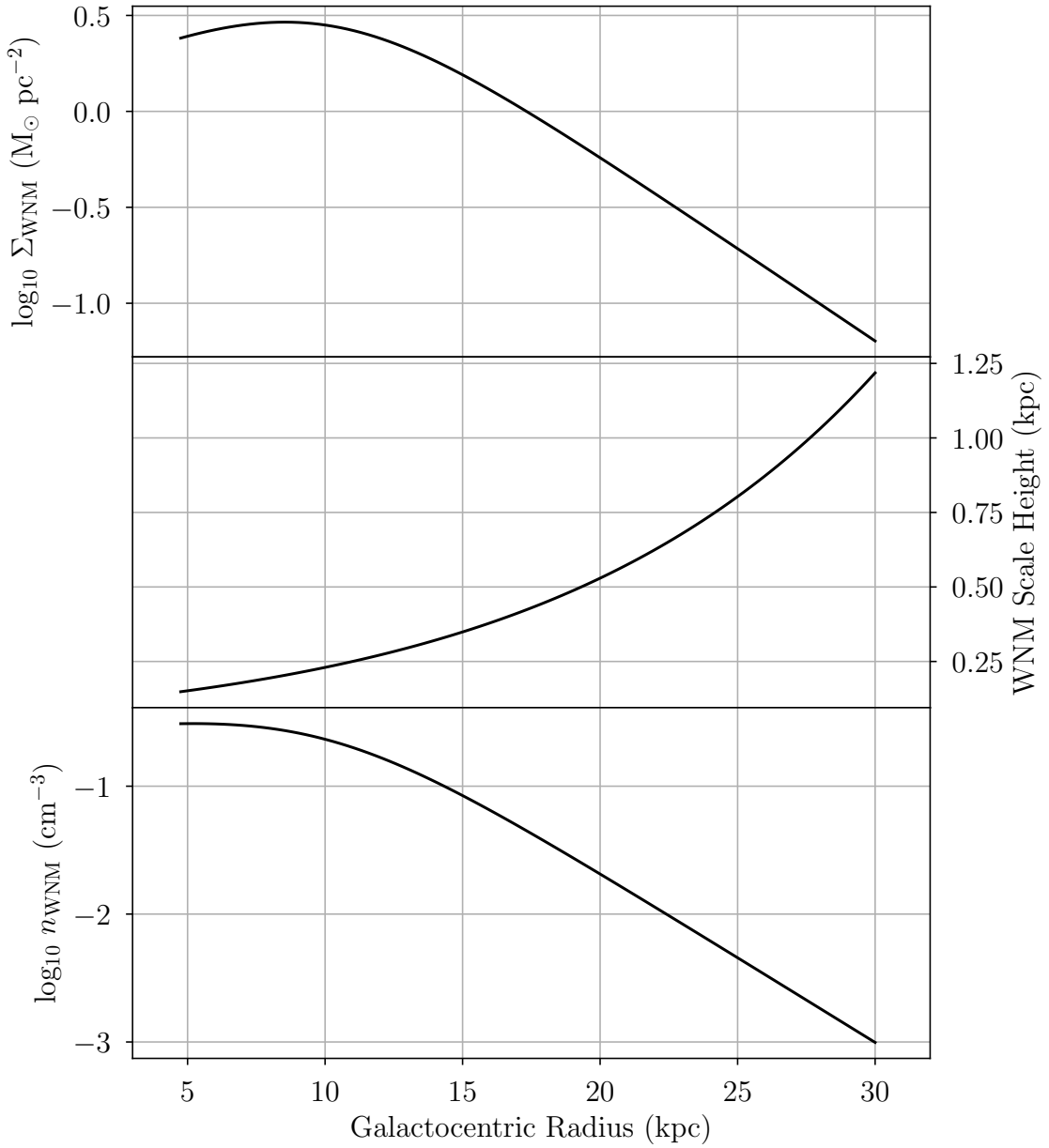

Figure 6.4: Model WNM surface density (top), scale height (middle), and midplane density (bottom) radial profiles, determined using the initial values in Table 6.1.

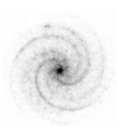

exponential, where the scale height of the WNM layer increases with Galactocentric radius (Kalberla & Kerp, 2009). We model the vertical WNM distribution as an axisymmetric Gaussian:

$$n_{\rm WNM}(R,Z) = n_{\rm WNM}(R,Z=0)\exp\left[-4\ln(2)\left(\frac{Z^2}{h^2_{\rm WNM}(R)}\right)\right] \tag{6.3}$$

where $h_{\rm WNM}(R)$ is the half width at half maximum (HWHM) scale height of the WNM at R, and $n_{\rm WNM}(R,Z=0)$ is the midplane density at R,

$$n_{\rm WNM}(R,Z=0) = \left(\frac{\ln(2)}{\pi}\right)^{1/2}\left(\frac{\Sigma_{WNM}(R)}{h_{\rm WNM}(R)}\right) \tag{6.4}$$

By integrating $n_{\rm WNM}(R,Z)$ over Z, we recover the WNM surface density, $\Sigma_{WNM}(R)$.

The HWHM scale height of the WNM layer grows exponentially with R (Kalberla & Dedes, 2008). We define this function as

$$h_{\rm WNM}(R) = h_0\exp\left[-\frac{R}{r_0}\right] \tag{6.5}$$

where h_0 is the scale height at the reference radius r_0. As initial parameters, we use $h_0 = 0.1\,$kpc and $r_0 = 12.0\,$kpc to approximately reproduce the Kalberla & Dedes (2008) fit. Figure 6.4 shows the WNM HWHM scale height (middle panel) and midplane density (bottom panel) using these initial values.

There are 6 free parameters, I_1, I_2, r_s, r_c, h_0, and r_0, that describe the morphology of the WNM in our model galaxy. The $(\ell, b, V_{\rm LSR})$ distribution of the WNM emission depends on the kinematics of the Galaxy, these morphological parameters, and the Doppler and spin temperatures of the WNM H I. The Doppler temperature characterizes the thermal and non-thermal (e.g., turbulent) motions of the gas (e.g., Balser, 1995). We assume that the WNM Doppler temperature, $T_{D,\rm WNM}$, and spin temperature, $T_{S,\rm WNM}$, are constant throughout the Galaxy, so there are 8 free parameters for the WNM component of our model.

6.3.4 Cold Neutral Medium (CNM) and Spiral Arms

The spatial distribution of the CNM, molecular gas, and H II regions in galaxies is strongly correlated with the locations of the galactic spiral arms (e.g., Burton et al., 1975; Young & Scoville, 1991; Koo et al., 2017). Although the morphology

of the Milky Way spiral arms is unknown and one of the parameters we wish to determine in this analysis, logarithmic spirals are typically good approximations for galactic spiral arms (e.g., Seigar & James, 1998; Davis et al., 2012; Reid et al., 2014). The Galactocentric radius, R, of a logarithmic spiral is related to its Galactocentric azimuth, θ, by

$$R = R_0 \exp\left[(\theta_0 - \theta)\tan\phi\right] \tag{6.6}$$

where θ_0 is the reference azimuth, at which the spiral has a radius R_0, and ϕ is the pitch angle. As initial parameters, we use the logarithmic spiral fits to the peaks of H I emission identified by Koo et al. (2017). They fit the Scutum-Centaurus (Scu-Cen) with $\phi = 12.4 \pm 1.8°$ and $\theta_0 = 252 \pm 47°$ (N.B. we define $\theta = 0°$ in the direction of the Sun and increasing in the direction of Galactic rotation; this differs from the Koo et al. (2017) definition). For the Sagittarius-Carina (Sgr-Car) arm, they fix ϕ and fit $\theta_0 = 317 \pm 17°$. They assume that the Perseus and Outer arm parameters are those of Scu-Cen and Sgr-Car, rotated by 180°. We force the spiral arms to lie in the Galactic midplane, although this midplane may be warped (see Section 6.3.7).

We model the CNM density as a Gaussian distribution centered on the spiral arms. This parametrization requires that we can determine the distance, $d_{\rm min}$, between any Galactocentric point (R, θ, Z) and a spiral arm. We are unable to find an analytical expression for $d_{\rm min}$, therefore we derive an approximation in Appendix E. We assume that the CNM density is a multiplicative factor of the WNM density, such that

$$n_{\rm CNM}(R,\theta,Z) = n_{\rm WNM}(R,Z) \sum_{i}^{n_{\rm arms}} \left[\left(\frac{n_{i,\rm CNM}}{n_{i,\rm WNM}} \right) \exp\left(-8\ln(2) \frac{d^2_{\rm min,i}(R,\theta,Z)}{\Delta_i^2} \right) \right] \tag{6.7}$$

where $d_{\rm min,i}$ is the distance between a point and the ith spiral, Δ_i is the CNM FWHM width of the ith spiral, $n_{i,\rm CNM}/n_{i,\rm WNM}$ is the ratio of the CNM density to the WNM density at the center of the ith spiral arm, and $n_{\rm arms}$ is the number of spiral arms. Figure 6.5 shows a face-on view of the midplane CNM density in a 4-armed model Galaxy using the initial parameters in Table 6.1. Since we are not modeling the Galactic bulge and bar, we mask out the Galactic center in the figure.

Each spiral arm has 4 free parameters, θ_i^0, ϕ_i, Δ_i, and $n_{i,\rm CNM}/n_{i,\rm WNM}$, which define the spiral morphology and the density of the CNM associated with that arm. Like the WNM, the CNM emission depends on the Doppler temperature, $T_{D,\rm CNM}$, and spin temperature, $T_{S,\rm CNM}$, of the gas. We assume that these temperatures are constant for

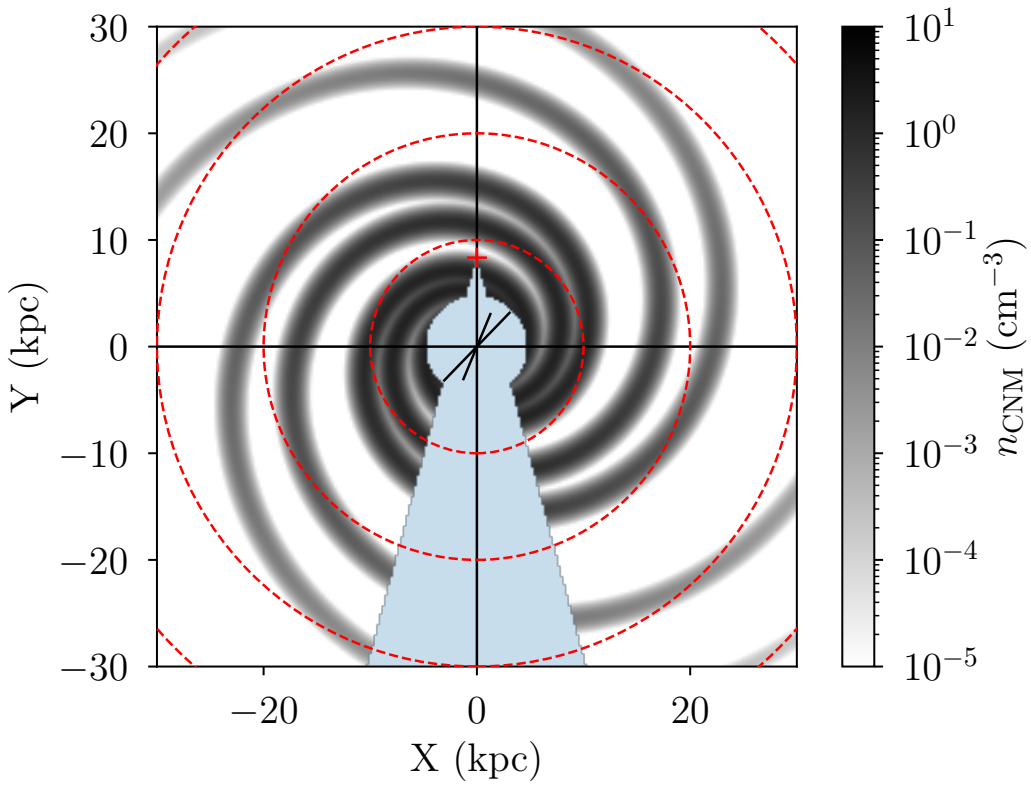

Figure 6.5: Initial model midplane CNM density, $n_{\rm CNM}$, determined using the parameters in Table 6.1. The Galactic center is at the origin, and the Sun is at the red cross. The two black lines at the origin represent the long and short Galactic bars (Benjamin et al., 2005). The red dashed circles are 10, 20, 30, and 40 kpc in radius. We do not model the Galactic center or the Galactic bars, so the inner Galaxy ($R < 4.5\,$kpc) and Galactic center direction ($|\ell| < 15°$) are masked in light blue.

all CNM gas in the model, and we select initial values such that the initial H I ℓ-$V_{\rm LSR}$ diagram is qualitatively similar to the HI4PI data.

The WNM and CNM make up the total neutral gas component of our model. In Figure 6.6 we show the radial (top) and face-on (bottom) distributions of the total H I surface density, determined by integrating the WNM and CNM densities from $Z = -10$ to 10 kpc. To compute the radial profile, we average the H I surface density over all Galactocentric azimuths. The total H I surface density matches the Kalberla & Kerp (2009) compilation, with $\Sigma_{\rm HI}$ ranging from $\sim 10^1\, M_\odot\,{\rm pc}^{-2}$ to $\sim 10^{-1}\, M_\odot\,{\rm pc}^{-2}$ between $R \simeq 5$ kpc and 30 kpc.

6.3.5 Molecular Gas

The physics of molecular gas in the ISM is an active area of research (e.g., Heyer & Dame, 2015). Since much of the molecular gas in galaxies is confined to spiral arms (e.g., Young & Scoville, 1991; García et al., 2014), and since we are not modeling individual GMCs, we adopt a very naïve scaling relation to relate the density of ^{12}CO to that of H I:

$$n_{\rm CO} = \begin{cases} 0 & n_{\rm HI} < n_{\rm HI}^{\rm COmin} \\ \left(\frac{n_{\rm CO}}{n_{\rm HI}}\right) n_{\rm HI} & n_{\rm HI} \geq n_{\rm HI}^{\rm COmin} \end{cases} \tag{6.8}$$

where $n_{\rm HI}^{\rm COmin}$ is the minimum H I density required for ^{12}CO presence, and $n_{\rm CO}/n_{\rm HI}$ is the ^{12}CO to total (CNM and WNM) H I density scaling factor. The minimum H I density cutoff restricts the ^{12}CO to the densest regions of the spiral arms. As a side effect, the ^{12}CO abruptly ceases to exist when $n_{\rm HI} < n_{\rm HI}^{\rm COmin}$. This parametrization is likely too simplistic to adequately reproduce the observed ^{12}CO $(\ell, b, V_{\rm LSR})$ distribution, since we are missing the GMCs in the outer Galaxy and inter-arm regions. Nonetheless, it is a sufficient approximation for this proof of concept analysis. Figure 6.7 shows the face-on distributions of the midplane ^{12}CO density (top) and ^{12}CO surface density for the initial model.

Including the Doppler temperature, $T_{\rm D,CO}$, and excitation temperature, $T_{\rm X,CO}$, which are assumed constant for all ^{12}CO gas, there are 4 free parameters for the ^{12}CO component of our model. We select initial values for each of these parameters such that the initial model ℓ-$V_{\rm LSR}$ diagram is qualitatively similar to the Dame et al. (2001) data.

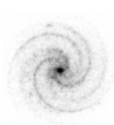

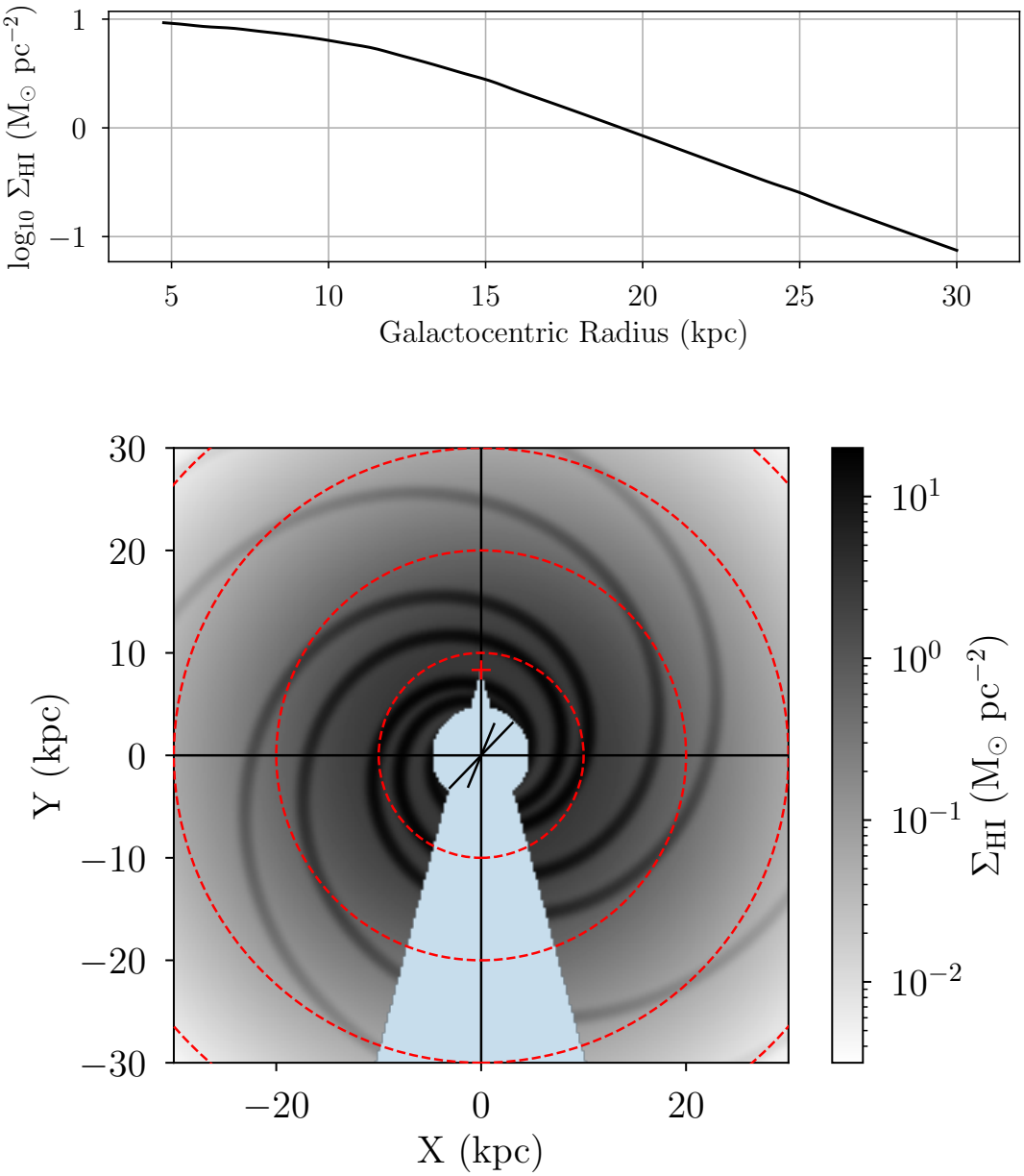

Figure 6.6: Initial model H I surface density, $\Sigma_{\rm HI}$, as a function of Galactocentric radius (top) and in a face-on view (bottom), determined using the parameters in Table 6.1. The radial profile is determined by averaging the H I surface density over all Galactocentric azimuths. The features in the face-on diagram are the same as in Figure 6.5.

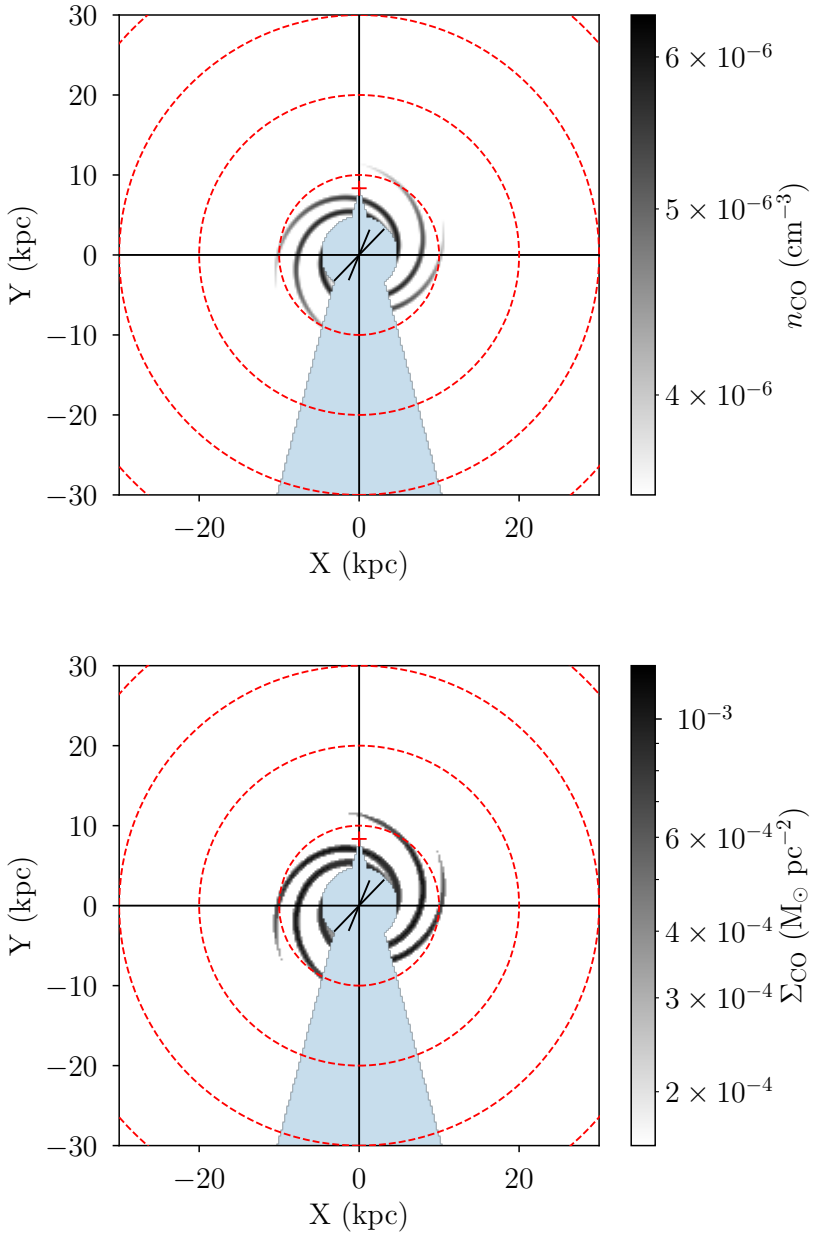

Figure 6.7: Face-on distribution of the initial model ^{12}CO midplane density, $n_{\rm CO}$ (top), and surface density, $\Sigma_{\rm CO}$ (bottom), determined using the parameters in Table 6.1. The features in the face-on diagrams are the same as in Figure 6.5. The ^{12}CO density sharply terminates where $n_{\rm HI} < n_{\rm HI}^{\rm COmin}$.

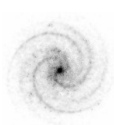

6.3.6 H II Regions

High-mass star formation is typically associated with molecular gas in galaxies (e.g., Anderson et al., 2009; Armentrout et al., 2017; Wenger et al., 2018b). Our simple treatment of molecular gas in the model means that there is no molecular gas where $n_{\rm HI} < n_{\rm HI}^{\rm COmin}$. We know there are H II regions in the outer Galaxy and inter-arm regions, therefore we can not only use the molecular gas density to set the H II region distribution. We assume that the H II region density depends on both the total H I and ^{12}CO densities with different scaling factors:

$$n_{\rm HII\,Regions} = \left(\frac{n_{\rm HII\,Regions}}{n_{\rm HI}}\right) n_{\rm HI} + \left(\frac{n_{\rm HII\,Regions}}{n_{\rm CO}}\right) n_{\rm CO} \tag{6.9}$$

where $n_{\rm HII\,Regions}/n_{\rm HI}$ and $n_{\rm HII\,Regions}/n_{\rm CO}$ are the H II region density scaling factors for H I and ^{12}CO, respectively. This is, again, a much too simplistic assumption, but it is sufficient for this exploratory analysis. We select initial values for these parameters such that the H II region ℓ-$V_{\rm LSR}$ diagram is qualitatively similar to the *WISE* Catalog data. Figure 6.8 shows the face-on view of the H II region midplane density (top) and surface density (bottom) for the initial parameters in Table 6.1.

In addition to the H II region density scaling factors, the velocity width of the H II region distribution, $\sigma_{V,\rm HII\,Regions}$ is a free parameter. We assume that the H II regions at any given position have a Gaussian velocity distribution centered on the nominal LSR velocity at that position. Therefore, $\sigma_{V,\rm HII\,Regions}$ is like the Doppler temperature of the H II region population.

6.3.7 Galactic Warp

The Milky Way disk is warped in the outer Galaxy as seen in the vertical distribution of stars (e.g., Poggio et al., 2018) and gas (e.g., Schmidt, 1957; Westerhout, 1957; Wouterloot et al., 1990; Levine et al., 2006; Voskes & Butler Burton, 2006). The warp of the Galactic plane is typically characterized by Fourier decomposition. Levine et al. (2006) and Kalberla et al. (2007), for example, decompose the Galactic warp into three modes, each with an amplitude, $W_i(R)$, and azimuthal offset, $\theta_{i,w}(R)$, that are a function of Galactocentric radius:

$$Z'(R) - Z(R) = W_0(R) + W_1(R)\cos\left[\theta - \theta_{w,1}(R)\right] + W_2(R)\cos\left[2\theta - \theta_{w,2}(R)\right] \tag{6.10}$$

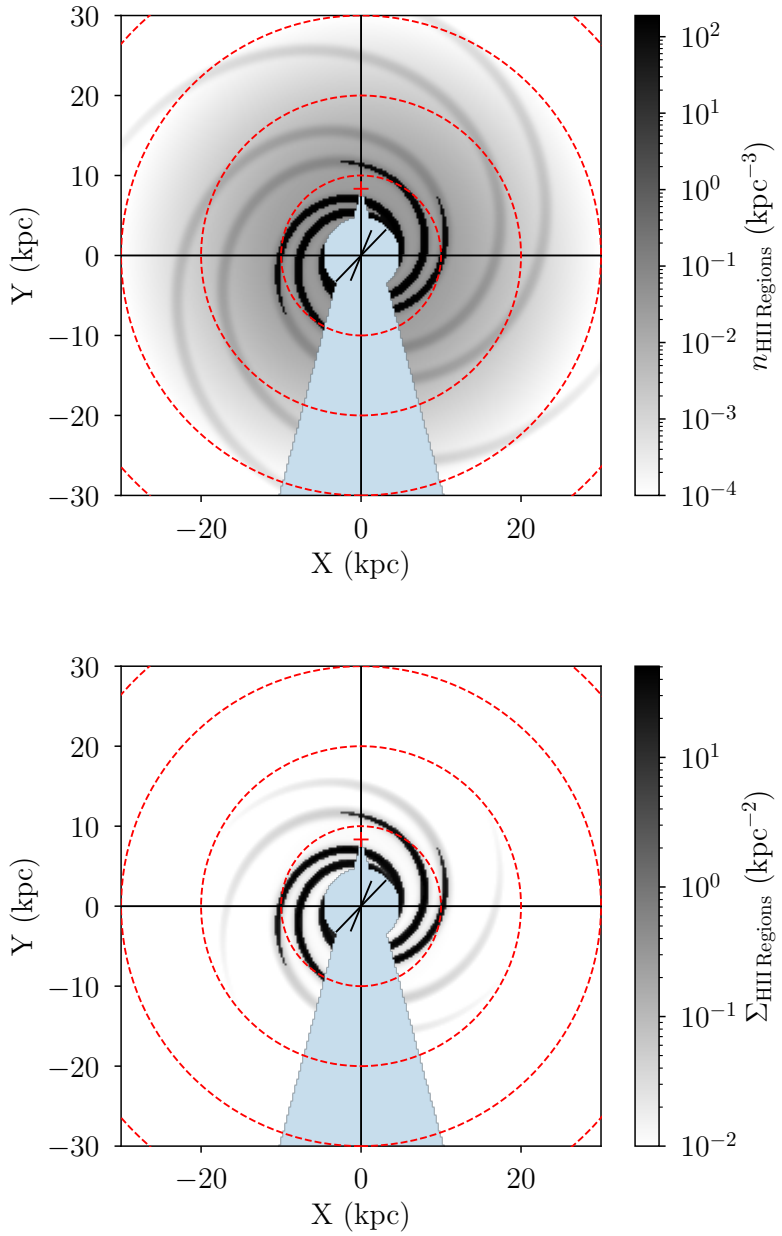

Figure 6.8: Same as Figure 6.7 for the initial model H II region distribution. The features in the face-on diagrams are the same as in Figure 6.5.

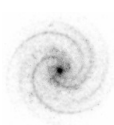

where $Z'(R) - Z(R)$ is the height of the warped midplane. The warp mode amplitudes and azimuthal offsets can, in principle, be complicated functions of R. The decomposition by Kalberla et al. (2007) shows that $W_i(R)$ is approximately linear in R up to $R \simeq 30$ kpc, whereas $\theta_{w,i}$ is more complicated, but varies by only $\sim 20°$ up to the same Galactocentric radius. We assume a linear model for these parameters, which we define as

$$W_i(R) = W_i + \left(\frac{dW_i}{dR}\right) R \tag{6.11}$$

$$\theta_{w,i}(R) = \theta_{w,i} + \left(\frac{d\theta_{w,i}}{dR}\right) R \tag{6.12}$$

where W_i and $\theta_{w,i}$ are the amplitude and azimuthal offset of the ith warp mode at $R = 0\,\mathrm{kpc}$, respectively, and dW_i/dR and $d\theta_{w,i}/dR$ are the slopes. We require $W_i(R) \geq 0$, so for any R where $W_i(R) < 0$, we set $W_i(R) = 0$. There is no $\theta_{w,0}$ component. The initial values for these three warp mode amplitudes and azimuthal offsets are selected to qualitatively match the Kalberla et al. (2007) decomposition. Figure 6.9 shows a face-on view of the warp of the Galactic midplane using the initial values in Table 6.1. The morphology and magnitude of this warp is similar to the face-on view of the H I warp in Levine et al. (2006).

6.4 Radiative Transfer

We derive the observed H I and ^{12}CO emission on a grid in $(\ell, b, V_{\mathrm{LSR}})$ space. In each direction, the line of sight is divided into many small segments such that the sum of the H I or ^{12}CO optical depths in these segments is a good approximation for the integral of the optical depth. Ideally, these line of sight segments would be infinitesimally small, but the limits of computation require that we make some approximations. Outside of Galactic spiral arms, the H I density varies slowly and the ^{12}CO gas is non-existent. Therefore, long line of sight segments are sufficient to estimate optical depths in these regions of the Galaxy. Within spiral arms, however, both the H I and ^{12}CO densities change rapidly, and we must use smaller segments to derive optical depths here.

We use an unsophisticated mesh-grid technique to divide the line of sight into sufficiently small distance segments and derive the H I and ^{12}CO optical depths. Given a line of sight direction (ℓ, b) and segment size, Δs, we derive the H I density at the

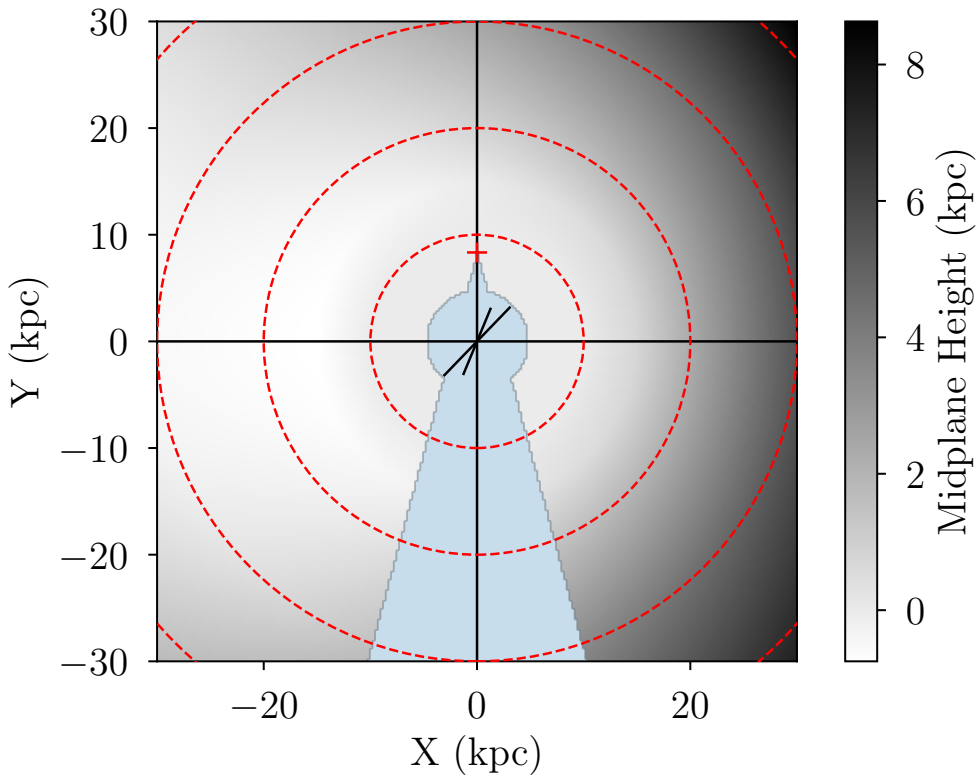

Figure 6.9: Face-on view of the Galactic warp height, $Z' - Z$, determined using the parameters in Table 6.1. The features in the face-on diagram are the same as in Figure 6.5.

center of each segment, s_i, up to some maximum distance, $d_{\rm max}$, or Galactocentric radius, $R_{\rm max}$, whichever is smaller. We also compute the H I density at $s_i + (\Delta s/4)$ and $s_i + (\Delta s/2)$ within each segment. If the H I density difference between any of these three positions is greater than some threshold, $n_{\rm thresh}$, then we divide the segment into sub-segments of size $\Delta s/2$ and recursively run the aforementioned procedure on the sub-segments. The recursion begins with some starting segment size $\Delta s_{\rm max}$ and continues until the H I density differences are less than $n_{\rm thresh}$ or until the minimum sub-segment size, $\Delta s_{\rm min}$, is reached.

The final $(\ell, b, V_{\rm LSR})$ H I distribution is sensitive to $\Delta s_{\rm max}$, which must be a few times smaller than the spiral arm CNM FWHM, whereas the ^{12}CO distribution is sensitive to both $\Delta s_{\rm max}$ and $\Delta s_{\rm min}$. If $\Delta s_{\rm max}$ is too large, then the inter-segment H I density fluctuations, such as the presence of a spiral arm, are missed and the segment resolution is not refined by the algorithm. Similarly, if $\Delta s_{\rm min}$ is too large, then the inter-segment ^{12}CO density fluctuations are not adequately sampled, and the final ^{12}CO optical depths are incorrect. We use $d_{\rm max} = R_{\rm max} = 30\,{\rm kpc}$, $n_{\rm thresh} = n_{\rm HI}^{\rm COmin}/50$, $\Delta s_{\rm max} = 100\,{\rm pc}$, and $\Delta s_{\rm min} = 25\,{\rm pc}$, which gives us a factor of 4 increase in line of sight distance resolution within the spiral arms. We also try $\Delta s_{\rm min} = 1\,{\rm pc}$, which increases the computation time by several orders of magnitude, but does not change the final $(\ell, b, V_{\rm LSR})$ H I and ^{12}CO distributions significantly ($\lesssim 1\%$ typically).

The observed $(\ell, b, V_{\rm LSR})$ brightness temperature distribution of H I or ^{12}CO depends on the spectral line physics and equations of radiative transfer. The opacity of a spectral line at some frequency ν is given by

$$\kappa(\nu) = \frac{c^2}{8\pi\nu_0^2}\left(\frac{g_U}{g_L}\right) n_L A_{UL}\left[1 - \exp\left(-\frac{h\nu_0}{kT_X}\right)\right]\phi(\nu) \tag{6.13}$$

where ν_0 is the emission line rest frequency, g_U and g_L are the statistical weights of the upper and lower energy levels, respectively, n_L is the density of the lower energy level, A_{UL} is the Einstein coefficient, T_X is the excitation temperature, $\phi(\nu)$ is the line profile, c is the speed of light, h is the Planck constant, and k is the Boltzmann constant (e.g., van de Hulst et al., 1954). We assume that the line widths are dominated by Doppler broadening, so the line profile is set by a Maxwellian

velocity distribution,

$$\phi(\nu) = \frac{c}{\nu_0}\left(\frac{M}{2\pi k T_D}\right)^{1/2} \exp\left[-\frac{Mc^2}{2kT_D}\left(\frac{\nu-\nu_{\rm LSR}}{\nu_{\rm LSR}}\right)^2\right] \tag{6.14}$$

where M is the mass of the emitter, T_D is the Doppler temperature, and $\nu_{\rm LSR}$ is the LSR rest frequency. The optical depth over some small line of sight distance segment with width Δs is approximately

$$\tau_i(\nu) = \kappa(\nu)\Delta s \tag{6.15}$$

and the brightness temperature contributed by the ith segment is given reciprocally by

$$T_{B,i}(\nu) = T_X\left(1-\exp[-\tau_i(\nu)]\right) + T_{B,i-1}(\nu)\exp\left[-\tau_i(\nu)\right] \tag{6.16}$$

where $T_{B,i-1}$ is the brightness temperature of the next more distant segment. The observed brightness temperature along some line of sight is $T_B(\nu) = \sum_i T_{B,i}(\nu)$.

The H I optical depth is set by a combination of the WNM and CNM densities, spin temperatures, and Doppler temperatures. The statistical weights in Equation 6.13 are $g_U/g_L = 3$ (van de Hulst et al., 1954). The ratio of the density of atoms in the upper energy state to the density of atoms in the lower energy state is given by the Boltzmann equation

$$\frac{n_{U,\rm HI}}{n_{L,\rm HI}} = \frac{g_U}{g_L}\exp\left(-\frac{h\nu_{UL}}{kT_X}\right) \tag{6.17}$$

where T_X is the H I spin temperature and ν_{UL} is the rest frequency of the transition. With $n_{\rm HI} = n_{U,\rm HI} + n_{L,\rm HI}$, this equation simplifies to

$$n_{L,\rm HI} = n_{\rm HI}\left[\frac{g_U}{g_L}\exp\left(-\frac{h\nu_0}{kT_S}\right)+1\right]^{-1} \tag{6.18}$$

where ν_0 is the H I rest frequency. For reasonable spin temperatures, $T_S \gtrsim 10\,{\rm K}$, the exponential term is $\sim$1 and $n_{L,\rm HI} \simeq n_{\rm HI}/4$. We determine the H I spin and Doppler temperatures by averaging the WNM and CNM temperatures weighted by the square of the WNM and CNM densities:

$$T = \frac{n_{\rm WNM}^2 T_{\rm WNM} + n_{\rm CNM}^2 T_{\rm CNM}}{n_{\rm WNM}^2 + n_{\rm CNM}^2} \tag{6.19}$$

where T is either the spin temperature or Doppler temperature. The LSR frequency is related to $V_{\rm LSR}$ by the Doppler equation:

$$\nu_{\rm LSR} = \nu_0 \left(1 - \frac{V_{\rm LSR}}{c}\right). \tag{6.20}$$

In each line of sight distance segment, the H I emission is confined to a small part of the LSR velocity space centered on the $V_{\rm LSR}$ of that position in the Galaxy. Therefore, to save computation time, we only compute the H I brightness temperature in the range $|V_{\rm LSR} - V_{\rm LSR}(\ell, b, s_i)| < 5\sigma_{V,\rm HI}$, where $V_{\rm LSR}(\ell, b, s_i)$ is the LSR velocity of this position and $\sigma_{V,\rm HI}$ is the Maxwellian velocity width from Equation 6.14.

The ^{12}CO optical depth is more complicated to derive because there are many possible energy levels. The statistical weight of the Jth state is $g_J = 2J + 1$ and the total ^{12}CO density is $n_{\rm CO} = \sum_J^\infty n_{J,\rm CO}$. The Boltzmann equation for ^{12}CO is

$$\frac{n_{J+1}}{n_J} = \frac{2J+3}{2J+1} \exp\left(-\frac{h\nu_{J+1\to J}}{kT_X}\right) \tag{6.21}$$

where $\nu_{J+1\to J}$ is the rest frequency of the $J+1$ to J transition, and T_X is the ^{12}CO excitation temperature, which we assume is constant for all transitions. The population of the $J = 0$ energy state is thus

$$n_{J=0} = n_{\rm CO} \left[\sum_{J=1}^{\infty} (2J+1) \prod_{J'=0}^{J} \exp\left(-\frac{h\nu_{J'+1\to J'}}{kT_x}\right)\right]^{-1} \tag{6.22}$$

where $n_{\rm CO}$ is the total ^{12}CO density. Numerically, we compute the summation to sufficiently high J such that the last term adds less than 0.1% to the total. As we did with H I, we only compute the ^{12}CO brightness temperature in the range $|V_{\rm LSR} - V_{\rm LSR}(\ell, b, s_i)| < 5\sigma_{V,\rm CO}$, where $\sigma_{V,\rm CO}$ is the ^{12}CO Maxwellian velocity width.

We determine the observed H I and ^{12}CO brightness temperatures on a $(\ell, b, V_{\rm LSR})$ grid with a 3 times finer resolution than the smoothed and gridded HI4PI and Dame et al. (2001) data. The native binning is 1° in ℓ, 0.5° in b, and 1.0 km s^{-1} in $V_{\rm LSR}$. These model data are smoothed and regridded to match the HI4PI and Dame et al. (2001) grid. Figures 6.10 and 6.11 show the ℓ-$V_{\rm LSR}$ brightness temperature distributions for H I and ^{12}CO, respectively, using the initial model parameters in Table 6.1 and this radiative transfer procedure. These data are integrated over all Galactic

latitudes. Many of the initial values for the model parameters, for example $T_{D,\mathrm{CO}}$ and $T_{X,\mathrm{CO}}$, are selected so that these model ℓ-V_{LSR} diagrams are qualitatively similar to the real data.

We compute the model H II region distribution on the same $(\ell, b, V_{\mathrm{LSR}})$ grid as the H I and ^{12}CO data. The number of H II regions in the line of sight distance segment s_i, which has an H II region density $n_{\mathrm{HII\,Regions}}$, is

$$N_i(V_{\mathrm{LSR}}) = n_{\mathrm{HII\,Regions}} |\sin\ell \sin b \cos b| s_i^2 \Delta s \phi_{\mathrm{HII\,Regions}}(V_{\mathrm{LSR}}) \tag{6.23}$$

where $|\sin\ell \sin b \cos b| s_i^2 \Delta s$ is the volume of the bin and $\phi_{\mathrm{HII\,Regions}}$ is the H II region velocity profile. We assume that the H II regions have a Gaussian V_{LSR} distribution centered at the V_{LSR} of that (ℓ, b, s_i) position, so

$$\phi_{\mathrm{HII\,Regions}}(V_{\mathrm{LSR}}) = \frac{1}{\sqrt{2\pi}\sigma_{\mathrm{HII\,Regions}}} \exp\left[-\frac{(V_{\mathrm{LSR}} - V_{\mathrm{LSR}}(\ell, b, s_i))^2}{2\sigma^2_{\mathrm{HII\,Regions}}}\right]. \tag{6.24}$$

The number of H II regions along any line of sight is $N_{\mathrm{HII\,Regions}}(V_{\mathrm{LSR}}) = \sum_i N_i(V_{\mathrm{LSR}})$. Figure 6.12 shows the ℓ-V_{LSR} distribution of H II regions using our initial model parameters (Table 6.1). These data are the sum of all Galactic latitudes. Since the model H II region data are the Poisson expectation values, they are not integers. Nonetheless, there are similarities between Figure 6.12 and the *WISE* Catalog H II region distribution (Figure 6.3).

6.5 Results

The ℓ-V_{LSR} diagrams of the initial model H I, ^{12}CO, and H II region distributions have similarities to the HI4PI, Dame et al. (2001), and *WISE* Catalog data. We use a Markov Chain Monte Carlo (MCMC) analysis to quantitatively determine the model parameters, and their uncertainties, which best reproduce the observed $(\ell, b, V_{\mathrm{LSR}})$ distributions of the data. The MCMC algorithm is implemented through the *emcee* package in *Python* (Foreman-Mackey et al., 2013). The *emcee* code uses the Goodman & Weare (2010) affine invariant ensemble sampler to maximize the posterior probability function, given by Bayes theorem as

$$P(\theta|X, D) \propto P(\theta)P(D|X, \theta) \tag{6.25}$$

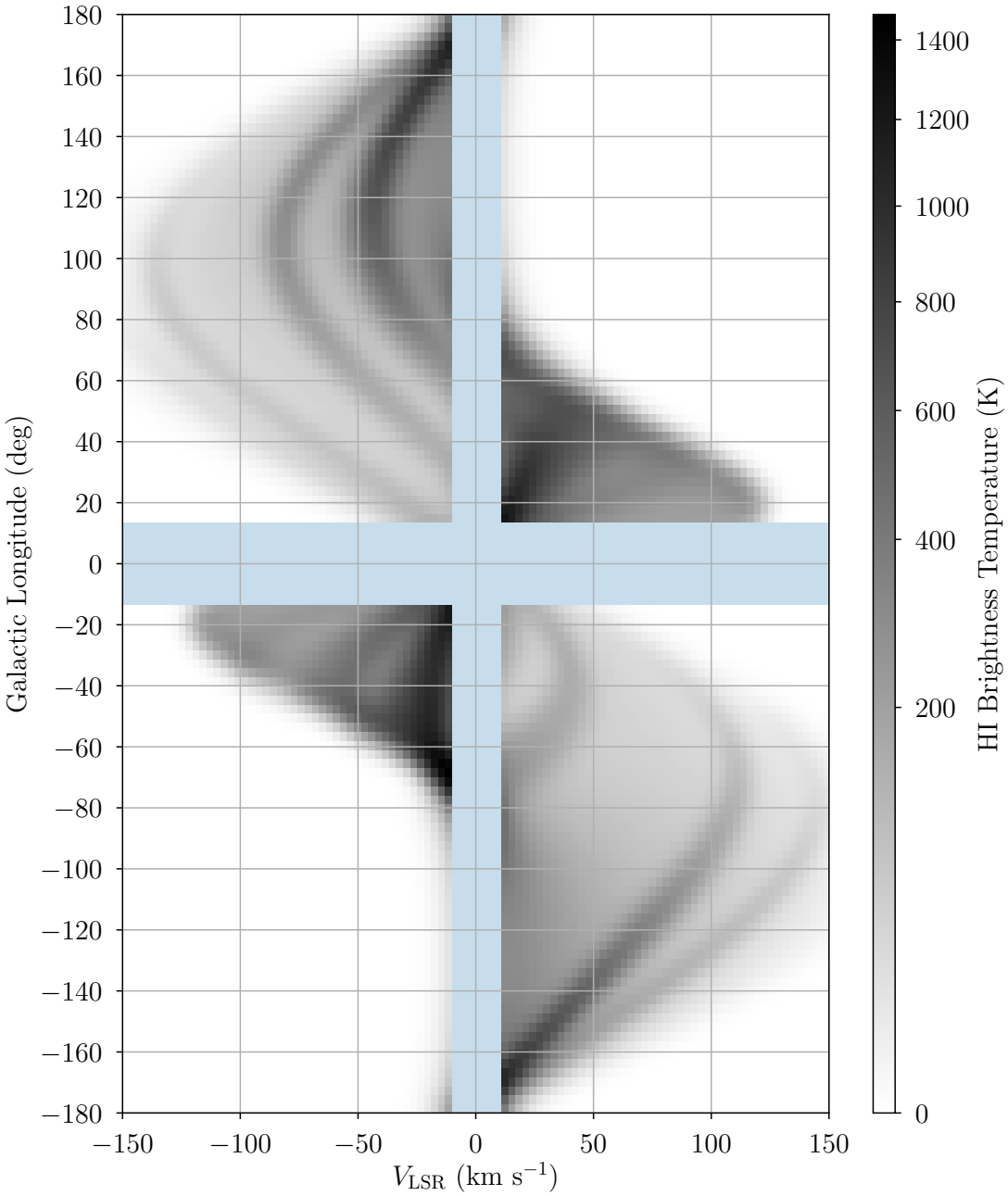

Figure 6.10: Model H I brightness temperature, $T_{B,\rm HI}$, integrated over Galactic latitude as a function of Galactic longitude and LSR velocity, $V_{\rm LSR}$. These data are determined using the initial parameters in Table 6.1. We mask in light blue the Galactic center ($|\ell| < 15°$) and low-velocity ($|V_{\rm LSR}| < 10\,{\rm km\,s^{-1}}$) regions of the diagram.

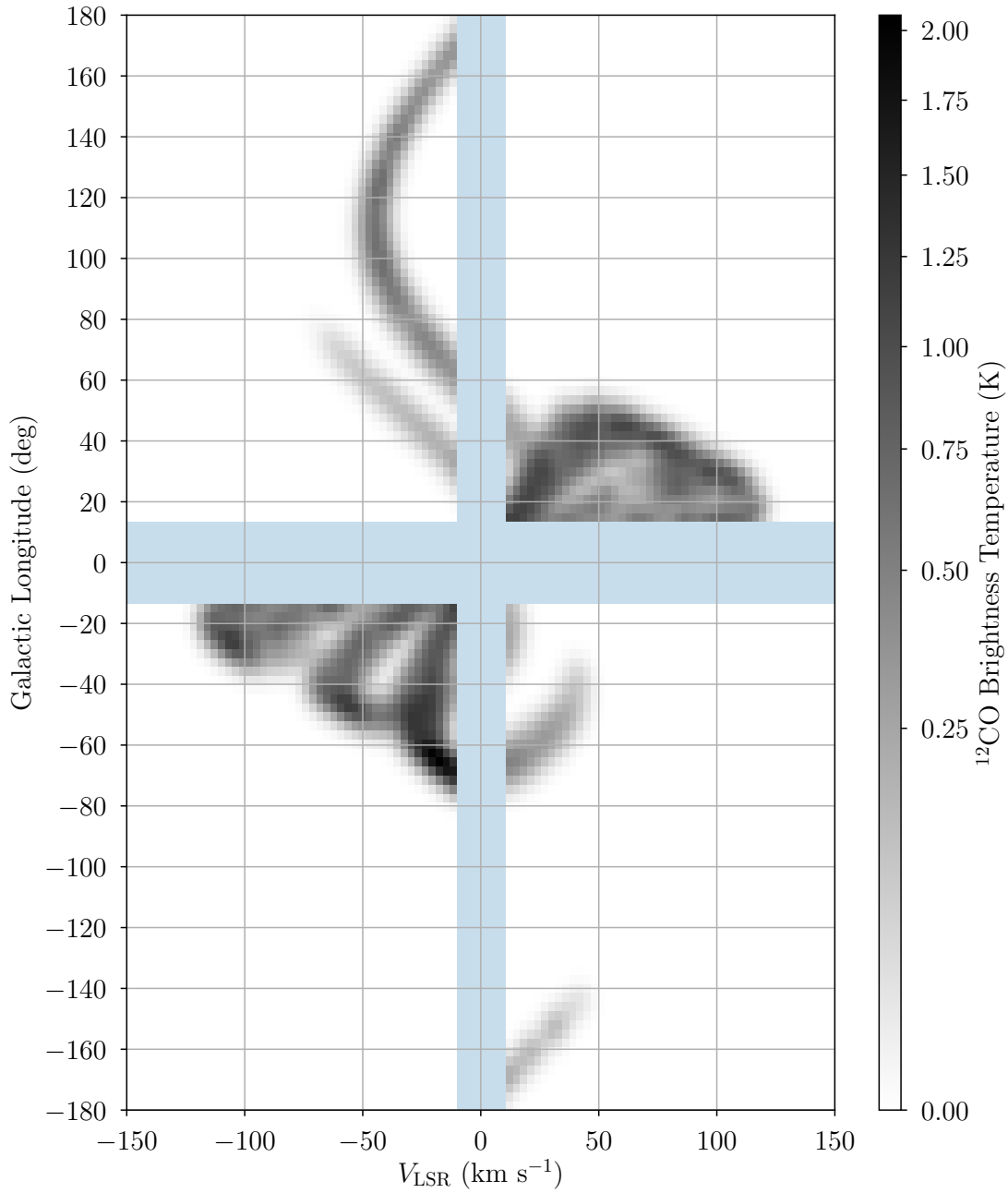

Figure 6.11: Same as Figure 6.10 for the initial model ^{12}CO brightness temperature distribution.

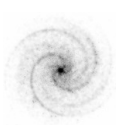

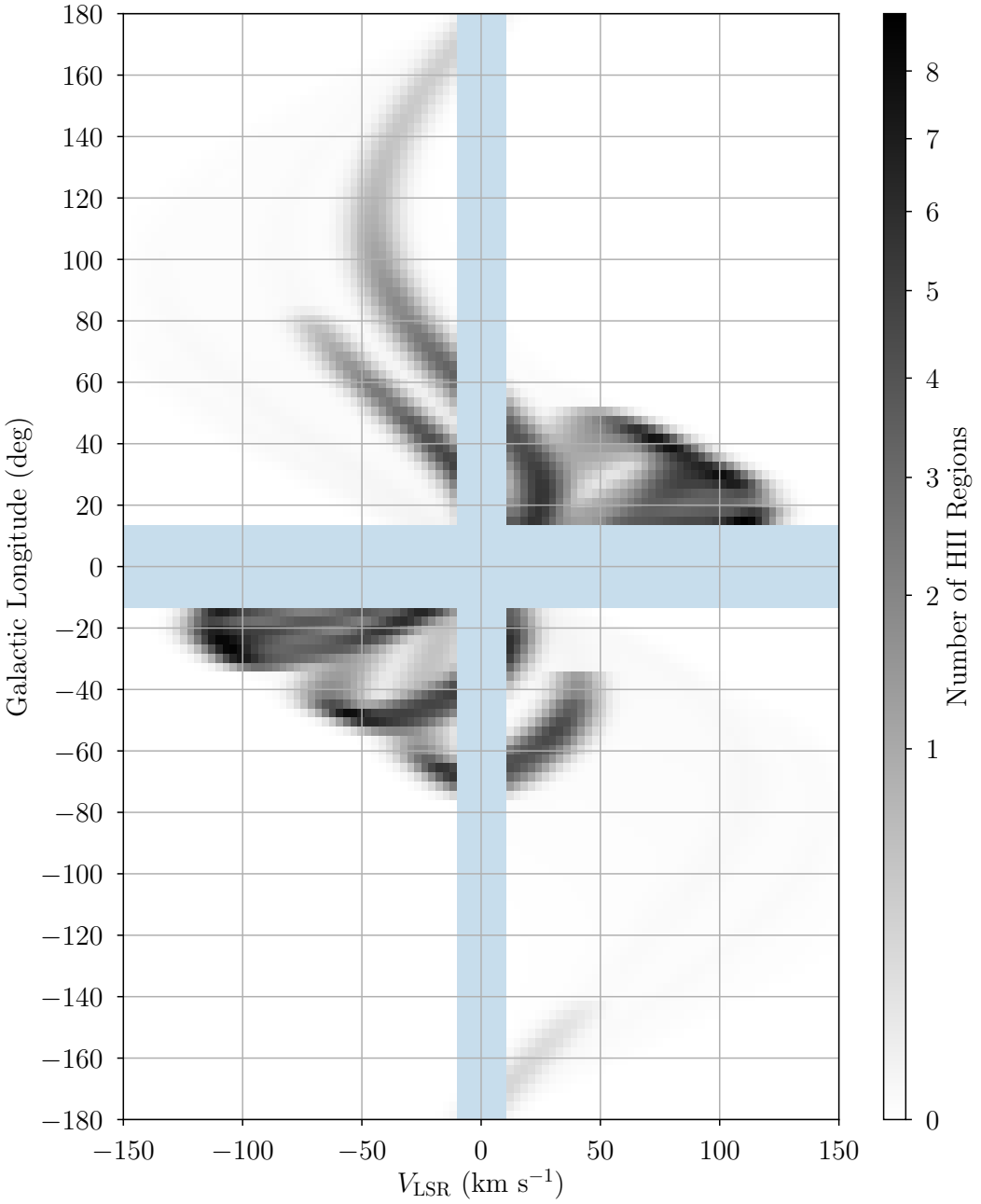

Figure 6.12: Same as Figure 6.10 for the initial model H II region distribution.

where θ is the set of model parameters, X is the set of $(\ell, b, V_{\rm LSR})$ positions, D is the set of real data at each position, $P(\theta)$ is prior on the model parameters, and $P(D|X,\theta)$ is the likelihood function. *emcee* minimizes the posterior by using a collection of random walkers to explore the parameter space (for more information, see Foreman-Mackey et al., 2013).

The likelihood function for this analysis is a complex combination of the H I, ^{12}CO, and H II region likelihoods. We assume that the H I and ^{12}CO data are drawn from a Gaussian probability distribution function, so

$$P(T_B|X,\theta) = \prod_i \frac{1}{\sqrt{2\pi}\sigma} \exp\left[-\frac{(T_{B,\rm data}(X_i) - T_{B,\rm model}(X_i,\theta))^2}{2\sigma^2}\right] \tag{6.26}$$

where T_B is either the H I or ^{12}CO brightness temperature, $T_{B,\rm data}$ is the HI4PI or Dame et al. (2001) data, σ is the (assumed) Gaussian uncertainty of T_B, $T_{B,\rm model}$ is the modeled H I or ^{12}CO brightness temperature determined using parameters θ, and X_i is the ith $(\ell, b, V_{\rm LSR})$ point. We use $\sigma_{\rm HI} = \sigma_{\rm CO} = 5\,{\rm mK}$ as an estimate for the point source sensitivity of the smoothed HI4PI and Dame et al. (2001) data. The H II region likelihood is a Poisson distribution:

$$P(N|X,\theta) = \prod_i \exp\left[-N_{\rm model}(X_i,\theta)\right] \left(\frac{N_{\rm model}(X_i,\theta)^{N_{\rm data}(X_i)}}{N_{\rm data}(X_i)!}\right) \tag{6.27}$$

where N is the number of H II regions, $N_{\rm data}$ is the *WISE* Catalog data, and $N_{\rm model}$ is the model. The total likelihood is thus

$$P(D|X,\theta) = P(T_{B,\rm HI}|X,\theta)P(T_{B,\rm CO}|X,\theta)P(N_{\rm HII\,Regions}|X,\theta). \tag{6.28}$$

We simplify the numerical computation by taking the logarithm of Bayes theorem and maximizing the log-posterior,

$$\ln P(\theta|X,D) \propto \ln P(\theta) + \ln P(D|X,\theta) \tag{6.29}$$

where

$$\ln P(D|X,\theta) = \ln P(T_{B,\rm HI}|X,\theta) + \ln P(T_{B,\rm CO}|X,\theta) + \ln P(N_{\rm HII\,Regions}|X,\theta) \tag{6.30}$$

This simplification means that the products in the H I, ^{12}CO, and H II region likelihood functions become summations in the log-likelihood functions.

We use strict priors on those model parameters with measured or derived uncertainties in Table 6.1. The priors for these parameters are Gaussian, centered at the derived value, and have a width equal to the derived uncertainty. Parameters without an uncertainty in Table 6.1 have a uniform, or uninformative, prior over a large range containing the initial value. These priors may be physically motivated; for example, the prior on I_1 is uniform between 0 and $200\,M_\odot\,\mathrm{pc}^{-2}$ since I_1 must be greater than zero. The total log-prior is

$$\ln P(\theta) = \sum_i \ln P(\theta_i) \tag{6.31}$$

where $P(\theta_i)$ is the prior on parameter θ_i.

We run five analyses to explore the robustness and variety of the MCMC results. In each analysis, we use $n_{\mathrm{arms}} = 4$ and $n_{\mathrm{warp}} = 3$. We ignore the Galactic center ($|\ell| < 15°$) and low-velocity ($|V_{\mathrm{LSR}}| < 10\,\mathrm{km\,s^{-1}}$) regions in the log-likelihood calculation since our simple model does not attempt to fit these features. Similarly, we ignore any $(\ell, b, V_{\mathrm{LSR}})$ point where the H I or ^{12}COdata are missing. We erroneously use $\theta_{w,i} = 180°$ as the initial Galactic warp azimuthal offset, rather than 90° as listed in Table 6.1.

The first analysis, Model A, fits a simulated dataset that is generated by our model using the initial model parameters in Table 6.1 (with $\theta_{w,i} = 180°$). We use our radiative transfer method to generate the $(\ell, b, V_{\mathrm{LSR}})$ distributions of H I, ^{12}CO, and H II regions with very high resolution, and then we smooth and grid those data to the HI4PI, Dame et al. (2001), and *WISE* Catalog resolution. After adding 5 mK of random, Gaussian noise to the H I and ^{12}CO data, we run the MCMC analysis with 200 random walkers to find the parameters that maximize the log-posterior. If the MCMC analysis is working properly, we should recover the input parameters.

The other four analyses, Models B, C, D, and E, attempt to maximize the log-posterior using the HI4PI, Dame et al. (2001), and *WISE* Catalog data. Each analysis uses a different number of random walkers (200 in Models B and C, 1000 in Models D and E) and/or fixed parameters (Models C and E). These fixed parameters are R_0, the solar non-circular motion parameters, the rotation curve parameters, and the

parameters describing the Galactic warp. In Models C and E, these parameters are fixed to their initial values.

The MCMC results are listed in Table 6.2. For each model, we list the number of random walkers; the number of Monte Carlo iterations; the best fit values for each parameter; and the best fit value uncertainties. We determine the best fit value as the median of the marginalized distributions of each parameter, ignoring the first 1000 Monte Carlo samples as "burn-in" (see Foreman-Mackey et al., 2013). The listed uncertainties are the 16th and 84th percentiles of the distributions, which mimics the $\pm 1\sigma$ uncertainties on a Gaussian distribution.

Each analysis is performed on the University of Virginia's Rivanna high-performance computing cluster. The radiative transfer methods, which require ∼30 seconds to generate the H I, ^{12}CO, and H II region $(\ell, b, V_{\rm LSR})$ data cubes, are the bottleneck of the analysis. The wall time for each model is approximately 72 hours distributed over 100-200 cores. The total computing time required to run all five analyses, including testing and debugging, is $\sim 100,000$ CPU hours.

6.6 DISCUSSION

Our simple morphological model of the Milky Way can not yet reproduce the observed H I, ^{12}CO, and H II region distribution of the Milky Way. The MCMC analysis is robust in that it is able to determine the model parameters for simulated datasets (i.e. Model A), but it is not able to adequately constrain the parameters for the real data. In particular, each of the real data analyses (Models B-E) converge such that the ^{12}CO brightness temperatures and H II region number densities are zero or extremely small. This is likely due to a combination of the simplistic parametrization of these components as well as the incorrect initial values for $\theta_{w,i}$. Below we discuss the results and failures of each model.

6.6.1 Model A

Model A is an MCMC analysis on simulated H I, ^{12}CO, and H II region datasets using 200 random walkers. We start the walkers near the initial parameters in Table 6.1, which are also the parameters used to generate the simulated data, and run 5000 Monte Carlo iterations. Figure 6.13 shows the MCMC samples for a subset of the parameters: the Galactocentric radius of the sun, R_0, a rotation curve parameter, a_1, and the tangent of the four spiral arm pitch angles, $\tan(\phi_0)$, $\tan(\phi_1)$, $\tan(\phi_2)$, and

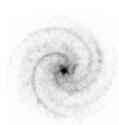

Table 6.2: MCMC Results

Parameter	Initial Value	Model A	Model B	Model C	Model D	Model E
Random Walkers		200	200	200	1000	1000
Monte Carlo Iterations		5000	5000	5000	4552	2553
R_0 (kpc)	8.34	$8.34^{+0.00}_{-0.00}$	$4.98^{+0.04}_{-0.00}$	8.34	$6.49^{+4.79}_{-1.72}$	8.34
$U_\odot^{\rm rev}$ (km s^{-1})	10.50	$10.50^{+0.00}_{-0.00}$	$11.59^{+0.05}_{-0.04}$	10.50	$11.24^{+0.23}_{-0.14}$	10.50
$V_\odot^{\rm rev}$ (km s^{-1})	14.40	$14.38^{+0.00}_{-0.00}$	$17.57^{+0.09}_{-0.06}$	14.40	$11.04^{+6.83}_{-6.06}$	14.40
$W_\odot^{\rm rev}$ (km s^{-1})	8.90	$8.93^{+0.00}_{-0.00}$	$14.23^{+0.11}_{-0.00}$	8.90	$15.67^{+1.25}_{-14.95}$	8.90
a_1 (km s^{-1})	241.00	$241.22^{+0.01}_{-0.01}$	$198.09^{+3.96}_{-0.05}$	241.00	$218.66^{+7.73}_{-8.19}$	241.00
a_2	0.90	$0.90^{+0.00}_{-0.00}$	$0.99^{+0.00}_{-0.01}$	0.90	$0.51^{+0.32}_{-0.09}$	0.90
a_3	1.46	$1.46^{+0.00}_{-0.00}$	$1.94^{+0.00}_{-0.05}$	1.46	$1.34^{+0.08}_{-0.07}$	1.46
I_1 (M$_\odot$ pc^{-2})	50.00	$49.84^{+0.00}_{-0.00}$	$12.31^{+0.01}_{-0.15}$	$45.97^{+9.62}_{-4.91}$	$57.22^{+5.95}_{-13.40}$	$104.26^{+15.78}_{-20.22}$
I_2	35.00	$35.03^{+0.00}_{-0.00}$	$42.11^{+0.33}_{-0.01}$	$98.81^{+0.85}_{-16.69}$	$53.60^{+4.11}_{-19.83}$	$75.64^{+16.02}_{-23.66}$
r_s (kpc)	4.50	$4.52^{+0.00}_{-0.00}$	$3.80^{+0.03}_{-0.00}$	$5.01^{+0.10}_{-0.09}$	$4.07^{+3.59}_{-1.24}$	$4.25^{+0.46}_{-0.15}$
r_c (kpc)	2.75	$2.75^{+0.00}_{-0.00}$	$1.33^{+0.04}_{-0.00}$	$1.92^{+0.16}_{-0.12}$	$2.07^{+1.16}_{-0.63}$	$2.48^{+0.24}_{-0.07}$
h_0 (kpc)	0.10	$0.10^{+0.00}_{-0.00}$	$0.06^{+0.00}_{-0.00}$	$0.03^{+0.00}_{-0.01}$	$0.03^{+0.10}_{-0.01}$	$0.02^{+0.00}_{-0.00}$
r_0 (kpc)	12.00	$11.95^{+0.00}_{-0.00}$	$7.49^{+0.41}_{-0.00}$	$4.49^{+0.19}_{-0.45}$	$4.34^{+8.00}_{-1.32}$	$3.43^{+0.03}_{-0.02}$
$T_{D,\rm WNM}$ (K)	6000.00	$6001.62^{+0.60}_{-0.59}$	$6902.42^{+138.77}_{-1.64}$	$10065.00^{+646.17}_{-428.44}$	$10202.01^{+762.85}_{-621.83}$	$11005.92^{+288.27}_{-173.92}$
$T_{S,\rm WNM}$ (K)	1000.00	$1002.86^{+0.04}_{-0.04}$	$207.33^{+5.41}_{-3.23}$	$179.87^{+24.98}_{-25.56}$	$182.23^{+97.02}_{-49.10}$	$140.56^{+3.61}_{-6.89}$
$\theta_{0,1}$ (rad)	1.26	$1.26^{+0.00}_{-0.00}$	$1.31^{+0.00}_{-0.02}$	$1.13^{+0.06}_{-0.18}$	$1.62^{+0.08}_{-0.17}$	$1.78^{+0.01}_{-0.01}$
$\tan(\phi_1)$	0.25	$0.25^{+0.00}_{-0.00}$	$0.29^{+0.00}_{-0.00}$	$0.51^{+0.22}_{-0.05}$	$0.26^{+0.03}_{-0.01}$	$0.23^{+0.00}_{-0.00}$
Δ_1 (kpc)	1.00	$1.00^{+0.00}_{-0.00}$	$2.00^{+0.02}_{-0.00}$	$0.74^{+1.34}_{-0.38}$	$0.66^{+0.18}_{-0.30}$	$1.09^{+0.23}_{-0.03}$
$n_{1,\rm CNM}/n_{1,\rm WNM}$	5.00	$4.99^{+0.00}_{-0.00}$	$2.78^{+0.13}_{-0.00}$	$3.91^{+1.80}_{-3.91}$	$2.90^{+4.37}_{-0.58}$	$12.58^{+0.97}_{-5.66}$
$\theta_{0,2}$ (rad)	4.40	$4.40^{+0.00}_{-0.00}$	$5.02^{+0.04}_{-0.00}$	$4.35^{+0.11}_{-0.10}$	$3.22^{+0.41}_{-0.62}$	$4.94^{+0.24}_{-0.13}$

Table 6.2 continued

Table 6.2: MCMC Results (continued)

Parameter	Initial Value	Model A	Model B	Model C	Model D	Model E
$\tan(\phi_2)$	0.25	$0.25^{+0.00}_{-0.00}$	$0.30^{+0.00}_{-0.00}$	$0.47^{+0.03}_{-0.06}$	$0.21^{+0.23}_{-0.05}$	$0.49^{+0.11}_{-0.06}$
Δ_2 (kpc)	1.00	$1.00^{+0.00}_{-0.00}$	$1.23^{+0.01}_{-0.02}$	$3.27^{+1.30}_{-0.74}$	$0.38^{+1.09}_{-0.10}$	$0.26^{+0.16}_{-0.17}$
$n_{2,\mathrm{CNM}}/n_{2,\mathrm{WNM}}$	5.00	$5.02^{+0.00}_{-0.00}$	$5.44^{+0.33}_{-0.00}$	$4.14^{+0.65}_{-2.21}$	$7.50^{+4.32}_{-6.15}$	$2.76^{+2.21}_{-0.71}$
$\theta_{0,3}$ (rad)	5.53	$5.53^{+0.00}_{-0.00}$	$6.28^{+0.00}_{-0.00}$	$3.80^{+0.65}_{-1.10}$	$4.44^{+0.69}_{-2.35}$	$2.79^{+0.01}_{-0.74}$
$\tan(\phi_3)$	0.25	$0.25^{+0.00}_{-0.00}$	$0.33^{+0.00}_{-0.01}$	$0.59^{+0.19}_{-0.07}$	$0.33^{+0.18}_{-0.10}$	$0.28^{+0.18}_{-0.01}$
Δ_3 (kpc)	1.00	$1.00^{+0.00}_{-0.00}$	$0.83^{+0.01}_{-0.00}$	$0.03^{+0.53}_{-0.03}$	$1.09^{+0.56}_{-0.35}$	$4.34^{+0.15}_{-0.57}$
$n_{3,\mathrm{CNM}}/n_{3,\mathrm{WNM}}$	5.00	$5.00^{+0.00}_{-0.00}$	$1.96^{+0.15}_{-0.00}$	$5.14^{+0.66}_{-1.66}$	$1.64^{+3.54}_{-0.70}$	$0.51^{+0.10}_{-0.03}$
$\theta_{0,4}$ (rad)	2.39	$2.39^{+0.00}_{-0.00}$	$2.62^{+0.01}_{-0.00}$	$2.11^{+0.04}_{-0.26}$	$3.10^{+1.95}_{-0.26}$	$5.26^{+0.01}_{-0.03}$
$\tan(\phi_4)$	0.25	$0.25^{+0.00}_{-0.00}$	$0.29^{+0.00}_{-0.00}$	$0.21^{+0.01}_{-0.00}$	$0.30^{+0.09}_{-0.04}$	$0.37^{+0.01}_{-0.05}$
Δ_4 (kpc)	1.00	$1.00^{+0.00}_{-0.00}$	$0.88^{+0.00}_{-0.04}$	$1.35^{+0.31}_{-0.31}$	$0.76^{+0.42}_{-0.31}$	$1.82^{+0.09}_{-0.26}$
$n_{4,\mathrm{CNM}}/n_{4,\mathrm{WNM}}$	5.00	$5.00^{+0.00}_{-0.00}$	$4.69^{+0.01}_{-0.20}$	$22.26^{+6.04}_{-3.90}$	$3.73^{+0.46}_{-3.02}$	$0.79^{+0.07}_{-0.08}$
$T_{D,\mathrm{CNM}}$ (K)	500.00	$499.81^{+0.10}_{-0.06}$	$254.47^{+36.83}_{-0.15}$	$433.77^{+606.62}_{-325.95}$	$634.22^{+294.67}_{-87.64}$	$3836.49^{+204.43}_{-1643.18}$
$T_{S,\mathrm{CNM}}$ (K)	100.00	$100.23^{+0.00}_{-0.01}$	$80.54^{+2.62}_{-0.03}$	$21.91^{+0.80}_{-1.35}$	$41.16^{+148.99}_{-24.12}$	$22.04^{+0.84}_{-0.60}$
$\log_{10} n_{\mathrm{HI}}^{\mathrm{COmin}}$ (cm^{-3})	0.00	$-0.00^{+0.00}_{-0.00}$	$0.53^{+0.00}_{-0.01}$	$2.51^{+1.50}_{-0.76}$	$-0.35^{+0.37}_{-0.30}$	$-0.54^{+0.02}_{-0.01}$
$\log_{10} n_{\mathrm{CO}}/n_{\mathrm{HI}}$	-5.50	$-5.50^{+0.00}_{-0.00}$	$-3.28^{+0.00}_{-0.29}$	$-16.45^{+6.57}_{-8.51}$	$-7.49^{+1.91}_{-2.86}$	$-24.36^{+2.07}_{-0.40}$
$T_{D,\mathrm{CO}}$ (K)	20.00	$20.00^{+0.00}_{-0.00}$	$28.38^{+0.00}_{-0.57}$	$37.59^{+16.22}_{-22.64}$	$8.87^{+20.15}_{-2.36}$	$0.83^{+0.87}_{-0.38}$
$T_{X,\mathrm{CO}}$ (K)	20.00	$20.07^{+0.00}_{-0.00}$	$21.41^{+1.70}_{-0.01}$	$65.06^{+25.88}_{-20.81}$	$28.04^{+3.58}_{-11.45}$	$46.81^{+23.19}_{-13.91}$
$\log_{10} n_{\mathrm{HII\,Regions}}/n_{\mathrm{HI}}$ ($\mathrm{cm}^3\ \mathrm{kpc}^{-3}$)	-1.00	$-1.00^{+0.00}_{-0.00}$	$-0.38^{+0.02}_{-0.00}$	$1.18^{+0.28}_{-0.65}$	$-0.98^{+0.33}_{-0.37}$	$-3.90^{+0.51}_{-0.37}$
$\log_{10} n_{\mathrm{HII\,Regions}}/n_{\mathrm{CO}}$ ($\mathrm{cm}^3\ \mathrm{kpc}^{-3}$)	7.50	$7.51^{+0.00}_{-0.00}$	$5.08^{+0.00}_{-0.20}$	$10.93^{+14.02}_{-6.82}$	$2.42^{+2.67}_{-0.58}$	$10.92^{+13.02}_{-9.23}$
$\sigma_{V,\mathrm{HII\,Regions}}$ ($\mathrm{km\ s}^{-1}$)	5.00	$4.99^{+0.00}_{-0.00}$	$4.17^{+0.08}_{-0.00}$	$13.08^{+7.85}_{-1.59}$	$5.80^{+1.11}_{-0.77}$	$5.77^{+10.76}_{-0.93}$
W_0 (kpc)	-2.50	$-2.50^{+0.00}_{-0.00}$	$-1.40^{+0.09}_{-0.00}$	-2.50	$-3.50^{+0.63}_{-0.73}$	-2.50
dW_0/dR	0.17	$0.17^{+0.00}_{-0.00}$	$0.10^{+0.00}_{-0.00}$	0.17	$0.20^{+0.03}_{-0.09}$	0.17
W_1 (kpc)	-1.50	$-1.50^{+0.00}_{-0.00}$	$-0.75^{+0.01}_{-0.00}$	-1.50	$-0.83^{+0.38}_{-2.95}$	-1.50

Table 6.2 continued

Table 6.2: MCMC Results (continued)

Parameter	Initial Value	Model A	Model B	Model C	Model D	Model E
dW_1/dR	0.15	$0.15^{+0.00}_{-0.00}$	$0.14^{+0.00}_{-0.00}$	0.15	$0.11^{+0.08}_{-0.01}$	0.15
W_2 (kpc)	-1.50	$-1.50^{+0.00}_{-0.00}$	$-1.66^{+0.00}_{-0.01}$	-1.50	$-1.18^{+0.24}_{-1.52}$	-1.50
dW_2/dR	0.05	$0.05^{+0.00}_{-0.00}$	$0.05^{+0.00}_{-0.00}$	0.05	$0.04^{+0.03}_{-0.02}$	0.05
$\theta_{w,1}$ (rad)	3.14^a	$3.13^{+0.00}_{-0.00}$	$2.18^{+0.00}_{-0.01}$	1.57	$2.11^{+0.09}_{-1.46}$	1.57
$d\theta_{w,1}/dR$ (rad kpc^{-1})	0.00	$0.00^{+0.00}_{-0.00}$	$-0.07^{+0.00}_{-0.00}$	0.00	$-0.03^{+0.90}_{-0.04}$	0.00
$\theta_{w,2}$ (rad)	3.14^a	$3.15^{+0.00}_{-0.00}$	$3.22^{+0.14}_{-0.00}$	1.57	$2.44^{+1.89}_{-2.41}$	1.57
$d\theta_{w,2}/dR$ (rad kpc^{-1})	0.00	$-0.00^{+0.00}_{-0.00}$	$-0.46^{+0.01}_{-0.00}$	0.00	$1.02^{+0.32}_{-0.63}$	0.00

[a] We incorrectly initialize and fix $\theta_{w,1}$ and $\theta_{w,2}$ to 180°.

$\tan(\phi_3)$. Figure 6.14 is a "corner plot" (Foreman-Mackey, 2016) showing the marginalized posterior distributions and the covariances between the parameters. We ignore the first 1000 "burn-in" samples to generate the corner plot. The parameters quickly converge with very little scatter. Each parameter is within 1% of the parameter used to generate the simulated data, thus proving the efficacy of our MCMC analysis.

6.6.2 Model B

We fit the HI4PI, Dame et al. (2001), and *WISE* Catalog data in Models B, C, D, and E. Model B uses 200 random walkers, initialized near the parameters in Table 6.1. We run 5000 Monte Carlo iterations. Figures 6.15 and 6.16 show the MCMC samples and covariances, respectively, for the same parameters as in Figures 6.13 and 6.14. Like in Model A, the parameters quickly converge with very little scatter. Due to the large parameter space and few random walkers, the walkers may become "stuck" in a local maximum of the posterior distribution. The walkers converge to $R_0 \simeq 5\,\mathrm{kpc}$, for example, despite the strict prior on R_0 at 8.34 kpc. This extremely unlikely result is probably due to the degeneracies of our model and the small number of random walkers.

6.6.3 Model C

Model C is the same as Model B, except we fix R_0, the solar non-circular motion parameters, the rotation curve parameters, and the parameters describing the Galactic warp to their initial values in Table 6.1 (we incorrectly fix $\theta_{w,i}$ to 180°). Figures 6.17 and 6.18 show the MCMC samples and covariances, respectively, for the following parameters: a WNM surface density parameter, I_1, the ^{12}CO Doppler temperature, $T_{D,\mathrm{CO}}$, and the tangent of the four spiral arm pitch angles, $\tan(\phi_0)$, $\tan(\phi_1)$, $\tan(\phi_2)$, and $\tan(\phi_3)$. We show different parameters because R_0 and a_1 are fixed in this analysis. The random walkers never converge, rather they continue to move around the parameter space through all of the Monte Carlo iterations. This is, again, probably because of the numerous parameter degeneracies, the limited number of MCMC walkers, and/or the incorrect value of $\theta_{w,i}$, the latter of which means that the outskirts of the Galaxy, where the warp becomes important, can never be properly fit by the MCMC walkers.

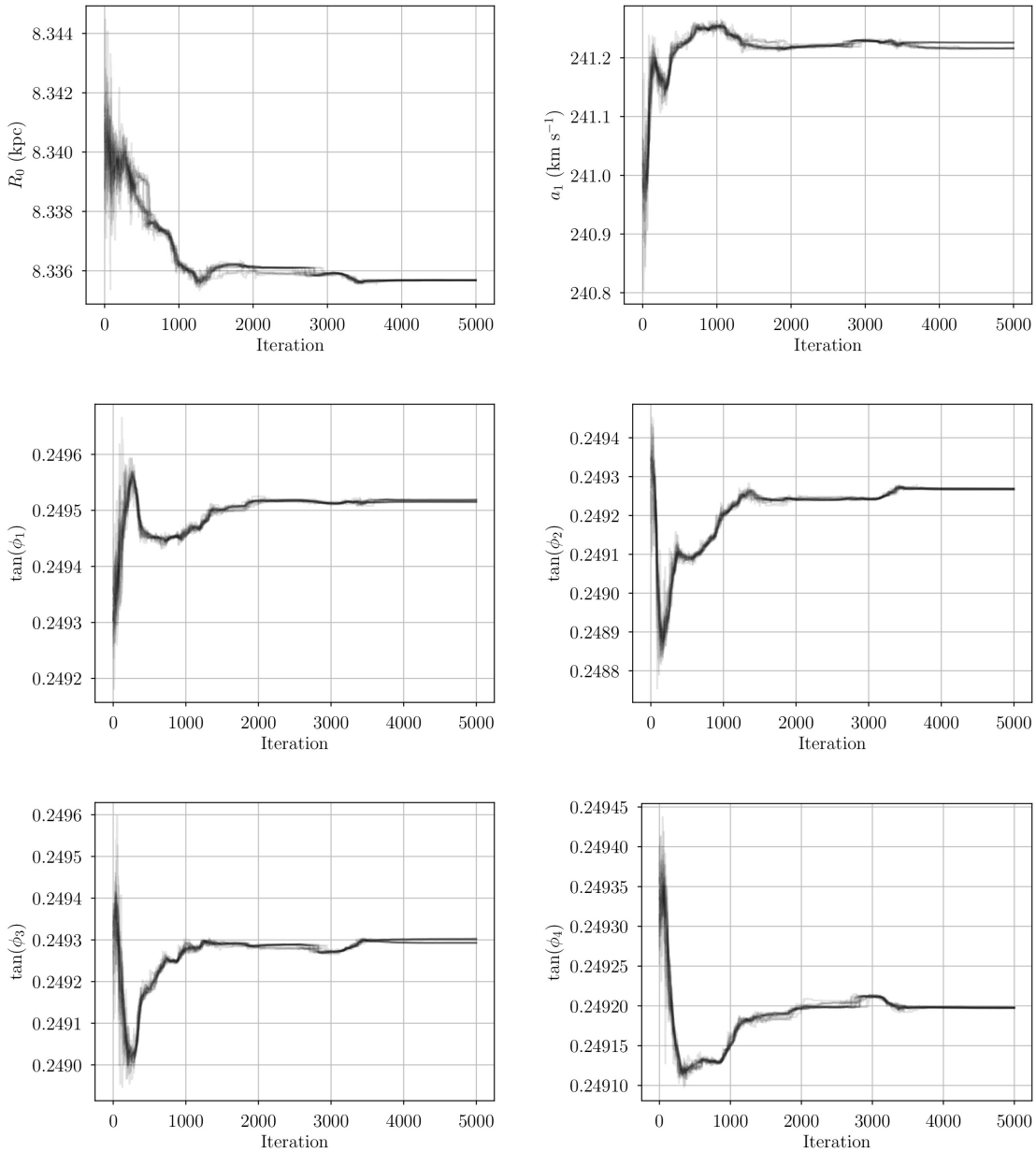

Figure 6.13: MCMC walkers for a subset of the Model A parameters: R_0, a_1, $\tan(\phi_0)$, $\tan(\phi_1)$, $\tan(\phi_2)$, and $\tan(\phi_3)$. Each curve is the path of one walker as a function of Monte Carlo iteration. Only the first 20 walkers are shown for clarity.

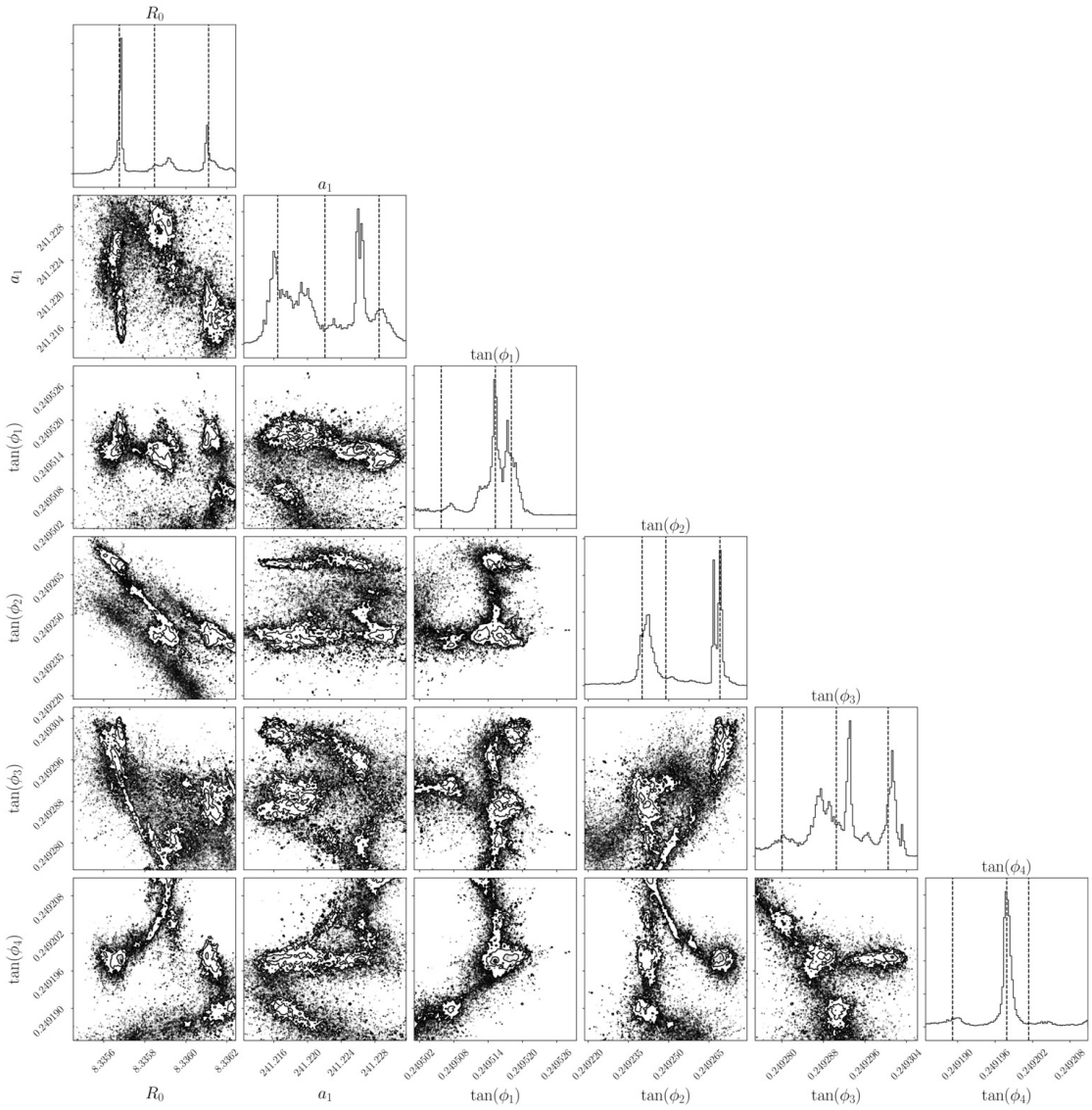

Figure 6.14: Corner plot (Foreman-Mackey, 2016) of the marginalized posterior distributions for a subset of the Model A parameters: R_0, a_1, tan(ϕ_0), tan(ϕ_1), tan(ϕ_2), and tan(ϕ_3). The one-dimensional posteriors are the histograms along the diagonal, and the dashed lines are the 16th, 50th, and 84th percentiles. The scatter plots are the two-dimensional posteriors, where each point is one random walker position at one Monte Carlo iteration. The densest regions of the scatter plots have density contours.

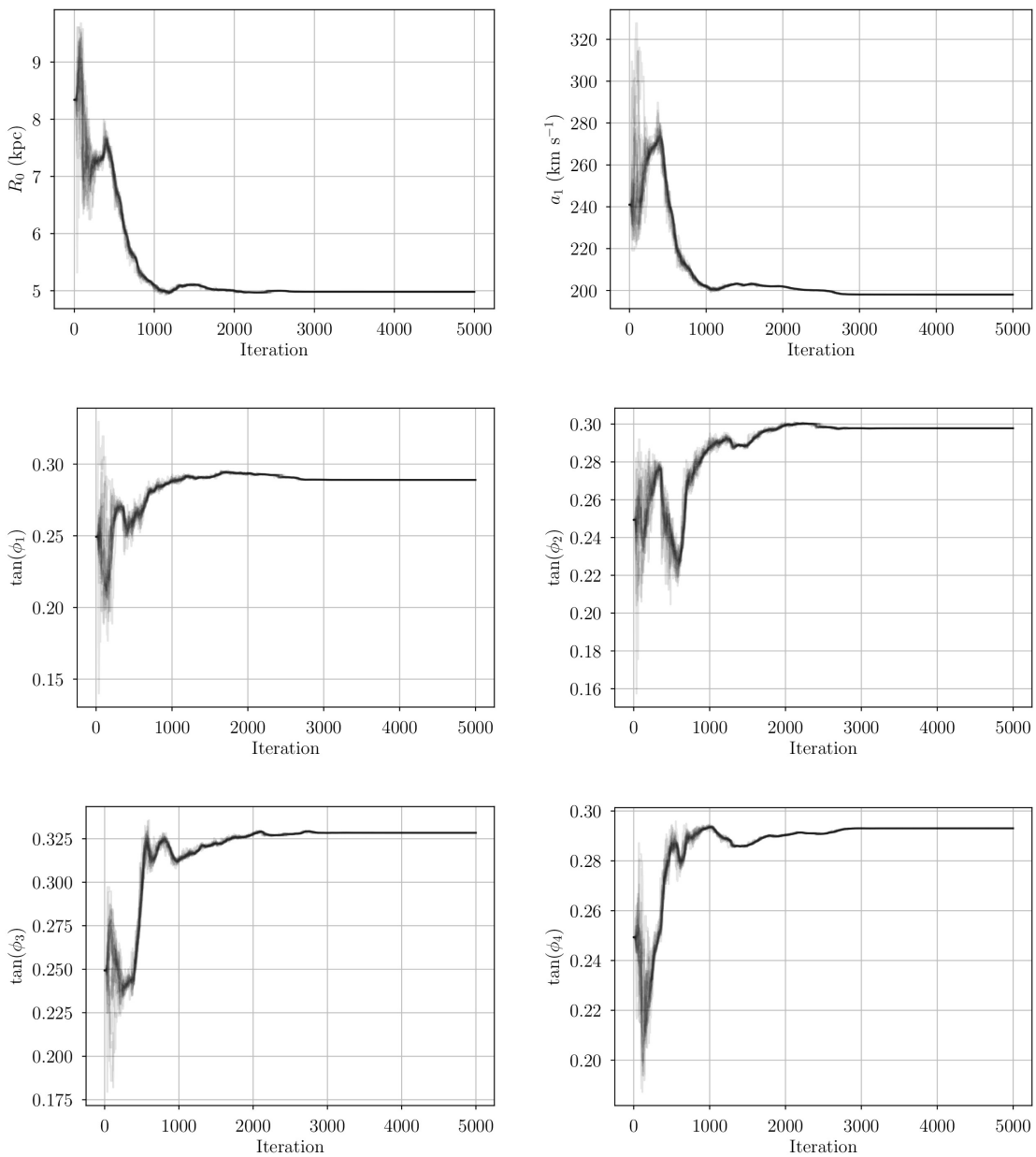

Figure 6.15: Same as Figure 6.13 for Model B.

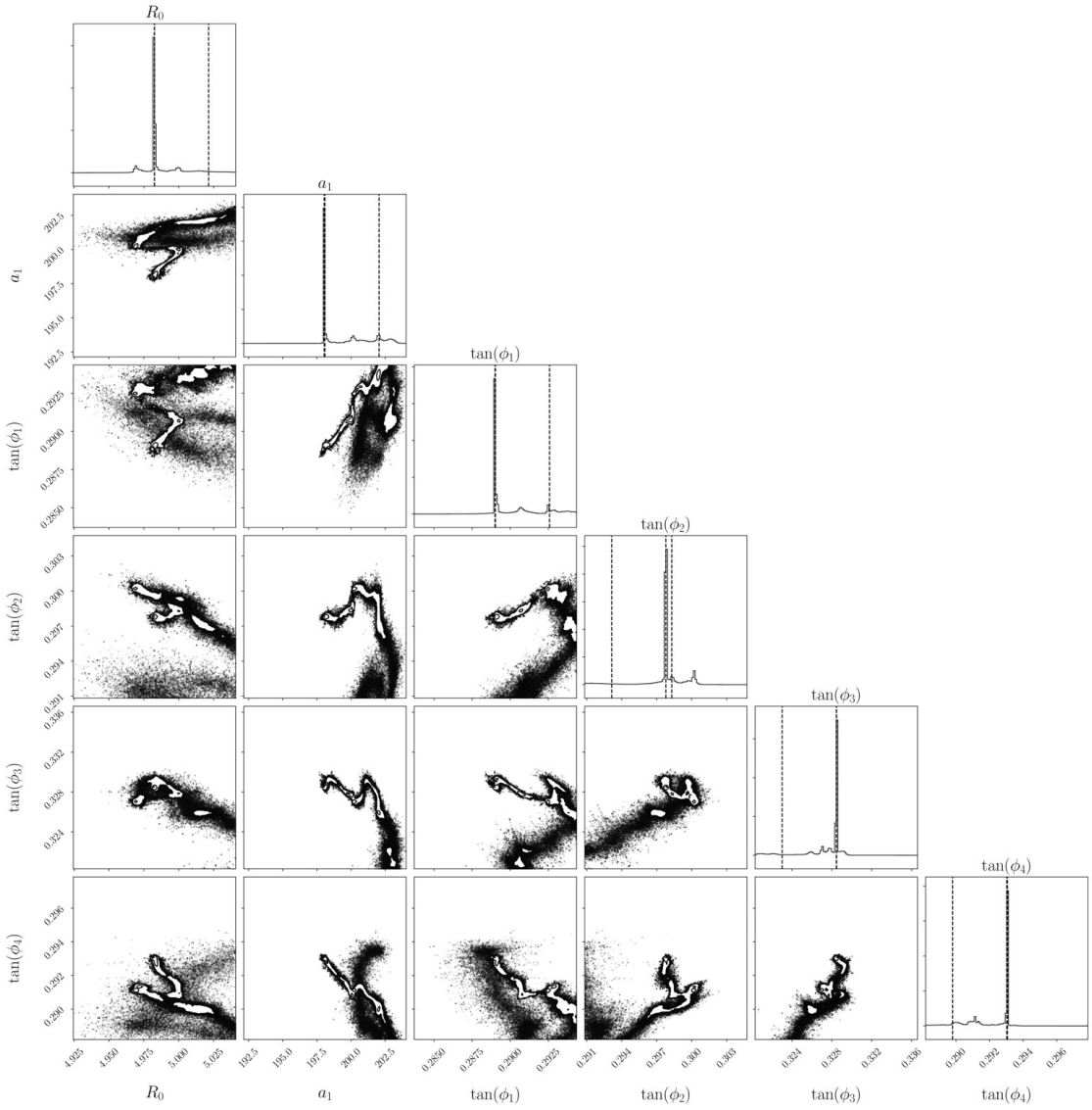

Figure 6.16: Same as Figure 6.14 for Model B. Note that the axis ranges are much different.

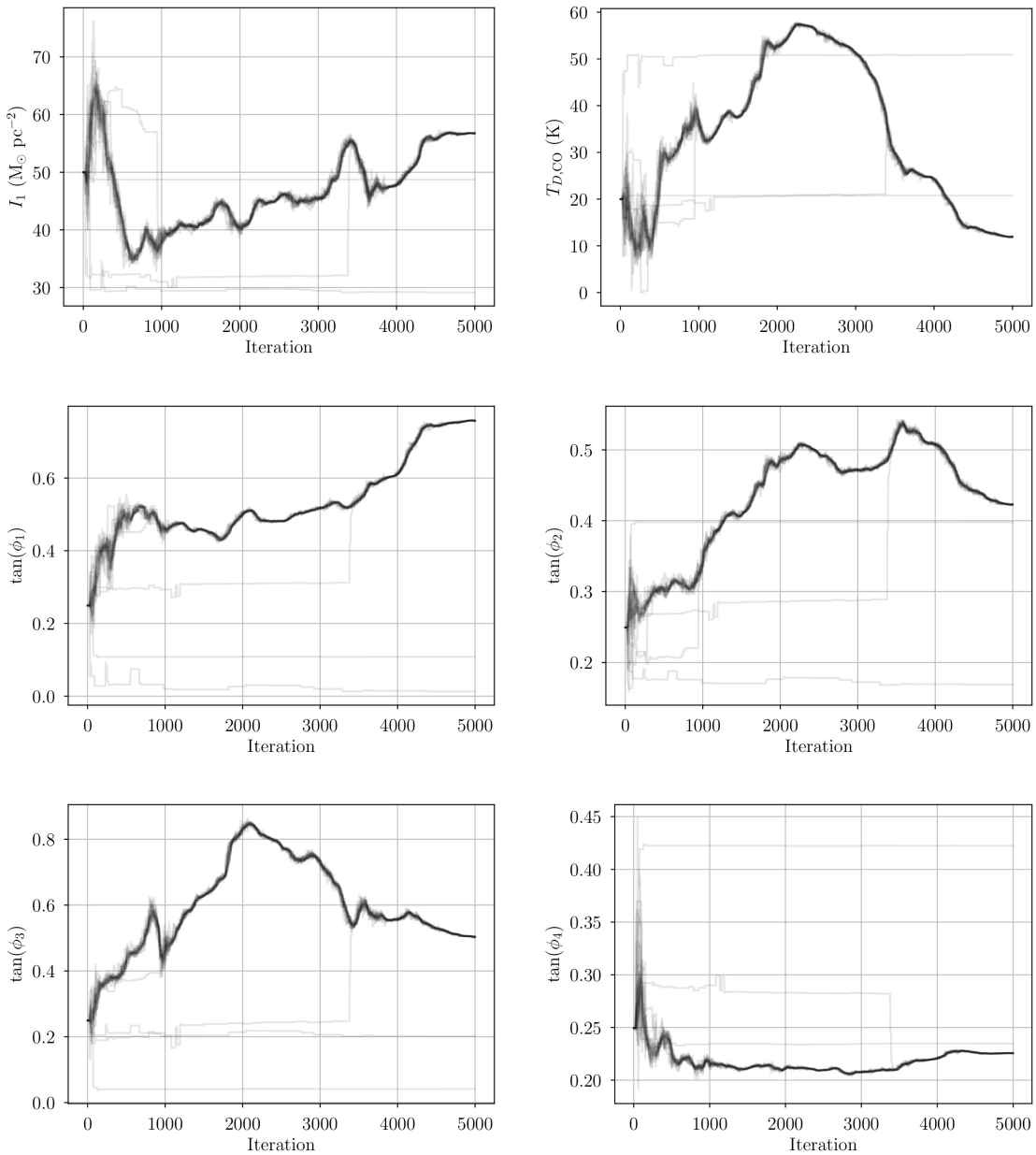

Figure 6.17: Same as Figure 6.13 for Model C and parameters I_1, $T_{D,\mathrm{CO}}$, $\tan(\phi_0)$, $\tan(\phi_1)$, $\tan(\phi_2)$, and $\tan(\phi_3)$.

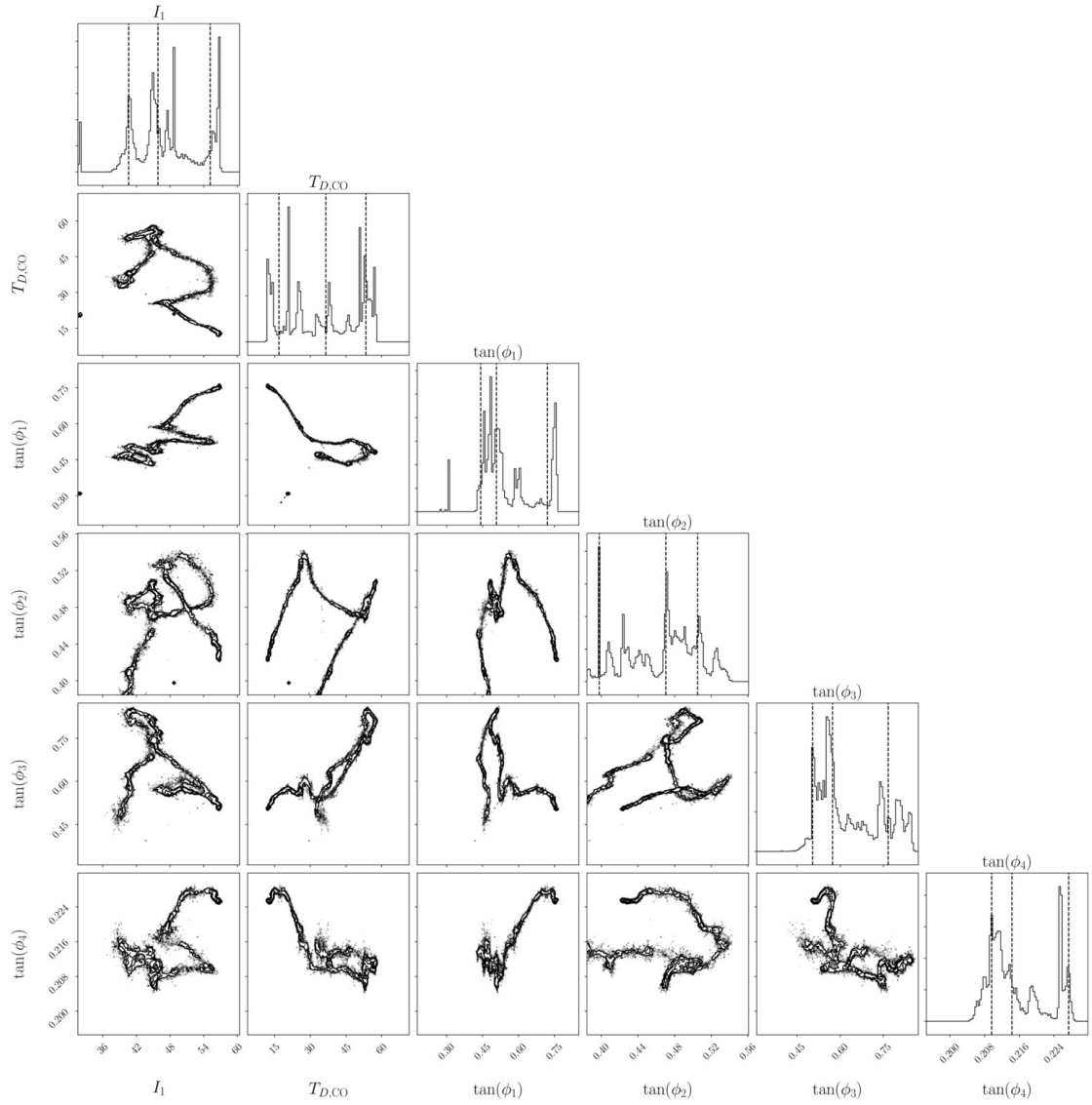

Figure 6.18: Same as Figure 6.14 for Model C and parameters I_1, $T_{D,\mathrm{CO}}$, $\tan(\phi_0)$, $\tan(\phi_1)$, $\tan(\phi_2)$, and $\tan(\phi_3)$. Note that the axis ranges are much different.

6.6.4 Model D

We attempt to fix the problems with the previous models by using many more random walkers. Model D uses ∼4500 Monte Carlo iterations and 1000 walkers, 5 times more walkers than in the previous three analyses. The MCMC samples and covariances for a subset of the model parameters, including R_0 and a_1, are shown in Figures 6.19 and 6.20, respectively. Here we see a new problem: the parameters are not well constrained. The random walkers populate several local maxima in the posterior distribution, due to the many degeneracies between the model parameters. With more Monte Carlo iterations, this model might eventually converge to the true local maximum in the posterior distribution.

6.6.5 Model E

Our final model, Model E, is the same as Model D, except we fix the same parameters as in Model C. This is an attempt to limit the parameter degeneracies and run the MCMC analysis with many random walkers. We only run ∼2500 Monte Carlo iterations due to limited computational resources. Figures 6.21 and 6.22 show the MCMC parameters and covariances, respectively. In this model, the random walkers do not get "stuck" in different local posterior maxima. Unfortunately, some of the parameters do not converge (e.g., I_1) and other parameters converge to unphysical values (e.g., $T_{D,\mathrm{CO}} \simeq 0\,\mathrm{K}$). Despite our attempts to limit the degeneracies of the model and increase the parameter space explored by the MCMC walkers, we are still unable to determine the best fit morphological parameters of the Galaxy. We suspect that an important factor in this failure is the incorrect value of $\theta_{w,i}$, which significantly affects the differences between the model and the real data in the outer Galaxy.

6.7 Summary and Future Work

We develop a simple morphological model of the H I, ^{12}CO, and H II region distribution of the Milky Way. Our model analytically parametrizes the kinematics of Galactic rotation and non-circular solar motion, the morphology of the spiral arms, the warp of the Galactic plane, and the H I, ^{12}CO, and H II region densities everywhere in the Galaxy. We use a mesh-grid radiative transfer tool to generate simulated $(\ell, b, V_{\mathrm{LSR}})$ distributions of the gas and the H II regions, which we compare to HI4PI H I data (HI4PI Collaboration et al., 2016), Dame et al. (2001) ^{12}CO data, and *WISE* Catalog H II region data (Anderson et al., 2014). We run a Bayesian MCMC analysis

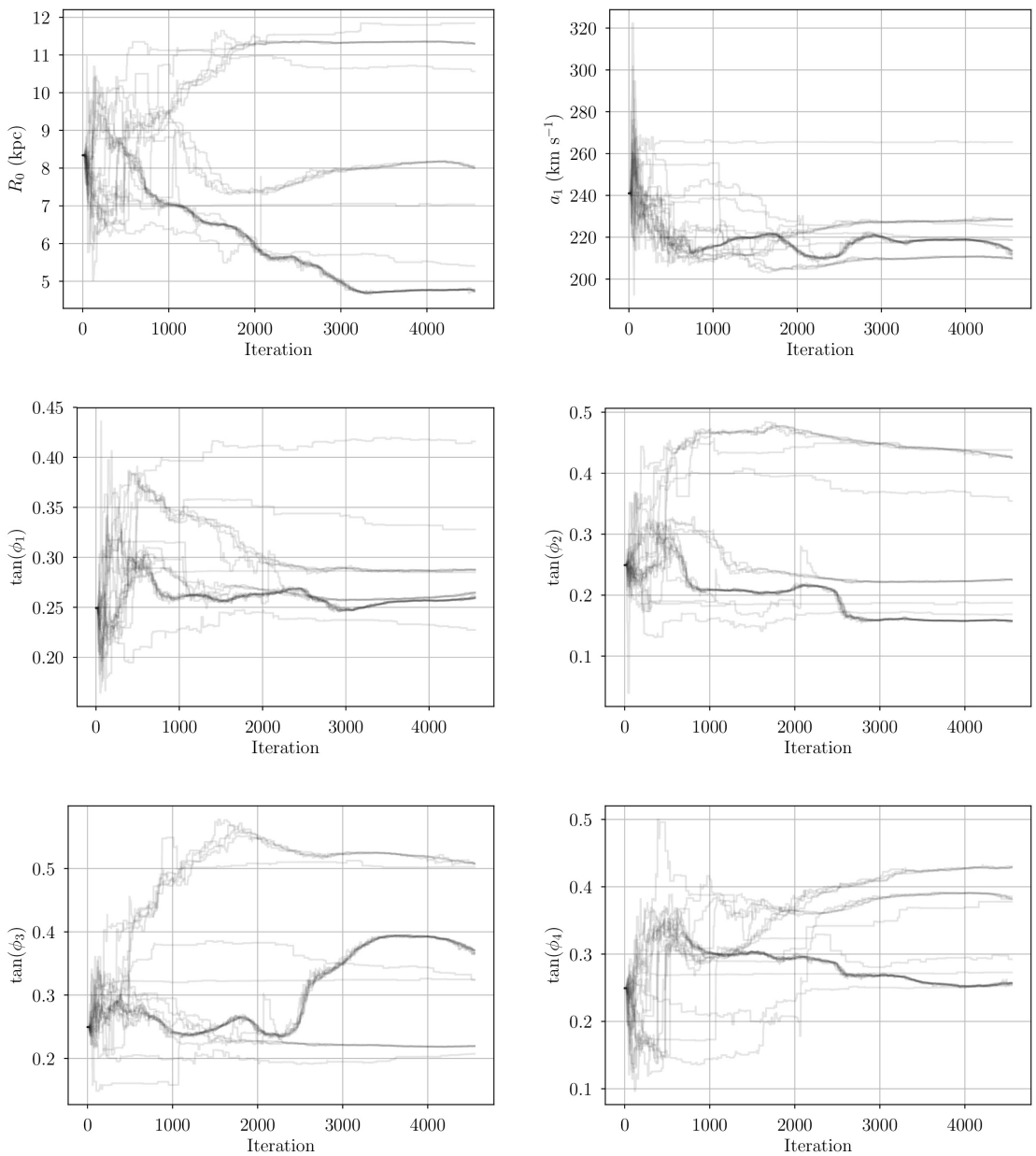

Figure 6.19: Same as Figure 6.13 for Model D.

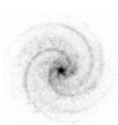

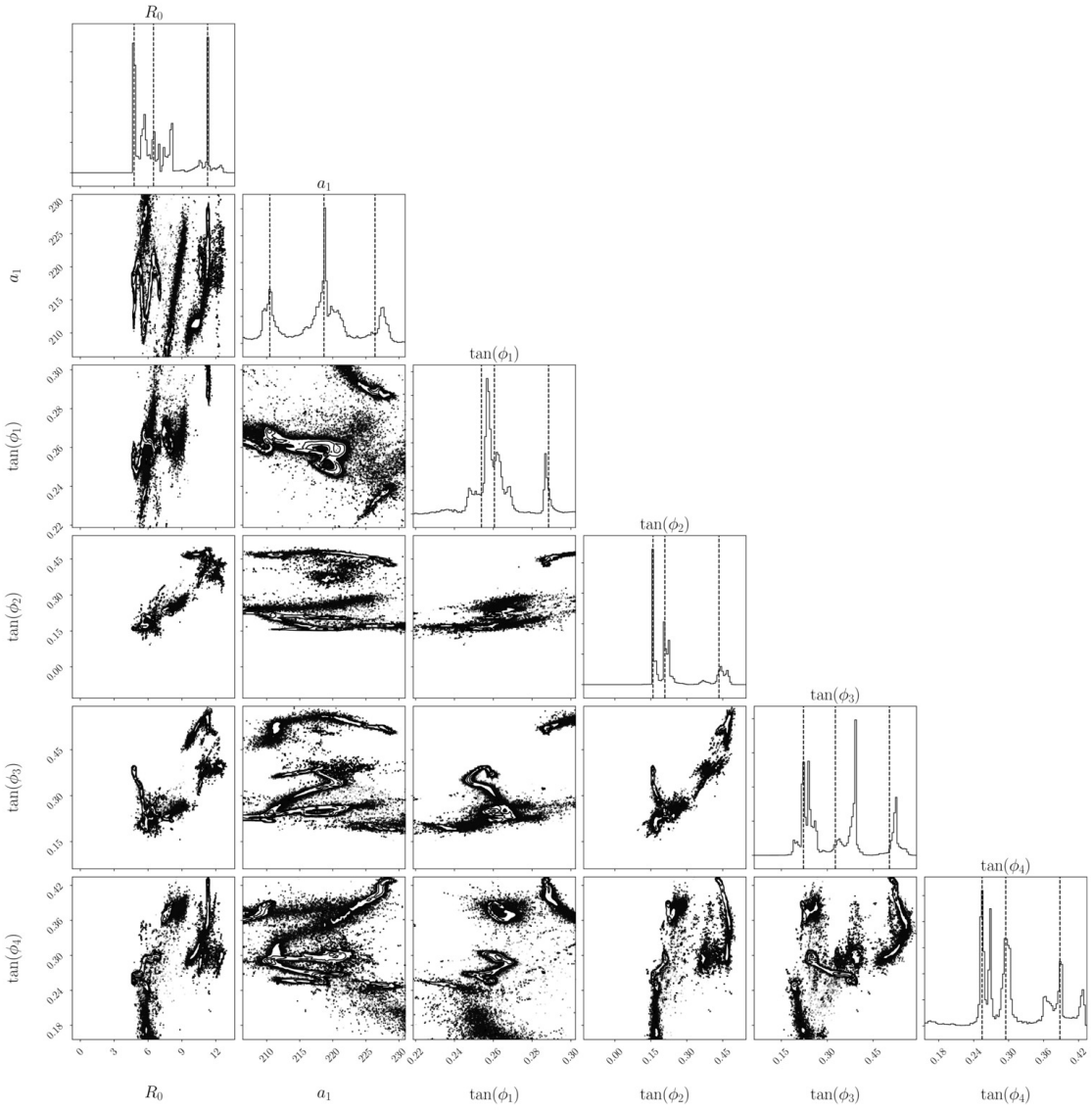

Figure 6.20: Same as Figure 6.14 for Model D. Note that the axis ranges are much different.

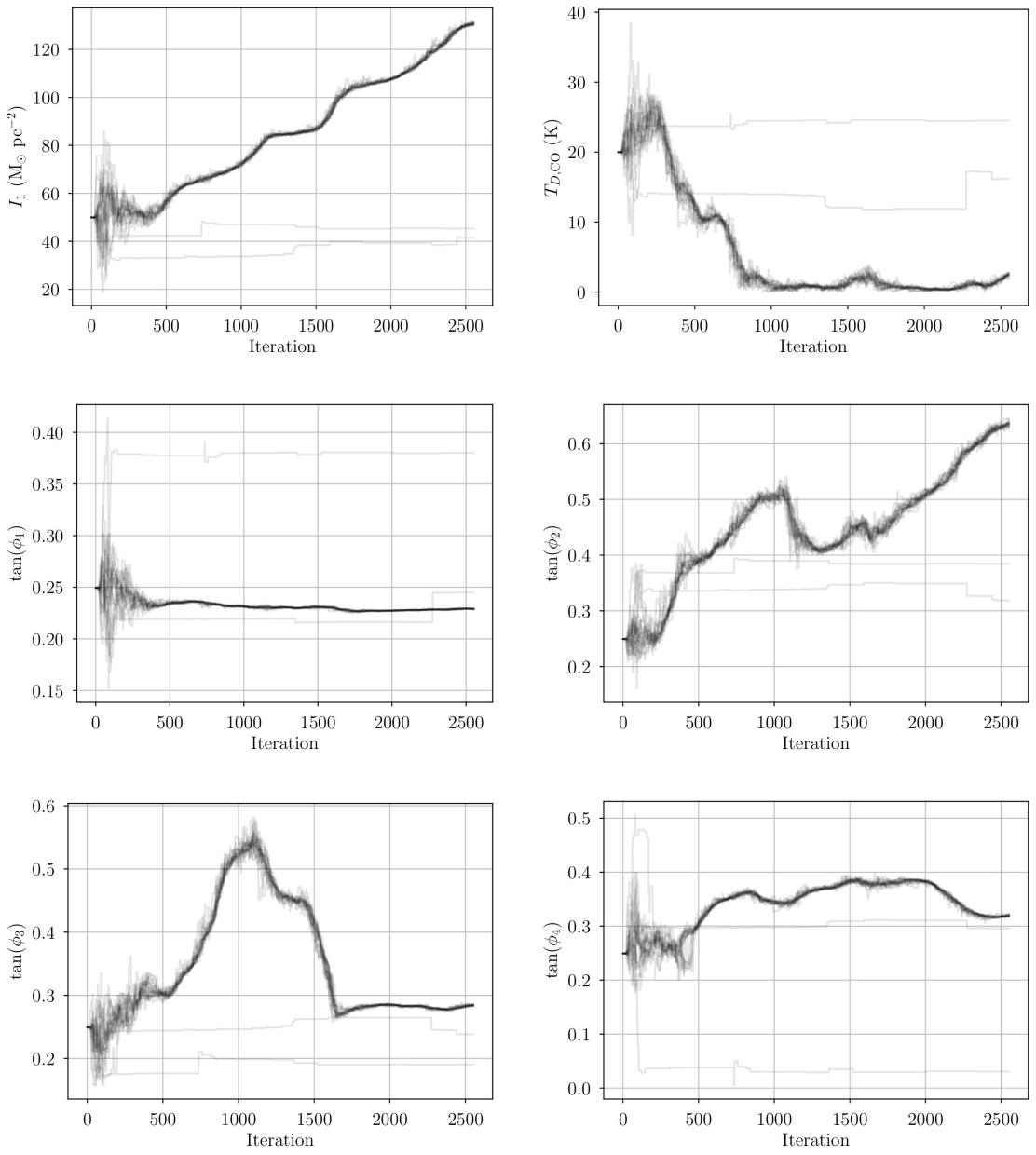

Figure 6.21: Same as Figure 6.17 for Model E.

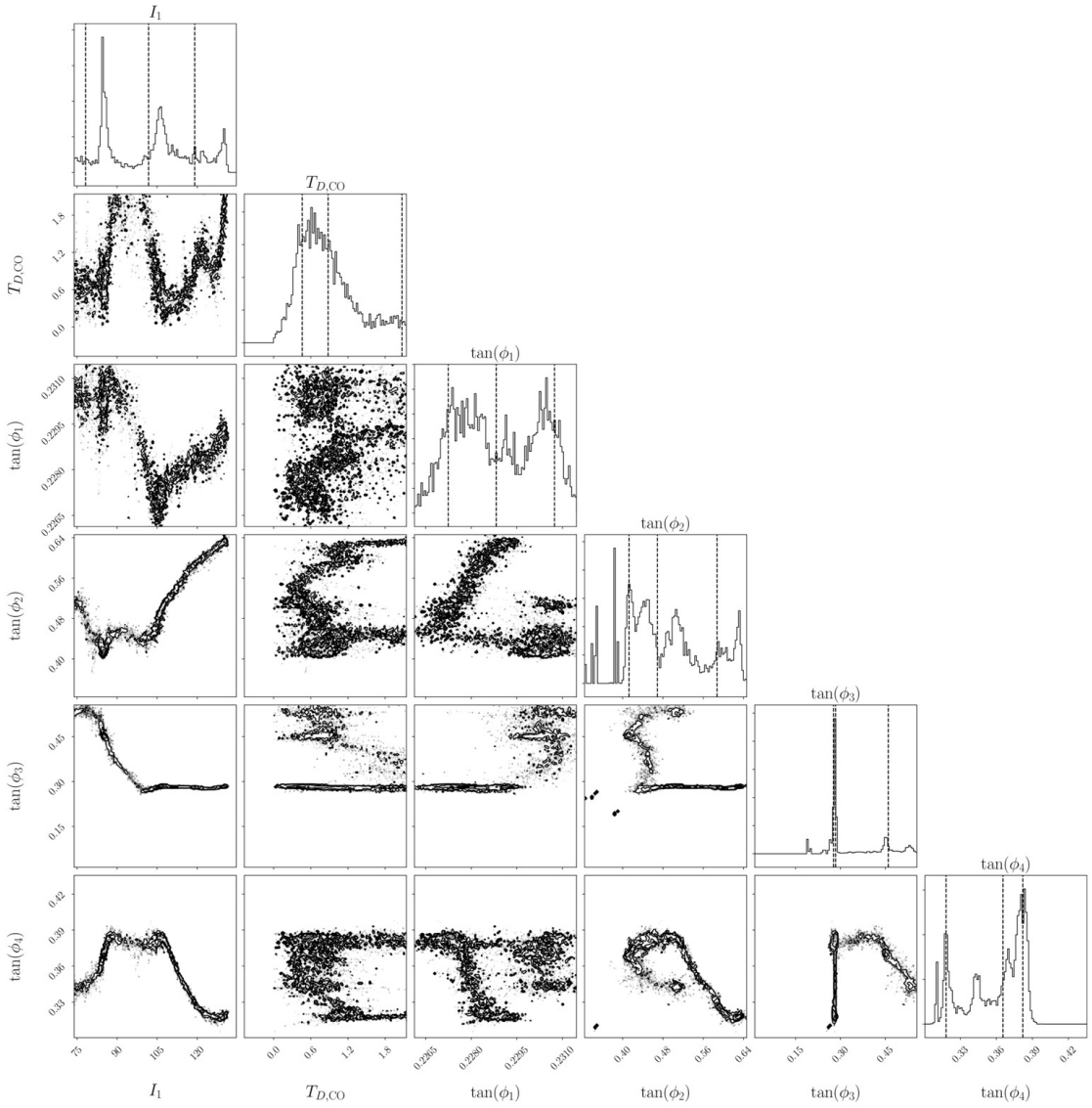

Figure 6.22: Same as Figure 6.18 for Model E. Note that the axis ranges are much different.

to determine the model parameters that best reproduce the observed H I, ^{12}CO, and H II region distribution in the Milky Way. Although we correctly recover the model parameters for a simulated dataset, we are unable to constrain the parameters using the real data.

There are several factors that are contributing to the failure of our MCMC analysis: (1) our model parameters are extremely degenerate, for example, R_0 is used to define the Galactic rotation curve as well as the reference radius for the Galactic spiral arms; (2) the H II region data are incomplete, especially in the 3rd and 4th Galactic quadrants (see Wenger et al., 2019, Chapter 4); (3) we use incorrect initial and fixed values for the Galactic warp azimuths, $\theta_{w,i}$; and (4) the number of MCMC random walkers may be insufficient given the large parameter space. We will resolve each of these issues by re-defining parameters in our model to remove degeneracies, using the complete SHRDS H II region catalog, correcting the initial and fixed values for $\theta_{w,i}$, and running the MCMC analysis with an adequate number of random walkers. This ongoing study is a proof of concept, which shows the capabilities of using a simple morphological to place constraints on Galactic spiral structure.

Chapter 7

Conclusions

The morphological, kinematic, and chemical structure of the Milky Way at the current epoch constrain models of Galactic formation and chemodynamical evolution. We explore all three of these structures using radio wavelength observations of Galactic H II regions. We discover hundreds of nebulae in the southern sky, and we use the latest and most complete catalog of Galactic H II regions to develop a new technique for determining H II region distances, to reveal azimuthal variations in the Milky Way's radial metallicity gradient, and to investigate Galactic spiral structure.

We test the accuracy of the kinematic distance technique by comparing the kinematic distance and maser parallax distances of 75 Galactic high-mass star forming regions (HMSFRs). Our new Monte Carlo method, which correctly accounts for the various uncertainties in the Galactic rotation model and the solar non-circular motion, is the most accurate kinematic distance technique to date. The median absolute difference between these kinematic distances and the parallax distances is 0.71 kpc. The derived uncertainties on the Monte Carlo kinematic distances are robust, and we show that kinematic distances are more accurate than parallax distances in a large portion of the Galactic disk. Our new method will improve both Galactic structure studies as well as any other work that relies on kinematic distances.

The number of known Galactic H II regions has doubled over the past decade, but most of these new nebulae are in the northern sky. We introduce the Southern H II Region Discovery Survey (SHRDS), an Australia Telescope Compact Array 4–10 GHz radio continuum and radio recombination line (RRL) survey of new Galactic H II regions. In our first data release, we detect RRL emission toward 76 previously known nebulae and we discover 256 new nebulae. These discoveries nearly double

the number of known Galactic H II regions in the longitude range ($259° < \ell < 344°$). We expect to discover ∼200 more nebulae upon the completion of the SHRDS, which will allow us to probe Galactic morphological structure, metallicity structure, and high-mass star formation across the entire Galactic disk. The SHRDS will complete the catalog of Galactic H II regions ionized by at least a single O star.

Recent single dish studies of H II region metallicities found evidence for unexpected azimuthal variations in the Galactic radial metallicity gradient. We use the National Radio Astronomy Observatory Karl G. Jansky Very Large Array to determine accurate RRL-to-continuum brightness ratios, electron temperatures, and metallicities of 82 Galactic H II regions. We combine these detections with previous single dish surveys and determine the nebular distances from maser parallax measurements or by using our new Monte Carlo kinematic distance technique. The catalog of Galactic H II regions with accurate distances and metallicities now contains 167 nebulae, which we use to map the metallicity structure of the Galactic disk. We measure a most likely radial oxygen abundance gradient of $0.052^{+0.004}_{-0.003}$ dex kpc^{-1}, which varies by a factor of ∼2 over the Galactocentric azimuth range 30°–100°. This variation is consistent with the simulated influence of spiral arms on the chemodynamical evolution of the Milky Way.

Finally, we develop a proof of concept morphological model of the neutral gas, molecular gas, and HMSFR content of the Galactic disk. We model Galactic kinematics, the morphology of spiral arms, the warp of the Galactic plane, and the densities of H I, ^{12}CO, and H II regions. Using a Markov Chain Monte Carlo analysis, we attempt to determine the model parameters that reproduce the observed Galactic longitude, latitude, and velocity distribution of H I 21 cm hyperfine emission, ^{12}CO ($J = 1 \rightarrow 0$) emission, and Galactic H II regions, including the newly discovered SHRDS nebulae. Our model is not yet able to reproduce the data, but we identify ways to improve the model and analysis strategy in this ongoing study.

The structure of the Milky Way remains an open question in astronomy. This dissertation answers some questions, but it raises many more. We create a novel and more accurate kinematic distance technique, but the impact of non-circular motions on kinematic distance determinations remains uncertain. We find significant azimuthal structure in the Milky Way's radial metallicity gradient, yet the cause of this structure is ill constrained. We create a model of spiral structure in the Galaxy, but the model is not yet able to explain the distributions of Galactic structure trac-

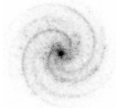

ers. H II regions, the primary tracer in our studies, are only one probe of Galactic structure. Several ongoing and planned projects, which span the full electromagnetic spectrum, target different tracers, and reveal a variety of structures, will undoubtedly revolutionize our understanding of the Galaxy and its place in the universe. We must combine the knowledge that we gain from all of these studies to create a complete map of the Galaxy and to uncover the formation and evolutionary history of the Milky Way.

Appendix A

Galactocentric Position Uncertainty Derivations

Here, we derive the relationship between uncertainties in the distance to an object, d, and the uncertainties in its Galactocentric position, $(R, \theta_{\rm Az})$. For simplicity, we assume all objects are in the Galactic plane ($b = 0°$ and $z = 0$).

An object's Galactocentric radius is given by

$$R = \left(d^2 + R_0^2 - 2dR_0 \cos \ell\right)^{1/2} \tag{A.1}$$

where R_0 is the Galactocentric radius of the solar orbit and ℓ is its Galactic longitude. The uncertainty in R is

$$\sigma_R^2 = \sigma_d^2 \left(\frac{\partial R}{\partial d}\right)^2 + \sigma_{R_0}^2 \left(\frac{\partial R}{\partial R_0}\right)^2 + \sigma_\ell^2 \left(\frac{\partial R}{\partial \ell}\right)^2 \tag{A.2}$$

where σ_R is the uncertainty in R, σ_{R_0} is the uncertainty in R_0, and σ_ℓ is the uncertainty in ℓ. For simplicity, we ignore cross-terms and assume $\sigma_{R_0} = \sigma_\ell = 0$. The above equation then reduces to

$$\sigma_R^2 = \sigma_d^2 \left(\frac{\partial R}{\partial d}\right)^2 . \tag{A.3}$$

This appendix previously appeared in the Astrophysical Journal. The original citation is as follows: T. V. Wenger, D. S. Balser, L. D. Anderson, and T. M. Bania. "Kinematic Distances: A Monte Carlo Method." *Astrophysical Journal*, 856:52, March 2018.

The partial derivative evaluates to

$$\frac{\partial R}{\partial d} = \frac{1}{2}\left(d^2 + R_0^2 - 2dR_0\cos\ell\right)^{-1/2}(2d - 2R_0\cos\ell) = \frac{d - R_0\cos\ell}{R}. \tag{A.4}$$

The uncertainty in the Galactocentric radius of an object is thus related to the uncertainty in its distance from the Sun by

$$\sigma_R = \frac{\sigma_d}{R}|d - R_0\cos\ell|. \tag{A.5}$$

This relationship is shown in the top panel of Figure A.1.

An object's Galactocentric azimuth is given by

$$\cos\theta_{\rm Az} = \frac{R^2 + R_0^2 - d^2}{2RR_0} = \frac{d^2 + R_0^2 - 2dR_0\cos\ell + R_0^2 - d^2}{2RR_0} = \frac{R_0 - d\cos\ell}{R}. \tag{A.6}$$

Again ignoring the σ_{R_0} and σ_ℓ terms, the uncertainty in $\theta_{\rm Az}$ is

$$\sigma_{\rm Az}^2 = \sigma_d^2\left(\frac{\partial\theta_{\rm Az}}{\partial d}\right)^2. \tag{A.7}$$

The partial derivative evaluates to

$$\frac{\partial\theta_{\rm Az}}{\partial d} = -\frac{1}{\sqrt{1-\cos^2\theta_{\rm Az}}}\frac{\partial\cos\theta_{\rm Az}}{\partial d} = -\frac{1}{\sin\theta_{\rm Az}}\frac{\partial\cos\theta_{\rm Az}}{\partial d}.$$

To evaluate the derivative of $\cos\theta_{\rm Az}$, we use our expression for R (Equation A.1) and define functions $f(d)$ and $g(d)$ such that

$$\cos\theta_{\rm Az} = \frac{R^2 + R_0^2 - d^2}{2RR_0} = \frac{d^2 + R_0^2 - 2dR_0\cos\ell + R_0^2 - d^2}{2RR_0} = \frac{R_0 - d\cos\ell}{R} \equiv \frac{f(d)}{g(d)} \tag{A.8}$$

where

$$\frac{\partial f(d)}{\partial d} = \frac{\partial(R_0 - d\cos\ell)}{\partial d} = -\cos\ell$$
$$\frac{\partial g(d)}{\partial d} = \frac{\partial R}{\partial d} = \frac{d - R_0\cos\ell}{R}.$$

We find

$$\begin{aligned}\frac{\partial \cos\theta_{\rm Az}}{\partial d} &= -\left[\frac{-R\cos\ell - (R_0 - d\cos\ell)\left(\frac{d-R_0\cos\ell}{R}\right)}{R^2\sin\theta_{\rm Az}}\right] \\ &= \left[\frac{\cos\ell}{R\sin\theta_{\rm Az}} + \frac{(R_0 - d\cos\ell)(d - R_0\cos\ell)}{R^3\sin\theta_{\rm Az}}\right].\end{aligned}$$

The uncertainty in the Galactic azimuth is thus

$$\begin{aligned}\sigma_{\rm Az}^2 &= \sigma_d^2\left(\frac{\cos\ell}{R\sin\theta_{\rm Az}} + \frac{(R_0 - d\cos\ell)(d - R_0\cos\ell)}{R^3\sin\theta_{\rm Az}}\right)^2 \\ \sigma_{\rm Az} &= \frac{\sigma_d}{R}\left|\csc\theta_{\rm Az}\left[\frac{\cos\ell}{\sin\theta_{\rm Az}} + \frac{(R_0 - d\cos\ell)(d - R_0\cos\ell)}{R^2\sin\theta_{\rm Az}}\right]\right|. \qquad \text{(A.9)}\end{aligned}$$

Rearranging, we see that the uncertainty in the Galactocentric azimuth of an object is related to the uncertainty in its distance from the Sun by

$$\sigma_{\rm Az} = \frac{\sigma_d}{R}\left|\frac{\cos\ell}{\sin\theta_{\rm Az}} + \frac{(R_0 - d\cos\ell)(d - R_0\cos\ell)}{R^2\sin\theta_{\rm Az}}\right|. \qquad \text{(A.10)}$$

This relationship is shown in the bottom panel of Figure A.1.

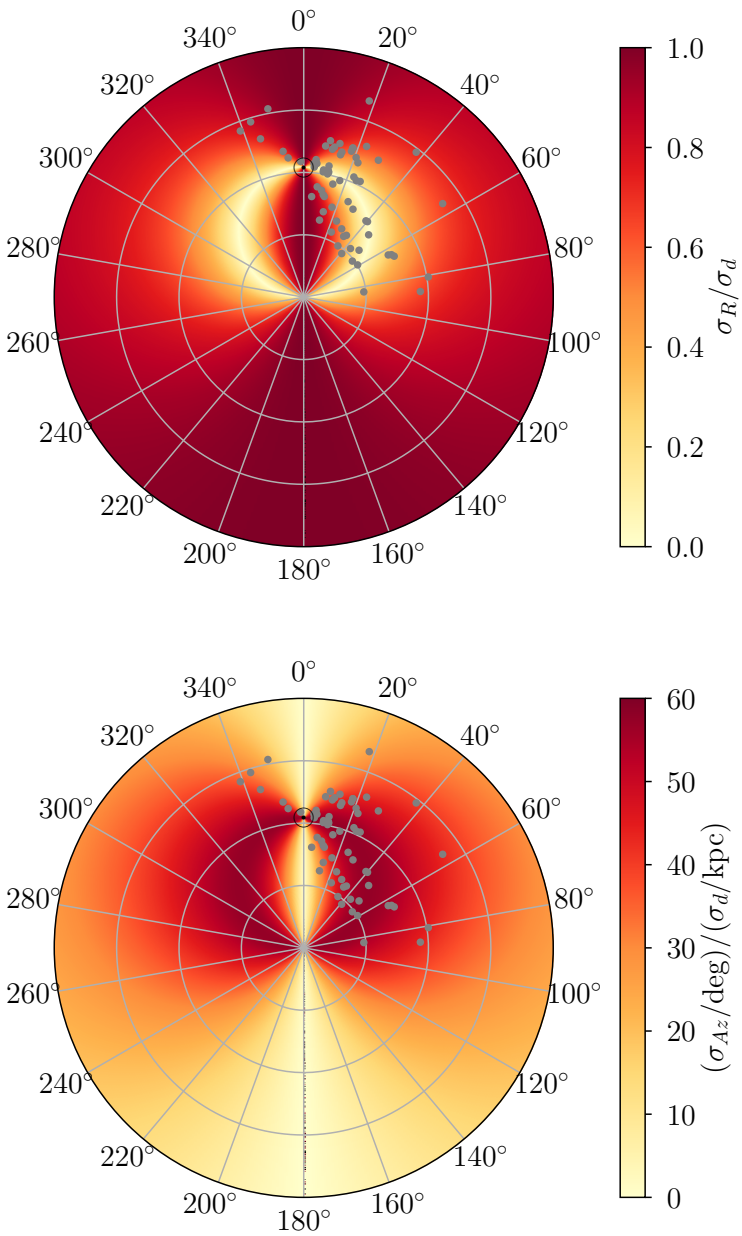

Figure A.1: The relationship between the uncertainty in distance, σ_d, and the uncertainty in Galactocentric radius (σ_R, Equation A.5, top) and Galactocentric azimuth (σ_{Az}, Equation A.10, bottom). The Galactic Center is located at the origin and the Sun is located 8.34 kpc in the direction $\theta_{\mathrm{Az}} = 0°$. The concentric circles are 4, 8, and 12 kpc in R and θ_{Az} is given in degrees. The color represents the uncertainty ratio. The gray points are the HMSFRs in our sample.

Appendix B

WISP: A General Radio Interferometry Data Reduction Package

Here, we introduce the data reduction and analysis tools developed for the SHRDS: the Wenger Interferometry Software Package (WISP; Wenger, 2018)[1]. WISP is a collection of *Python* code implemented through the Common Astronomy Software Applications (CASA) package (McMullin et al., 2007). Its generic and modular framework is designed to handle any continuum or spectral line radio interferometry data. We are motivated to create our own data reduction pipeline for three reasons: (1) the large quantity of data in the SHRDS, (2) missing functionality in CASA, and (3) the lack of automatically generated quality diagnostics in existing pipelines.

Our primary motivation for WISP is the overwhelmingly large quantity of data produced in the SHRDS. The calibration process for a single ∼8 hr observing session of the SHRDS, for example, takes ∼16 hr of raw computing time on a reasonably powerful machine, not including the downtime between individual calibration tasks, while inspecting the data, etc. Including this overhead, the entire calibration process

---

This appendix previously appeared in the Astrophysical Journal Supplement Series. The original citation is as follows: T. V. Wenger, J. M. Dickey, C. H. Jordan, D. S. Balser, W. P. Armentrout, L. D. Anderson, T. M. Bania, J. R. Dawson, N. M. McClure-Griffiths, and J. Shea. "The Southern H II Region Discovery Survey. I. The Bright Catalog." *Astrophysical Journal Supplement Series*, 240:24, February 2019.

[1] `https://doi.org/10.5281/zenodo.2225273`

for a single observing session can take a week if done interactively. This is impractical considering the hundreds of hours of data accumulated by the SHRDS. With WISP, all of the calibration steps are automated so that there is no downtime between the completion of one task and the start of the next. The total time it takes to calibrate a single observing session using WISP is reduced to only ∼24 hr including the manual data inspection.

The imaging process is equally as time consuming if done interactively. To *CLEAN* a single spectral line window data cube for a single field can take ∼15 minutes. Given the ∼300 fields and ∼20 spectral line windows, the total computation time required to generate all of the images for the SHRDS Bright Catalog is nearly two months. Interactive cleaning (i.e. determining *CLEAN* masks by hand) would add substantially to the imaging time, so WISP uses automatic *CLEAN* mask generation and other tricks to automate the entire imaging process.

The SHRDS Bright Catalog data grows from about 10 terabytes in its raw form to nearly 50 terabytes after each field and spectral window are imaged ("data reduction" should really be called "data expansion" when discussing radio interferometry). All of the images and data cubes generated for a single source total about 150 gigabytes. WISP (via CASA) generates several intermediate images and data cubes for each field and spectral window, most of which are not needed for the final data analysis. By converting the required images and cubes to Flexible Image Transport System (FITS) files and by deleting all CASA-generated images and cubes, we reduce the disk space for a single source to about 30 gigabytes.

Our second motivation for WISP is a lack of some required functionality in CASA. For example, CASA cannot interpolate through missing or flagged data. The ATCA correlator, CABB, has several known bad channels ("birdies"). If these channels are flagged throughout all of the data, CASA fails to account correctly for the missing data when regridding the velocity axis of our spectral line windows. This failure produces large, periodic ripples in the spectra. WISP has the functionality to interpolate seamlessly through any known bad channels by directly editing the visibility data. Without missing data, the velocity axis regridding works correctly.

Finally, existing pipelines (at least those that existed when the SHRDS began) lack the ability to automatically generate calibration and imaging diagnostics to assess the quality of the data reduction process. For example, after the calibration process, we wish to inspect the derived calibration solutions and the calibrated visibilities. In

CASA, this requires the user to run a task, wait (sometimes several minutes) for the plot(s) to be generated, inspect the plots, then repeat for the next calibration solution or visibility set. In total, this can take several hours depending on the number of calibrator sources and calibration solutions to inspect. WISP automatically generates all of the necessary calibration solution and visibility plots and compiles them into a single document. We can then quickly scroll through the plots and identify any issues.

Below, we describe, in detail, the specific calibration and imaging steps performed by WISP.

B.1 Calibration

The calibration pipeline in WISP handles all of the necessary calibration steps: (1) flags bad data, (2) computes calibration solutions, and (3) applies calibration solutions. Using a combination of automated flagging and manual flagging, this pipeline is extremely time-efficient. A summary of the calibration process is shown in Figure B.1.

The raw data are contaminated by several sources of bad data, including bad channels in the correlator ("birdies"), shadowed antennas, the beginning and end of scans when the antennas are not on source, and radio frequency interference (RFI). The pipeline begins by flagging the known sources of bad data: birdies, shadowed antennas, and off-source antennas. We then use the automatic flagging algorithm *TFCROP*, as implemented in CASA, to catch any RFI. This task is the recommended auto-flagging task to use on uncalibrated data by detecting outliers in the time-frequency domain. Our tests show that *TFCROP* is excellent at finding ∼95% of bright, short-duration, limited-frequency RFI but often misses complex RFI, which can completely compromise the data quality of a spectral line window.

The data are now pruned of obvious RFI, but some low-level RFI may still remain. Using the calibrator data, we compute preliminary calibration solutions for the absolute flux, bandpass, delays, and complex gains. We apply these calibration solutions to the calibrators, thereby removing any instrumental effects from the data. These calibrated data should be well-behaved, and thus, it is easier to identify any RFI or otherwise bad data. Using the CASA algorithm *RFLAG*, we again automatically flag the calibrator data to identify any remaining bad data. This algorithm differs from *TFCROP* in that it requires the data to be calibrated. It then computes statistics on small chunks of the data and flags data using a threshold determined by

these statistics. The *RFLAG* algorithm successfully flags most of the RFI missed by *TFCROP*, but it often misses other bad data, such as misbehaving antennas or RFI compromising an entire spectral line window. This algorithm will also flag the peak of our spectral lines if the spectral line is very bright ($\gtrsim$500 mJy beam^{-1}). In these cases, we must manually unflag the spectral lines.

At this stage, we have run the data through two independent automatic flagging algorithms. We recompute and reapply the calibration solutions. We then generate diagnostic plots to inspect the quality of the calibrator data and calibration solutions. These diagnostic plots are slices of the data in many dimensions: for example, complex amplitude as a function of complex phase, real amplitude as a function of time, and complex phase as a function of frequency. If we notice any heretofore unidentified bad data, we manually flag it, recalculate and reapply the calibration solutions, regenerate the diagnostic plots, and reinspect them. We iterate this process until the calibrator data are free of any bad data.

After accurate calibration solutions are established, the science target data can be calibrated. Using the final calibration solutions, we calibrate the absolute flux, bandpass, delay, and complex gain of the science target data using the secondary calibrator located closest to the science target on the sky. We then run the *RFLAG* algorithm on the science target data to identify any RFI. Finally, we generate diagnostic plots for the science target data and manually flag any remaining bad data.

The final data products generated by the WISP calibration pipeline are: (1) fully calibrated visibilities, (2) a flag table identifying all of the flagged data, (3) the final calibration solution tables, (4) the final diagnostic plots, and (5) a copy of the fully calibrated visibilities for each individual field. We use WISP to calibrate each observing session of the SHRDS. If a given field is observed in multiple sessions, we combine all of the data for that field before imaging.

B.2 IMAGING

The imaging pipeline in WISP automatically creates several images for each of our fields. This automation is necessary due to the large amount of computing time required to image and to *CLEAN* each field. The *CLEAN* and other imaging parameters are initially set by the user and then applied to every image. All of the imaging and *CLEAN*ing is performed using the CASA task *TCLEAN*. We generate the following images for each field: (1) a multiscale, multi-frequency synthesis

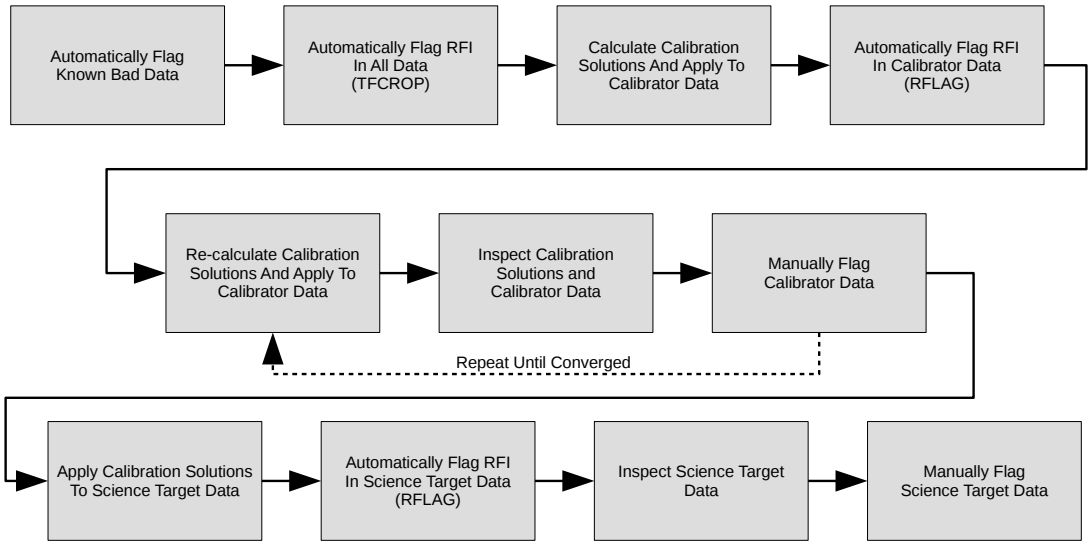

Figure B.1: Steps performed by the WISP calibration pipeline.

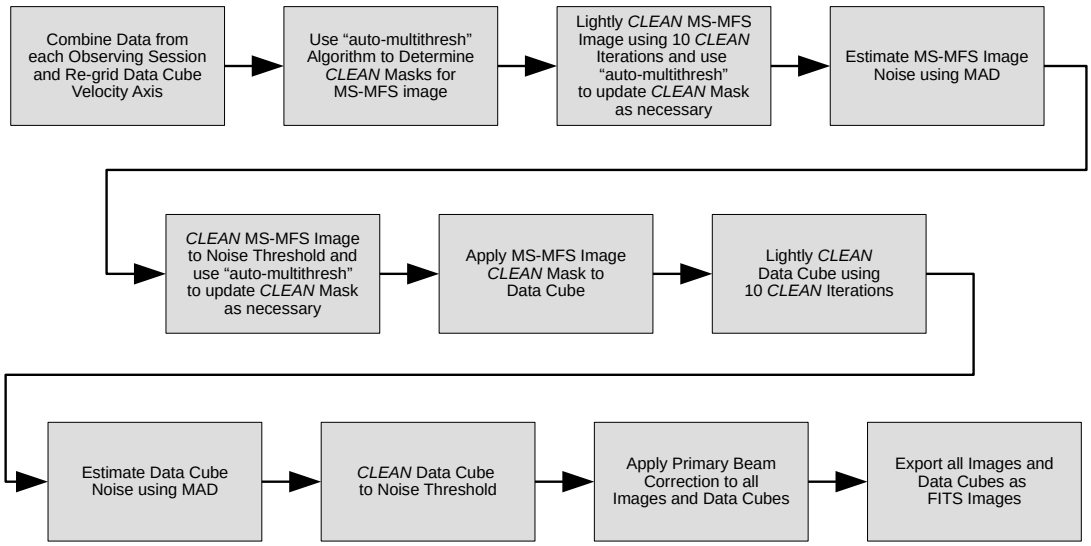

Figure B.2: Steps performed by the WISP imaging pipeline for a single spectral line window.

(MS-MFS) image produced by combining the two 2 GHz continuum windows, (2) an MS-MFS image of each 2 GHz bandwidth continuum window, (3) MS-MFS images of each 64 MHz bandwidth spectral line window, and (4) multiscale data cubes of each spectral line window. Figure B.2 summarizes the imaging process for a single spectral line window.

We use the newly implemented "auto-multithresh" algorithm to automatically determine *CLEAN* masks in our images (Kepley et al, in prep.). This algorithm applies user-defined thresholds to determine the locations of "real" emission around which to place a *CLEAN* mask. It first masks any emission brighter than a given threshold above the brightest sidelobe in the image, based on the *TCLEAN*-generated dirty beam image. After several iterations of *CLEAN*, the dirty beam sidelobes are suppressed and the algorithm begins masking any emission brighter than a given threshold above the estimated noise in the *TCLEAN*-generated residual image. The sidelobe masking threshold is very sensitive to the *uv*-coverage of the data; images with very complete *uv*-coverage, either because of large bandwidths or more hour angle coverage, have dirty beams with lower sidelobes, whereas images with poor *uv*-coverage may have sidelobes comparable in gain to the synthesized beam. Therefore, we use a separate set of thresholds for the large-bandwidth continuum windows and the small-bandwidth spectral line windows.

The "auto-multithresh" algorithm is time consuming when applied to each channel of a data cube independently. We reduce the *CLEAN* computation time by applying the "auto-multithresh" *CLEAN* mask from the MS-MFS image of a given spectral window to all of the channels in the data cube for that spectral window. This is possible because the morphology of our target H II regions and H II region candidates should not change from channel to channel; the free-free continuum and RRL emission originate in the same volume of gas.

Each image and data cube is "lightly *CLEAN*ed" by running only 10 iterations of *CLEAN*. From these data we estimate the image noise and *CLEAN* stopping criterion (i.e. *CLEAN* threshold). We compute the median absolute deviation (MAD) of the *TCLEAN*-generated residual image to estimate the *CLEAN* threshold. The MAD is a robust estimator of the noise of a data set even in the presence of outliers. For Gaussian noise, MAD is related to the root-mean-square, rms, by rms $\simeq 1.4826$ MAD. We use this rms as the stopping criterion for *CLEAN*: when the maximum absolute value of the residual image within the *CLEAN* mask is below this value, we stop

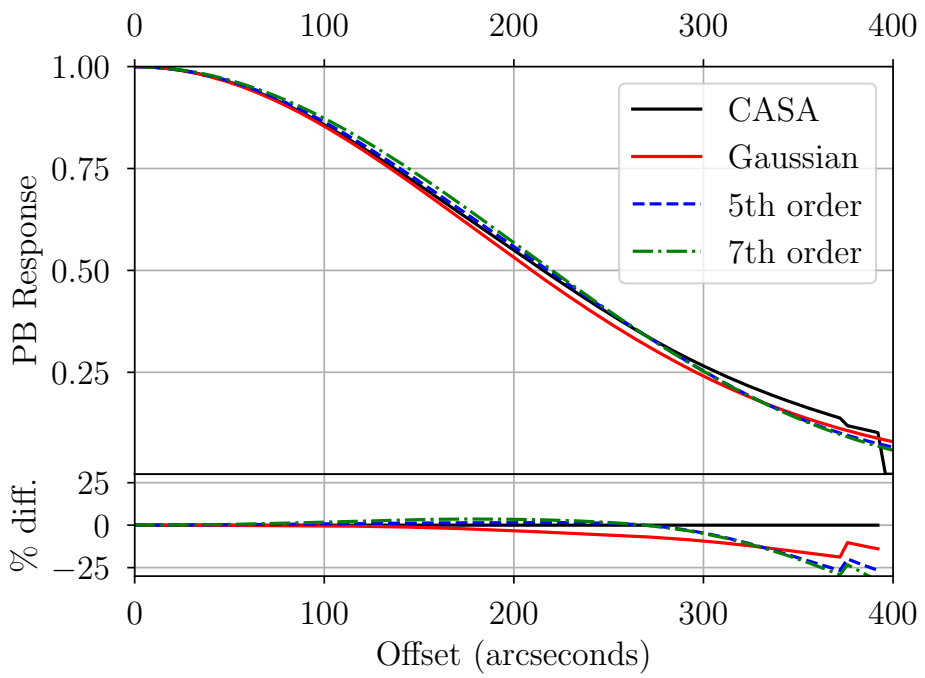

Figure B.3: The primary beam response generated by *TCLEAN* (black solid line) and three empirical models by Wieringa & Kesteven (1992): a Gaussian (red solid line), a 5th order polynomial (blue dashed line), and a 7th order polynomial (green dashed–dotted line). The bottom panel shows the percent difference between the three Wieringa & Kesteven (1992) models and the *TCLEAN*-generated profile.

CLEAN. This entire process usually takes fewer than 50 iterations of *CLEAN* for the MS-MFS images and 200 iterations for the spectral data cubes.

In order to average together each spectral window into a final <H$n\alpha$> spectrum, we must regrid the spectral windows to a common velocity frame. Using the CASA task *CVEL2*, we linearly interpolate each spectral line window to the kinematic local standard of rest (LSRK) reference frame in 321 velocity channels with a $2.5\,\mathrm{km\,s^{-1}}$ width starting at $-400\,\mathrm{km\,s^{-1}}$. This gives us velocity coverage from $V_{\mathrm{LSR}} = -400\,\mathrm{km\,s^{-1}}$ to $+400\,\mathrm{km\,s^{-1}}$, sufficient to detect all Galactic H II regions.

Finally, each image and data cube is primary beam corrected. We divide each image and cube by the *TCLEAN*-generated primary beam image. For our full 4GHz bandwidth continuum images, we use the CASA task *WIDEBANDPBCOR* which considers the varying primary beam over a large fractional bandwidth ($4-10$GHz in our case). For all other images, we use *IMPBCOR* which applies the primary beam correction using the primary beam of the center frequency. Figure B.3 shows the *TCLEAN*-generated primary beam profile for a 4GHz bandwidth MS-MFS image. We also show the Gaussian, 5th order polynomial, and 7th order polynomial empirical primary beam models from Wieringa & Kesteven (1992). The CASA primary beam deviates significantly ($\gtrsim 10\%$) from these models beyond $\sim$300 arcsec from the primary beam center. Thus the continuum and RRL intensities of sources at the edges of an observed field are inaccurate.

The final data products generated by the WISP imaging pipeline for each field are: (1) an MS-MFS image of the combined 4 GHz bandwidth continuum windows, (2) an MS-MFS image of each 2 GHz bandwidth continuum window, (3) MS-MFS images of each 64 MHz bandwidth spectral line window, and (4) multiscale data cubes of each spectral line window. These images are saved both as CASA and FITS images. All subsequent analyses are performed using the FITS images, so the CASA images are deleted.

Appendix C

SHRDS Bright Catalog: Multiple Detections

A *WISE* Catalog source may appear in multiple fields. The data with the highest quality factor and/or thw largest signal-to-noise ratio are included in the main catalogs (Tables 4.4–4.7). Here we give the radio continuum and <H$n\alpha$> RRL properties for these "multiple detections" as measured in each independent field. Most of these sources are located near the edge of the field, so the continuum and RRL intensities may be inaccurate (see Appendix B). The data in the main catalogs, not the multiple detections catalogs, should be used for all subsequent analyses. In the next data release, we will combine the data from each field to improve our sensitivity and to measure the continuum and RRL properties of these sources more accurately.

The continuum properties of the multiple detections are listed in Table C.1 (non-tapered) and Table C.2 (uv-tapered). For each source, we list the *WISE* Catalog name; the position of the peak radio continuum emission; the fields containing the source; the epoch; the synthesized beam area in the continuum image; the separation between the observed continuum peak position and infrared position, $\Delta\theta$; the MFS-synthesized frequency of the continuum image, ν_C; the peak continuum flux density, S_C; the rms noise, rms_C; and a quality factor, QF. These tables contain one row for

This appendix previously appeared in the Astrophysical Journal Supplement Series. The original citation is as follows: T. V. Wenger, J. M. Dickey, C. H. Jordan, D. S. Balser, W. P. Armentrout, L. D. Anderson, T. M. Bania, J. R. Dawson, N. M. McClure-Griffiths, and J. Shea. "The Southern H II Region Discovery Survey. I. The Bright Catalog." *Astrophysical Journal Supplement Series*, 240:24, February 2019.

each field in which the source is found.

The <H$n\alpha$> RRL properties of the multiple detections are listed in Table C.3 (non-tapered) and Table C.4 (uv-tapered). For each source, we give the *WISE* Catalog name; the field; the epoch; the weighted-average frequency of the <H$n\alpha$> RRL, ν_L; the Gaussian fits to the peak intensity, S_L; the LSR velocity, $V_{\rm LSR}$; and the FWHM line width, ΔV; the rms spectral noise in the line-free region of the spectrum, rms$_L$; the signal-to-noise ratio, S/N; and a quality factor, QF. These tables also contain one row for each field in which the source is found.

Table C.1: Non-tapered Image Continuum Properties of Multiple Detections

Target	R.A. J2000 (hh:mm:ss)	Decl. J2000 (dd:mm:ss)	Field	Epoch[a]	Beam Area (arcsec^2)	$\Delta\theta^b$ (arcsec)	ν_C (MHz)	S_C (mJy beam^{-1})	rms$_C$ (mJy beam^{-1})	QF
G289.944−00.889	11:01:11.1	−60:56:48.0	shrds191	2015	2502	10.2	7023	123.68	1.47	A
G289.944−00.889	11:01:09.7	−60:56:40.8	g290.012-00.867	2014	5394	16.4	6050	135.43	7.10	C
G290.012−00.867	11:01:59.2	−60:56:48.8	g290.012-00.867	2014	5394	106.4	6050	200.17	3.66	B
G290.012−00.867	11:01:45.4	−60:57:25.8	g290.012-00.867	2014*	···	0.8	···	···	···	···
G290.323−02.984	10:56:33.0	−63:00:43.9	g290.323-02.984	2014	5453	26.8	6050	28.85	0.34	A
G290.323−02.984	10:56:36.4	−63:00:35.0	g290.323-02.984	2014*	···	2.9	···	···	···	···
G290.385−01.042	11:03:59.6	−61:16:04.4	g290.385-01.042	2014	5384	2.0	6050	23.30	0.87	A
G290.385−01.042	11:03:59.4	−61:16:06.7	g290.385-01.042	2014*	···	0.6	···	···	···	···
G290.674−00.133	11:08:43.9	−60:31:29.3	g290.674-00.133	2014	5351	187.1	6050	-0.73	0.88	C
G290.674−00.133	11:09:07.0	−60:32:47.0	g290.674-00.133	2014*	···	2.0	···	···	···	···
G291.281−00.726	11:11:52.3	−61:18:48.4	caswell3	2016	2238	40.6	7023	38233.32	102.06	B
G291.281−00.726	11:11:52.4	−61:18:42.7	shrds1034	2016	1813	46.1	7023	34864.83	128.60	B
G291.596−00.239	11:15:49.4	−60:59:20.4	g291.596-00.239	2014	5376	9.7	6050	32.12	13.76	A
G291.596−00.239	11:15:48.1	−60:59:17.7	g291.596-00.239	2014*	···	2.5	···	···	···	···
G292.889−00.831	11:24:08.6	−61:58:27.7	g292.889-00.831	2014	5402	74.7	6050	4.43	0.62	C
G292.889−00.831	11:24:15.3	−61:59:26.9	g292.889-00.831	2014*	···	2.0	···	···	···	···
G293.936−00.873	11:32:38.8	−62:21:31.7	g293.936-00.873	2014	5536	6.8	6050	112.29	1.91	B
G293.936−00.873	11:32:39.3	−62:21:38.8	g293.936-00.873	2014*	···	1.6	···	···	···	···
G293.952−00.894	11:32:43.9	−62:23:12.0	g293.936-00.873	2014	5536	4.0	6050	127.21	2.15	B
G293.952−00.894	11:32:43.7	−62:23:05.4	g293.994-00.934	2014	5531	3.3	6050	124.77	4.09	B
G293.967−00.984	11:32:36.0	−62:28:14.3	shrds219	2015	2584	19.2	7023	174.35	0.62	B
G293.967−00.984	11:32:36.1	−62:28:21.4	g293.994-00.934	2014	5531	13.4	6050	172.05	3.96	B
G293.994−00.934	11:32:58.6	−62:26:05.5	g293.994-00.934	2014	5531	3.1	6050	289.85	2.45	A
G293.994−00.934	11:32:58.5	−62:26:02.4	shrds219	2015	2584	6.2	7023	256.90	1.07	B
G293.994−00.934	11:32:59.0	−62:26:11.6	g293.936-00.873	2014	5536	3.8	6050	300.88	5.64	C
G293.994−00.934	11:32:58.5	−62:26:10.8	g293.994-00.934	2014*	···	2.3	···	···	···	···
G294.988−00.538	11:42:10.3	−62:20:09.5	g294.988-00.538	2014	6672	0.9	6050	157.84	0.92	A

Table C.1 continued

Table C.1: Non-tapered Image Continuum Properties of Multiple Detections (continued)

Target	R.A. J2000 (hh:mm:ss)	Decl. J2000 (dd:mm:ss)	Field	Epoch[a]	Beam Area (arcsec^2)	$\Delta\theta^b$ (arcsec)	ν_C (MHz)	S_C (mJy beam^{-1})	rms$_C$ (mJy beam^{-1})	QF
G294.988−00.538	11:42:10.1	−62:20:11.7	g294.988-00.538	2014*	···	2.9	···	···	···	···
G295.275−00.255	11:44:54.8	−62:08:08.9	g295.275-00.255	2014	8350	112.5	6050	20.75	1.14	C
G295.275−00.255	11:45:10.8	−62:08:15.7	g295.275-00.255	2014*	···	2.0	···	···	···	···
G295.748−00.207	11:49:12.7	−62:12:25.1	g295.748-00.207	2014	8361	1.2	6050	82.13	0.62	A
G295.748−00.207	11:49:12.5	−62:12:27.5	g295.748-00.207	2014*	···	1.5	···	···	···	···
G297.248−00.754	12:00:55.4	−63:04:09.4	g297.248-00.754	2014	8311	10.1	6050	304.13	1.45	A
G297.248−00.754	12:00:55.3	−63:04:00.9	g297.248-00.754	2014*	···	1.6	···	···	···	···
G297.626−00.906	12:03:58.2	−63:17:09.2	g297.626-00.906	2014	8396	6.3	6050	169.81	2.30	A
G297.626−00.906	12:03:57.4	−63:17:15.2	g297.626-00.906	2014*	···	1.8	···	···	···	···
G298.473+00.104	12:12:50.5	−62:25:59.1	g298.473+00.104	2014	8329	36.6	6050	113.65	1.85	A
G298.473+00.104	12:12:45.3	−62:25:56.6	g298.473+00.104	2014*	···	1.8	···	···	···	···
G299.349−00.267	12:19:54.2	−62:55:25.7	caswell6	2016	2031	21.7	7023	179.70	0.65	B
G299.349−00.267	12:19:54.2	−62:55:26.6	shrds1046	2016	1683	22.3	7023	162.61	0.84	C
G300.983+01.117	12:35:01.2	−61:41:46.9	g300.983+01.117	2014	8253	19.5	6050	69.44	3.97	A
G300.983+01.117	12:34:52.5	−61:39:32.6	caswell7	2016	2049	129.0	7023	809.67	2.55	B
G300.983+01.117	12:34:59.4	−61:41:33.0	g300.983+01.117	2014*	···	1.4	···	···	···	···
G311.629+00.289	14:04:55.1	−61:20:05.4	caswell12	2016	2248	6.7	7023	2274.81	4.88	A
G311.629+00.289	14:04:55.1	−61:20:03.4	shrds428	2016	1679	6.9	7023	2064.37	4.72	C
G312.675+00.048	14:13:54.0	−61:15:51.2	shrds462	2015	1614	40.9	7023	55.22	0.59	B
G312.675+00.048	14:13:53.7	−61:15:59.9	shrds458	2016	1483	47.6	7023	51.64	1.70	C
G313.671−00.105	14:22:02.3	−61:04:16.0	atca348	2013	4257	13.4	8450	69.25	0.32	B
G313.671−00.105	14:22:04.1	−61:04:18.7	atca348	2013*	···	1.0	···	···	···	···
G313.790+00.705	14:20:41.3	−60:15:55.8	atca352	2013	4231	24.7	8450	275.24	0.95	A
G313.790+00.705	14:20:43.8	−60:16:11.0	atca352	2013*	···	1.0	···	···	···	···
G314.219+00.343	14:25:02.2	−60:27:44.8	atca361	2013	4132	17.0	8450	270.48	3.50	B
G314.219+00.343	14:24:59.9	−60:27:40.0	atca361	2013*	···	1.1	···	···	···	···
G315.312−00.272	14:35:09.7	−60:37:38.1	ch87.1	2013	4158	22.5	8450	149.80	1.34	A

Table C.1 continued

Table C.1: Non-tapered Image Continuum Properties of Multiple Detections (continued)

Target	R.A. J2000 (hh:mm:ss)	Decl. J2000 (dd:mm:ss)	Field	Epoch[a]	Beam Area (arcsec^2)	$\Delta\theta^b$ (arcsec)	ν_C (MHz)	S_C (mJy beam^{-1})	rms$_C$ (mJy beam^{-1})	QF
G315.312−00.272	14:35:07.1	−60:37:41.7	ch87.1	2013*	···	6.6	···	···	···	···
G316.516−00.600	14:45:05.2	−60:26:30.8	atca382	2013	4075	29.3	8450	75.30	0.42	A
G316.516−00.600	14:45:08.6	−60:26:15.6	atca382	2013*	···	0.2	···	···	···	···
G317.570−00.257	14:51:26.3	−59:40:08.5	shrds521	2015	1582	52.8	7023	19.75	0.49	A
G317.570−00.257	14:51:26.7	−59:40:08.8	atca397	2013	4057	49.9	8450	13.84	0.81	C
G317.861+00.160	14:52:04.9	−59:10:09.8	atca402	2013	3989	27.4	8450	340.89	2.42	B
G317.861+00.160	14:52:08.4	−59:10:03.4	atca402	2013*	···	1.3	···	···	···	···
G318.248+00.150	14:55:04.9	−59:00:39.8	atca406	2013	4015	109.0	8450	38.43	1.69	C
G318.248+00.150	14:54:51.5	−59:00:02.7	atca406	2013*	···	1.2	···	···	···	···
G319.229+00.225	15:01:21.6	−58:26:59.7	atca412	2013	4105	104.0	8450	54.52	0.87	B
G319.229+00.225	15:01:16.7	−58:28:37.4	atca412	2013*	···	1.3	···	···	···	···
G320.778+00.241	15:11:24.2	−57:41:50.1	shrds1146	2016	1680	2.6	7023	109.30	3.09	B
G320.778+00.241	15:11:24.1	−57:41:52.0	shrds1147	2016	1681	3.5	7023	104.42	4.92	C
G322.162+00.625	15:18:39.3	−56:38:52.6	caswell15	2016	2062	7.5	7023	6041.97	19.36	A
G322.162+00.625	15:18:39.2	−56:38:54.7	shrds1151	2016	1698	8.1	7023	5526.11	26.24	B
G323.449+00.095	15:28:32.5	−56:22:57.8	atca449	2013	4209	9.2	8450	85.45	0.78	A
G323.449+00.095	15:28:33.2	−56:23:06.2	atca449	2013*	···	0.8	···	···	···	···
G323.464−00.079	15:29:19.6	−56:31:19.6	atca450	2013	4077	15.0	8450	672.79	1.46	A
G323.464−00.079	15:29:21.2	−56:31:12.7	atca450	2013*	···	0.9	···	···	···	···
G323.743−00.249	15:31:43.9	−56:30:14.7	atca456	2013	4090	14.0	8450	136.29	0.42	A
G323.743−00.249	15:31:43.1	−56:30:03.9	atca456	2013*	···	1.0	···	···	···	···
G323.806+00.020	15:31:05.7	−56:14:21.0	atca459	2013	4083	61.6	8450	205.68	1.10	B
G323.806+00.020	15:30:58.6	−56:14:36.8	atca459	2013*	···	0.2	···	···	···	···
G323.936−00.038	15:31:37.2	−56:11:44.0	shrds590	2015	2550	197.0	7023	36.85	1.39	B
G323.936−00.038	15:31:58.6	−56:11:08.6	atca462	2013	4280	112.0	8450	27.87	1.61	C
G323.936−00.038	15:31:58.9	−56:13:00.3	atca462	2013*	···	0.4	···	···	···	···
G324.642−00.321	15:37:23.7	−56:01:49.9	atca466	2013	4148	58.5	8450	275.18	1.12	A

Table C.1 continued

Table C.1: Non-tapered Image Continuum Properties of Multiple Detections (continued)

Target	R.A. J2000 (hh:mm:ss)	Decl. J2000 (dd:mm:ss)	Field	Epoch[a]	Beam Area (arcsec^2)	$\Delta\theta^b$ (arcsec)	ν_C (MHz)	S_C (mJy beam^{-1})	rms$_C$ (mJy beam^{-1})	QF
G324.642−00.321	15:37:26.8	−56:02:00.6	atca466	2013*	···	80.7	···	···	···	···
G325.108+00.053	15:38:35.7	−55:28:10.9	atca472	2013	4125	111.7	8450	72.62	0.74	B
G325.108+00.053	15:38:23.2	−55:27:33.6	atca472	2013*	···	1.6	···	···	···	···
G325.354−00.036	15:40:11.4	−55:23:08.8	atca475	2013	3999	18.3	8450	158.27	0.80	A
G325.354−00.036	15:40:09.2	−55:23:04.2	atca475	2013*	···	0.9	···	···	···	···
G326.657+00.588	15:44:43.3	−54:05:51.9	shrds1163	2016	1609	11.6	7023	6421.29	20.52	A
G326.657+00.588	15:44:43.1	−54:05:50.7	shrds1164	2016	1588	13.3	7023	6344.41	29.30	C
G326.721+00.773	15:44:14.9	−53:54:45.8	atca484	2013	4118	36.5	8450	116.41	4.18	B
G326.721+00.773	15:44:19.0	−53:54:54.6	atca484	2013*	···	1.2	···	···	···	···
G326.728+00.616	15:44:59.5	−54:02:14.6	shrds1164	2016	1588	11.2	7023	3633.95	9.90	A
G326.728+00.616	15:44:59.6	−54:02:15.5	shrds1163	2016	1609	11.2	7023	3601.45	56.80	C
G326.890−00.277	15:49:39.1	−54:38:18.1	atca486	2013	3904	8.5	8450	378.29	2.62	A
G326.890−00.277	15:49:40.0	−54:38:14.1	atca486	2013*	···	0.8	···	···	···	···
G326.916−01.100	15:53:26.9	−55:15:15.9	atca487	2013	4023	26.4	8450	88.72	0.80	A
G326.916−01.100	15:53:25.0	−55:15:36.9	atca487	2013*	···	0.8	···	···	···	···
G327.300−00.548	15:53:03.3	−54:35:25.5	caswell18	2016	2005	7.1	7023	17063.66	33.10	B
G327.300−00.548	15:53:02.9	−54:35:26.2	shrds1168	2016	1603	5.0	7023	15389.62	42.40	B
G327.300−00.548	15:53:03.1	−54:35:24.8	ch87.3.1	2013	3749	5.2	8450	21242.49	94.24	B
G327.300−00.548	15:53:03.7	−54:34:20.8	ch87.3.1	2013*	···	62.3	···	···	···	···
G327.400+00.444	15:49:19.7	−53:45:13.8	shrds621	2016	2009	9.3	7023	123.26	1.00	A
G327.400+00.444	15:49:19.8	−53:45:19.1	atca492	2013	3904	10.0	8450	118.56	2.23	B
G327.401+00.483	15:49:09.3	−53:44:17.8	shrds621	2016	2009	51.3	7023	65.96	1.25	B
G327.401+00.483	15:49:09.0	−53:44:14.8	atca492	2013	3904	48.3	8450	99.12	1.47	B
G327.401+00.483	15:49:09.1	−53:43:25.3	atca492	2013*	···	1.6	···	···	···	···
G327.555−00.829	15:55:46.3	−54:38:57.6	atca495	2013	3818	72.0	8450	98.22	1.99	B
G327.555−00.829	15:55:38.4	−54:38:38.5	atca495	2013*	···	0.8	···	···	···	···
G327.714+00.576	15:50:16.9	−53:27:43.7	atca498	2013	4075	71.7	8450	58.96	0.46	B

Table C.1 continued

Table C.1: Non-tapered Image Continuum Properties of Multiple Detections (continued)

Target	R.A. J2000 (hh:mm:ss)	Decl. J2000 (dd:mm:ss)	Field	Epoch[a]	Beam Area (arcsec^2)	$\Delta\theta^b$ (arcsec)	ν_C (MHz)	S_C (mJy beam^{-1})	rms$_C$ (mJy beam^{-1})	QF
G327.714+00.576	15:50:24.4	−53:27:19.9	atca498	2013*	···	0.3	···	···	···	···
G327.763+00.163	15:52:28.2	−53:44:54.9	atca501	2013	3782	27.9	8450	126.83	2.23	B
G327.763+00.163	15:52:25.2	−53:44:47.2	atca501	2013*	···	0.8	···	···	···	···
G331.057−00.229	16:10:36.6	−51:53:03.1	shrds711	2015	1749	27.7	7023	82.37	4.54	A
G331.057−00.229	16:10:36.7	−51:52:57.6	shrds716	2015	1346	25.4	7023	72.85	4.83	C
G331.123−00.530	16:12:14.0	−52:02:39.7	shrds717	2015	2302	36.8	7023	577.16	6.28	B
G331.123−00.530	16:12:13.9	−52:02:44.3	shrds721	2015	2268	32.0	7023	595.83	12.68	C
G331.127−00.481	16:12:01.4	−52:00:55.6	shrds717	2015	2302	3.2	7023	94.51	6.16	B
G331.127−00.481	16:12:01.3	−52:00:56.3	shrds721	2015	2268	2.3	7023	97.55	6.66	B
G331.129−00.243	16:10:59.1	−51:50:25.8	shrds716	2015	1346	5.7	7023	352.22	1.82	A
G331.129−00.243	16:10:59.5	−51:50:22.9	shrds711	2015	1749	9.3	7023	367.12	11.86	C
G331.172−00.460	16:12:07.8	−51:58:16.3	shrds721	2015	2268	7.6	7023	408.98	4.33	A
G331.172−00.460	16:12:07.5	−51:58:15.6	shrds717	2015	2302	9.7	7023	407.89	10.82	B
G331.172−00.460	16:12:08.2	−51:58:15.3	shrds720	2015	2176	4.2	7023	444.77	10.83	C
G332.382+00.080	16:15:30.9	−50:44:30.5	shrds763	2015	1448	72.7	7023	49.94	1.00	B
G332.382+00.080	16:15:30.7	−50:44:32.8	shrds766	2015	1605	70.2	7023	51.47	1.95	B
G332.415+00.053	16:16:01.2	−50:43:26.0	shrds763	2015	1448	216.6	7023	149.76	3.23	C
G332.415+00.053	16:16:00.6	−50:43:28.8	shrds766	2015	1605	209.9	7023	155.10	1.12	C
G332.657−00.622	16:19:39.0	−51:03:12.6	shrds771	2015	2190	56.4	7023	2236.41	20.17	C
G332.657−00.622	16:19:37.6	−51:03:17.7	shrds1181	2016	1967	68.0	7023	2004.47	22.09	C
G333.962+00.063	16:22:30.4	−49:39:00.3	shrds806	2015	3681	7.1	7022	149.25	1.27	A
G333.962+00.063	16:22:30.4	−49:38:54.8	shrds807	2016	1501	11.9	7023	105.09	2.40	B
G336.900−00.033	16:35:12.8	−47:35:34.2	shrds1212	2016	1972	0.8	7022	186.87	15.94	A
G336.900−00.033	16:35:12.2	−47:35:32.8	shrds862	2015	1279	7.0	7022	172.60	10.45	C
G337.709+00.091	16:37:52.4	−46:54:33.3	shrds886	2015	2094	6.1	7023	348.35	3.37	A
G337.709+00.091	16:37:52.5	−46:54:34.2	shrds881	2015	1502	4.9	7023	334.94	5.86	B
G337.754+00.057	16:38:05.4	−46:56:05.4	shrds886	2015	2094	144.1	7023	49.44	3.69	B

Table C.1 continued

Table C.1: Non-tapered Image Continuum Properties of Multiple Detections (continued)

Target	R.A. J2000 (hh:mm:ss)	Decl. J2000 (dd:mm:ss)	Field	Epoch[a]	Beam Area (arcsec^2)	$\Delta\theta^b$ (arcsec)	ν_C (MHz)	S_C (mJy beam^{-1})	rms$_C$ (mJy beam^{-1})	QF
G337.754+00.057	16:38:26.1	−46:54:51.1	shrds888	2015	1416	152.2	7023	36.73	1.23	B
G337.996+00.081	16:39:03.5	−46:42:22.9	shrds890	2015	1447	13.5	7023	111.64	3.20	A
G337.996+00.081	16:39:03.2	−46:42:28.3	shrds892	2015	1340	16.4	7023	103.67	4.90	C
G338.075+00.016	16:39:39.0	−46:41:24.2	shrds892	2015	1340	11.9	7023	1818.34	6.19	B
G338.075+00.016	16:39:38.7	−46:41:25.3	shrds893	2015	2084	10.5	7023	1915.16	6.74	B
G338.075+00.016	16:39:38.3	−46:41:24.5	shrds1219	2016	1480	7.9	7022	1745.44	12.60	C
G338.374−00.152	16:41:30.8	−46:34:32.4	caswell22	2016	1718	3.5	7022	263.24	12.01	B
G338.374−00.152	16:41:31.2	−46:34:31.4	shrds896	2015	1779	1.4	7023	273.87	16.09	C
G338.405−00.203	16:41:51.7	−46:35:08.2	caswell22	2016	1718	1.2	7022	1974.80	5.90	A
G338.405−00.203	16:41:51.0	−46:35:05.7	shrds898	2015	2221	8.4	7023	2036.43	11.09	C
G338.917+00.382	16:41:16.6	−45:48:50.3	shrds905	2015	1187	3.2	7022	249.13	1.91	C
G338.917+00.382	16:41:16.1	−45:48:50.3	shrds906	2015	1838	5.4	7023	281.16	1.63	C

[a] Rows with epochs with an asterisk (*) are copied directly from Brown et al. (2017). They did not give the continuum fluxes for their detections.

[b] The separation between the *WISE* Catalog infrared position and the position of the SHRDS continuum peak.

Table C.2: *uv*-tapered Image Continuum Properties of Multiple Detections

Target	R.A. J2000 (hh:mm:ss)	Decl. J2000 (dd:mm:ss)	Field	Epoch[a]	Beam Area (arcsec^2)	$\Delta\theta^b$ (arcsec)	ν_C (MHz)	S_C (mJy beam^{-1})	rms$_C$ (mJy beam^{-1})	QF
G289.944−00.889	11:01:11.1	−60:56:48.0	shrds191	2015	9232	10.1	7023	145.89	3.69	A
G289.944−00.889	11:01:09.7	−60:56:44.3	g290.012-00.867	2014	7104	13.1	6050	131.86	10.48	B
G290.012−00.867	11:01:59.1	−60:56:49.2	g290.012-00.867	2014	7104	105.8	6050	196.21	5.43	B
G290.012−00.867	11:01:45.4	−60:57:25.8	g290.012-00.867	2014*	···	0.8	···	···	···	···
G290.323−02.984	10:56:33.0	−63:00:44.2	g290.323-02.984	2014	7202	27.2	6050	29.11	0.46	A
G290.323−02.984	10:56:36.4	−63:00:35.0	g290.323-02.984	2014*	···	2.9	···	···	···	···
G290.385−01.042	11:03:59.5	−61:16:04.9	g290.385-01.042	2014	7084	1.4	6050	24.97	1.35	A
G290.385−01.042	11:03:59.4	−61:16:06.7	g290.385-01.042	2014*	···	0.6	···	···	···	···
G291.281−00.726	11:11:52.9	−61:18:48.3	caswell3	2016	9253	40.1	7023	60503.27	235.80	A
G291.281−00.726	11:11:54.1	−61:18:38.8	shrds1034	2016	9325	49.6	7023	62445.63	357.51	C
G291.596−00.239	11:15:49.9	−60:59:20.6	g291.596-00.239	2014	7121	13.1	6050	37.46	25.11	C
G291.596−00.239	11:15:48.1	−60:59:17.7	g291.596-00.239	2014*	···	2.5	···	···	···	···
G293.936−00.873	11:32:38.8	−62:21:31.8	g293.936-00.873	2014	7287	6.8	6050	121.99	2.82	B
G293.936−00.873	11:32:39.3	−62:21:38.8	g293.936-00.873	2014*	···	1.6	···	···	···	···
G293.952−00.894	11:32:43.4	−62:23:11.8	g293.936-00.873	2014	7287	5.7	6050	127.53	3.16	B
G293.952−00.894	11:32:43.6	−62:23:05.5	g293.994-00.934	2014	7289	3.4	6050	120.46	5.91	B
G293.967−00.984	11:32:36.6	−62:28:22.4	shrds219	2015	9356	10.3	7023	224.20	1.04	A
G293.967−00.984	11:32:36.1	−62:28:25.4	g293.994-00.934	2014	7289	11.2	6050	177.95	5.79	B
G293.994−00.934	11:32:58.6	−62:26:05.2	g293.994-00.934	2014	7289	3.4	6050	294.20	3.54	A
G293.994−00.934	11:32:59.7	−62:25:58.4	shrds219	2015	9356	12.5	7023	302.07	1.88	B
G293.994−00.934	11:32:59.0	−62:26:11.6	g293.936-00.873	2014	7287	3.8	6050	306.45	8.32	C
G293.994−00.934	11:32:58.5	−62:26:10.8	g293.994-00.934	2014*	···	2.3	···	···	···	···
G294.988−00.538	11:42:10.3	−62:20:09.5	g294.988-00.538	2014	9367	0.9	6050	163.76	1.64	A
G294.988−00.538	11:42:10.1	−62:20:11.7	g294.988-00.538	2014*	···	2.9	···	···	···	···
G295.275−00.255	11:44:54.8	−62:08:05.1	g295.275-00.255	2014	10997	112.4	6050	23.73	1.98	B
G295.275−00.255	11:45:10.8	−62:08:15.7	g295.275-00.255	2014*	···	2.0	···	···	···	···
G295.748−00.207	11:49:12.1	−62:12:25.3	g295.748-00.207	2014	11002	3.2	6050	83.80	1.08	A

Table C.2 continued

Table C.2: *uv*-tapered Image Continuum Properties of Multiple Detections (continued)

Target	R.A. J2000 (hh:mm:ss)	Decl. J2000 (dd:mm:ss)	Field	Epoch[a]	Beam Area (arcsec^2)	$\Delta\theta^b$ (arcsec)	ν_C (MHz)	S_C (mJy beam^{-1})	rms$_C$ (mJy beam^{-1})	QF
G295.748−00.207	11:49:12.5	−62:12:27.5	g295.748-00.207	2014*	···	1.5	···	···	···	···
G297.248−00.754	12:00:55.5	−63:04:05.6	g297.248-00.754	2014	10913	6.3	6050	316.90	2.12	A
G297.248−00.754	12:00:55.3	−63:04:00.9	g297.248-00.754	2014*	···	1.6	···	···	···	···
G297.626−00.906	12:03:58.2	−63:17:09.1	g297.626-00.906	2014	11074	6.5	6050	174.48	3.49	A
G297.626−00.906	12:03:57.4	−63:17:15.2	g297.626-00.906	2014*	···	1.8	···	···	···	···
G298.473+00.104	12:12:49.9	−62:25:54.9	g298.473+00.104	2014	11055	32.3	6050	121.93	3.60	A
G298.473+00.104	12:12:45.3	−62:25:56.6	g298.473+00.104	2014*	···	1.8	···	···	···	···
G299.349−00.267	12:19:53.0	−62:55:13.6	caswell6	2016	8956	7.3	7023	371.53	1.81	B
G299.349−00.267	12:19:51.3	−62:55:22.5	shrds1046	2016	8725	18.8	7023	374.57	3.48	C
G300.983+01.117	12:35:01.3	−61:41:47.3	g300.983+01.117	2014	10927	20.3	6050	74.99	4.49	A
G300.983+01.117	12:34:53.0	−61:39:20.6	caswell7	2016	9123	138.7	7023	1600.66	5.87	B
G300.983+01.117	12:34:59.4	−61:41:33.0	g300.983+01.117	2014*	···	1.4	···	···	···	···
G311.629+00.289	14:04:54.6	−61:20:05.5	caswell12	2016	9111	10.6	7023	2461.56	10.74	A
G311.629+00.289	14:04:56.2	−61:19:47.3	shrds428	2016	8625	17.5	7023	2407.24	14.59	C
G313.671−00.105	14:22:04.0	−61:04:19.8	atca348	2013	8829	0.8	8450	102.68	0.58	A
G313.671−00.105	14:22:04.1	−61:04:18.7	atca348	2013*	···	1.0	···	···	···	···
G313.790+00.705	14:20:41.9	−60:15:51.9	atca352	2013	9016	24.8	8450	361.87	1.69	A
G313.790+00.705	14:20:43.8	−60:16:11.0	atca352	2013*	···	1.0	···	···	···	···
G314.219+00.343	14:25:01.6	−60:27:52.8	atca361	2013	8689	16.9	8450	382.92	7.50	A
G314.219+00.343	14:24:59.9	−60:27:40.0	atca361	2013*	···	1.1	···	···	···	···
G315.312−00.272	14:35:07.0	−60:37:29.7	ch87.1	2013	8758	6.2	8450	264.75	2.92	A
G315.312−00.272	14:35:07.1	−60:37:41.7	ch87.1	2013*	···	6.6	···	···	···	···
G316.516−00.600	14:45:05.7	−60:26:18.6	atca382	2013	8604	21.4	8450	116.46	0.64	A
G316.516−00.600	14:45:08.6	−60:26:15.6	atca382	2013*	···	0.2	···	···	···	···
G317.570−00.257	14:51:26.9	−59:40:12.5	shrds521	2015	8261	48.3	7023	18.76	2.11	A
G317.570−00.257	14:51:28.2	−59:40:16.6	atca397	2013	8465	38.1	8450	15.66	3.79	A
G317.861+00.160	14:52:05.9	−59:10:09.8	atca402	2013	8615	19.7	8450	458.63	4.18	B

Table C.2 continued

Table C.2: *uv*-tapered Image Continuum Properties of Multiple Detections (continued)

Target	R.A. J2000 (hh:mm:ss)	Decl. J2000 (dd:mm:ss)	Field	Epoch[a]	Beam Area (arcsec^2)	$\Delta\theta^b$ (arcsec)	ν_C (MHz)	S_C (mJy beam^{-1})	rms$_C$ (mJy beam^{-1})	QF
G317.861+00.160	14:52:08.4	−59:10:03.4	atca402	2013*	···	1.3	···	···	···	···
G318.248+00.150	14:55:05.0	−59:00:55.9	atca406	2013	8603	115.7	8450	57.09	5.74	B
G318.248+00.150	14:54:51.5	−59:00:02.7	atca406	2013*	···	1.2	···	···	···	···
G319.229+00.225	15:01:21.1	−58:27:15.9	atca412	2013	8934	87.6	8450	96.09	1.61	B
G319.229+00.225	15:01:16.7	−58:28:37.4	atca412	2013*	···	1.3	···	···	···	···
G322.162+00.625	15:18:38.8	−56:38:52.8	caswell15	2016	9149	3.9	7023	8280.75	47.65	A
G322.162+00.625	15:18:37.8	−56:38:43.1	shrds1151	2016	9252	8.8	7023	8348.90	59.60	C
G323.449+00.095	15:28:32.0	−56:22:57.8	atca449	2013	9069	11.8	8450	95.96	1.91	A
G323.449+00.095	15:28:33.2	−56:23:06.2	atca449	2013*	···	0.8	···	···	···	···
G323.464−00.079	15:29:19.1	−56:31:23.8	atca450	2013	9153	20.6	8450	677.85	2.51	A
G323.464−00.079	15:29:21.2	−56:31:12.7	atca450	2013*	···	0.9	···	···	···	···
G323.743−00.249	15:31:44.0	−56:30:14.9	atca456	2013	9097	14.2	8450	146.61	0.81	A
G323.743−00.249	15:31:43.1	−56:30:03.9	atca456	2013*	···	1.0	···	···	···	···
G323.806+00.020	15:31:05.2	−56:14:29.0	atca459	2013	9034	56.2	8450	291.92	1.97	A
G323.806+00.020	15:30:58.6	−56:14:36.8	atca459	2013*	···	0.2	···	···	···	···
G323.936−00.038	15:31:56.6	−56:11:04.9	atca462	2013	9085	117.3	8450	41.94	4.57	B
G323.936−00.038	15:31:58.9	−56:13:00.3	atca462	2013*	···	0.4	···	···	···	···
G324.642−00.321	15:37:23.2	−56:01:50.1	atca466	2013	9060	54.6	8450	317.76	2.08	A
G324.642−00.321	15:37:26.8	−56:02:00.6	atca466	2013*	···	80.7	···	···	···	···
G325.108+00.053	15:38:35.7	−55:28:23.0	atca472	2013	8900	115.9	8450	97.88	1.57	B
G325.108+00.053	15:38:23.2	−55:27:33.6	atca472	2013*	···	1.6	···	···	···	···
G325.354−00.036	15:40:11.4	−55:23:05.1	atca475	2013	8825	17.9	8450	198.02	1.71	A
G325.354−00.036	15:40:09.2	−55:23:04.2	atca475	2013*	···	0.9	···	···	···	···
G326.657+00.588	15:44:43.2	−54:05:55.8	shrds1163	2016	9201	9.4	7023	10592.22	86.86	A
G326.657+00.588	15:44:41.7	−54:06:10.5	shrds1164	2016	8874	23.7	7023	10967.80	148.99	C
G326.721+00.773	15:44:16.8	−53:54:34.0	atca484	2013	8945	27.4	8450	193.77	7.41	A
G326.721+00.773	15:44:19.0	−53:54:54.6	atca484	2013*	···	1.2	···	···	···	···

Table C.2 continued

Table C.2: *uv*-tapered Image Continuum Properties of Multiple Detections (continued)

Target	R.A. J2000 (hh:mm:ss)	Decl. J2000 (dd:mm:ss)	Field	Epoch[a]	Beam Area (arcsec^2)	$\Delta\theta^b$ (arcsec)	ν_C (MHz)	S_C (mJy beam^{-1})	rms$_C$ (mJy beam^{-1})	QF
G326.728+00.616	15:44:59.5	−54:02:14.7	shrds1164	2016	8874	11.2	7023	3975.21	41.68	A
G326.728+00.616	15:45:01.0	−54:01:55.6	shrds1163	2016	9201	12.0	7023	4156.23	289.37	C
G326.890−00.277	15:49:39.1	−54:38:18.1	atca486	2013	8685	8.5	8450	408.89	7.41	A
G326.890−00.277	15:49:40.0	−54:38:14.1	atca486	2013*	···	0.8	···	···	···	···
G326.916−01.100	15:53:25.5	−55:15:15.9	atca487	2013	8763	21.0	8450	135.18	1.54	A
G326.916−01.100	15:53:25.0	−55:15:36.9	atca487	2013*	···	0.8	···	···	···	···
G327.300−00.548	15:53:03.3	−54:35:21.6	caswell18	2016	8991	6.4	7023	26594.54	85.78	A
G327.300−00.548	15:53:02.5	−54:35:22.4	shrds1168	2016	9148	1.0	7023	26946.33	194.38	B
G327.300−00.548	15:53:03.5	−54:35:24.8	ch87.3.1	2013	8209	8.8	8450	25983.44	170.90	B
G327.300−00.548	15:53:03.7	−54:34:20.8	ch87.3.1	2013*	···	62.3	···	···	···	···
G327.400+00.444	15:49:19.6	−53:45:13.9	shrds621	2016	8563	9.0	7023	138.57	4.51	B
G327.400+00.444	15:49:19.4	−53:45:14.7	atca492	2013	8493	6.7	8450	123.04	8.87	B
G327.401+00.483	15:49:09.2	−53:43:57.9	shrds621	2016	8563	31.4	7023	151.98	5.98	B
G327.401+00.483	15:49:08.6	−53:43:58.8	atca492	2013	8493	32.8	8450	149.56	5.88	B
G327.401+00.483	15:49:09.1	−53:43:25.3	atca492	2013*	···	1.6	···	···	···	···
G327.555−00.829	15:55:46.3	−54:39:05.9	atca495	2013	8320	74.5	8450	143.61	4.46	B
G327.555−00.829	15:55:38.4	−54:38:38.5	atca495	2013*	···	0.8	···	···	···	···
G327.714+00.576	15:50:17.3	−53:27:51.9	atca498	2013	8768	71.6	8450	90.89	0.91	A
G327.714+00.576	15:50:24.4	−53:27:19.9	atca498	2013*	···	0.3	···	···	···	···
G327.763+00.163	15:52:27.7	−53:44:46.6	atca501	2013	8494	22.7	8450	197.40	5.52	A
G327.763+00.163	15:52:25.2	−53:44:47.2	atca501	2013*	···	0.8	···	···	···	···
G331.123−00.530	16:12:12.7	−52:02:39.6	shrds717	2015	8983	35.9	7023	1265.81	18.02	B
G331.123−00.530	16:12:13.0	−52:03:04.2	shrds721	2015	8878	11.2	7023	1276.29	53.15	C
G331.172−00.460	16:12:07.8	−51:58:12.3	shrds721	2015	8878	6.6	7023	548.35	15.69	A
G331.172−00.460	16:12:07.9	−51:58:03.8	shrds717	2015	8983	10.3	7023	582.63	34.14	B
G331.172−00.460	16:12:09.5	−51:58:27.3	shrds720	2015	8907	17.0	7023	664.03	65.70	C
G333.962+00.063	16:22:30.5	−49:39:00.0	shrds806	2015	9436	7.1	7022	176.02	2.84	A

Table C.2 continued

Table C.2: *uv*-tapered Image Continuum Properties of Multiple Detections (continued)

Target	R.A. J2000 (hh:mm:ss)	Decl. J2000 (dd:mm:ss)	Field	Epoch[a]	Beam Area (arcsec^2)	$\Delta\theta^b$ (arcsec)	ν_C (MHz)	S_C (mJy beam^{-1})	rms$_C$ (mJy beam^{-1})	QF
G333.962+00.063	16:22:30.4	−49:39:14.8	shrds807	2016	8219	9.6	7023	172.61	10.79	B
G337.709+00.091	16:37:52.8	−46:54:37.4	shrds886	2015	8825	1.3	7023	418.78	10.95	A
G337.709+00.091	16:37:54.1	−46:54:30.0	shrds881	2015	7206	16.3	7023	413.27	28.84	C
G338.075+00.016	16:39:39.3	−46:41:16.0	shrds892	2015	8013	13.8	7023	2077.43	29.09	B
G338.075+00.016	16:39:38.7	−46:41:29.3	shrds893	2015	8991	13.9	7023	2122.57	19.69	B
G338.405−00.203	16:41:52.1	−46:35:08.4	caswell22	2016	8110	4.1	7022	2508.80	17.22	A
G338.405−00.203	16:41:50.2	−46:35:09.6	shrds898	2015	8631	15.7	7023	2582.93	26.35	C

[a] Rows with epochs with an asterisk (*) are copied directly from Brown et al. (2017). They did not give the continuum fluxes for their detections.

[b] The separation between the *WISE* Catalog infrared position and the position of the SHRDS continuum peak.

Table C.3: Non-tapered Image RRL Properties of Multiple Detections

Target	Field	Epoch[a]	ν_L[b] (MHz)	S_L (mJy beam^{-1})	$V_{\rm LSR}$ (km s^{-1})	ΔV (km s^{-1})	rms$_L$ (mJy beam^{-1})	S/N	QF
G289.944−00.889	shrds191	2015	6800	8.60 ± 0.50	31.50 ± 0.70	23.60 ± 1.70	1.40	13.6	B
G289.944−00.889	g290.012-00.867	2014	5193	11.70 ± 3.10	31.80 ± 1.70	13.10 ± 4.20	5.10	3.7	C
G290.012−00.867	g290.012-00.867	2014	6134	···	···	···	3.00	···	D
G290.012−00.867	g290.012-00.867	2014*	···	3.60 ± 2.50	14.70 ± 8.30	24.90 ± 8.60	1.80	4.5	C
G290.323−02.984	g290.323-02.984	2014	5874	···	···	···	2.50	···	D
G290.323−02.984	g290.323-02.984	2014*	···	3.50 ± 2.10	-17.70 ± 8.00	28.30 ± 8.30	1.50	5.6	C
G290.385−01.042	g290.385-01.042	2014	5911	···	···	···	2.30	···	D
G290.385−01.042	g290.385-01.042	2014*	···	4.00 ± 2.90	9.91 ± 4.60	13.20 ± 4.70	1.90	3.4	C
G290.674−00.133	g290.674-00.133	2014	6624	···	···	···	7.40	···	D
G290.674−00.133	g290.674-00.133	2014*	···	5.20 ± 2.40	19.30 ± 5.20	23.20 ± 5.30	1.40	8.0	C
G291.281−00.726	caswell3	2016	5468	2534.20 ± 27.10	-24.10 ± 0.20	33.20 ± 0.40	59.80	108.1	A
G291.281−00.726	shrds1034	2016	5766	2468.10 ± 18.10	-24.60 ± 0.10	31.40 ± 0.30	71.80	85.4	A
G291.596−00.239	g291.596-00.239	2014	6415	···	···	···	3.80	···	D
G291.596−00.239	g291.596-00.239	2014*	···	15.30 ± 3.70	11.40 ± 5.10	44.20 ± 5.40	2.50	18.0	A
G292.889−00.831	g292.889-00.831	2014	6224	···	···	···	2.40	···	D
G292.889−00.831	g292.889-00.831	2014*	···	4.80 ± 2.30	21.80 ± 7.10	30.00 ± 7.30	1.40	8.4	C
G293.936−00.873	g293.936-00.873	2014	6118	···	···	···	2.90	···	D
G293.936−00.873	g293.936-00.873	2014*	···	16.40 ± 2.20	36.60 ± 1.40	22.30 ± 1.50	2.00	17.0	A
G293.952−00.894	g293.936-00.873	2014	6173	···	···	···	3.30	···	D
G293.952−00.894	g293.994-00.934	2014	5855	···	···	···	4.00	···	D
G293.967−00.984	shrds219	2015	6710	10.60 ± 0.50	27.80 ± 0.70	30.50 ± 1.60	1.30	20.2	A
G293.967−00.984	g293.994-00.934	2014	5610	···	···	···	4.50	···	D
G293.994−00.934	shrds219	2015	6070	16.20 ± 0.90	46.30 ± 0.70	25.10 ± 1.60	2.20	16.2	A
G293.994−00.934	g293.936-00.873	2014	5279	···	···	···	8.90	···	D
G293.994−00.934	g293.994-00.934	2014	5902	16.80 ± 1.60	45.80 ± 0.90	20.00 ± 2.20	3.40	9.9	C
G293.994−00.934	g293.994-00.934	2014*	···	18.60 ± 2.60	46.50 ± 1.70	25.60 ± 1.80	1.30	32.0	A
G294.988−00.538	g294.988-00.538	2014	6017	9.10 ± 0.80	39.40 ± 1.10	26.20 ± 2.70	2.00	10.1	B
G294.988−00.538	g294.988-00.538	2014*	···	9.70 ± 1.40	39.80 ± 1.90	27.40 ± 2.00	1.20	19.0	A

Table C.3 continued

Table C.3: Non-tapered Image RRL Properties of Multiple Detections (continued)

Target	Field	Epoch[a]	ν_L[b] (MHz)	S_L (mJy beam^{-1})	$V_{\rm LSR}$ (km s^{-1})	ΔV (km s^{-1})	rms$_L$ (mJy beam^{-1})	S/N	QF
G295.275−00.255	g295.275-00.255	2014	5900	···	···	···	2.70	···	D
G295.275−00.255	g295.275-00.255	2014*	···	5.60 ± 2.30	30.10 ± 6.20	30.60 ± 6.30	1.60	8.7	C
G295.748−00.207	g295.748-00.207	2014	6001	···	···	···	3.00	···	D
G295.748−00.207	g295.748-00.207	2014*	···	7.20 ± 2.10	23.30 ± 3.50	23.90 ± 3.50	1.60	9.8	C
G297.248−00.754	g297.248-00.754	2014	5957	16.20 ± 1.50	24.10 ± 1.30	28.90 ± 3.20	3.00	12.7	B
G297.248−00.754	g297.248-00.754	2014*	···	22.60 ± 2.90	22.60 ± 1.50	24.40 ± 1.60	1.90	26.0	A
G297.626−00.906	g297.626-00.906	2014	6168	7.30 ± 1.10	32.60 ± 2.50	32.40 ± 5.90	3.00	6.2	C
G297.626−00.906	g297.626-00.906	2014*	···	16.10 ± 2.50	31.30 ± 2.10	28.40 ± 2.20	1.50	26.0	A
G298.473+00.104	g298.473+00.104	2014	5992	···	···	···	3.30	···	D
G298.473+00.104	g298.473+00.104	2014*	···	12.20 ± 2.20	32.90 ± 2.00	23.50 ± 2.10	2.00	13.0	B
G299.349−00.267	caswell6	2016	6535	19.40 ± 0.60	-40.50 ± 0.30	20.60 ± 0.70	1.30	29.5	A
G299.349−00.267	shrds1046	2016	5557	23.00 ± 1.80	-41.80 ± 0.70	19.00 ± 1.70	2.70	16.6	A
G300.983+01.117	caswell7	2016	6611	67.40 ± 0.80	-38.60 ± 0.10	25.50 ± 0.30	3.00	50.3	A
G300.983+01.117	g300.983+01.117	2014	6169	···	···	···	2.20	···	D
G300.983+01.117	g300.983+01.117	2014*	···	83.80 ± 2.80	-42.00 ± 0.40	26.50 ± 0.40	3.30	26.0	A
G311.629+00.289	caswell12	2016	6807	133.50 ± 1.10	-56.30 ± 0.10	35.30 ± 0.30	2.60	136.9	A
G311.629+00.289	shrds428	2016	5589	97.70 ± 1.30	-55.60 ± 0.20	37.50 ± 0.60	2.80	95.9	A
G312.675+00.048	shrds462	2015	5945	9.90 ± 0.60	-61.60 ± 0.60	21.20 ± 1.50	1.30	15.4	A
G312.675+00.048	shrds458	2016	5311	11.40 ± 1.80	-63.00 ± 1.90	24.40 ± 4.60	3.00	8.3	C
G313.671−00.105	atca348	2013	7941	8.70 ± 0.50	-53.20 ± 0.60	21.10 ± 1.30	1.10	15.6	A
G313.671−00.105	atca348	2013*	···	12.00 ± 1.40	-54.60 ± 1.40	24.60 ± 1.50	1.60	17.0	A
G313.790+00.705	atca352	2013	8045	34.20 ± 1.10	-57.90 ± 0.30	21.60 ± 0.80	2.30	31.1	A
G313.790+00.705	atca352	2013*	···	38.70 ± 3.00	-57.20 ± 0.90	22.60 ± 0.90	2.60	32.0	A
G314.219+00.343	atca361	2013	7922	42.90 ± 1.50	-63.30 ± 0.30	20.10 ± 0.80	2.30	36.6	A
G314.219+00.343	atca361	2013*	···	66.40 ± 3.10	-62.50 ± 0.40	20.00 ± 0.50	3.50	38.0	A
G315.312−00.272	ch87.1	2013	7878	20.10 ± 1.00	15.20 ± 0.60	24.50 ± 1.40	2.30	19.5	A
G315.312−00.272	ch87.1	2013*	···	30.00 ± 3.60	14.20 ± 1.40	24.00 ± 1.40	3.60	18.0	A
G316.516−00.600	atca382	2013	7889	13.30 ± 0.50	-45.60 ± 0.40	19.10 ± 0.90	1.20	21.7	A

Table C.3 continued

Table C.3: Non-tapered Image RRL Properties of Multiple Detections (continued)

Target	Field	Epoch[a]	ν_L[b] (MHz)	S_L (mJy beam^{-1})	$V_{\rm LSR}$ (km s^{-1})	ΔV (km s^{-1})	rms$_L$ (mJy beam^{-1})	S/N	QF
G316.516−00.600	atca382	2013*	···	19.00 ± 1.70	-45.60 ± 0.90	19.90 ± 0.90	1.70	22.0	A
G317.570−00.257	shrds521	2015	6309	···	···	···	1.70	···	D
G317.570−00.257	atca397	2013	7721	···	···	···	1.50	···	D
G317.861+00.160	atca402	2013	7905	37.50 ± 1.10	1.30 ± 0.30	24.10 ± 0.80	2.20	36.9	A
G317.861+00.160	atca402	2013*	···	55.60 ± 4.60	1.53 ± 0.90	22.90 ± 0.90	2.70	44.0	A
G318.248+00.150	atca406	2013	7818	4.90 ± 1.10	-36.80 ± 3.30	28.70 ± 9.50	2.00	5.9	C
G318.248+00.150	atca406	2013*	···	17.00 ± 3.70	-39.90 ± 2.00	19.00 ± 2.00	2.80	12.0	B
G319.229+00.225	atca412	2013	7476	7.80 ± 0.80	-68.70 ± 1.00	20.90 ± 2.50	1.50	10.4	B
G319.229+00.225	atca412	2013*	···	12.90 ± 2.20	-66.10 ± 1.80	20.90 ± 1.80	1.90	14.0	B
G320.778+00.241	shrds1146	2016	6095	14.10 ± 0.70	-5.60 ± 0.60	26.00 ± 1.50	1.70	18.5	A
G320.778+00.241	shrds1147	2016	5698	11.80 ± 0.90	-4.60 ± 1.20	30.30 ± 2.90	2.70	10.6	B
G322.162+00.625	caswell15	2016	5966	501.90 ± 1.70	-52.10 ± 0.00	28.10 ± 0.10	4.10	287.7	A
G322.162+00.625	shrds1151	2016	5634	456.00 ± 2.20	-52.10 ± 0.10	28.60 ± 0.20	6.20	173.4	A
G323.449+00.095	atca449	2013	8183	11.70 ± 0.80	-75.00 ± 0.80	22.10 ± 1.80	1.30	18.3	A
G323.449+00.095	atca449	2013*	···	13.80 ± 2.10	-75.10 ± 1.70	22.50 ± 1.70	2.00	15.0	B
G323.464−00.079	atca450	2013	8285	30.40 ± 0.80	-67.50 ± 0.60	29.90 ± 1.40	1.20	61.3	C
G323.464−00.079	atca450	2013*	···	28.00 ± 2.20	-68.80 ± 1.20	38.30 ± 1.20	1.30	45.0	A
G323.743−00.249	atca456	2013	8234	21.90 ± 0.50	-47.90 ± 0.20	17.40 ± 0.40	1.40	28.2	A
G323.743−00.249	atca456	2013*	···	22.80 ± 1.80	-47.30 ± 0.70	19.20 ± 0.70	2.20	20.0	A
G323.806+00.020	atca459	2013	7902	22.40 ± 0.50	-60.80 ± 0.30	25.30 ± 0.70	1.90	26.8	A
G323.806+00.020	atca459	2013*	···	31.60 ± 2.70	-58.90 ± 0.90	21.60 ± 0.90	2.70	24.0	A
G323.936−00.038	shrds590	2015	6418	···	···	···	1.50	···	D
G323.936−00.038	atca462	2013	7328	7.20 ± 1.60	-60.30 ± 1.90	17.80 ± 4.50	2.00	6.7	C
G323.936−00.038	atca462	2013*	···	13.80 ± 5.20	-57.30 ± 4.50	24.50 ± 4.60	2.40	12.7	B
G324.642−00.321	atca466	2013	8084	31.20 ± 1.30	-47.00 ± 0.40	21.90 ± 1.00	2.30	28.3	A
G324.642−00.321	atca466	2013*	···	28.70 ± 4.80	-47.80 ± 1.70	21.30 ± 1.80	2.90	20.0	A
G325.108+00.053	atca472	2013	7770	11.20 ± 0.70	-61.20 ± 0.70	21.10 ± 1.60	1.70	13.1	B
G325.108+00.053	atca472	2013*	···	11.50 ± 3.10	-67.80 ± 2.70	20.40 ± 2.70	3.20	7.3	C

Table C.3 continued

Table C.3: Non-tapered Image RRL Properties of Multiple Detections (continued)

Target	Field	Epoch[a]	ν_L[b] (MHz)	S_L (mJy beam^{-1})	$V_{\rm LSR}$ (km s^{-1})	ΔV (km s^{-1})	rms$_L$ (mJy beam^{-1})	S/N	QF
G325.354−00.036	atca475	2013	8034	14.60 ± 0.90	-62.80 ± 0.70	25.20 ± 1.70	1.60	20.4	A
G325.354−00.036	atca475	2013*	···	15.00 ± 1.50	-63.80 ± 0.60	34.40 ± 1.50	1.40	26.0	A
G326.657+00.588	shrds1163	2016	5998	630.20 ± 1.60	-44.10 ± 0.00	26.00 ± 0.10	7.20	197.4	A
G326.657+00.588	shrds1164	2016	5493	611.90 ± 2.60	-44.00 ± 0.10	26.50 ± 0.10	8.10	171.4	A
G326.721+00.773	atca484	2013	7623	20.80 ± 0.80	-38.20 ± 0.40	22.20 ± 1.00	2.60	16.5	A
G326.721+00.773	atca484	2013*	···	45.50 ± 3.70	-40.60 ± 0.90	22.60 ± 0.90	4.90	20.0	A
G326.728+00.616	shrds1163	2016	5574	198.90 ± 1.90	-40.50 ± 0.20	35.00 ± 0.40	5.20	100.0	A
G326.728+00.616	shrds1164	2016	6426	236.70 ± 1.60	-41.00 ± 0.10	33.70 ± 0.30	1.80	340.7	A
G326.890−00.277	atca486	2013	8168	59.50 ± 0.90	-44.40 ± 0.10	19.20 ± 0.40	1.90	60.5	A
G326.890−00.277	atca486	2013*	···	63.20 ± 4.50	-44.20 ± 0.70	19.10 ± 0.70	3.50	35.0	A
G326.916−01.100	atca487	2013	7797	14.50 ± 1.20	-51.40 ± 0.90	20.30 ± 2.00	2.10	13.8	B
G326.916−01.100	atca487	2013*	···	18.90 ± 3.40	-49.80 ± 1.80	21.00 ± 1.90	4.40	8.8	C
G327.300−00.548	caswell18	2016	5795	1508.20 ± 8.60	-48.30 ± 0.10	29.40 ± 0.20	15.60	231.6	A
G327.300−00.548	shrds1168	2016	5836	1390.90 ± 8.50	-48.20 ± 0.10	29.50 ± 0.20	20.90	160.1	A
G327.300−00.548	ch87.3.1	2013	7349	2288.20 ± 12.60	-48.20 ± 0.10	28.20 ± 0.20	24.90	215.9	A
G327.300−00.548	ch87.3.1	2013*	···	2280.00 ± 41.70	-48.50 ± 0.20	28.10 ± 0.30	33.10	163.0	A
G327.400+00.444	shrds621	2016	7127	2.30 ± 0.20	-80.10 ± 5.10	102.90 ± 16.40	0.90	12.0	C
G327.400+00.444	atca492	2013	7945	···	···	···	3.60	···	D
G327.401+00.483	shrds621	2016	6253	12.80 ± 0.60	-76.50 ± 0.40	18.10 ± 1.00	1.30	19.1	A
G327.401+00.483	atca492	2013	7794	19.80 ± 1.30	-75.40 ± 0.60	19.00 ± 1.50	2.40	16.2	A
G327.401+00.483	atca492	2013*	···	31.50 ± 6.10	-76.30 ± 1.70	17.70 ± 1.70	2.60	23.0	A
G327.555−00.829	atca495	2013	7827	11.80 ± 1.00	-38.40 ± 1.10	26.50 ± 2.80	2.20	12.1	B
G327.555−00.829	atca495	2013*	···	16.50 ± 3.50	-41.70 ± 2.60	24.80 ± 2.60	4.00	9.2	C
G327.714+00.576	atca498	2013	7691	8.10 ± 0.50	-52.10 ± 0.80	25.10 ± 1.90	1.30	13.9	B
G327.714+00.576	atca498	2013*	···	12.00 ± 2.70	-47.40 ± 2.40	21.90 ± 2.50	2.10	12.0	B
G327.763+00.163	atca501	2013	7916	18.90 ± 0.90	-92.40 ± 0.60	22.80 ± 1.30	1.80	22.4	A
G327.763+00.163	atca501	2013*	···	30.10 ± 3.40	-92.80 ± 1.20	21.60 ± 1.20	2.60	24.0	A
G331.057−00.229	shrds711	2015	6553	6.60 ± 0.90	-92.00 ± 1.60	24.90 ± 3.90	2.10	7.0	C

Table C.3 continued

Table C.3: Non-tapered Image RRL Properties of Multiple Detections (continued)

Target	Field	Epoch[a]	ν_L[b] (MHz)	S_L (mJy beam^{-1})	$V_{\rm LSR}$ (km s^{-1})	ΔV (km s^{-1})	rms$_L$ (mJy beam^{-1})	S/N	QF
G331.057−00.229	shrds716	2015	5518	11.00 ± 1.20	-90.50 ± 0.90	16.60 ± 2.10	2.60	7.7	C
G331.123−00.530	shrds717	2015	6247	84.00 ± 1.20	-67.90 ± 0.10	19.90 ± 0.30	2.90	57.3	A
G331.123−00.530	shrds721	2015	5539	82.50 ± 2.40	-67.90 ± 0.30	21.50 ± 0.70	5.30	32.3	A
G331.127−00.481	shrds717	2015	6523	11.50 ± 1.00	-66.20 ± 0.80	18.30 ± 1.90	1.90	11.6	B
G331.127−00.481	shrds721	2015	6147	10.30 ± 1.40	-65.60 ± 1.20	17.80 ± 2.80	2.50	7.8	C
G331.129−00.243	shrds711	2015	5756	27.40 ± 1.90	-81.50 ± 1.00	31.40 ± 2.50	5.10	13.4	B
G331.129−00.243	shrds716	2015	6997	35.20 ± 0.50	-84.30 ± 0.20	23.10 ± 0.60	0.90	79.4	C
G331.172−00.460	shrds717	2015	5802	50.30 ± 1.70	-69.80 ± 0.40	23.00 ± 0.90	3.50	30.7	A
G331.172−00.460	shrds720	2015	5521	50.30 ± 2.80	-71.70 ± 0.60	22.40 ± 1.40	4.50	23.7	A
G331.172−00.460	shrds721	2015	6534	49.20 ± 0.90	-70.90 ± 0.20	22.20 ± 0.40	2.00	52.4	A
G332.382+00.080	shrds763	2015	6299	7.10 ± 0.50	-41.50 ± 0.70	20.10 ± 1.70	1.00	13.6	B
G332.382+00.080	shrds766	2015	5758	7.50 ± 1.20	-40.80 ± 1.50	19.30 ± 3.50	1.70	8.5	C
G332.415+00.053	shrds763	2015	5331	···	···	···	3.00	···	D
G332.415+00.053	shrds766	2015	6103	···	···	···	1.30	···	D
G332.657−00.622	shrds771	2015	5500	224.70 ± 3.60	-46.60 ± 0.20	24.40 ± 0.50	7.40	66.2	A
G332.657−00.622	shrds1181	2016	5343	255.40 ± 2.00	-47.20 ± 0.10	25.00 ± 0.20	7.10	80.0	A
G333.962+00.063	shrds806	2015	6683	14.50 ± 0.50	-64.10 ± 0.30	21.10 ± 0.80	1.40	21.8	A
G333.962+00.063	shrds807	2016	5541	14.60 ± 1.00	-66.00 ± 0.60	17.30 ± 1.40	3.10	8.6	C
G336.900−00.033	shrds862	2015	5611	7.90 ± 1.50	-119.50 ± 2.10	23.30 ± 4.90	2.60	6.6	C
G336.900−00.033	shrds1212	2016	6310	···	···	···	3.00	···	D
G337.709+00.091	shrds881	2015	5692	21.70 ± 1.90	-78.50 ± 1.60	37.80 ± 4.30	5.00	11.9	B
G337.709+00.091	shrds886	2015	6602	27.60 ± 0.70	-78.30 ± 0.40	30.90 ± 1.00	1.80	38.7	A
G337.754+00.057	shrds886	2015	6153	13.10 ± 1.00	-46.00 ± 0.60	16.30 ± 1.50	1.90	12.2	B
G337.754+00.057	shrds888	2015	6303	6.80 ± 0.50	-50.10 ± 0.70	16.80 ± 1.50	1.20	10.3	B
G337.996+00.081	shrds890	2015	6536	14.90 ± 1.40	-129.90 ± 0.90	19.40 ± 2.20	2.50	11.7	B
G337.996+00.081	shrds892	2015	5945	15.40 ± 0.90	-130.20 ± 0.60	21.60 ± 1.50	1.80	17.4	A
G338.075+00.016	shrds892	2015	5751	116.80 ± 1.20	-37.10 ± 0.20	31.20 ± 0.40	2.50	115.3	A
G338.075+00.016	shrds893	2015	6129	134.50 ± 1.30	-37.30 ± 0.10	30.60 ± 0.30	2.60	124.9	A

Table C.3 continued

Table C.3: Non-tapered Image RRL Properties of Multiple Detections (continued)

Target	Field	Epoch[a]	ν_L[b] (MHz)	S_L (mJy beam^{-1})	$V_{\rm LSR}$ (km s^{-1})	ΔV (km s^{-1})	rms$_L$ (mJy beam^{-1})	S/N	QF
G338.075+00.016	shrds1219	2016	5361	106.60 ± 1.90	-37.00 ± 0.30	30.90 ± 0.60	4.60	56.8	A
G338.374−00.152	shrds896	2015	5589	···	···	···	4.70	···	D
G338.374−00.152	caswell22	2016	6056	13.10 ± 0.90	8.40 ± 1.10	31.70 ± 2.80	3.00	10.9	B
G338.405−00.203	shrds898	2015	5623	106.90 ± 2.10	-0.40 ± 0.30	32.90 ± 0.70	6.30	43.3	A
G338.405−00.203	caswell22	2016	6265	110.90 ± 1.10	-0.20 ± 0.20	33.80 ± 0.40	1.90	148.3	A
G338.917+00.382	shrds905	2015	5385	16.30 ± 1.80	-25.40 ± 1.70	31.20 ± 4.00	3.30	12.1	B
G338.917+00.382	shrds906	2015	6604	19.20 ± 0.70	-24.70 ± 0.60	30.50 ± 1.40	1.90	24.6	A

[a] Rows with epochs with an asterisk (*) are copied directly from Brown et al. (2017). They did not give the weigted-average frequency of their H$n\alpha$ RRL spectra.

[b] This is the weighted-average frequency of the <H$n\alpha$> spectrum.

Table C.4: *uv*-tapered Image RRL Properties of Multiple Detections

Target	Field	Epoch[a]	ν_L[b] (MHz)	S_L (mJy beam^{-1})	$V_{\rm LSR}$ (km s^{-1})	ΔV (km s^{-1})	rms$_L$ (mJy beam^{-1})	S/N	QF
G289.944−00.889	shrds191	2015	6429	8.90 ± 0.80	32.30 ± 0.90	21.40 ± 2.10	1.70	11.0	B
G289.944−00.889	g290.012-00.867	2014	5276	···	···	···	4.40	···	D
G290.012−00.867	g290.012-00.867	2014	6035	···	···	···	3.00	···	D
G290.012−00.867	g290.012-00.867	2014*	···	3.60 ± 2.50	14.70 ± 8.30	24.90 ± 8.60	1.80	4.5	C
G290.323−02.984	g290.323-02.984	2014	5819	···	···	···	2.50	···	D
G290.323−02.984	g290.323-02.984	2014*	···	3.50 ± 2.10	-17.70 ± 8.00	28.30 ± 8.30	1.50	5.6	C
G290.385−01.042	g290.385-01.042	2014	5921	···	···	···	2.40	···	D
G290.385−01.042	g290.385-01.042	2014*	···	4.00 ± 2.90	9.91 ± 4.60	13.20 ± 4.70	1.90	3.4	C
G291.281−00.726	caswell3	2016	5492	3208.30 ± 38.10	-24.10 ± 0.20	33.90 ± 0.50	74.70	110.7	A
G291.281−00.726	shrds1034	2016	5639	3245.30 ± 23.30	-24.10 ± 0.10	32.90 ± 0.30	99.90	82.6	A
G291.596−00.239	g291.596-00.239	2014	6246	···	···	···	3.90	···	D
G291.596−00.239	g291.596-00.239	2014*	···	15.30 ± 3.70	11.40 ± 5.10	44.20 ± 5.40	2.50	18.0	A
G293.936−00.873	g293.936-00.873	2014	6080	···	···	···	3.10	···	D
G293.936−00.873	g293.936-00.873	2014*	···	16.40 ± 2.20	36.60 ± 1.40	22.30 ± 1.50	2.00	17.0	A
G293.952−00.894	g293.936-00.873	2014	6090	···	···	···	3.50	···	D
G293.952−00.894	g293.994-00.934	2014	5744	···	···	···	4.30	···	D
G293.967−00.984	shrds219	2015	6348	12.90 ± 0.60	27.20 ± 0.70	30.40 ± 1.70	1.60	19.9	A
G293.967−00.984	g293.994-00.934	2014	5539	···	···	···	4.80	···	D
G293.994−00.934	shrds219	2015	5829	17.40 ± 1.00	46.20 ± 0.70	25.20 ± 1.70	2.50	15.7	A
G293.994−00.934	g293.936-00.873	2014	5268	···	···	···	8.50	···	D
G293.994−00.934	g293.994-00.934	2014	5843	17.90 ± 1.50	46.00 ± 0.80	20.20 ± 2.00	3.50	10.2	B
G293.994−00.934	g293.994-00.934	2014*	···	18.60 ± 2.60	46.50 ± 1.70	25.60 ± 1.80	1.30	32.0	A
G294.988−00.538	g294.988-00.538	2014	5959	8.90 ± 0.90	40.00 ± 1.30	25.10 ± 3.10	2.10	9.3	C
G294.988−00.538	g294.988-00.538	2014*	···	9.70 ± 1.40	39.80 ± 1.90	27.40 ± 2.00	1.20	19.0	A
G295.275−00.255	g295.275-00.255	2014	6253	···	···	···	3.30	···	D
G295.275−00.255	g295.275-00.255	2014*	···	5.60 ± 2.30	30.10 ± 6.20	30.60 ± 6.30	1.60	8.7	C
G295.748−00.207	g295.748-00.207	2014	5957	···	···	···	3.10	···	D
G295.748−00.207	g295.748-00.207	2014*	···	7.20 ± 2.10	23.30 ± 3.50	23.90 ± 3.50	1.60	9.8	C

Table C.4 continued

Table C.4: *uv*-tapered Image RRL Properties of Multiple Detections (continued)

Target	Field	Epoch[a]	ν_L[b] (MHz)	S_L (mJy beam^{-1})	$V_{\rm LSR}$ (km s^{-1})	ΔV (km s^{-1})	rms$_L$ (mJy beam^{-1})	S/N	QF
G297.248−00.754	g297.248-00.754	2014	5926	16.40 ± 1.60	24.40 ± 1.40	29.40 ± 3.40	3.20	12.2	B
G297.248−00.754	g297.248-00.754	2014*	···	22.60 ± 2.90	22.60 ± 1.50	24.40 ± 1.60	1.90	26.0	A
G297.626−00.906	g297.626-00.906	2014	6145	7.10 ± 1.20	33.10 ± 3.20	36.80 ± 8.00	3.20	5.9	C
G297.626−00.906	g297.626-00.906	2014*	···	16.10 ± 2.50	31.30 ± 2.10	28.40 ± 2.20	1.50	26.0	A
G298.473+00.104	g298.473+00.104	2014	6020	···	···	···	3.30	···	D
G298.473+00.104	g298.473+00.104	2014*	···	12.20 ± 2.20	32.90 ± 2.00	23.50 ± 2.10	2.00	13.0	B
G299.349−00.267	caswell6	2016	6254	33.40 ± 0.90	-39.30 ± 0.30	20.40 ± 0.60	1.90	35.7	A
G299.349−00.267	shrds1046	2016	5494	33.90 ± 2.30	-40.50 ± 0.60	18.00 ± 1.40	3.80	16.7	A
G300.983+01.117	caswell7	2016	6060	118.40 ± 1.00	-43.00 ± 0.10	26.20 ± 0.20	2.50	106.6	A
G300.983+01.117	g300.983+01.117	2014	5848	···	···	···	2.70	···	D
G300.983+01.117	g300.983+01.117	2014*	···	83.80 ± 2.80	-42.00 ± 0.40	26.50 ± 0.40	3.30	26.0	A
G311.629+00.289	caswell12	2016	6514	137.40 ± 1.50	-55.60 ± 0.20	34.70 ± 0.40	3.10	114.8	A
G311.629+00.289	shrds428	2016	5408	102.60 ± 1.70	-55.10 ± 0.30	36.20 ± 0.70	3.70	74.2	A
G313.671−00.105	atca348	2013	7734	9.90 ± 0.60	-53.80 ± 0.60	20.50 ± 1.40	1.40	14.0	B
G313.671−00.105	atca348	2013*	···	12.00 ± 1.40	-54.60 ± 1.40	24.60 ± 1.50	1.60	17.0	A
G313.790+00.705	atca352	2013	7846	40.70 ± 1.40	-58.30 ± 0.40	21.90 ± 0.90	3.00	28.3	A
G313.790+00.705	atca352	2013*	···	38.70 ± 3.00	-57.20 ± 0.90	22.60 ± 0.90	2.60	32.0	A
G314.219+00.343	atca361	2013	7739	53.00 ± 1.90	-63.00 ± 0.30	19.90 ± 0.80	2.80	37.2	A
G314.219+00.343	atca361	2013*	···	66.40 ± 3.10	-62.50 ± 0.40	20.00 ± 0.50	3.50	38.0	A
G315.312−00.272	ch87.1	2013	7762	30.10 ± 1.40	15.20 ± 0.50	23.90 ± 1.20	2.70	23.9	A
G315.312−00.272	ch87.1	2013*	···	30.00 ± 3.60	14.20 ± 1.40	24.00 ± 1.40	3.60	18.0	A
G316.516−00.600	atca382	2013	7679	17.60 ± 0.70	-45.70 ± 0.30	18.40 ± 0.80	1.60	21.3	A
G316.516−00.600	atca382	2013*	···	19.00 ± 1.70	-45.60 ± 0.90	19.90 ± 0.90	1.70	22.0	A
G317.570−00.257	shrds521	2015	5935	···	···	···	2.70	···	D
G317.570−00.257	atca397	2013	7466	···	···	···	1.80	···	D
G317.861+00.160	atca402	2013	7572	45.30 ± 1.20	1.60 ± 0.30	24.10 ± 0.70	2.80	34.7	A
G317.861+00.160	atca402	2013*	···	55.60 ± 4.60	1.53 ± 0.90	22.90 ± 0.90	2.70	44.0	A
G318.248+00.150	atca406	2013	7422	9.90 ± 1.60	-41.90 ± 1.40	17.90 ± 3.40	2.40	7.7	C

Table C.4 continued

Table C.4: *uv*-tapered Image RRL Properties of Multiple Detections (continued)

Target	Field	Epoch[a]	ν_L[b] (MHz)	S_L (mJy beam^{-1})	$V_{\rm LSR}$ (km s^{-1})	ΔV (km s^{-1})	rms$_L$ (mJy beam^{-1})	S/N	QF
G318.248+00.150	atca406	2013*	···	17.00 ± 3.70	-39.90 ± 2.00	19.00 ± 2.00	2.80	12.0	B
G319.229+00.225	atca412	2013	7306	11.40 ± 0.70	-68.10 ± 0.70	23.00 ± 1.70	1.80	13.8	B
G319.229+00.225	atca412	2013*	···	12.90 ± 2.20	-66.10 ± 1.80	20.90 ± 1.80	1.90	14.0	B
G322.162+00.625	caswell15	2016	6042	622.00 ± 2.20	-52.40 ± 0.00	28.20 ± 0.10	4.40	334.6	A
G322.162+00.625	shrds1151	2016	5432	570.60 ± 3.10	-52.50 ± 0.10	28.60 ± 0.20	7.50	180.3	A
G323.449+00.095	atca449	2013	7885	12.80 ± 0.90	-75.10 ± 0.70	21.00 ± 1.70	1.60	15.8	A
G323.449+00.095	atca449	2013*	···	13.80 ± 2.10	-75.10 ± 1.70	22.50 ± 1.70	2.00	15.0	B
G323.464−00.079	atca450	2013	8010	29.40 ± 0.70	-67.50 ± 0.40	29.20 ± 1.00	1.30	52.7	B
G323.464−00.079	atca450	2013*	···	28.00 ± 2.20	-68.80 ± 1.20	38.30 ± 1.20	1.30	45.0	A
G323.743−00.249	atca456	2013	7881	22.50 ± 0.60	-48.10 ± 0.20	16.70 ± 0.50	1.70	24.7	A
G323.743−00.249	atca456	2013*	···	22.80 ± 1.80	-47.30 ± 0.70	19.20 ± 0.70	2.20	20.0	A
G323.806+00.020	atca459	2013	7617	29.90 ± 0.80	-60.30 ± 0.30	23.70 ± 0.80	2.10	30.7	A
G323.806+00.020	atca459	2013*	···	31.60 ± 2.70	-58.90 ± 0.90	21.60 ± 0.90	2.70	24.0	A
G323.936−00.038	atca462	2013	7306	8.30 ± 1.70	-62.40 ± 1.40	13.90 ± 3.40	2.50	5.4	C
G323.936−00.038	atca462	2013*	···	13.80 ± 5.20	-57.30 ± 4.50	24.50 ± 4.60	2.40	12.7	B
G324.642−00.321	atca466	2013	7822	35.00 ± 1.70	-47.50 ± 0.50	21.60 ± 1.20	2.70	26.2	A
G324.642−00.321	atca466	2013*	···	28.70 ± 4.80	-47.80 ± 1.70	21.30 ± 1.80	2.90	20.0	A
G325.108+00.053	atca472	2013	7455	15.30 ± 1.00	-62.80 ± 0.70	22.10 ± 1.70	2.20	14.7	B
G325.108+00.053	atca472	2013*	···	11.50 ± 3.10	-67.80 ± 2.70	20.40 ± 2.70	3.20	7.3	C
G325.354−00.036	atca475	2013	7810	17.00 ± 1.20	-63.10 ± 0.90	25.10 ± 2.10	2.10	17.6	A
G325.354−00.036	atca475	2013*	···	15.00 ± 1.50	-63.80 ± 0.60	34.40 ± 1.50	1.40	26.0	A
G326.657+00.588	shrds1163	2016	6062	837.90 ± 3.00	-43.70 ± 0.00	26.20 ± 0.10	7.30	259.3	A
G326.657+00.588	shrds1164	2016	5452	803.90 ± 4.40	-43.70 ± 0.10	26.90 ± 0.20	15.50	119.0	A
G326.721+00.773	atca484	2013	7670	30.10 ± 1.30	-38.50 ± 0.50	22.50 ± 1.10	3.10	20.6	A
G326.721+00.773	atca484	2013*	···	45.50 ± 3.70	-40.60 ± 0.90	22.60 ± 0.90	4.90	20.0	A
G326.728+00.616	shrds1163	2016	5664	205.00 ± 4.40	-40.70 ± 0.40	37.40 ± 0.90	14.20	39.1	A
G326.728+00.616	shrds1164	2016	6661	258.10 ± 1.90	-40.70 ± 0.10	33.90 ± 0.30	2.80	234.2	A
G326.890−00.277	atca486	2013	7832	60.00 ± 1.30	-44.50 ± 0.20	19.90 ± 0.50	2.50	48.1	A

Table C.4 continued

Table C.4: *uv*-tapered Image RRL Properties of Multiple Detections (continued)

Target	Field	Epoch[a]	ν_L[b] (MHz)	S_L (mJy beam^{-1})	$V_{\rm LSR}$ (km s^{-1})	ΔV (km s^{-1})	rms$_L$ (mJy beam^{-1})	S/N	QF
G326.890−00.277	atca486	2013*	···	63.20 ± 4.50	-44.20 ± 0.70	19.10 ± 0.70	3.50	35.0	A
G326.916−01.100	atca487	2013	7594	19.80 ± 1.40	-51.80 ± 0.70	21.40 ± 1.80	2.50	16.0	A
G326.916−01.100	atca487	2013*	···	18.90 ± 3.40	-49.80 ± 1.80	21.00 ± 1.90	4.40	8.8	C
G327.300−00.548	caswell18	2016	5772	1999.60 ± 13.20	-48.60 ± 0.10	29.30 ± 0.20	20.40	235.2	A
G327.300−00.548	shrds1168	2016	5634	1962.60 ± 14.90	-48.70 ± 0.10	29.70 ± 0.30	27.10	174.5	A
G327.300−00.548	ch87.3.1	2013	7320	2584.50 ± 12.00	-48.40 ± 0.10	28.30 ± 0.20	26.40	230.6	A
G327.300−00.548	ch87.3.1	2013*	···	2280.00 ± 41.70	-48.50 ± 0.20	28.10 ± 0.30	33.10	163.0	A
G327.400+00.444	shrds621	2016	6511	2.80 ± 0.30	-83.70 ± 5.40	90.60 ± 15.70	1.40	8.6	C
G327.400+00.444	atca492	2013	7425	···	···	···	4.40	···	D
G327.401+00.483	shrds621	2016	6099	24.10 ± 0.80	-76.70 ± 0.30	17.20 ± 0.70	1.80	25.1	A
G327.401+00.483	atca492	2013	7402	27.50 ± 1.70	-76.50 ± 0.60	18.60 ± 1.30	3.00	17.5	A
G327.401+00.483	atca492	2013*	···	31.50 ± 6.10	-76.30 ± 1.70	17.70 ± 1.70	2.60	23.0	A
G327.555−00.829	atca495	2013	7459	15.30 ± 1.30	-40.10 ± 1.20	28.50 ± 2.80	2.70	13.2	B
G327.555−00.829	atca495	2013*	···	16.50 ± 3.50	-41.70 ± 2.60	24.80 ± 2.60	4.00	9.2	C
G327.714+00.576	atca498	2013	7438	10.80 ± 0.70	-50.60 ± 0.80	25.70 ± 1.80	1.70	14.1	B
G327.714+00.576	atca498	2013*	···	12.00 ± 2.70	-47.40 ± 2.40	21.90 ± 2.50	2.10	12.0	B
G327.763+00.163	atca501	2013	7745	24.40 ± 1.10	-92.30 ± 0.50	22.90 ± 1.10	2.50	20.9	A
G327.763+00.163	atca501	2013*	···	30.10 ± 3.40	-92.80 ± 1.20	21.60 ± 1.20	2.60	24.0	A
G331.123−00.530	shrds717	2015	6068	147.20 ± 1.70	-68.30 ± 0.10	21.80 ± 0.30	3.50	87.6	A
G331.123−00.530	shrds721	2015	5386	131.40 ± 2.10	-68.30 ± 0.20	22.70 ± 0.40	7.40	37.5	A
G331.172−00.460	shrds717	2015	5703	61.20 ± 2.00	-70.20 ± 0.40	23.40 ± 0.90	4.50	29.1	A
G331.172−00.460	shrds720	2015	5466	62.80 ± 3.40	-71.80 ± 0.60	21.20 ± 1.40	7.60	16.9	A
G331.172−00.460	shrds721	2015	6372	60.40 ± 1.20	-71.00 ± 0.20	22.00 ± 0.50	2.50	50.2	A
G333.962+00.063	shrds806	2015	6368	14.80 ± 0.80	-64.50 ± 0.60	22.20 ± 1.40	1.80	17.2	A
G333.962+00.063	shrds807	2016	5460	15.90 ± 1.40	-65.60 ± 0.60	13.60 ± 1.40	4.20	6.2	C
G337.709+00.091	shrds881	2015	5710	27.10 ± 3.90	-79.90 ± 2.10	29.40 ± 5.90	8.40	7.8	C
G337.709+00.091	shrds886	2015	6184	33.60 ± 1.60	-78.80 ± 0.70	28.60 ± 1.60	2.70	29.0	A
G338.075+00.016	shrds892	2015	5510	120.20 ± 1.20	-36.60 ± 0.10	30.70 ± 0.40	4.30	69.1	A

Table C.4 continued

Table C.4: *uv*-tapered Image RRL Properties of Multiple Detections (continued)

Target	Field	Epoch[a]	ν_L[b] (MHz)	S_L (mJy beam^{-1})	$V_{\rm LSR}$ (km s^{-1})	ΔV (km s^{-1})	rms$_L$ (mJy beam^{-1})	S/N	QF
G338.075+00.016	shrds893	2015	5996	142.60 ± 1.80	-37.10 ± 0.20	30.20 ± 0.40	3.40	102.4	A
G338.405−00.203	shrds898	2015	5577	117.50 ± 2.30	-0.20 ± 0.30	31.40 ± 0.70	8.40	34.5	A
G338.405−00.203	caswell22	2016	6235	126.70 ± 1.20	0.00 ± 0.20	34.10 ± 0.40	2.70	119.4	A

[a] Rows with epochs with an asterisk (*) are copied directly from Brown et al. (2017). They did not give the weigted-average frequency of their H$n\alpha$ RRL spectra.

[b] This is the weighted-average frequency of the <H$n\alpha$> spectrum.

Appendix D

Electron Temperature Derivations

Here we derive the relationship between the nebular electron temperature, hydrogen radio recombination line (RRL) brightness, and radio continuum brightness of an H II region. This derivation relies on several assumptions: (1) the nebula is homogeneous, isothermal, and in local thermodynamic equilibrium (LTE), (2) the nebula is optically thin in both radio continuum and RRL emission, (3) the nebula is composed primarily of ionized hydrogen and singly-ionized helium, and (4) the RRL and continuum brightness are measured with the same telescope in the Raleigh-Jeans limit.

The free-free radio continuum absorption coefficient of an isothermal plasma is

$$\begin{aligned}\frac{k_C(\nu)}{\mathrm{pc}^{-1}} =& 3.014\times10^{-2}\left(\frac{T_e}{\mathrm{K}}\right)^{-1.5}\left(\frac{\nu}{\mathrm{GHz}}\right)^{-2}\\ &\times\left[\ln\left(4.955\times10^{-2}\left(\frac{\nu}{\mathrm{GHz}}\right)^{-1}\right)+1.5\ln\left(\frac{T_e}{\mathrm{K}}\right)\right]\left(\frac{n_i n_e}{\mathrm{cm}^{-6}}\right),\end{aligned} \tag{D.1}$$

where T_e is the electron temperature, ν is the observed frequency, n_i is the ion number density, and n_e is the electron number density (Oster, 1961). Altenhoff et al. (1960) approximate the absorption coefficient as

$$\frac{k_C(\nu)}{\mathrm{pc}^{-1}} \simeq 8.235\times10^{-2}\left(\frac{T_e}{\mathrm{K}}\right)^{-1.35}\left(\frac{\nu}{\mathrm{GHz}}\right)^{-2.1}\left(\frac{n_i n_e}{\mathrm{cm}^{-6}}\right), \tag{D.2}$$

which is accurate within 10% for $100\,\mathrm{MHz} < \nu < 35\,\mathrm{GHz}$ and $5000\,\mathrm{K} < T_e < 12000\,\mathrm{K}$ (Mezger & Henderson, 1967). The free-free optical depth is the integral of this ab-

sorption coefficient along the line of sight, $\tau_C(\nu) = \int k_C(\nu)\, dl$. In a homogeneous medium with line of sight depth l, the optical depth simplifies to $\tau_C(\nu) = k_C l$.

The LTE hydrogen RRL absorption coefficient for the transition from principle quantum state m to n is

$$k_L^*(\nu) = \left(\frac{h\nu_L}{kT_e}\right)\left(\frac{\pi e^2}{m_e c}\right)\left(\frac{h^2}{2\pi m_e kT_e}\right)^{3/2} n_e n_p \exp\left(\frac{\chi_n}{kT_e}\right) n^2 f_{nm}\phi_\nu(\nu), \tag{D.3}$$

where ν_L is the RRL rest frequency, χ_n is the energy required to ionize the atom from state n, f_{nm} is the oscillator strength of the m to n transition, $\phi_\nu(\nu)$ is the normalized line profile with inverse frequency units, n_p is the hydrogen number density, h is the Planck constant, k is the Boltzmann constant, e is the electron charge, m_e is the electron mass, and c is the speed of light (Brocklehurst & Seaton, 1972; Balser, 1995). The Rydberg formula determines the transition frequency between state m and n:

$$\nu_L = Z^2 Rc\left(n^{-2} - m^{-2}\right), \tag{D.4}$$

where Z is the effective nuclear charge and R is the Rydberg constant. For hydrogen, $Z = 1$ and $R = R_\infty(1 - m_e/m_p)$, where R_∞ is the Rydberg constant for an infinite mass and m_p is the proton mass. If we let $\Delta n = m - n$, the hydrogen transition frequencies are

$$\nu_L = R_\infty c\left(1 - \frac{m_e}{m_p}\right)\left[n^{-2} - (n + \Delta n)^{-1}\right]. \tag{D.5}$$

For the low Δn transitions in the radio regime (e.g. H109α), $\Delta n \ll n$ and

$$\nu_L \simeq 2R_\infty c\left(1 - \frac{m_e}{m_p}\right)\frac{\Delta n}{n^3}. \tag{D.6}$$

Substituting these frequencies into Equation D.3, and assuming that we are observing in the Rayleigh-Jean limit $\chi_n \ll kT_e$, the LTE RRL absorption coefficient simplifies to

$$k_L^*(\nu) = 2R_\infty c\left(\frac{h}{kT_e}\right)\left(1 - \frac{m_e}{m_p}\right)\left(\frac{\pi e^2}{m_e c}\right)\left(\frac{h^2}{2\pi m_e kT_e}\right)^{3/2} n_e n_p \frac{\Delta n}{n} f_{nm}\phi_\nu(\nu). \tag{D.7}$$

Evaluating the constants and moving to astrophysically relevant units, this equation

becomes

$$\frac{k_L^*(\nu)}{\mathrm{pc}^{-1}} \simeq 1.070 \times 10^7 \left(\frac{T_e}{\mathrm{K}}\right)^{-2.5} \left(\frac{n_e n_p}{\mathrm{cm}^{-6}}\right) \frac{\Delta n}{n} f_{nm} \left(\frac{\phi_\nu(\nu)}{\mathrm{Hz}^{-1}}\right). \tag{D.8}$$

The RRL optical depth is the integral of this absorption coefficient along the line of sight, which is $\tau_L^*(\nu) = k_L^*(\nu) l$ for a homogeneous medium.

In an optically thin medium, the specific intensity of some emission with optical depth τ is $I_\nu \simeq B_\nu(T)\tau$, where $B_\nu(T)$ is the Planck function at some temperature T. Assuming the RRL and continuum emission originate in the same volume of isothermal and homogeneous gas and with electron temperature, T_e, the RRL-to-continuum specific intensity ratio at ν_L is

$$\begin{aligned} \frac{I_L(\nu_L)}{I_C(\nu_L)} &= \frac{\tau_L^*(\nu_L)}{\tau_C(\nu_L)} = \frac{k_L^*(\nu_L)}{k_C(\nu_L)} \\ \frac{I_L(\nu_L)}{I_C(\nu_L)} &= 1.300 \times 10^8 \left(\frac{T_e}{\mathrm{K}}\right)^{-1.15} \left(\frac{\nu_L}{\mathrm{GHz}}\right)^{2.1} \frac{n_p}{n_i} \frac{\Delta n}{n} f_{nm} \left(\frac{\phi_\nu(\nu_L)}{\mathrm{Hz}^{-1}}\right). \end{aligned} \tag{D.9}$$

For a Gaussian line profile with full-width half-maximum line width $\Delta\nu$,

$$\phi_\nu(\nu) = \frac{2}{\Delta\nu} \left(\frac{\ln 2}{\pi}\right)^{1/2} \exp\left[-4 \ln 2 \frac{(\nu - \nu_L)^2}{\Delta\nu^2}\right] \tag{D.10}$$

and

$$\phi_\nu(\nu_L) = \frac{2}{\Delta\nu} \left(\frac{\ln 2}{\pi}\right)^{1/2}. \tag{D.11}$$

Using Equation D.11 in Equation D.9, we find

$$\frac{I_L(\nu_L)}{I_C(\nu_L)} = 1.221 \times 10^8 \frac{\Delta n}{n} \left(\frac{T_e}{\mathrm{K}}\right)^{-1.15} \left(\frac{\nu_L}{\mathrm{GHz}}\right)^{2.1} \left(\frac{\Delta\nu}{\mathrm{Hz}}\right)^{-1} \frac{n_p}{n_i} f_{nm}. \tag{D.12}$$

If the nebulae is composed of only hydrogen and singly ionized helium, then

$$\frac{n_p}{n_i} = \frac{n_p}{n_p + n_{\mathrm{He}^+}} = \left(1 + \frac{n_{\mathrm{He}^+}}{n_p}\right)^{-1} = (1+y)^{-1}, \tag{D.13}$$

where n_{He^+} is the singly ionized helium number density and $y \equiv n_{\mathrm{He}^+}/n_p$ is the ratio of helium to hydrogen by number. We use the Doppler equation to convert the FWHM

line width from frequency to velocity units:

$$\frac{\Delta\nu}{\mathrm{Hz}} = \frac{\Delta V}{c}\left(\frac{\nu_L}{\mathrm{Hz}}\right) = 3.336\times10^3\left(\frac{\nu_L}{\mathrm{GHz}}\right)\left(\frac{\Delta V}{\mathrm{km\ s^{-1}}}\right) \tag{D.14}$$

where ΔV is the FWHM line width in velocity units. The RRL-to-continuum specific intensity ratio at ν_L is thus

$$\frac{I_L(\nu_L)}{I_C(\nu_L)} = 3.661\times10^4\left(\frac{T_e}{\mathrm{K}}\right)^{-1.15}\left(\frac{\nu_L}{\mathrm{GHz}}\right)^{1.1}\left(\frac{\Delta V}{\mathrm{km\ s^{-1}}}\right)^{-1}(1+y)^{-1}\frac{\Delta n}{n}f_{nm}. \tag{D.15}$$

The expression $(f_{nm}\Delta n/n)$ is not a strong function of n for $\Delta n = 1$ hydrogen RRLs. For example, $(f_{nm}\Delta n/n) = 0.19435$, 0.19395, and 0.19363 for $\Delta n = 1$ and $n = 80$, 90, and 100, respectively, using the oscillator strengths from Menzel (1968). This variation is less than 0.3% across these H$n\alpha$ transitions, so we adopt the H90α oscillator strength to simplify the RRL-to-continuum specific intensity equation as

$$\frac{I_L(\nu_L)}{I_C(\nu_L)} = 7.100\times10^3\left(\frac{T_e}{\mathrm{K}}\right)^{-1.15}\left(\frac{\nu_L}{\mathrm{GHz}}\right)^{1.1}\left(\frac{\Delta V}{\mathrm{km\ s^{-1}}}\right)^{-1}(1+y)^{-1}. \tag{D.16}$$

Solving for the electron temperature, we find

$$\frac{T_e}{\mathrm{K}} = \left[7.100\times10^3\left(\frac{I_C(\nu_L)}{I_L(\nu_L)}\right)\left(\frac{\nu_L}{\mathrm{GHz}}\right)^{1.1}\left(\frac{\Delta V}{\mathrm{km\ s^{-1}}}\right)^{-1}(1+y)^{-1}\right]^{0.87} \tag{D.17}$$

D.1 SINGLE DISH OBSERVATIONS

Single dish telescopes measure intensity in units of antenna temperature, T_A. The antenna temperature is related to the brightness temperature distribution, $T_B(\theta)$, by

$$T_A = \frac{\eta_b}{\Omega_b}2\pi\int_0^\infty f(\theta)T_B(\theta)\,\sin\theta\,d\theta, \tag{D.18}$$

where η_b is the telescope beam efficiency, Ω_b is the telescope main beam solid angle, $f(\theta)$ is the telescope beam pattern, and the integral is the convolution of the source brightness distribution with the telescope beam (Mezger & Henderson, 1967). For a Gaussian beam with half-power beam width (HPBW) θ_b, the beam pattern is $f(\theta) = \exp[-4\ln(2)\,\theta^2/\theta_b^2]$ and the beam solid angle is $\Omega_b = 2\pi\int_0^\infty f(\theta)\theta\,d\theta = \pi\theta_b^2/(4\ln 2)$. Similarly, if the source brightness distribution is Gaussian with amplitude T_B and

half-power width θ_s, then the source brightness temperature distribution is $T_B(\theta) = T_B \exp[-4\ln(2)\,\theta^2/\theta_s^2]$. In astronomy, θ is typically very small, $\sin\theta \simeq \theta$, and the integral in Equation D.20 is

$$\begin{aligned}\int_0^\infty f(\theta)T_B(\theta)\,\sin\theta\,d\theta &\simeq \int_0^\infty f(\theta)T_B(\theta)\,\theta\,d\theta \\ &= T_B\int_0^\infty \exp\left[-4\ln(2)\theta^2\left(\frac{\theta_s^2+\theta_b^2}{\theta_s^2\theta_b^2}\right)\right]\theta\,d\theta \\ &= \frac{T_B}{8\ln 2}\left(\frac{\theta_s^2\theta_b^2}{\theta_s^2+\theta_b^2}\right),\end{aligned} \tag{D.19}$$

where we use $\int_0^\infty x\exp(-ax^2)\,dx = 1/(2a)$. The antenna temperature is thus

$$T_A = \eta_b T_B\left(\frac{\theta_s^2}{\theta_s^2+\theta_b^2}\right). \tag{D.20}$$

For a very resolved source, $\theta_s \gg \theta_b$ and $T_A \simeq \eta_b T_B$. For a very small source, $\theta_s \ll \theta_b$ and $T_A \simeq \eta_b T_B(\theta_s^2/\theta_b^2)$.

Brightness temperature is defined as

$$T_B \equiv \frac{c^2}{2k\nu^2}I_\nu, \tag{D.21}$$

where I_ν is the specific intensity. For an optically thin medium, $I_\nu = B_\nu(T)\tau$, where T is the blackbody temperature of the emission and τ is the optical depth. In the Rayleigh-Jeans limit, the brightness temperature is simply

$$T_B = \frac{c^2}{2k\nu^2}B_\nu(T)\tau \simeq T\tau. \tag{D.22}$$

Substituting Equation D.22 into Equation D.20, we find

$$T_A = \eta_b T\tau\left(\frac{\theta_s^2}{\theta_s^2+\theta_b^2}\right). \tag{D.23}$$

If the RRL and continuum antenna temperatures are measured with the same telescope and at the same frequency, and if both sources of emission originate from the same volume of homogeneous and isothermal gas with electron temperature T_e,

Equation D.16 is trivially

$$\frac{T_L(\nu_L)}{T_C(\nu_L)} = 7.100 \times 10^3 \left(\frac{T_e}{\mathrm{K}}\right)^{-1.15} \left(\frac{\nu_L}{\mathrm{GHz}}\right)^{1.1} \left(\frac{\Delta V}{\mathrm{km\ s^{-1}}}\right)^{-1} (1+y)^{-1}, \tag{D.24}$$

where $T_C(\nu_L)$ and $T_L(\nu_L)$ are the continuum and RRL antenna temperatures measured at the RRL frequency ν_L, respectively. Equation D.17 becomes

$$\frac{T_e}{\mathrm{K}} \simeq \left[7.100 \times 10^3 \left(\frac{T_C(\nu_L)}{T_L(\nu_L)}\right) \left(\frac{\nu_L}{\mathrm{GHz}}\right)^{1.1} \left(\frac{\Delta V}{\mathrm{km\ s^{-1}}}\right)^{-1} (1+y)^{-1}\right]^{0.87}. \tag{D.25}$$

D.2 Averaging Single Dish RRLs

In Galactic H II region surveys, we average multiple RRL transitions to increase the RRL signal-to-noise ratio. Each RRL transition is an independent measurement of the nebular electron temperature, so the electron temperature derived from many RRL-to-continuum antenna temperature measurements is

$$\frac{T_e}{\mathrm{K}} = \left[7.100 \times 10^3 \left(\frac{\mathrm{km\ s^{-1}}}{\Delta V}\right) (1+y)^{-1}\right]^{0.87} \left\langle \left[\left(\frac{T_C(\nu_L)}{T_L(\nu_L)}\right) \left(\frac{\nu_L}{\mathrm{GHz}}\right)^{1.1}\right]^{0.87} \right\rangle, \tag{D.26}$$

assuming that adjacent RRL transitions have similar FWHM line widths in velocity units (e.g., Balser et al., 2011). Previous single dish RRL studies have used different strategies for averaging RRL transitions. Balser et al. (2011) and Balser et al. (2015), for example, scale each RRL antenna temperature to account for the variations in telescope beam size with frequency, then average the re-scaled RRL spectra. They measure the continuum antenna temperature at one frequency within the RRL frequency range, then take the ratio of the average RRL antenna temperatures to this continuum temperature. This strategy is an approximation to Equation D.26.

Here we compute the difference between the true electron temperature and the Balser et al. (2011) and Balser et al. (2015) approximation using multiple RRL tran-

sitions. From Equation D.26, the factor we need to derive is

$$X_{\rm true} = \left\langle \left[\left(\frac{T_C(\nu_L)}{T_L(\nu_L)} \right) \left(\frac{\nu_L}{\rm GHz} \right)^{1.1} \right]^{0.87} \right\rangle$$
$$= \left(\frac{T_e}{\rm K} \right) \left[7.100 \times 10^3 \left(\frac{\Delta V}{\rm km\ s^{-1}} \right)^{-1} (1+y)^{-1} \right]^{-0.87}, \tag{D.27}$$

where $T_e \propto X_{\rm true}$ and $X_{\rm true}$ is the only variable in Equation D.26 that depends on the RRL transition. Balser et al. (2011) and Balser et al. (2015) approximate this factor as

$$X = \left[\left(\frac{T_C(\nu_C)}{\langle T_L^*(\nu_L) \rangle} \right) \left(\frac{\langle \nu_L \rangle}{\rm GHz} \right)^{1.1} \right]^{0.87}, \tag{D.28}$$

where ν_C is the observed continuum frequency and $T_L^*(\nu_L)$ is the RRL antenna temperature corrected for the variation of telescope beam size with frequency. They re-scale the observed RRL antenna temperature, $T_L(\nu_L)$, using

$$T_L^*(\nu_L) = T_L(\nu_L) \left(\frac{\theta_s^2 + \theta_b^2}{\theta_s^2 + (\theta_b^*)^2} \right), \tag{D.29}$$

where θ_b is the HPBW at ν_L, and θ_b^* is the HPBW at ν_C, and θ_s is the half-power width of the source. The observed source brightness distribution is the convolution of the actual source brightness and the telescope beam. With the assumption that the telescope beam and source brightness distribution are Gaussian, the convolution is also a Gaussian with half-power width $\theta_o^2 = \theta_s^2 + \theta_b^2$. Balser et al. (2011) and Balser et al. (2015) measure the source half-power width at ν_C, which is $(\theta_o^*)^2 = \theta_s^2 + (\theta_b^*)^2$. The true, deconvolved source size is $\theta_s^2 = (\theta_o^*)^2 - (\theta_b^*)^2$, and the re-scaled antenna temperature in terms of observables is

$$T_L^*(\nu_L) = T_L(\nu_L) \left(\frac{(\theta_o^*)^2 - (\theta_b^*)^2 + \theta_b^2}{(\theta_o^*)^2} \right). \tag{D.30}$$

For a point source, $(\theta_o^*)^2 \simeq (\theta_b^*)^2$ and $T_L^*(\nu_L) \simeq T_L(\nu_L)[\theta_b^2/(\theta_b^*)^2]$, whereas if the source is very resolved, $(\theta_o^*)^2 \gg (\theta_b^*)^2$ and $T_L^*(\nu_L) \simeq T_L(\nu_L)$.

Using Equations D.8, D.11, and D.14, the line center LTE optical depth of the ith

RRL transition is

$$\tau^*_{L,i}(\nu_{L,i}) = 584.47 \left(\frac{T_e}{\mathrm{K}}\right)^{-2.5} \left(\frac{n_e n_p}{\mathrm{cm}^{-6}}\right) \left(\frac{\nu_{L,i}}{\mathrm{GHz}}\right)^{-1} \left(\frac{\Delta V}{\mathrm{km\ s}^{-1}}\right)^{-1} \left(\frac{l}{\mathrm{pc}}\right), \tag{D.31}$$

where we have assumed $\tau^*_{L,i} = \int k^*_{L,i}\, dl = k^*_{L,i} l$ for a homogeneous medium with an LTE absorption coefficient $k^*_{L,i}$ and a line of sight depth l. The antenna temperature of this transition is

$$\begin{aligned} T_{L,i}(\nu_{L,i}) &= T_e \tau^*_{L,i}(\nu_{L,i}) \eta_b \left(\frac{\theta_s^2}{\theta_s^2 + \theta_b^2}\right) \\ &= 584.47 \eta_b \left(\frac{T_e}{\mathrm{K}}\right)^{-1.5} \left(\frac{n_e n_p}{\mathrm{cm}^{-6}}\right) \left(\frac{\nu_{L,i}}{\mathrm{GHz}}\right)^{-1} \left(\frac{\Delta V}{\mathrm{km\ s}^{-1}}\right)^{-1} \left(\frac{l}{\mathrm{pc}}\right) \\ &\times \left(\frac{\theta_s^2}{\theta_s^2 + \theta_b^2}\right) \end{aligned} \tag{D.32}$$

and the re-scaled RRL antenna temperature is

$$\begin{aligned} T^*_{L,i}(\nu_{L,i}) &= 584.47 \eta_b \left(\frac{T_e}{\mathrm{K}}\right)^{-1.5} \left(\frac{n_e n_p}{\mathrm{cm}^{-6}}\right) \left(\frac{\nu_{L,i}}{\mathrm{GHz}}\right)^{-1} \left(\frac{\Delta V}{\mathrm{km\ s}^{-1}}\right)^{-1} \left(\frac{l}{\mathrm{pc}}\right) \\ &\times \left(\frac{\theta_s^2}{\theta_s^2 + (\theta_b^*)^2}\right). \end{aligned} \tag{D.33}$$

The average re-scaled RRL antenna temperature of several RRL transitions is

$$\begin{aligned} \langle T^*_L(\nu_L) \rangle &= 584.47 \eta_b \left(\frac{T_e}{\mathrm{K}}\right)^{-1.5} \left(\frac{n_e n_p}{\mathrm{cm}^{-6}}\right) \left(\frac{\Delta V}{\mathrm{km\ s}^{-1}}\right)^{-1} \left(\frac{l}{\mathrm{pc}}\right) \\ &\times \left\langle \left(\frac{\nu_L}{\mathrm{GHz}}\right)^{-1} \left(\frac{\theta_s^2}{\theta_s^2 + (\theta_b^*)^2}\right) \right\rangle \end{aligned} \tag{D.34}$$

assuming that the RRLs have similar FWHM line widths in velocity units.

From Equation D.2, the continuum optical depth at frequency ν_C is

$$\tau_C(\nu_C) = 8.235 \times 10^{-2} \left(\frac{T_e}{\mathrm{K}}\right)^{-1.35} \left(\frac{\nu_C}{\mathrm{GHz}}\right)^{-2.1} \left(\frac{n_i n_e}{\mathrm{cm}^{-6}}\right) \left(\frac{l}{\mathrm{pc}}\right), \tag{D.35}$$

where, again, we have assumed that the medium is homogeneous. The continuum

antenna temperature is

$$\begin{aligned} T_C(\nu_C) &= T_e \tau_C(\nu_C) \eta_b \left(\frac{\theta_s^2}{\theta_s^2 + (\theta_b^*)^2} \right) \\ &= 8.235 \times 10^{-2} \eta_b \left(\frac{T_e}{\mathrm{K}} \right)^{-0.35} \left(\frac{\nu_C}{\mathrm{GHz}} \right)^{-2.1} \left(\frac{n_i n_e}{\mathrm{cm}^{-6}} \right) \left(\frac{l}{\mathrm{pc}} \right) \\ &\times \left(\frac{\theta_s}{\theta_s + (\theta_b^*)^2} \right). \end{aligned} \tag{D.36}$$

Substituting Equations D.34 and D.36 into the Balser et al. (2011) and Balser et al. (2015) approximation of X, we find

$$\begin{aligned} X = &\left(\frac{T_e}{\mathrm{K}} \right) \left[1.409 \times 10^{-4} \left(\frac{\nu_C}{\mathrm{GHz}} \right)^{-2.1} \left(\frac{\Delta V}{\mathrm{km\ s^{-1}}} \right) (1+y) \left(\frac{\langle \nu_L \rangle}{\mathrm{GHz}} \right)^{1.1} \right]^{0.87} \\ &\times \left\langle \left(\frac{\nu_L}{\mathrm{GHz}} \right)^{-1} \right\rangle^{-0.87}. \end{aligned} \tag{D.37}$$

The ratio of the X approximation and X_{true} is

$$\frac{X}{X_{\mathrm{true}}} = \left(\frac{\nu_C}{\mathrm{GHz}} \right)^{-1.827} \left(\frac{\langle \nu_L \rangle}{\mathrm{GHz}} \right)^{0.957} \left\langle \left(\frac{\nu_L}{\mathrm{GHz}} \right)^{-1} \right\rangle^{-0.87}. \tag{D.38}$$

As a sanity check on this expression, if the RRL and continuum antenna temperatures are measured at only one RRL frequency, then $\nu_C = \nu_L = \langle \nu_L \rangle$ and this ratio is unity. Balser et al. (2015) measured the continuum antenna temperature at $\nu_C = 8.556$GHz and the RRL antenna temperature for 6 H$n\alpha$ transitions (H87α to H93α, excluding H90α). The average RRL frequency is $\langle \nu_L \rangle = 8.903$GHz, but Balser et al. (2015) use $\langle \nu_L \rangle = 9$GHz. With these values, the X ratio is

$$\frac{X}{X_{\mathrm{true}}} = 1.057. \tag{D.39}$$

Therefore, Balser et al. (2015) and other studies that average the same RRL transitions and observe the same continuum frequency will overestimate the derived electron temperatures by ∼5.7%.

Quireza et al. (2006a) and Quireza et al. (2006b) use different RRL transitions and calibration strategies to derive electron temperatures. In their C II survey, they

observe H91α and H92α. They assume both transitions have the same antenna temperature in the bright H II region W3, and they use this assumption to calibrate H92α relative to H91α. From Equation D.32, this calibration factor is

$$\frac{T_{L,\,\mathrm{H91}\alpha}}{T_{L,\,\mathrm{H92}\alpha}} = \left(\frac{\nu_{\mathrm{H92}\alpha}}{\nu_{\mathrm{H91}\alpha}}\right)\left(\frac{\theta_s^2 + \theta_{b,\,\mathrm{H92}\alpha}^2}{\theta_s^2 + \theta_{b,\,\mathrm{H91}\alpha}^2}\right). \tag{D.40}$$

W3 is unresolved in their survey, so $\theta_s^2 + \theta_b^2 \simeq \theta_b^2$. Using $\theta_b^2 \propto \nu^{-2}$ for a Gaussian beam, this factor becomes

$$\frac{T_{L,\,\mathrm{H91}\alpha}}{T_{L,\,\mathrm{H92}\alpha}} \simeq \left(\frac{\nu_{\mathrm{H91}\alpha}}{\nu_{\mathrm{H92}\alpha}}\right) = 1.033. \tag{D.41}$$

Therefore, the average RRL antenna temperature in their surveys is

$$\begin{aligned}
\langle T_L(\nu_L)\rangle &= \frac{1}{2}\left(T_{L,\,\mathrm{H91}\alpha} + 1.033 T_{L,\,\mathrm{H92}\alpha}\right) \\
\langle T_L(\nu_L)\rangle &= 292.235\eta_b \left(\frac{T_e}{\mathrm{K}}\right)^{-1.5}\left(\frac{n_e n_p}{\mathrm{cm}^{-6}}\right)\left(\frac{\Delta V}{\mathrm{km\ s}^{-1}}\right)^{-1} l \\
&\quad\times\left[\left(\frac{\nu_{\mathrm{H91}\alpha}}{\mathrm{GHz}}\right)^{-1}\left(\frac{\theta_s^2}{\theta_s^2 + \theta_{b,\,\mathrm{H91}\alpha}^2}\right) + 1.033\left(\frac{\nu_{\mathrm{H92}\alpha}}{\mathrm{GHz}}\right)^{-1}\left(\frac{\theta_s^2}{\theta_s^2 + \theta_{b,\,\mathrm{H92}\alpha}^2}\right)\right].
\end{aligned} \tag{D.42}$$

The continuum antenna temperature at ν_C is given by Equation D.36, and the Quireza et al. (2006a,b) X is

$$\begin{aligned}
X &= \left(\frac{T_e}{\mathrm{K}}\right)\left[2.818\times 10^{-4}\left(\frac{\nu_C}{\mathrm{GHz}}\right)^{-2.1}\left(\frac{\Delta V}{\mathrm{km\ s}^{-1}}\right)(1+y)\left(\frac{\langle\nu_L\rangle}{\mathrm{GHz}}\right)^{1.1}\right]^{0.87} \\
&\quad\times\left[\left(\frac{\nu_{\mathrm{H91}\alpha}}{\mathrm{GHz}}\right)^{-1}\left(\frac{\theta_s^2 + (\theta_b^*)^2}{\theta_s^2 + \theta_{b,\,\mathrm{H91}\alpha}^2}\right) + 1.033\left(\frac{\nu_{\mathrm{H92}\alpha}}{\mathrm{GHz}}\right)^{-1}\left(\frac{\theta_s^2 + (\theta_b^*)^2}{\theta_s^2 + \theta_{b,\,\mathrm{H92}\alpha}^2}\right)\right]^{-0.87}.
\end{aligned} \tag{D.43}$$

The ratio of this X approximation to $X_{\rm true}$ is

$$\frac{X}{X_{\rm true}} = 1.829\left(\frac{\nu_C}{\rm GHz}\right)^{-1.827}\left(\frac{\langle\nu_L\rangle}{\rm GHz}\right)^{0.957} \times\left[\left(\frac{\nu_{\rm H91\alpha}}{\rm GHz}\right)^{-1}\left(\frac{\theta_s^2+(\theta_b^*)^2}{\theta_s^2+\theta_{b,\,\rm H91\alpha}^2}\right)+1.033\left(\frac{\nu_{\rm H92\alpha}}{\rm GHz}\right)^{-1}\left(\frac{\theta_s^2+(\theta_b^*)^2}{\theta_s^2+\theta_{b,\,\rm H92\alpha}^2}\right)\right]^{-0.87}. \tag{D.44}$$

Quireza et al. (2006a) and Quireza et al. (2006b) did not account for the variation in telescope beam size in their analysis. Therefore, their ratio $X/X_{\rm true}$ has a dependence on the source size. In the limit that the source is unresolved at all frequencies, $\theta_s^2 \ll \theta_b^2$. For Gaussian beams with $\theta^2 \propto \nu^{-2}$, the ratio in this limit simplifies to

$$\begin{aligned}
\lim_{\theta_s^2\ll\theta_b^2}\frac{X}{X_{\rm true}} &= 1.829\left(\frac{\nu_C}{\rm GHz}\right)^{-1.827}\left(\frac{\langle\nu_L\rangle}{\rm GHz}\right)^{0.957} \\
&\quad\times\left[\left(\frac{\nu_{\rm H91\alpha}}{\rm GHz}\right)^{-1}\left(\frac{(\theta_b^*)^2}{\theta_{b,\,\rm H91\alpha}^2}\right)+1.033\left(\frac{\nu_{\rm H92\alpha}}{\rm GHz}\right)^{-1}\left(\frac{(\theta_b^*)^2}{\theta_{b,\,\rm H92\alpha}^2}\right)\right]^{-0.87} \\
\lim_{\theta_s^2\ll\theta_b^2}\frac{X}{X_{\rm true}} &= 1.829\left(\frac{\nu_C}{\rm GHz}\right)^{-1.827}\left(\frac{\langle\nu_L\rangle}{\rm GHz}\right)^{0.957} \\
&\quad\times\left[\left(\frac{\nu_{\rm H91\alpha}}{\rm GHz}\right)^{-1}\left(\frac{\nu_{\rm H91\alpha}^2}{\nu_C^2}\right)+1.033\left(\frac{\nu_{\rm H92\alpha}}{\rm GHz}\right)^{-1}\left(\frac{\nu_{\rm H92\alpha}^2}{\nu_C^2}\right)\right]^{-0.87} \\
\lim_{\theta_s^2\ll\theta_b^2}\frac{X}{X_{\rm true}} &= 1.829\left(\frac{\nu_C}{\rm GHz}\right)^{-0.087}\left(\frac{\langle\nu_L\rangle}{\rm GHz}\right)^{0.957}\left[\left(\frac{\nu_{\rm H91\alpha}}{\rm GHz}\right)+1.033\left(\frac{\nu_{\rm H92\alpha}}{\rm GHz}\right)\right]^{-0.87}.
\end{aligned} \tag{D.45}$$

Using the RRL frequencies, $\nu_C = 8.665$GHz, and $\langle\nu_L\rangle = \nu_{\rm H91\alpha}$, which is what Quireza et al. (2006a,b) use, we find

$$\lim_{\theta_s^2\ll\theta_b^2}\frac{X}{X_{\rm true}} = 1.0. \tag{D.46}$$

For unresolved sources, Quireza et al. (2006a,b) correctly calculate the electron tem-

peratures in their C II survey. In the resolved case, $\theta_s^2 \gg \theta_b^2$ and

$$\lim_{\theta_s^2 \gg \theta_b^2} \frac{X}{X_{\rm true}} = 1.829 \left(\frac{\nu_C}{\rm GHz}\right)^{-1.827} \left(\frac{\langle \nu_L \rangle}{\rm GHz}\right)^{0.957} \left[\left(\frac{\nu_{\rm H91\alpha}}{\rm GHz}\right)^{-1} + 1.033 \left(\frac{\nu_{\rm H92\alpha}}{\rm GHz}\right)^{-1}\right]^{-0.87}$$
$$\lim_{\theta_s^2 \gg \theta_b^2} \frac{X}{X_{\rm true}} = 0.956. \tag{D.47}$$

Therefore, the Quireza et al. (2006b) electron temperatures for the C II survey nebulae are underestimated by up to 5% depending on the source morphology.

In their ^{3}He survey, Quireza et al. (2006a,b) only observe the H91α transition. The X ratio for this survey is simpler:

$$\frac{X}{X_{\rm true}} = \left(\frac{\nu_C}{\rm GHz}\right)^{-1.827} \left(\frac{\nu_{\rm H91\alpha}}{\rm GHz}\right)^{1.827} \left(\frac{\theta_s^2 + (\theta_b^*)^2}{\theta_s^2 + \theta_{b,\,\rm H91\alpha}^2}\right)^{-0.87}, \tag{D.48}$$

with limits

$$\lim_{\theta_s^2 \ll \theta_b^2} \frac{X}{X_{\rm true}} = \left(\frac{\nu_C}{\rm GHz}\right)^{-1.827} \left(\frac{\nu_{\rm H91\alpha}}{\rm GHz}\right)^{1.827} \left(\frac{(\theta_b^*)^2}{\theta_{b,\,\rm H91\alpha}^2}\right)^{-0.87}$$
$$= \left(\frac{\nu_C}{\rm GHz}\right)^{-0.087} \left(\frac{\nu_{\rm H91\alpha}}{\rm GHz}\right)^{0.087}$$
$$\lim_{\theta_s^2 \ll \theta_b^2} \frac{X}{X_{\rm true}} = 1.0 \tag{D.49}$$

and

$$\lim_{\theta_s^2 \gg \theta_b^2} \frac{X}{X_{\rm true}} = \left(\frac{\nu_C}{\rm GHz}\right)^{-1.827} \left(\frac{\nu_{\rm H91\alpha}}{\rm GHz}\right)^{1.827}$$
$$\lim_{\theta_s^2 \gg \theta_b^2} \frac{X}{X_{\rm true}} = 0.983. \tag{D.50}$$

Quireza et al. (2006b) underestimate their electron temperatures by up to 2% in their ^{3}He survey.

In Table D.1 we list the $X/X_{\rm true}$ factors for the single dish surveys used in Chapter 5. For each survey, we list the author; the observed RRL transitions; the observed continuum frequency; the average RRL frequency they used in the electron temperature equation; and the $X/X_{\rm true}$ factor.

Table D.1: Single Dish Electron Temperature Corrections

Author	RRLs	ν_C GHz	$< \nu_L >^a$ GHz	$X/X_{\rm true}$
Quireza et al. (2006a,b) C II Survey	H91α;H92α	8.665	8.585	0.956 to 1.0
Quireza et al. (2006a,b) ^{3}He Survey	H91α	8.665	8.585	0.983 to 1.0
Balser et al. (2011, 2015)	H87α to H93α	8.665	9.0	1.057

[a] This is the average RRL frequency used by the author, which is not the actual average RRL frequency

D.3 Interferometric Observations

Interferometers measure intensity in units of flux density per synthesized beam, S, which is related to brightness temperature, T_B, by Rayleigh-Jeans law:

$$S = \frac{2kc^2}{\nu^2} T_B. \tag{D.51}$$

If the RRL and continuum flux densities are measured at the same frequency, with the same telescope, and with the same synthesized beam size, the RRL-to-continuum flux density ratio and electron temperature are given by Equations D.16 and D.17, respectively, where I_C is the continuum flux density and I_L is the RRL flux density.

D.4 Averaging Interferometric RRLs

An important difference between the interferometric observations in Chapter 5 and single dish observations is that interferometers measure the RRL and continuum emission simultaneously. At each RRL frequency, we measure the RRL flux density and continuum flux density with the same synthesized beam. If the source is homogeneous and isothermal, we can ignore all effects of the varying beam size.

In Chapter 5, we extract spectra from our data cubes in two ways: from the pixel of brightest continuum emission, such that the spectrum has units of flux density per beam, or from the sum of all pixels within a region, such that the spectrum has units of flux density. We average these spectra weighted by the continuum brightness and rms noise in the line-free regions, so our interferometric X factor is

$$X = \left[\left(\frac{\langle S_C(\nu_L) \rangle^*}{\langle S_L(\nu_L) \rangle^*} \right) \left(\frac{\langle \nu_L \rangle^*}{\mathrm{GHz}} \right)^{1.1} \right]^{0.87}, \tag{D.52}$$

where S_C and S_L are the continuum and RRL brightness or flux density, respectively, and $\langle\rangle^*$ indicates a weighted average. If we assume that the spectral rms noise is the

same in each RRL transition, then the weighted average values are simply

$$\langle S_C(\nu_L)\rangle^* = \frac{\sum_i S_C^2(\nu_{L,i})}{\sum_i S_C(\nu_{L,i})} \tag{D.53}$$

$$\langle S_L(\nu_L)\rangle^* = \frac{\sum_i S_L(\nu_{L,i}) S_C(\nu_{L,i})}{\sum_i S_C(\nu_{L,i})} \tag{D.54}$$

$$\langle \nu_L\rangle^* = \frac{\sum_i \nu_{L,i} S_C(\nu_{L,i})}{\sum_i S_C(\nu_{L,i})}. \tag{D.55}$$

From Equations D.2 and D.51, the continuum brightness at the ith RRL frequency is

$$\begin{aligned} S_C(\nu_{L,i}) &= \frac{2k\nu_{L,i}^2}{c^2} T_e \tau_C(\nu_{L,i}) \\ \frac{S_C(\nu_{L,i})}{\mathrm{Jy\ sr^{-1}}} &= 2.530 \times 10^3 \left(\frac{T_e}{\mathrm{K}}\right)^{-0.35} \left(\frac{\nu_{L,i}}{\mathrm{GHz}}\right)^{-0.1} \left(\frac{n_i n_e}{\mathrm{cm^{-6}}}\right) \left(\frac{l}{\mathrm{pc}}\right) \end{aligned} \tag{D.56}$$

for a homogeneous nebula with depth l. The RRL frequency is the only factor that depends on RRL transition, so

$$\sum_i \frac{S_C(\nu_{L,i})}{\mathrm{Jy\ sr^{-1}}} = 2.530 \times 10^3 \left(\frac{T_e}{\mathrm{K}}\right)^{-0.35} \left(\frac{n_i n_e}{\mathrm{cm^{-6}}}\right) \left(\frac{l}{\mathrm{pc}}\right) \sum_i \left(\frac{\nu_{L,i}}{\mathrm{GHz}}\right)^{-0.1} \tag{D.57}$$

and

$$\begin{aligned} \frac{\langle S_C(\nu_L)\rangle^*}{\mathrm{Jy\ sr^{-1}}} &= 2.530 \times 10^3 \left(\frac{T_e}{\mathrm{K}}\right)^{-0.35} \left(\frac{n_i n_e}{\mathrm{cm^{-6}}}\right) \left(\frac{l}{\mathrm{pc}}\right) \\ &\quad \times \left[\sum_i \left(\frac{\nu_{L,i}}{\mathrm{GHz}}\right)^{-0.2}\right] \left[\sum_i \left(\frac{\nu_{L,i}}{\mathrm{GHz}}\right)^{-0.1}\right]^{-1}. \end{aligned} \tag{D.58}$$

Using Equations D.8 and D.51, the LTE brightness of the ith RRL is

$$\begin{aligned} S_L(\nu_{L,i}) &= \frac{2k\nu_{L,i}^2}{c^2} T_e \tau_L^*(\nu_{L,i}) \\ \frac{S_L(\nu_{L,i})}{\mathrm{Jy\ sr^{-1}}} &= 1.796 \times 10^7 \left(\frac{T_e}{\mathrm{K}}\right)^{-1.5} \left(\frac{\nu_{L,i}}{\mathrm{GHz}}\right) \left(\frac{n_p n_e}{\mathrm{cm^{-6}}}\right) \left(\frac{\Delta V}{\mathrm{km\ s^{-1}}}\right)^{-1} \left(\frac{l}{\mathrm{pc}}\right) \end{aligned} \tag{D.59}$$

for a homogeneous medium with depth l. The average RRL brightness is

$$\frac{\langle S_L(\nu_L)\rangle^*}{\mathrm{Jy\ sr^{-1}}} = 1.796\times 10^7 \left(\frac{T_e}{\mathrm{K}}\right)^{-0.5} \left(\frac{n_p n_e}{\mathrm{cm^{-6}}}\right) \left(\frac{\Delta V}{\mathrm{km\ s^{-1}}}\right)^{-1} \left(\frac{l}{\mathrm{pc}}\right) \times \left[\sum_i \left(\frac{\nu_{L,i}}{\mathrm{GHz}}\right)^{0.9}\right] \left[\sum_i \left(\frac{\nu_{L,i}}{\mathrm{GHz}}\right)^{-0.1}\right]^{-1}. \tag{D.60}$$

The average RRL frequency is

$$\frac{\langle \nu_L\rangle^*}{\mathrm{GHz}} = \left[\sum_i \left(\frac{\nu_{L,i}}{\mathrm{GHz}}\right)^{0.9}\right] \left[\sum_i \left(\frac{\nu_{L,i}}{\mathrm{GHz}}\right)^{-0.1}\right]^{-1}, \tag{D.61}$$

so the interferometric X approximation simplifies to

$$X = \left(\frac{T_e}{\mathrm{K}}\right) \left[1.409\times 10^{-4} \left(\frac{\Delta V}{\mathrm{km\ s^{-1}}}\right) (1+y) \left(\frac{\sum_i \nu_{L,i}^{-0.2}}{\sum_i \nu_{L,i}^{0.9}}\right) \left(\frac{\sum_i \nu_{L,i}^{0.9}}{\sum_i \nu_{L,i}^{-0.1}}\right)^{1.1}\right]^{0.87}. \tag{D.62}$$

The ratio of this approximation to X_{true} is

$$\frac{X}{X_{\mathrm{true}}} = \left[\left(\frac{\sum_i \nu_{L,i}^{-0.2}}{\sum_i \nu_{L,i}^{0.9}}\right) \left(\frac{\sum_i \nu_{L,i}^{0.9}}{\sum_i \nu_{L,i}^{-0.1}}\right)^{1.1}\right]^{0.87} \tag{D.63}$$

In Chapter 5, we observe the seven RRL transitions from H87α to H93α. Our X factor ratio is thus

$$\frac{X}{X_{\mathrm{true}}} = 1.0 \tag{D.64}$$

Our strategy for averaging multiple RRL transitions to compute electron temperatures is accurate.

Appendix E

Logarithmic Spiral Derivations

The Galactocentric radius, $R_{\rm sp}$, of a logarithmic spiral is related to its Galactocentric azimuth, $\theta_{\rm sp}$, by

$$R_{\rm sp} = R_0 \exp\left[(\theta_0 - \theta_{\rm sp}) \tan\phi\right] \tag{E.1}$$

where θ_0 is the reference azimuth, at which the spiral crosses R_0, and ϕ is the pitch angle. The distance between a Galactocentric point (R, θ, Z) and a logarithmic spiral is given by the law of cosines:

$$d_{\rm sp}^2 = R^2 + R_{\rm sp}^2(\theta_{\rm sp}) - 2RR_{\rm sp}(\theta_{\rm sp})\cos(\theta - \theta_{\rm sp} - 2\pi n) + [Z - Z_{\rm sp}(\theta_{\rm sp})]^2. \tag{E.2}$$

where n is an integer representing the "wrap" of the spiral such that $0° < \theta_{\rm sp} + 2\pi n < 360°$. In our simple model in Chapter 6, we assume that the logarithmic spiral arms of the model galaxy are confined to the galactic midplane, so $Z_{\rm sp}(\theta_{\rm sp}) = 0$ always.

We derive the minimum distance between some point and the logarithmic spiral arm by finding the $\theta_{\rm sp}$ that minimizes Equation E.2. Naïvely, this is accomplished by differentiating that equation with respect to $\theta_{\rm sp}$, setting the derivative equal to zero, and solving for $\theta_{\rm sp}$. If we let $\gamma \equiv \theta - \theta_{\rm sp} - 2\pi n$, then

$$R_{\rm sp} = R_0 \exp\left[(\theta_0 - \theta + 2\pi n + \gamma) \tan\phi\right] \tag{E.3}$$

$$\frac{dR_{\rm sp}}{d\theta_{\rm sp}} = R_0 \exp\left[(\theta_0 - \theta + 2\pi n + \gamma) \tan\phi\right] \tan\phi = R_{\rm sp} \tan\phi \tag{E.4}$$

and

$$\frac{d}{d\theta_{\rm sp}}d_{\rm sp}^2 = 2R_{\rm sp}\left(\frac{dR_{\rm sp}}{d\theta_{\rm sp}}\right) - 2R\cos\gamma\left(\frac{dR_{\rm sp}}{d\theta_{\rm sp}}\right) - 2RR_{\rm sp}\sin\gamma$$
$$\frac{d}{d\theta_{\rm sp}}d_{\rm sp}^2 = 2R_{\rm sp}^2\tan\phi - 2RR_{\rm sp}\cos\gamma\tan\phi - 2RR_{\rm sp}\sin\gamma. \tag{E.5}$$

Unfortunately, this derivative is a transcendental equation for which we have found no analytical solution to $dd_{\rm sp}^2/d\theta_{\rm sp} = 0$.

To approximate the minimum value of Equation E.2, we define $Q \equiv R_0\exp[(\theta_0 - \theta + 2\pi n)\tan\phi]$. The minimum distance between a point and the spiral will have $\gamma \sim 0$, so we expand $R_{\rm sp}$, $\cos\gamma$, and $R_{\rm sp}\cos\gamma$ around $\gamma = 0$ to $O(\gamma^2)$:

$$R_{\rm sp} = Q\exp\left[\gamma\tan\phi\right] \simeq Q\left(1 + \gamma\tan\phi + \frac{\gamma^2\tan^2\phi}{2}\right) \tag{E.6}$$
$$\cos\gamma \simeq 1 - \frac{\gamma^2}{2} \tag{E.7}$$
$$R_{\rm sp}\cos\gamma \simeq Q\left(1 + \gamma\tan\phi - \frac{\gamma^2}{2} + \frac{\gamma^2\tan^2\phi}{2}\right) \tag{E.8}$$

The expansion of Equation E.2 around $\gamma = 0$ is thus

$$d_{\rm sp}^2 \simeq R^2 + Q^2\left(1 + \gamma\tan\phi + \frac{\gamma^2\tan^2\phi}{2}\right)^2 - 2RQ\left(1 + \gamma\tan\phi - \frac{\gamma^2}{2} + \frac{\gamma^2\tan^2\phi}{2}\right) + Z^2$$
$$d_{\rm sp}^2 \simeq R^2 + Q^2\left(1 + 2\gamma\tan\phi + 2\gamma^2\tan^2\phi\right) - 2RQ\left(1 + \gamma\tan\phi - \frac{\gamma^2}{2} + \frac{\gamma^2\tan^2\phi}{2}\right) + Z^2 \tag{E.9}$$

where we keep only $O(\gamma^2)$ terms. Differentiating this equation with respect to γ, we find

$$\frac{d}{d\gamma}d_{\rm sp}^2 \simeq 2Q^2\left(\tan\phi + 2\gamma\tan^2\phi\right) - 2RQ\left(\tan\phi - \gamma + \gamma\tan^2\phi\right)$$
$$\frac{d}{d\gamma}d_{\rm sp}^2 \simeq 2Q^2\tan\phi + 4Q^2\gamma\tan^2\phi - 2RQ\tan\phi + 2RQ\gamma - 2RQ\gamma\tan^2\phi$$
$$\frac{d}{d\gamma}d_{\rm sp}^2 \simeq 2Q\tan\phi\left(Q - R\right) + 2Q\gamma\left(2Q\tan^2\phi + R - R\tan^2\phi\right) \tag{E.10}$$

Setting this derivative equal to zero, requiring $Q \neq 0$, and solving for $\gamma \equiv \gamma_{\rm min}$, we

find

$$0 \simeq \tan\phi\,(Q-R) + 2Q\gamma_{\rm min}\tan^2\phi + R\gamma_{\rm min} - R\gamma_{\rm min}\tan^2\phi$$
$$\gamma_{\rm min} \simeq \frac{\tan\phi\,(R-Q)}{2Q\tan^2\phi + R - R\tan^2\phi}. \tag{E.11}$$

This is the value of γ that minimizes Equation E.2.

The Galactocentric azimuth of the spiral that minimizes Equation E.2 is

$$\theta_{\rm sp,min} = \theta - \gamma_{\rm min} - 2\pi n \tag{E.12}$$

Since $\gamma_{\rm min} \sim 0$, we estimate n as

$$n = {\rm nint}\left(\frac{\theta - \theta_{\rm guess}}{2\pi}\right) \tag{E.13}$$

where nint() is the nearest integer (rounding) function and

$$\theta_{\rm guess} = \theta_0 - \frac{1}{\tan\phi}\ln\left(\frac{R}{R_0}\right) \tag{E.14}$$

The Galactocentric radius of the spiral that minimizes Equation E.2 is simply

$$R_{\rm sp,min} = R_0 {\rm exp}\left[(\theta_0 - \theta_{\rm sp,min})\tan\phi\right] \tag{E.15}$$

and the minimum distance is

$$d^2_{\rm min} = R^2 + R^2_{\rm sp,min} - 2RR_{\rm sp,min}\cos(\theta - \theta_{\rm sp,min} - 2\pi n) + Z^2. \tag{E.16}$$

Figure E.1 shows a face-on view of the midplane ($Z = 0$) distance between every point and the nearest spiral in a galaxy with four logarithmic spiral arms.

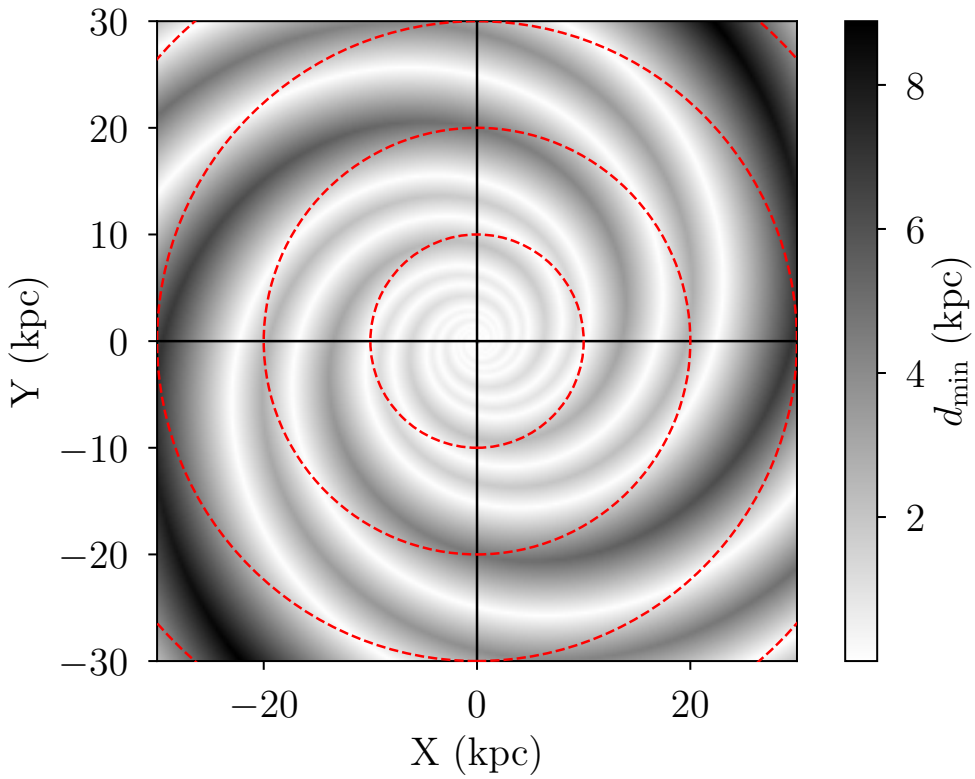

Figure E.1: Face-on view of the midplane ($Z = 0$) minimum distance, $d_{\rm min}$, between each point and the nearest logarithmic spiral. This example has four logarithmic spirals with $\phi = 14°$ and $\theta_0 = (72°, 252°, 317°, 137°)$. The red dashed circles have radius 10, 20, 30, and 40 kpc.

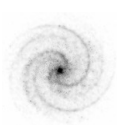

References

Alexander, S. 1852, The Astronomical Journal, 2, 95

Allende Prieto, C., Majewski, S. R., Schiavon, R., et al. 2008, Astronomische Nachrichten, 329, 1018

Altenhoff, W. J., Downes, D., Pauls, T., & Schraml, J. 1979, Astronomy and Astrophysics Supplement Series, 35, 23

Altenhoff, W. J., Mezger, P. G., Wendker, H., & Westerhout, G. 1960, Veröffentlichungen der Univer-sitäts-Sternwarte zu Bonn, 59, 48

Anders, F., Chiappini, C., Rodrigues, T. S., et al. 2017, Astronomy and Astrophysics, 597, A30

Anderson, L. D., Armentrout, W. P., Johnstone, B. M., et al. 2015a, The Astrophysical Journal Supplement Series, 221, 26

Anderson, L. D., Armentrout, W. P., Luisi, M., et al. 2018, The Astrophysical Journal Supplement Series, 234, 33

Anderson, L. D., & Bania, T. M. 2009, The Astrophysical Journal, 690, 706

Anderson, L. D., Bania, T. M., Balser, D. S., et al. 2014, The Astrophysical Journal Supplement Series, 212, 1

Anderson, L. D., Bania, T. M., Balser, D. S., & Rood, R. T. 2011, The Astrophysical Journal Supplement Series, 194, 32

—. 2012, The Astrophysical Journal, 754, 62

Anderson, L. D., Bania, T. M., Jackson, J. M., et al. 2009, The Astrophysical Journal Supplement Series, 181, 255

Anderson, L. D., Hough, L. A., Wenger, T. V., Bania, T. M., & Balser, D. S. 2015b, The Astrophysical Journal, 810, 42

Ando, K., Nagayama, T., Omodaka, T., et al. 2011, Publications of the Astronomical Society of Japan, 63, 45

Araya, E., Hofner, P., Churchwell, E., & Kurtz, S. 2002, The Astrophysical Journal Supplement Series, 138, 63

Armentrout, W. P., Anderson, L. D., Balser, D. S., et al. 2017, The Astrophysical Journal, 841, 121

Arnal, E. M., Bajaja, E., Larrarte, J. J., Morras, R., & Pöppel, W. G. L. 2000, Astronomy and Astrophysics Supplement Series, 142, 35

Asaki, Y., Deguchi, S., Imai, H., et al. 2010, The Astrophysical Journal, 721, 267

Baade, W. 1944, The Astrophysical Journal, 100, 137

Bajaja, E., Arnal, E. M., Larrarte, J. J., et al. 2005, Astronomy and Astrophysics, 440, 767

Balser, D. S. 1995, PhD thesis, Boston University

Balser, D. S., Anish Roshi, D., Jeyakumar, S., et al. 2016, The Astrophysical Journal, 816, 22

Balser, D. S., Bania, T. M., Rood, R. T., & Wilson, T. L. 1999, The Astrophysical Journal, 510, 759

Balser, D. S., Rood, R. T., Bania, T. M., & Anderson, L. D. 2011, The Astrophysical Journal, 738, 27

Balser, D. S., Wenger, T. V., Anderson, L. D., & Bania, T. M. 2015, The Astrophysical Journal, 806, 199

Bania, T. M. 1977, The Astrophysical Journal, 216, 381

Bania, T. M., Anderson, L. D., & Balser, D. S. 2012, The Astrophysical Journal, 759, 96

Bania, T. M., Anderson, L. D., Balser, D. S., & Rood, R. T. 2010, The Astrophysical Journal Letters, 718, L106

Bartkiewicz, A., Brunthaler, A., Szymczak, M., van Langevelde, H. J., & Reid, M. J. 2008, Astronomy and Astrophysics, 490, 787

Becker, R. H., White, R. L., Helfand, D. J., & Zoonematkermani, S. 1994, The Astrophysical Journal Supplement Series, 91, 347

Benjamin, R. A., Churchwell, E., Babler, B. L., et al. 2005, The Astrophysical Journal Letters, 630, L149

Bergemann, M., Ruchti, G. R., Serenelli, A., et al. 2014, Astronomy and Astrophysics, 565, A89

Bertrand, G. 2005, Journal of Mathematical Imaging and Vision, 22, 217

Bigiel, F., & Blitz, L. 2012, The Astrophysical Journal, 756, 183

Bihr, S., Johnston, K. G., Beuther, H., et al. 2016, Astronomy and Astrophysics, 588, A97

Binney, J., & Merrifield, M. 1998, Galactic Astronomy (Princeton University Press)

Bird, J. C., Kazantzidis, S., & Weinberg, D. H. 2012, Monthly Notices of the Royal Astronomical Society, 420, 913

Blaauw, A. 1995, in IAU Symposium, Vol. 164, Stellar Populations, ed. P. C. van der Kruit & G. Gilmore, 39

Bland-Hawthorn, J., & Gerhard, O. 2016, Annual Review of Astronomy and Astrophysics, 54, 529

Bock, D. C.-J., Large, M. I., & Sadler, E. M. 1999, The Astronomical Journal, 117, 1578

Bovy, J., Nidever, D. L., Rix, H.-W., et al. 2014, The Astrophysical Journal, 790, 127

Brand, J., & Blitz, L. 1993, Astronomy and Astrophysics, 275, 67

Brocklehurst, M., & Seaton, M. J. 1972, Monthly Notices of the Royal Astronomical Society, 157, 179

Brown, C., Dickey, J. M., Dawson, J. R., & McClure-Griffiths, N. M. 2014, The Astrophysical Journal Supplement Series, 211, 29

Brown, C., Jordan, C., Dickey, J. M., et al. 2017, The Astronomical Journal, 154, 23

Brunthaler, A., Reid, M. J., Menten, K. M., et al. 2009, The Astrophysical Journal, 693, 424

—. 2011, Astronomische Nachrichten, 332, 461

Burton, W. B. 1966, Bulletin of the Astronomical Institutes of the Netherlands, 18, 247

—. 1971, Astronomy and Astrophysics, 10, 76

—. 1972, Astronomy and Astrophysics, 19, 51

—. 1973, Publications of the Astronomical Society of the Pacific, 85, 679

Burton, W. B., Gordon, M. A., Bania, T. M., & Lockman, F. J. 1975, The Astrophysical Journal, 202, 30

Caswell, J. L., & Haynes, R. F. 1987, Astronomy and Astrophysics, 171, 261

Cheng, J. Y., Rockosi, C. M., Morrison, H. L., et al. 2012, The Astrophysical Journal, 746, 149

Chiappini, C., Romano, D., & Matteucci, F. 2003, Monthly Notices of the Royal Astronomical Society, 339, 63

Choi, Y. K., Hachisuka, K., Reid, M. J., et al. 2014, The Astrophysical Journal, 790, 99

Choi, Y. K., Hirota, T., Honma, M., et al. 2008, Publications of the Astronomical Society of Japan, 60, 1007

Christiansen, W. N., & Hindman, J. V. 1952a, The Observatory, 72, 149

—. 1952b, Australian Journal of Scientific Research A Physical Sciences, 5, 437

Churchwell, E., & Walmsley, C. M. 1975, Astronomy and Astrophysics, 38, 451

Condon, J. J., Cotton, W. D., Greisen, E. W., et al. 1998, The Astronomical Journal, 115, 1693

Conselice, C. J. 2014, Annual Review of Astronomy and Astrophysics, 52, 291

Cox, D. P. 2005, Annual Review of Astronomy and Astrophysics, 43, 337

Dame, T. M., Elmegreen, B. G., Cohen, R. S., & Thaddeus, P. 1986, The Astrophysical Journal, 305, 892

Dame, T. M., Hartmann, D., & Thaddeus, P. 2001, The Astrophysical Journal, 547, 792

Dame, T. M., & Thaddeus, P. 2008, The Astrophysical Journal, 683, L143

—. 2011, The Astrophysical Journal Letters, 734, L24

Davis, B. L., Berrier, J. C., Shields, D. W., et al. 2012, The Astrophysical Journal Supplement Series, 199, 33

de Sitter, W. 1934, Kosmos (van Stockum & Zoon, Den Haag)

Di Matteo, P., Haywood, M., Combes, F., Semelin, B., & Snaith, O. N. 2013, Astronomy and Astrophysics, 553, A102

Dickey, J. M., & Lockman, F. J. 1990, Annual Review of Astronomy and Astrophysics, 28, 215

Diplas, A., & Savage, B. D. 1991, The Astrophysical Journal, 377, 126

Dobbs, C., & Baba, J. 2014, Publications of the Astronomical Society of Australia, 31, e035

Downes, D., Wilson, T. L., Bieging, J., & Wink, J. 1980, Astronomy and Astrophysics Supplement Series, 40, 379

Easton, C. 1900, The Astrophysical Journal, 12, 136

Ewen, H. I., & Purcell, E. M. 1951, Nature, 168, 356

Feigelson, E. D., & Babu, G. J. 2012, Modern Statistical Methods for Astronomy (Cambridge University Press)

Foreman-Mackey, D. 2016, The Journal of Open Source Software, 24, doi:10.21105/joss.00024

Foreman-Mackey, D., Hogg, D. W., Lang, D., & Goodman, J. 2013, Publications of the Astronomical Society of the Pacific, 125, 306

Friel, E. D., Janes, K. A., Tavarez, M., et al. 2002, The Astronomical Journal, 124, 2693

Gaia Collaboration, Katz, D., Antoja, T., et al. 2018, Astronomy and Astrophysics, 616, A11

Galilei, G. 1610, Sidereus Nuncius (Thomas Baglioni)

García, P., Bronfman, L., Nyman, L.-Å., Dame, T. M., & Luna, A. 2014, The Astrophysical Journal Supplement Series, 212, 2

Georgelin, Y. M., & Georgelin, Y. P. 1976, Astronomy and Astrophysics, 49, 57

Gingerich, O. 1985, in IAU Symposium, Vol. 106, The Milky Way Galaxy, ed. H. van Woerden, R. J. Allen, & W. B. Burton, 59–70

Gómez, G. C. 2006, The Astronomical Journal, 132, 2376

Goodman, J., & Weare, J. 2010, Communications in Applied Mathematics and Computational Science, 5, 65

Grand, R. J. J., Kawata, D., & Cropper, M. 2014, Monthly Notices of the Royal Astronomical Society, 439, 623

Grand, R. J. J., Springel, V., Kawata, D., et al. 2016, Monthly Notices of the Royal Astronomical Society, 460, L94

Gum, C. S. 1955, Memoirs of the Royal Astronomical Society, 67, 155

Hachisuka, K., Brunthaler, A., Menten, K. M., et al. 2009, The Astrophysical Journal, 696, 1981

Hachisuka, K., Choi, Y. K., Reid, M. J., et al. 2015, The Astrophysical Journal, 800, 2

Hachisuka, K., Brunthaler, A., Menten, K. M., et al. 2006, The Astrophysical Journal, 645, 337

Haffner, L. M., Reynolds, R. J., & Tufte, S. L. 1999, The Astrophysical Journal, 523, 223

Hartmann, D., & Burton, W. B. 1997, Atlas of Galactic Neutral Hydrogen (Cambridge: Cambridge University Press), 243

Hayden, M. R., Holtzman, J. A., Bovy, J., et al. 2014, The Astronomical Journal, 147, 116

Hayden, M. R., Bovy, J., Holtzman, J. A., et al. 2015, The Astrophysical Journal, 808, 132

Helfand, D. J., Becker, R. H., White, R. L., Fallon, A., & Tuttle, S. 2006, The Astronomical Journal, 131, 2525

Herschel, W. 1785, Philosophical Transactions of the Royal Society of London Series I, 75, 213

Heyer, M., & Dame, T. M. 2015, Annual Review of Astronomy and Astrophysics, 53, 583

HI4PI Collaboration, Ben Bekhti, N., Flöer, L., et al. 2016, Astronomy and Astrophysics, 594, A116

Hirota, T., Ando, K., Bushimata, T., et al. 2008, Publications of the Astronomical Society of Japan, 60, 961

Ho, I.-T., Seibert, M., Meidt, S. E., et al. 2017, The Astrophysical Journal, 846, 39

Hoglund, B., & Mezger, P. G. 1965a, Sci., 150, 339

—. 1965b, The Astronomical Journal, 70, 678

Honma, M., Bushimata, T., Choi, Y. K., et al. 2007, Publications of the Astronomical Society of Japan, 59, 889

Hou, L. G., & Han, J. L. 2014, Astronomy and Astrophysics, 569, A125

Hubble, E. P. 1925, Popular Astronomy, 33

Immer, K., Reid, M. J., Menten, K. M., Brunthaler, A., & Dame, T. M. 2013, Astronomy and Astrophysics, 553, A117

Jansky, K. G. 1933, Nature, 132, 66

Jones, M. C. 1993, Statistics and Computing, 3, 135

Kalberla, P. M. W., Burton, W. B., Hartmann, D., et al. 2005, Astronomy and Astrophysics, 440, 775

Kalberla, P. M. W., & Dedes, L. 2008, Astronomy and Astrophysics, 487, 951

Kalberla, P. M. W., Dedes, L., Kerp, J., & Haud, U. 2007, Astronomy and Astrophysics, 469, 511

Kalberla, P. M. W., & Haud, U. 2015, Astronomy and Astrophysics, 578, A78

Kalberla, P. M. W., & Kerp, J. 2009, Annual Review of Astronomy and Astrophysics, 47, 27

Kalberla, P. M. W., McClure-Griffiths, N. M., Pisano, D. J., et al. 2010, Astronomy and Astrophysics, 521, A17

Kant, I. 1755, Universal Natural History and Theory of the Heavens (Scottish Academic Press)

Kapteyn, J. C. 1922, The Astrophysical Journal, 55, 302

Kardashev, N. S. 1959, Soviet Astronomy, 3, 813

Kerp, J., Winkel, B., Ben Bekhti, N., Flöer, L., & Kalberla, P. M. W. 2011, Astronomische Nachrichten, 332, 637

Kerr, F. J., & Lynden-Bell, D. 1986, Monthly Notices of the Royal Astronomical Society, 221, 1023

Kim, M. K., Hirota, T., Honma, M., et al. 2008, Publications of the Astronomical Society of Japan, 60, 991

King, H. 2003, The History of the Telescope, Dover Books on Astronomy Series (Dover Publications)

Kolpak, M. A., Jackson, J. M., Bania, T. M., Clemens, D. P., & Dickey, J. M. 2003, The Astrophysical Journal, 582, 756

Koo, B.-C., Park, G., Kim, W.-T., et al. 2017, Publications of the Astronomical Society of the Pacific, 129, 094102

Kovalevsky, J. 1998, Astronomy and Astrophysics, 340, L35

Kuchar, T. A., & Bania, T. M. 1994, The Astrophysical Journal, 436, 117

Kurayama, T., Nakagawa, A., Sawada-Satoh, S., et al. 2011, Publications of the Astronomical Society of Japan, 63, 513

Leavitt, H. S. 1908, Annals of Harvard College Observatory, 60, 87

Lenz, D. D., & Ayres, T. R. 1992, Publications of the Astronomical Society of the Pacific, 104, 1104

Leroy, A. K., Walter, F., Brinks, E., et al. 2008, The Astronomical Journal, 136, 2782

Levine, E. S., Blitz, L., & Heiles, C. 2006, The Astrophysical Journal, 643, 881

Lin, C. C., & Shu, F. H. 1964, The Astrophysical Journal, 140, 646

Lindblad, B. 1925, Arkiv for Matematik, Astronomi och Fysik, 19A, 21

—. 1926, Arkiv for Matematik, Astronomi och Fysik, 19B, 7

Lockman, F. J. 1989, The Astrophysical Journal Supplement Series, 71, 469

Lockman, F. J., & Brown, R. L. 1975, The Astrophysical Journal, 201, 134

Lockman, F. J., Pisano, D. J., & Howard, G. J. 1996, The Astrophysical Journal, 472, 173

Luck, R. E., Kovtyukh, V. V., & Andrievsky, S. M. 2006, The Astronomical Journal, 132, 902

Luisi, M., Anderson, L. D., Balser, D. S., Wenger, T. V., & Bania, T. M. 2017, The Astrophysical Journal, 849, 117

Majewski, S. R., APOGEE Team, & APOGEE-2 Team. 2016, Astronomische Nachrichten, 337, 863

Mauch, T., Murphy, T., Buttery, H. J., et al. 2003, Monthly Notices of the Royal Astronomical Society, 342, 1117

McClure-Griffiths, N. M., & Dickey, J. M. 2007, The Astrophysical Journal, 671, 427

McClure-Griffiths, N. M., Dickey, J. M., Gaensler, B. M., et al. 2005, The Astrophysical Journal Supplement Series, 158, 178

McClure-Griffiths, N. M., Pisano, D. J., Calabretta, M. R., et al. 2009, The Astrophysical Journal Supplement Series, 181, 398

McKee, C. F., & Williams, J. P. 1997, The Astrophysical Journal, 476, 144

McMullin, J. P., Waters, B., Schiebel, D., Young, W., & Golap, K. 2007, in ASPC, Vol. 376, Astronomical Data Analysis Software and Systems XVI, ed. R. A. Shaw, F. Hill, & D. J. Bell, 127

Menten, K. M., Reid, M. J., Forbrich, J., & Brunthaler, A. 2007, Astronomy and Astrophysics, 474, 515

Menzel, D. H. 1968, Nature, 218, 756

Mezger, P. G., & Henderson, A. P. 1967, The Astrophysical Journal, 147, 471

Mezger, P. G., & Hoglund, B. 1967, The Astrophysical Journal, 147, 490

Minchev, I., Chiappini, C., & Martig, M. 2013, Astronomy and Astrophysics, 558, A9

—. 2014, Astronomy and Astrophysics, 572, A92

Minchev, I., Anders, F., Recio-Blanco, A., et al. 2018, Monthly Notices of the Royal Astronomical Society, 481, 1645

Moellenbrock, G. A., Claussen, M. J., & Goss, W. M. 2009, The Astrophysical Journal, 694, 192

Moisés, A. P., Damineli, A., Figuerêdo, E., et al. 2011, Monthly Notices of the Royal Astronomical Society, 411, 705

Mollá, M., Díaz, Á. I., Cavichia, O., et al. 2019, Monthly Notices of the Royal Astronomical Society, 482, 3071

Morgan, W. W., Sharpless, S., & Osterbrock, D. 1952, The Astronomical Journal, 57, 3

Moscadelli, L., Cesaroni, R., Rioja, M. J., Dodson, R., & Reid, M. J. 2011, Astronomy and Astrophysics, 526, A66

Moscadelli, L., Reid, M. J., Menten, K. M., et al. 2009, The Astrophysical Journal, 693, 406

Muller, C. A., & Oort, J. H. 1951, Nature, 168, 357

Nagayama, T., Omodaka, T., Nakagawa, A., et al. 2011, Publications of the Astronomical Society of Japan, 63, 23

Nidever, D. L., Bovy, J., Bird, J. C., et al. 2014, The Astrophysical Journal, 796, 38

Oh, C. S., Kobayashi, H., Honma, M., et al. 2010, Publications of the Astronomical Society of Japan, 62, 101

Oort, J. H. 1922, Bulletin of the Astronomical Institutes of the Netherlands, 1, 133

—. 1927, Bulletin of the Astronomical Institutes of the Netherlands, 3, 275

Oort, J. H., Kerr, F. J., & Westerhout, G. 1958, Monthly Notices of the Royal Astronomical Society, 118, 379

Oster, L. 1961, The Astronomical Journal, 66, 50

Pawsey, J. L. 1951, Nature, 168, 358

Persic, M., Salucci, P., & Stel, F. 1996, Monthly Notices of the Royal Astronomical Society, 281, 27

Poggio, E., Drimmel, R., Lattanzi, M. G., et al. 2018, Monthly Notices of the Royal Astronomical Society, 481, L21

Proctor, R. A. 1869, Monthly Notices of the Royal Astronomical Society, 30, 50

Quireza, C., Rood, R. T., Balser, D. S., & Bania, T. M. 2006a, The Astrophysical Journal Supplement Series, 165, 338

Quireza, C., Rood, R. T., Bania, T. M., Balser, D. S., & Maciel, W. J. 2006b, The Astrophysical Journal, 653, 1226

Reid, M. J., & Dame, T. M. 2016, The Astrophysical Journal, 832, 159

Reid, M. J., Dame, T. M., Menten, K. M., & Brunthaler, A. 2016, The Astrophysical Journal, 823, 77

Reid, M. J., & Honma, M. 2014, Annual Review of Astronomy and Astrophysics, 52, 339

Reid, M. J., Menten, K. M., Brunthaler, A., et al. 2009a, The Astrophysical Journal, 693, 397

Reid, M. J., Menten, K. M., Zheng, X. W., Brunthaler, A., & Xu, Y. 2009b, The Astrophysical Journal, 705, 1548

Reid, M. J., Menten, K. M., Zheng, X. W., et al. 2009c, The Astrophysical Journal, 700, 137

Reid, M. J., Menten, K. M., Brunthaler, A., et al. 2014, The Astrophysical Journal, 783, 130

Reifenstein, E. C., Wilson, T. L., Burke, B. F., Mezger, P. G., & Altenhoff, W. J. 1970, Astronomy and Astrophysics, 4, 357

Rodgers, A. W., Campbell, C. T., & Whiteoak, J. B. 1960, Monthly Notices of the Royal Astronomical Society, 121, 103

Roman-Duval, J., Jackson, J. M., Heyer, M., et al. 2009, The Astrophysical Journal, 699, 1153

Rosse, F. E. o., & Parsons, L. 1880, Scientific Transactions of the Royal Dublin Society, 2, 1

Rosse, T. E. O. 1850, Philosophical Transactions of the Royal Society of London Series I, 140, 499

Rygl, K. L. J., Brunthaler, A., Reid, M. J., et al. 2010, Astronomy and Astrophysics, 511, A2

Rygl, K. L. J., Brunthaler, A., Sanna, A., et al. 2012, Astronomy and Astrophysics, 539, A79

Sandstrom, K. M., Peek, J. E. G., Bower, G. C., Bolatto, A. D., & Plambeck, R. L. 2007, The Astrophysical Journal, 667, 1161

Sanna, A., Reid, M. J., Dame, T. M., et al. 2012, The Astrophysical Journal, 745, 82

Sanna, A., Reid, M. J., Menten, K. M., et al. 2014, The Astrophysical Journal, 781, 108

Sato, M., Reid, M. J., Brunthaler, A., & Menten, K. M. 2010, The Astrophysical Journal, 720, 1055

Sato, M., Hirota, T., Honma, M., et al. 2008, Publications of the Astronomical Society of Japan, 60, 975

Sato, M., Wu, Y. W., Immer, K., et al. 2014, The Astrophysical Journal, 793, 72

Schmidt, M. 1957, Bulletin of the Astronomical Institutes of the Netherlands, 13, 247

Searle, L. 1971, The Astrophysical Journal, 168, 327

Seigar, M. S., & James, P. A. 1998, Monthly Notices of the Royal Astronomical Society, 299, 685

Sellwood, J. A., & Binney, J. J. 2002, Monthly Notices of the Royal Astronomical Society, 336, 785

Sellwood, J. A., & Carlberg, R. G. 1984, The Astrophysical Journal, 282, 61

Sewilo, M., Watson, C., Araya, E., et al. 2004, The Astrophysical Journal Supplement Series, 154, 553

Shapley, H. 1918, The Astrophysical Journal, 48, doi:10.1086/142423

Sharpless, S. 1953, The Astrophysical Journal, 118, 362

—. 1959, The Astrophysical Journal Supplement Series, 4, 257

Shaver, P. A., McGee, R. X., Newton, L. M., Danks, A. C., & Pottasch, S. R. 1983, Monthly Notices of the Royal Astronomical Society, 204, 53

Shu, F. H. 2016, Annual Review of Astronomy and Astrophysics, 54, 667

Smith, T. R., & Kennicutt, Jr., R. C. 1989, Publications of the Astronomical Society of the Pacific, 101, 649

Snaith, O., Haywood, M., Di Matteo, P., et al. 2015, Astronomy and Astrophysics, 578, A87

Spitzer, Jr., L. 1956, The Astrophysical Journal, 124, 20

Stanghellini, L., & Haywood, M. 2010, The Astrophysical Journal, 714, 1096

Stil, J. M., Taylor, A. R., Dickey, J. M., et al. 2006, The Astronomical Journal, 132, 1158

Strömgren, B. 1948, The Astrophysical Journal, 108, 242

Struve, O. 1953, Leaflets of the Astronomical Society of the Pacific, 285

Su, Y., Yang, J., Zhang, S., et al. 2019, The Astrophysical Journal Supplement Series, 240, 9

Taylor, A. R., Gibson, S. J., Peracaula, M., et al. 2003, The Astronomical Journal, 125, 3145

Urquhart, J. S., Hoare, M. G., Lumsden, S. L., et al. 2012, Monthly Notices of the Royal Astronomical Society, 420, 1656

van de Hulst, H. C. 1945, Ned. Tijd. Natuurkunde, 11, 120

van de Hulst, H. C., Muller, C. A., & Oort, J. H. 1954, Bulletin of the Astronomical Institutes of the Netherlands, 12, 117

Voskes, T., & Butler Burton, W. 2006, arXiv Astrophysics e-prints, astro-ph/0601653

Wang, J., Fu, J., Aumer, M., et al. 2014, Monthly Notices of the Royal Astronomical Society, 441, 2159

Watson, C., Araya, E., Sewilo, M., et al. 2003, The Astrophysical Journal, 587, 714

Wenger, T. 2018, Astrophysics Source Code Library, ascl:1812.001

Wenger, T., Balser, D., Anderson, L., & Bania, T. 2017, Astrophysics Source Code Library, ascl:1712.001

Wenger, T. V., Balser, D. S., Anderson, L. D., & Bania, T. M. 2018a, The Astrophysical Journal, 856, 52

Wenger, T. V., Bania, T. M., Balser, D. S., & Anderson, L. D. 2013, The Astrophysical Journal, 764, 34

Wenger, T. V., Khan, A. A., Ferraro, N. G., et al. 2018b, The Astrophysical Journal, 852, 2

Wenger, T. V., Dickey, J. M., Jordan, C. H., et al. 2019, The Astrophysical Journal Supplement Series, 240, 24

Westerhout, G. 1957, Bulletin of the Astronomical Institutes of the Netherlands, 13, 201

Wieringa, M. H., & Kesteven, M. J. 1992, Measurements of the ATCA primary beam, ATNF Technical Memo 39.2/010, Australia Telescope National Facility

Wilson, R. W., Jefferts, K. B., & Penzias, A. A. 1970a, The Astrophysical Journal Letters, 161, L43

Wilson, T. L., Mezger, P. G., Gardner, F. F., & Milne, D. K. 1970b, Astronomy and Astrophysics, 6, 364

Winkel, B., Kerp, J., Flöer, L., et al. 2016, Astronomy and Astrophysics, 585, A41

Wolfire, M. G., McKee, C. F., Hollenbach, D., & Tielens, A. G. G. M. 2003, The Astrophysical Journal, 587, 278

Wouterloot, J. G. A., Brand, J., Burton, W. B., & Kwee, K. K. 1990, Astronomy and Astrophysics, 230, 21

Wright, E. L., Eisenhardt, P. R. M., Mainzer, A. K., et al. 2010, The Astronomical Journal, 140, 1868

Wright, T. 1750, An Original Theory Or New Hypothesis of the Universo, Founded Upon the Laws of Nature, and Solving by Mathematical Principles the General Phaenomena of the Visible Creation and Particularly the Via Lactea (Chapelle)

Wu, Y. W., Xu, Y., Menten, K. M., Zheng, X. W., & Reid, M. J. 2012, in IAU Symposium, Vol. 287, Cosmic Masers - from OH to H0, ed. R. S. Booth, W. H. T. Vlemmings, & E. M. L. Humphreys, 425–426

Wu, Y. W., Sato, M., Reid, M. J., et al. 2014, Astronomy and Astrophysics, 566, A17

Xu, Y., Moscadelli, L., Reid, M. J., et al. 2011, The Astrophysical Journal, 733, 25

Xu, Y., Reid, M. J., Menten, K. M., et al. 2009, The Astrophysical Journal, 693, 413

Xu, Y., Reid, M. J., Zheng, X. W., & Menten, K. M. 2006, Science, 311, 54

Xu, Y., Li, J. J., Reid, M. J., et al. 2013, The Astrophysical Journal, 769, 15

Young, J. S., & Scoville, N. Z. 1991, Annual Review of Astronomy and Astrophysics, 29, 581

Zhang, B., Reid, M. J., Menten, K. M., & Zheng, X. W. 2012a, The Astrophysical Journal, 744, 23

Zhang, B., Reid, M. J., Menten, K. M., Zheng, X. W., & Brunthaler, A. 2012b, Astronomy and Astrophysics, 544, A42

Zhang, B., Reid, M. J., Menten, K. M., et al. 2013, The Astrophysical Journal, 775, 79

Zhang, B., Zheng, X. W., Reid, M. J., et al. 2009, The Astrophysical Journal, 693, 419

Zhang, B., Moscadelli, L., Sato, M., et al. 2014, The Astrophysical Journal, 781, 89

Biographical Sketch

Trey Vaughn Wenger was born 3 May 1991 in Indianapolis, Indiana to Koral L. Frost and Dennis S. Wenger. He graduated from Northrop High School in Fort Wayne, Indiana in 2009, and subsequently enrolled in the physics and astronomy program at Boston University (BU). At BU, Trey worked with Professor Teresea Brainerd on topics related to cosmology before beginning a summer student research program at the Arecibo Observatory. Dr. Tapasi Ghosh and Dr. Chris Salter mentored Trey for the 10-week program, during which Trey discovered his passion for radio astronomy. Upon his return to BU, Trey began working with Professor Thomas Bania on topics related to H II regions and Galactic structure, thus setting the foundation for this dissertation. Following another summer student research program at the National Radio Astronomy Observatory in Charlottesville, Virginia, mentored by his now doctoral advisor, Dr. Dana S. Balser, Trey graduated *summa cum laude* from BU in May 2013.

Enchanted by the Virginia scenery and research opportunities in Charlottesville, Trey enrolled in the astronomy Ph.D. program at the University of Virginia (UVA) as the D. N. Batten Foundation Jefferson Fellow. Among his many extracurricular activities at UVA, he was a volunteer with *Dark Skies, Bright Kids*, an outreach program designed to bolster scientific interest and literacy in rural Virginia elementary schools, he was president of the Raven Society, the oldest and most prestigious honor and philanthropic society at UVA, and he was the founder of Astronomy on Tap C'ville, a community engagement program that brings astronomy to the public at local bars and restaurants. Trey graduated with his Ph.D. in May 2019 before moving to the frigid north as the Covington Fellow at the National Research Council of Canada Dominion Radio Astrophysical Observatory.

Trey V. Wenger at the Leander McCormick Observatory in Charlottesville, Virginia.

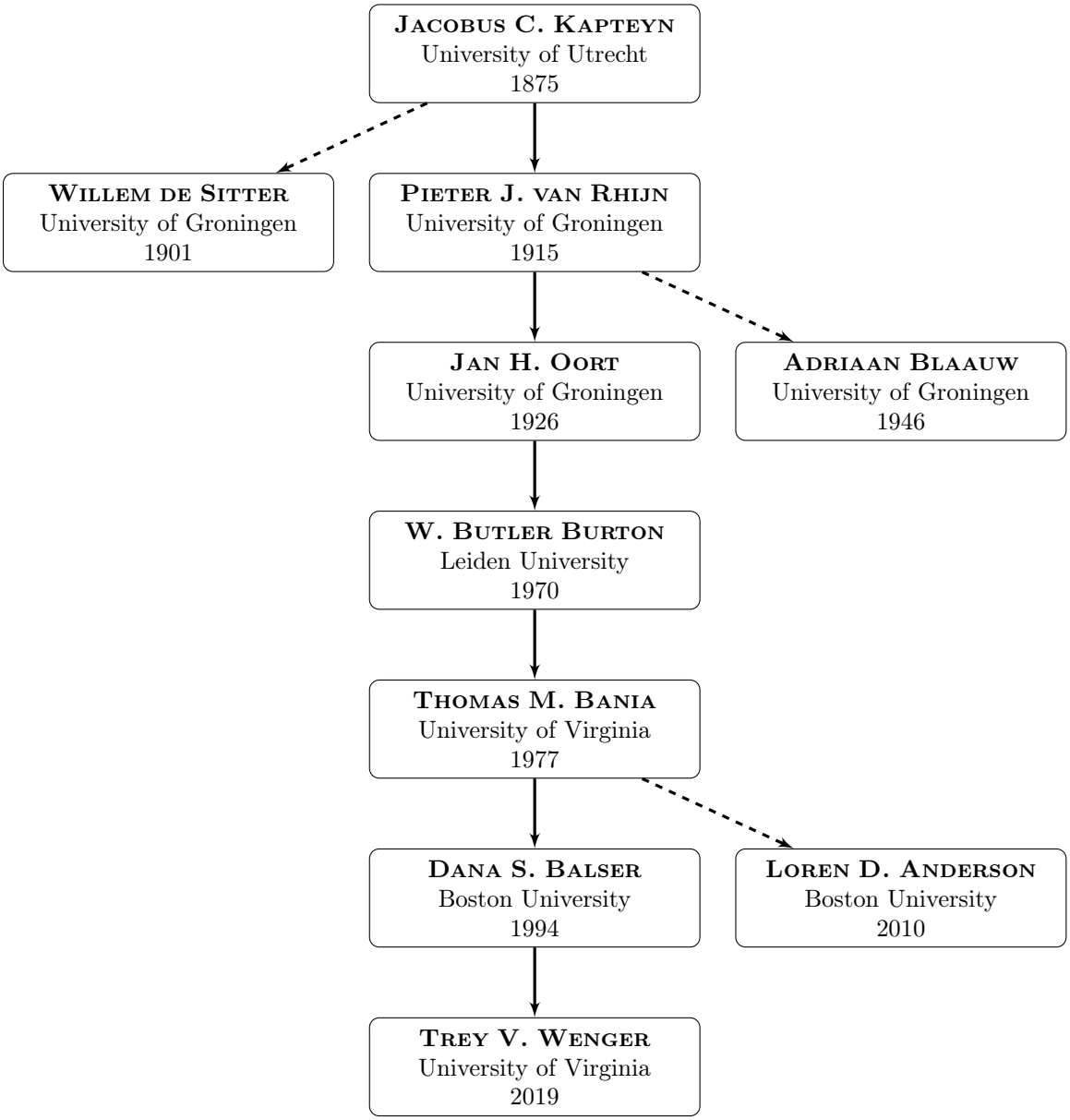

The Wenger academic family tree, which spans seven generations and nearly 150 years of Galactic structure astronomers.

Curriculum Vitae

Personal:

Name:	Trey V. Wenger
Address:	Department of Astronomy, University of Virginia 530 McCormick Road, Charlottesville, VA, USA
Email:	`tvw2pu@virginia.edu`
Website:	`www.treywenger.com`

Education:	Ph.D., Astronomy, University of Virginia (2015 – 2019) M.S., Astronomy, University of Virginia (2013 – 2015) B.A., Astronomy and Physics, Boston University (2009 – 2013)
Dissertation:	"Structure in the Milky Way"
Advisor:	Dr. Dana S. Balser, National Radio Astronomy Observatory
Research Areas:	Milky Way structure; interstellar medium; H II regions; high-mass star formation; galaxy formation and evolution; radio recombination lines

Employment:

Research Fellow, University of Virginia, 2013 – 2019
Advisor: Dr. Dana S. Balser, National Radio Astronomy Observatory
Teaching Assistant, University of Virginia, 2014 – 2016
Instructor, University of Virginia, 2014
Research Assistant, Boston University, 2012 – 2013
Advisor: Prof. Thomas M. Bania, Boston University
REU Student, National Radio Astronomy Observatory, 2012
Advisor: Dr. Dana S. Balser, National Radio Astronomy Observatory
REU Student, Arecibo Observatory, 2011
Advisors: Dr. Tapasi Ghosh and Dr. Chris Salter, Arecibo Observatory
Assistant Curator, J. B. Coit Observatory, 2010 – 2013

Research Grants:

Graduate Research Fellowship, Virginia Space Grant Consortium, 2017 – 2018
Grote Reber Doctoral Fellowship, National Radio Astronomy Observatory, 2016 – 2018
Raven Fellowship, Raven Society, University of Virginia, 2016
Graduate Research Fellowship, Virginia Space Grant Consortium, 2016 – 2017
ARCS Scholarship, Achievement Rewards for College Scientists, 2016 – 2017
D. N. Batten Foundation Jefferson Fellowship, Jefferson Scholars Foundation, 2013 – 2019
Undergraduate Research Outreach Program Award, Boston University, 2012 – 2013
NSF Research Experiences for Undergraduates, National Radio Astronomy Observatory, 2012
NSF Research Experiences for Undergraduates, Arecibo Observatory, 2011

Honors & Awards:

Raven Award, Raven Society, University of Virginia, 2019
Chambliss Astronomy Achievement Award, American Astronomical Society, 2018
Laurence W. Fredrick Teaching Award, University of Virginia, 2016
First Place Award and Scholarship, Huskey Research Exhibition, University of Virginia, 2015
Inductee, Raven Society, University of Virginia, 2015
Second Place Award and Scholarship, Huskey Research Exhibition, University of Virginia, 2014
College Prize in Astronomy, Boston University, 2013
Institute for Astrophysical Research Prize, Boston University, 2013

Professional Society Memberships:

Junior Fellow, Society of Fellows, University of Virginia, 2018 – 2019
Member, Raven Society, University of Virginia, 2015 – Present
Member, Phi Beta Kappa, Epsilon Chapter of Massachusetts, 2013 – Present
Junior/Graduate Student Member, American Astronomical Society, 2011 – Present
Member, Boston University Astronomical Society, 2009 – 2013

Research Mentoring Experience:

Maryam Hami, National Radio Astronomy Observatory, 2018
Wesley Red, National Radio Astronomy Observatory, 2017
Jeanine Shea, National Radio Astronomy Observatory, 2016
Nicholas Ferraro, University of Virginia, 2015 – 2018
Asad Khan, University of Virginia, 2015 – 2018

Jonathan Barnes, National Radio Astronomy Observatory, 2015

Outreach & Service:

Founder & Lead Organizer, Astronomy on Tap C'ville, 2018 – 2019
Organizer, Bob Rood Memorial Symposium, University of Virginia, 2018
President, Raven Society, University of Virginia, 2017 – 2018
Chair, Gray-Carrington Memorial Fellowship Committee, University of Virginia, 2017
Member, Astronomy Graduate Admissions Committee, University of Virginia, 2017
Organizer, Bob Rood Memorial Symposium, University of Virginia, 2017
Member, Raven Society Leadership Council, University of Virginia, 2016 – 2019
Volunteer Speaker, Charlottesville Astronomical Society, 2016
Organizer, Forum for Interdisciplinary Dialogue Research Symposium, University of Virginia, 2015
Co-founder, Astronomy Undergraduate Mentorship Program, University of Virginia, 2013 – 2019
Volunteer Webmaster, Astronomy Department, University of Virginia, 2013 – 2019
Volunteer, *Dark Skies, Bright Kids*, University of Virginia, 2013 – 2019
President, Boston University Astronomical Society, 2010 – 2012

Refereed Publications

C. D. Weins, T. V. Wenger, K. E. Johnson, L. Xiao, S. C. Gallagher, and P. Tzanavaris. The Occurance of Compact Groups of Galaxies Through Cosmic Time. Astrophysical Journal, in press.

T. V. Wenger, J. M. Dickey, C. H. Jordan, D. S. Balser, W. P. Armentrout, L. D. Anderson, T. M. Bania, J. R. Dawson, N. M. McClure-Griffiths, and J. Shea. The Southern H II Region Discovery Survey. I. The Bright Catalog. Astrophysical Journal Supplement Series, 240:24, February 2019.

L. D. Anderson, T. V. Wenger, W. P. Armentrout, D. S. Balser, and T. M. Bania. A Galactic Plane Defined by the Milky Way H II Region Distribution. Astrophysical Journal, 871:145, February 2019.

D. M. Maffucci, T. V. Wenger, R. Le Gal, and E. Herbst. Astrochemical Kinetic Grid Models of Groups of Observed Molecular Abundances: Taurus Molecular Cloud 1 (TMC-1). Astrophysical Journal, 868:41, November 2018.

M. Luisi, L. D. Anderson, T. M. Bania, D. S. Balser, T. V. Wenger, and A. A. Kepley. Hydrogen Radio Recombination Line Emission from M51 and NGC 628. Publications of the Astronomical Society of the Pacific, 130(8):084101, August 2018.

T. V. Wenger, D. S. Balser, L. D. Anderson, and T. M. Bania. Kinematic Distances: A Monte Carlo Method. Astrophysical Journal, 856:52, March 2018.

L. D. Anderson, W. P. Armentrout, M. Luisi, T. M. Bania, D. S. Balser, and T. V. Wenger. A Green Bank Telescope Survey of Large Galactic H II Regions. Astrophysical Journal Supplement Series, 234:33, February 2018.

T. V. Wenger, A. A. Khan, N. G. Ferraro, D. S. Balser, W. P. Armentrout, L. D. Anderson, and T. M. Bania. Carbon Monoxide Observations toward Star-forming Regions in the Outer Scutum- Centaurus Spiral Arm. Astrophysical Journal, 852:2, January 2018.

M. Luisi, L. D. Anderson, D. S. Balser, T. V. Wenger, and T. M. Bania. Diffuse Ionized Gas in the Milky Way Disk. Astrophysical Journal, 849:117, November 2017.

B.-C. Koo, G. Park, W.-T. Kim, M. G. Lee, D. S. Balser, and T. V. Wenger. Tracing the Spiral Structure of the Outer Milky Way with Dense Atomic Hydrogen Gas. Publications of the Astronomical Society of the Pacific, 129(9):094102, September 2017.

D. S. Balser, T. V. Wenger, W. M. Goss, K. E. Johnson, and A. A. Kepley. JVLA Observations of IC 342: Probing Star Formation in the Nucleus. Astrophysical Journal, 844:73, July 2017.

C. Brown, C. Jordan, J. M. Dickey, L. D. Anderson, W. P. Armentrout, D. S. Balser, T. M. Bania, J. R. Dawson, N. M. McClure-Griffiths, and T. V. Wenger. The Southern H II Region Discovery Survey (SHRDS): Pilot Survey. Astronomical Journal, 154:23, July 2017.

W. P. Armentrout, L. D. Anderson, D. S. Balser, T. M. Bania, T. M. Dame, and T. V. Wenger. High-mass Star Formation in the Outer Scutum-Centaurus Arm. Astrophysical Journal, 841:121, June 2017.

M. Luisi, L. D. Anderson, D. S. Balser, T. M. Bania, and T. V. Wenger. H II Region Ionization of the Interstellar Medium: A Case Study of NGC 7538. Astrophysical Journal, 824:125, June 2016.

L. D. Anderson, W. P. Armentrout, B. M. Johnstone, T. M. Bania, D. S. Balser, T. V. Wenger, and V. Cunningham. Finding Distant Galactic HII Regions. Astrophysical Journal Supplement Series, 221:26, December 2015.

L. D. Anderson, L. A. Hough, T. V. Wenger, T. M. Bania, and D. S. Balser. Untangling the Recombination Line Emission from H II Regions with Multiple Velocity Components. Astrophysical Journal, 810:42, September 2015.

D. S. Balser, T. V. Wenger, L. D. Anderson, and T. M. Bania. Azimuthal Metallicity Structure in the Milky Way Disk. Astrophysical Journal, 806:199, June 2015.

L. D. Anderson, T. M. Bania, D. S. Balser, V. Cunningham, T. V. Wenger, B. M. Johnstone, and W. P. Armentrout. The WISE Catalog of Galactic H II Regions. Astrophysical Journal Supplement Series, 212:1, May 2014.

T. V. Wenger, T. M. Bania, D. S. Balser, and L. D. Anderson. The Green Bank Telescope H II Region Discovery Survey. IV. Helium and Carbon Recombination Lines. Astrophysical Journal, 764:34, February 2013.

Other Publications

D. S. Balser, L. D. Anderson, T. M. Bania, J. M. Dickey, D. Anish Roshi, T. V. Wenger, and T. L. Wilson. Science with an ngVLA: Radio Recombination Lines from HII Regions. Science with a Next-Generation VLA, October 2018.

Published Software

T. V. Wenger. WISP: Wenger Interferometry Software Package. Astrophysics Source Code Library, December 2018.

T. Wenger and C. Wiens. MillCgs: Searching for Compact Groups in the Millennium Simulation. Astrophysics Source Code Library, November 2018.

T. V. Wenger, D. S. Balser, L. D. Anderson, and T. M. Bania. KDUtils: Kinematic Distance Utilities. Astrophysics Source Code Library, December 2017.

T. V. Wenger, A. K. Kepley, and D. S. Balser. HRM: H II Region Models. Astrophysics Source Code Library, July 2017.

T. Bania, T. Wenger, D. Balser, and L. Anderson. TMBIDL: Single dish radio astronomy data reduction package. Astrophysics Source Code Library, May 2016.

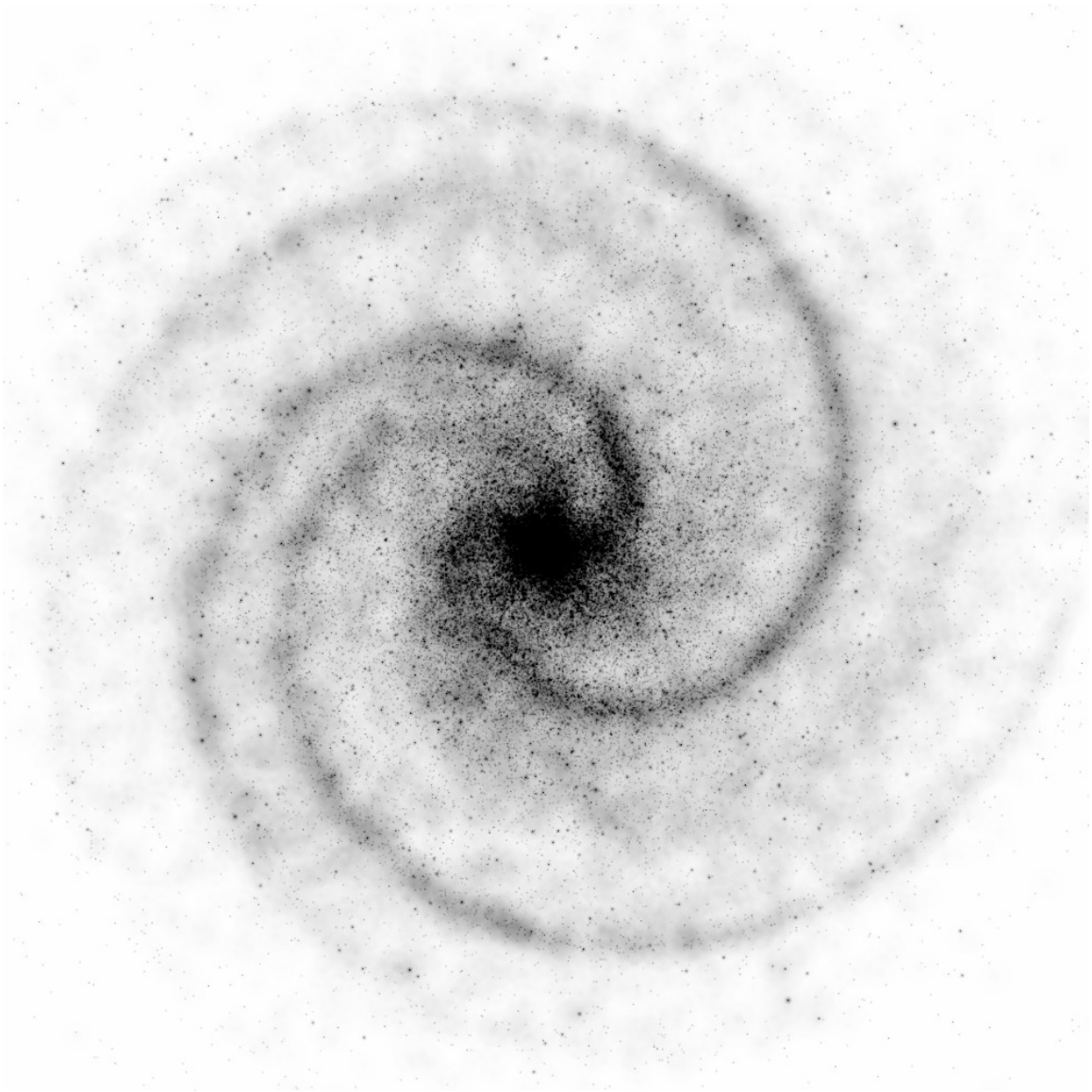

The flip book at the bottom of each page is a
simulation of spiral density waves in a four-armed spiral galaxy.
The simulation code is by Ingo Berg (`http://beltoforion.de`)
and available under a Creative Commons Attribution 4.0 license.